frontiers | Research Topics

Studying the immune microenvironment of liver cancer using artificial intelligence

Edited by
Dake Zhang, Jieliang Chen and Bing Yang

Published in
Frontiers in Immunology
Frontiers in Oncology

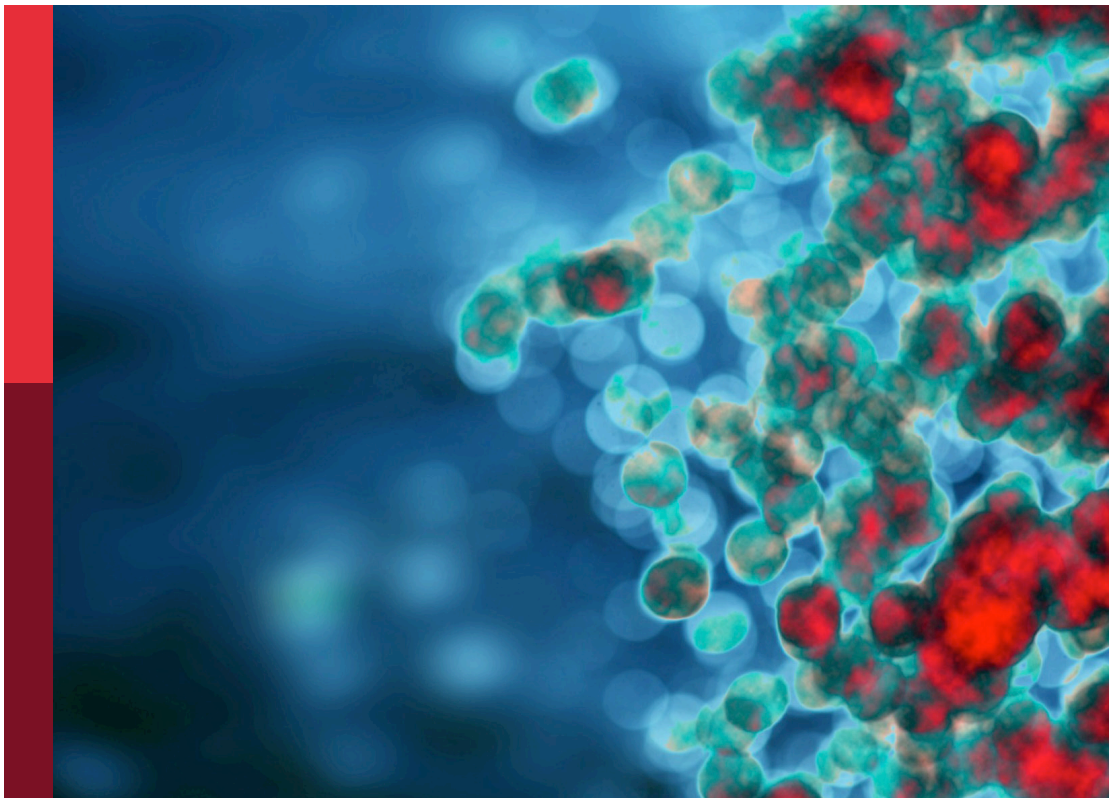

ISSN 1664-8714
ISBN 978-2-8325-6822-4
DOI 10.3389/978-2-8325-6822-4

Generative AI statement
Any alternative text (Alt text) provided alongside figures in the articles in this ebook has been generated by Frontiers with the support of artificial intelligence and reasonable efforts have been made to ensure accuracy, including review by the authors wherever possible. If you identify any issues, please contact us.

About Frontiers

Frontiers is more than just an open access publisher of scholarly articles: it is a pioneering approach to the world of academia, radically improving the way scholarly research is managed. The grand vision of Frontiers is a world where all people have an equal opportunity to seek, share and generate knowledge. Frontiers provides immediate and permanent online open access to all its publications, but this alone is not enough to realize our grand goals.

Frontiers journal series

The Frontiers journal series is a multi-tier and interdisciplinary set of open-access, online journals, promising a paradigm shift from the current review, selection and dissemination processes in academic publishing. All Frontiers journals are driven by researchers for researchers; therefore, they constitute a service to the scholarly community. At the same time, the *Frontiers journal series* operates on a revolutionary invention, the tiered publishing system, initially addressing specific communities of scholars, and gradually climbing up to broader public understanding, thus serving the interests of the lay society, too.

Dedication to quality

Each Frontiers article is a landmark of the highest quality, thanks to genuinely collaborative interactions between authors and review editors, who include some of the world's best academicians. Research must be certified by peers before entering a stream of knowledge that may eventually reach the public - and shape society; therefore, Frontiers only applies the most rigorous and unbiased reviews. Frontiers revolutionizes research publishing by freely delivering the most outstanding research, evaluated with no bias from both the academic and social point of view. By applying the most advanced information technologies, Frontiers is catapulting scholarly publishing into a new generation.

What are Frontiers Research Topics?

Frontiers Research Topics are very popular trademarks of the *Frontiers journals series*: they are collections of at least ten articles, all centered on a particular subject. With their unique mix of varied contributions from Original Research to Review Articles, Frontiers Research Topics unify the most influential researchers, the latest key findings and historical advances in a hot research area.

Find out more on how to host your own Frontiers Research Topic or contribute to one as an author by contacting the Frontiers editorial office: frontiersin.org/about/contact

Studying the immune microenvironment of liver cancer using artificial intelligence

Topic editors

Dake Zhang — Beihang University, China

Jieliang Chen — Fudan University, China

Bing Yang — Tianjin Medical University, China

Citation

Zhang, D., Chen, J., Yang, B., eds. (2025). *Studying the immune microenvironment of liver cancer using artificial intelligence*. Lausanne: Frontiers Media SA.

doi: 10.3389/978-2-8325-6822-4

Table of contents

frontiers | Frontiers in Immunology

TYPE Editorial
PUBLISHED 26 August 2025
DOI 10.3389/fimmu.2025.1679921

OPEN ACCESS

EDITED AND REVIEWED BY
Peter Brossart,
University of Bonn, Germany

*CORRESPONDENCE
Bing Yang
bingyang@tmu.edu.cn;
yang.bing@krirk.ac.th

RECEIVED 05 August 2025
ACCEPTED 11 August 2025
PUBLISHED 26 August 2025

CITATION
Zhang D-k, Chen J-l, Yang B-r and Yang B (2025) Editorial: Studying the immune microenvironment of liver cancer using artificial intelligence. *Front. Immunol.* 16:1679921. doi: 10.3389/fimmu.2025.1679921

Editorial: Studying the immune microenvironment of liver cancer using artificial intelligence

Da-ke Zhang[1], Jie-liang Chen[2], Bo-ran Yang[3] and Bing Yang[4,5]*

[1]Key Laboratory of Biomechanics and Mechanobiology, Ministry of Education, Beijing Advanced Innovation Center for Biomedical Engineering, School of Engineering Medicine, Beihang University, Beijing, China, [2]Shanghai Medical College, Fudan University, Shanghai, China, [3]Tianjin Wutong High School, Tianjin, China, [4]Department of Cell Biology, College of Basic Medical Sciences, Tianjin Medical University, Tianjin, China, [5]Department of Public Health, International School, Krirk University, Bangkok, Thailand

KEYWORDS

artificial intelligence - AI, liver disease, immunotherapy, hepatocellular carcinoma, cancer immune microenvironment, cancer precision medicine

Editorial on the Research Topic
Studying the immune microenvironment of liver cancer using artificial intelligence

A significant number of deaths each year can be attributed to liver cancer, which is known for its rapid progression and poor prognosis (1). It has a severe impact on quality of life and continues to present a major global public health challenge.

Liver cancer often renders chemotherapy and radiation ineffective, complicating treatment. The need for more effective treatment options has led to pioneering technologies being investigated, including artificial intelligence (Figure 1).

Cancer precision medicine aims to ensure treatments work as well as possible for each patient, while also trying to reduce any nasty side effects. Significant progress in oncology has been made by artificial intelligence through high-dimensional datasets and computing/deep learning (2, 3).

Nevertheless, the use of artificial intelligence in medicine is still in its infancy (4). Despite rapid advancements in algorithmic development, significant challenges remain in the areas of clinical data accumulation, data standardization, and quality verification. The accuracy of artificial intelligence in clinical practice still needs to be improved.

The present editorial introduces the compendium of articles that have been published in Frontiers in Immunology: Cancer Immunity and Immunotherapy Research Topic. We hope that this will encourage high-quality research on artificial intelligence in the field of relativity.

Harnessing multi-omics and artificial intelligence: revolutionizing prognosis and treatment in hepatocellular carcinoma by Wang et al. The study gained an

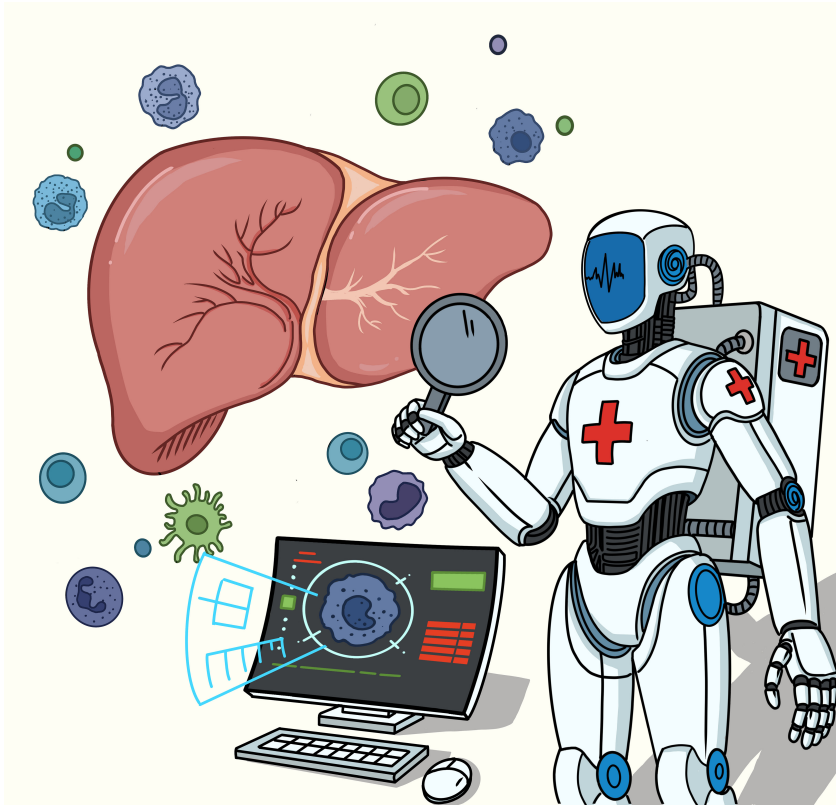

FIGURE 1
Amazing helping hand: Artificial Intelligence in immunological management of liver disease.

understanding of the different types of this cancer, improving prediction and treatment by combining different kinds of data.

Machine learning-driven prediction of immune checkpoint inhibitor responses against cholangiocarcinoma: a bile biopsy perspective by Zhang et al. Research aims to develop models to detect and treat cholangiocarcinoma early.

Preoperative assessment of liver regeneration using T1 mapping and the functional liver imaging score derived from Gd-EOB-DTPA-enhanced magnetic resonance for patient with hepatocellular carcinoma after hepatectomy by Li et al. The author proves that T1 mapping parameters and functional liver imaging score are potential non-invasive indicators of liver regeneration.

Multiomic analysis of lactylation and mitochondria-related genes in hepatocellular carcinoma identified MRPL3 as a new prognostic biomarker by Xing et al. The author demonstrates that MRPL3 is a dependable predictive biomarker in diagnosing and treating hepatocellular carcinoma.

Pinpointing the integration of artificial intelligence in liver cancer immune microenvironment by Bukhari et al. This review covers recent progress in the immune microenvironment of hepatocellular carcinoma using artificial intelligence.

Integrative multi-omics analysis reveals a novel subtype of hepatocellular carcinoma with biological and clinical relevance by Li et al. This study has built an effective model to predict outcomes for patients with this type of cancer and identified new subgroups.

The complex role of immune cells in antigen presentation and regulation of T-cell responses in hepatocellular carcinoma: progress, challenges, and future directions by Ning et al. This review gives the latest information about this field by studying how liver cancer antigen presentation works.

Screening of genes co-associated with osteoporosis and chronic HBV infection based on bioinformatics analysis and machine learning by Yang et al. The study also focuses on diagnosing and treating chronic HBV. New insights have been gained into the relationship between osteoporosis and chronic HBV infection.

Lactylation signature identifies liver fibrosis phenotypes and traces fibrotic progression to hepatocellular carcinoma by Li et al. This research focuses on hepatocellular carcinoma arising from liver fibrosis, particularly lactylation and related immune infiltration.

Causal relationship between immune cell phenotypes and risk of biliary tract cancer: evidence from Mendelian randomization analysis by Hu et al. Mendelian randomization was employed in this study to explore the potential association between immune cell phenotypes and biliary tract cancer.

Hepatitis B-related hepatocellular carcinoma: classification and prognostic model based on programmed cell death genes by Tian et al. This study used various bioinformatics techniques to analyze RNA sequencing data from patients with Hepatitis B - hepatocellular carcinoma. A prognostic model was also developed, based on genomic and clinical information.

Author contributions

DZ: Writing – original draft. JC: Writing – original draft. BrY: Visualization, Writing – original draft. BY: Supervision, Writing – original draft, Writing – review & editing.

Acknowledgments

The authors would like to express their gratitude to the coeditors of this Research Topic and the contribution of the reviewers.

Conflict of interest

The authors declare that the research was conducted in the absence of any commercial or financial relationships that could be construed as a potential conflict of interest.

The author(s) declared that they were an editorial board member of Frontiers, at the time of submission. This had no impact on the peer review process and the final decision.

Generative AI statement

The author(s) declare that no Generative AI was used in the creation of this manuscript.

Any alternative text (alt text) provided alongside figures in this article has been generated by Frontiers with the support of artificial intelligence and reasonable efforts have been made to ensure accuracy, including review by the authors wherever possible. If you identify any issues, please contact us.

Publisher's note

References

1. Wang L, Qiu M, Wu L, Li Z, Meng X, He L, et al. Construction and validation of prognostic signature for hepatocellular carcinoma basing on hepatitis B virus related specific genes. *Infect Agents Cancer*. (2022) 17:60. doi: 10.1186/s13027-022-00470-y

2. Chokkakula S, Chong S, Yang B, Jiang H, Yu J, Han R, et al. Quantum leap in medical mentorship: exploring ChatGPT's transition from textbooks to terabytes. *Front Med*. (2025) 12:1517981. doi: 10.3389/fmed.2025.1517981

3. Wu L-l, Yang B, Meng X, Fan G, Yang B. Artificial intelligence: new hope for critically ill cardiovascular patients. *Front Med*. (2024) 11:1453169. doi: 10.3389/fmed.2024.1453169

4. Xianyu Z, Correia C, Yong Ung C, Zhu S, Billadeau DD, Li H. The rise of hypothesis-driven artificial intelligence in oncology. *Cancers*. (2024) 16:822. doi: 10.3390/cancers16040822

frontiers | Frontiers in Immunology

TYPE Original Research
PUBLISHED 10 May 2024
DOI 10.3389/fimmu.2024.1411161

OPEN ACCESS

EDITED BY
Bing Yang,
Tianjin Medical University, China

REVIEWED BY
Guan Guiwen,
Peking University, China
Yu Zhu,
Tianjin Haihe Hospital, China

*CORRESPONDENCE
Xinyi Jiang
xyjiang@njmu.edu.cn
Jian Zou
zoujan@njmu.edu.cn

RECEIVED 02 April 2024
ACCEPTED 29 April 2024
PUBLISHED 10 May 2024

CITATION
Tian J, Meng J, Yang Z, Song L, Jiang X and Zou J (2024) Hepatitis B-related hepatocellular carcinoma: classification and prognostic model based on programmed cell death genes. *Front. Immunol.* 15:1411161. doi: 10.3389/fimmu.2024.1411161

Hepatitis B-related hepatocellular carcinoma: classification and prognostic model based on programmed cell death genes

Jinyue Tian, Jiao Meng, Zhenkun Yang, Li Song, Xinyi Jiang* and Jian Zou*

Department of Clinical Laboratory, Wuxi People's Hospital Affiliated Nanjing Medical University, Wuxi, China

Instruction: Hepatitis B virus (HBV) infection is a major risk factor for hepatocellular carcinoma (HCC). Programmed cell death (PCD) is a critical process in suppressing tumor growth, and alterations in PCD-related genes may contribute to the progression of HBV-HCC. This study aims to develop a prognostic model that incorporates genomic and clinical information based on PCD-related genes, providing novel insights into the molecular heterogeneity of HBV-HCC through bioinformatics analysis and experimental validation.

Methods: In this study, we analyzed 139 HBV-HCC samples from The Cancer Genome Atlas (TCGA) and validated them with 30 samples from the Gene Expression Omnibus (GEO) database. Various bioinformatics tools, including differential expression analysis, gene set variation analysis, and machine learning algorithms were used for comprehensive analysis of RNA sequencing data from HBV-HCC patients. Furthermore, among the PCD-related genes, we ultimately chose *DLAT* for further research on tissue chips and patient cohorts. Besides, immunohistochemistry, qRT-PCR and Western blot analysis were conducted.

Results: The cluster analysis identified three distinct subgroups of HBV-HCC patients. Among them, Cluster 2 demonstrated significant activation in DNA replication-related pathways and tumor-related processes. Analysis of copy number variations (CNVs) of PCD-related genes also revealed distinct patterns in the three subgroups, which may be associated with differences in pathway activation and survival outcomes. *DLAT* in tumor tissues of HBV-HCC patients is upregulated.

Discussion: Based on the PCD-related genes, we developed a prognostic model that incorporates genomic and clinical information and provided novel insights into the molecular heterogeneity of HBV-HCC. In our study, we emphasized the significance of PCD-related genes, particularly *DLAT*, which was examined in vitro to explore its potential clinical implications.

KEYWORDS

hepatocellular carcinoma, hepatitis B virus infection, programmed cell death, clinical characteristics, prognostic model

1 Introduction

Chronic hepatitis B virus (HBV) infection is a major risk factor for the development of Hepatocellular carcinoma (HCC), particularly in regions with high HBV prevalence (1, 2). Despite advances in treatment, the prognosis of HBV-related HCC remains poor, with a high rate of recurrence and metastasis (3, 4). Therefore, there is an urgent need to identify novel prognostic biomarkers and therapeutic targets for HBV-related HCC.

Programmed cell death (PCD) is a critical process in the regulation of tissue homeostasis and the elimination of damaged or abnormal cells (5). Several types of PCD have been identified, including apoptosis, necroptosis, pyroptosis, and ferroptosis (6). Recently, several studies have suggested that PCD plays a critical role in the development and progression of HCC (7–9). However, the role of different types of PCD in HBV-related HCC and their clinical significance remains unclear.

In this study, we aimed to identify distinct subgroups of HBV-HCC patients based on clinical characteristics and expression profiles of PCD-related genes. Various bioinformatics tools, including differential expression analysis, gene set variation analysis, and machine learning algorithms were used for comprehensive analysis of RNA sequencing data from HBV-HCC patients. The identification of subgroups with distinct clinical characteristics, immune microenvironments, metabolic states, and drug sensitivities may facilitate the development of effective therapies for HBV-HCC. Furthermore, among the PCD-related genes, we ultimately chose *DLAT* for further research on tissue chips and patient cohorts. Upon analyzing the relationship between *DLAT* and patient survival prognosis, it was discovered that patients with deep *DLAT* staining had significantly shorter survival times than those with light *DLAT* staining. Through our study, we can classify HBV-HCC subgroups based on different PCD-related genes and construct prognostic models. It suggests that PCD-related genes can serve as potential biomarkers for patient stratification and personalized treatment.

2 Material and methods

2.1 NMF unsupervised clustering of HBV-HCC samples

We analyzed 139 HBV-HCC samples from TCGA using non-negative matrix factorization (NMF) to perform unsupervised clustering. The cophenetic value and clustering heatmap were used to determine the optimal number of clusters, and we found that three clusters showed the greatest inter-group variability and the least intra-group variability. We then compared the overall survival (OS) rates of the three clusters using the "survival" and "survminer" packages in R software. The expression of genes related to programmed cell death (PCD) in the three clusters was visualized using a heatmap generated with the "pheatmap" package. We also analyzed the clinical characteristics of the three clusters using a stacked bar plot generated with the "ggplot2" package.

2.2 Immune cell infiltration analysis and prediction of response to immunotherapy

Analysis of immune cell infiltration was performed using TIMER2.0 (http://timer.cistrome.org), which utilizes gene expression data to estimate the abundance of various immune cell types in tumor tissues. Seven different methods were used to evaluate immune cell infiltration. Heatmap visualization of differentially expressed immune cells was generated using the "pheatmap" package. The microenvironment of each cluster was evaluated using the "estimate" package, and boxplots were generated using the "ggpubr" package to compare the stromal score, immune score, and ESTIMATE score between clusters. The Tumor Immune Dysfunction and Exclusion (TIDE) algorithm (http://tide.dfci.harvard.edu) was used to predict the response to immune checkpoint blockade therapy, and the results were visualized using violin plots and boxplots with the "ggpubr" package.

2.3 GSVA and CNV analysis of PCD-related genes in HBV-HCC

Gene set variation analysis (GSVA) was performed using the "GSVA" and "GSEABase" packages in R to calculate the pathway activity of HALLMARK gene sets in the three HBV-HCC subgroups. Heatmaps were generated to visualize the pathway activity using the "pheatmap" package. The HALLMARK gene sets were obtained from the Molecular Signatures Database (MSigDB) (http://www.gsea-msigdb.org/gsea/msigdb). Additionally, Copy number variations (CNVs) of PCD-related genes in HBV-HCC subgroups were analyzed using CNV data obtained from the UCSC Xena browser. Lollipop charts were generated to visualize the CNV variations using the "ggplot2" package.

2.4 Differential gene expression analysis and enrichment analysis of HBV-HCC subgroups

RNA sequencing data from three subgroups of HBV-HCC were obtained and analyzed using R software. Differential expression analysis was performed using the "limma" package to identify differentially expressed genes (DEGs) between each subgroup. DEGs with an adjusted p-value < 0.05 and a log2 fold change > 1 were considered significant. Gene ontology (GO) and Kyoto Encyclopedia of Genes and Genomes (KEGG) enrichment analysis were performed on the DEGs for each subgroup using the "clusterProfiler" package in R. The enriched GO terms and KEGG pathways with a p-value < 0.05 were considered significant. To visualize the GO enrichment results, GO circle plots were generated using the "circlize" and "ComplexHeatmap" packages in R.

2.5 Identification of survival-associated genes and construction of a prognostic model

The univariate cox regression analysis was performed to identify genes significantly associated with OS with p-value<0.05. Two methods, LASSO regression and random survival forest (RSF), were used for further screening of survival-associated genes. The optimal lambda value was used to select genes in the LASSO regression, and the top 10 genes with the highest importance score based on the Gini coefficient were selected in the RSF analysis. The intersection of genes selected by the two methods was used for further analysis. A stepwise multiple cox regression was conducted to build a prognostic model using the selected genes, and hub genes were identified. Risk scores were calculated based on the expression levels and coefficients of the hub genes for distinguishing patients into high- and low-risk groups. Kaplan-Meier survival curves and receiver operating characteristic (ROC) curves were used to evaluate the performance of the model. Principal component analysis (PCA) and t-distributed stochastic neighbor embedding (t-SNE) were used to explore the expression pattern of the hub genes and to visualize the clustering of patients in the high- and low-risk groups.

2.6 Evaluation of prognostic value and gene expression patterns in high- and low-risk groups

We used the same risk score formula derived from the stepwise multivariate Cox regression analysis in the training and validation sets. Patients were ranked according to their risk scores, and the risk score distribution and survival curves were plotted to evaluate the prognostic value of the risk score. In addition, to compare the gene expression patterns between the high- and low-risk groups, we selected the top five genes from the multivariate Cox regression analysis and compared their expression levels in the two groups. The expression levels were presented as a heatmap using the "pheatmap" package.

2.7 Immune cell and immune process enrichment analysis and evaluation of immune therapy and MSI score in HBV-HCC

GSVA method was used to evaluate the relative enrichment score of 29 immune cell types and immune processes in HBV-HCC samples. The ssGSEA score of each immune cell type and immune process was calculated using the "GSVA" and "GSEABase" packages in R. The ImmunCellAI algorithm was used to evaluate the sensitivity of immune therapy for HBV-HCC patients. The immune cell score, immunotherapy exclusion score, and cytotoxic score were obtained through the ImmunCellAI web tool (http://bioinfo.life.hust.edu.cn/ImmuCellAI#!/analysis). The tumor immune dysfunction and exclusion (TIDE) algorithm was used to evaluate the MSI (Microsatellite instability, MSI) score of HBV-HCC samples. MSI is an important factor in the occurrence and development of tumors. The results were visualized using violin plots and boxplots with the "ggpubr" package.

2.8 Drug sensitivity analysis using IC50 data from the GDSC database

Drug IC50 data were obtained from the Genomics of Drug Sensitivity in Cancer (GDSC) database. Drug sensitivity analysis was conducted with "pRRophetic" and box plots were drawn by "ggplot2" in R software. IC50 values between the high- and low-risk groups were compared using the t-test. Drugs with significantly lower IC50 values in the low-risk group were considered potentially suitable for low-risk patients, while drugs with significantly lower IC50 values in the high-risk group were considered potentially suitable for high-risk patients.

2.9 Construction and evaluation of clinical prediction model for HBV-HCC patients

Patients with complete clinical information and survival data were included in this study. Univariate cox regression analysis was performed to extract factors with p<0.05 with "graphics" package and construct a multivariate cox regression model with "StepReg" and "regplot" packages. The ROC curve was evaluated to assess the discrimination ability of the model using "timeROC" package. The calibration curve was plotted with "timeROC" package to evaluate the calibration of the model. The clinical prediction model was divided into high and low-risk groups based on the model with "survival" package.

2.10 Western blot and qRT-PCR

Liver cancer cells were lysed using RIPA buffer (Cell Signal Technology, MA), centrifuged for the supernatant. The protein concentration was measured using bicinchoninic acid (BCA) assay (Cwbio, Beijing, China). The lysates were then diluted in loading buffer and denatured by heating at 100°C. Standard Western blot assay were performed using *DLAT* antibody (Proteintech, 68303) and GAPDH antibody (Abcam, ab77109) as the loading control.

Total RNA was extracted from the liver cancer cells using Trizol reagent (Invitrogen, USA) and cDNA was synthesized using the M-MLV Reverse Transcriptase Kit (Cwbio) following the manufacturer's instructions. RT-PCR was performed using Real SYBR Mixture (Cwbio) on a Lightcycler 480 II instrument (Roche Applied Science, USA). GAPDH severed as the internal control.

DLAT forward primer: 5′-CCGCCGCTATTACAGTCTTCC-3′;

DLAT reverse primer: 5′-CTCTGCAATTAGGTCACCTTCAT-3′.

GAPDH forward primer: 5′-TGTTGCCATCAATGACCCCTT-3′;

GAPDH reverse primer: 5′-CTCCACGACGTACTCAGCG-3′

2.11 Tissue microarray and immunohistochemistry

Immunohistochemistry staining was performed using the streptavidin-peroxidase method according to the manufacturer's instructions (Ultrasensitive; MaiXin, Fuzhou, China). The tissue microarray HLivH180Su09 which was related to HBV infection were incubated with an anti-*DLAT* antibody (mouse anti-human; dilution, 1:2000; HPA040786) at 4°C overnight, followed by the biotinylated anti-mouse IgG secondary antibody. The result of IHC were independently scored by two investigators who were blinded to the clinical data. The scores were obtained by evaluating the staining intensity and percentage of positive cells in representative areas. We used the following strategy to assess the results: intensity, 0 (no signal), 1 (weak), 2 (moderate), or 3 (high); percentage of cells, 0%-100%. We multiplied the scores of the staining intensity and percentage to obtain a final score (range 0–3). When the IHC score≥1.5, they had a high *DLAT* expression. When the IHC score<1.5, they were defined as low *DLAT* expression.

3 Results

3.1 Identification of three subgroups of HBV-HCC samples with distinct clinical characteristics and survival outcomes

We collected 139 HBC-HCC samples from TCGA-LIHC which contained clinical information and survival outcomes. According to NMF unsupervised clustering (Figure 1A), the samples were divided into three subgroups, labeled Cluster 1, Cluster 2, and Cluster 3. Among them, Cluster 2 showed the worst Overall Survival (OS) probability (Figure 1B), and contained more overexpressed PCD-related genes in the heatmap (Figure 1C). Moreover, exploration of clinical characteristics revealed that Cluster 2 had the largest proportion of high-risk groups: more samples were at stage of G3/G4, III/IV and T3/T4 grade in histological grade, pathological stage, and T stage, respectively (Figures 1D-F).

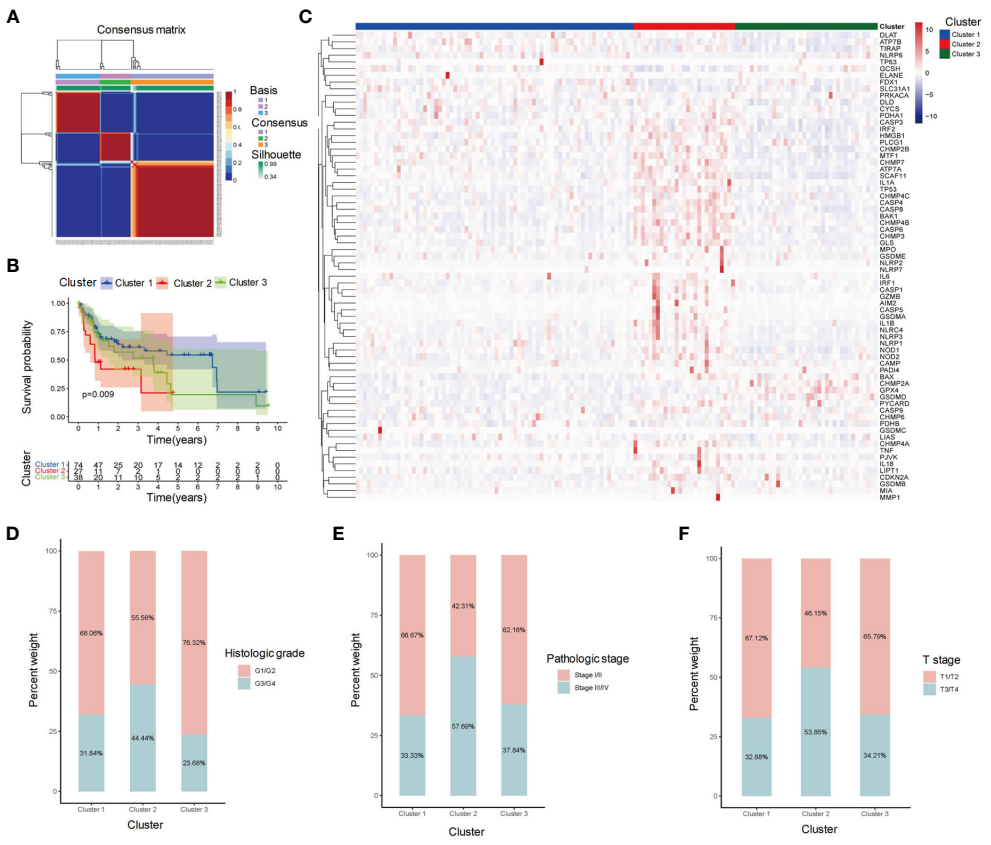

FIGURE 1
Clustering analysis of HBV-HCC samples based on gene expression profiles. **(A)** Clustering heatmap shows the identification of three distinct subgroups of HBV-HCC samples, labeled as Cluster 1, Cluster 2, and Cluster 3. **(B)** Kaplan-Meier survival analysis shows the overall survival (OS) of patients in each cluster. **(C)** Heatmap shows the expression levels of PCD-related genes in each cluster. **(D-F)** Stacked bar plot shows the distribution of histological grade, pathological stage, and T stage in each cluster. OS, Overall survival; PCD, Programmed cell death.

10.3389/fimmu.2024.1411161

3.2 Microenvironment and immunotherapy sensitivity evaluation

We perform 7 algorithms to evaluate the immune infiltration of three clusters (Figure 2A). Cluster 2 displayed higher abundance of immune cells compared to the other clusters. Consistent with the above results, Cluster 2 had the highest stromal score, immune score and estimate score (Figures 2B-D), indicating that more active microenvironments existed in Cluster 2. The TIDE evaluation revealed that the exclusion score of Cluster 2 was also the highest (Figure 2E). Although Cluster 2 contained more immune cells, the cells were undergoing immune rejection and were unable to infiltrate. In the evaluation of dysfunctions, Cluster 1 received the lowest score (Figure 2F). This indicates that Cluster 1 was supposed to have the least immune rejection and dysfunction, which could be associated with better survival outcomes. Meanwhile, both Cluster 1 and Cluster 3 had a higher MSI score compared to Cluster 2, suggesting that immunotherapy was least effective in Cluster 2 (Figure 2G).

3.3 Pathway and CNV analysis reveals differences among HBV-HCC subgroups

We further explored the pathway activation in three distinct clusters (Figure 3A). The heatmap revealed that metabolism-related pathways, such as fatty acid and bile acid metabolism, were significantly activated in Cluster 1. Cluster 2 exhibited activation of DNA replication pathways, including the G2M checkpoint, and tumor-related processes, such as p53 pathway, were significantly activated in

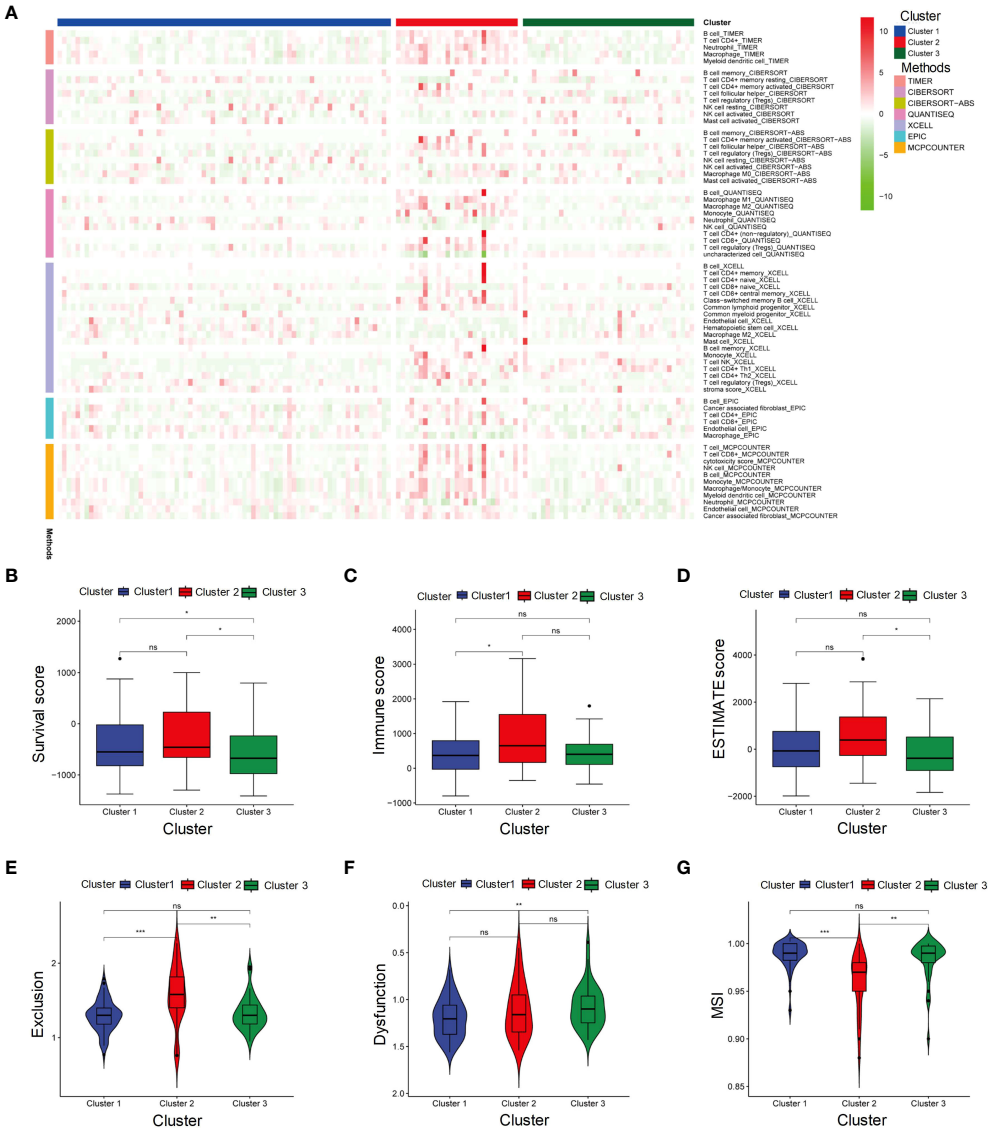

FIGURE 2
Microenvironment and immunotherapy sensitivity evaluation of three subgroups. **(A)** Heatmap represents immune cell infiltration in three subgroups of HBV-HCC using seven algorithms. **(B-G)** Stromal score, Immune score, ESTIMATE score, Exclusion score, Dysfunction score and MSI in Cluster 1, Cluster 2, and Cluster 3. MSI, Microsatellite instability. It signifies a lack of significant differences. *p≤0.05, **p≤0.01, ***p≤0.001. ns means p>0.05.

10.3389/fimmu.2024.1411161

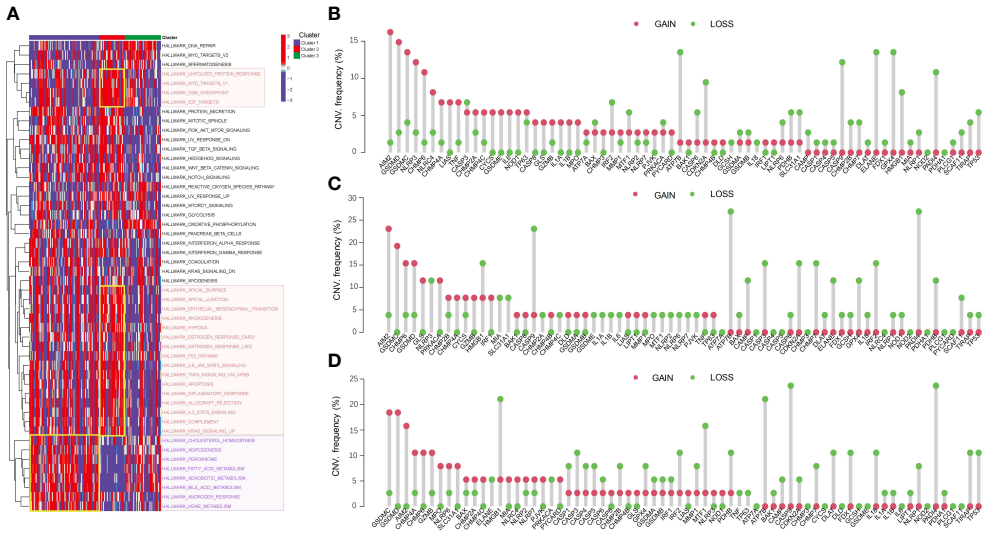

FIGURE 3
Pathway activation and CNV analysis reveal differences among HBV-HCC subgroups. **(A)** GSVA analysis shows the differences in pathway activity among the three HBV-HCC subgroups. The color red denotes DNA replication pathways, whereas purple signifies pathways related to metabolism. **(B-D)** Frequencies of CNV gain, loss, and non-CNV among PCD-related genes in the three HBV-HCC subgroups. CNV, Copy number variation; GSVA, Gene set variation analysis.

Cluster 2, suggesting that Cluster 2 may have a closer relation to tumor progression. Analysis of CNVs in PCD-related genes revealed distinct patterns in the three HBV-HCC subgroups. In Cluster 1 (Figure 3B), 32 genes had more samples with amplifications in gene copy number compared to losses, while Cluster 2 and Cluster 3 had 22 and 24 genes, respectively (Figures 3C, D). These CNV variations may be correlated with the differences in pathway activation and survival outcomes among the subgroups.

3.4 Metabolic differences between HBV-HCC subgroups

We conducted GO and KEGG enrichment analyses on the differentially expressed genes within the three subgroups. The results of the GO enrichment analysis indicated that both Cluster 1 and Cluster 2 exhibited significant enrichment in GO terms related to metabolism (Figures 4A-C). However, the biological processes and

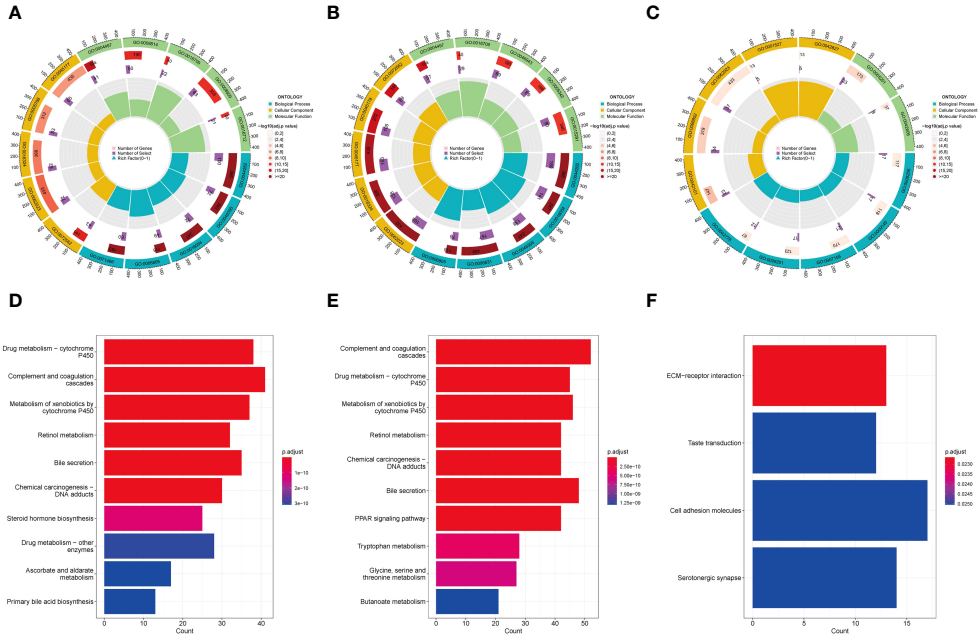

FIGURE 4
GO and KEGG analysis in HBV-HCC subgroups. GO enrichment analysis of Cluster 1 **(A)**, Cluster 2 **(B)**, and Cluster 3 **(C)**. KEGG pathway analysis of Cluster 1 **(D)**, Cluster 2 **(E)**, and Cluster 3 **(F)**. GO, Gene ontology; KEGG, Kyoto encyclopedia of genes and genomes.

signaling pathways related to metabolism were activated (GO z-scores > 0) in Cluster 1, while they were inhibited (GO z-scores < 0) in Cluster 2. KEGG pathway analysis showed that both Cluster 1 and Cluster 2 also shared significant enrichment in metabolic pathways (Figures 4D-F). However, the enriched pathways were mainly upregulated in Cluster 1, while they were downregulated in Cluster 2. These results suggest that the three subgroups have distinct metabolic states, with Cluster 1 showing activated metabolism, Cluster 2 showing inhibited metabolism, and Cluster 3 showing a different metabolic state.

3.5 Identification and validation of prognostic gene signature for HBV-HCC

We screened 20 PCD-related genes associated with OS using univariate Cox regression analysis. Two screening methods were used to identify potential genes: (1) According to LASSO regression, we selected 12 genes with the optimal lambda value (Figures 5A, B); (2) RSF analysis ranked the genes based on their importance, and we selected the top 10 genes (Figure 5C). The intersection of these two methods resulted in nine genes, which were further analyzed using multivariable Cox regression analysis. From this analysis, five genes (*CHMP4C, DLAT, MMP1, NLRP6, and NOD2*), were found to be associated with OS (Figure 5D). The risk score was calculated based on these five genes, and patients were divided into high-risk and low-risk groups. The KM survival curves showed that the high-risk group had significantly poorer OS than the low-risk group ($p < 0.05$) (Figure 5E). The ROC curves showed that the risk score had good accuracy in predicting 1-year (AUC: 0.766), 3-year (AUC: 0.804) and 5-year (AUC: 0.782) survival (Figure 5F). Additionally, PCA and tSNE analyses showed that the high-risk and low-risk groups were well separated based on their risk scores, indicating that the risk

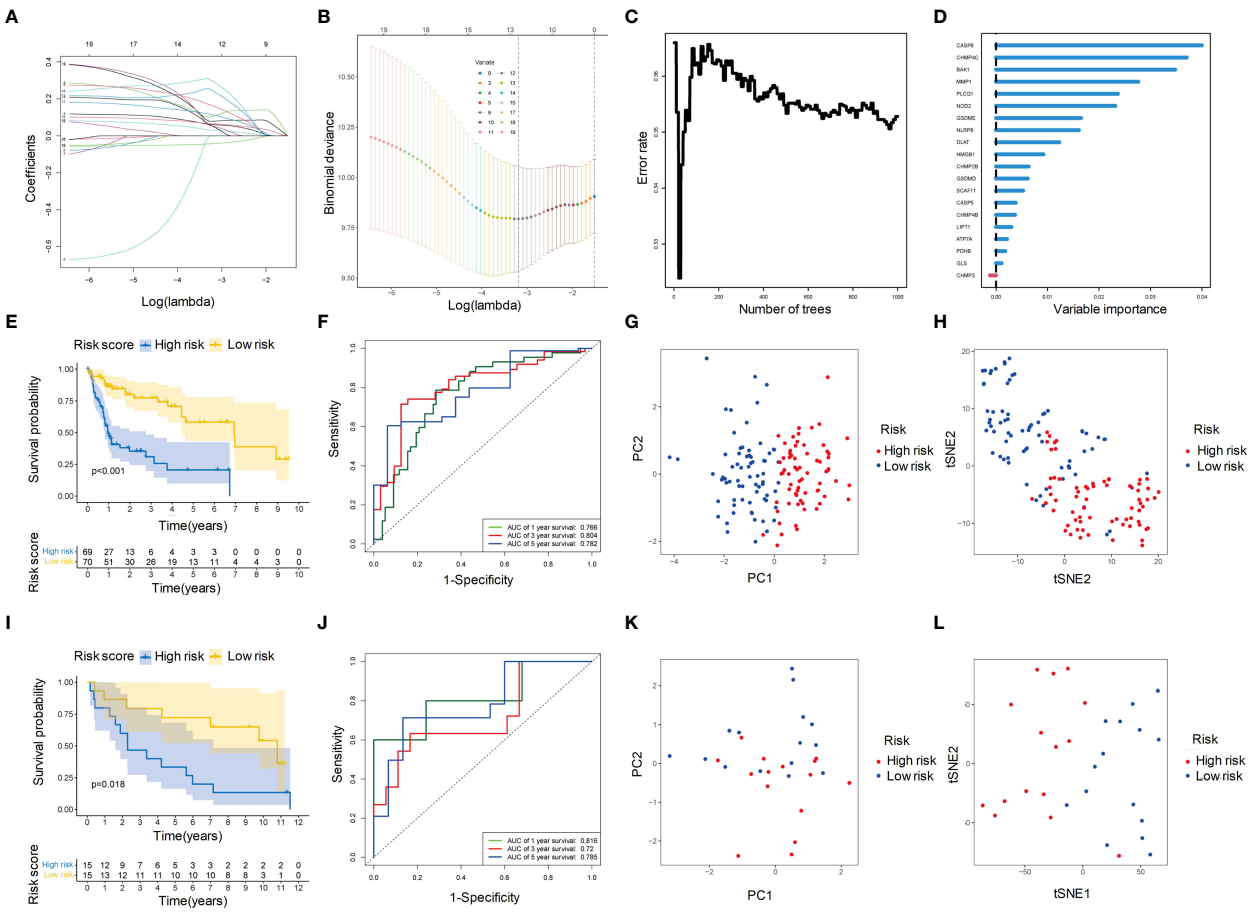

FIGURE 5
Identification of hub genes and construction of PCD-related prognostic model for HBV-HCC. **(A)** Univariate Cox regression analysis profiles 20 genes significantly associated with OS. **(B)** LASSO regression showed that when the error of the model was minimized, 12 variables were selected for further logistic regression analysis. **(C)** Variable importance plot for the top 10 genes identified by RSF analysis. **(D)** Classification error rates of the RSF analysis for different numbers of genes. **(E)** Kaplan-Meier survival curves for patients in the high- and low-risk groups defined by the five-gene prognostic model. **(F)** ROC curve analysis of the five-gene prognostic model for 1-year, 3-year and 5-year OS. **(G)** PCA analysis of the high- and low-risk groups based on the five-gene prognostic model. **(H)** tSNE analysis of the high- and low-risk groups based on the five-gene prognostic model. **(I-L)** The prognostic value of the five-gene signature was validated in an independent cohort. The Kaplan-Meier survival curves **(I)**, ROC curve analysis **(J)**, PCA analysis **(K)**, and tSNE analysis **(L)** showed consistent results with those of the training cohort. OS, Overall survival; LASSO, Least absolute shrinkage and selection operator; RSF, Random survival forest; ROC, Receiver operating characteristic curve; PCA, Principal components analysis; tSNE, t-distributed stochastic neighbor embedding.

score represented the major differences in the patient samples (Figures 5G, H). These findings were consistent with those in the independent validation cohort (Figures 5I-L).

3.6 Identification and validation of prognostic gene signature for HBV-HCC

We ranked the patients according to the risk score of the training set, and found that patients with higher risk scores had significantly worse survival outcomes, indicating that the risk score was a reliable prognostic indicator (Figures 6A, B). Compared the expression levels of the five selected genes between the high-risk and low-risk groups, we found NLRP6 exhibited higher expression levels in the low-risk group while the other four genes expressed at higher levels in the high-risk group (Figure 6C). The same results were observed in the validation set (Figures 6D-F). These findings confirmed the prognostic value of the risk score and the potential clinical significance of the selected genes in HBV-HCC.

3.7 Immune cell infiltration and microenvironment in HBV-HCC

We evaluated the immune infiltration with ssGSEA analysis and discovered eight immune cell types were positively correlated with risk score, while two immune cell types were negatively correlated with the risk score (Figures 7A-J). In the high-risk group, most immune processes were significantly activated (Figure 7K), indicating a higher abundance of immune cells in this group. While low-risk group showed higher ImmunCellAI score, higher MSI score and lower exclusion score (Figures 7L-O) compared to high-risk group, indicating that the low-risk group was more likely to benefit from immunotherapy.

3.8 Drug sensitivity analysis reveals potential therapeutic options for high-risk and low-risk HCC patients

The IC50 values of 12 drugs were collected from GDSC. Among them, the IC50 of four drugs in the low-risk group was significantly

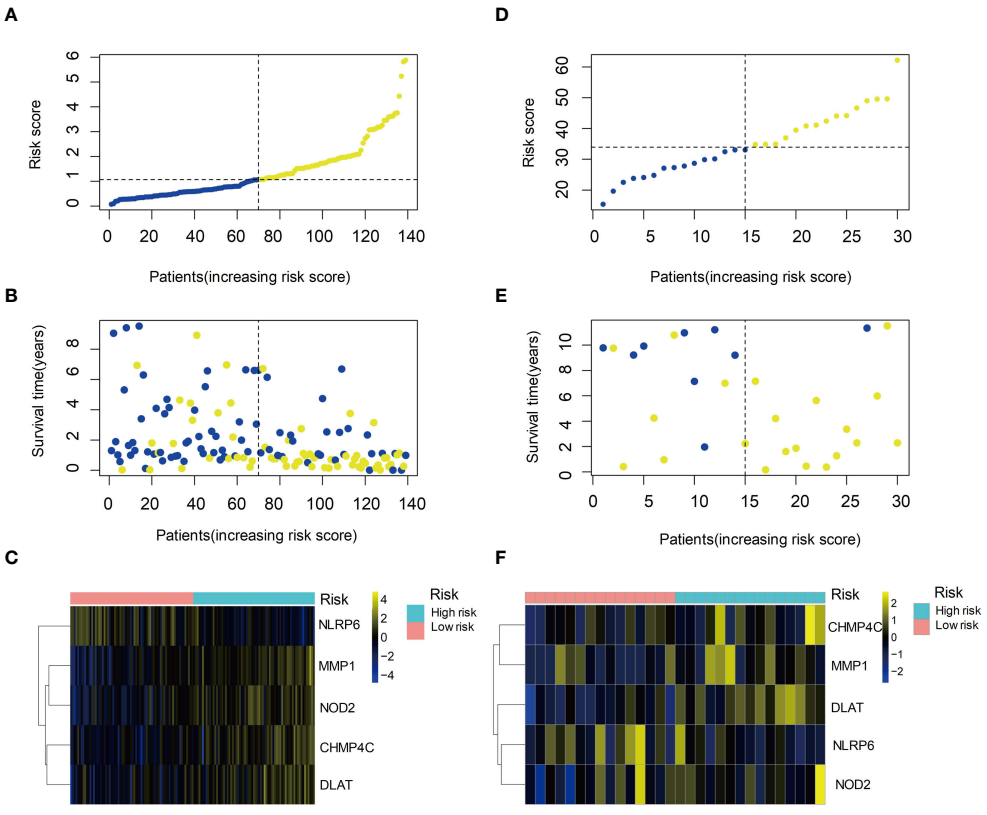

FIGURE 6
Prognostic value of the risk score and expression of hub genes in HBV-HCC. **(A)** Kaplan-Meier survival curves of the high- and low-risk groups based on the risk score. **(B)** Time-dependent ROC curves of the risk score for predicting survival outcomes. **(C)** Heatmap showing the expression levels of the five hub genes in the high- and low-risk groups. **(D)** Kaplan-Meier survival curves of the high- and low-risk groups in the validation set. **(E)** Time-dependent ROC curves of the risk score in the validation set. **(F)** Heatmap showing the expression levels of the five hub genes in the high- and low-risk groups in the validation set. ROC, Receiver operating characteristic curve.

10.3389/fimmu.2024.1411161

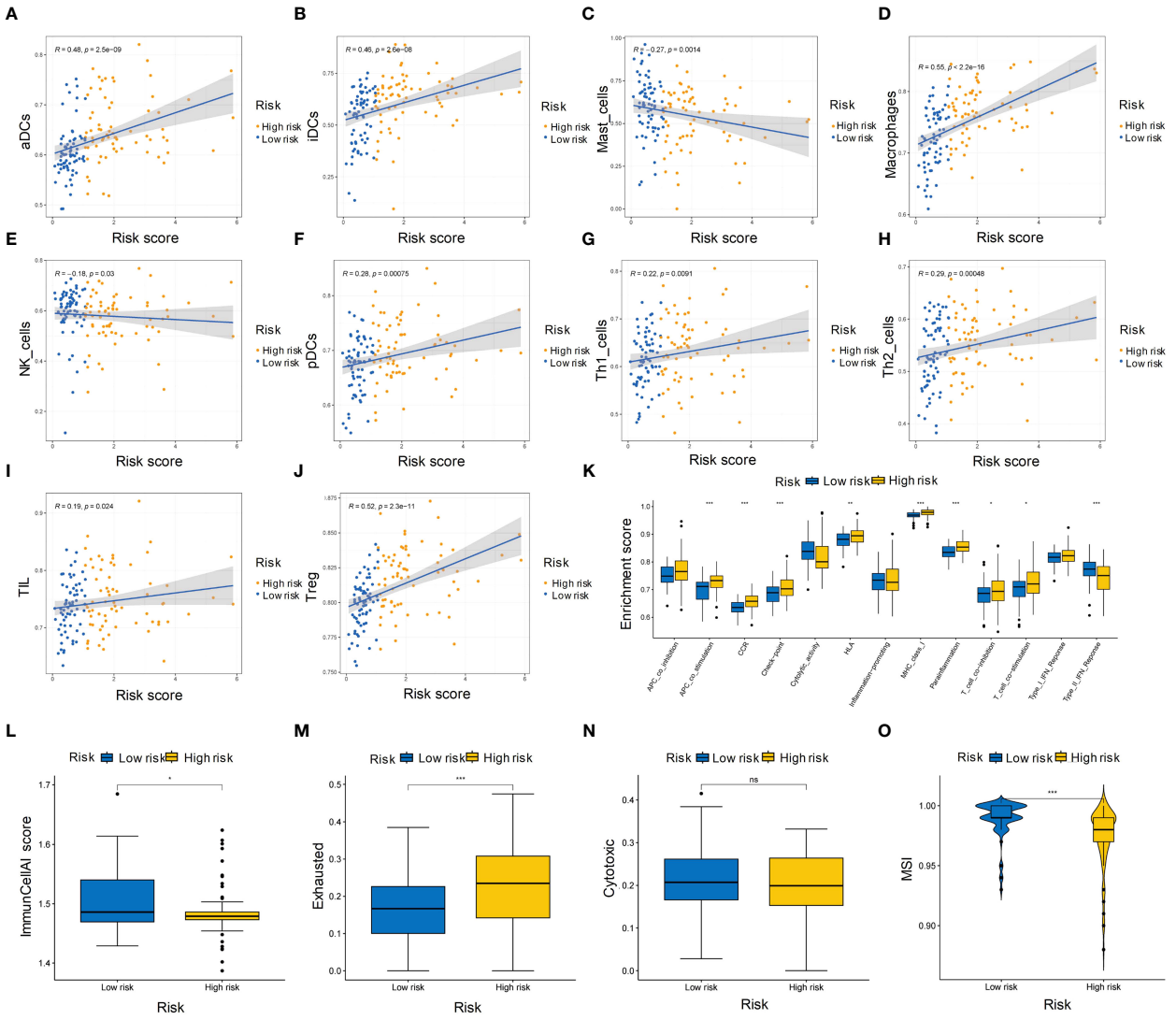

FIGURE 7
Immune cell infiltration and microenvironment in high- and low-risk groups of HBV-HCC patients. **(A-J)** Heatmap showing the ssGSEA scores of immune cell types in the high- and low-risk groups. **(K)** Boxplot showing the distribution of ssGSEA scores of immune processes in the high-risk and low-risk groups. **(L-N)** ImmunCellAI scores of the high-risk and low-risk groups for immunotherapy sensitivity, immunotherapy exclusion, and cytotoxic activity, respectively. **(O)** Boxplot showing the MSI scores of the high-risk and low-risk groups. ssGSEA, single sample gene set enrichment analysis; MSI, Microsatellite instability. *p≤0.05, **p≤0.01, ***p≤0.001. ns means p>0.05.

lower than that in the high-risk group, indicating that these drugs may be more suitable for low-risk patients. On the other hand, the IC50 of 8 drugs was lower in the high-risk group, making them more suitable for high-risk patients (Supplementary Figure S1).

3.9 Development of a clinical prediction model based on T stage and risk score for HBV-HCC patients

Combined with the risk score and clinical information (age, sex, T stage, N stage, M stage, and histological stage), univariate Cox regression analysis was performed yielding two factors T stage and risk score (p<0.05). These factors were closely associated with poor survival (Figure 8A). They were further used to construct a multivariate Cox regression model, visualized with a survival nomogram (Figure 8B). The ROC curve was drawn to assess the discrimination ability of the model (Figure 8C), with a larger AUC indicating better discrimination. The calibration curve was plotted to evaluate the calibration of the model, and the deviation between the actual curve and the ideal curve was small (Figure 8D). The clinical prediction model was further divided into high-risk and low-risk groups based on the model and significant survival differences were observed between the two groups (Figure 8E). Based on the risk score calculated by the 5 PCD-related genes and T stage of HBV-HCC tumors, we constructed a clinical model with good discrimination ability, calibration, and survival prediction.

10.3389/fimmu.2024.1411161

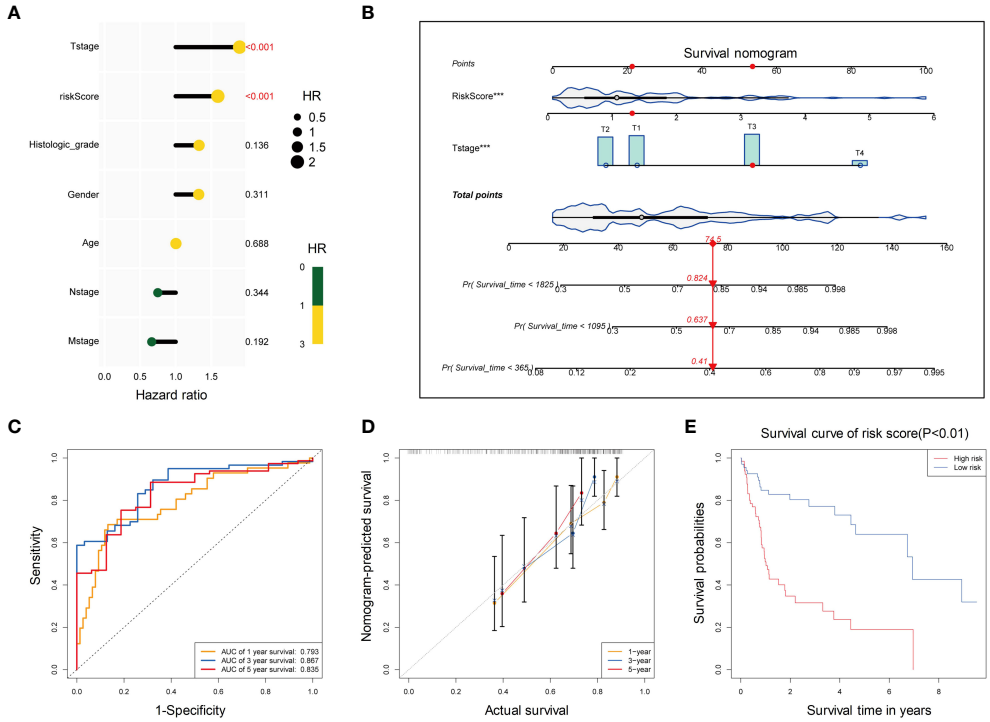

FIGURE 8
Development of a clinical prediction model based on T stage and risk score for HBV-HCC patients. **(A)** Univariate cox regression analysis of T stage and risk score for OS. **(B)** The distribution of risk scores in the training set. The dotted line represents the cut-off point for dividing patients into high- and low-risk groups. **(C)** The ROC curve of the multivariate Cox regression model based on T stage and risk score. **(D)** Calibration curves for 1-year, 3-year, and 5-year OS of HBV-HCC patients in the training cohort for the multivariate Cox regression model. **(E)** Kaplan-Meier curves for OS of patients in the high-risk and low-risk groups. OS, Overall survival; ROC, Receiver operating characteristic curve.

3.9 Upregulation of *DLAT* in tumor tissues of HBV-HCC patients

We compared the expression of *DLAT* at both the mRNA and protein levels in Huh-7, and Huh-7 cells transfected with a plasmid containing the whole HBV genome (Huh-7/HBV). The results showed that *DLAT* levels increased after HBV transfection, both in terms of RNA and protein levels. (Figures 9A, B). Immunohistochemical staining was conducted on a tissue microarray of 76 HBV-HCC patients' tumors and adjacent tissues. Three fields of view with high, medium, and low staining were chosen, revealing that the tumor exhibited stronger staining compared to the adjacent tissues. The immunohistochemical staining score of *DLAT* in cancer tissue was also significantly higher than in the adjacent tissues ($p<0.001$) (Figures 9C, D). Further analysis of the relationship between *DLAT* and the clinical characteristics of patients revealed that *DLAT* was associated with abnormal ALT and GGT levels (Figures 9E, F). It was speculated that *DLAT* is a gene associated with adverse effects in patients with HBV-HCC.

4 Discussion

HBV-related HCC is a complex and heterogeneous disease with pessimistic clinical outcomes (10–13). In this study, we focused on the role of three types of PCDs (cuproptosis, netotic cell death, and pyroptosis) and investigated their values in the progression and prognosis of HBV-HCC.

Several previous studies have identified subtypes in HCC (14, 15), and classified HCC patients with distinct clinical outcomes. Our study differed from those previous ones in the methods used to identify subtypes, and found specific clinical characteristics and immune features of each subtype. Through unsupervised clustering analysis, we firstly discovered three distinct subgroups of HBV-HCC patients with different clinical characteristics and survival outcomes. Cluster 2 was associated with the worst OS, and it had the highest abundance of immune cells, suggesting a more active microenvironment. However, TIDE analysis showed that Cluster 2 had significantly higher exclusion scores, indicating an immunosuppressive state and an inability for immune cells to infiltrate into the tumors, which may be related to its poor survival outcomes. MSI analysis also indicated that Cluster 2 was the least likely to benefit from immune checkpoint blockade therapy, while both Cluster 1 and Cluster 3 had higher MSI scores, suggesting that these two subgroups may be more sensitive to immunotherapy.

Previous studies have reported that dysregulated metabolism is a hallmark of cancer, especially in HCC (16–18), for example, glycolytic pathway (9) and lipid metabolism pathway (19) were found to be upregulated in HCC, and targeting these pathways may have therapeutic potential. In our study, we performed more detailed research and found that metabolic pathways were

10.3389/fimmu.2024.1411161

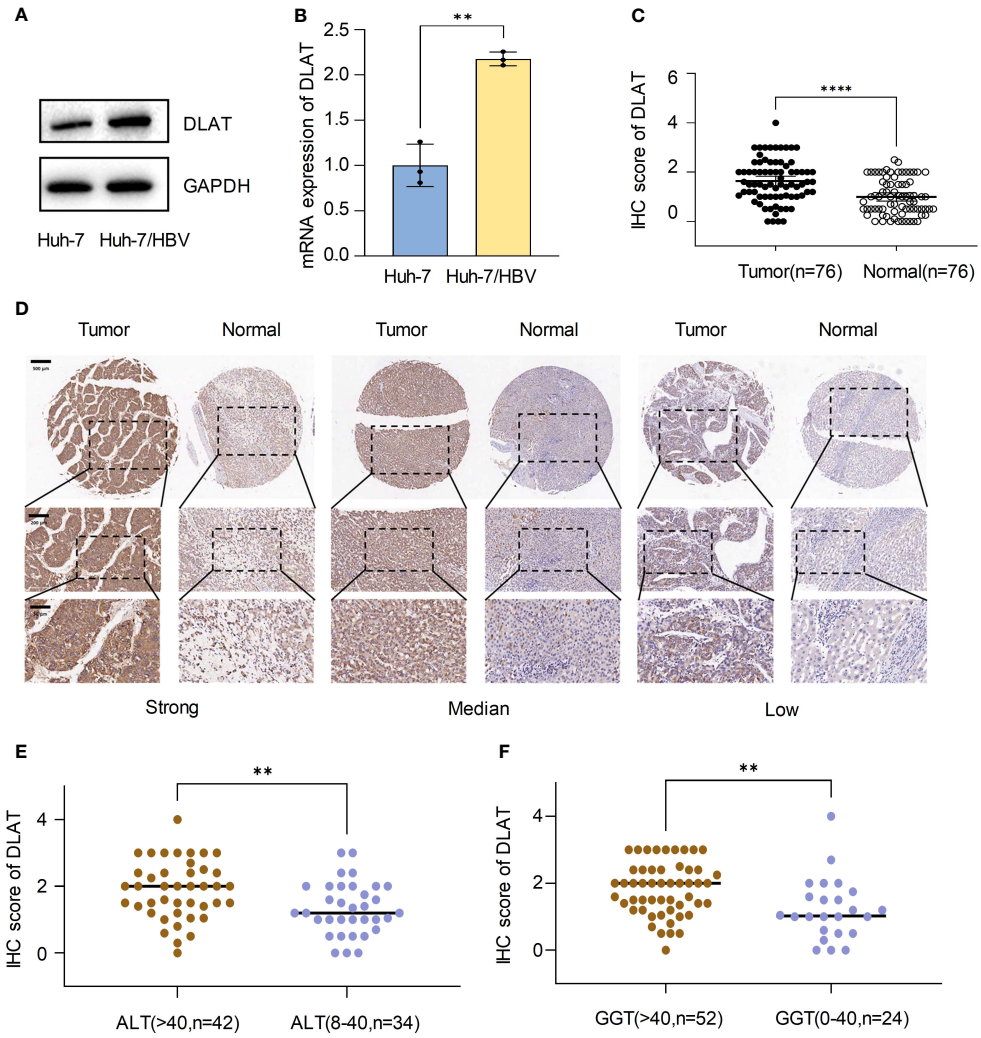

FIGURE 9
Upregulation of *DLAT* in tumor tissues of HBV-HCC patients. **(A, B)** Verify the expression of *DLAT* protein and mRNA levels in cells through *in vitro* experiments. **(C, D)** IHC staining of a tissue microarray was used to verify the expression of *DLAT* in HBV-HCC patients. **(E, F)** The relationship between *DLAT* IHC scores and levels of ALT and GGT. ** means p≤0.01, *** means p≤0.001, they all indicate significant differences.

activated or inhibited in different immune subtypes of HBV-HCC. Small molecules, carboxylic acid, organic acid and other catabolic process related pathways were upregulated in Cluster 1 and downregulated in Cluster 2. The subgroups with distinct characteristics and activated pathways found in our study may bring implications for the development of personalized therapies for HBV-HCC patients.

Using a combination of univariate Cox regression analysis, LASSO regression, and random forest analysis, we identified five genes (*CHMP4C*, *DLAT*, *MMP1*, *NLRP6*, and *NOD2*) associated with OS. Among them, *MMP1* is a biomarker related to netotic cell death, *NOD2* and *NLRP6* associates with both autophagy and pyroptosis. Furthermore, *CHMP4C* and *DLAT* are related to pyroptosis and cuproptosis, respectively. We then developed a risk score formula based on their expression levels. The risk score had good predictive accuracy in differentiating high-risk and low-risk patients, and patients in the high-risk group had significantly poorer OS than those in the low-risk group. Furthermore, we evaluated the potential for drug sensitivity analysis based on the risk score. We found that four drugs had significantly lower IC50 values in the low-risk group, indicating that these drugs may be more effective in low-risk patients, while eight drugs had significantly lower IC50 values in the high-risk group. These genes may serve as potential prognostic biomarkers and therapeutic targets for HBV-HCC. As part of the pyruvate dehydrogenase complex, *DLAT* plays an important role in glucose metabolism and the TCA cycle. However, the relevance and function of *DLAT* in cancers such as HCC, are unclear (20, 21). It has been found that *DLAT* is a gene related to cuproptosis and glucose metabolism (22, 23). Therefore, *DLAT* was selected for further research.

Our study has several limitations. First, the sample size is relatively small, and external validation with a larger sample size is needed to confirm our findings. Second, the molecular mechanisms underlying the identified pathways and PCD-related genes need further investigation. Genes from different types of PCD that influence HBV-HCC progression independently or synergistically remains to be explored. Third, our study is based

on transcriptomic data of HBV-HCC liver tissues, and further validation of the prediction model using other omics data from different HBV-HCC samples (such as blood samples, urine specimen and stool samples with better access) is warranted. Fourth, we selected *DLAT in vitro* experiments to verify its correlation with the poor prognosis of HBV-HCC. Subsequent functional experiments are needed to further explore how upstream HBV regulates *DLAT* and the effect of the increase in downstream *DLAT* on cuproptosis and metabolism.

In conclusion, our study identified distinct subgroups of HBV-HCC patients with different clinical characteristics, survival outcomes, and metabolic states, providing new insights into the heterogeneity of HBV-HCC. A prognostic model based on five PCD-related genes (specifically *DLAT*) and tumor stage that may serve as potential biomarkers for patient stratification and personalized therapy. Finally, our study highlights the potential for drug sensitivity analysis based on the risk score, which may facilitate the development of targeted therapies for HBV-HCC.

Data availability statement

The datasets presented in this study can be found in online repositories. The names of the repository/repositories and accession number(s) can be found in the article/Supplementary Material.

Author contributions

JT: Data curation, Writing – original draft. JM: Data curation, Methodology, Writing – original draft. ZY: Formal analysis, Methodology, Writing – original draft. LS: Formal analysis, Investigation, Writing – original draft. XJ: Project administration, Software, Supervision, Writing – original draft, Writing – review & editing. JZ: Conceptualization, Project administration, Supervision, Writing – review & editing.

Funding

The author(s) declare financial support was received for the research, authorship, and/or publication of this article. This work was supported by funding from NSFC: 82172954, 82300692; NFS-JS: BK20230186; Jiangsu Young Medical Talents (QNRC2016188); Top Talent Support Program for young and middle-aged people of Wuxi Health Committee (HB2023002); Nanjing Medical University (NMUB20220171); Wuxi Medical Center, Nanjing Medical University (WMCG202311, WMCQ202301).

Conflict of interest

The authors declare that the research was conducted in the absence of any commercial or financial relationships that could be construed as a potential conflict of interest.

Publisher's note

Supplementary material

The Supplementary Material for this article can be found online at: https://www.frontiersin.org/articles/10.3389/fimmu.2024.1411161/full#supplementary-material

References

1. Feng X, Lu H, Wei Y, Guan M, Wang J, Liu C, et al. Prognostic impact of hepatitis B virus infection in patients with primary cervical cancer. *Cancer Med*. (2021) 10:8310–9. doi: 10.1002/cam4.4358

2. Conners EE, Panagiotakopoulos L, Hofmeister MG, Spradling PR, Hagan LM, Harris AM, et al. Screening and testing for hepatitis B virus infection: CDC recommendations - United States 2023. *MMWR Recomm Rep*. (2023) 72:1–25. doi: 10.15585/mmwr.rr7201a1

3. Li Q, Chen C, Huang C, Xu W, Hu Q, Chen L. Noninvasive models for predicting poor prognosis of chronic HBV infection patients precipitating acute HEV infection. *Sci Rep*. (2020) 10:2753. doi: 10.1038/s41598-020-59670-4

4. Ndow G, Vo-Quang E, Shimakawa Y, Ceesay A, Tamba S, Njai HF, et al. Clinical characteristics and outcomes of patients with cirrhosis and hepatocellular carcinoma in The Gambia, west Africa: a prospective cohort study. *Lancet Glob Health*. (2023) 11: e1383–92. doi: 10.1016/S2214-109X(23)00263-2

5. Griffioen AW, Nowak-Sliwinska P. Programmed cell death lives. *Apoptosis*. (2022) 27:619–21. doi: 10.1007/s10495-022-01758-5

6. Hojo T, Skarzynski DJ, Okuda K. Apoptosis, autophagic cell death, and necroptosis: different types of programmed cell death in bovine corpus luteum regression. *J Reprod Dev*. (2022) 68:355–60. doi: 10.1262/jrd.2022-097

7. Zhang G, Liu Z, Duan S, Han Q, Li Z, Lv Y, et al. Association of polymorphisms of programmed cell death-1 gene with chronic hepatitis B virus infection. *Hum Immunol*. (2010) 71:1209–13. doi: 10.1016/j.humimm.2010.08.014

8. Liao G, Liu Z, Xia M, Chen H, Wu H, Li B, et al. Soluble programmed cell death-1 is a novel predictor of HBsAg loss in chronic hepatitis B patients when long-term nucleos(t)ide analog treatment is discontinued. *Infect Drug Resist*. (2022) 15:2347–57. doi: 10.2147/IDR.S360202

9. Ren YX, Li XB, Liu W, Yang XG, Liu X, Luo Y. The mechanism of Rac1 in regulating HCC cell glycolysis which provides underlying therapeutic target for HCC therapy. *J Oncol*. (2022) 2022:7319641. doi: 10.1155/2022/7319641

10. Chacko S, Samanta S. "Hepatocellular carcinoma: A life-threatening disease". *BioMed Pharmacother*. (2016) 84:1679–88. doi: 10.1016/j.biopha.2016.10.078

11. Forner A, Reig M, Bruix J. Hepatocellular carcinoma. *Lancet*. (2018) 391:1301–14. doi: 10.1016/S0140-6736(18)30010-2

12. Sayiner M, Golabi P, Younossi ZM. Disease burden of hepatocellular carcinoma: A global perspective. *Dig Dis Sci*. (2019) 64:910–7. doi: 10.1007/s10620-019-05537-2

13. Nishida N. Metabolic disease as a risk of hepatocellular carcinoma. *Clin Mol Hepatol*. (2021) 27:87–90. doi: 10.3350/cmh.2020.0302

14. Wang G, Xiao R, Zhao S, Sun L, Guo J, Li W, et al. Cuproptosis regulator-mediated patterns associated with immune infiltration features and construction of cuproptosis-related signatures to guide immunotherapy. *Front Immunol*. (2022) 13:945516. doi: 10.3389/fimmu.2022.945516

15. Zheng C, Peng Y, Wang H, Wang Y, Liu L, Zhao Q. Identification and validation of ferroptosis-related subtypes and a predictive signature in hepatocellular carcinoma. *Pharmgenomics Pers Med*. (2023) 16:39–58. doi: 10.2147/PGPM.S397892

16. Geyer T, Rübenthaler J, Alunni-Fabbroni M, Schinner R, Weber S, Mayerle J, et al. NMR-based lipid metabolite profiles to predict outcomes in patients undergoing interventional therapy for a hepatocellular carcinoma (HCC): A substudy of the SORAMIC trial. *Cancers (Basel)*. (2021) 13, 6–13. doi: 10.3390/cancers13112787

17. Berardi G, Ratti F, Sposito C, Nebbia M, D'Souza DM, Pascual F, et al. Model to predict major complications following liver resection for HCC in patients with metabolic syndrome. *Hepatology*. (2023) 77:1527–39. doi: 10.1097/HEP.0000000000000027

18. Cucchetti A, Casadei-Gardini A. Liver resection for HCC in patients with metabolic syndrome: questions answered, questions raised. *Hepatology*. (2023) 77:1463–4. doi: 10.1097/HEP.0000000000000034

19. Lee S, Mardinoglu A, Zhang C, Lee D, Nielsen J. Dysregulated signaling hubs of liver lipid metabolism reveal hepatocellular carcinoma pathogenesis. *Nucleic Acids Res*. (2016) 44:5529–39. doi: 10.1093/nar/gkw462

20. Bai WD, Liu JY, Li M, Yang X, Wang YL, Wang GJ, et al. A novel cuproptosis-related signature identified DLAT as a prognostic biomarker for hepatocellular carcinoma patients. *World J Oncol*. (2022) 13:299–310. doi: 10.14740/wjon1529

21. Zhang P, Zhao JH, Yuan LX, Ju LL, Wang HX, Wang F, et al. DLAT is a promising prognostic marker and therapeutic target for hepatocellular carcinoma: a comprehensive study based on public databases. *Sci Rep*. (2023) 13:17295. doi: 10.1038/s41598-023-43835-y

22. Ke C, Dai S, Xu F, Yuan J, Fan S, Chen Y, et al. Cuproptosis regulatory genes greatly contribute to clinical assessments of hepatocellular carcinoma. *BMC Cancer*. (2023) 23:25. doi: 10.1186/s12885-022-10461-2

23. Li Z, Zhou H, Zhai X, Gao L, Yang M, An B, et al. MELK promotes HCC carcinogenesis through modulating cuproptosis-related gene DLAT-mediated mitochondrial function. *Cell Death Dis*. (2023) 14:733. doi: 10.1038/s41419-023-06264-3

frontiers | Frontiers in Immunology

TYPE Original Research
PUBLISHED 10 July 2024
DOI 10.3389/fimmu.2024.1430551

OPEN ACCESS

EDITED BY
Bing Yang,
Tianjin Medical University, China

REVIEWED BY
Zhijia Xia,
Ludwig Maximilian University of Munich, Germany
Jun Hu,
Tianjin Medical University Cancer Institute and Hospital, China
Beibei Jiang,
Peking University, China

*CORRESPONDENCE
Qiang Guo
gqkj003@sina.com
Hui Tang
htang1122@aliyun.com

†These authors have contributed equally to this work

RECEIVED 10 May 2024
ACCEPTED 03 June 2024
PUBLISHED 10 July 2024

CITATION
Hu YL, Wang K, Chen Y, Jin Y, Guo Q and Tang H (2024) Causal relationship between immune cell phenotypes and risk of biliary tract cancer: evidence from Mendelian randomization analysis.
Front. Immunol. 15:1430551.
doi: 10.3389/fimmu.2024.1430551

Causal relationship between immune cell phenotypes and risk of biliary tract cancer: evidence from Mendelian randomization analysis

YaLan Hu[1†], Kui Wang[1,2†], Yuhua Chen[3†], Yongli Jin[4†], Qiang Guo[1*] and Hui Tang[1*]

[1]Department of Gastroenterology, The First People's Hospital of Yunnan Province, The Affiliated Hospital of Kunming University of Science and Technology, Kunming, Yunnan, China, [2]Department of Gastroenterology, Qilu Hospital of Shandong University, Jinan, Shandong, China, [3]The First Clinical Medical College, Lanzhou University, Lanzhou, China, [4]Department of Anesthesiology, Yanbian University Hospital, Yanji, China

Background: Biliary tract cancer stands as a prevalent illness, posing significant risks to human health, where immune cells are pivotal in both its development and recovery processes. Due to the diverse functionalities exhibited by different immune cell phenotypes within the organism, and the relatively limited research on their relationship with biliary tract cancer, this study employed Mendelian randomization (MR) to explore their potential association, thereby aiding in a better understanding of the causal link between immune cell phenotypes and biliary tract cancer.

Methods: In this study, the causative association of 731 immunophenotype with biliary tract cancer was established using publicly accessible genome-wide association study (GWAS) genetic data through two-sample MR analysis. Sensitivity analyses assess horizontal pleiotropy and heterogeneity of the study findings.

Results: Among the 731 immunophenotypes examined, a total of 26 immune cell phenotypes were found to exhibit positive results, indicating a significant association with the risk of biliary tract cancer. We confirmed that among these 26 types of immune cells, there are primarily 13 types of B cells; three types of classical dendritic cells (CDCs), including CD80 on myeloid DC, HLA DR on myeloid DC, and Myeloid DC %DC; one type of mature stage T cell,CD4RA on TD CD4+; six types of regulatory T cells; and three types of myeloid cells.

KEYWORDS

immune cell phenotypes, Mendelian randomization (MR) analysis, biliary tract cancer, causal relationship, malignant tumors

Introduction

Biliary tract cancer (BTC) pertains to a neoplastic condition affecting the biliary system, involving the development of malignant tumors within its structures. This encompasses gallbladder cancer (GBC) and cholangiocarcinoma (CCA). Among them, CCA stands as the second most prevalent primary liver tumor worldwide, with its incidence steadily increasing over recent decades (1). Cholangiocarcinoma refers to the malignant proliferation of epithelial cells in the bile duct, forming tumors, according to its location in the bile duct, cholangiocarcinoma is classified into intrahepatic cholangiocarcinoma, hilar cholangiocarcinoma, and distal cholangiocarcinoma. Additionally, gallbladder cancer is a common malignant biliary tract cancer characterized by a mere 5% survival rate in late-stage patients (2, 3). On a global scale, the incidence of CCA varies significantly due to differences in living environments, dietary habits, geographical factors, and racial disparities. Several factors influence the incidence of biliary tract cancer, besides well-established age-related factors, these risk factors also include genetic, parasitic infections such as liver fluke, bacterial infections, smoking, alcohol consumption, dietary behaviors, and environmental factors, etc. Statistically, during the 2010–2014 timeframe, mortality rates from intrahepatic cholangiocarcinoma in men ranged between 1–2/100,000 person-years in the majority of countries (4). Due to its asymptomatic presentation, highly invasive nature, and chemotherapy resistance, the mortality rate of patients with bile duct cancer is concerning, accounting for 2% of all cancer-related deaths globally (5). In short, the mortality rate of biliary tract cancer is high, posing significant health risks, and imposing substantial financial burdens on many patients' families. Furthermore, despite progress in therapeutic approaches, the expected outcome of individuals diagnosed with biliary tract cancer remains notably grim, rate of survival over a five-year period falls within the range of 7% to 20% (1). Currently, therapeutic modalities for BTC mainly consist of Surgical treatment, Hepatic transplantation, Chemotherapeutic treatment, radiotherapy, and immunotherapy, etc. Tumor immunotherapy, is a burgeoning field internationally, with extensive research ongoing, Immunotherapy has shown superiority over Chemotherapeutic treatment and radiotherapy. Immunotherapy is increasingly recognized as one of the most promising therapeutic strategies for advanced cancer patients (6, 7).

With the development of medicine, the role of immune cell phenotypes has emerged as pivotal in cancer treatment. In the realm of immunotherapy research, there is interest in developing patient-specific immunotherapies based on tumor-infiltrating immune cell types and their characteristics. Numerous immunotherapies, such as immune checkpoint inhibitors or cellular immunotherapy, are utilized in cancer treatment, targeting diverse immune cell populations within the immune system (8, 9). Studies targeting immunotherapy for biliary tract tumors. Increasing evidence from biological research suggests a multifaceted and close interconnection between immune cells and biliary tract cancer (10). For example, Immune therapy targets for T cells in biliary tract cancer are very attractive. Studies have shown that T cell immunotherapy targets for gallbladder cancer are attractive, with adoptive cell transfer therapy (ACT) representing a prominent approach in cancer immunotherapy (11, 12). T cells, including CD4+ and CD8+ subsets, are key players in immunotherapy.CD4+ T cells support immune responses by acting as helper T cells, aiding in the proliferation and differentiation of CD8+ T cells into cytotoxic T lymphocytes, while also boosting the phagocytic activity of macrophages. The role of tumor-infiltrating CD8+ T lymphocytes in tumor development has been examined across various human malignancies (13–15). In biliary tract cancer, cytotoxic CD8+ T lymphocytes play a crucial role and are associated with cancer prognosis. The surface MHC I molecules of biliary tract cancer tumor cells present endogenous antigens to CD8+ T cells, which in turn produce interferon-γ to attack biliary tract cancer tumor cells. Furthermore, the production of cytokines by CD4+ T lymphocytes enables indirect inhibition of tumor growth. Within the epithelial tumor infiltration in biliary tract cancer, CD4+ and CD8+ T lymphocytes exhibit synergistic anti-tumor effects (15). Studies have found that patients with biliary tract cancer who have intraepithelial tumor-infiltrating CD4+, CD8+, and Foxp3+ T lymphocytes exhibit significantly longer overall survival (16). B lymphocytes can produce various types of antibodies to recognize tumor-specific antigens and antigens associated with tumors. In the tumor microenvironment of cholangiocarcinoma, tumor-associated Immune cells, including macrophages, B cell, and T cell interact with the tumor microenvironment to inhibit tumor formation. Immune cells significantly influence the regulation of distinct biological processes in CCA, encompassing invasion, angiogenesis, lymphangiogenesis, tumor growth, and metastasis, which are also associated with the clinical prognosis of this cancer (17). These investigations into the role of immune cells in biliary tract cancer offer novel insights into potential immunotherapeutic approaches for the condition. However, the precise relationship between specific immune cell types and biliary tract cancer remains insufficiently explored. In order to propel the progression of immunotherapeutic approaches for biliary tract cancer and ameliorate patient morbidity, this investigation chose to analyze the relationship between immune cell phenotypes and biliary tract malignancies. This helps to study the pathogenesis of biliary tract cancer, provide more methods for the treatment of biliary tract malignancies, and contribute to people's health.

Mendelian Randomization employs single nucleotide polymorphisms (SNPs) linked to exposure in publicly accessible Genome-Wide Association Study (GWAS) datasets as instrumental variables (IVs) to evaluate the potential causal link between exposure and outcome. Mendelian randomization is similar to randomized controlled trials and its analysis is rapid and inexpensive. The purpose of this method is to emulate a randomized controlled trial, thereby reducing the impact of potential confounders and reverse causation present in observational studies. And this method approach enhances causal inference regarding exposure-outcome associations (18, 19). Relatively little measurement error is associated with genetic variants and their effects. The present research employed a two-

sample MR analysis to explore the causal association between immune cell characteristics and biliary tract malignancies. We used SNPs linked to immune cell phenotypes as IVs and immune cell phenotypes as exposure.

Study design

Our study utilized a two-sample Mendelian Randomization analysis to investigate the potential causal relationship between immune cell phenotypes and biliary tract cancer with SNPs strongly correlated with Immunocyte phenotypes serving as IVs, immune cell phenotype as the exposure, and biliary tract cancer as the outcome. These SNPs were identified from extensively documented Genome-Wide Association Studies literature, with 731 immune cell phenotypes obtained from published Waste SNPs adhere to three key assumptions of Mendelian Randomization analysis, as illustrated in Figure 1: (1) Correlation hypothesis: SNPs exhibit a pronounced correlation with he phenotypes of immune cells; (2) Independence Assumption: SNP can only affect the biliary tract cancer through the immune cell phenotypes and not through any other pathways; (3) Assuming restriction: SNPs were found to be unrelated to confounding factors such as smoking and diet (20, 21). Moreover, their impact on the outcome is exclusively mediated by their effect on the exposure, precluding any alternative causal pathways. The analysis process is shown in Figure 2.

Materials and methods

Source of data

SNPs associated with immune cells and biliary tract cancer were derived from GWAS datasets. The database GWAS used in this study is open and accessible data, and the data involved in the research were approved by the respective local ethical committees. The data originate from the FinnGen 10 local download and can be accessed at the website (https://storage.googleapis.com/finngen-public-data-r10/summary_stats/finngen_R10_C3_BILIARY_GALLBLADDER_EXALLC.gz). Accession numbers ranging from ebi-a-GCST90001391 to ebi-a-GCST90002121 were obtained from the GWAS catalog, encompassing a total of 731 immune phenotypes (Supplementary Table S1), Correlation analyses were conducted using a reference panel derived from Sardinian genomic sequences, based on a dataset comprising 22 million SNPs.

These 731 immune cell phenotypes encompass B cells, classical dendritic cells (CDCs), mature stages of T cells, monocytes, regulatory T cells (Tregs), myeloid cells, and TBNK cells. And these 731 immune cell phenotypes have four distinct immunological patterns:absolute cell counts (AC) encompassing 118, relative cell counts (RC) comprising 92, morphological parameters (MP) consisting of 32, and median fluorescence intensity (MFI) reflects the levels of surface antigens, with 389. Both immune cell and cholangiocarcinoma data are derived from European populations. Biliary tract cancer data include 1207 cases and 314,193 controls from European populations.

Instrument variables selection

For the instrumental variables(IV) used in MR, three main hypotheses are satisfied. The selection criteria for IV linked to immune cell phenotypes are as follows: The threshold for single nucleotide polymorphisms associated with cell phenotypes is set at a p-value less than 1×10^{-5}. Although a p-value$< 5\times10^{-8}$ is less stringent than p-value$< 5\times10^{-8}$ (22, 23), the small quantity of SNPs meeting the $< 5\times10^{-8}$ criterion is inadequate for subsequent analyses (24, 25). In SNP selection, those with lower Minor Allele Frequency (MAF) are filtered out from the analysis due to their potentially minor impact on immune cell phenotypes, which could

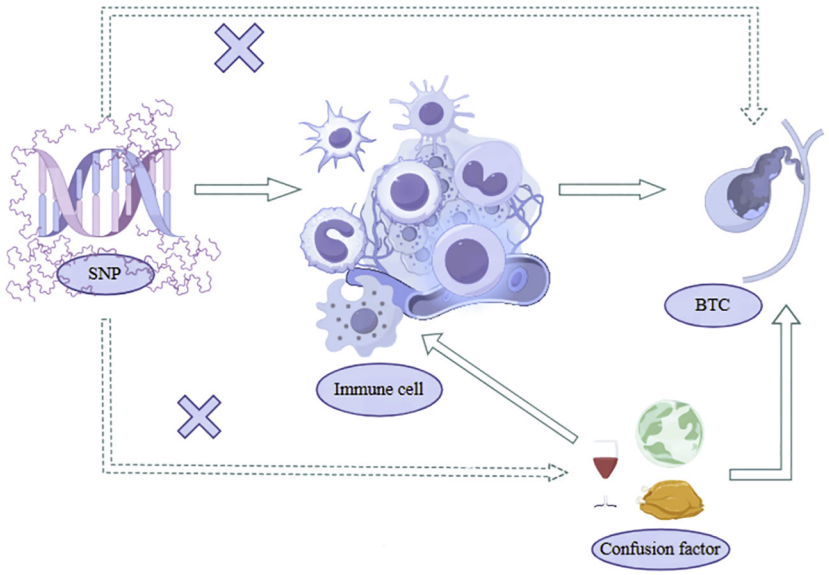

FIGURE 1
Three key assumptions of Mendelian randomization.

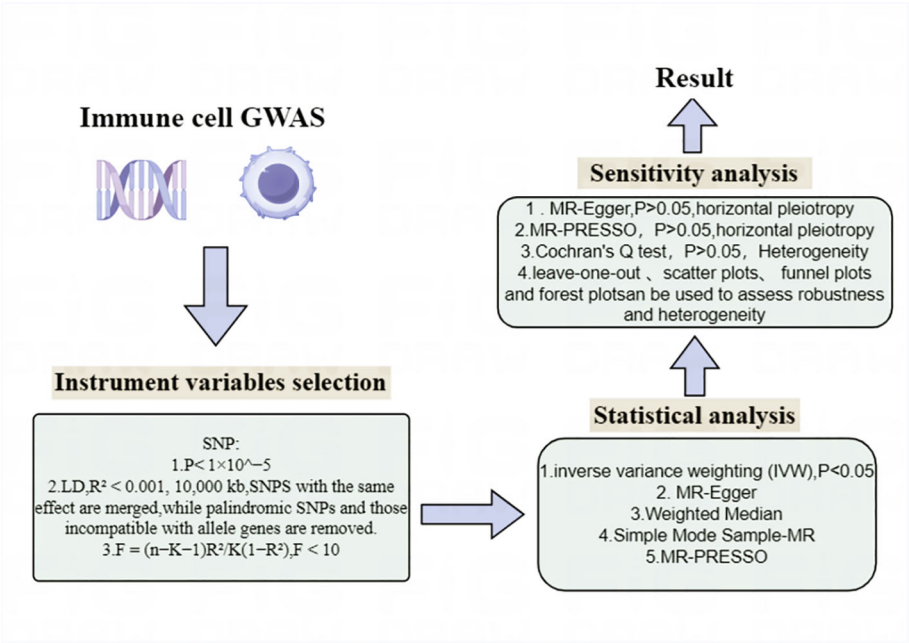

FIGURE 2
MR analysis process.

increase the risk of false positives. A threshold of 0.01 is set for MAF, and SNPs with MAF greater than 0.01 are retained for analysis. Additionally, by utilizing Phenoscanner for the identification of SNPs potentially linked to confounding factors, the exclusion of such SNPs serves to diminish the interference posed by these factors. This, in turn, enables a more accurate inference of causal relationships between exposure variables and outcomes. Due to the potential presence of linkage disequilibrium (LD) in SNPs, which will affect the analysis results, it is necessary to eliminate or weaken the impact of linkage disequilibrium, and remove linkage disequilibrium to obtain more precise and dependable outcomes. To attain analysis results with enhanced precision and reliability, the standard for testing LD is set at (R^2 < 0.001, 5000 kb) (26), where SNPs with R^2 greater than 0.001 within a 5000 kb range are removed. SNPS with the same effect are merged, while palindromic SNPs and those incompatible with allele genes are removed. Subsequently, each instrumental variable is evaluated using an F-test,calculating the F-statistic for each SNP.The formula for calculating F is $F = (n-K-1)R^2/K(1-R^2)$, where the F-statistic threshold is used to determine IV effectiveness, set at F > 10.SNPs with F < 10 are considered weak instrumental variables and are removed.After filtering, only robust instrumental variables with F-values exceeding 10 remain, ensuring a more rigorous analysis. Finally, SNPs related to biliary tract cancer that meet the specified criteria are obtained (Supplementary Table S2).

Statistical analysis

Statistical analysis was performed utilizing R software (Version 4.2.2), augmented by the TwosampleMR package (Version 0.56), to explore the association between 731 immune cell phenotypes and biliary tract cancer via a series of Mendelian randomization analyses. This research employed various MR analysis techniques, encompassing MR-Egger, Weighted mode, Simple mode, Weighted median, and Inverse variance weighted (IVW). Among these, IVW is often preferred as the main analytical approach due to its ability to minimize the effects of confounding factors when assessing the impact of genotypes on outcome variables, thereby enhancing the accuracy of the results. For SNPs with a *P*-value exceeding 0.05 in the IVW analysis, indicating no effect, they should be excluded, leaving only SNPs with a *P*-value below 0.05. Subsequently, sensitivity analyses were conducted, primarily examining horizontal pleiotropy and heterogeneity. Horizontal pleiotropy was assessed using MR-Egger and MR-PRESSO global tests. The intercept and *P*-value from MR-Egger can be used to assess horizontal pleiotropy, where a non-zero intercept with a *P*-value less than 0.05 suggests the presence of horizontal pleiotropy. The MR-PRESSO global test is a method for detecting horizontal pleiotropy, identifying and adjusting for outliers and potential horizontal pleiotropy in MR analysis.A *P*-value less than 0.05 indicates the presence of horizontal pleiotropy, with the global test's *P*-value also set at (P > 0.05). Heterogeneity was assessed using Cochran's Q test, and the *P* value of Cochran's Q test was set to (P>0.05) (Supplementary Table S3). The presence of outlier data points can be evaluated through scatter plots, validating horizontal pleiotropy. A sensitivity analysis, conducted by leaving out one SNP at a time, was performed to evaluate the individual impact of SNPs to the overall causal effect. Leave-one-out sensitivity analysis, funnel plots, and forest plots verify heterogeneity and robustness (Figure 3; Supplementary Figure)

10.3389/fimmu.2024.1430551

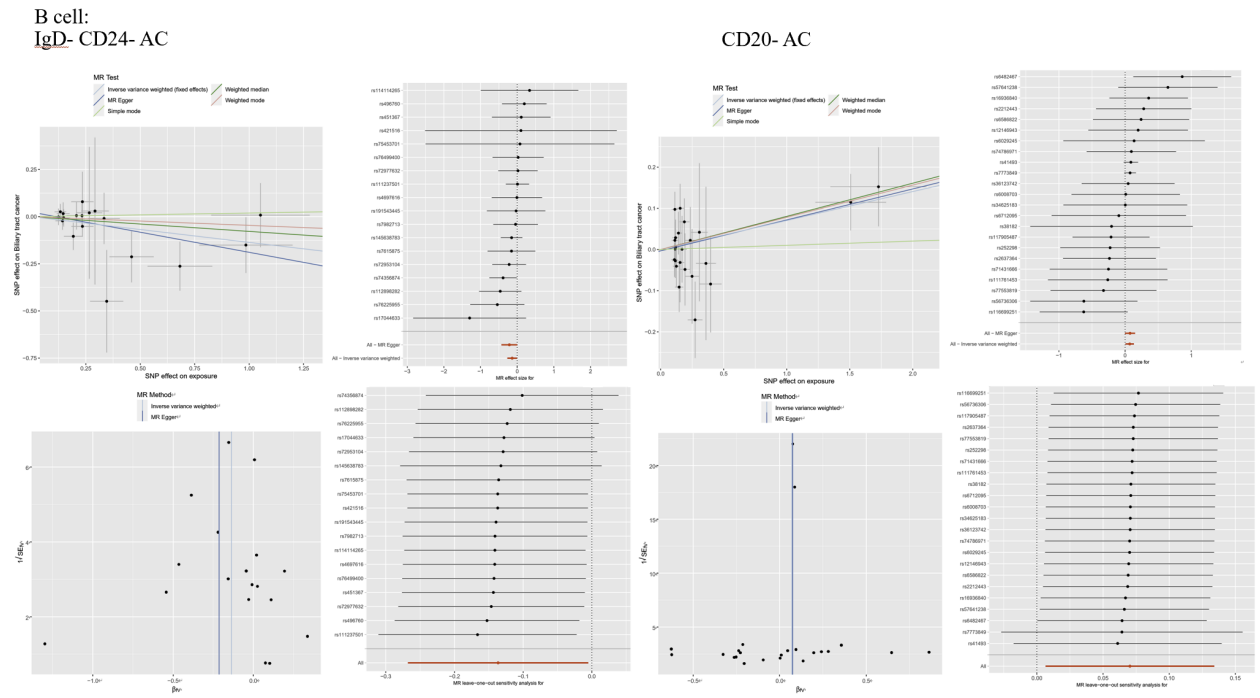

FIGURE 3
Immunophenotype and MR Analysis of Biliary Tract Cancer: **(A)** Scatter plot, forest plot, funnel plot.and sensitivity analysis of the risk association between B cell laD- CD24- AC and biliary tractcancer. **(B)** Scatter plot, forest plot, funnel plot, and sensitivity analysis of the risk association between B cellaD-CD20- AC and biliary tract cancer.

Results

Exploration of the causal effect of immune cell phenotypes on biliary tract cancer

This research aimed to analyze the causal link between immune cell phenotypes and biliary tract cancer. Following a comprehensive series of MR analyses on 731 immune cell phenotypes, detailed specifics for each immune cell phenotype were obtained, as outlined in Supplementary Table S2. Through IVW and sensitivity analyses, as well as assessments for horizontal pleiotropy and heterogeneity, and with an F-statistic > 10,26 types of immune cell phenotypes were finally positive, which means that among 731 types of immune cell phenotypes, 26 types of immune cell phenotypes were associated with biliary tract cancer. Among these, we confirmed that 13 were B cells, three were classical dendritic cells, including Myeloid DC %DC, CD80 on myeloid DC, and HLA DR on myeloid DC, one was CD4RA on TD CD4+ representing a mature stage of T cells, six were regulatory T cells, and three were myeloid cells (Figure 4). Details are provided in Supplementary Table S3 (Supplementary Tables S3, S4).

Causal relationship between immunophenotypes of B cells and biliary tract cancer

Thirteen immune cell phenotypes of B cells were found to be associated with biliary tract cancer. Among these,six B cell immune phenotypes exhibited positive associations with biliary tract cancer as detected by the IVW method. The IVW findings exhibited significance, consistent with the results obtained from MR-Egger, Weighted Median, and Weighted Mode analyses. Similarly, the risk estimation for biliary tract cancer by CD25 on CD24+ CD27+ was 1.04, CD25 on CD24+ CD27+ showed a significant association with biliary tract cancer risk (OR=1.04, 95% CI=1.01–1.08, *P*=0.0074). The IVW analysis of CD25 on IgD+ CD38- naive (OR=1.08, 95% CI=1.01–1.16, *P*=0.025) indicated an increased risk of biliary tract cancer. Furthermore, IVW analysis revealed positive correlations between biliary tract cancer and CD27 on CD20- CD38- (OR=1.14, 95% CI=1.02–1.28, *P*=0.0198), as well as IgD on IgD+ CD38- unsw mem (OR=1.12, 95% CI=1.03–1.23, *P*=0.01), IgD on IgD+ CD38br (OR=1.10, 95% CI=1.01–1.20, *P*=0.034), and IgD on IgD+ (OR=1.11, 95% CI=1.01–1.22, *P*=0.02). On the contrary, we identified six B cell immune phenotypes that exhibited a negative correlation with biliary tract cancer. Through IVW analysis, their respective odds ratios (ORs) were 0.87, 0.93, 0.91, 0.92, 0.85, and 0.96. The immunophenotype OR values of these immune cells were all <1, indicating that they were negatively correlated with the biliary tract cancer and had a protective effect against reduced biliary tract cancer risk. These findings were consistent across IVW analysis and other methods including MR-Egger, Weighted Median, and Weighted Mode analyses (Figure 4).

Immunophenotypes of CDC and biliary tract cancer

The IVW analysis for classical dendritic cells revealed that CD80 on myeloid dendritic cells had an IVW result of (OR=1.09,

10.3389/fimmu.2024.1430551

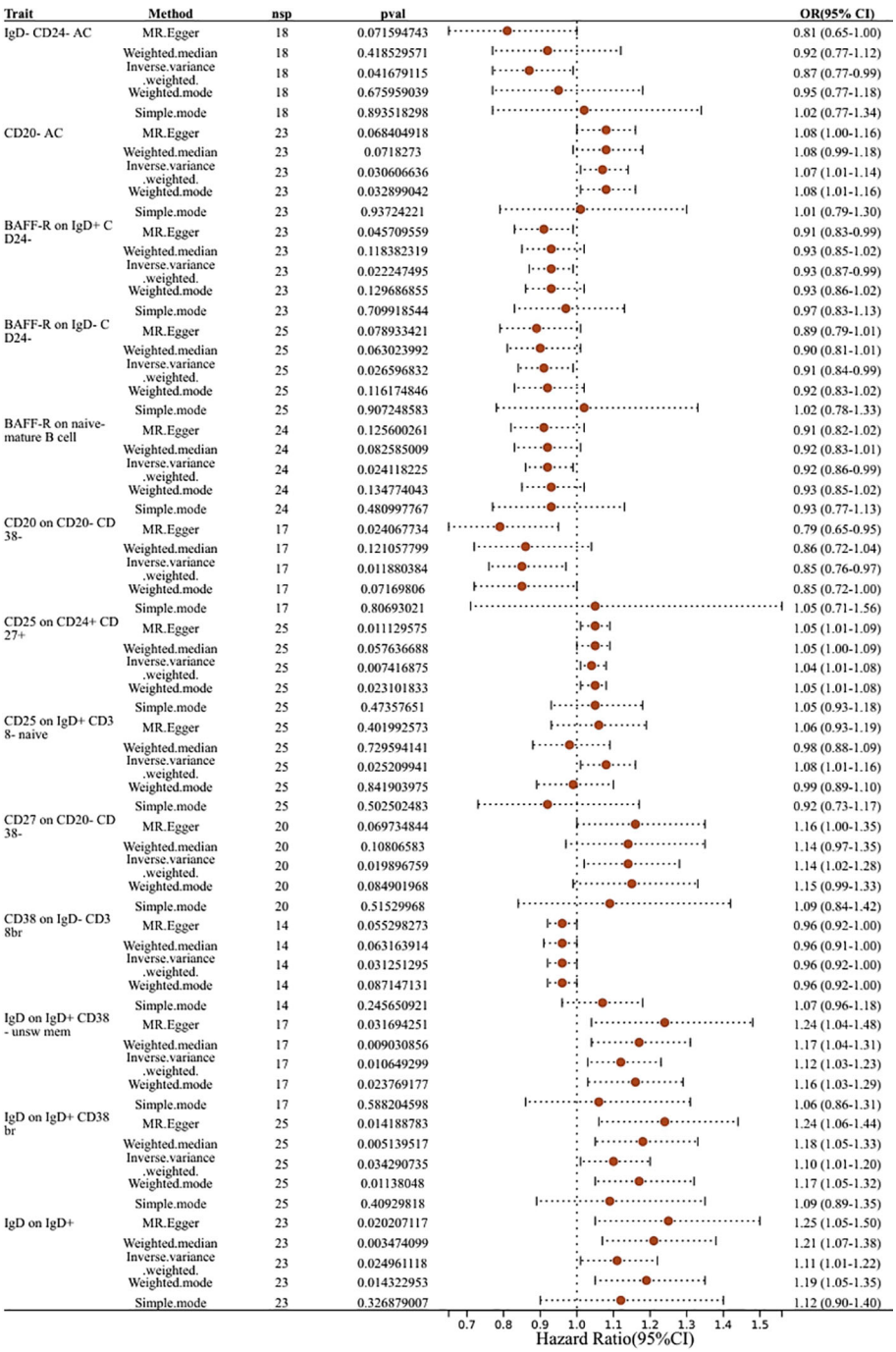

FIGURE 4
Forest plots showed the causal effect of B cell immunophenotypes on biliary tract cancer. nsnp, nonsynonymoussingle-nucleotide polymorphism; OR, odds ratio; CI, confidence interval; P yalye, IVW analysis results P value.

95% CI=1.00–1.19, *P*=0.04), indicating a positive correlation with biliary tract cancer as OR > 1 suggests. Conversely, Immune phenotypes associated with a protective effect against reduced biliary tract cancer risk include HLA DR on myeloid DC and Myeloid DC %DC. The effect size for HLA DR on myeloid DC was (OR=0.94, 95% CI=0.88–1.00, *P*=0.046), while Myeloid DC %DC was detected as (OR= 0.88, 95% CI=0.79–0.98, *P*=0.024), with OR < 1 indicating a negative correlation with biliary tract cancer. These findings regarding the phenotypes of classical dendritic cells are consistent across IVW effects and other MR analysis method (Figure 5).

Immunophenotyping of T cells in relation to biliary tract cancer

In the mature stage of T cells, only one immunophenotype of T-cells in the maturation stage was negatively associated with risk

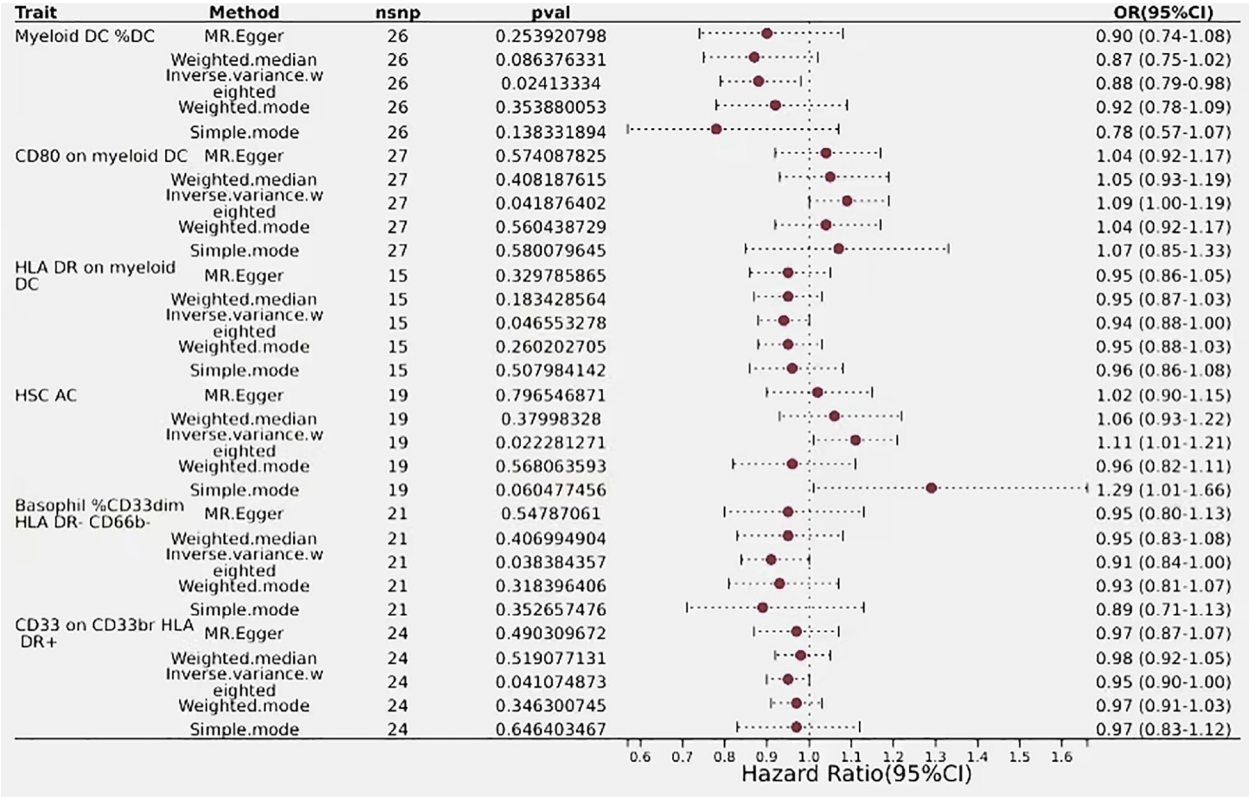

FIGURE 5
Forest plots showed the causal effect of T cells immunophenotypes on biliary tract cancer. nsnp, nonsynonymous single-nucleotide polymorphism; OR, odds ratio; CI, confidence interval; P value, IVW analysis results P value.

of biliary tract cancer, CD4RA on TD CD4+, which was protective against a reduced risk of biliary tract cancer, as detected by an OR<1 (OR=0.95, 95% CI=0.90–1.00, *P*=0.034). Additionally, six immune phenotypes associated with regulatory T cells showed positive detection results, indicating a causal relationship with biliary tract cancer, with the majority of these phenotypes demonstrated protective properties, while only one immune trait was identified as a risk factor. The detection result for CD45RA- CD28- CD8br%CD8br was an odds ratio of 1 (95% CI=1.00–1.00, *P*=0.009), with similar outcomes observed using MR-Egger and Weighted Median,indicating that this immunophenotype has no impact on the risk of biliary tract cancer. Conversely, CD39+ resting Treg %resting Treg exhibited a negative correlation with biliary tract cancer risk, with a detection result of (OR=0.92, 95% CI=0.85–0.99, *P*=0.034), suggesting an association with an increased risk of biliary tract cancer, thus representing a risk factor for the disease. Regulatory T cells with similar outcomes included CD28 on CD4+ (OR=0.91, 95% CI=0.84–0.99, *P*=0.02), CD25 on CD39+ activated Treg (OR=0.87, 95% CI=0.78–0.97, *P*=0.01), CD25 on CD39+ secreting Treg (OR=0.93, 95% CI=0.88–1.00, *P*=0.036), and CD4 on CD39+ resting Treg (OR=0.89, 95% CI=0.81–0.99, *P*=0.028), all of which had a predictive outcome OR of less than 1 and were protective factors for a reduced risk of biliary tract cancer (Figure 6).

Immunophenotype of myeloid cells in relation to biliary tract cancer

The estimated effect of HSC AC on biliary tract cancer was determined to be (OR=1.11, 95% CI=1.01–1.21, *P*=0.02), with OR > 1 indicating a positive correlation with an increased risk of biliary tract cancer, thus serving as a risk factor. Results from the Weighted Median and MR-Egger methods also support this relationship. Basophil %CD33dim HLA DR- CD66b- (OR=0.91, 95% CI=0.84–1.00, *P*=0.038) and CD33 on CD33br HLA DR+ (OR=0.95, 95% CI=0.90–1.00, *P*=0.04) from the myeloid lineage showed a negative correlation with biliary tract cancer risk, indicating an association with a decreased risk of biliary tract cancer (Figure 5).

Discussion

We conducted a study to investigate the association between 731 immune cell phenotypes and biliary tract cancer. Through a series of MR analyses following strict criteria, we pinpointed 26 Immunocyte phenotypes correlation with biliary tract cancer. This is also the first study to explore the genetic contributions of these 26 immune cell phenotypes to biliary tract cancer.

In tumors, T lymphocytes and B lymphocytes exert inhibitory effects on tumor progression, which correlates with the prognosis of

10.3389/fimmu.2024.1430551

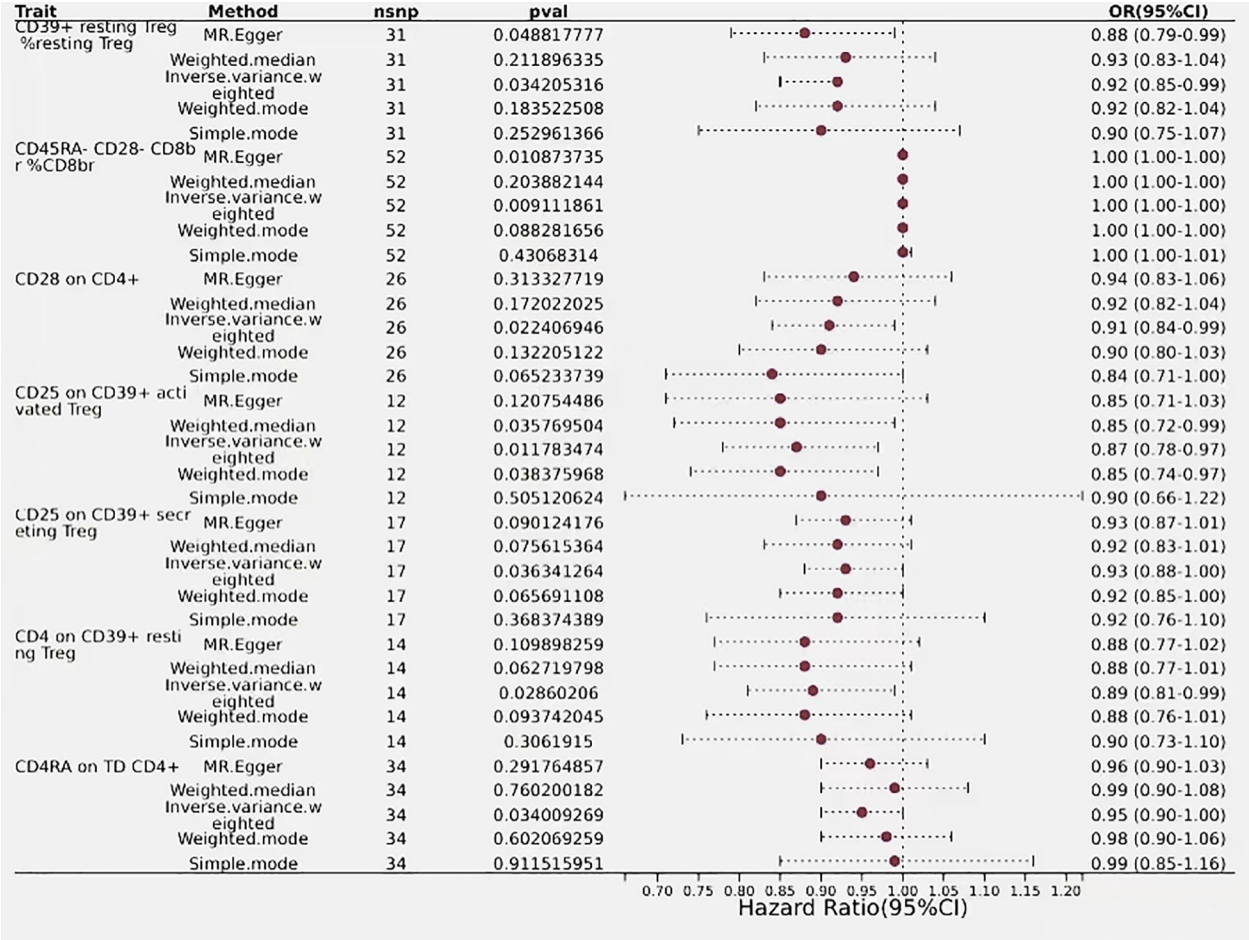

FIGURE 6
Forest plots showed the causal effect of CDC and myeloid cells immunophenotypes on biliary tract cancer, nsnp, nonsynonymous single-nucleotidepolymorphism; OR, odds ratio; CI,confidence interval; P value, IVW analysis results P value.

biliary tract malignancies patients. Within the framework of biliary tract cancer, tumors infiltrated by immune cells trigger an immune response (27, 28), and these immune cells infiltrating the tumor include T cells, B cells, myeloid cells, natural killer(NK) cells, dendritic cells, and macrophages, which interact with each other to generate an immune response to inhibit tumor progression. Tumor-infiltrating lymphocytes (TILs) play a pivotal role in fostering anti-tumor immune responses by detecting tumor antigens and executing the destruction of tumor cells (29). Among these immune cells infiltrating the tumor, T cells and B cells are the primary cells involved in anti-tumor activity and are also the main cells generating immune responses. B cells have the capability to produce antibodies and participate in immune responses through various mechanisms. This research indicates a significant negative relationship between CD20 on expression of CD20 on B cells and the risk of biliary tract cancer. The results indicate that elevated levels of CD20 on B cells could potentially exert a protective influence against the onset of biliary tract cancer. Within the phenotype of immune cells expressing CD20 on CD20- CD38-, B cells exert a protective effect against biliary tract cancer risk, whereas cells lacking CD20 expression such as CD20- AC and CD27 on CD20- CD38- promote the risk of biliary tract cancer. CD20, a surface molecule on B cells, is expressed at almost every stage of B cell development. Its expression is crucial for aiding in the development, maturation, and activation of B cells, playing a vital role in the regulation of B cell functions. CD20 is not known to have a natural ligand. Its primary function is to enhance B cell immune responses, playing a pivotal part in the initiation of T cell independent antibody responses (30). Kasper et al. found a significant increase in CD20+ B cell abundance within the TILs of Intrahepatic cholangiocarcinoma (ICC) patients infected with EB virus, the heightened density of CD20+ B cells correlates significantly with extended survival rates in ICC (31). Additionally, upon binding with antibodies, CD20 is capable of generating signals that regulate cell proliferation and programmed cell death in diverse cell types, including neoplastic cells (32). It is noteworthy that anti-CD20 therapies are applicable across various diseases, with several pharmaceutical companies investing in robust research on CD20. CD20 antibodies currently represent one of the most successful anti-tumor treatment strategies. Moreover, the heightened occurrence of CD20+ B cells shows a positive correlation with the clinical outcomes of patients afflicted with breast cancer, melanoma, colon cancer, and biliary tract cancer (33). These research elucidate the role of CD20 in

inhibiting the progression of biliary tract cancer, consistent with our research findings predicting a correlation between. The results of the current study show that BAFF-R on IgD+ CD24-, BAFF-R on IgD- CD24-, and BAFF-R on naive-mature B cells are inversely associated with biliary tract cancer, contributing to the prognosis of patients with this condition. Conversely, the expression of CD24 on CD25+ CD24+ CD27+ B cells is positively correlated with biliary tract cancer, confirming CD24 as a risk factor and BAFF-R (B-cell activating factor receptor) as a protective factor.BAFF-R is a surface receptor found on B cells that specifically binds to BAFF. This interaction fosters the viability, proliferation, and differentiation of B cells. BAFF transmits co-stimulatory cues to T cells, fostering inflammation through the Th1/Th17 pathways (34). BAFF functions as a co-stimulatory signal that assists in the activation of both naïve and memory CD4 and CD8 T cells (35–37). CD4 and CD8 T cells are pivotal in orchestrating anti-tumor immunity in the biliary tract cancer microenvironment (38–40). These findings underscore the importance of the interaction between BAFF-R on the surface of B cells and BAFF for their normal function and immune responses, particularly in tumor immunity. BAFF-R emerges as a protective factor in reducing the risk of biliary tract cancer. Tumor-initiating cells (CSCs), alternatively termed as tumor stem cells,exhibit drug-resistant, can metastasize and spread, which is the key to tumor development, metastasis as well as recurrence. And CD24 is one of the markers expressed by tumor stem cells. Evidence suggests that 20%-30% of CCA tumors express cancer stem cell markers, heightening the risk of tumor progression and recurrence among patients with unfavorable prognoses (41). Furthermore, CD24 overexpression in primary gallbladder carcinoma (GBC) correlates with Lymph node spread and invasion into lymphatic and vascular channels, and the worst prognosis was observed in patients with primary gallbladder carcinoma who were in the CD24+ subgroup (42). Studies have indicated that CD24 serves as a notable indicator of malignancy and predictor of poor outcomes in GBC (43). These studies are consistent with our analysis, demonstrating that CD24 is a risk factor for biliary tract cancer.Additionally, research has revealed a positive correlation between CD25 on IgD+ CD38- naive B cells and biliary tract cancer.

The detection of CD4RA on TD CD4+ within mature T cells showed an inverse link with the risk of cholangiocarcinoma. Specifically, it is the CD4+ T cells that express CD4 during the mature stage. This study implies an association between CD4RA+CD4+ T cells and a decreased risk of biliary tract cancer. In addition to promoting clonal expansion, CD4 T cells are also involved in the differentiation of CD8 T cells into effectors and effector/memory cells (44). Activated CD4 T cells provide not only CD40L, but also IFN-I, which act nonredundantly to cross-prime cDC1s against tumor cell-associated antigens (45). A follow-up investigation involving 306 individuals diagnosed with biliary tract cancers demonstrated a positive correlation between longer overall survival (OS) and increased tumor infiltration of total CD4+ tumor-infiltrating lymphocytes (46). Helper T cells that express CD4RA+CD4+ acquire the capability to recognize CD4 antigen peptides consisting of amino acid residues. Upon activation, naive CD4RA+CD4+ T cells can differentiate into different types of Th cells (e.g., Th1, Th2, Th17), which can present antigens and secrete cytokines to promote inflammation and promote the proliferation. Moreover, they have the capacity to stimulate CD8+ T cells, guiding them toward targeted tumor cell destruction, while also fostering B cell differentiation, thereby enhancing the immune response. They exhibit a suppressive effect on the progression of biliary tract malignancies. The immunophenotypes of regulatory T cells, including CD28 on CD4+, CD4 on CD39+ resting Treg, CD4 on CD39+ resting Treg, and CD39+ resting Treg % resting Treg, CD25 on CD39+ activated Treg, exhibit a significant causal relationship with biliary tract cancer, serving as protective factors against its development. This underscores the association between CD4-expressing regulatory T cells and biliary tract cancer. Biliary tract cancer typically arises from conditions such as gallstones, pancreaticobiliary maljunction (PBM), or infrequently, gallbladder polyps. These malignancies are frequently associated with chronic inflammation (47). CD4+ Tregs are crucial in inflammation-linked diseases, exerting a suppressive impact on inflammatory responses within the tumor microenvironment (TME) (48–50). In addition, studies have shown that CD39 Tregs efficiently suppress T cell proliferation and the secretion of inflammatory cytokines like interferon (IFN)-γ and interleukin (IL)-17 (51, 52). In the context of biliary tract cancer inflammation, immune cells may mitigate immune inflammation, thereby potentially reducing tumor growth and metastatic potential within the tumor microenvironment.Thus, the increased expression of CD4 or CD39 regulatory T cells contributes to dampening inflammation in biliary tract cancer.

Our study determined that myeloid DC %DC and myeloid dendritic cell HLA DR were protective factors for biliary tract cancer.Myeloid dendritic cells assume a central role in the process of antigen presentation, wherein they capture, process, and present antigens to T cells, thereby instigating and coordinating adaptive immune responses.Moreover, myeloid DCs participate in the activation and differentiation of diverse subsets of immune cells. they endowed with the remarkable ability to activate both cytotoxic CD8+ T cells and helper CD4+ T cells (53–55). In patients with biliary tract cancer, those with dendritic cells tend to survive longer compared to those without DC (56). The study indicates that biliary tract cancer patients with myeloid dendritic cells have a more hopeful prognosis for treatment. DCs capable of initiating specific cellular responses against tumor and infectious antigens within the context of humoral immunity (57). The antigen presentation molecule HLA-DR expressed on myeloid dendritic cells plays a pivotal role in immune response, HLA-DR is a crucial antigen presentation molecule.Myeloid DC expression of HLA-DR DCs enhances their antigen presentation capacity, facilitating the immune system's response to infections and diseases.In addition,basophil% CD33dim HLA DR - CD66b -CD33 on CD33br HLA DR+ and CD33 on CD33br HLA DR+ are negatively correlated with biliary cancer, while CD80 on myoid DC is positively correlated with biliary cancer. The research on these immune phenotypes is not very clear. Moreover, HSC AC in Myeloid cells is a risk factor for biliary cancer. Evidence suggests that cancer-associated fibroblasts (CAFs), derived from hepatic stellate cells (HSCs), facilitate the growth of intrahepatic cholangiocarcinoma by releasing hepatocyte growth factor via direct

interaction in the HSC-CAFa-tumor pathway, thus activating the tumor-expressed MET pathway (58).

Our study's strength lies in being the first to conduct MR analysis on the correlation between Immunotherapy and biliary tract malignancies. The results, Incorporating genetic factors and GWAS data, underwent rigorous assessments for horizontal pleiotropy and heterogeneity, thereby reducing confounding factors' interference. We identified 26 immune cell phenotypes associated with biliary tract cancer, providing novel insights and avenues for exploring treatments, potential targets, and prognosis in biliary tract cancer research. However, In the aggregated data of GWAS, Analyzing overarching determinants such as age and gender in segmented form is impractical due to inherent limitations. Additionally, Our study is limited in its scope to the European population, thereby restricting the generalizability of findings to broader demographic cohorts. GWAS data from different populations or regions may exhibit significant disparities, leading to variations in the distribution and impact of various overarching determinants, including age and gender, across different demographic groups. And, we only explored the causal correlation between immunophenotypes and biliary tract malignancies, without delving into their mechanisms.In future research, our aim is to significantly increase the sample size and broaden the scope to include diverse populations. This will enable us to offer more robust theoretical support for understanding the mechanisms linking immunophenotypes and biliary tract malignancies.

Conclusion

This study elucidates the causal relationship between immune cell phenotypes and biliary tract cancer, identifying 26 immune cell phenotypes associated with biliary tract cancer. Specifically, it highlights the association of B cells expressing CD20 and BAFF-R with reduced biliary tract cancer risk, while CD4RA+CD4+ T cells exhibit anti-tumor effects in biliary tract cancer. Conversely, Certain immunophenotypes of regulatory T cells that inhibit immune inflammation serve as protective factors against biliary tract cancer.Additionally, myeloid DCs show a negative correlation with biliary tract cancer, whereas HSC AC in Myeloid cells promotes biliary tract cancer tumor development. These discoveries offer valuable comprehension of Potential pathways and therapeutic targets for understanding and studying biliary tract cancer. A comprehensive understanding of the intricate pathways involved and potential intervention points is crucial for advancing research in this area.

Data availability statement

The original contributions presented in the study are included in the article/Supplementary Material. Further inquiries can be directed to the corresponding authors.

Ethics statement

The studies involving humans were approved by The First People's Hospital of Yunnan Province. The studies were conducted in accordance with the local legislation and institutional requirements. The human samples used in this study were acquired from primarily isolated as part of your previous study for which ethical approval was obtained. Written informed consent for participation was not required from the participants or the participants' legal guardians/next of kin in accordance with the national legislation and institutional requirements. Written informed consent was obtained from the individual(s) for the publication of any potentially identifiable images or data included in this article.

Author contributions

YH: Writing – original draft, Data curation, Formal analysis, Investigation, Methodology, Project administration, Software, Supervision, Validation, Writing – review & editing. KW: Data curation, Formal analysis, Investigation, Methodology, Project administration, Software, Supervision, Validation, Writing – original draft, Writing – review & editing. YC: Formal analysis, Investigation, Methodology, Project administration, Writing – review & editing. YJ: Investigation, Methodology, Project administration, Software, Supervision, Validation, Writing – review & editing. QG: Data curation, Investigation, Project administration, Resources, Supervision, Validation, Visualization, Writing – review & editing. HT: Conceptualization, Formal analysis, Funding acquisition, Methodology, Project administration, Resources, Supervision, Validation, Visualization, Writing – review & editing.

Funding

The author(s) declare financial support was received for the research, authorship, and/or publication of this article. This study was supported by National Natural Science Foundation of China [No.82260483]; Yunnan Provincial Department of Science and Technology Foundation for Applied Basic Research [202301AS070015].

Acknowledgments

We express our sincere gratitude to the MiBioGen Consortium and the GWAS Catalog database for generously sharing their GWAS summary data, which greatly facilitates our research endeavors. Additionally, we appreciate the expert assistance in figure preparation provided by Figdraw (www.figdraw.com).

Conflict of interest

The authors declare that the research was conducted in the absence of any commercial or financial relationships that could be construed as a potential conflict of interest.

Publisher's note

All claims expressed in this article are solely those of the authors and do not necessarily represent those of their affiliated organizations, or those of the publisher, the editors and the reviewers. Any product that may be evaluated in this article, or claim that may be made by its manufacturer, is not guaranteed or endorsed by the publisher.

Supplementary material

The Supplementary Material for this article can be found online at: https://www.frontiersin.org/articles/10.3389/fimmu.2024.1430551/full#supplementary-material

References

1. Steffani M, Nitsche U, Ollesky J, Kaufmann B, Schulze S, Novotny A, et al. Liver fibrosis is associated with poorer overall survival and higher recurrence rate in patients with cholangiocarcinoma. *Dig Surg*. (2024) 41:53–62. doi: 10.1159/000535733

2. Li Y, Yuan R, Ren T, Yang B, Miao H, Liu L, et al. Role of Sciellin in gallbladder cancer proliferation and formation of neutrophil extracellular traps. *Cell Death Dis*. (2021) 12:30. doi: 10.1038/s41419-020-03286-z

3. Wang Z, Wang S, Jia Z, Hu Y, Cao D, Yang M, et al. YKL-40 derived from infiltrating macrophages cooperates with GDF15 to establish an immune suppressive microenvironment in gallbladder cancer. *Cancer Lett*. (2023) 563:216184. doi: 10.1016/j.canlet.2023.216184

4. Bertuccio P, Malvezzi M, Carioli G, Hashim D, Boffetta P, El-Serag HB, et al. Global trends in mortality from intrahepatic and extrahepatic cholangiocarcinoma. *J Hepatol*. (2019) 71:104–14. doi: 10.1016/j.jhep.2019.03.013

5. Banales JM, Marin J, Lamarca A, Rodrigues PM, Khan SA, Roberts LR, et al. Cholangiocarcinoma 2020: the next horizon in mechanisms and management. *Nat Rev Gastroenterol Hepatol*. (2020) 17:557–88. doi: 10.1038/s41575-020-0310-z

6. Ilyas SI, Affo S, Goyal L, Lamarca A, Sapisochin G, Yang JD, et al. Cholangiocarcinoma - novel biological insights and therapeutic strategies. *Nat Rev Clin Oncol*. (2023) 20:470–86. doi: 10.1038/s41571-023-00770-1

7. Ruiz-Cordero R, Devine WP. Targeted therapy and checkpoint immunotherapy in lung cancer. *Surg Pathol Clin*. (2020) 13:17–33. doi: 10.1016/j.path.2019.11.002

8. Hadfield MJ, DeCarli K, Bash K, Sun G, Almhanna K. Current and emerging therapeutic targets for the treatment of cholangiocarcinoma: an updated review. *Int J Mol Sci*. (2023) 25(1):543. doi: 10.3390/ijms25010543

9. Tang T, Huang X, Zhang G, Hong Z, Bai X, Liang T. Advantages of targeting the tumor immune microenvironment over blocking immune checkpoint in cancer immunotherapy. *Signal Transduct Target Ther*. (2021) 6:72. doi: 10.1038/s41392-020-00449-4

10. Gonzalez H, Hagerling C, Werb Z. Roles of the immune system in cancer: from tumor initiation to metastatic progression. *Genes Dev*. (2018) 32:1267–84. doi: 10.1101/gad.314617.118

11. Zhang Y, Zuo C, Li Y, Liu L, Yang B, Xia J, et al. Single-cell characterization of infiltrating T cells identifies novel targets for gallbladder cancer immunotherapy. *Cancer Lett*. (2024) 586:216675. doi: 10.1016/j.canlet.2024.216675

12. Chen W, Hu Z, Li G, Zhang L, Li T. The state of systematic therapies in clinic for hepatobiliary cancers. *J Hepatocell Carcinoma*. (2024) 11:629–49. doi: 10.2147/JHC.S454666

13. Fukunaga A, Miyamoto M, Cho Y, Murakami S, Kawarada Y, Oshikiri T, et al. CD8+ tumor-infiltrating lymphocytes together with CD4+ tumor-infiltrating lymphocytes and dendritic cells improve the prognosis of patients with pancreatic adenocarcinoma. *Pancreas*. (2004) 28:e26–31. doi: 10.1097/00006676-200401000-00023

14. Guedj N, Zhan Q, Perigny M, Rautou PE, Degos F, Belghiti J, et al. Comparative protein expression profiles of hilar and peripheral hepatic cholangiocarcinomas. *J Hepatol*. (2009) 51:93–101. doi: 10.1016/j.jhep.2009.03.017

15. Goeppert B, Frauenschuh L, Zucknick M, Stenzinger A, Andrulis M, Klauschen F, et al. Prognostic impact of tumour-infiltrating immune cells on biliary tract cancer. *Br J Cancer*. (2013) 109:2665–74. doi: 10.1038/bjc.2013.610

16. Eroglu Z, Zaretsky JM, Hu-Lieskovan S, Kim DW, Algazi A, Johnson DB, et al. High response rate to PD-1 blockade in desmoplastic melanomas. *Nature*. (2018) 553:347–50. doi: 10.1038/nature25187

17. Yang S, Zou R, Dai Y, Hu Y, Li F, Hu H. Tumor immune microenvironment and the current immunotherapy of cholangiocarcinoma (Review). *Int J Oncol*. (2023) 63(6):137. doi: 10.3892/ijo

18. Bowden J, Holmes MV. Meta-analysis and Mendelian randomization: A review. *Res Synth Methods*. (2019) 10:486–96. doi: 10.1002/jrsm.1346

19. Xue H, Chen J, Zeng L, Fan W. Causal relationship between circulating immune cells and the risk of Alzheimer's disease: A Mendelian randomization study. *Exp Gerontol*. (2024) 187:112371. doi: 10.1016/j.exger.2024.112371

20. Xiao X, Ding Z, Shi Y, Zhang Q. Causal role of immune cells in chronic obstructive pulmonary disease: A two-sample mendelian randomization study. *COPD*. (2024) 21:2327352. doi: 10.1080/15412555.2024.2327352

21. Wang K, Wang S, Qin X, Chen Y, Chen Y, Wang J, et al. The causal relationship between gut microbiota and biliary tract cancer: comprehensive bidirectional Mendelian randomization analysis. *Front Cell Infect Microbiol*. (2024) 14:1308742. doi: 10.3389/fcimb.2024.1308742

22. Chen Y, Yang L, Wang K, An Y, Wang Y, Zheng Y, et al. Relationship between fatty acid intake and aging: a Mendelian randomization study. *Aging (Albany NY)*. (2024) 16:5711–39. doi: 10.18632/aging.v16i6

23. Wang S, Wang K, Chen X, Chen D, Lin S. Autoimmune thyroid disease and myasthenia gravis: a study bidirectional Mendelian randomization. *Front Endocrinol (Lausanne)*. (2024) 15:1310083. doi: 10.3389/fendo.2024.1310083

24. Chen C, Liu Q, Li Y, Yu J, Wang S, Liu L. Impact of immune cells on stroke limited to specific subtypes: evidence from mendelian randomization study. *Neurol Ther*. (2024) 13(3):599–609. doi: 10.1007/s40120-024-00592-y

25. Wang K, Wang S, Chen Y, Lu X, Wang D, Zhang Y, et al. Causal relationship between gut microbiota and risk of gastroesophageal reflux disease: a genetic correlation and bidirectional Mendelian randomization study. *Front Immunol*. (2024) 15:1327503. doi: 10.3389/fimmu.2024.1327503

26. Shi X, Wang T, Teng D, Hou S, Lin N. A mendelian randomization study investigates the causal relationship between immune cell phenotypes and cerebral aneurysm. *Front Genet*. (2024) 15:1333855. doi: 10.3389/fgene.2024.1333855

27. Job S, Rapoud D, Dos SA, Gonzalez P, Desterke C, Pascal G, et al. Identification of four immune subtypes characterized by distinct composition and functions of tumor microenvironment in intrahepatic cholangiocarcinoma. *Hepatology*. (2020) 72:965–81. doi: 10.1002/hep.31092

28. Gajewski TF, Schreiber H, Fu YX. Innate and adaptive immune cells in the tumor microenvironment. *Nat Immunol*. (2013) 14:1014–22. doi: 10.1038/ni.2703

29. Hodi FS, Dranoff G. The biologic importance of tumor-infiltrating lymphocytes. *J Cutan Pathol*. (2010) 37 Suppl 1:48–53. doi: 10.1111/j.1600-0560.2010.01506.x

30. Kuijpers TW, Bende RJ, Baars PA, Grummels A, Derks IA, Dolman KM, et al. CD20 deficiency in humans results in impaired T cell-independent antibody responses. *J Clin Invest*. (2010) 120:214–22. doi: 10.1172/JCI40231

31. Huang YH, Zhang CZ, Huang QS, Yeong J, Wang F, Yang X, et al. Clinicopathologic features, tumor immune microenvironment and genomic landscape of Epstein-Barr virus-associated intrahepatic cholangiocarcinoma. *J Hepatol*. (2021) 74:838–49. doi: 10.1016/j.jhep.2020.10.037

32. Shan D, Ledbetter JA, Press OW. Apoptosis of Malignant human B cells by ligation of CD20 with monoclonal antibodies. *Blood*. (1998) 91:1644–52. doi: 10.1182/blood.V91.5.1644.1644_1644_1652

33. Fan Y, Mao R, Yang J. NF-kappaB and STAT3 signaling pathways collaboratively link inflammation to cancer. *Protein Cell*. (2013) 4:176–85. doi: 10.1007/s13238-013-2084-3

34. Uzzan M, Colombel JF, Cerutti A, Treton X, Mehandru S. B cell-activating factor (BAFF)-targeted B cell therapies in inflammatory bowel diseases. *Dig Dis Sci*. (2016) 61:3407–24. doi: 10.1007/s10620-016-4317-9

35. Hu S, Wang R, Zhang M, Liu K, Tao J, Tai Y, et al. BAFF promotes T cell activation through the BAFF-BAFF-R-PI3K-Akt signaling pathway. *BioMed Pharmacother*. (2019) 114:108796. doi: 10.1016/j.biopha.2019.108796

36. Yu G, Boone T, Delaney J, Hawkins N, Kelley M, Ramakrishnan M, et al. APRIL and TALL-I and receptors BCMA and TACI: system for regulating humoral immunity. *Nat Immunol*. (2000) 1:252–6. doi: 10.1038/79802

37. Kalled SL. The role of BAFF in immune function and implications for autoimmunity. *Immunol Rev*. (2005) 204:43–54. doi: 10.1111/j.0105-2896.2005.00219.x

38. Tanaka R, Kimura K, Eguchi S, Tauchi J, Shibutani M, Shinkawa H, et al. Preoperative neutrophil-to-lymphocyte ratio predicts tumor-infiltrating CD8(+) T cells in biliary tract cancer. *Anticancer Res*. (2020) 40:2881–7. doi: 10.21873/anticanres.14264

39. Takagi S, Miyagawa S, Ichikawa E, Soeda J, Miwa S, Miyagawa Y, et al. Dendritic cells, T-cell infiltration, and Grp94 expression in cholangiocellular carcinoma. *Hum Pathol*. (2004) 35:881–6. doi: 10.1016/j.humpath.2004.03.016

40. Oshikiri T, Miyamoto M, Shichinohe T, Suzuoki M, Hiraoka K, Nakakubo Y, et al. Prognostic value of intratumoral CD8+ T lymphocyte in extrahepatic bile duct carcinoma as essential immune response. *J Surg Oncol*. (2003) 84:224–8. doi: 10.1002/jso.10321

41. Na YJ, Lee HK, Choi KC. Amurensin G sensitized cholangiocarcinoma to the anti-cancer effect of gemcitabine via the downregulation of cancer stem-like properties. *Nutrients*. (2023) 16(1):73. doi: 10.3390/nu16010073

42. Song SP, Zhang SB, Liu R, Yao L, Hao YQ, Liao MM, et al. NDRG2 down-regulation and CD24 up-regulation promote tumor aggravation and poor survival in patients with gallbladder carcinoma. *Med Oncol*. (2012) 29:1879–85. doi: 10.1007/s12032-011-0110-y

43. Lim SC, Oh SH. The role of CD24 in various human epithelial neoplasias. *Pathol Res Pract*. (2005) 201:479–86. doi: 10.1016/j.prp.2005.05.004

44. Fluxa P, Rojas-Sepulveda D, Gleisner MA, Tittarelli A, Villegas P, Tapia L, et al. High CD8(+) and absence of Foxp3(+) T lymphocytes infiltration in gallbladder tumors correlate with prolonged patients survival. *BMC Cancer*. (2018) 18:243. doi: 10.1186/s12885-018-4147-6

45. Lei X, de Groot DC, Welters M, de Wit T, Schrama E, van Eenennaam H, et al. CD4(+) T cells produce IFN-I to license cDC1s for induction of cytotoxic T-cell activity in human tumors. *Cell Mol Immunol*. (2024) 21:374–92. doi: 10.1038/s41423-024-01133-1

46. Kasper HU, Drebber U, Stippel DL, Dienes HP, Gillessen A. Liver tumor infiltrating lymphocytes: comparison of hepatocellular and cholangiolar carcinoma. *World J Gastroenterol*. (2009) 15:5053–7. doi: 10.3748/wjg.15.5053

47. Brown PA, Shah B, Advani A, Aoun P, Boyer MW, Burke PW, et al. Acute lymphoblastic leukemia, version 2.2021, NCCN clinical practice guidelines in oncology. *J Natl Compr Canc Netw*. (2021) 19:1079–109. doi: 10.6004/jnccn.2021.0042

48. Sakaguchi S, Mikami N, Wing JB, Tanaka A, Ichiyama K, Ohkura N. Regulatory T cells and human disease. *Annu Rev Immunol*. (2020) 38:541–66. doi: 10.1146/annurev-immunol-042718-041717

49. Luo Y, Acevedo D, Vlagea A, Codina A, García-García A, Deyà-Martínez A, et al. Changes in Treg and Breg cells in a healthy pediatric population. *Front Immunol*. (2023) 14:1283981. doi: 10.3389/fimmu.2023.1283981

50. Al-Mterin MA, Murshed K, Elkord E. Correlations between circulating and tumor-infiltrating CD4(+) treg subsets with immune checkpoints in colorectal cancer patients with early and advanced stages. *Vaccines (Basel)*. (2022) 10(9):1471. doi: 10.3390/vaccines10091471

51. Gupta V, Katiyar S, Singh A, Misra R, Aggarwal A. CD39 positive regulatory T cell frequency as a biomarker of treatment response to methotrexate in rheumatoid arthritis. *Int J Rheum Dis*. (2018) 21:1548–56. doi: 10.1111/1756-185X.13333

52. Rissiek A, Baumann I, Cuapio A, Mautner A, Kolster M, Arck PC, et al. The expression of CD39 on regulatory T cells is genetically driven and further upregulated at sites of inflammation. *J Autoimmun*. (2015) 58:12–20. doi: 10.1016/j.jaut.2014.12.007

53. Dolan BP, Gibbs KJ, Ostrand-Rosenberg S. Dendritic cells cross-dressed with peptide MHC class I complexes prime CD8+ T cells. *J Immunol*. (2006) 177:6018–24. doi: 10.4049/jimmunol.177.9.6018

54. Hey YY, Quah B, O'Neill HC. Antigen presenting capacity of murine splenic myeloid cells. *BMC Immunol*. (2017) 18:4. doi: 10.1186/s12865-016-0186-4

55. Rolinski J, Hus I. Breaking immunotolerance of tumors: a new perspective for dendritic cell therapy. *J Immunotoxicol*. (2014) 11:311–8. doi: 10.3109/1547691X.2013.865094

56. Rannikko JH, Verlingue L, de Miguel M, Pasanen A, Robbrecht D, Skytta T, et al. Bexmarilimab-induced macrophage activation leads to treatment benefit in solid tumors: The phase I/II first-in-human MATINS trial. *Cell Rep Med*. (2023) 4:101307. doi: 10.1016/j.xcrm.2023.101307

57. Palomares F, Pina A, Dakhaoui H, Leiva-Castro C, Munera-Rodriguez AM, Cejudo-Guillen M, et al. Dendritic cells as a therapeutic strategy in acute myeloid leukemia: vaccines. *Vaccines (Basel)*. (2024) 12(2):165. doi: 10.3390/vaccines12020165

58. Cao H, Huang T, Dai M, Kong X, Liu H, Zheng Z, et al. Tumor microenvironment and its implications for antitumor immunity in cholangiocarcinoma: future perspectives for novel therapies. *Int J Biol Sci*. (2022) 18:5369–90. doi: 10.7150/ijbs.73949

frontiers | Frontiers in Immunology

TYPE Original Research
PUBLISHED 27 August 2024
DOI 10.3389/fimmu.2024.1433393

OPEN ACCESS

EDITED BY
Bing Yang,
Tianjin Medical University, China

REVIEWED BY
Jun Hu,
Tianjin Medical University Cancer Institute and Hospital, China
BL Gan,
Guangxi Medical University, China
Wenli Zhao,
Saga University, Japan

*CORRESPONDENCE
Wei-nan Lai
Laiwn123@smu.edu.cn
Lu-shan Xiao
15622178423@163.com

†These authors have contributed equally to this work and share first authorship

RECEIVED 15 May 2024
ACCEPTED 31 July 2024
PUBLISHED 27 August 2024

CITATION
Li L-n, Li W-w, Xiao L-s and Lai W-n (2024) Lactylation signature identifies liver fibrosis phenotypes and traces fibrotic progression to hepatocellular carcinoma. *Front. Immunol.* 15:1433393. doi: 10.3389/fimmu.2024.1433393

Lactylation signature identifies liver fibrosis phenotypes and traces fibrotic progression to hepatocellular carcinoma

Lin-na Li[1†], Wen-wen Li[2†], Lu-shan Xiao[3*] and Wei-nan Lai[4*]

[1]Department of Endocrinology and Metabolism, Nanfang Hospital, Southern Medical University, Guangzhou, Guangdong, China, [2]Guangzhou Wondfo Health Science and Technology Co., Ltd, Guangzhou, China, [3]Department of Infectious Diseases, Nanfang Hospital, Southern Medical University, Guangzhou, China, [4]Department of Rheumatology and Immunology, Nanfang Hospital, Southern Medical University, Guangzhou, China

Introduction: Precise staging and classification of liver fibrosis are crucial for the hierarchy management of patients. The roles of lactylation are newly found in the progression of liver fibrosis. This study is committed to investigating the signature genes with histone lactylation and their connection with immune infiltration among liver fibrosis with different phenotypes.

Methods: Firstly, a total of 629 upregulated and 261 downregulated genes were screened out of 3 datasets of patients with liver fibrosis from the GEO database and functional analysis confirmed that these differentially expressed genes (DEGs) participated profoundly in fibrosis-related processes. After intersecting with previously reported lactylation-related genes, 12 DEGs related to histone lactylation were found and narrowed down to 6 core genes using R algorithms, namely S100A6, HMGN4, IFI16, LDHB, S100A4, and VIM. The core DEGs were incorporated into the Least absolute shrinkage and selection operator (LASSO) model to test their power to distinguish the fibrotic stage.

Results: Advanced fibrosis presented a pattern of immune infiltration different from mild fibrosis, and the core DEGs were significantly correlated with immunocytes. Gene set and enrichment analysis (GSEA) results revealed that core DEGs were closely linked to immune response and chemokine signaling. Samples were classified into 3 clusters using the LASSO model, followed by gene set variation analysis (GSVA), which indicated that liver fibrosis can be divided into status featuring lipid metabolism reprogramming, immunity immersing, and intermediate of both. The regulatory networks of the core genes shared several transcription factors, and certain core DEGs also presented dysregulation in other liver fibrosis and idiopathic pulmonary fibrosis (IPF) cohorts, indicating that lactylation may exert comparable functions in various fibrotic pathology. Lastly, core DEGs also exhibited upregulation in HCC.

Discussion: Lactylation extensively participates in the pathological progression and immune infiltration of fibrosis. Lactylation and related immune infiltration could be a worthy focus for the investigation of HCC developed from liver fibrosis.

KEYWORDS

liver fibrosis, lactylation, machine learning, immune infiltration, hepatocellular carcinoma

1 Introduction

Liver fibrosis, or hepatic fibrosis, often begins with a fibrous scar arising from extracellular matrix (ECM) accumulation, especially crosslinked collagens type I and type III (1). Fibrous scar formation, in replacement of damaged normal tissue, is constantly triggered following chronic liver injury. Viral infection (2), alcohol abuse (3), metabolic dysfunction-associated steatohepatitis (MASH), and metabolic-associated fatty liver disease (MAFLD) foster persistent activation of inflammatory response and fibrogenesis, leading to the development of liver fibrosis (4). Fibrosis progression from reversible to advanced stage may deteriorate into cirrhosis, liver failure, and portal hypertension (5). Cirrhosis is one of the intermediate processes of liver diseases developing hepatocellular carcinoma (HCC), no matter whether it originated from alcohol abuse, hepatitis virus infection, or metabolic dysfunction (6). The last decades have witnessed an epidemic of liver fibrosis, despite social efforts on HBV/HCV (hepatitis B virus and hepatitis C virus) delimitation. Non-viral etiology for liver fibrosis increased due to superfluous living supplies. Infection rates of hepatitis virus, prevalence of metabolism-related liver diseases, and per capita consumption of alcohol in China surpassed those in other countries and regions; moreover, liver fibrosis and cirrhosis largely account for hospitalization of patients with liver disease (7). Fibrotic progression to liver failure can only be treated by liver transplantation (8), highlighting the hierarchical management of patients with liver fibrosis. Therefore, reversing early-stage fibrosis and curbing advanced fibrosis from progressing into liver failure is one of the most urgent challenges for public health.

Recent studies underscore the roles of histone lactylation in various diseases (9–11). Lactylation, a novel histone acetylation that was newly defined in 2019, has emerged to the sight of researchers with its modulatory roles in inflammation, fibrosis, cell differentiation, and cancerous development (10). Lactylation can exert reparative (12) and injurious (13) functions concerning all kinds of immunocytes, stroma cells, and histiocytes (14–16). Immunocytes, in response to anti/pro-inflammatory and angiogenetic signals, undergo metabolic reprogramming and a drastic increase in glycolysis produces abundant lactide that fuels histone lactylation and subsequent modulation of gene expression (17).

Lactylation in liver fibrosis is under intensive study but far from fully elucidated. Liver fibrosis involves joint action from hepatic stellate cells (HSCs), immunocytes, and hepatocytes (18). HSC activation features dynamic glycolysis and entails histone lactylation for transcriptional activation of key genes sustaining fibrotic pathology (19, 20). However, lactylation of hepatocytes and its impact on the infiltration and activation of immune cells has been scarcely studied.

Enlightened by the prerequisite role of lactylation in HSC activation and fibrotic phenotypes, the study aims to comprehensively assess the activity and staging value of lactylation in liver fibrosis. Combining the Gene Expression Omnibus (GEO) database and documented lactylation-related genes (21–23), we screened differentially expressed genes (DEGs) with lactylation and tested their power to distinguish early and advanced fibrosis. Functional and enrichment analyses as well as immune infiltration analysis validated that the DEGs were closely related to fibrosis progression and immune infiltration.

2 Method and materials

2.1 Data sources

Raw gene expression and stage data of patients with liver fibrosis from three datasets, namely GSE130970, GSE84044, and GSE49541 were downloaded from the GEO database (http://www.ncbi.nlm.nih.gov/geo/). In GSE130970, fibrosis was staged by scoring tissue sections stained with Masson's trichrome stain using the NIDDK NASH CRN staging system, and stages 1a, 1b, and 1c were classified as stage 1 (24). The dataset contained 23 control subjects, 28 fibrosis cases at stage 1, 9 at stage 2, 14 at stage 3, and 2 at stage 4, and gene expressions were detected by Illumina HiSeq 2500 (Homo sapiens) on the GPL16791 platform. GSE84044 provides data on 43 non-fibrotic livers, 20 fibrosis cases at stage 1, 33 at stage 2, 18 at stage 3, and 10 at stage 4 (25). The dataset applied the Affymetrix Human Genome U133 Plus 2.0 Array [HG-U133_Plus_2] on GPL570 for gene sequencing. A total of 40 control and fibrotic livers at stage 1 were grouped against 32 cases of fibrosis at stages 2 to 4 in GSE49541(GPL570[HG-U133_Plus_2] Affymetrix Human Genome U133 Plus 2.0 Array).

Therefore, we defined stages F0 to F1 as mild fibrosis and stages F2 to F4 as advanced fibrosis. Datasets were merged and batch effects were adjusted using the limma and sva packages in R language. R version 4.2.2 was used for all analyses in this article. The FactoMineR and factoextra packages were utilized for principal component analysis (PCA) and plotting to visualize the adjustment on three-dimensional scatter plots.

To verify the generalization of core DEGs in fibrosis, GSE14323, GSE103580, GSE110147, and GSE150910 from the GEO database were collected. GSE14323 and GSE103580 provided liver specimen expression data of patients with HCV-related and alcohol-related cirrhosis, respectively. Gene expression of lung samples from patients with idiopathic pulmonary fibrosis and normal controls were gathered from GSE110147 and GSE150910.

Expression and survival data of patients with HCC (TCGA-LIHC cohort) were obtained from the TCGA website (https://www.cancer.gov/ccg/research/genome-sequencing/tcga).

2.2 Screening of differentially expressed genes

A linear model for microarray data (LIMMA) package (26) from R language was used for DEG screening. To improve the reliability of differentially expressed genes, probe sets for which the adjusted P was <0.05, and |logFC| was > 0.25 between mild and advanced fibrosis were defined as significantly differentially expressing.

2.3 Functional analyses of DEGs and gene set enrichment analysis

In order to investigate the biological functions of DEGs, ClusterProfiler package (27) was utilized for functional analyses. The analyses incorporated Gene Ontology (GO) and Kyoto Encyclopedia of Genes and Genomes (KEGG), and the GO category delineated functional pathways into three aspects including biological processes (BP), molecular functions (MF), and cellular components (CC). The P-value was adjusted using the Benjamini–Hochberg approach or FDR for multiple testing corrections. The threshold was set at FDR<0.05.

In gene set enrichment analysis (GSEA) for core DEGs, the clusterProfiler package was utilized to calculate the enrichment score of pathways with the given genes.

2.4 Selection of core DEGs

After intersection with the lactylation-related gene list, 12 candidates were subjected to two machine learning algorithms, random forest (RSF) and support vector machine (SVM), for characteristic gene selection. The harvested six genes were further tested by least absolute shrinkage and selection operator (LASSO), another machine learning algorithm characteristic of dimension reduction. LASSO analysis was implemented with a turning/penalty parameter utilizing a 10-fold cross-verification via the glmnet package (28). Receiver operating characteristic (ROC) curves and the area under the curve (AUC) were used to estimate the diagnostic efficacy.

In detail, to model the degree of liver fibrosis, we used the "glmnet" function in LASSO regression and the variable type was binomial. When performing 10-fold cross-validation using the cv.glmnet function, the "coef" function was utilized to extract the coefficients of the model. The parameter s=cvfit$lambda.min specifies the coefficient corresponding to the minimum lambda value selected using cross-validation.

This article uses two machine learning methods to screen key genes, SVM and RSF. SVM and RSF are commonly used machine learning methods. SVM is a supervised learning algorithm primarily used for classification and regression problems. Its basic principle is to find the optimal boundary between data points (hyperplane), which can maximize the boundary distance between different categories. SVM uses kernel functions to map data to high-dimensional space to handle nonlinear separable problems. In gene screening, SVM can be used to distinguish samples with different biological characteristics or phenotypes by identifying which genes are most important for classification. RSF is an ensemble learning method based on decision tree construction. It improves the accuracy and robustness of the model by constructing multiple decision trees (forests) and voting or averaging their results. Each decision tree uses a random subset of the dataset during training (achieved through self-sampling), which increases model diversity and reduces the risk of overfitting. An important feature of RSF is its feature importance assessment, which can identify the genes that impact classification most greatly. In gene screening, RSF can be used to evaluate the contribution of genes to sample classification and select key genes through feature importance scores. Combining SVM and RSF can improve the accuracy of predictions.

2.5 Immune cell infiltration analysis

Single-sample gene set enrichment analysis (ssGSEA) was implemented to analyze the immune infiltration based on the expression profiling of 29 immunity-relevant signatures. The analyses were composed of reciprocal relevance between different types of immune cells, differences in immune infiltration between mild and advanced fibrosis, and correlation of immune cells with core DEGs.

The ssGSEA function in the Gene Set Variation Analysis (GSVA) package evaluates the degree of association between a single sample and a predefined gene set. It is comprised of the following key steps:

2.5.1 Immune cell infiltration analysis

Pre-processing of gene expression data: First, gene expression data must be converted into a format suitable for GSVA analysis.

2.5.2 Preparation of gene sets

The gene sets used in this article represent cell types and pathways.

2.5.3 Non-parametric pathway enrichment analysis

GSVA uses nonparametric methods to evaluate the degree of association between each sample in the gene expression profile and every certain gene set, and converts the associations into a continuous score.

2.5.4 Kernel density estimation

GSVA estimates the expression distribution of gene sets through kernel functions (Gaussian kernel in this paper).

2.5.5 Empirical cumulative distribution function

GSVA uses eCDF to evaluate the position of gene sets in gene expression ranking lists.

2.5.6 Enrichment score

ES was calculated by taking the maximum absolute value of the difference between the cumulative distribution function of all genes in the gene set and the cumulative distribution function of the entire gene set.

2.5.7 Statistical test

Finally, linear models and empirical Bayesian methods are used to perform statistical tests on the ES to determine whether the enrichment of the gene set is statistically significant.

The p-value ranged from 0 to 1, and less than 0.05 was considered significant.

2.6 Unsupervised hierarchical clustering

The normalized expression microarray data for each patient were collected and subjected to unsupervised hierarchical clustering with the ConsensusClusterPlus package in R.

2.7 Gene set variation analysis

KEGG and Reactome pathways were downloaded from the MSigDB database as the reference set. The GSVA scores of each pathway were calculated using the ssGSEA function in the GSVA package from R. The GSVA score denoted the degree of absolute enrichment of each gene set, and was compared across two clusters using the limma package.

2.8 Construction of regulatory network

Regulator data concerning miRNA and transcriptional factors were obtained from the regnetwork database(https://regnetworkweb.org/) for upstream prediction of core DEGs. The regulatory network was constructed using Cytoscape software.

2.9 Statistical analysis

All the statistical analyses were performed using R-4.1.3. Heatmaps were plotted using R package "pheatmap". The KM method was performed using the R package "survminer". LASSO analysis was performed using the R package "glmnet". The KM plots, violin plots, volcano plots were plotted using the R package "ggplot2". For comparison between two groups, Student's t-test was performed.

3 Results

3.1 Integrating microarray datasets of liver fibrosis

The three liver fibrosis datasets (GSE130970, GSE84044, and GSE49541) were incorporated into the study and merged using the limma and sva algorithms to remove batch effects. Distribution patterns of the fibrotic cases before and after normalization were visualized using principal component analysis (PCA) (Figures 1A, B) and box plots (Figures 1C, D).

3.2 Differentially expressed genes between mild and advanced liver fibrosis

After homogenization, the samples were subjected to variance analysis using the limma package. Distinct gene expression patterns between mild and advanced fibrosis were identified (adj.P.val < 0.05, and |log2FC| > 0.25), with 629 DEGs upregulated and 261 downregulated for liver fibrosis, as shown in the volcano plot and heatmap (Figures 1E, F).

3.3 Enrichment analyses of DEGs

Next, we performed pathway enrichment analyses on the DEGs of liver fibrosis. GO analysis revealed that these DEGs were enriched in fibrotic processes, such as "cytokine–mediated signaling", "cell chemotaxis", and "extracellular matrix organization" (Figures 2A–C). KEGG analysis highlighted their involvement in "cytokine–cytokine receptor interaction", "chemokine signaling pathway", "ECM–receptor interaction", etc (Figure 2D). Enrichment for these pathways suggested that these DEGs were associated with chemokine signaling and excessive production of extracellular matrix, which are responsible for liver fibrosis.

3.4 Lactylation underscores the core predictive DEGs in fibrotic livers

By intersecting these DEGs with 336 lactylation–modified genes (21–23), we found that among the upregulated DEGs, 12 genes were modulated by lactylation (Figure 3A), while none of the downregulated DEGs were related to lactylation (Figure 3B). We

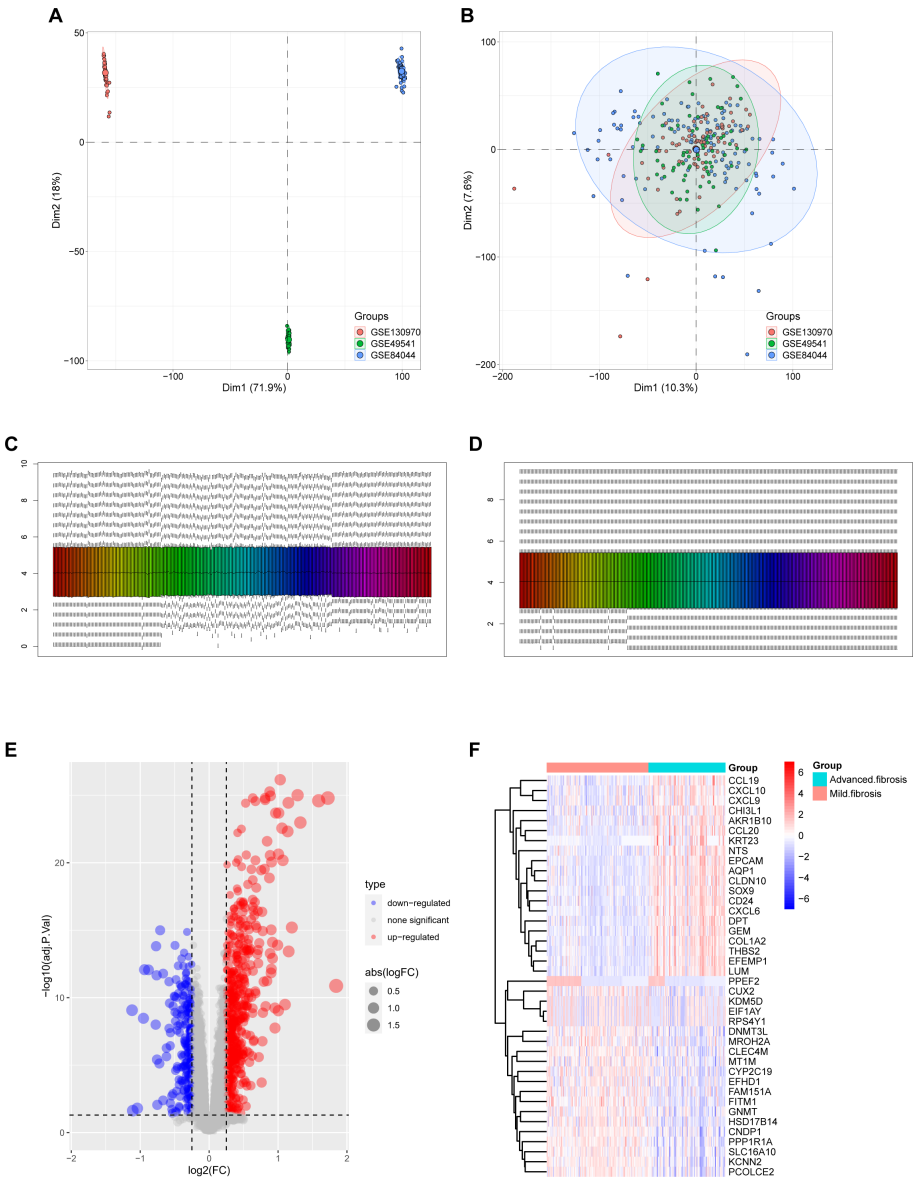

FIGURE 1
Merging the database and screening differential expressed genes (DEGs). **(A)** Principal Component Analysis (PCA) of samples from the three databases before data merging. **(B)** PCA of 274 samples covering 16,243 genes after data merging using the FactoMineR and factoextra packages from R. **(C, D)** sample distribution before **(C)** and after **(D)** homogenization of the datasets using the preprocessCore package of R language. **(E, F)** DEGs were screened using the limma package under the standard of adj.P.Val<0.05, and |logFC| > 0.25. Upregulated genes were plotted in red and downregulated genes in blue in a volcano plot **(E)**. The heatmap **(F)** displays a group of genes differentially expressed in mild and advanced fibrosis.

further analyzed the 336 lactylation–related genes in patients with or without liver fibrosis and the results validated that the expression level of only these 12 upregulated DEGs fluctuated between fibrotic and normal livers (Figure 3C). The 12 genes included S100A6, HMGN4, IFI16, LDHB, S100A4, S100A11, VIM, TMSB4X, FABP5, RACGAP1, CCNA2, and MNDA, and their expression patterns in advanced fibrosis were distinct from mildly fibrotic livers (Figures 3D, E). Thus, these genes might have crucial functions in the pathology of liver fibrosis.

We applied two machine algorithms to screen out signature genes from the 12 lactylation–related DEGs in liver fibrosis. Six candidates of predictive value for liver fibrosis were selected by SVM (Figure 4A) and ten by random forest (Figure 4B). The harvested key DEGs were further intersected (Figure 4C), which returned six core candidates, namely S100A6, HMGN4, IFI16, LDHB, S100A4, and VIM, with significantly and reciprocally positive correlations (Figure 4D). We constructed a LASSO regression model based on the six core genes (Figure 4E), which manifested better predictive power than each single DEG as shown by the ROC curve (Figure 4F), with the AUC reaching 0.828 in LASSO model and ranging from 0.719 (VIM) to 0.773 (S100A6 and HMGN4).

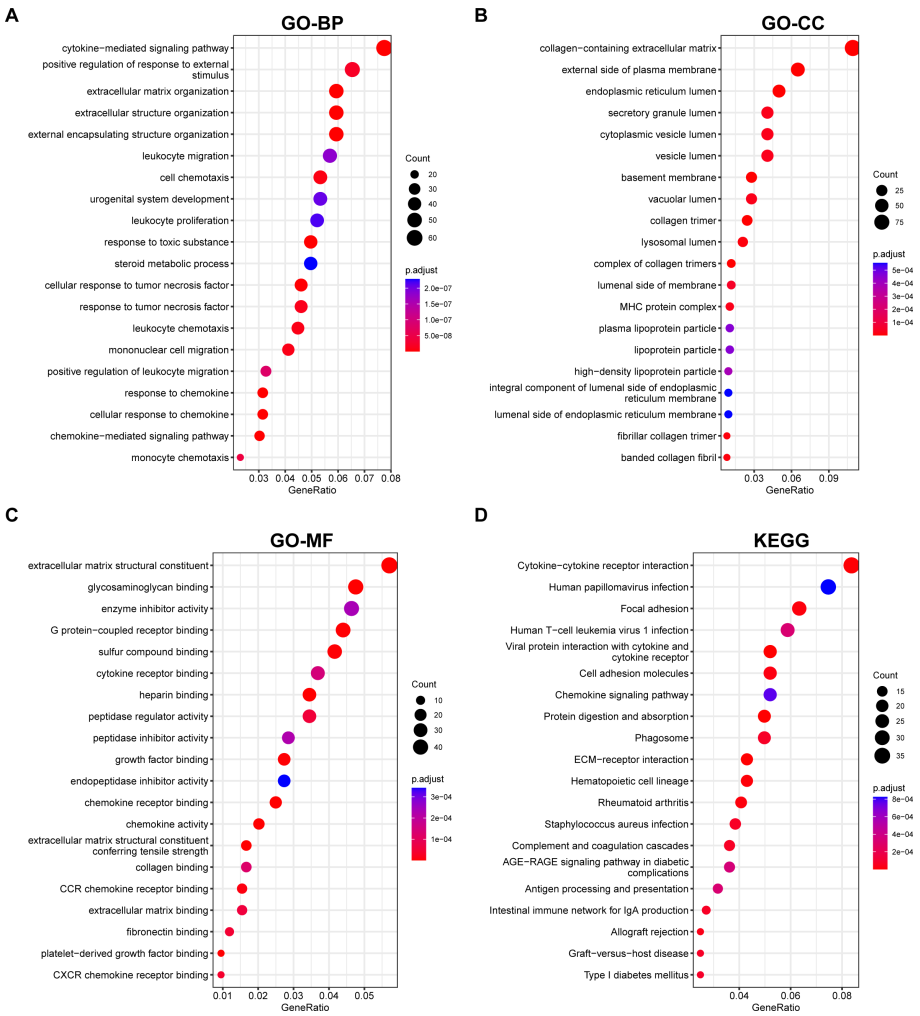

FIGURE 2
GO Annotation and KEGG Enrichment analyses of DEGs. **(A–C)** GO annotation of the DEGs in association with annotated **(A)** biological process (BP), **(B)** cellular component (CC), and **(C)** molecular function (MF). **(D)** demonstration of KEGG enrichment results. Pathways were ranked according to their GeneRatio, and the sizes of the bubbles represent the number of enriched genes, and the colors represent *p* values.

3.5 Liver fibrosis progression involves variations in immune infiltration and gene expression

We continued to investigate the immune infiltration in the fibrotic livers. Cross infiltration of all kinds of immune cells revealed the intertwined inflammatory status along fibrotic progression (Figure 5A), especially the strongly significant coexistence of activated B cells with activated CD4, CD8 T cells, and γδ T cells that are responsible for the pro-inflammatory process, as well as the myeloid-derived suppressor cells (MDSCs) and regulatory T cells that exert immunoregulatory functions. Moreover, infiltration of immunocytes presented distinctive alterations along the progression of liver fibrosis (Figure 5B). Most immunocytes, including activated B cells, activated CD4 and CD8 T cells, dendritic cells, γδ T cells, MDSCs, and regulatory T cells increased while macrophages and neutrophils decreased along with fibrosis advancement. Moreover, infiltration of different immunocytes was associated with the core DEGs (Figure 5C). Typically, activated CD4 T cells were the top immunocyte correlated with HMGN4, IFI16, and LDHB, while MDSCs and mast cells were closely related to S100A4, S100A6, and VIM. In addition, immunocytes that distinctively infiltrated in mild and advanced fibrosis also exhibited significant correlations with the core DEGs. These results suggested that not only did immune infiltration participate in fibrotic progression, but also certain core genes might be involved in the proportion variation of immunocytes.

3.6 Phenotyping power of the core DEGs in liver fibrosis

In order to catalog liver fibrosis with core DEGs, we screened genes notably related to each core DEG (Figure 6), which were sequentially subjected to GSEA (Figure 7). Per the aforementioned results that these DEGs were linked to immune infiltration in liver fibrosis (Figure 5), genes screened by their relationship with core DEGs were enriched in pathways involving immune responses and

10.3389/fimmu.2024.1433393

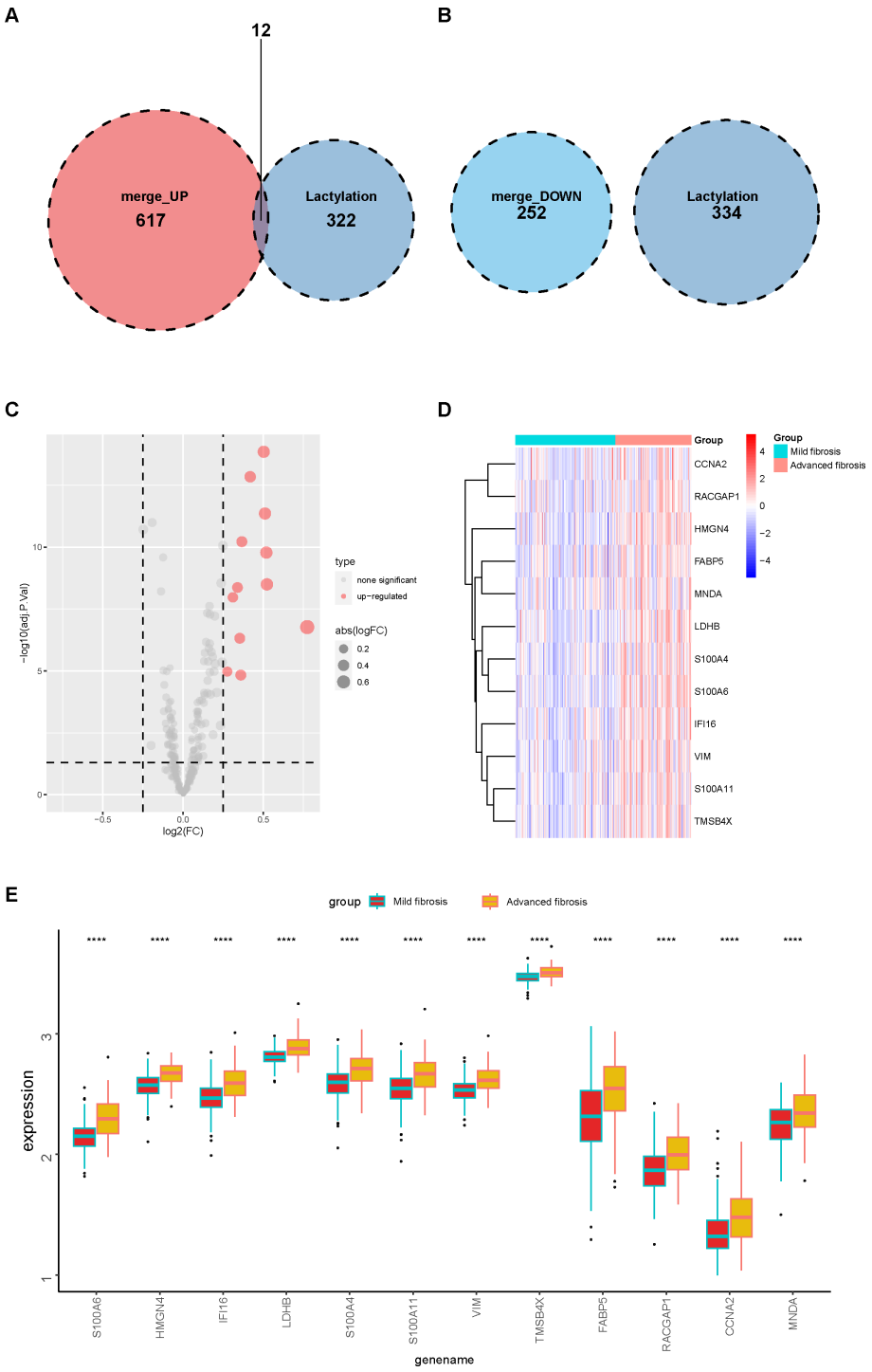

FIGURE 3
Lactylation of DEGs in mild and advanced fibrotic livers. **(A, B)** Venn plot displaying the intersection of upregulated **(A)** and downregulated **(B)** DEGs with lactylation−related genes. **(C)** a volcano plot displaying the expressions of lactylation−related genes in mild and advanced fibrotic livers. **(D, E)** heatmap **(D)** and boxplot **(E)** displaying the expression patterns of the 12 lactylation−related genes in mild and advanced fibrotic livers. ****p<0.001.

chemokine signaling including “immunoregulatory interactions between a Lymphoid and a non-Lymphoid cell”, “neutrophil degranulation”, “interferon signaling”, “neutrophil degranulation”, “cytokine signaling in immune system”, and “chemokine receptors bind chemokines”.

We then classified 274 samples from three databases into three phenotypes according to their expression of core DEGs (Figure 8A). The PCA results confirmed that these samples were discriminately stratified (Figure 8B). In detail, advanced fibrosis accumulated in clusters B and C more than in cluster A; furthermore, cluster A

10.3389/fimmu.2024.1433393

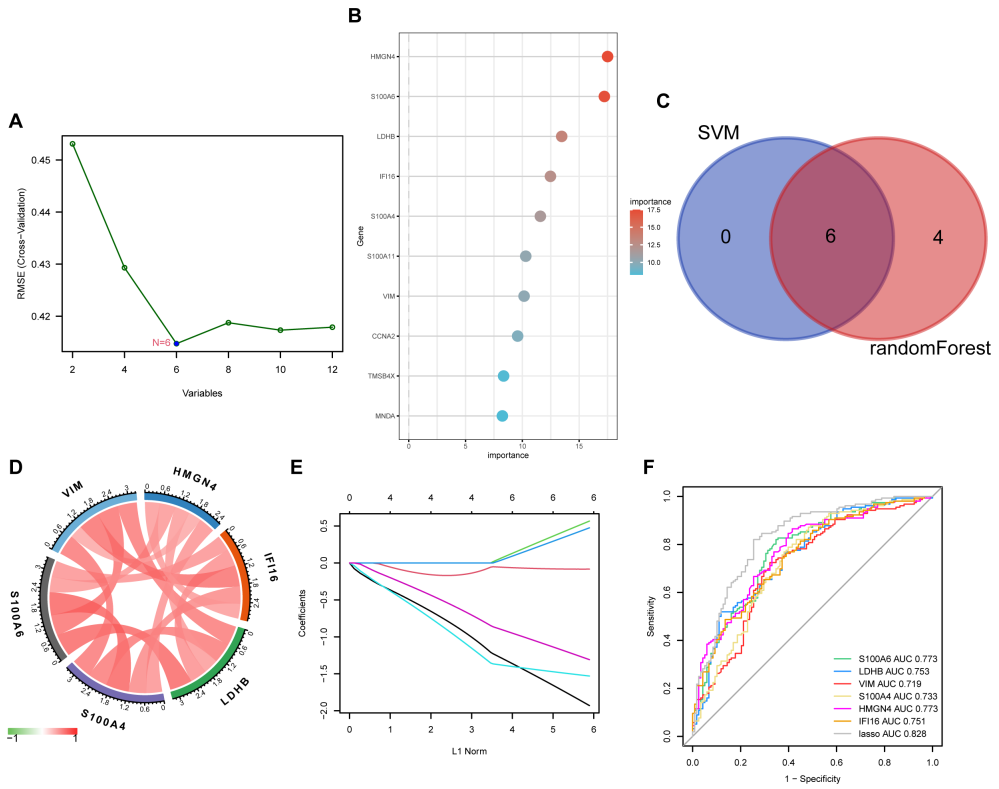

FIGURE 4
Key DEG screening using machine learning. **(A)** key DEGs screened by SVM (support vector machine) using the kernlab package from R. **(B)** key DEGs elected by random forest using the randomForest package of R and ranked in order of their importance. **(C)** key DEGs selected by SVM and random forest were intersected and six candidates were obtained. **(D)** chord diagram displaying the correlation of six core DEGs. Positive correlations were plotted in red and negative in green. **(E)** the LASSO coefficient profiles of the six core DEGs in predicting liver fibrosis plotted by the glmnet package from R. **(F)** ROC (receiver operating characteristic) curve of the six core DEGs and their LASSO model in predicting disease occurrence plotted using the pROC package from R. AUC, area under the curve.

featured low expression of the core DEGs, which were moderately upregulated in cluster B and drastically increased in cluster C (Figures 8C, D). GSVA revealed that pathways related to immune response, such as "primary immunodeficiency", and "cytokine receptor interaction" were enriched in clusters B and C (Figure 9A); also, clusters A and B were characterized by activated lipid metabolism and signaling, including pathways involving "peroxisomal lipid metabolism", and "fatty acids". (Figure 9B). In light of this, we named cluster A as "metabolic phenotype, C as "immune phenotype", and B as "mixed phenotype". These results indicated that fibrotic livers presented crosswise variances and similarities; accordingly, classification into three clusters might help distinguish different phenotypes.

3.7 Upstream regulators of core DEGs and their expression evolution along liver pathology

With the help of the regnetwork database(https://regnetworkweb.org/) and cytoscape software, we mapped the regulatory network of core DEGs in liver fibrosis (Figure 10). Core DEGs shared several transcriptional factors, namely E2F4, MAX, TP53, USF1, MXI1, CLEC5A, SP1, E2F1, and JUM. As liver fibrosis arises from various etiologies and leads to cirrhosis once it progresses towards irreversible stages, we examine the roles of core DEGs in different etiologies. By comparing their expression in HCV- and alcohol-related cirrhosis, we found that most of the core DEGs were significantly upregulated in HCV- and alcohol-related cirrhosis; specifically, S100A4 and S100A6 were upregulated in HCV-related cirrhosis but presented comparable expression in alcoholic cirrhosis and control livers (Figures 11A, B). These results indicated that they might exert distinct functions in liver fibrosis of different origins. As for fibrosis in other tissue types, idiopathic pulmonary fibrosis (IPF), for instance, manifested another expression pattern of the core DEGs against liver cirrhosis. S100A6, VIM, S100A4, and HMGN4 were downregulated or unchanged, while LDHB was upregulated or remained unchanged in IPF. Only IFI16 was upregulated in both IPF and liver cirrhosis, indicating that it was universally activated in fibrosis (Figures 11C, D).

3.8 Tumorigenic roles of core DEGs

As the core DEGs function universally in fibrotic pathology, we hypothesized that they might participate in fibrotic progression to liver tumors as well. By comparing their expression in tumor and

10.3389/fimmu.2024.1433393

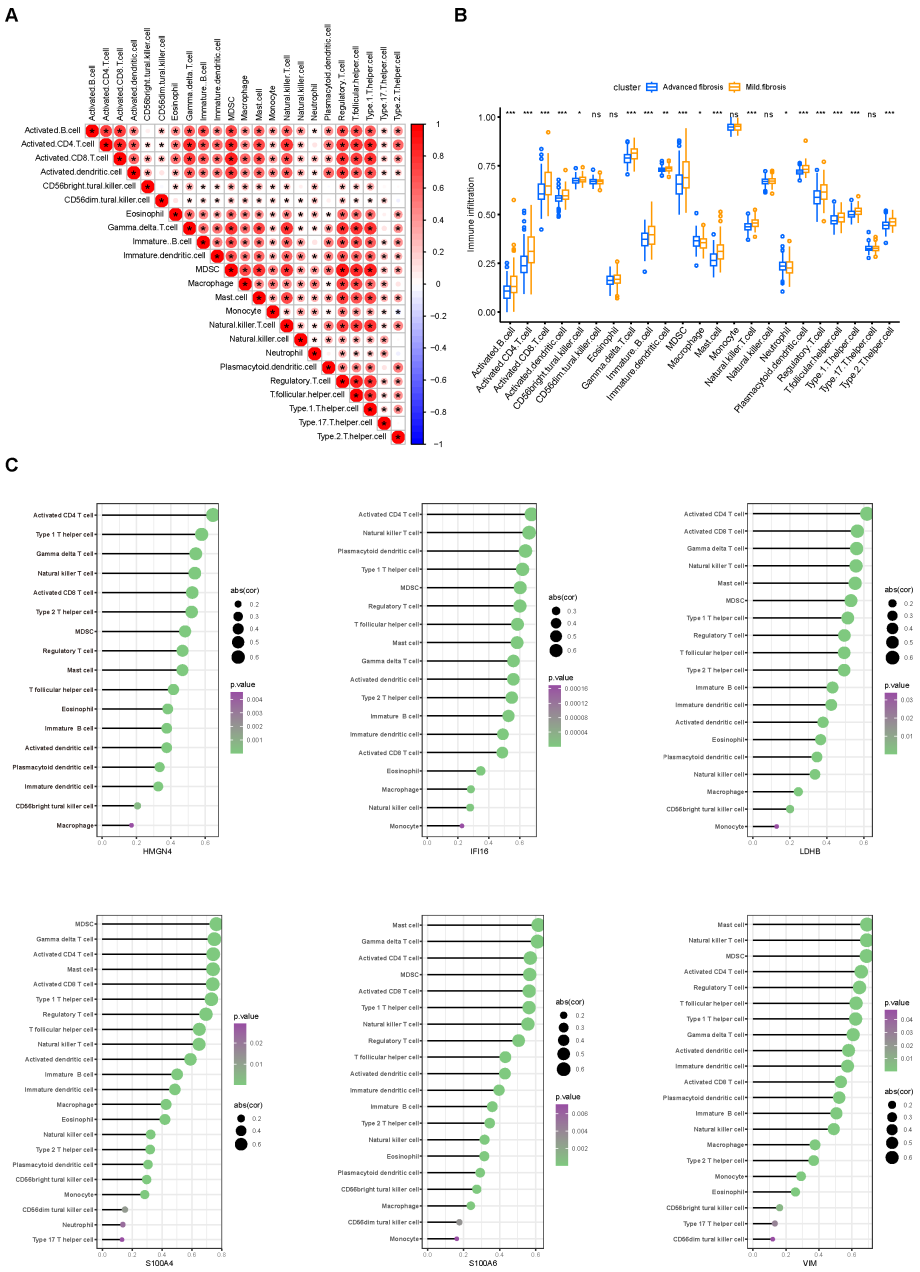

FIGURE 5
Immune infiltration in fibrotic livers and its correlation with core DEGs. **(A)** correlation heatmap displaying the correlation of various immune cells in the aspect of their proportion in fibrotic livers. **(B)** differences in immunocyte infiltration between mild and advanced fibrosis. Ns, not significant, *p<0.05, **p<0.01, ***p<0.001. **(C)** associations between the degree of immune infiltration and each core DEG were plotted using the ggplot2 package on R. Immunocytes with p values less than 0.05 are displayed, sizes of the bubbles represent correlation coefficients and colors represent p values.

non-tumor tissues from the TCGA-LIHC database, we found that all core DEGs were upregulated in tumoral specimens (Figure 12A); moreover, HMGN4 (log-rank p= 0.039) and S100A6 (log-rank p= 0.014) expressions in HCC patients were significantly correlated with their overall survival (Figure 12B), suggesting their tumorigenic potential in liver fibrosis progression.

VIM and S100A4 were upregulated in liver fibrosis but downregulated in IPF; we further collected mice fibrotic livers to examine their expression. As expected, fibrotic mice presented higher expression of VIM and S100A4 in the liver than normal mice (Figure 12C).

4 Discussion

Staging of liver fibrosis currently relies upon liver biopsy and noninvasive imaging is increasingly applied for screening and diagnosis (29, 30). Fibrosis staging indicates the severity of the

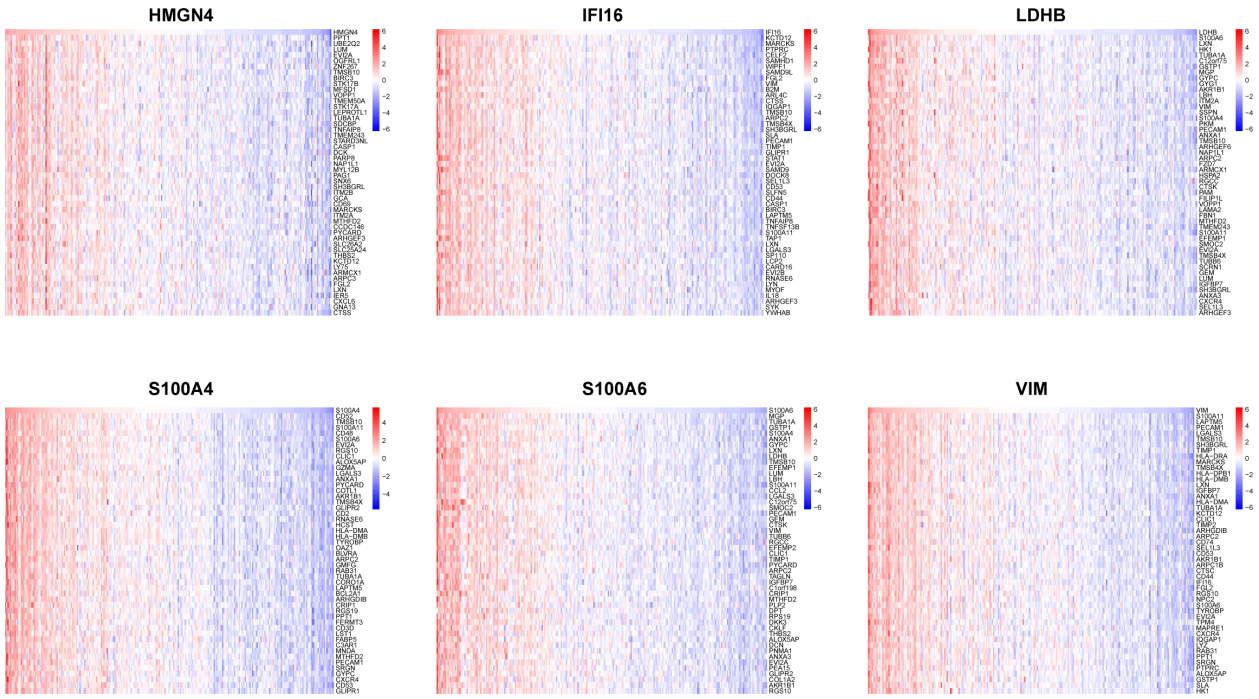

FIGURE 6
Association of core DEGs with genome variants. Correlation heatmaps illustrating the association between a single core DEG and 50 top-related genes.

FIGURE 7
GSEA of genes correlated with core DEGs. GSEA was performed based on the genes selected by correlation analysis using clusterProfiler from R. Top20 Reactome pathways of GSEA results are plotted with the enrichment score on the x-axis.

10.3389/fimmu.2024.1433393

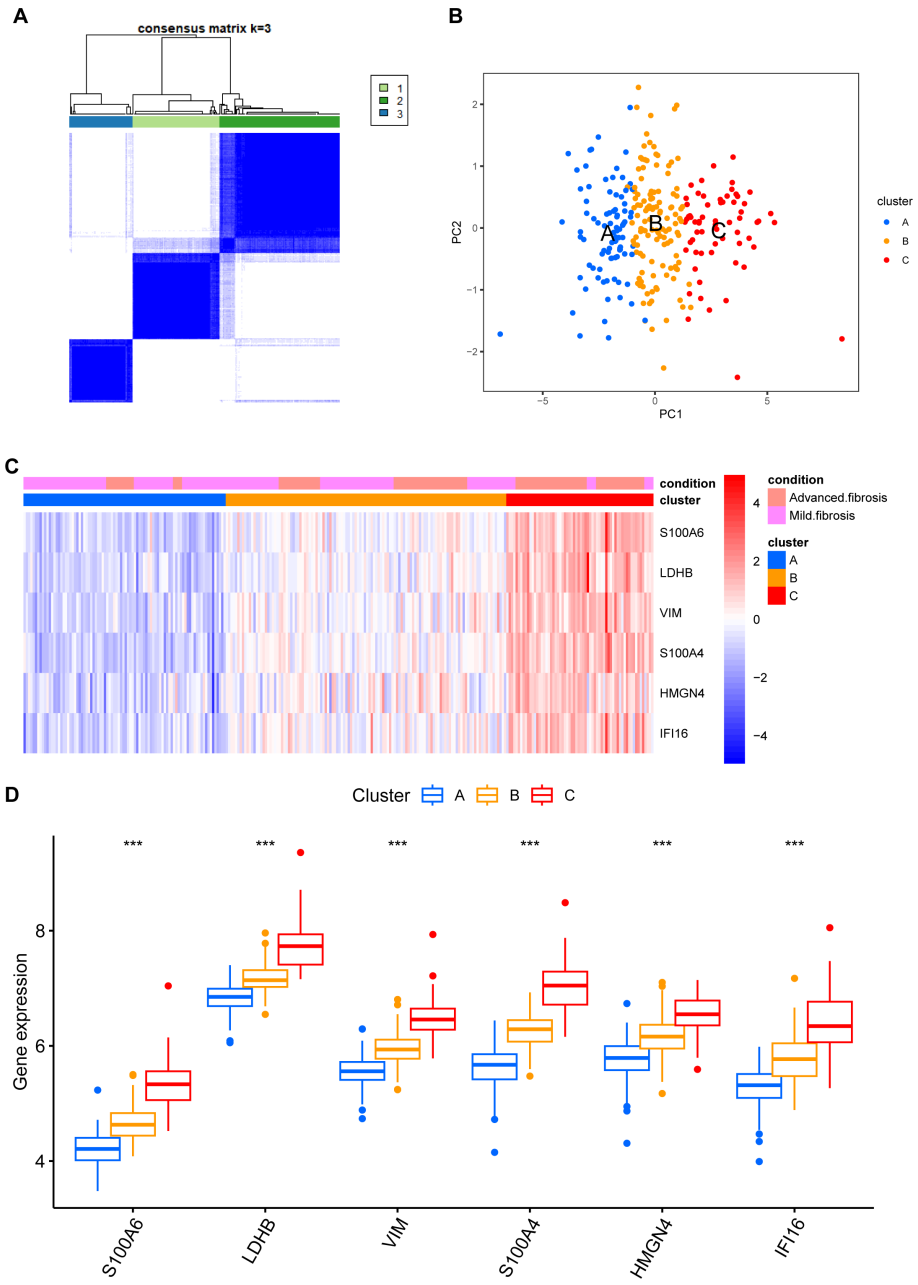

FIGURE 8
Phenotype clustering by the expression of core DEGs. **(A)** consensus clustering on liver fibrosis samples based on the six core DEGs using the ConsensusClusterPlus package from R. **(B)** PCA of the sample distribution across different phenotypes. **(C)** heatmap showing the association between gene expression and different phenotypes plotted by pheatmap from R. **(D)** expression distinction of core DEGs across different phenotypes. ***$p<0.001$.

condition and the study proposed a model for fibrosis classification that also reflected the immune and metabolic status of the nidus. We screened lactylation-related core DEGs between mild and advanced fibrosis and discovered that fibrosis stages are associated with immune infiltration. One of the core DEGs, IFI16, might also play certain roles in lung fibrosis as suggested by its upregulation in IPF.

The model integrated the feature of disease progression with immunity and metabolism as constructed with concerns of fibrotic stage and lactylation activity. The phenotypes cataloged by the model exhibit varied inclinations in immune infiltration and metabolic reprogramming. The metabolic phenotype features activated lipid metabolism, the immune phenotype involves more immune components, and the mixed phenotype stands as the intermediated state of both clusters. As early-stage samples made up the majority of the metabolic phenotype and advanced fibrosis mainly fell under the immune phenotype, we inferred that the main cause of fibrotic pathology begins at lipid metabolic reprogramming and turns to

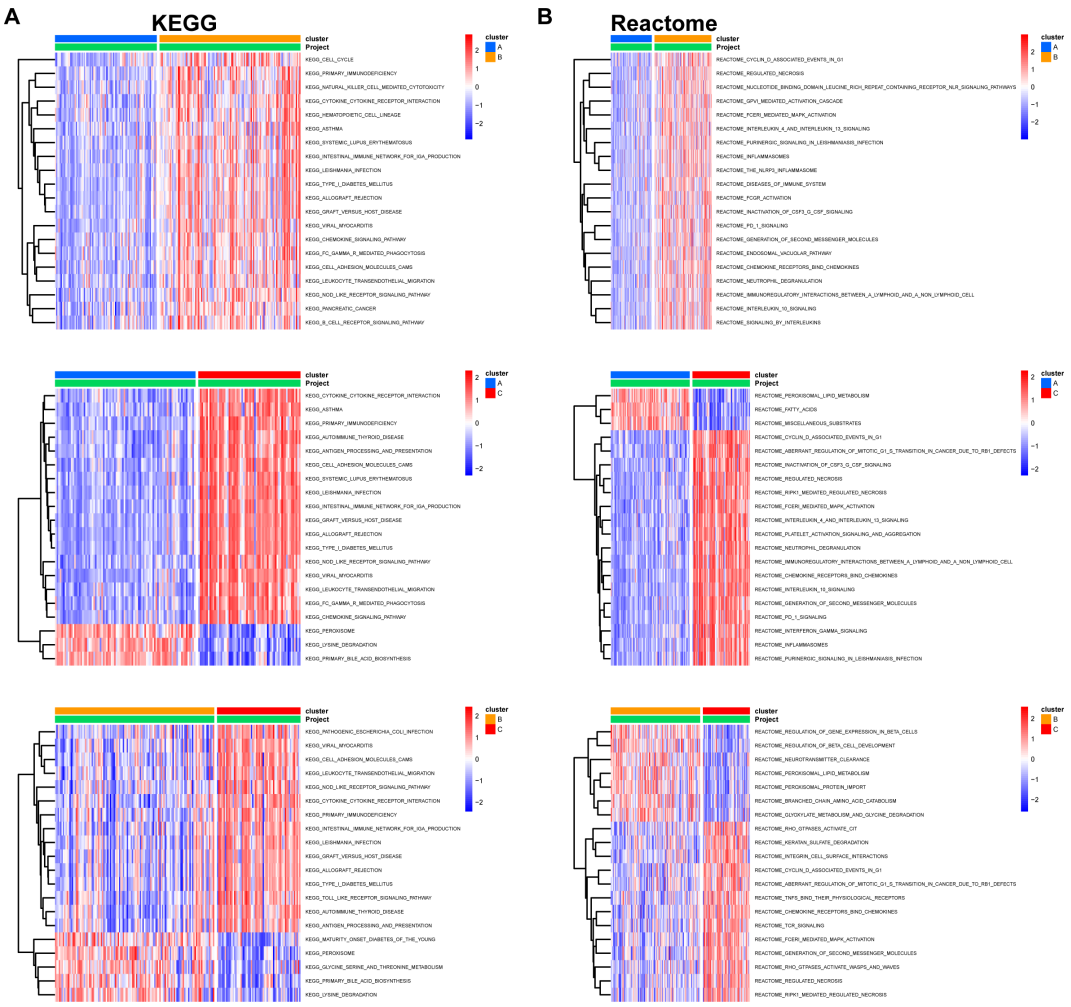

FIGURE 9
Pairwise GSVA between different clusters. KEGG **(A)** and Reactome **(B)** pathways enriched for indicated clusters. GSVA package in R was used to compare pathway enrichment reciprocally between each two clusters. Pathways with significant differences were plotted on heatmaps using the pheatmap package from R. The color columns represent enrichment scores for the pathways in each cluster.

immune response, which might enlighten our presupposition of fibrosis progression and direct further investigation.

The study found that immune infiltration exhibited distinct patterns in mild and advanced fibrosis (Figure 5B). Besides the relay of metabolic reprogramming and immunity, the discrepancy might also result from the deterioration of etiology such as the progression of MAFLD to MASH (4, 31, 32). B cells, CD4 T cells, CD8 T cells, and dendritic cells were activated in advanced fibrosis, accompanied by increased infiltration of γδ T cells, MDSCs, and natural killer T cells (NKTs), and most of these are established pro-fibrosis immunocytes (31, 33, 34). In contrast, macrophages and neutrophils, mediators of tissue repair (31), were reduced in proportion during disease advancement. These findings not only correspond to previous reports but also summarize cell types with pro/anti-fibrotic functions.

In corroboration of our hypothesis that lactylation might influence the infiltration and activation of immune cells, core DEGs sifted from lactylation-related genes demonstrated significant correlations with immune infiltration and functioning (Figures 5C, 7). Lactylation-related core genes were subjected to ssGSEA (Figure 5C) and GSEA (Figure 7) to examine the pathways mediating the crosstalk between gene expression and immune cell infiltration. For example, almost all core DEGs were found to be closely related to activated CD4 T cells, natural killer T cells, MDSCs, regulatory T cells, and so forth (Figure 5C). In the GSEA results (Figure 7), "Immunoregulatory interactions between a Lymphoid and a non-Lymphoid cell" and "Interferon Signaling" pathways, which involve the interaction between the above cells and mediate the killing activity of T cells, were enriched for the core DEGs. Therefore, lactylation might modulate the inclination between immune killing and immune regulation through these core DEGs. Histone lactylation has been widely documented with immunoregulatory functions. For instance, glycolysis was boosted by STAT5 (signal transducer and activator of transcription 5A) in acute myeloid leukemia (AML) cells to provide excessive lactide for lactylation of PD-1, making tumor cells susceptible to immune checkpoint inhibitors (ICIs) (35). Activated glycolysis facilitated H3K18la lactylation at the promoter region of FOXP3 to

10.3389/fimmu.2024.1433393

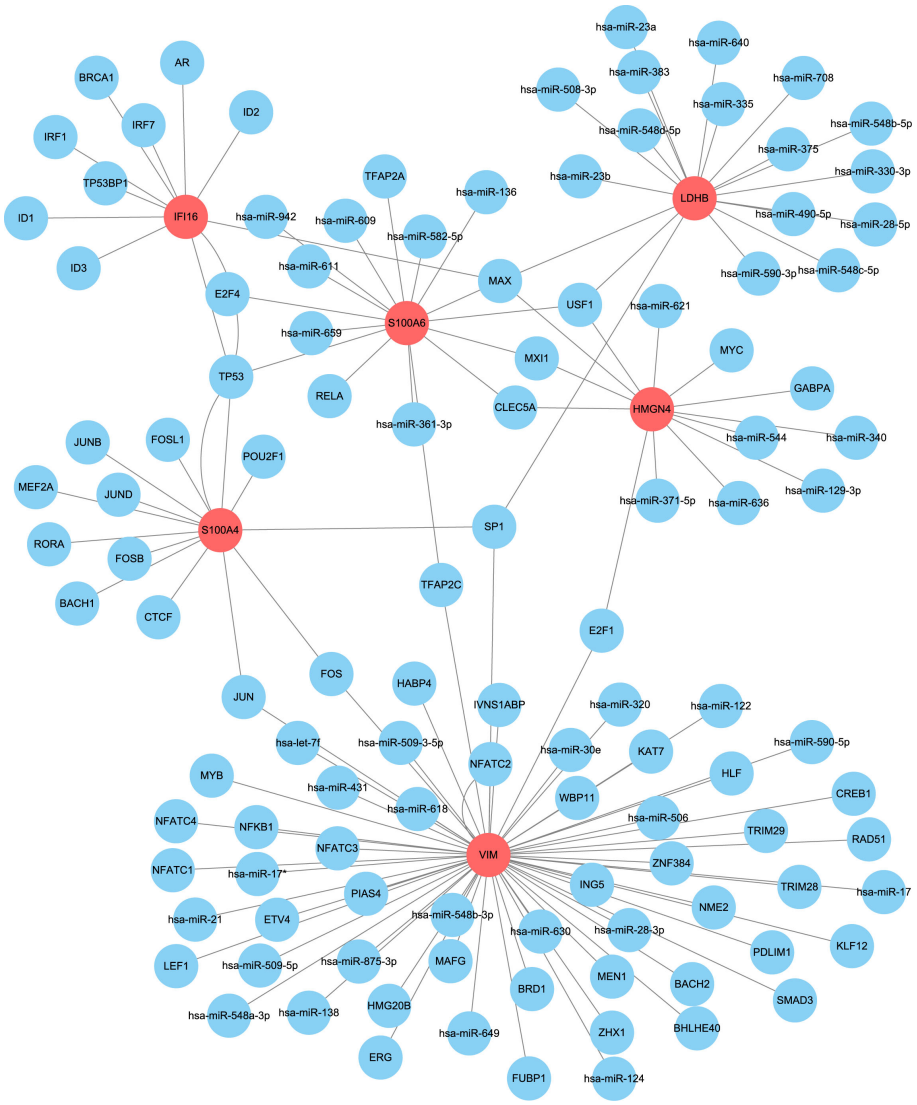

FIGURE 10
Upstream regulatory network of core DEGs. Core DEGs (red) and their predicted upstream regulators (blue) in the regulatory network constructed by Cytoscape software.

compromise the immune killing of NKT-like cells (36). Our analysis of immune infiltration in liver fibrosis unveiled the association of lactylation with mast cells and MDSCs, which has barely been reported. There is a high probability that lactylation extensively functions in all kinds of immunocytes to participate in their immune responses, which are commonly accompanied by activated glycolysis (9, 37). Thus, research to expand our knowledge on the crosstalk between lactylation and immunocytes and delineate the underlying mechanisms might be promising in the field of immunoregulation.

In addition, lactylation might have universal impacts on fibrotic pathologies. Most core DEGs were upregulated in HCV-related and alcohol-related cirrhosis except S100A4 and S100A6 (Figures 11A, B). Though sharing some common pathology concerning inflammation (38), fibrosis originating from hepatitis viral infection or alcohol abuse might manifest some inclination to immune response, lipid toxicity, and oxidative stress (39). Thus, a variety of gene functions in cirrhosis with different etiologies is not uncommon. For example, the genetic variant rs738409 (G) in the PNPLA3 gene was an independent risk factor for the development of HCC in patients with alcoholic cirrhosis but showed no influence in the progression of HCV-related cirrhosis to HCC (40). At the same time, fibrosis in the liver and lungs also share certain functional molecules such as TGF-β (41) and serotonin (5-hydroxytryptamine(5-HT)) (42). In the study, we found that most core DEGs manifested dysregulation in IPF, especially IFI16, the expression of which was increased in both validation datasets (Figures 11C, D). IFI16 has been previously reported to function in lung cystic fibrosis (43), while its role in liver fibrosis has scarcely been researched (44). Therefore, our data excavated a profibrotic gene with pan-tissue potential.

10.3389/fimmu.2024.1433393

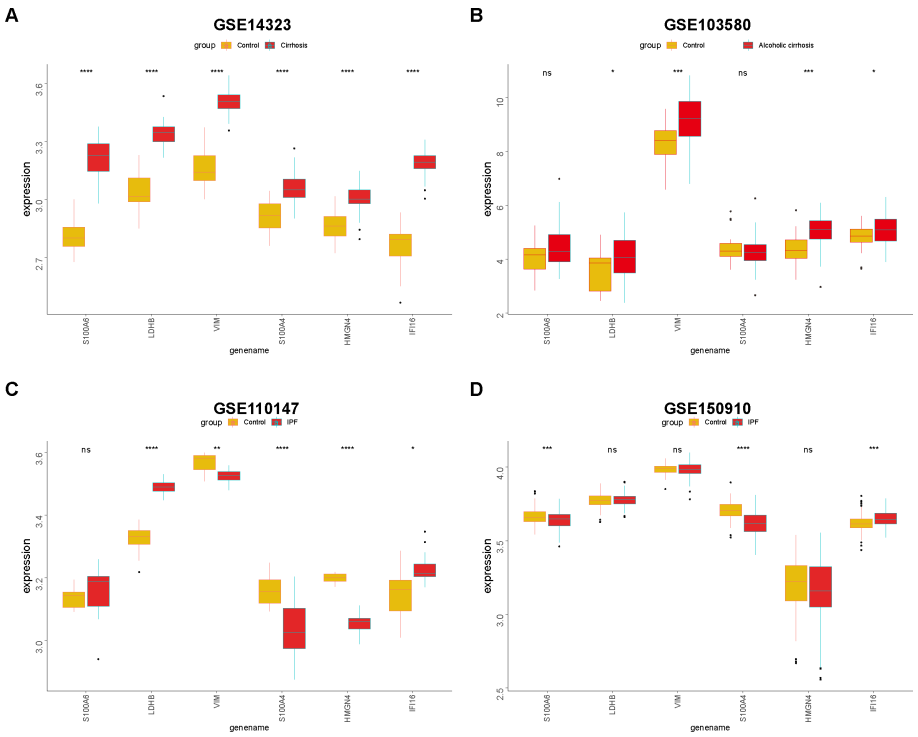

FIGURE 11
Expression of core DEGs in fibrosis, cirrhosis, and IPF. Differences in core DEG expressions in HCV-related cirrhosis **(A)**, alcoholic cirrhosis **(B)**, and IPF **(C, D)** were compared with the control. *p<0.05, **p<0.01, ***p<0.005, ****p<0.001, and ns, non-significant.

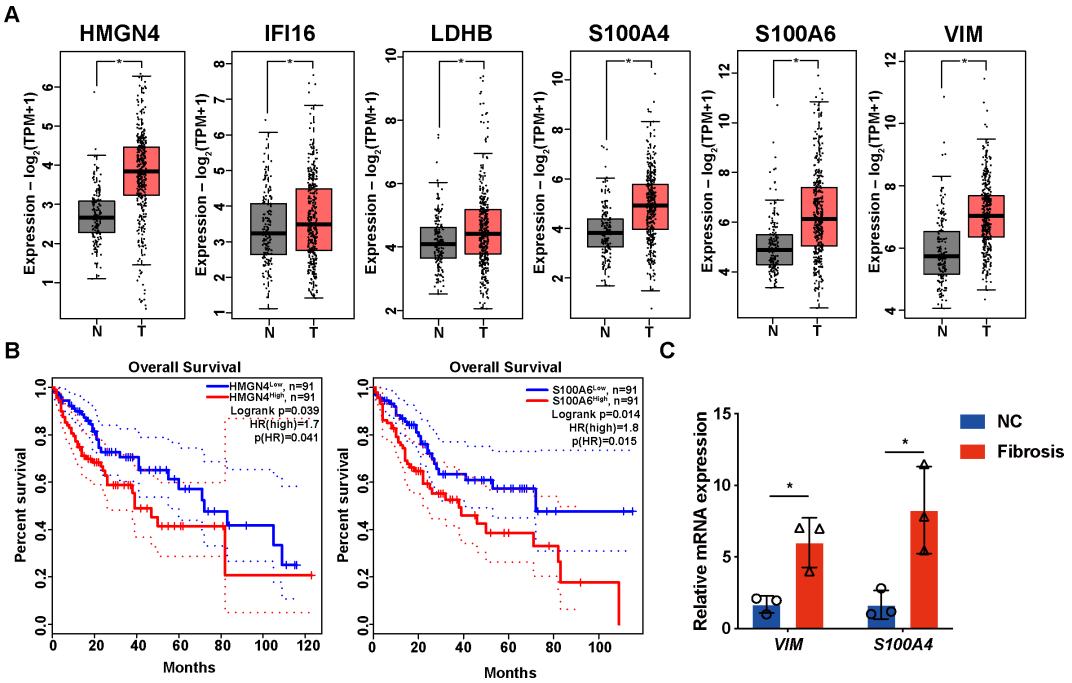

FIGURE 12
Expression and prognostic values of core DEGs in patients with HCC. **(A)** expressions of core DEG in the TCGA-LIHC patients. **(B)** overall survival of HCC patients with high or low expression of core DEGs. Only genes with significant association with survival are displayed. **(C)** mRNA expressions of VIM and S100A4 in normal and fibrotic mice detected by RT-qPCR. *p<0.05.

Last but not least, the expression of the core DEGs also reflected the tumorigenic risks underlying liver fibrosis (Figure 12). HCC is one of the most unfavorable outcomes of liver fibrosis and cirrhosis, and there might be shared molecules that function throughout fibrosis to tumorigenesis. For example, depletion of Apobec1 complementation factor (A1CF) in a mouse model upregulated genes responsible for oxidative stress, inflammatory response, extracellular matrix organization, and proliferation, resulting in spontaneous fibrosis, dysplasia, and HCC (45). On one hand, genes with accepted fibrotic roles might exert certain functions in hepatocellular carcinoma; on the other hand, our results underscore the consistent involvement of lactylation in liver fibrosis advancement and HCC development (46, 47). During the process, immunocytes might be the main executive component (48). Therefore, it would be worth investigating the roles of lactylation-associated immune infiltration in liver fibrosis progression to HCC for precise treatment (49, 50).

In summary, the study constructed a phenotyping model of liver fibrosis with lactylation-related DEGs between early- and later-stage patients, which can classify the cases into metabolic, immune, and intermediate clusters as well as predict the tumorigenic potential of liver fibrosis. The distinct inclination of the clusters revealed the interplay of metabolism and immunity in the progression of fibrotic pathology. To what extent these two forces function at different stages of liver fibrosis and how they are poised for HCC development may be interesting propositions in future investigations.

Data availability statement

The original contributions presented in the study are included in the article/supplementary material. Further inquiries can be directed to the corresponding authors.

Author contributions

L-nL: Writing – original draft, Visualization, Validation, Supervision, Software, Methodology, Investigation, Formal analysis, Data curation. W-wL: Writing – review & editing, Validation, Methodology, Investigation. L-sX: Writing – review & editing, Validation, Supervision, Conceptualization. W-nL: Writing – review & editing, Validation, Supervision, Conceptualization.

Funding

The author(s) declare financial support was received for the research, authorship, and/or publication of this article. The study was supported by Guangdong Natural Science Foundation (No.2022A1515110656).

Conflict of interest

Author W-wL was employed by the company Guangzhou Wondfo Health Science and Technology Co., Ltd.

The remaining authors declare that the research was conducted in the absence of any commercial or financial relationships that could be construed as a potential conflict of interest.

Publisher's note

References

1. Kisseleva T, Brenner D. Molecular and cellular mechanisms of liver fibrosis and its regression. *Nat Rev Gastroenterol Hepatol.* (2021) 18:151–66. doi: 10.1038/s41575-020-00372-7

2. Tang X, Yang L, Zhang P, Wang C, Luo S, Liu B, et al. Occult hepatitis B virus infection and liver fibrosis in Chinese patients. *J Infect Dis.* (2023) 228:1375–84. doi: 10.1093/infdis/jiad140

3. Lackner C, Tiniakos D. Fibrosis and alcohol-related liver disease. *J Hepatol.* (2019) 70:294–304. doi: 10.1016/j.jhep.2018.12.003

4. Parola M, Pinzani M. Liver fibrosis in NAFLD/NASH: from pathophysiology towards diagnostic and therapeutic strategies. *Mol Aspects Med.* (2024) 95:101231. doi: 10.1016/j.mam.2023.101231

5. Bataller R, Brenner DA. Liver fibrosis. *J Clin Invest.* (2005) 115:209–18. doi: 10.1172/JCI24282

6. Toh MR, Wong EYT, Wong SH, Ng AWT, Loo LH, Chow PK, et al. Global epidemiology and genetics of hepatocellular carcinoma. *Gastroenterology.* (2023) 164:766–82. doi: 10.1053/j.gastro.2023.01.033

7. Xiao J, Wang F, Wong NK, He J, Zhang R, Sun R, et al. Global liver disease burdens and research trends: Analysis from a Chinese perspective. *J Hepatol.* (2019) 71:212–21. doi: 10.1016/j.jhep.2019.03.004

8. Ling S, Jiang G, Que Q, Xu S, Chen J, Xu X. Liver transplantation in patients with liver failure: Twenty years of experience from China. *Liver Int.* (2022) 42:2110–6. doi: 10.1111/liv.15288

9. Sun L, Zhang H, Gao P. Metabolic reprogramming and epigenetic modifications on the path to cancer. *Protein Cell.* (2022) 13:877–919. doi: 10.1007/s13238-021-00846-7

10. Chen AN, Luo Y, Yang YH, Fu JT, Geng XM, Shi JP, et al. Lactylation, a novel metabolic reprogramming code: current status and prospects. *Front Immunol.* (2021) 12:688910. doi: 10.3389/fimmu.2021.688910

11. Zhang Y, Song H, Li M, Lu P. Histone lactylation bridges metabolic reprogramming and epigenetic rewiring in driving carcinogenesis: Oncometabolite fuels oncogenic transcription. *Clin Transl Med.* (2024) 14:e1614. doi: 10.1002/ctm2.1614

12. Wang N, Wang W, Wang X, Fu JT, Geng XM, Shi JP, et al. Histone lactylation boosts reparative gene activation post-myocardial infarction. *Circ Res.* (2022) 131:893–908. doi: 10.1161/CIRCRESAHA.122.320488

13. Yang K, Fan M, Wang X, Xu J, Wang Y, Tu F, et al. Lactate promotes macrophage HMGB1 lactylation, acetylation, and exosomal release in polymicrobial sepsis. *Cell Death Differ.* (2022) 29:133–46. doi: 10.1038/s41418-021-00841-9

14. Wang T, Ye Z, Li Z, Jing DS, Fan GX, Liu MQ, et al. Lactate-induced protein lactylation: A bridge between epigenetics and metabolic reprogramming in cancer. *Cell Prolif.* (2023) 56:e13478. doi: 10.1111/cpr.13478

15. Du S, Zhang X, Jia Y, Peng P, Kong Q, Jiang S, et al. Hepatocyte HSPA12A inhibits macrophage chemotaxis and activation to attenuate liver ischemia/reperfusion injury via suppressing glycolysis-mediated HMGB1 lactylation and secretion of hepatocytes. *Theranostics.* (2023) 13:3856–71. doi: 10.7150/thno.82607

16. Fan M, Yang K, Wang X, Chen L, Gill PS, Ha T, et al. Lactate promotes endothelial-to-mesenchymal transition via Snail1 lactylation after myocardial infarction. *Sci Adv*. (2023) 9:eadc9465. doi: 10.1126/sciadv.adc9465

17. Ye L, Jiang Y, Zhang M. Crosstalk between glucose metabolism, lactate production and immune response modulation. *Cytokine Growth Factor Rev*. (2022) 68:81–92. doi: 10.1016/j.cytogfr.2022.11.001

18. Parola M, Pinzani M. Liver fibrosis: Pathophysiology, pathogenetic targets and clinical issues. *Mol Aspects Med*. (2019) 65:37–55. doi: 10.1016/j.mam.2018.09.002

19. Zhou Y, Yan J, Huang H, Liu L, Ren L, Hu J, et al. The m(6)A reader IGF2BP2 regulates glycolytic metabolism and mediates histone lactylation to enhance hepatic stellate cell activation and liver fibrosis. *Cell Death Dis*. (2024) 15:189. doi: 10.1038/s41419-024-06509-9

20. Rho H, Terry AR, Chronis C, Hay N. Hexokinase 2-mediated gene expression via histone lactylation is required for hepatic stellate cell activation and liver fibrosis. *Cell Metab*. (2023) 35:1406–1423 e8. doi: 10.1016/j.cmet.2023.06.013

21. Cheng Z, Huang H, Li M, Liang X, Tan Y, Chen Y. Lactylation-related gene signature effectively predicts prognosis and treatment responsiveness in hepatocellular carcinoma. *Pharm (Basel)*. (2023) 16. doi: 10.3390/ph16050644

22. Liu X, Zhang Y, Li W, Zhou X. Lactylation, an emerging hallmark of metabolic reprogramming: Current progress and open challenges. *Front Cell Dev Biol*. (2022) 10:972020. doi: 10.3389/fcell.2022.972020

23. Wan N, Wang N, Yu S, Zhang H, Tang S, Wang D, et al. Cyclic immonium ion of lactyllysine reveals widespread lactylation in the human proteome. *Nat Methods*. (2022) 19:854–64. doi: 10.1038/s41592-022-01523-1

24. Hoang SA, Oseini A, Feaver RE, Cole BK, Asgharpour A, Vincent R, et al. Gene expression predicts histological severity and reveals distinct molecular profiles of nonalcoholic fatty liver disease. *Sci Rep*. (2019) 9:12541. doi: 10.1038/s41598-019-48746-5

25. Wang M, Gong Q, Zhang J, Chen L, Zhang Z, Lu L, et al. Characterization of gene expression profiles in HBV-related liver fibrosis patients and identification of ITGBL1 as a key regulator of fibrogenesis. *Sci Rep*. (2017) 7:43446. doi: 10.1038/srep43446

26. Ritchie ME, Phipson B, Wu D, Hu Y, Law CW, Shi W, et al. limma powers differential expression analyses for RNA-sequencing and microarray studies. *Nucleic Acids Res*. (2015) 43:e47. doi: 10.1093/nar/gkv007

27. Yu G, Wang LG, Han Y, He QY. clusterProfiler: an R package for comparing biological themes among gene clusters. *OMICS*. (2012) 16:284–7. doi: 10.1089/omi.2011.0118

28. Engebretsen S, Bohlin J. Statistical predictions with glmnet. *Clin Epigenet*. (2019) 11:123. doi: 10.1186/s13148-019-0730-1

29. Anteby R, Klang E, Horesh N, Nachmany I, Shimon O, Barash Y, et al. Deep learning for noninvasive liver fibrosis classification: A systematic review. *Liver Int*. (2021) 41:2269–78. doi: 10.1111/liv.14966

30. Acharya UR, Raghavendra U, Koh JEW, Meiburger KM, Ciaccio EJ, Hagiwara Y, et al. Automated detection and classification of liver fibrosis stages using contourlet transform and nonlinear features. *Comput Methods Programs BioMed*. (2018) 166:91–8. doi: 10.1016/j.cmpb.2018.10.006

31. Hammerich L, Tacke F. Hepatic inflammatory responses in liver fibrosis. *Nat Rev Gastroenterol Hepatol*. (2023) 20:633–46. doi: 10.1038/s41575-023-00807-x

32. Peiseler M, Schwabe R, Hampe J, Kubes P, Heikenwälder M, Tacke F. Immune mechanisms linking metabolic injury to inflammation and fibrosis in fatty liver disease - novel insights into cellular communication circuits. *J Hepatol*. (2022) 77:1136–60. doi: 10.1016/j.jhep.2022.06.012

33. Zhou Y, Zhang H, Yao Y, Zhang X, Guan Y, Zheng F. CD4(+) T cell activation and inflammation in NASH-related fibrosis. *Front Immunol*. (2022) 13:967410. doi: 10.3389/fimmu.2022.967410

34. Kotsiliti E, Leone V, Schuehle S, Govaere O, Li H, Wolf MJ, et al. Intestinal B cells license metabolic T-cell activation in NASH microbiota/antigen-independently and contribute to fibrosis by IgA-FcR signalling. *J Hepatol*. (2023) 79:296–313. doi: 10.1016/j.jhep.2023.04.037

35. Huang ZW, Zhang XN, Zhang L, Liu LL, Zhang JW, Sun YX, et al. STAT5 promotes PD-L1 expression by facilitating histone lactylation to drive immunosuppression in acute myeloid leukemia. *Signal Transduct Target Ther*. (2023) 8:391. doi: 10.1038/s41392-023-01605-2

36. Wang ZH, Zhang P, Peng WB, Ye LL, Xiang X, Wei XS, et al. Altered phenotypic and metabolic characteristics of FOXP3(+)CD3(+)CD56(+) natural killer T (NKT)-like cells in human Malignant pleural effusion. *Oncoimmunology*. (2023) 12:2160558. doi: 10.1080/2162402X.2022.2160558

37. Sun L, Yang X, Yuan Z, Wang H. Metabolic reprogramming in immune response and tissue inflammation. *Arterioscler Thromb Vasc Biol*. (2020) 40:1990–2001. doi: 10.1161/ATVBAHA.120.314037

38. Das UN. Beneficial role of bioactive lipids in the pathobiology, prevention, and management of HBV, HCV and alcoholic hepatitis, NAFLD, and liver cirrhosis: A review. *J Adv Res*. (2019) 17:17–29. doi: 10.1016/j.jare.2018.12.006

39. Distler JHW, Gyorfi AH, Ramanujam M, Whitfield ML, Königshoff M, Lafyatis R. Shared and distinct mechanisms of fibrosis. *Nat Rev Rheumatol*. (2019) 15:705–30. doi: 10.1038/s41584-019-0322-7

40. Guyot E, Sutton A, Rufat P, Laguillier C, Mansouri A, Moreau R, et al. PNPLA3 rs738409, hepatocellular carcinoma occurrence and risk model prediction in patients with cirrhosis. *J Hepatol*. (2013) 58:312–8. doi: 10.1016/j.jhep.2012.09.036

41. El-Tanbouly DM, Wadie W, Sayed RH. Modulation of TGF-beta/Smad and ERK signaling pathways mediates the anti-fibrotic effect of mirtazapine in mice. *Toxicol Appl Pharmacol*. (2017) 329:224–30. doi: 10.1016/j.taap.2017.06.012

42. Lofdahl A, Rydell-Tormanen K, Muller C, Martina Holst C, Thiman L, Ekström G, et al. 5-HT2B receptor antagonists attenuate myofibroblast differentiation and subsequent fibrotic responses in vitro and in *vivo*. *Physiol Rep*. (2016) 4. doi: 10.14814/phy2.12873

43. Trouve P, Genin E, Ferec C. In silico search for modifier genes associated with pancreatic and liver disease in Cystic Fibrosis. *PloS One*. (2017) 12:e0173822. doi: 10.1371/journal.pone.0173822

44. Minisini R, Giarda P, Grossi G, Bitetto D, Toniutto P, Falleti E, et al. Early activation of interferon-stimulated genes in human liver allografts: relationship with acute rejection and histological outcome. *J Gastroenterol*. (2011) 46:1307–15. doi: 10.1007/s00535-011-0440-8

45. Blanc V, Riordan JD, Soleymanjahi S, Nadeau JH, Nalbantoglu I, Xie Y, et al. Apobec1 complementation factor overexpression promotes hepatic steatosis, fibrosis, and hepatocellular cancer. *J Clin Invest*. (2021) 131. doi: 10.1172/JCI138699

46. Pan L, Feng F, Wu J, Fan S, Han J, Wang S, et al. Demethylzeylasteral targets lactate by inhibiting histone lactylation to suppress the tumorigenicity of liver cancer stem cells. *Pharmacol Res*. (2022) 181:106270. doi: 10.1016/j.phrs.2022.106270

47. Jin J, Bai L, Wang D, Ding W, Cao Z, Yan P, et al. SIRT3-dependent delactylation of cyclin E2 prevents hepatocellular carcinoma growth. *EMBO Rep*. (2023) 24:e56052. doi: 10.15252/embr.202256052

48. Gu J, Zhou J, Chen Q, Xu X, Gao J, Li X, et al. Tumor metabolite lactate promotes tumorigenesis by modulating MOESIN lactylation and enhancing TGF-beta signaling in regulatory T cells. *Cell Rep*. (2022) 39:110986. doi: 10.1016/j.celrep.2022.110986

49. Yang X, Yang C, Zhang S, Geng H, Zhu AX, Bernards R, et al. Precision treatment in advanced hepatocellular carcinoma. *Cancer Cell*. (2024) 42:180–97. doi: 10.1016/j.ccell.2024.01.007

50. Xiao LS, Hu CY, Cui H, Li RN, Hong C, Li QM, et al. Splenomegaly in predicting the survival of patients with advanced primary liver cancer treated with immune checkpoint inhibitors. *Cancer Med*. (2022) 11:4880–8. doi: 10.1002/cam4.4818

frontiers | Frontiers in Immunology

TYPE Original Research
PUBLISHED 16 September 2024
DOI 10.3389/fimmu.2024.1472354

OPEN ACCESS

EDITED BY
Dake Zhang,
Beihang University, China

REVIEWED BY
Jun Hu,
Tianjin Medical University Cancer Institute and Hospital, China
Ye Zhao,
Krirk University, Thailand

*CORRESPONDENCE
Zhiming Sun
szhm618@163.com
Bei Jiang
beier0131@163.com

†These authors have contributed equally to this work

RECEIVED 29 July 2024
ACCEPTED 28 August 2024
PUBLISHED 16 September 2024

CITATION
Yang J, Yang W, Hu Y, Tong L, Liu R, Liu L, Jiang B and Sun Z (2024) Screening of genes co-associated with osteoporosis and chronic HBV infection based on bioinformatics analysis and machine learning.
Front. Immunol. 15:1472354.
doi: 10.3389/fimmu.2024.1472354

Screening of genes co-associated with osteoporosis and chronic HBV infection based on bioinformatics analysis and machine learning

Jia Yang[1†], Weiguang Yang[2†], Yue Hu[3†], Linjian Tong[1], Rui Liu[1], Lice Liu[1], Bei Jiang[3*] and Zhiming Sun[1*]

[1]Clinical College of Neurology, Neurosurgery and Neurorehabilitation, Tianjin Medical University, Tianjin, China, [2]Department of Cardiovascular Surgery, Tianjin Medical University General Hospital, Tianjin, China, [3]Clinical School of the Second People's Hospital, Tianjin Medical University, Tianjin, China

Objective: To identify HBV-related genes (HRGs) implicated in osteoporosis (OP) pathogenesis and develop a diagnostic model for early OP detection in chronic HBV infection (CBI) patients.

Methods: Five public sequencing datasets were collected from the GEO database. Gene differential expression and LASSO analyses identified genes linked to OP and CBI. Machine learning algorithms (random forests, support vector machines, and gradient boosting machines) further filtered these genes. The best diagnostic model was chosen based on accuracy and Kappa values. A nomogram model based on HRGs was constructed and assessed for reliability. OP patients were divided into two chronic HBV-related clusters using non-negative matrix factorization. Differential gene expression analysis, Gene Ontology, and KEGG enrichment analyses explored the roles of these genes in OP progression, using ssGSEA and GSVA. Differences in immune cell infiltration between clusters and the correlation between HRGs and immune cells were examined using ssGSEA and the Pearson method.

Results: Differential gene expression analysis of CBI and combined OP dataset identified 822 and 776 differentially expressed genes, respectively, with 43 genes intersecting. Following LASSO analysis and various machine learning recursive feature elimination algorithms, 16 HRGs were identified. The support vector machine emerged as the best predictive model based on accuracy and Kappa values, with AUC values of 0.92, 0.83, 0.74, and 0.7 for the training set, validation set, GSE7429, and GSE7158, respectively. The nomogram model exhibited AUC values of 0.91, 0.79, and 0.68 in the training set, GSE7429, and GSE7158, respectively. Non-negative matrix factorization divided OP patients into two clusters, revealing statistically significant differences in 11 types of immune cell infiltration between clusters. Finally, intersecting the HRGs obtained from LASSO analysis with the HRGs identified three genes.

Conclusion: This study successfully identified HRGs and developed an efficient diagnostic model based on HRGs, demonstrating high accuracy and strong

predictive performance across multiple datasets. This research not only offers new insights into the complex relationship between OP and CBI but also establishes a foundation for the development of early diagnostic and personalized treatment strategies for chronic HBV-related OP.

KEYWORDS

osteoporosis, HBV, bioinformatics, machine learning, disease typing, immune cell infiltration

Introduction

Hepatitis B virus (HBV) infection is a significant global public health issue, affecting millions of people's health (1, 2). Chronic HBV infection (CBI) can lead to chronic liver diseases, including cirrhosis and hepatocellular carcinoma, severely impacting patients' quality of life (3). Recent studies have found that CBI is not only associated with liver-related diseases but may also increase the risk of other comorbidities, including osteoporosis (OP) (4, 5). OP is a bone disease characterized by low bone density and deterioration of bone tissue structure, leading to fragile bones and an increased risk of fractures (6, 7). This disease is common in middle-aged and elderly people, especially postmenopausal women, but men and younger individuals are also at risk (8, 9). The development of OP is related to various factors, including genetics, diet, lifestyle, and the impact of chronic diseases (10).

"Hepatic osteodystrophy" is a common complication of chronic liver disease, characterized by increased bone resorption and decreased bone formation, leading to metabolic bone disease (11, 12). It has been reported that the incidence of OP in chronic liver disease ranges from 12% to 55%, with fracture risk reaching up to 40% (13). In patients with chronic hepatitis, OP is considered one of the most significant complications (14). The connection between CBI and OP is not yet fully understood, but research suggests that HBV may impact bone health through direct and indirect mechanisms. These mechanisms include the chronic inflammatory response induced by the viral infection, low serum levels of insulin-like growth factor I, the induction of tumor necrosis factor which inhibits bone formation, and the potential effects of HBV-related drug treatments on bone density (15–18).

Bioinformatics is an interdisciplinary scientific field that combines biology, computer science, and statistics (19). It utilizes computational technology and mathematical methods to process and analyze the massive amount of data produced in biological research, revealing the nature and mechanisms of biological phenomena (20). Bioinformatics is widely applied in areas such as genomics, transcriptomics, proteomics, and metabolomics (21). The rapid development of this discipline has been facilitated by high-throughput technologies, such as gene chips, high-throughput sequencing, and mass spectrometry analysis (22). These advanced technologies generate a vast amount of biological data, which require in-depth analysis with bioinformatics tools. Research topics include data mining, sequence alignment, protein structure prediction, and biological network analysis (23). These methods help to unearth valuable information from the data, such as gene function, metabolic pathways, and protein interactions, which are crucial biological questions (24). Machine learning (ML), a branch of computer science, provides machines with the ability to learn autonomously. Machine learning algorithms are widely used in bioinformatics for prediction, classification, and feature selection tasks, and their application in the field of bioinformatics has become an important force driving biological research and medical development (25). By analyzing clinical data, medical images, and transcriptome data, machine learning can help doctors diagnose diseases more accurately, classify diseases, and identify disease-specific gene expression patterns (26).

In this study, we collected four OP datasets and one HBV dataset from the Gene Expression Omnibus (GEO) database. Bioinformatics-based analysis and machine learning methods were used to screen for common pathogenic genes of HBV and OP, and predictive models were constructed. In addition, a column-line graph prediction model was constructed, and the prediction performance was evaluated using calibration curves, decision curve analysis (DCA), and clinical impact curves. OP patients were classified into cluster1 and cluster2 according to HBV-related genes (HRGs), and the mechanisms by which HRGs affect the occurrence and development of OP were further explored by enrichment analysis and immune cell infiltration analysis. Three core genes were finally identified, and samples from 10 patients with

Abbreviations: OP, Osteoporosis; HBV, Hepatitis B virus; HRGs, HBV-related genes; DEGs, differentially expressed genes; GEO, Gene Expression Omnibus; CBI, Chronic HBV infection; ssGSEA, single-sample gene set enrichment analysis; ML, Machine learning; GSVA, gene set variation analysis; DCA, decision curve analysis; RFE, recursive feature elimination; RF, Random Forest; SVM, Support Vector Machine; and GBM, Gradient Boosting Machine; AUC, Area Under the Curve; NMF, non-negative matrix factorization; GO, Gene Ontology; KEGG, Kyoto Encyclopedia of Genes and Genomes; GSEA, Gene Set Enrichment Analysis; PBMC, Peripheral blood mononuclear cell.

CBI and 10 patients with combined OP with CBI were collected from Tianjin Second People's Hospital for molecular biology experiments.

Methods

Data collection and processing

This study collected five datasets from the Gene Expression Omnibus (GEO) database (https://www.ncbi.nlm.nih.gov/geo/) (27). The GSE83148 dataset includes liver tissue samples from 122 CBI patients and 6 healthy controls. GSE56815, GSE56814, GSE7429, and GSE7158 consist of peripheral blood mononuclear cell samples from OP patients and controls. The "sva" and "limma" packages in R software were used for data normalization and batch effect elimination (28, 29). The information for each dataset was shown in Table 1.

Gene differential expression analysis

The R package "limma" was used to perform gene differential expression analysis on the combined datasets of GSE56815 and GSE56814, and separately on GSE83148. The criteria for inclusion of differentially expressed genes in the GSE83148 dataset were $P<0.05$ and $|LogFC|>1$. For the combined dataset, the criterion for differentially expressed genes was $P<0.05$. Subsequently, an intersection of differentially expressed genes between the two datasets was taken.

Screening genes by least absolute shrinkage selection operator analysis and machine learning

The "glmnet" package was used for LASSO analysis to further select genes within both the combined dataset and the GSE83148 dataset, choosing the lambda corresponding to the smallest Binomial Deviance as the optimal value (30). Within the combined dataset, the "caret" package was utilized to compare the effects of recursive feature elimination (RFE) between models such as Random Forest (RF), Support Vector Machine (SVM), and Gradient Boosting Machine (GBM), to determine the final HRGs. The combined dataset was divided into a training set and an internal validation set in an 0.8:0.2 ratio, followed by the construction of an SVM model through ten-fold cross-validation. The "caret" package automatically selects the optimal model. The "DALEX" package was used to interpret the SVM model and generate results for the distribution of residuals and gene importance ranking (31). The "pROC" package was employed to draw the ROC curve and calculate the Area Under the Curve (AUC) to assess the accuracy of the predictive model (32). The GSE7429 and GSE7158 datasets were used to validate the accuracy of the model.

TABLE 1 Basic information of GEO datasets.

ID	Sample source	Number of cases	Number of controls
GSE83148	Liver	122	6
GSE56815	Peripheral blood mononuclear cell	40	40
GSE56814	Peripheral blood mononuclear cell	31	42
GSE7429	Peripheral blood mononuclear cell	10	10
GSE7158	Peripheral blood mononuclear cell	12	14

Construction and evaluation of the nomogram model

A nomogram model was constructed for the combined dataset using the Logistic regression method, and validated with the test datasets GSE7429 and GSE7158. The R software packages "rms" and "VRPM" were utilized to establish the nomogram model for OP risk assessment. In the nomogram, each of the HRGs is assigned a specific score; the individual scores of the 18 HRGs are summed to derive a total score. The risk of OP can be inferred based on the total score. The predictive capability of the nomogram model was evaluated using ROC curves, calibration curves, Decision Curve Analysis (DCA), and Clinical Impact Curves (33).

Identification and functional enrichment analysis of HBV-related OP patient clusters

To explore the differences in HBV-related clusters among OP patients, we clustered OP patients using the non-negative matrix factorization (NMF) method (34). The clustering was executed using the R package "NMF", applying the "brunet" algorithm over 50 iterations. Gene Ontology (GO) analysis, a common method for large-scale functional enrichment studies, encompasses biological processes (BP), molecular functions (MF), and cellular components (CC). The Kyoto Encyclopedia of Genes and Genomes (KEGG), a database widely used for biological pathway analysis (35), alongside the R package "clusterProfiler", was employed for conducting and visualizing GO and KEGG enrichment analyses. Gene Set Variation Analysis (GSVA), facilitating gene set (pathway) level differential analysis (36), was performed using the R packages "GSVA" and "limma". The R package "ggplot2" was utilized for visualization of the analysis results. GO, KEGG, and GSVA enrichment analyses were conducted to explore the differences in biological processes between aging-related clusters. GO and KEGG enrichment analyses were carried out using the Gene Set Enrichment Analysis (GSEA) method. Differentially expressed genes between clusters with $|LogFC|>1$ and $P<0.05$ were included in the analysis, and results with $P<0.05$ in the enrichment analyses were considered statistically significant. The GSVA enrichment analysis employed the single-sample gene set enrichment analysis (ssGSEA) method, which

calculates pathway scores based on gene expression matrices (37). In the GSVA enrichment results, |t|>2 and $P<0.05$ were deemed statistically significant.

Immune cell infiltration analysis

To identify differences in immune cell infiltration status among different HBV-related clusters, this study downloaded the commonly used immune cell-related gene set "LM22" from the literature (38). Using the R package "GSVA" and the ssGSEA algorithm, the immune cell infiltration scores of 71 OP samples in the GSE56815 dataset were evaluated to distinguish between the immune cell infiltration statuses of different clusters (39). Additionally, the R package "psych" was utilized to calculate the correlation between HRGs and 28 types of immune cells through Pearson correlation analysis.

Patients' samples collection and peripheral blood mononuclear cell isolation

In this study, 10 mL of fresh peripheral blood specimens were collected from 10 patients with CBI and 10 patients with CBI combined with OP at Tianjin Second People's Hospital. PBMCs were prepared from peripheral blood specimens by density gradient centrifugation using Ficoll cushion. The clinical information of patients was shown in Table 2. The study was approved by the Ethics Committee of Tianjin Second People's Hospital (No. [2018]15) and written informed consent was obtained from all participants.

The validation of the expression of hub genes between CBI and CBI combined with osteoporosis groups

Total RNA extraction was adopted using the Trizol reagent (Thermo Fisher Scientific, Darmstadt, Germany), followed by reverse transcription with a Reverse Transcription Kit (Takara Code No.RR 037A) following the instruction of the manufacturer. Real-time quantitative PCR (RT-qPCR) was performed by adopting a TaqMan PCR Kit (ThermoFisher). All reactions were conducted in duplicate, and the relative mRNA expression was calculated based on the $2^{-\Delta\Delta Ct}$ approach. Primer sequences are listed as follows: USP10-F, 5′-ATTGAGTTTGGTGTCGATGAAGT3′; USP10-R, 5′-GGAGCCATAGCTTGCTTCTTTAG3′; ECM1-F, 5′-GCTTCACGGCTACAGGACAG3′; ECM1-R, 5′-GAGGCTTCGGGATAGGGGT3′; ERAL1-F, 5′-TCAATCGGTGTTAAGAGTCTGGC3; ERAL1-R, 5′-TCCGTTGGAAGCCTAAGAGTG3′.

TABLE 2 Patient demographics.

Characteristics	CBI (n=10)	CBI combined with OP (n=10)	*P* value
Age (years)	38.4 ± 4.8	63.2 ± 3.1	*<0.001*
Male sex	8 (80.0%)	7 (70.0%)	*0.605*
HBV DNA (Log10 IU/mL)	1.4 (1.2-1.7)	1.3 (1.1-1.4)	*0.912*
ALT(U/L)	17.9 ± 6.5	25.4 ± 11.9	*0.123*
AST(U/L)	27.4 ± 8.7	35.4 ± 12.1	*0.105*
GGT (U/L)	47.6 ± 9.3	45.5 ± 10.3	*0.109*

ALT, alanine aminotransferase; AST, aspartate aminotransferase; GGT, glutamyltransferase.

Statistical analysis

R version 4.2.3 and GraphPad Prism version 9.0.2 (GraphPad Software Inc., San Diego, CA, USA) and SPSS 21.0 software (Chicago, IL, USA) were used for statistical analysis. The counting data were expressed as cases and percentages, and Chi-square test was used for comparison between groups. The statistical description of non-normal distribution data was expressed by median and quartile, and Mann–Whitney U test was used for comparison between groups. All tests were performed by two-tailed and P value of <0.05 was statistically significant.

Results

Gene differential expression analysis and screening of HRGs

The bioinformatics analysis strategy is illustrated in Figure 1. The combined dataset of GSE56815 and GSE56814, including 71 OP patients and 82 healthy control samples, yielded 822 differentially expressed genes (DEGs) after gene differential expression analysis (Figure 2A). The GSE83148 dataset resulted in 776 DEGs after gene expression differential analysis (Figure 2B). An intersection of the two datasets revealed a total of 43 common genes (Figure 2C).

To select HRGs, LASSO analysis was performed on the combined dataset. Figure 2D illustrates the coefficient of each gene varying with lambda. At lambda = 0.02887027, where the Binomial Deviance was minimized, the number of HRGs was determined to be 18 (Figure 2E). Subsequently, this study aimed to further filter the HRGs using three machine learning methods: RF-RFE, SVM-RFE, and GBM-RFE, evaluating the predictive performance of each method through Accuracy and Kappa. The results indicated that SVM-RFE outperformed RF-RFE and GBM-RFE in both Accuracy and Kappa. Moreover, among the three machine learning methods, when the number of HRGs was 18, the SVM-RFE method exhibited the highest Accuracy and Kappa, at 0.78 and 0.56, respectively (Figures 3A, B). These 18 HRGs were identified as USP10, ERAL1, ECM1, CTSD, BRD4, LCP2, PLAUR, NCKAP1L, EGR2, GPR56, GSN, CDC42EP3, FPR3, ARL4C, RCAN2, AIM2, GNMT, and SCD5. Figure 3C illustrates the expression of HRGs in OP patients and healthy controls.

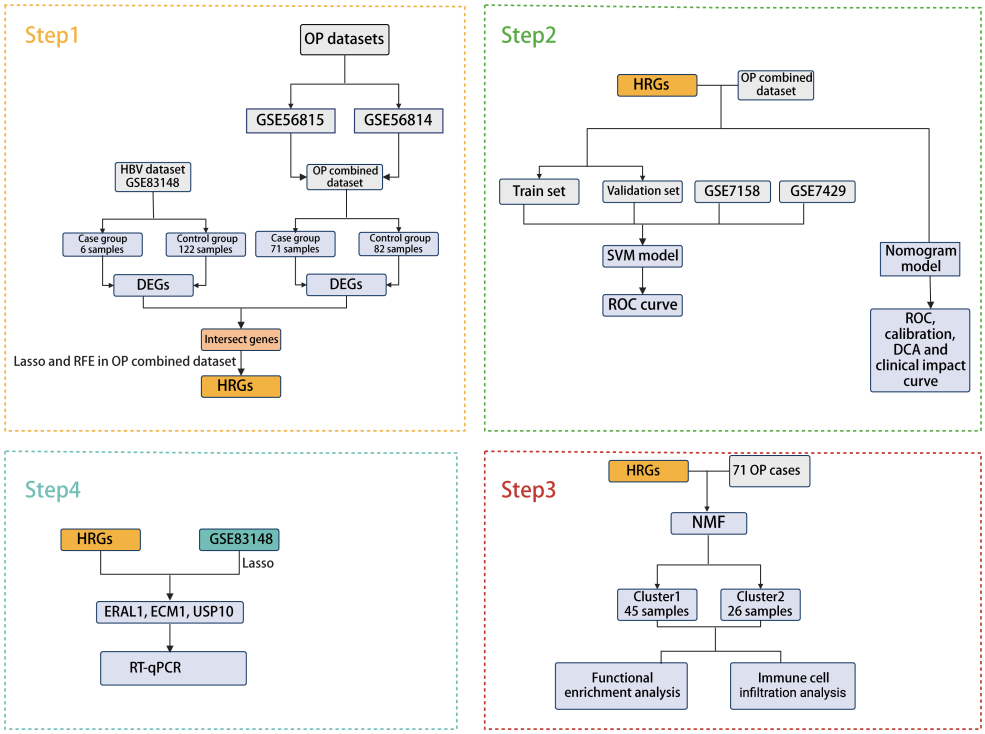

FIGURE 1
Flowchart of this study.

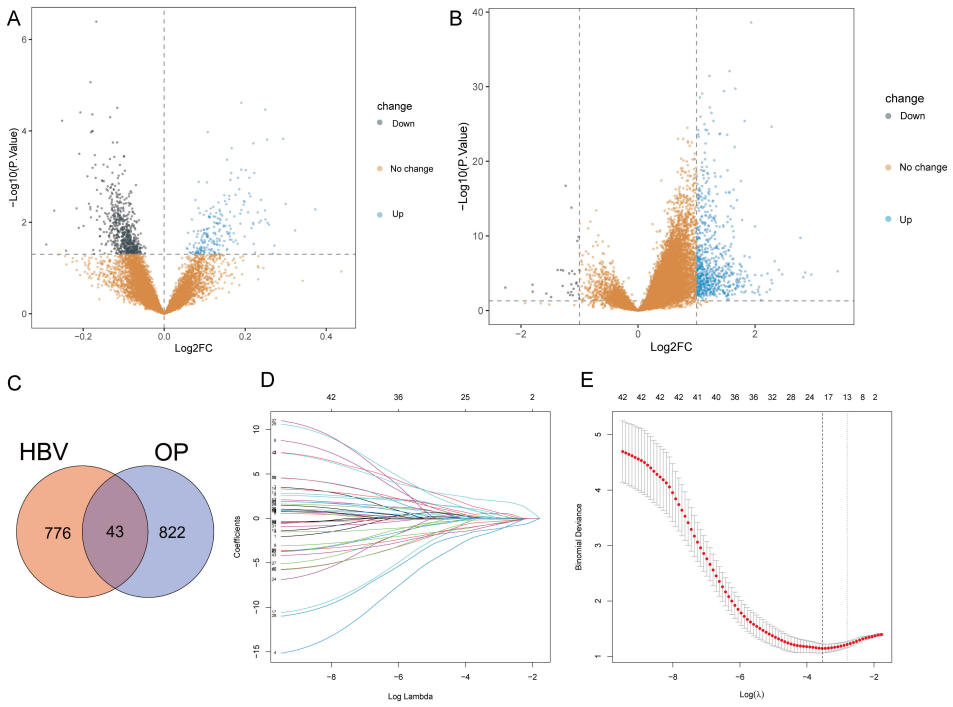

FIGURE 2
Gene differential expression analysis and Lasso analysis. **(A)** OP dataset. **(B)** GSE83148. **(C)** Intersection of DEGs from both datasets. **(D)** Coefficients of each gene as the penalty parameter lambda varies. Each line represents a gene. **(E)** Ten-fold cross-validation graph. The left dashed line represents the lambda value when the binomial deviation is minimal.

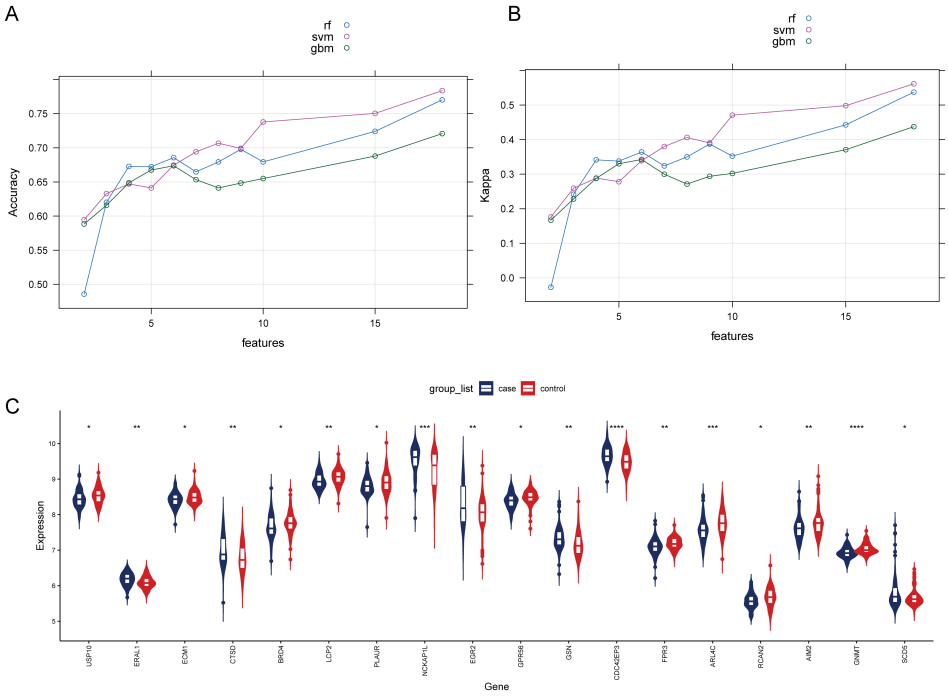

FIGURE 3
Comparison of machine learning models and expression of HRGs in the OP **(A)** Change in the accuracy of machine learning recursive feature elimination algorithms with the number of genes. **(B)** Change in the kappa of machine learning recursive feature elimination algorithms with the number of genes. **(C)** Expression of HRGs in the OP dataset. *P<0.05, **P<0.01, ***P<0.001, ****P<0.0001.

Construction and evaluation of predictive models for OP of HRGs

Next, we divided the combined dataset into a training set and a validation set in an 0.8:0.2 ratio and constructed an SVM model based on the 18 identified HRGs. We then analyzed and interpreted the distribution of residuals and the importance of features in the SVM model and evaluated the model's performance through ROC curves. Figures 4A, B display the residual inverse cumulative distribution curve and box plot, respectively. Figure 4C shows the importance of HRGs in the SVM model, evaluated using Root Mean Square Error (RMSE) loss, with GPR56 ranked as the most important. Finally, we used the GSE7428 and GSE7158 datasets to validate and test the effectiveness of our predictive model. Figure 4D presents the AUC values of the ROC curve for the SVM model. The AUC values in the training set, validation set, GSE7429, and GSE7158 were 0.92, 0.83, 0.74, and 0.7, respectively. The results indicate that the SVM model constructed based on HRGs demonstrates good predictive ability and can be used to predict the risk of OP.

To further evaluate the predictive performance of HRGs, we constructed a nomogram model based on the 18 HRGs using the combined dataset as the training set (Figure 5A). The ROC curve, calibration curve, Decision Curve Analysis (DCA) curve, and clinical impact curve were utilized to further assess the predictive performance of the nomogram. The nomogram model demonstrated an AUC of 0.91 in the training set, with AUCs of 0.79 and 0.68 in the GSE7429 and GSE7158 datasets, respectively (Figure 5B), indicating strong diagnostic value for OP. The calibration curve shows that the predicted performance of the constructed nomogram model aligns closely with the actual outcomes (Figure 5C). Similarly, the DCA curve illustrates the net benefit of the nomogram model across different risk thresholds, showing that decisions based on the nomogram model yield a net benefit compared to either intervening in all or none (Figure 5D). The clinical impact curve displays the estimated number of individuals identified as high risk by the model and the number of true positives across varying risk thresholds, aiding in assessing the model's efficacy in identifying true cases (Figure 5E).

Identification and functional enrichment analysis of CBI combined with OP patient clusters

Based on the 18 HRGs, patients in the combined dataset with OP were clustered using the Non-negative Matrix Factorization (NMF) method. A total of 71 OP patients were divided into cluster1 (N=45) and cluster2 (N=26). Figures 6A, B display the distinction between cluster1 and cluster2 through heatmaps. Subsequently, GO and KEGG enrichment analyses were performed between cluster1 and cluster2. Figure 7A and Figure 7B show the top 10 results of GSEA for GO and KEGG respectively, respectively. In the GSEA results for GO, compared to cluster2, cluster1 showed upregulation in response to type I interferon, tertiary granule, tube closure, negative regulation of cytoskeleton organization, neural tube

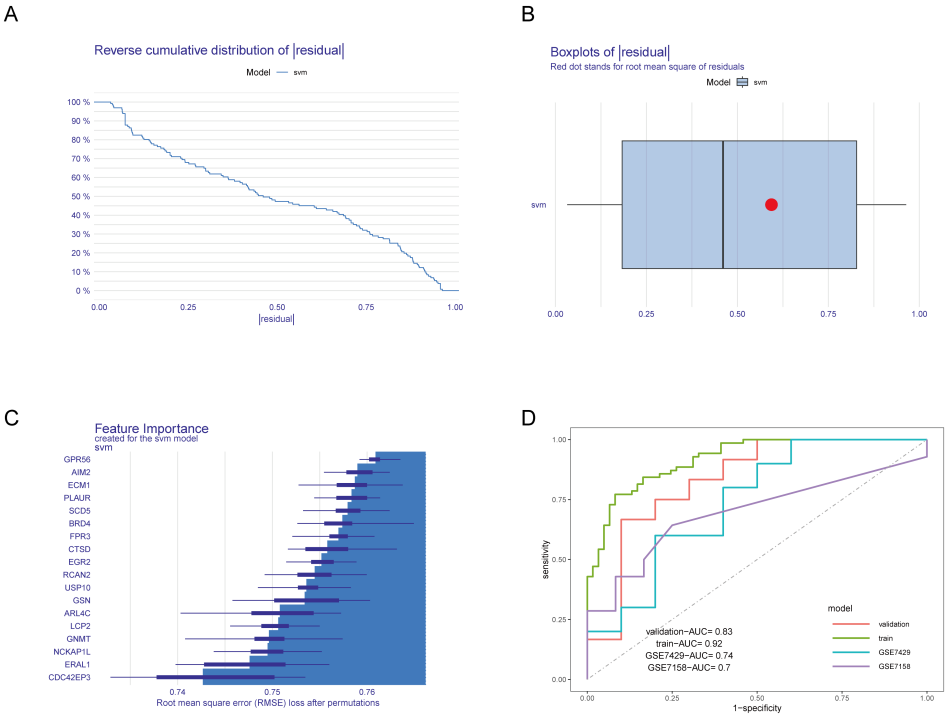

FIGURE 4
Construction and evaluation of the SVM model. **(A)** Residual inverse cumulative distribution curve. The X-axis represents the residual value. The Y-axis represents cumulative frequency. This means for any point on the graph, what frequency of samples have residuals greater than or equal to the value on the X-axis. **(B)** Residual box plot. The X-axis represents the residual value. The red dot represents the root mean square of residuals. **(C)** Importance of HRGs. The greater the RMSE loss, the more important the gene. **(D)** ROC curves of the SVM model in various datasets.

closure, and cellular response to type I interferon, and downregulation in recombinational repair, muscle organ development, DNA recombination, and ATP-dependent activity acting on DNA. In the GSEA results for KEGG, cluster1, in comparison to cluster2, indicated upregulation in the Adipocytokine signaling pathway, B cell receptor signaling pathway, Diabetic cardiomyopathy, FcγR-mediated phagocytosis, GnRH secretion, Influenza A, Neutrophil extracellular trap formation, RIG-I-like receptor signaling pathway, Th1 and Th2 cell differentiation, Thyroid hormone signaling pathway. Similarly, Figure 7C shows the top ten results for upregulated and downregulated GO terms in GSVA for cluster1 relative to cluster2. Figure 7D presents the results for upregulated and downregulated KEGG pathways in GSVA, with 10 pathways being upregulated and only 7 downregulated. In other words, the upregulated results represent pathways primarily involved by cluster1, while the downregulated results represent pathways mainly involved by cluster2.

Immune cell infiltration analysis

We analyzed the differences in immune cell infiltration levels between cluster1 and cluster2 (Figure 8A). The results indicated that, compared to cluster2, cluster1 exhibited upregulated infiltration of $CD56^{dim}$ natural killer cells, immature dendritic cells, T follicular helper cells, type 1 T helper cells, and type 17 T helper cells, and downregulated infiltration of eosinophils, gamma delta T cells, immature B cells, mast cells, and plasmacytoid dendritic cells. Figure 8B shows the correlation between HRGs and immune cells.

LASSO analysis for selecting HBV-related genes

After analyzing the OP dataset, we performed LASSO analysis on the GSE83148 dataset to further select HRGs Figure 9A illustrates the change in gene coefficients with lambda during the LASSO analysis. At lambda = 0.0002521665, where the Binomial Deviance was minimized, 6 genes were identified (Figure 9B). An intersection with HRGs yielded 3 genes: USP10, ERAL1, and ECM1. Figures 9C, D show the expression of these three genes in the OP and CBI datasets, respectively.

The validation of the expression pattern of three hub genes

To further confirm the accuracy of the above integrated bioinformatics analysis, we firstly examined the expression pattern of the three hub genes in the recruited patients. The RT-qPCR results confirmed expression pattern of three hub genes in CBI and CBI combined with OP. Figure 10 shows the relative

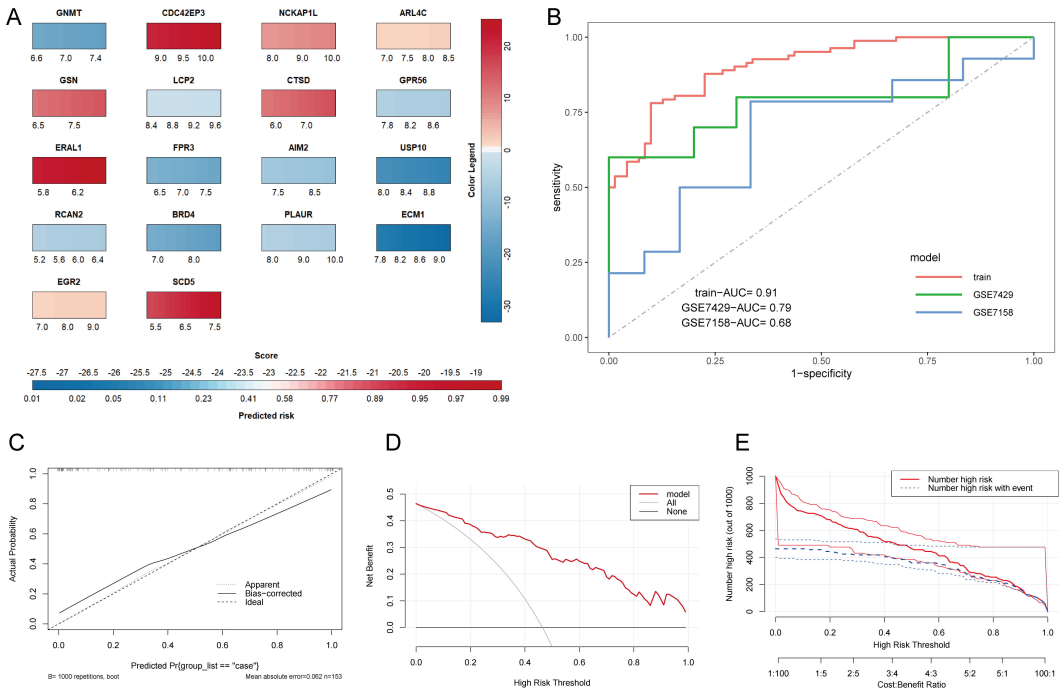

FIGURE 5
Construction and evaluation of the nomogram model. **(A)** Nomogram prediction model. The color legend on the right represents the score of each gene, adding up each gene's score to get the Score below and the Predicted risk of OP. **(B)** ROC curves of the nomogram model in various datasets. **(C)** Calibration curve. The X-axis represents predicted probability, and the Y-axis represents actual outcomes. Apparent represents uncorrected model predictions. Bias-corrected represents model predictions after bootstrapping correction. Ideal represents absolute ideal model predictions. **(D)** DCA curve. The X-axis is the threshold probability for being judged as high-risk, and the Y-axis represents net benefit. All and None represent the extreme cases of all interventions and no interventions. **(E)** Clinical impact curve. The dual X-axis represents the threshold probability of being judged as high risk and the cost: benefit ratio. Number high risk represents the number of cases judged positive by the model, Number high risk with event represents the number of true positives.

expression levels of the hub genes we identified in patients from the CBI group and the CBI combined with OP group. The relative expression levels of ERAL1 and USP10 in the CBI combined with OP group were significantly higher than those in the CBI group, consistent with the machine learning results (Figures 10A, C). Probably due to insufficient sample size, we did not observe differences in another hub gene ECM1 between the two groups (Figure 10B).

Discussion

CBI is a global public health issue that not only significantly affects the liver but is also associated with a variety of non-hepatic complications, including OP (40, 41). OP is a systemic bone disease caused by multiple factors, leading to decreased bone density and quality, as well as the deterioration of bone microarchitecture (42). An increasing body of research suggests that CBI can elevate the

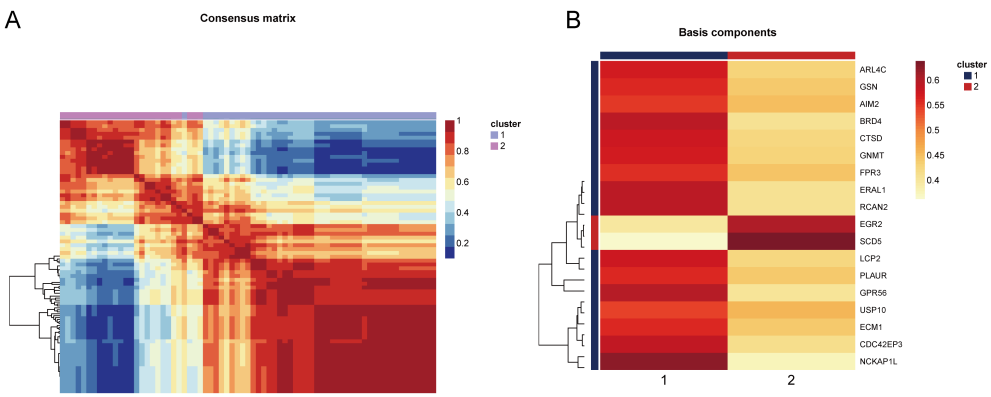

FIGURE 6
Heatmap showing the distinction between cluster1 and cluster2. **(A)** The consensus matrix of NMF clustering. **(B)** The co-clustering coefficient of HRGs.

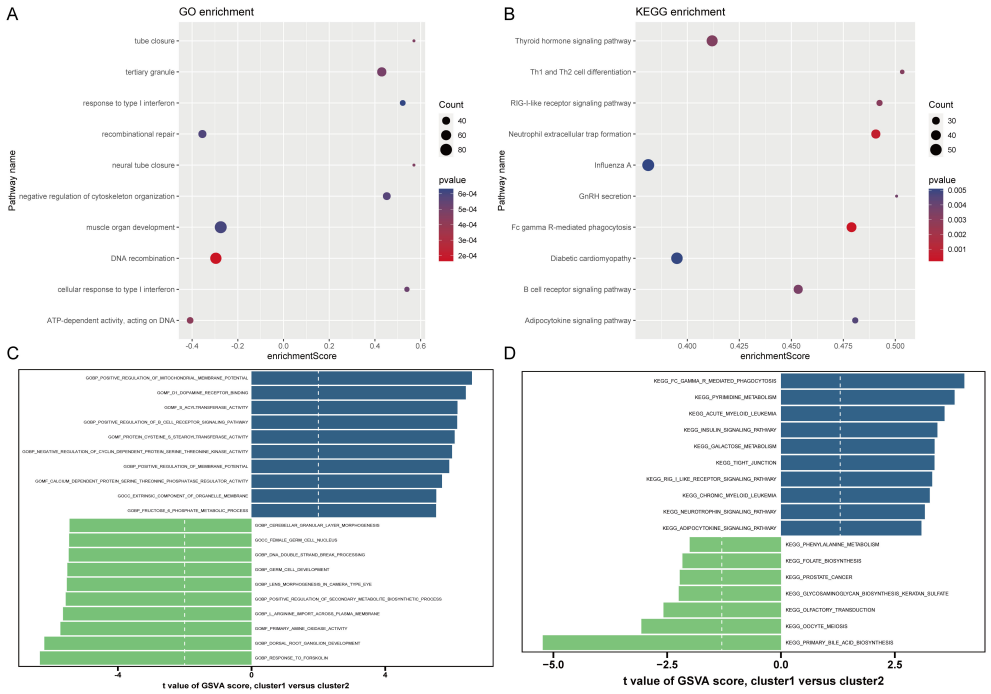

FIGURE 7
Results of GO and KEGG enrichment analysis. **(A, B)** GSEA results of GO and KEGG. The X-axis represents enrichment score. The Y-axis represents pathway names. Count represents the number of genes. **(C, D)** GSVA results of GO and KEGG. The X-axis is the t-value. The Y-axis represents pathway names.

risk of developing OP. Several studies have indicated that CBI may lead to osteoporosis through several mechanisms. Firstly, vitamin D deficiency, which is common in CBI patients, adversely affects bone metabolism and results in decreased bone mineral density. Additionally, long-term use of antiviral drugs, particularly tenofovir disoproxil fumarate (TDF), has been associated with bone mineral density reduction, likely due to its impact on renal phosphate handling, leading to bone demineralization. As CBI patients age, the presence of comorbidities such as diabetes, hypertension, and cardiovascular diseases further exacerbates the risk of osteoporosis by altering calcium metabolism and increasing bone fragility. Chronic inflammation associated with CBI may also contribute to bone loss by promoting the production of cytokines that enhance bone resorption. Although the direct effects of HBV on bone cells are still under investigation, these combined factors indicate that CBI patients, especially those on long-term TDF therapy and those with additional risk factors like age and comorbidities, are at a significantly increased risk of developing osteoporosis (43). Therefore, careful monitoring and individualized treatment strategies are recommended to mitigate this risk. Recently, the widespread adoption of microarray technologies and sequencing methods has significantly advanced the investigation of molecular mechanisms and landscapes of various diseases (44, 45). With the advent of big data, there is a growing utilization of comprehensive bioinformatics analysis and machine learning tools. These methods are instrumental in discovering new genes and potential diagnostic markers, as well as in unveiling the underlying mechanisms of diseases and identifying novel therapeutic targets (46, 47). This opens new avenues for understanding and treating diseases.

To our knowledge, this study is the first to explore the complex interactions between CBI and OP through the synergistic integration of bioinformatics analysis and machine learning techniques. In this research, we utilized datasets from the GEO database to identify HRGs by intersecting differentially expressed genes, conducting LASSO analysis, and employing machine learning recursive feature elimination. Notably, the HRGs selected by the three methods—RF-RFE, SVM-RFE, and GBM-RFE were consistent at 18, matching the LASSO analysis, indicating that HRGs are robust enough for predicting OP risk. Furthermore, the SVM model exhibited AUC values of 0.92, 0.83, 0.74, and 0.7 in the training set, validation set, GSE7429, and GSE7158, respectively. The nomogram model showed an AUC of 0.91 in the training set, with AUCs of 0.79 and 0.68 in the GSE7429 and GSE7158 datasets, respectively. Several OP prediction models based on biomarkers have been developed. The SVM prediction model constructed by Zhang Peng and others, based on m6A regulatory factors, achieved an AUC of 0.848 (48). The SVM prediction model constructed by Lai Jinzhi and colleagues, based on genes related to the Wnt pathway, achieved an AUC of 0.762, and the nomogram model also reached a high AUC of 0.7 (49). The prediction models developed by Zheng Zhenlong and his team showed AUCs ranging from 0.667 to 0.999 in the training set and from 0.603 to 0.662 in the test set (50). These results all emphasize the effectiveness of

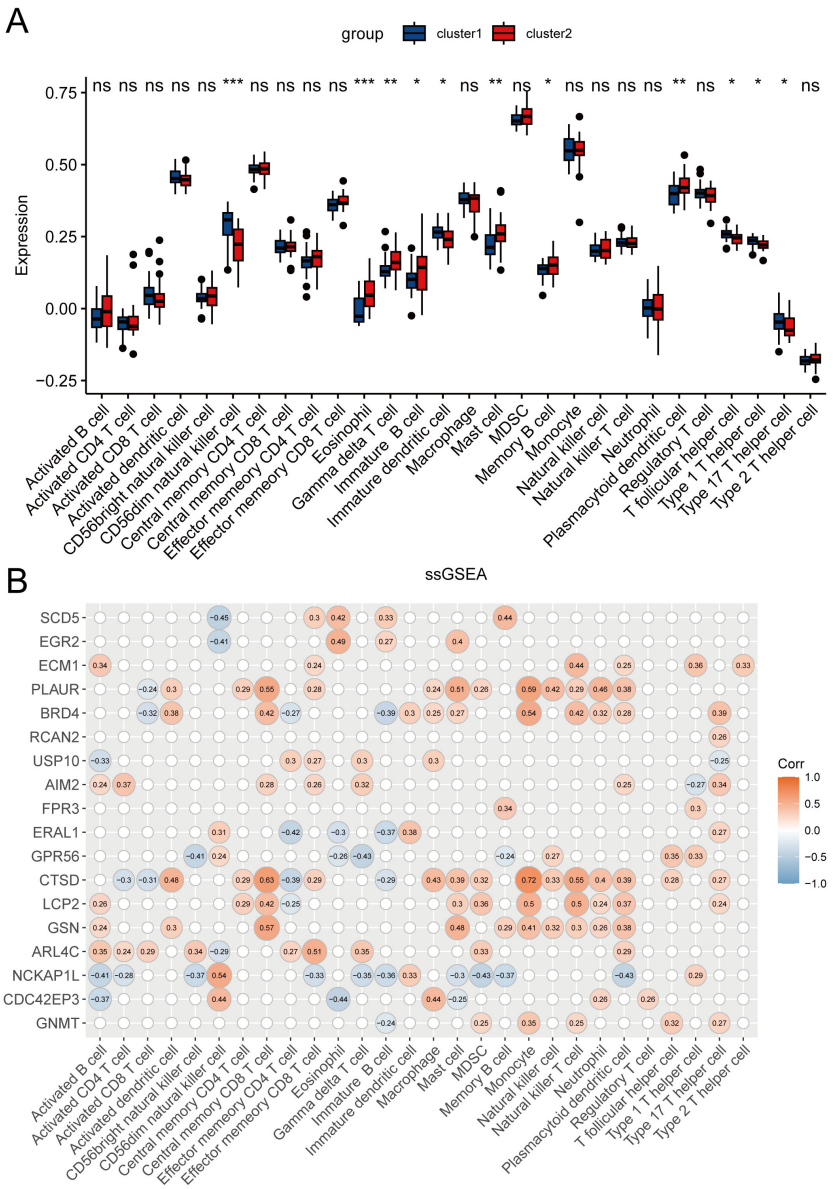

FIGURE 8
Immune cell infiltration analysis. **(A)** Differences in 28 types of immune cell infiltration between clusters evaluated by the ssGSEA algorithm. *$P < 0.05$, **$P < 0.01$, ***$P < 0.001$, ns represents $P \geq 0.05$. **(B)** Pearson correlation assessing the relationship between HRGs and 28 types of immune cells.

using machine learning to predict OP. Compared to other studies, our research, whether through the SVM based on HRGs or the nomogram model, demonstrates good predictive ability.

Patients with OP were divided into two distinct clusters using NMF clustering. Functional enrichment analysis further elucidated the different biological processes and pathways regulated in each cluster. These analyses revealed potential complex molecular mechanisms through identified upregulated and downregulated pathways, which may underlie the clinical manifestations of OP observed in patients with CBI. For instance, the differential regulation of pathways such as the Thyroid hormone signaling pathway, Th1 and Th2 cell differentiation, and the Adipocytokine signaling pathway in the GSEA results for KEGG highlighted the multifaceted nature of the pathogenesis of OP in the context of CBI (51–53). Additionally, pathways related to immune regulation, including Neutrophil extracellular trap formation, RIG-I-like receptor signaling pathway, Th1 and Th2 cell differentiation, FcγR-mediated phagocytosis, Adipocytokine signaling pathway, and B cell receptor signaling pathway, were upregulated in cluster1. Therefore, we speculate that cluster1 may predominantly influence the progression of OP through immune regulation. Conversely, in the GSVA results for KEGG, cluster2 exhibited upregulation in pathways such as primary bile acid biosynthesis, glycosaminoglycan biosynthesis - keratan sulfate, folate biosynthesis, and phenylalanine metabolism. Thus, we infer that cluster2 mainly affects the progression of OP through the synthesis

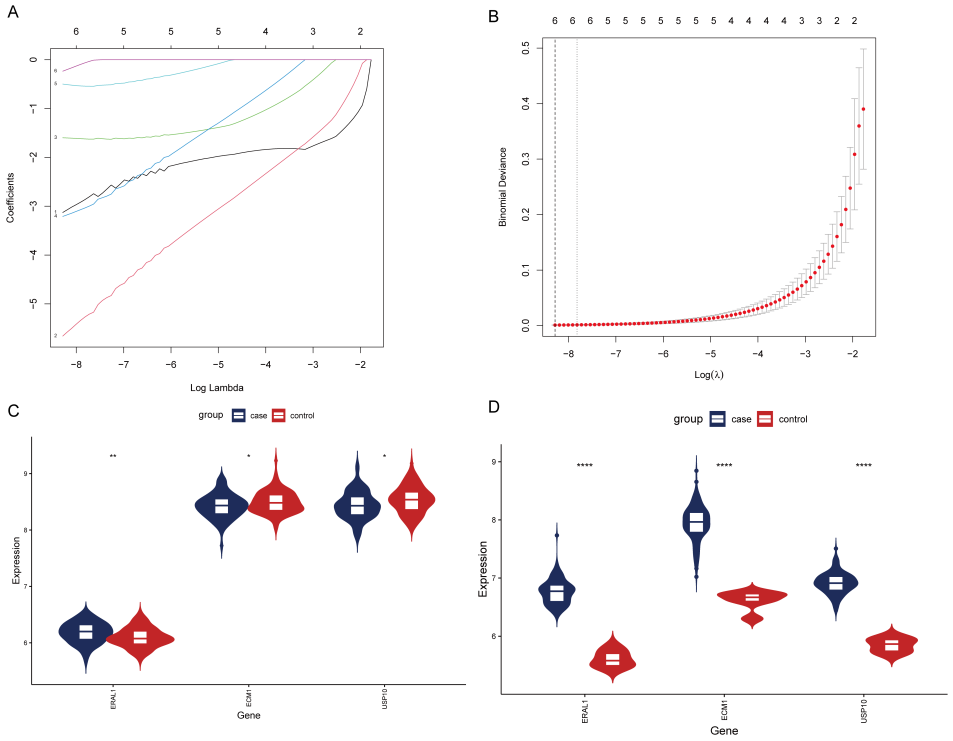

FIGURE 9
Screening of HRGs and expression of HRGs in the dataset. **(A)** Coefficients of each gene as the penalty parameter lambda varies. **(B)** Ten-fold cross-validation graph. **(C)** Expression of HRGs in the OP dataset. **(D)** Expression of HRGs in the HBV dataset. *$P < 0.05$, **$P < 0.01$, ****$P < 0.0001$.

and metabolism of condition-specific substances. These findings underscore the inherent heterogeneity of CBI combined with OP, indicating that the pathogenesis of OP in the context of CBI is not uniform but exhibits significant variation among individuals.

The analysis of immune cell infiltration has provided additional insights into the role of the immune system in the pathophysiology of chronic HBV-related OP. The differences in specific types of immune cell infiltrations between the two clusters emphasize the importance of the immune microenvironment in bone health and disease. The complex interactions between immune cells and bone cells, such as osteoblasts and osteoclasts, may influence bone density and structure, leading to the development or exacerbation of OP (54). Compared to cluster2, cluster1 exhibited increased infiltration of $CD56^{dim}$ natural killer cells, immature dendritic cells, T follicular helper cells, Th1 cells, and Th17 cells, while showing decreased infiltration of eosinophils, γδT cells, immature B cells, mast cells, and plasmacytoid dendritic cells. These findings highlight the need for targeted therapeutic strategies that address both the viral infection and its immunological consequences to effectively manage chronic HBV-related OP.

Finally, the intersection of HRGs identified three genes: USP10, ERAL1, and ECM1. USP10 is an enzyme belonging to the ubiquitin-specific proteases (USPs) family, playing a key role in the de-ubiquitination process (55). De-ubiquitination refers to the removal of ubiquitin from ubiquitinated proteins, a post-translational modification that can signal protein degradation, alter protein location, affect activity, and promote or inhibit protein-protein interactions (56). The differentiation of mesenchymal stem cells into

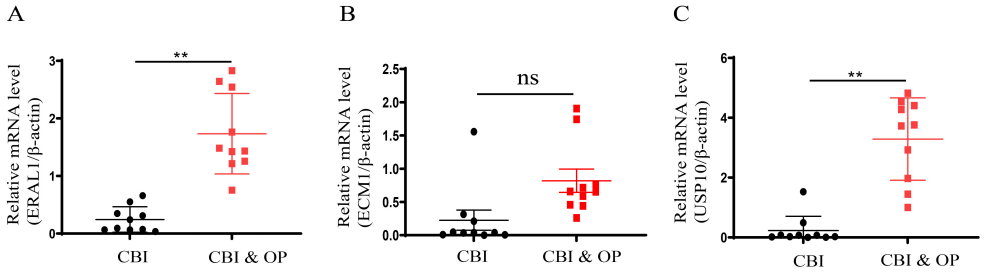

FIGURE 10
Expression of the three hub genes in CBI and CBI combined OP was detected by RT-qPCR. **(A)** ERAL1. **(B)** ECM1. **(C)** USP10. ns represents $P \geq 0.05$, **$P < 0.01$.

osteoblasts or the differentiation of monocytes into osteoclasts is regulated by USPs (57, 58). USP10 may participate in regulating bone metabolism processes through its specific de-ubiquitination activity, affecting the development of OP. Yu Wei and others found that estrogen can prevent cell aging and bone loss by regulating the degradation of p53 dependent on Usp10 in bone cells and osteoblasts (59). ERAL1 is an RNA chaperone located in mitochondria, mainly involved in the maturation and stability of mitochondrial 12s rRNA (60). ERAL1 is crucial for ensuring normal mitochondrial protein synthesis since 12s rRNA is a component of the mitochondrial ribosomal small subunit involved in protein synthesis within mitochondria (61, 62). Numerous studies have shown that mitochondrial dysfunction can lead to cellular disorder or dysfunction, disrupting the balance of osteoblast and osteoclast activity, thereby leading to the occurrence of OP (63, 64). Additionally, ERAL1 can promote the RIG-I-like receptor signaling pathway to inhibit viral infections (65). However, direct studies linking ERAL1 to OP have not been found. ECM1 is a widely expressed extracellular matrix protein that plays a role in various biological processes, including cell proliferation, differentiation, migration, and the organization and remodeling of the extracellular matrix (66–68). ECM1 influences the structure and function of the extracellular matrix through interactions with other extracellular matrix components such as collagens, glycoproteins, and proteoglycans (69). ECM can regulate the osteoblast lineage and osteoclast lineage, including their crosstalk, thereby affecting the occurrence of OP (70). It has been reported that Hepatocyte Growth Factor (HGF) and Epidermal Growth Factor (EGF) are increased in patients with HBV infection, enhancing the cell-protective intracellular signaling of ECM from the outside to the inside (71).

However, our study has some limitations. The research relied on datasets from publicly available data, with a limited number of samples and without specific datasets for CBI combined with OP, which may restrict the broad applicability of our findings. Furthermore, although we collected PBMCs from clinical patients and utilized qPCR to verify the expression levels of the hub genes for validation, the next step should involve collecting real-world data and detailed clinical information as supplements to verify the accuracy of the prediction models constructed with HRGs. Future studies should include additional experiments to explore the expression and mechanisms of USP10, ERAL1, and ECM in the context of CBI combined with OP. In clinical practice, particular attention should be given to patients with CBI exhibiting abnormal expression of USP10, ERAL1, and ECM, as this may indicate a higher risk of OP.

Conclusion

In conclusion, this study successfully identified HRGs using a combination of bioinformatics analysis and machine learning. Furthermore, the SVM and nomogram models built based on HRGs demonstrated excellent predictive performance across various OP datasets. The HRGs divided OP patients into two HBV-related subgroups, which exhibited significant differences in immune cell infiltration and biological pathways.

Data availability statement

The raw data supporting the conclusions of this article will be made available by the authors, without undue reservation.

Ethics statement

The study was approved by the Ethics Committee of Tianjin Second People's Hospital (No. [2018]15). The studies were conducted in accordance with the local legislation and institutional requirements. Written informed consent for participation in this study was provided by the participants' legal guardians/next of kin. Written informed consent was obtained from the individual(s) for the publication of any potentially identifiable images or data included in this article.

Author contributions

JY: Investigation, Methodology, Writing – original draft. WY: Investigation, Methodology, Software, Writing – original draft. YH: Investigation, Methodology, Software, Writing – original draft. LT: Investigation, Methodology, Writing – original draft. RL: Investigation, Methodology, Validation, Writing – original draft. LL: Data curation, Investigation, Methodology, Writing – original draft. BJ: Data curation, Investigation, Methodology, Supervision, Visualization, Writing – original draft, Writing – review & editing. ZS: Investigation, Methodology, Resources, Validation, Writing – original draft, Writing – review & editing.

Funding

The author(s) declare financial support was received for the research, authorship, and/or publication of this article. This study was supported by grants from the Natural Science Foundation of Tianjin Municipality (23JCYBJC01740).

Acknowledgments

The authors thank "home-for researchers (www.home-for-researchers.com)" for their help in polishing our English writing.

Conflict of interest

The authors declare that the research was conducted in the absence of any commercial or financial relationships that could be construed as a potential conflict of interest.

The reviewer JH declared a shared affiliation, with no collaboration, with several of the authors JY, WY, LT, RL, LL, ZS to the handling editor at the time of the review.

Publisher's note

References

1. Hsu Y-C, Huang DQ, Nguyen MH. Global burden of hepatitis B virus: current status, missed opportunities and a call for action. *JNRG Hepatol.* (2023) 20:524–37. doi: 10.1038/s41575-023-00760-9

2. Hou J, Liu Z, Gu F. Epidemiology and prevention of hepatitis B virus infection. *Int J Med Sci.* (2005), 50–7. doi: 10.7150/ijms.2.50

3. Cortesi PA, Conti S, Scalone L, Jaffe A, Ciaccio A, Okolicsanyi S, et al. Health related quality of life in chronic liver diseases. *Liver Int.* (2020) 40:2630–42. doi: 10.1111/liv.14647

4. Wang L, Qiu M, Wu L, Li Z, Meng X, He L, et al. Construction and validation of prognostic signature for hepatocellular carcinoma basing on hepatitis B virus related specific genes. *Infect Agent Cancer.* (2022) 17:60. doi: 10.1186/s13027-022-00470-y

5. Oh H, Jun DW, Lee IH, Ahn HJ, Kim BO, Jung S, et al. Increasing comorbidities in a South Korea insured population-based cohort of patients with chronic hepatitis B. *Aliment Pharmacol Ther.* (2020) 52:371–81. doi: 10.1111/apt.15867

6. Sobh MM, Abdalbary M, Elnagar S, Nagy E, Elshabrawy N, Abdelsalam M, et al. Secondary osteoporosis and metabolic bone diseases. *J Clin Med.* (2022) 11:2382. doi: 10.3390/jcm11092382

7. Raisz LG. Pathogenesis of osteoporosis: concepts, conflicts, and prospects. *J Clin Invest.* (2005) 115:3318–25. doi: 10.1172/jci27071

8. Ji MX, Yu Q. Primary osteoporosis in postmenopausal women. *Chronic Dis Trans Med.* (2015) 1:9–13. doi: 10.1016/j.cdtm.2015.02.006

9. Rinonapoli G, Ruggiero C, Meccariello L, Bisaccia M, Ceccarini P, Caraffa A. Osteoporosis in men: A review of an underestimated bone condition. *Int J Mol Sci.* (2021) 22:2105. doi: 10.3390/ijms22042105

10. Guo D, Zhao M, Xu W, He H, Li B, Hou T. Dietary interventions for better management of osteoporosis: An overview. *Crit Rev Food Sci Nutr.* (2021) 63:125–44. doi: 10.1080/10408398.2021.1944975

11. Rouillard S. Hepatic osteodystrophy. *Hepatology.* (2001) 33:301–7. doi: 10.1053/jhep.2001.20533

12. Ehnert S, Aspera-Werz RH, Ruoß M, Dooley S, Hengstler JG, Nadalin S, et al. Hepatic osteodystrophy—Molecular mechanisms proposed to favor its development. *Int J Mol Sci.* (2019) 20:2555. doi: 10.3390/ijms20102555

13. Gatta A. Hepatic osteodystrophy. *Clin cases Mineral Bone Metab.* (2014) 11:185–191. doi: 10.11138/ccmbm/2014.11.3.185

14. Wariaghli G, Mounach A, Achemlal L, Benbaghdadi I, Aouragh A, Bezza A, et al. Osteoporosis in chronic liver disease: a case–control study. *Rheumatol Int.* (2009) 30:893–9. doi: 10.1007/s00296-009-1071-8

15. Yang YJ, Kim DJ. An overview of the molecular mechanisms contributing to musculoskeletal disorders in chronic liver disease: osteoporosis, sarcopenia, and osteoporotic sarcopenia. *Int J Mol Sci.* (2021) 22:2604. doi: 10.3390/ijms22052604

16. Jeong H, Kim D. Bone diseases in patients with chronic liver disease. *Int J Mol Sci.* (2019) 20:4270. doi: 10.3390/ijms20174270

17. Gallego-Rojo FJ, Gonzalez-Calvin JL, Muñoz-Torres M, Mundi JL, Fernandez-Perez R, Rodrigo-Moreno D. Bone mineral density, serum insulin-like growth factor I, and bone turnover markers in viral cirrhosis. *Hepatology.* (1998) 28:695–9. doi: 10.1002/hep.510280315

18. Gonzalez-Calvin JL, Mundi JL, Casado-Caballero FJ, Abadia AC, Martin-Ibanez JJ. Bone mineral density and serum levels of soluble tumor necrosis factors, estradiol, and osteoprotegerin in postmenopausal women with cirrhosis after viral hepatitis. *JTJoCE Metab.* (2009) 94:4844–50. doi: 10.1210/jc.2009-0835

19. Benton D. Bioinformatics — principles and potential of a new multidisciplinary tool. *Trends Biotechnol.* (1996) 14:261–72. doi: 10.1016/0167-7799(96)10037-8

20. Mehmood MA, Sehar U, Ahmad NJ. Use of bioinformatics tools in different spheres of life sciences. *J Data Min Genomics Proteomics.* (2014) 5:1. doi: 10.4172/2153-0602.1000158

21. Ogunjobi TT, Ohaeri PN, Akintola OT, Atanda DO, Orji FP, Adebayo JO, et al. Bioinformatics applications in chronic diseases: A comprehensive review of genomic, transcriptomics, proteomic, metabolomics, and machine learning approaches. *Medinformatics.* (2024) 52:371–81. doi: 10.47852/bonviewMEDIN42022335

22. Schmidt B, Hildebrandt A. Next-generation sequencing: big data meets high performance computing. *Drug Discovery Today.* (2017) 22:712–7. doi: 10.1016/j.drudis.2017.01.014

23. Lan K, Wang D-t, Fong S, L-s L, Wong KKL, Dey N. A survey of data mining and deep learning in bioinformatics. *J Med Syst.* (2018) 42:139. doi: 10.1007/s10916-018-1003-9

24. Dale JM, Popescu L, Karp PD. Machine learning methods for metabolic pathway prediction. *BMC Bioinf.* (2010) 11:15. doi: 10.1186/1471-2105-11-15

25. Shastry KA, Sanjay HA. Machine learning for bioinformatics. In: *Statistical Modelling and Machine Learning Principles for Bioinformatics Techniques, Tools, and Applications.* Algorithms for Intelligent Systems. Singapore: Springer Nature Singapore Pte Ltd (2020). p. 25–39. doi: 10.1007/978-981-15-2445-5

26. Larrañaga P, Calvo B, Santana R, Bielza C, Galdiano J, Inza I, et al. Machine learning in bioinformatics. *Briefings Bioinf.* (2006) 7:86–112. doi: 10.1093/bib/bbk007

27. Edgar R, Domrachev M, Lash AE. Gene Expression Omnibus: NCBI gene expression and hybridization array data repository. *Nucleic Acids Res.* (2002) 30:207–10. doi: 10.1093/nar/30.1.207

28. Leek JT, Johnson WE, Parker HS, Jaffe AE, Storey JD. The sva package for removing batch effects and other unwanted variation in high-throughput experiments. *Bioinformatics.* (2012) 28:882–3. doi: 10.1093/bioinformatics/bts034

29. Ritchie ME, Phipson B, Wu D, Hu Y, Law CW, Shi W, et al. limma powers differential expression analyses for RNA-sequencing and microarray studies. *Nucleic Acids Res.* (2015) 43:e47. doi: 10.1093/nar/gkv007

30. Frost HR, Amos CI. Gene set selection via LASSO penalized regression (SLPR). *Nucleic Acids Res.* (2017) 45:e114. doi: 10.1093/nar/gkx291

31. Su Z, Su W, Li C, Ding P, Wang Y. Identification and immune features of cuproptosis-related molecular clusters in polycystic ovary syndrome. *Sci Rep.* (2023) 13:980. doi: 10.1038/s41598-022-27326-0

32. Robin X, Turck N, Hainard A, Tiberti N, Lisacek F, Sanchez JC, et al. pROC: an open-source package for R and S+ to analyze and compare ROC curves. *BMC Bioinf.* (2011) 12:77. doi: 10.1186/1471-2105-12-77

33. Vickers AJ, van Calster B, Steyerberg EW. A simple, step-by-step guide to interpreting decision curve analysis. *Diagn Progn Res.* (2019) 3:18. doi: 10.1186/s41512-019-0064-7

34. Brunet JP, Tamayo P, Golub TR, Mesirov JP. Metagenes and molecular pattern discovery using matrix factorization. *Proc Natl Acad Sci U S A.* (2004) 101:4164–9. doi: 10.1073/pnas.0308531101

35. Kanehisa M, Goto S. KEGG: kyoto encyclopedia of genes and genomes. *Nucleic Acids Res.* (2000) 28:27–30. doi: 10.1093/nar/28.1.27

36. Subramanian A, Tamayo P, Mootha VK, Mukherjee S, Ebert BL, Gillette MA, et al. Gene set enrichment analysis: a knowledge-based approach for interpreting genome-wide expression profiles. *Proc Natl Acad Sci U S A.* (2005) 102:15545–50. doi: 10.1073/pnas.0506580102

37. Lei C, Zhongyan Z, Wenting S, Jing Z, Liyun Q, Hongyi H, et al. Identification of necroptosis-related genes in Parkinson's disease by integrated bioinformatics analysis and experimental validation. *Front Neurosci.* (2023) 17:1097293. doi: 10.3389/fnins.2023.1097293

38. Newman AM, Liu CL, Green MR, Gentles AJ, Feng W, Xu Y, et al. Robust enumeration of cell subsets from tissue expression profiles. *Nat Methods.* (2015) 12:453–7. doi: 10.1038/nmeth.3337

39. Zheng H, Liu H, Li H, Dou W, Wang J, Zhang J, et al. Characterization of stem cell landscape and identification of stemness-relevant prognostic gene signature to aid immunotherapy in colorectal cancer. *Stem Cell Res Ther.* (2022) 13:244. doi: 10.1186/s13287-022-02913-0

40. Shahriar S, Araf Y, Ahmad R, Kattel P, Sah GS, Rahaman TI, et al. Insights into the coinfections of human immunodeficiency virus-hepatitis B virus, human immunodeficiency virus-hepatitis C virus, and hepatitis B virus-hepatitis C virus: prevalence, risk factors, pathogenesis, diagnosis, and treatment. *Front Microbiol.* (2022) 12:780887. doi: 10.3389/fmicb.2021.780887

41. Hwang EW, Cheung R. Global epidemiology of hepatitis B virus (HBV) infection. *Am Chin J Med Science.* (2012) 4:7. doi: 10.7156/v4i1p007

42. Montoya MJ, Giner M, Miranda C, Vázquez MA, Caeiro JR, Guede D, et al. Microstructural trabecular bone from patients with osteoporotic hip fracture or osteoarthritis: Its relationship with bone mineral density and bone remodelling markers. *Maturitas.* (2014) 79:299–305. doi: 10.1016/j.maturitas.2014.07.006

43. Yip TC, Lai JC, Yam TF, Tse YK, Hui VW, Lai MS, et al. Long-term use of tenofovir disoproxil fumarate increases fracture risk in elderly patients with chronic hepatitis B. *J Hepatol.* (2024) 80:553–63. doi: 10.1016/j.jhep.2023.12.001

44. Karczewski KJ, Snyder MP. Integrative omics for health and disease. *Nat Rev Genet.* (2018) 19:299–310. doi: 10.1038/nrg.2018.4

45. Yang Y, Adelstein SJ, Kassis AI. Target discovery from data mining approaches. *Drug Discovery Today*. (2012) 17:S16–23. doi: 10.1016/j.drudis.2011.12.006

46. Auslander N, Gussow AB, Koonin EV. Incorporating machine learning into established bioinformatics frameworks. *Int J Mol Sci*. (2021) 22:2903. doi: 10.3390/ijms22062903

47. Li R, Li L, Xu Y, Yang J. Machine learning meets omics: applications and perspectives. *Briefings Bioinf*. (2022) 23:bbab560. doi: 10.1093/bib/bbab460

48. Zhang P, Chen H, Xie B, Zhao W, Shang Q, He J, et al. Bioinformatics identification and experimental validation of m6A-related diagnostic biomarkers in the subtype classification of blood monocytes from postmenopausal osteoporosis patients. *Front Endocrinol*. (2023) 14:990078. doi: 10.3389/fendo.2023.990078

49. Lai J, Yang H, Huang J, He L. Investigating the impact of Wnt pathway-related genes on biomarker and diagnostic model development for osteoporosis in postmenopausal females. *Sci Rep*. (2024) 14:2880. doi: 10.1038/s41598-024-52429-1

50. Zheng Z, Zhang X, Oh B-K, Kim K-Y. Identification of combined biomarkers for predicting the risk of osteoporosis using machine learning. *Aging*. (2022) 14:4270–80. doi: 10.18632/aging.204084

51. Bassett JHD, Williams GR. Role of thyroid hormones in skeletal development and bone maintenance. *Endocrine Rev*. (2016) 37:135–87. doi: 10.1210/er.2015-1106

52. Zhang J, Fu Q, Ren Z, Wang Y, Wang C, Shen T, et al. Changes of serum cytokines-related Th1/Th2/Th17 concentration in patients with postmenopausal osteoporosis. *Gynecological Endocrinology*. (2014) 31:183–90. doi: 10.3109/09513590.2014.975683

53. Patil JD, Fredericks S. The role of adipokines in osteoporosis management: a mini review. *Front Endocrinology*. (2024) 15:1336543. doi: 10.3389/fendo.2024.1336543

54. Clowes JA, Riggs BL, Khosla S. The role of the immune system in the pathophysiology of osteoporosis. *Immunol Rev*. (2005) 208:207–27. doi: 10.1111/j.0105-2896.2005.00334.x

55. Chen S, Liu Y, Zhou H. Advances in the development ubiquitin-specific peptidase (USP) inhibitors. *Int J Mol Sci*. (2021) 22:4546. doi: 10.3390/ijms22094546

56. Wang Y, Wang F. Post-translational modifications of deubiquitinating enzymes: expanding the ubiquitin code. *Front Pharmacol*. (2021) 12:685011. doi: 10.3389/fphar.2021.685011

57. Shen J, Lin X, Dai F, Chen G, Lin H, Fang B, et al. Ubiquitin-specific peptidases: Players in bone metabolism. *Cell Proliferation*. (2023) 56:e13444. doi: 10.1111/cpr.13444

58. Luo W, Zhang G, Wang Z, Wu Y, Xiong Y. Ubiquitin-specific proteases: Vital regulatory molecules in bone and bone-related diseases. *Int Immunopharmacology*. (2023) 118:110075. doi: 10.1016/j.intimp.2023.110075

59. Wei Y, Fu J, Wu W, Ma P, Ren L, Wu J. Estrogen prevents cellular senescence and bone loss through Usp10-dependent p53 degradation in osteocytes and osteoblasts: the role of estrogen in bone cell senescence. *Cell Tissue Res*. (2021) 386:297–308. doi: 10.1007/s00441-021-03496-7

60. Uchiumi T, Ohgaki K, Yagi M, Aoki Y, Sakai A, Matsumoto S, et al. ERAL1 is associated with mitochondrial ribosome and elimination of ERAL1 leads to mitochondrial dysfunction and growth retardation. *Nucleic Acids Res*. (2010) 38:5554–68. doi: 10.1093/nar/gkq305

61. Mai N, Chrzanowska-Lightowlers ZMA, Lightowlers RN. The process of mammalian mitochondrial protein synthesis. *Cell Tissue Res*. (2016) 367:5–20. doi: 10.1007/s00441-016-2456-0

62. Dennerlein S, Rozanska A, Wydro M, Chrzanowska-Lightowlers Zofia MA, Lightowlers Robert N. Human ERAL1 is a mitochondrial RNA chaperone involved in the assembly of the 28S small mitochondrial ribosomal subunit. *Biochem J*. (2010) 430:551–8. doi: 10.1042/bj20100757

63. Liu J, Gao Z, Liu X. Mitochondrial dysfunction and therapeutic perspectives in osteoporosis. *Front Endocrinol*. (2024) 15:1325317. doi: 10.3389/fendo.2024.1325317

64. Yan C, Shi Y, Yuan L, Lv D, Sun B, Wang J, et al. Mitochondrial quality control and its role in osteoporosis. *Front Endocrinol*. (2023) 14:1077058. doi: 10.3389/fendo.2023.1077058

65. Li S, Kuang M, Chen L, Li Y, Liu S, Du H, et al. The mitochondrial protein ERAL1 suppresses RNA virus infection by facilitating RIG-I-like receptor signaling. *Cell Rep*. (2021) 34:108631. doi: 10.1016/j.celrep.2020.108631

66. Mongiat M, Andreuzzi E, Tarticchio G, Paulitti A. Extracellular matrix, a hard player in angiogenesis. *Int J Mol Sci*. (2016) 17:1822. doi: 10.3390/ijms17111822

67. Mongiat M, Fu J, Oldershaw R, Greenhalgh R, Gown AM, Iozzo RV. Perlecan protein core interacts with extracellular matrix protein 1 (ECM1), a glycoprotein involved in bone formation and angiogenesis. *J Biol Chem*. (2003) 278:17491–9. doi: 10.1074/jbc.M210529200

68. Theocharis AD, Manou D, Karamanos NK. The extracellular matrix as a multitasking player in disease. *FEBS J*. (2019) 286:2830–69. doi: 10.1111/febs.14818

69. Järveläinen H, Sainio A, Koulu M, Wight TN, Penttinen R. Extracellular matrix molecules: potential targets in pharmacotherapy. *Pharmacol Rev*. (2009) 61:198–223. doi: 10.1124/pr.109.001289

70. Alcorta-Sevillano N, Macías I, Infante A, Rodríguez CI. Deciphering the relevance of bone ECM signaling. *Cells*. (2020) 9:2630. doi: 10.3390/cells9122630

71. Barreiros AP, Sprinzl M, Rosset S, Höhler T, Otto G, Theobald M, et al. EGF and HGF levels are increased during active HBV infection and enhance survival signaling through extracellular matrix interactions in primary human hepatocytes. *Int J Cancer*. (2008) 124:120–9. doi: 10.1002/ijc.23921

frontiers | Frontiers in Immunology

TYPE Review
PUBLISHED 22 October 2024
DOI 10.3389/fimmu.2024.1483834

OPEN ACCESS

EDITED BY
Bing Yang,
Tianjin Medical University, China

REVIEWED BY
Jun Hu,
Tianjin Medical University Cancer Institute and Hospital, China
Shengshan Xu,
Jiangmen Central Hospital, China
Dong Wu,
Zhuanghe Central Hospital, China

*CORRESPONDENCE
Yutao Wang
pumch_ytwang@126.com
Zijia Tao
zjtao@cmu.edu.cn

RECEIVED 20 August 2024
ACCEPTED 30 September 2024
PUBLISHED 22 October 2024

CITATION
Ning J, Wang Y and Tao Z (2024) The complex role of immune cells in antigen presentation and regulation of T-cell responses in hepatocellular carcinoma: progress, challenges, and future directions. *Front. Immunol.* 15:1483834. doi: 10.3389/fimmu.2024.1483834

The complex role of immune cells in antigen presentation and regulation of T-cell responses in hepatocellular carcinoma: progress, challenges, and future directions

Jianbo Ning[1], Yutao Wang[2]* and Zijia Tao[3]*

[1]The Fourth Clinical College, China Medical University, Shenyang, China, [2]Department of Urology, Peking Union Medical College Hospital, Chinese Academy of Medical Sciences and Peking Union Medical College, Beijing, China, [3]Department of Interventional Radiology, the First Hospital of China Medical University, Shenyang, China

Hepatocellular carcinoma (HCC) is a prevalent form of liver cancer that poses significant challenges regarding morbidity and mortality rates. In the context of HCC, immune cells play a vital role, especially concerning the presentation of antigens. This review explores the intricate interactions among immune cells within HCC, focusing on their functions in antigen presentation and the modulation of T-cell responses. We begin by summarizing the strategies that HCC uses to escape immune recognition, emphasizing the delicate equilibrium between immune surveillance and evasion. Next, we investigate the specific functions of various types of immune cells, including dendritic cells, natural killer (NK) cells, and CD8+ T cells, in the process of antigen presentation. We also examine the impact of immune checkpoints, such as cytotoxic T-lymphocyte-associated protein 4 (CTLA-4) and the pathways involving programmed cell death protein 1 (PD-1) and programmed death ligand 1 (PD-L1), on antigen presentation, while taking into account the clinical significance of checkpoint inhibitors. The review further emphasizes the importance of immune-based therapies, including cancer vaccines and CAR-T cell therapy, in improving antigen presentation. In conclusion, we encapsulate the latest advancements in research, propose future avenues for exploration, and stress the importance of innovative technologies and customized treatment strategies. By thoroughly analyzing the interactions of immune cells throughout the antigen presentation process in HCC, this review provides an up-to-date perspective on the field, setting the stage for new therapeutic approaches.

KEYWORDS

hepatocellular carcinoma, dendritic cells, natural killer cells, CTLA-4, PD-1/PD-L1

1 Introduction

Hepatocellular carcinoma (HCC), the predominant type of liver cancer, poses a considerable challenge to global health, illustrated by rising incidence figures and concerning mortality rates (1–3). The complex relationships between cancerous cells and the host's immune system are crucial in influencing the development and progression of HCC. Understanding how immune cells participate in the antigen presentation process related to HCC is vital, as this insight is fundamental to improving our grasp of tumor immunology and formulating effective therapeutic strategies (4). This review seeks to explore the complex interactions between immune cells and HCC, emphasizing their functions in antigen presentation and the regulation of T cell responses (5). HCC is frequently associated with chronic liver conditions, such as viral hepatitis, alcoholic liver disease, and non-alcoholic fatty liver disease (5, 6). These risk factors lead to a microenvironment that fosters immune dysregulation, allowing tumor cells to escape immune detection and grow (7, 8).

The immune system's ability to recognize and destroy abnormal cells is fundamental to cancer progression. In this context, the process of antigen presentation acts as a critical checkpoint (9, 10). Antigen-presenting cells (APCs), including dendritic cells (DCs) and macrophages, play a vital role in the capture of tumor-specific antigens and their subsequent delivery to CD8+ cytotoxic T cells. This process initiates a cascade of immune responses aimed at targeting cancerous cells. Nevertheless, the complex mechanisms linked to antigen presentation in HCC and their influence on the anti-tumor immune response remain subjects of ongoing research.

Understanding the immune dynamics related to HCC antigen presentation carries important therapeutic implications. While immune checkpoint inhibitors have achieved impressive results across various types of cancer, their effectiveness in HCC has been limited. This discovery suggests that gaining a deeper insight into the immune landscape within the microenvironment of HCC is essential for creating improved immunotherapy approaches (11, 12). Additionally, creating personalized treatment modalities, such as cancer vaccines and adoptive T cell therapies, relies on a clear understanding of the mechanisms of antigen presentation (13, 14).

As investigations reveal the complex interactions among immune cells and HCC, it is essential to present a thorough summary of the current understanding. This review aims to consolidate existing research to illuminate the varied functions of immune cells in relation to antigen presentation within HCC. By exploring the detailed communication among immune cells, tumor cells, and the tumor microenvironment, we seek to clarify the elements that contribute to immune evasion and identify potential pathways for enhancing anti-tumor immune responses. Through this analysis, the review enhances the overall comprehension of tumor immunology and establishes a foundation for developing innovative and focused immunotherapeutic approaches targeting HCC.

1.1 Immune escape mechanism of hepatocellular carcinoma

HCC is recognized as the main liver cancer that often arises in the context of ongoing liver inflammation, particularly associated with conditions such as viral hepatitis and liver damage from alcohol (15–17). The management of immune surveillance plays a crucial role in identifying and eliminating cancerous cells. Nevertheless, HCC has skillfully developed various strategies to avoid immune detection, promoting its unrestricted growth and advancement (18). An essential factor contributing to the immune evasion observed in HCC is the increased expression of inhibitory immune checkpoint proteins. Among these, programmed death ligand 1 (PD-L1) stands out prominently, alongside cytotoxic T-lymphocyte-associated protein 4 (CTLA-4) (19–21). These molecules interact with their corresponding receptors on T cells, hindering their activation and subsequent effector functions, thereby weakening the immune response aimed at cancerous cells.

Furthermore, the microenvironment surrounding tumors in hepatocellular carcinoma (HCC) frequently exhibits a suppressive immune profile, largely as a result of the buildup of regulatory T cells (Tregs) and myeloid-derived suppressor cells (MDSCs) (22–24). This aggregation of cells leads to the suppression of effector T cells and natural killer (NK) cells, ultimately undermining the immune response directed at malignant cells (25, 26). At the same time, HCC cells display a tendency to release a variety of immunosuppressive cytokines and chemokines, particularly transforming growth factor-beta (TGF-β) and interleukin-10 (IL-10), contributing to the overall reduction of anti-tumoral immune responses (Figure 1).

Alterations in both genetic and epigenetic factors observed in HCC cells contribute to immune evasion, as demonstrated by changes in human leukocyte antigen (HLA) expression and modifications in mechanisms for antigen presentation (27–29). These irregularities enable HCC cells to avoid detection and destruction by cytotoxic T cells, crafting a sophisticated evasion strategy. Recently, clinical studies have highlighted the effectiveness of immunotherapeutic approaches aimed at these immune escape routes. In these initiatives, immune checkpoint blockers like anti-programmed cell death protein 1 (PD-1) and anti-PD-L1 antibodies have demonstrated effectiveness in certain groups of HCC patients by re-energizing the inhibited immune response directed towards the tumor. Furthermore, investigating combination therapies targeting various immune evasion pathways shows potential in enhancing the effectiveness of treatment option.

1.2 Interaction between immune cells and tumor microenvironment

The complex interactions between various groups of immune cells and the tumor microenvironment (TME) in HCC represent a dynamic and multifaceted mechanism that significantly influences the progression of the disease (11, 30). A broad spectrum of research has uncovered important elements of this relationship, emphasizing the sophisticated ways in which distinct immune cell populations interact and communicate within the TME. Tumor-associated macrophages (TAMs) are key players in the immune milieu, predominantly exhibiting a pro-tumoral M2 phenotype in the context of HCC. This behavior fosters both tumor development

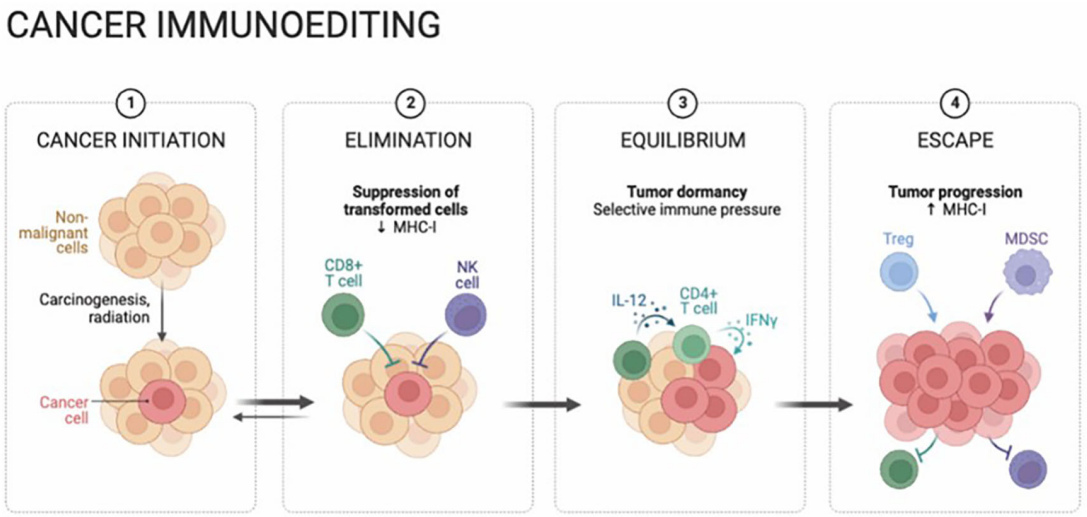

FIGURE 1
Hepatocellular carcinoma (HCC) cancer immunoediting is a dynamic and multifaceted process, comprising the stages of cancer initiation, elimination, equilibrium, and eventual escape. Immune surveillance initially destroys nascent cells, followed by immune equilibrium controlling growth. Over time, HCC evades detection, leading to progression. Understanding these stages reveals the complex immune-HCC relationship, emphasizing therapeutic potential.

and neovascularization by releasing factors such as vascular endothelial growth factor (VEGF) and IL-10 (31, 32). Tregs, another critical aspect of the immune response, build up in the TME and considerably influence antitumor immunity by effectively inhibiting cytotoxic T cells and establishing an immunosuppressive environment (33). Concurrently, MDSCs play a pivotal role in promoting immune evasion mechanisms, as they reduce T cell functionality and stimulate angiogenesis, further complicating the already intricate landscape of immune escape within the TME (34).

Additionally, the complex interactions of immune checkpoints in the HCC microenvironment trigger a series of sophisticated molecular exchanges that shape the trajectory of antitumor immune responses. Importantly, PD-1 found on T cells, when engaging with its corresponding ligand PD-L1 on tumor cells, induces a state of immune exhaustion, undermining the processes of effective tumor recognition and elimination (35, 36). In a similar vein, CTLA-4 inhibits the activation of antitumor T cell responses through its proficient suppression of costimulatory signals (37, 38). These diverse interactions collectively create a complex landscape dependent on a fragile balance between immune activation and inhibition, a balance that is significantly disrupted in the context of HCC.

Deepening our understanding of these complex interactions offers considerable potential for identifying new therapeutic avenues for HCC. Targeted strategies that modulate immune cell dynamics and interrupt the detailed network of immune evasion mechanisms may prove effective in halting tumor progression and enhancing antitumor immune responses. The rapid progress of breakthroughs in immunotherapy, including immune checkpoint blockers and adoptive T cell treatments, underscores the growing dynamism within this field. Furthermore, the integration of cutting-edge methodologies, including single-cell genomics and spatial transcriptomics, has the potential to reveal previously unexplored complexities within the immune environment of HCC (39). These revelations could lead to the creation of precision immunotherapeutic strategies specifically designed to address the unique immunological context of individual HCC patients, signaling a new era in the management of this challenging malignancy.

1.3 Balance of immune surveillance and escape

The intricate equilibrium between immune monitoring and evasion significantly impacts the advancement of HCC. A range of research efforts supports the complex interactions between tumor cells and the immune system of the host. While immune surveillance conducts a complex process to recognize and eliminate cancerous cells, HCC employs various strategies to evade detection and destruction by the immune system. The mechanisms of immune evasion in HCC are illustrated by the heightened expression of inhibitory immune checkpoint proteins, notably characterized by increased levels of PD-L1 (40, 41). This orchestrated interaction with PD-1 on T cells leads to their exhaustion and results in a weakened antineoplastic effector response (42). The TME within HCC acts as an architect, shaping an environment conducive to immunosuppression, which is significantly influenced by the recruitment of regulatory Tregs and MDSCs. The consolidation of these immunosuppressive entities ultimately suppresses the functionality of effector immune cells. This delicate equilibrium is further influenced by fluctuating levels of pro-inflammatory cytokines, notably IL-6 and tumor necrosis factor-alpha (TNF-α), which play dual roles by enhancing antitumoral immunity while also promoting inflammation within the tumor microenvironment (43–45).

Therapeutic strategies designed to counteract these complex mechanisms include immune checkpoint inhibitors and adoptive T cell therapies. The primary aim of these therapeutic approaches is to

restore balance, thereby enhancing immune responses against HCC cells. Immune checkpoint inhibitors, known for their ability to disrupt immune inhibitory interactions, represent a powerful front in overcoming the immune-suppressive barriers established by HCC. In conjunction with this, adoptive T cell therapies provide a means to rejuvenate the functionality of effector T cells, thereby revitalizing the immune response. Together, these therapeutic modalities hold transformative potential, envisioning a therapeutic landscape that favors a recalibrated immune response against HCC and, consequently, a more effective therapeutic trajectory.

2 Role of immune cells in HCC antigen presentation

In the realm of HCC, the coordination of immune cells is vital to the intricate process of presenting antigens, which is essential for triggering adaptive immune responses aimed at combating cancer cells. Dendritic cells (DCs) are particularly important in this immune response, as they adeptly capture antigens from tumor cells, process them, and present tumor-derived peptides on their surface within the major histocompatibility complex (MHC) framework (46, 47). This essential interaction between antigens and MHC molecules is recognized by CD4+ and CD8+ T cells, which in turn triggers a specific immune response against HCC (48–50). However, HCC can evade this immune response through various mechanisms that interfere with antigen presentation, leading to immune resistance. Notably, tumor-infiltrating myeloid cells, including DCs, undergo changes that render them immunosuppressive, diminishing their ability to present antigens effectively. Moreover, HCC cells themselves can modulate MHC expression or suppress antigen processing and presentation, enabling them to escape detection by T cells. Therapeutic strategies, such as immune checkpoint inhibitors, are designed to counter these inhibitory signals and enhance antigen presentation, aiming to elicit robust antitumor immune responses, which holds promise in the treatment of HCC (Figure 2).

As we delve deeper into this intricate environment, the expanding array of immune cell subsets within the HCC microenvironment significantly influences the dynamics of antigen presentation. Regulatory T cells (Tregs), known for their suppressive effects on immune responses, interact closely with antigen-presenting DCs, modulating the strength and effectiveness of immune activation (51) (Figure 2). MDSCs, characterized by their strong immunosuppressive properties, contribute to a complex interplay that dampens antigen presentation, creating a microenvironment that supports HCC progression. Understanding and targeting this complex interplay is crucial for developing new therapies that overcome immune suppression, enhance antigen presentation, and strengthen antitumor immune responses (52).

From a broader therapeutic perspective, the quest to enhance antigen presentation and reinvigorate immune responses is fraught with challenges. The inherent plasticity of the immune landscape, coupled with the complexity of the HCC microenvironment, complicates the development of effective interventions. While immune checkpoint inhibitors have shown promise, ongoing efforts must balance the enhancement of immune responses with the potential for immune-related adverse effects. The potential for combination therapies, including but not limited to immune checkpoint inhibitors, offers hope in dismantling the mechanisms of immune escape (53, 54). Identifying the most effective and lasting therapeutic approaches will require careful exploration through a multidisciplinary approach that integrates experimental findings with clinical observations.

2.1 Function and regulation of dendritic cells

DCs play a crucial role at the crossroads of the immune system, orchestrating key regulatory functions within both the innate and adaptive immune responses (55, 56). As specialized antigen-presenting cells, DCs are responsible for capturing, processing, and presenting antigens to T cells, thereby initiating and modulating a range of immune responses. In the complex environment of HCC, the essential role of DCs is evident in their ability to recognize tumor-derived antigens and initiate the priming of tumor-specific T cells (57, 58, 108). DCs utilize a variety of mechanisms, including phagocytosis, macropinocytosis, and receptor-mediated endocytosis, to capture tumor antigens. The antigens that have been captured are subsequently transformed into peptide fragments, which are displayed on the surface of DCs through major histocompatibility complex (MHC) molecules. This process of presenting antigens, aided by co-stimulatory signals from DCs, triggers the activation of naïve T cells, ultimately leading to the formation of tumor-specific cytotoxic CD8+ T cells and CD4+ T helper cells.

The functionality of DCs is closely tied to their maturation process, which is meticulously regulated. While immature DCs are highly efficient at capturing antigens, they have limited ability to stimulate T cells (59, 60). This changes when DCs are exposed to inflammatory signals, such as pathogen-associated molecular patterns (PAMPs) or danger-associated molecular patterns (DAMPs). These signals drive DCs into a mature state, characterized by increased surface expression of co-stimulatory molecules like CD80 and CD86, and the release of various cytokines. Maturation is critical for equipping DCs with the capacity to effectively prime T cells (61, 62). However, the tumor microenvironment in HCC can influence DC function, potentially leading to the development of tolerogenic DCs. These tolerogenic DCs exhibit reduced antigen presentation and diminished T cell activation, contributing to immune evasion by the tumor.

2.2 Role of natural killer cells

NK cells are a critical component of the innate immune defense, playing a vital role in the surveillance of HCC and other

10.3389/fimmu.2024.1483834

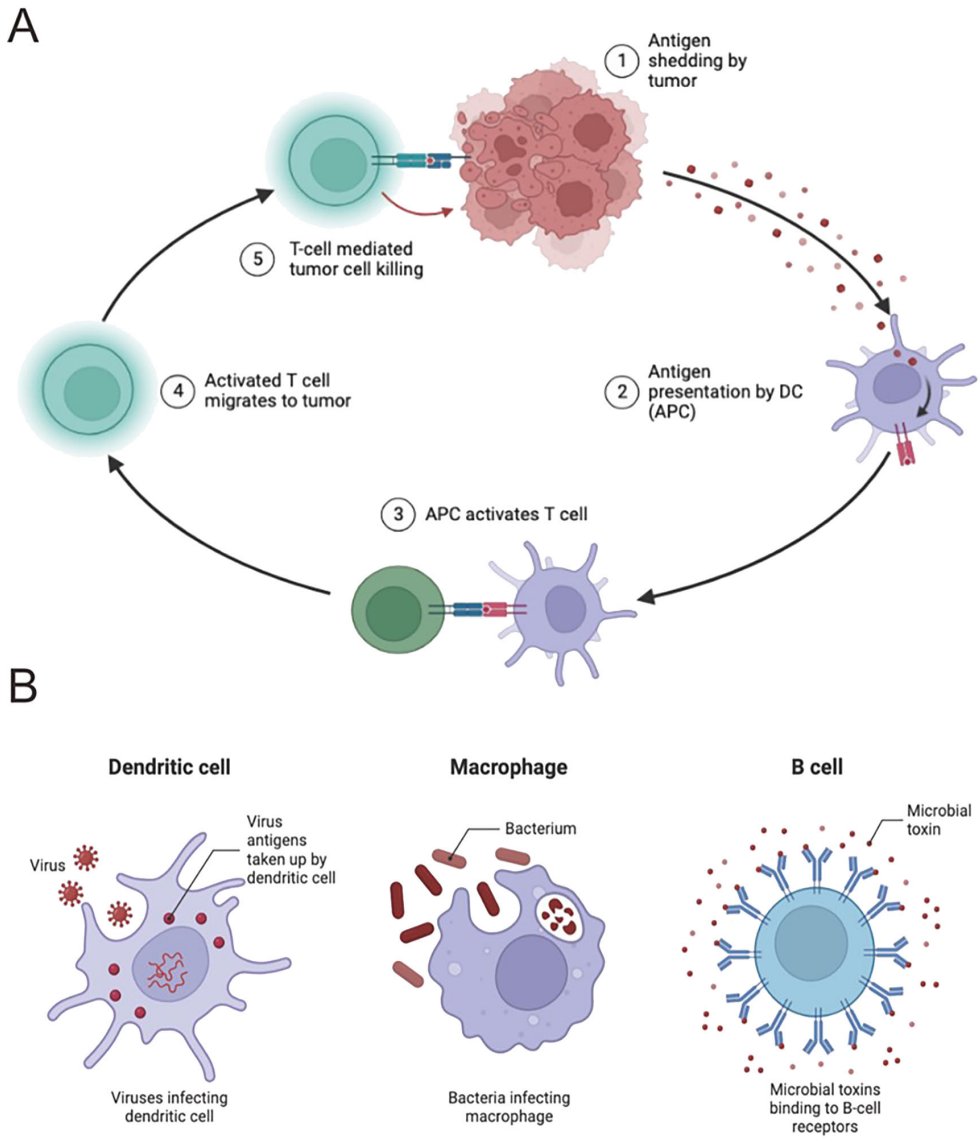

FIGURE 2
Immune cells play a pivotal role in HCC antigen presentation. **(A)** Antigen presentation by immune cells orchestrates anticancer responses. Dendritic cells (DCs) capture antigens and present to CD8+ T cells, with CD4+ T cells enhancing this process. HCC develops immune escape mechanisms, impairing antigen presentation. In-depth study may reveal new immunotherapy targets. **(B)** DCs capture and process antigens for presentation to CD8+ T cells. NK cells directly kill HCC cells. CD4+ T cells assist in antitumor immunity. HCC employs immune escape mechanisms; comprehensive understanding is crucial for treatment strategies.

malignancies. These specialized lymphocytes have the unique ability to detect and eliminate target cells, including tumor cells, without requiring prior sensitization (63, 64). In HCC, NK cells are key players in antitumor immunity, primarily due to their capacity to recognize stress-induced ligands such as MHC class I-related chain A/B (MICA/B) and UL16-binding proteins (ULBPs) on the surface of cancer cells. The cytotoxic arsenal of activated NK cells, which includes perforin and granzymes, is instrumental in triggering apoptosis in tumor cells. Beyond direct cytotoxicity, NK cells also secrete immune-modulatory cytokines, notably interferon-gamma (IFN-γ), which amplify the immune response and contribute to a coordinated antitumor effect (65). Nonetheless, the function of NK cells in HCC is intricate and greatly influenced by the tumor microenvironment. The immunosuppressive nature of the HCC microenvironment can dampen NK cell activity through various mechanisms. A major factor is the upregulation of inhibitory ligands, such as PD-L1, on tumor cells, which interact with PD-1 receptors on NK cells, leading to functional exhaustion. Additionally, the presence of Tregs and MDSCs further suppresses NK cell function. To counteract these inhibitory influences and

enhance NK cell activity in HCC, research is increasingly focused on innovative immunotherapies, including immune checkpoint inhibitors and adoptive NK cell therapies.

To summarize, NK cells have an essential yet intricate function in the immune response to HCC. While they contribute significantly to tumor surveillance and destruction, the tumor microenvironment presents formidable challenges that undermine their effectiveness. Advances in immunotherapy that harness the full potential of NK cells may offer new therapeutic avenues and transform treatment strategies for HCC.

2.3 CD8+ T cell function and activation

Cytotoxic T cells (CTLs), referred to as CD8+ T lymphocytes, play a crucial role in the immune system's response to HCC and various other cancers (66). These cells are highly adept at recognizing and eliminating infected or transformed cells, making them crucial for maintaining immune surveillance. In the HCC microenvironment, their activation is initiated when their T cell receptors (TCRs) interact with tumor-associated antigens presented by major histocompatibility complex class I (MHC-I) molecules, typically facilitated by professional antigen-presenting cells such as dendritic cells (67). This interaction triggers the activation of CD8+ T cells, leading to their clonal expansion and differentiation into effector CTLs. These effector cells then migrate to the tumor site, where they deploy their cytotoxic arsenal, including perforin and granzymes, to induce apoptosis in cancer cells. Additionally, CD8+ T cells produce cytokines like IFN-γ, which not only enhance the antitumor immune response but also activate other immune cells, thereby contributing to the establishment of an immunogenic environment within the tumor microenvironment.

Despite their significant role, CD8+ T cells face numerous challenges within the HCC microenvironment. A major obstacle is the creation of an immunosuppressive environment, rich in soluble factors such as vascular endothelial growth factor (VEGF) and transforming growth factor-beta (TGF-β), which negatively impact CD8+ T cell activation and function (68). Moreover, HCC cells often downregulate MHC-I expression, rendering themselves less visible to CD8+ T cells and disrupting their ability to recognize and target malignant cells (69). To overcome these challenges, therapeutic strategies have been developed, focusing on immune checkpoints like the PD-1/PD-L1 axis (109). These approaches aim to block inhibitory pathways, thereby restoring the full functional capacity of CD8+ T cells and improving clinical outcomes for patients with HCC.

2.4 Other immune cell types contribute

Besides the main immune cell subsets mentioned earlier, a varied range of additional immune cell populations contributes significantly to the intricate immune reaction against HCC (70, 71). Neutrophils, for instance, exhibit a dual role depending on their polarization, functioning both in promoting tumor growth and in exerting antitumor effects. Some subsets of neutrophils contribute to inflammation and cancer progression, while others support antitumor immunity by enhancing T cell infiltration and activation. Mast cells also significantly influence the tumor microenvironment by releasing various mediators that promote angiogenesis and recruit other immune cells. Although present in lower numbers within the HCC microenvironment, B cells contribute to antitumor immunity through antibody production and antigen presentation. Recent research has emphasized the role of γδ T cells and innate lymphoid cells (ILCs) in regulating the immune response in HCC, which may impact tumor development and alter treatment results.

3 Regulation of immune checkpoint in HCC during antigen presentation

The control of immune checkpoints while presenting antigens is vital for maintaining a balance between immune activation and tolerance in the context of HCC (37, 72). The intricate relationship involving immune checkpoints like PD-1 and its ligand, PD-L1, plays a significant role in influencing the immune response directed at cancer cells (73). Within the HCC environment, inflammatory signals promote the increased expression of PD-L1 on tumor cells, which aids in forming an immunosuppressive microenvironment. This process involves the interaction between CD8+ T cells and antigen-presenting cells (APCs), including dendritic cells. The interaction between PD-1 on T cells and PD-L1 on APCs results in T cell fatigue, which diminishes their ability to produce cytokines and perform cytotoxic functions. This mechanism, while preventing excessive immune activity, also allows tumor cells to evade immune detection.

Findings from clinical research underscore the promise of immune checkpoint blockade as a treatment strategy. Employing anti-PD-1/PD-L1 antibodies represents a potentially effective method to rejuvenate fatigued CD8+ T cells, thus amplifying the immune response toward tumors in patients with HCC (74). As our understanding of the delicate interplay between immune checkpoints, antigen presentation, and immune evasion in HCC expands, strategies aimed at deciphering and modifying this complex relationship offer the potential for substantial progress in boosting the effectiveness of antitumor immunotherapy. The active modulation of immune checkpoints during the process of antigen presentation highlights their essential function in influencing the immune response against HCC. Approaches focused on modifying immune checkpoint interactions could significantly enhance antitumor immunity and improve clinical outcomes for HCC patients.

3.1 The role of CTLA-4 and PD-1/PD-L1 pathways

The intricate involvement of the CTLA-4 and PD-1/PD-L1 pathways in HCC underscores their essential roles in regulating

immune responses and significantly impacting tumor development (Figure 3A). CTLA-4, a key receptor expressed on activated T cells, competes with the CD28 receptor for binding to B7 ligands on antigen-presenting cells. By doing so, CTLA-4 functions as a negative regulator, effectively inhibiting T cell activation and acting as an immune checkpoint that prevents hyperactive immune responses, which could otherwise lead to autoimmune damage (75). In the context of HCC, CTLA-4 exerts its suppressive effects by curtailing the activity of tumor-infiltrating lymphocytes, thereby facilitating tumor immune evasion and contributing to the progression of the malignancy (Figure 3).

Conversely, the PD-1 pathway serves a unique function in preserving peripheral tolerance and inhibiting autoimmunity. PD-1 is expressed on the surface of activated T cells, B cells, and myeloid cells, and interacts with its ligands, PD-L1 and PD-L2, which are expressed on a variety of cell types, including both neoplastic and immune cells (76, 77). This interaction is particularly relevant in the microenvironment of HCC, where the binding of PD-1 on T cells to PD-L1 on tumor or immune cells creates an immunosuppressive environment that promotes T cell exhaustion. The fatigue reduces T cells' capability to efficiently target cancer cells, thereby undermining the immune system's effectiveness in regulating tumor development.

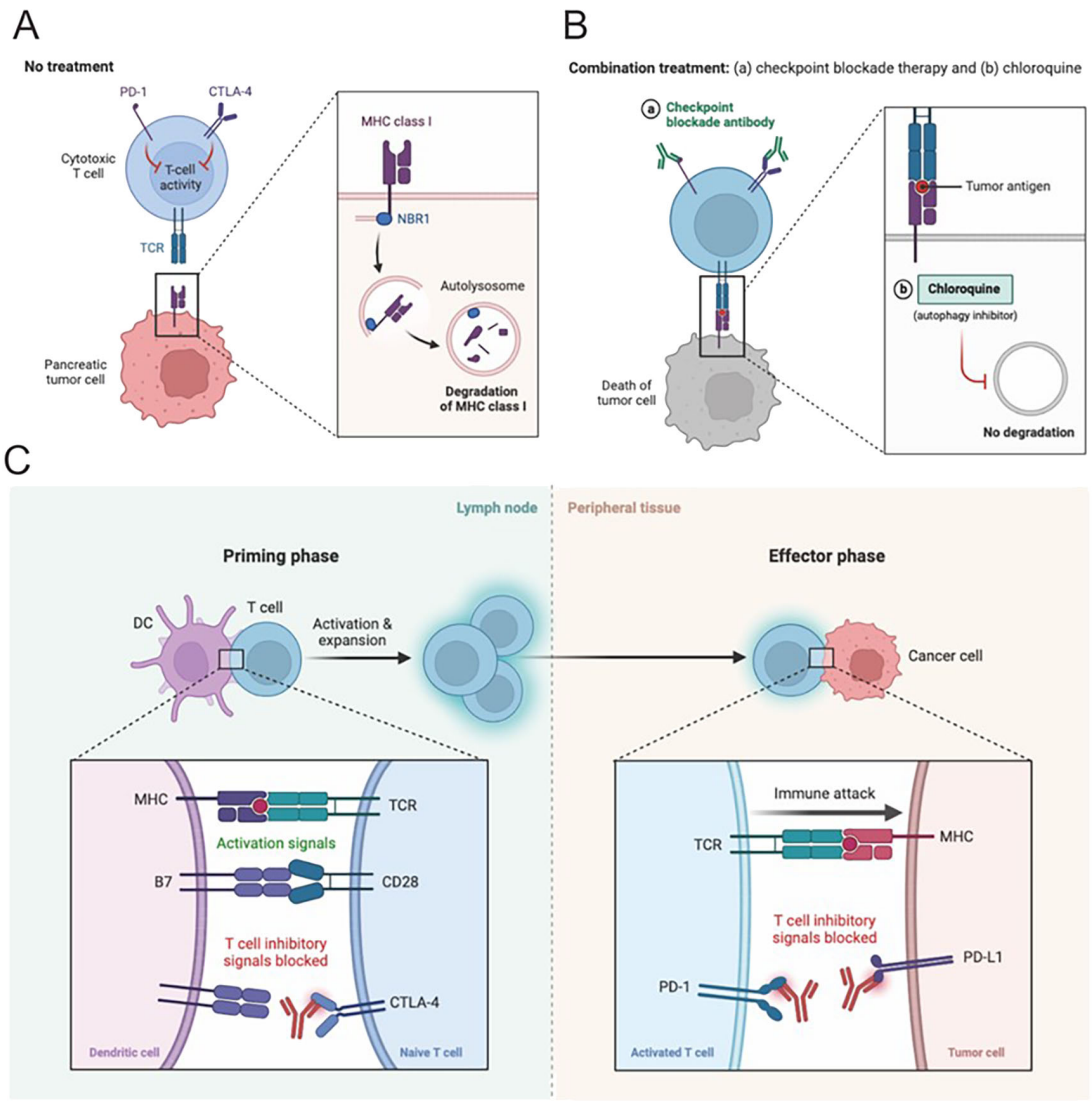

FIGURE 3
Combination therapies hold great potential for HCC. **(A, B)** Pancreatic cancer in the context of HCC often requires multifaceted treatment. The combination of immune checkpoint inhibitors with tyrosine kinase inhibitors or locoregional therapies is an attractive strategy, aiming to synergistically impede tumor growth, etc. This leverages complementary mechanisms of different treatments, laying the foundation for effective therapy. **(C)** Blocking CTLA-4 or PD-1 signaling is a promising approach in HCC immunotherapy. These checkpoints regulate T cell activity and are exploited by tumor cells to evade immune surveillance. Inhibitors targeting them release T cell responses. Clinical trials show encouraging results, potentially revolutionizing HCC treatment. Manipulating these pathways is a promising strategy to enhance immunity and improve outcomes.

Clinical studies have provided compelling evidence for the therapeutic potential of targeting these immune checkpoints in HCC. The development and application of immune checkpoint inhibitors, such as ipilimumab, which targets CTLA-4, and nivolumab, which targets the PD-1/PD-L1 axis, have shown promising results in enhancing antitumor immune responses. These inhibitors work by reinvigorating exhausted T cells, thereby restoring their ability to fight against tumor cells and leading to improved survival rates among HCC patients. The success of these therapies has opened new avenues for the treatment of HCC and has underscored the critical importance of continued research into the mechanisms of immune checkpoint regulation.

3.2 Clinical application of immune checkpoint inhibitors

The clinical integration of immune checkpoint inhibitors has revolutionized the therapeutic landscape for HCC and various other malignancies (78). By strategically focusing on regulatory pathways like CTLA-4 and PD-1/PD-L1, these inhibitors activate the immune system's natural ability to identify and destroy cancerous cells. In the context of HCC, these agents have shown significant promise. Notably, well-conducted clinical trials, including KEYNOTE-240 and CheckMate-040, have provided robust evidence of the efficacy and safety of immune checkpoint inhibitors like pembrolizumab and nivolumab in treating advanced HCC (79–81). These trials have demonstrated notable improvements in overall survival and sustained responses in a specific subset of patients. Combination therapies involving immune checkpoint inhibitors and other immunotherapies exhibit substantial potential in HCC. Evidence indicates that these combinations can synergistically enhance efficacy by activating the immune system through multiple pathways, thereby improving therapeutic outcomes (82, 83). As our understanding of HCC immunological mechanisms advances and new therapies continue to emerge, these combination strategies are likely to be further refined, offering improved survival benefits for HCC patients. The potential of combining immune checkpoint inhibitors with other therapeutic strategies, such as tyrosine kinase inhibitors and locoregional treatments, holds great promise for enhancing therapeutic outcomes (84). However, as this therapeutic approach continues to gain traction, several critical considerations must be addressed. Essential elements comprise the classification of patients according to significant clinical indicators, the discovery of predictive biomarkers, and the meticulous management of adverse immune-related effects. These aspects are vital for enhancing the clinical application of immune checkpoint inhibitors. The main challenges in implementing personalized immunotherapy for HCC include tumor heterogeneity, the complexity of immune escape mechanisms, and the lack of effective biomarkers for predicting therapeutic efficacy. Future studies should concentrate on a more thorough investigation of the immune evasion mechanisms in HCC, the identification of novel therapeutic targets and biomarkers, as well as the evaluation of the safety and effectiveness of new treatments via extensive clinical trials. The scientific community must continue to advance research efforts, focusing on strategies that effectively integrate immune checkpoint inhibitors with other treatments and identify prognostic markers. This ongoing research is essential to developing personalized treatment regimens tailored to the unique characteristics of individual patients.

4 Application of antitumor immunotherapy in enhancing antigen presentation

Antitumor immunotherapy signifies a groundbreaking method for treating cancer, improving the presentation of antigens and bolstering the immune system's reaction to malignant cells. This method leverages the complex interactions among immune cells, tumor antigens, and the tumor microenvironment to thwart immune evasion and reinstate effective immune surveillance. In the context of HCC and various other malignancies, treatment approaches seek to enhance the pathways for antigen presentation, thereby promoting the activation of CTLs along with other essential immune cells.

A fundamental component of antitumor immunotherapy is the deployment of immune checkpoint inhibitors (ICIs). These inhibitors target suppressive molecules on immune cells—for instance, PD-1 on T cells and its ligand PD-L1 on tumor cells (85, 86). By inhibiting these interactions, ICIs remove inhibitory controls on the immune system, enhancing T cells' ability to recognize and eliminate cancer cells more effectively. Clinical research, including the KEYNOTE-240 and CheckMate-040 trials, has substantiated the effectiveness of ICIs like pembrolizumab and nivolumab in boosting antigen presentation and fostering antitumor immunity in advanced HCC cases. These treatments not only reactivate exhausted CD8+ T cells but also increase tumor-infiltrating lymphocytes (TILs) and amplify tumor antigen-specific immune responses (87–89).

Another strategy to augment antigen presentation involves cancer vaccines, which are designed to elicit a targeted immune response against tumor antigens (90). Comprising either tumor-associated antigens (TAAs) or neoantigens from mutated cancer-specific proteins, these vaccines are pivotal in initiating an immune reaction. DCs are crucial in the process of capturing, processing, and presenting antigens to T cells. Clinical trials investigating various cancer vaccine modalities, including peptide-based, protein-based, and nucleic acid-based vaccines in HCC, have demonstrated encouraging results in enhancing antigen-specific T cell responses and improving clinical outcomes. Additionally, adoptive T cell therapy (ACT) involves the ex vivo expansion and modification of patient-derived T cells to boost their antigen recognition and cytotoxic activity (91–93). Chimeric antigen receptor (CAR) T cell therapy, a subset of ACT, involves engineering T cells to express CARs that target specific tumor antigens. While CAR T cell therapy has achieved significant success in treating hematological malignancies, its application in HCC is under investigation. ACT enhances antigen presentation by directly infusing highly specific and potent T cells into the patient, counteracting tumor-induced immunosuppression and enhancing the potential for tumor eradication.

4.1 Overview and application prospect of cancer vaccine

The development of immunotherapy is propelled by cancer vaccines that harness the immune system's ability to recognize and destroy tumor cells (94, 95). Specifically tailored to induce targeted immune responses against cancer-specific antigens, these vaccines activate CTLs and foster the development of immunological memory, thereby enhancing antigen presentation and triggering robust immune responses in HCC and other malignancies, which may improve clinical outcomes.

Various types of cancer vaccines exist, including peptide-based, protein-based, nucleic acid-based, and whole-cell vaccines (96, 97). Peptide-based vaccines administer short peptides derived from tumor antigens to prime T cells for cancer cell recognition and targeting. Protein-based vaccines use entire proteins or their fragments from tumor cells to provoke immune reactions. Vaccines that utilize nucleic acids deliver either DNA or RNA encoding tumor antigens, which aids in the synthesis of these proteins and stimulates the immune response. Whole-cell vaccines employ either intact tumor cells or their lysates to prompt immune recognition of a wide array of tumor antigens. At the core of these vaccination approaches are DCs, which take up, process, and present antigens to T cells, thereby initiating the immune response. In clinical settings, the use of cancer vaccines in HCC has been evaluated, such as in a phase III trial of the peptide-based vaccine adjuvant MelCancerVac, which targets melanoma-associated antigens in HCC patients. Although primary endpoints were not met, the trial underscored the potential to induce tumor-specific immune responses. Additionally, early-phase trials of the TERT-encoding DNA vaccine GRANITE-001 have yielded promising results by stimulating T cell responses against telomerase reverse transcriptase (TERT), an antigen prevalent in various cancers, including HCC.

The future of cancer vaccines in HCC appears promising but is not without its challenges. The heterogeneity of tumor antigens and immune responses among patients calls for the identification of both unique and common antigens to optimize vaccine design. Additionally, the tumor microenvironment's immunosuppressive characteristics and possible mechanisms of immune tolerance might reduce the effectiveness of vaccines. To overcome these barriers, combination strategies, including the integration of cancer vaccines with immune checkpoint inhibitors, are under investigation to enhance therapeutic outcomes. The potential of cancer vaccines to improve antigen presentation and target specific immune responses against cancer cells underscores their role in advancing personalized immunotherapy approaches in HCC. Ongoing investigations and clinical studies are crucial for the advancement and enhancement of cancer vaccine approaches, offering the potential to greatly influence the treatment of HCC.

4.2 Role of CAR-T cell therapy in antigen presentation

CAR-T cell therapy, a pivotal advancement in immunotherapy, has profoundly influenced antigen presentation and the immune response to cancers, including HCC. This therapy involves T lymphocytes engineered to express chimeric antigen receptors (CARs) that merge the antigen-binding domain of an antibody with T cell signaling domains (98). These engineered receptors allow CAR-T cells to identify specific tumor-associated antigens without the need for major histocompatibility complex (MHC) presentation, circumventing conventional antigen presentation pathways. In practice, T cells are harvested from patients, genetically modified to bear CARs that target tumor-specific antigens, and then reinfused (99). These CAR-T cells then recognize and bind to tumor cells displaying these antigens, triggering direct cytotoxic attacks and cytokine release, which not only promotes tumor cell destruction but also enhances antigen presentation through direct T-cell engagement.

Research in the clinical field highlights the considerable potential of CAR-T cell therapy for the treatment of HCC. A noteworthy investigation centered on CAR-T cells targeting glypican-3 (GPC3), a unique antigen commonly found in advanced HCC cases, revealed impressive antitumor effectiveness, with several patients showing marked tumor reduction and increased survival duration (100). Additional investigations into CAR-T cells targeting other antigens like alpha-fetoprotein (AFP) and mesothelin in preclinical and early clinical phases further attest to the adaptability of this approach in HCC. However, challenges such as the immunosuppressive nature of the tumor microenvironment, tumor antigen variability, and potential antigen escape mechanisms pose hurdles to the lasting effectiveness of CAR-T cell therapy. Additionally, immune checkpoint inhibitors and CAR-T cell therapies are associated with certain adverse effects, including skin toxicity, gastrointestinal reactions, and cytokine release syndrome. To address these issues, strategies that combine CAR-T therapy with immune checkpoint inhibitors are being explored to counteract immunosuppression and enhance therapeutic results. Adverse reactions can be effectively mitigated through close monitoring, appropriate medication, and supportive care, thereby ensuring patient safety. Ongoing research into identifying optimal antigens and developing effective and safe CAR constructs is critical to refining and expanding the utility of CAR-T cell therapy in HCC treatment.

5 Research progress and future prospects

5.1 Application of new technologies in the study of immune cell function

Recent advancements have significantly enhanced our understanding of immune cells in both healthy and diseased states, including HCC. Single-cell RNA sequencing (scRNA-seq) has proven to be a powerful tool for delineating gene expression at the individual cell level (101). In HCC, scRNA-seq has exposed the diversity within immune cell populations in the tumor microenvironment, offering insights into their functional states and interactions (90). Further, developments in high-dimensional flow cytometry and mass cytometry have enabled the simultaneous

measurement of multiple markers on individual cells, improving our grasp of immune cell phenotypes and functionalities. Spatial transcriptomics have also been employed to map immune cells within tumors, illuminating their spatial distribution and intercellular communication. These technological breakthroughs collectively provide a detailed picture of the dynamic immune responses and the mechanisms of immune escape in HCC, setting the stage for more targeted therapeutic approaches.

5.2 Development of individualized treatment strategies

The transition to personalized medicine is increasingly evident in the realm of HCC immunotherapy, underscored by the unique immune profiles and tumor characteristics exhibited by each patient (102). Detailed profiling of tumor antigens and immune cell infiltrates enhances the formulation of customized treatment plans (103). The identification of neoantigens through genomic sequencing has facilitated the creation of personalized vaccines and adoptive T cell therapies (104). Additionally, the discovery of biomarkers that predict responses to immune checkpoint inhibitors aids in selecting appropriate treatments, reducing ineffective approaches and improving patient outcomes. The combination of various omics data, such as genomic, transcriptomic, and proteomic analyses, assists in identifying the key molecular factors and pathways that contribute to immune dysfunction in HCC (105, 106). Looking ahead, the amalgamation of these insights with cutting-edge immunotherapies promises to refine clinical results by aligning interventions with the specific immunological profiles of HCC patients.

5.3 Directions and challenges for future research

Despite substantial progress, numerous pivotal challenges and directions remain in the domain of HCC immunotherapy. Initially, deciphering the intricate relationships between immune cells and the tumor microenvironment remains a challenging endeavor. It is crucial to comprehend the diverse functionalities of immune cells and their communication networks to devise potent combination therapies. Secondly, addressing the immunosuppression prevalent within the HCC microenvironment demands innovative approaches. The synergy of immune checkpoint inhibitors, immune modulators, and targeted therapies presents a promising route to counteract immune escape mechanisms (107). Thirdly, the enhancement of adoptive T cell therapies, such as CAR-T cells, hinges on refining engineering techniques to boost tumor specificity and longevity. Additionally, the development of universally applicable CAR-T cells or allogeneic methods could mitigate logistical and manufacturing hurdles (7). Lastly, the quest for biomarkers that can stratify patients and predict treatment responses is critical. Effective predictive markers are essential to tailor therapy choices, minimizing adverse effects while maximizing therapeutic efficacy.

6 Conclusion and discussion

In summary, a detailed investigation of immune cell dynamics and antigen presentation within HCC has revealed complex interaction layers that critically affect tumor progression, immune reactions, and therapeutic results. The immune evasion tactics utilized by HCC illustrate the tumor's capacity to circumvent immune surveillance and underscore the importance of immune checkpoints like CTLA-4 and PD-1/PD-L1 in regulating the intricate equilibrium between immune activation and suppression. Various immune cells, including DCs, NK cells, and CD8+ T cells, engage in a sophisticated interaction within the tumor microenvironment. This interaction influences antigen presentation, immune infiltration, and ultimately, tumor control. The introduction of novel approaches such as cancer vaccines and CAR-T cell therapies opens promising pathways to enhance antigen presentation and empower the immune system to more effectively recognize and combat cancer cells.

Clinical investigations, such as the KEYNOTE-240 and CheckMate-040 trials, have corroborated the significant clinical advantages of immune checkpoint inhibitors in reinvigorating immune responses and enhancing outcomes for advanced HCC. Nevertheless, hurdles in patient stratification, biomarker identification, and the management of immune-related side effects persist. The integration of innovative technologies, such as single-cell RNA sequencing and high-dimensional flow cytometry, has afforded profound insights into the functionality of immune cells. This technological prowess has unraveled the complexities of immune cell populations and their interplay within HCC, thereby facilitating the crafting of personalized treatment modalities that leverage unique patient characteristics to maximize therapeutic efficacy. Furthermore, advancements in CAR-T cell therapy underscore its potential in augmenting antigen presentation, thus spearheading a new frontier in immunotherapy for HCC and potentially other malignancies.

Looking forward, the unraveling of the complex interactions between immune cells and tumors within the HCC microenvironment is imperative. This understanding is critical for the informed development of combination therapies aimed at counteracting immunosuppression. The quest for biomarkers that accurately predict treatment responses continues to be a focal point, promising to refine therapy selection to enhance patient outcomes and minimize side effects. Ongoing research is essential to perfect adoptive T cell therapies and address challenges such as immunosuppression, tumor heterogeneity, and scalability of manufacturing processes.

In summary, the comprehensive analysis of immune cell function and antigen presentation within HCC has laid a robust groundwork for innovative cancer immunotherapy strategies. The synergy of cutting-edge technologies, tailored treatment

approaches, and a nuanced comprehension of the immune landscape is poised to transform the management of HCC, thereby reshaping the therapeutic paradigm for patients in dire need.

Author contributions

JN: Conceptualization, Investigation, Visualization, Writing – original draft, Writing – review & editing. YW: Conceptualization, Investigation, Project administration, Resources, Software, Writing – original draft, Writing – review & editing. ZT: Conceptualization, Investigation, Project administration, Resources, Software, Visualization, Writing – original draft, Writing – review & editing.

Funding

The author(s) declare that no financial support was received for the research, authorship, and/or publication of this article.

Acknowledgments

Here, we would like to express our gratitude to Jingyi Zhang for her support during the process of writing the article.

Conflict of interest

The authors declare that the research was conducted in the absence of any commercial or financial relationships that could be construed as a potential conflict of interest.

Publisher's note

References

1. Vogel A, Meyer T, Sapisochin G, Salem R, Saborowski A. Hepatocellular carcinoma. *Lancet*. (2022) 400(10360):1345–62. doi: 10.1016/S0140-6736(22)01200-4

2. Chidambaranathan-Reghupaty S, Fisher PB, Sarkar D. Hepatocellular carcinoma (HCC): Epidemiology, etiology and molecular classification. *Adv Cancer Res*. (2021) 149:1–61. doi: 10.1016/bs.acr.2020.10.001

3. Ganesan P, Kulik LM. Hepatocellular carcinoma: new developments. *Clin Liver Dis*. (2023) 27:85–102. doi: 10.1016/j.cld.2022.08.004

4. Hartke J, Johnson M, Ghabril M. The diagnosis and treatment of hepatocellular carcinoma. *Semin Diagn Pathol*. (2017) 34:153–9. doi: 10.1053/j.semdp.2016.12.011

5. Galle PR, Dufour JF, Peck-Radosavljevic M, Trojan J, Vogel A. Systemic therapy of advanced hepatocellular carcinoma. *Future Oncol*. (2021) 17(10):1237–51. doi: 10.2217/fon-2020-0758

6. Rajendran L, Ivanics T, Claasen MP, Muaddi H, Sapisochin G. The management of post-transplantation recurrence of hepatocellular carcinoma. *Clin Mol Hepatol*. (2022) 28(1):1–16. doi: 10.3350/cmh.2021.0217

7. Alizadeh D, Wong RA, Yang X, Wang D, Pecoraro JR, Kuo CF, et al. IL15 enhances CAR-T cell antitumor activity by reducing mTORC1 activity and preserving their stem cell memory phenotype. *Cancer Immunol Res*. (2019) 7(5):759–72. doi: 10.1158/2326-6066.CIR-18-0466

8. Chen X, Wang Z, Han S, Wang Z, Zhang Y, Li X, et al. Targeting SYK of monocyte-derived macrophages regulates liver fibrosis via crosstalking with Erk/Hif1α and remodeling liver inflammatory environment. *Cell Death Dis*. (2021) 12(12):1123. doi: 10.1038/s41419-021-04403-2

9. Zhang H, Zhang N, Wu W, Wang Z, Dai Z, Liang X, et al. Pericyte mediates the infiltration, migration, and polarization of macrophages by CD163/MCAM axis in glioblastoma. *iScience*. (2022) 25(9):104918. doi: 10.1016/j.isci.2022.104918

10. Chew GL, Campbell AE, De Neef E, Sutliff NA, Shadle SC, Tapscott SJ, et al. DUX4 suppresses MHC class I to promote cancer immune evasion and resistance to checkpoint blockade. *Dev Cell*. (2019) 50(5):658–671.e7. doi: 10.1016/j.devcel.2019.06.011

11. Zhang Z, Zeng X, Wu Y, Liu Y, Zhang X, Song Z. Cuproptosis-related risk score predicts prognosis and characterizes the tumor microenvironment in hepatocellular carcinoma. *Front Immunol*. (2022) 13:925618. doi: 10.3389/fimmu.2022.925618

12. Wei CY, Zhu MX, Zhang PF, Huang XY, Wan JK, Yao XZ, et al. PKCα/ZFP64/CSF1 axis resets the tumor microenvironment and fuels anti-PD1 resistance in hepatocellular carcinoma. *J Hepatol*. (2022) 77(1):163–76. doi: 10.1016/j.jhep.2022.02.019

13. Zuo B, Zhang Y, Zhao K, Wu L, Qi H, Yang R, et al. Universal immunotherapeutic strategy for hepatocellular carcinoma with exosome vaccines that engage adaptive and innate immune responses. *J Hematol Oncol*. (2022) 15 (1):46. doi: 10.1186/s13045-022-01266-8

14. Lu Z, Zuo B, Jing R, Gao X, Rao Q, Liu Z, et al. Dendritic cell-derived exosomes elicit tumor regression in autochthonous hepatocellular carcinoma mouse models. *J Hepatol*. (2017) 67(4):739–48. doi: 10.1016/j.jhep.2017.05.019

15. Wen N, Cai Y, Li F, Ye H, Tang W, Song P, et al. The clinical management of hepatocellular carcinoma worldwide: A concise review and comparison of current guidelines: 2022 update. *Biosci Trends*. (2022) 16(1):20–30. doi: 10.5582/bst.2022.01061

16. Heller M, Parikh ND, Fidelman N, Owen D. Frontiers of therapy for hepatocellular carcinoma. *Abdom Radiol (NY)*. (2021) 46(8):3648–59. doi: 10.1007/s00261-021-03065-0

17. von Felden J, Garcia-Lezana T, Schulze K, Losic B, Villanueva A. Liquid biopsy in the clinical management of hepatocellular carcinoma. *Gut*. (2020) 69(11):2025–34. doi: 10.1136/gutjnl-2019-320282

18. Chen QF, Li W, Wu PH, Shen LJ, Huang ZL. Significance of tumor-infiltrating immunocytes for predicting prognosis of hepatitis B virus-related hepatocellular carcinoma. *World J Gastroenterol*. (2019) 25(35):5266–82. doi: 10.3748/wjg.v25.i35.5266

19. Lu LG, Zhou ZL, Wang XY, Liu BY, Lu JY, Liu S, et al. PD-L1 blockade liberates intrinsic antitumourigenic properties of glycolytic macrophages in hepatocellular carcinoma. *Gut*. (2022) 71(12):2551–60. doi: 10.1136/gutjnl-2021-326350

20. Li Q, Zhang L, You W, Xu J, Dai J, Hua D, et al. PRDM1/BLIMP1 induces cancer immune evasion by modulating the USP22-SPI1-PD-L1 axis in hepatocellular carcinoma cells. *Nat Commun*. (2022) 13(1):7677. doi: 10.1038/s41467-022-35469-x

21. Sové RJ, Verma BK, Wang H, Ho WJ, Yarchoan M, Popel AS. Virtual clinical trials of anti-PD-1 and anti-CTLA-4 immunotherapy in advanced hepatocellular carcinoma using a quantitative systems pharmacology model. *J Immunother Cancer*. (2022) 10(11). doi: 10.1136/jitc-2022-005414

22. Zheng C, Zheng L, Yoo JK, Guo H, Zhang Y, Guo X, et al. Landscape of infiltrating T cells in liver cancer revealed by single-cell sequencing. *Cell*. (2017) 169 (7):1342–56.e16. doi: 10.1016/j.cell.2017.05.035

23. Zakeri N, Hall A, Swadling L, Pallett LJ, Schmidt NM, Diniz MO, et al. Characterisation and induction of tissue-resident gamma delta T-cells to target hepatocellular carcinoma. *Nat Commun*. (2022) 13(1):1372. doi: 10.1038/s41467-022-29012-1

24. Ma J, Zheng B, Goswami S, Meng L, Zhang D, Cao C, et al. PD1(Hi) CD8(+) T cells correlate with exhausted signature and poor clinical outcome in hepatocellular carcinoma. *J Immunother Cancer*. (2019) 7(1):331. doi: 10.1186/s40425-019-0814-7

25. Wang S, Wu Q, Chen T, Su R, Pan C, Qian J, et al. Blocking CD47 promotes antitumour immunity through CD103(+) dendritic cell-NK cell axis in murine hepatocellular carcinoma model. *J Hepatol*. (2022) 77(2):467–78. doi: 10.1016/j.jhep.2022.03.011

26. Yu W, He J, Wang F, He Q, Shi Y, Tao X, et al. NR4A1 mediates NK-cell dysfunction in hepatocellular carcinoma via the IFN-γ/p-STAT1/IRF1 pathway. *Immunology*. (2023) 169(1):69–82. doi: 10.1111/imm.13611

27. Catamo E, Zupin L, Crovella S, Celsi F, Segat L. Non-classical MHC-I human leukocyte antigen (HLA-G) in hepatotropic viral infections and in hepatocellular carcinoma. *Hum Immunol*. (2014) 75(12):1225–31. doi: 10.1016/j.humimm.2014.09.019

28. Matsui M, Machida S, Itani-Yohda T, Akatsuka T. Downregulation of the proteasome subunits, transporter, and antigen presentation in hepatocellular carcinoma, and their restoration by interferon-gamma. *J Gastroenterol Hepatol*. (2002) 17(8):897–907. doi: 10.1046/j.1440-1746.2002.02837.x

29. Tang PM, Bui-Xuan NH, Wong CK, Fong WP, Fung KP. Pheophorbide a-mediated photodynamic therapy triggers HLA class I-restricted antigen presentation in human hepatocellular carcinoma. *Transl Oncol*. (2010) 3(2):114–22. doi: 10.1593/tlo.09262

30. Donne R, Lujambio A. The liver cancer immune microenvironment: Therapeutic implications for hepatocellular carcinoma. *Hepatology*. (2023) 77(5):1773–96. doi: 10.1002/hep.32740

31. Lu Z, Liu R, Wang Y, Jiao M, Li Z, Wang Z, et al. Ten-eleven translocation-2 inactivation restrains IL-10-producing regulatory B cells to enable antitumor immunity in hepatocellular carcinoma. *Hepatology*. (2023) 77(3):745–59. doi: 10.1002/hep.32442

32. Barooah P, Saikia S, Kalita MJ, Bharadwaj R, Sarmah P, Bhattacharyya M, et al. IL-10 polymorphisms and haplotypes predict susceptibility to hepatocellular carcinoma occurrence in patients with hepatitis C virus infection from northeast India. *Viral Immunol*. (2020) 33(6):457–67. doi: 10.1089/vim.2019.0170

33. Sakaguchi S, Yamaguchi T, Nomura T, Ono M. Regulatory T cells and immune tolerance. *Cell*. (2008) 133(5):775–87. doi: 10.1016/j.cell.2008.05.009

34. Gabrilovich DI, Nagaraj S. Myeloid-derived suppressor cells as regulators of the immune system. *Nat Rev Immunol*. (2009) 9:162–74. doi: 10.1038/nri2506

35. Hu B, Yu M, Ma X, Sun J, Liu C, Wang C, et al. IFNα Potentiates anti-PD-1 efficacy by remodeling glucose metabolism in the hepatocellular carcinoma microenvironment. *Cancer Discov*. (2022) 12(7):1718–41. doi: 10.1158/2159-8290.CD-21-1022

36. Tan Z, Chiu MS, Yang X, Yue M, Cheung TT, Zhou D, et al. Isoformic PD-1-mediated immunosuppression underlies resistance to PD-1 blockade in hepatocellular carcinoma patients. *Gut*. (2023) 72(8):1568–80. doi: 10.1136/gutjnl-2022-327133

37. Shang BB, Chen J, Wang ZG, Liu H. Significant correlation between HSPA4 and prognosis and immune regulation in hepatocellular carcinoma. *PeerJ*. (2021) 9:e12315. doi: 10.7717/peerj.12315

38. Kudo M. Combination cancer immunotherapy with molecular targeted agents/anti-CTLA-4 antibody for hepatocellular carcinoma. *Liver Cancer*. (2019) 8:1–11. doi: 10.1159/000496277

39. Bidkhori G, Benfeitas R, Klevstig M, Zhang C, Nielsen J, Uhlen M, et al. Metabolic network-based stratification of hepatocellular carcinoma reveals three distinct tumor subtypes. *Proc Natl Acad Sci USA*. (2018) 115(50):E11874–e83. doi: 10.1073/pnas.1807305115

40. Cheng AL, Qin S, Ikeda M, Galle PR, Ducreux M, Kim TY, et al. Updated efficacy and safety data from IMbrave150: Atezolizumab plus bevacizumab vs. sorafenib for unresectable hepatocellular carcinoma. *J Hepatol*. (2022) 76(4):862–73. doi: 10.1016/j.jhep.2021.11.030

41. Du SS, Chen GW, Yang P, Chen YX, Hu Y, Zhao QQ, et al. Radiation Therapy Promotes Hepatocellular Carcinoma Immune Cloaking via PD-L1 Upregulation Induced by cGAS-STING Activation. *Int J Radiat Oncol Biol Phys*. (2022) 112(5):1243–55. doi: 10.1016/j.ijrobp.2021.12.162

42. Teng MW, Ngiow SF, Ribas A, Smyth MJ. Classifying cancers based on T-cell infiltration and PD-L1. *Cancer Res*. (2015) 75(11):2139–45. doi: 10.1158/0008-5472.CAN-15-0255

43. Yin Z, Ma T, Lin Y, Lu X, Zhang C, Chen S, et al. IL-6/STAT3 pathway intermediates M1/M2 macrophage polarization during the development of hepatocellular carcinoma. *J Cell Biochem*. (2018) 119(11):9419–32. doi: 10.1002/jcb.27259

44. Zhang W, Liu Y, Yan Z, Yang H, Sun W, Yao Y, et al. IL-6 promotes PD-L1 expression in monocytes and macrophages by decreasing protein tyrosine phosphatase receptor type O expression in human hepatocellular carcinoma. *J Immunother Cancer*. (2020) 8(1). doi: 10.1136/jitc-2019-000285

45. Dai Z, Wang X, Peng R, Zhang B, Han Q, Lin J, et al. Induction of IL-6Rα by ATF3 enhances IL-6 mediated sorafenib and regorafenib resistance in hepatocellular carcinoma. *Cancer Lett*. (2022) 524:161–71. doi: 10.1016/j.canlet.2021.10.024

46. Fujiwara K, Higashi T, Nouso K, Nakatsukasa H, Kobayashi Y, Uemura M, et al. Decreased expression of B7 costimulatory molecules and major histocompatibility complex class-I in human hepatocellular carcinoma. *J Gastroenterol Hepatol*. (2004) 19:1121–7. doi: 10.1111/j.1440-1746.2004.03467.x

47. Haber PK, Castet F, Torres-Martin M, Andreu-Oller C, Puigvehí M, Miho M, et al. Molecular markers of response to anti-PD1 therapy in advanced hepatocellular carcinoma. *Gastroenterology*. (2023) 164(1):72–88.e18. doi: 10.1053/j.gastro.2022.09.005

48. Magen A, Hamon P, Fiaschi N, Soong BY, Park MD, Mattiuz R, et al. Intratumoral dendritic cell-CD4(+) T helper cell niches enable CD8(+) T cell differentiation following PD-1 blockade in hepatocellular carcinoma. *Nat Med*. (2023) 29(6):1389–99. doi: 10.1038/s41591-023-02345-0

49. Ma C, Kesarwala AH, Eggert T, Medina-Echeverz J, Kleiner DE, Jin P, et al. NAFLD causes selective CD4(+) T lymphocyte loss and promotes hepatocarcinogenesis. *Nature*. (2016) 531(7593):253–7. doi: 10.1038/nature16969

50. Dai Z, Wang Z, Lei K, Liao J, Peng Z, Lin M, et al. Irreversible electroporation induces CD8(+) T cell immune response against post-ablation hepatocellular carcinoma growth. *Cancer Lett*. (2021) 503:1–10. doi: 10.1016/j.canlet.2021.01.001

51. Guermonprez P, et al. Antigen presentation and T cell stimulation by dendritic cells. *Annu Rev Immunol*. (2002) 20:621–67. doi: 10.1146/annurev.immunol.20.100301.064828

52. Xing R, et al. Strategies to improve the antitumor effect of immunotherapy for hepatocellular carcinoma. *Front Immunol*. (2021) 12:783236. doi: 10.3389/fimmu.2021.783236

53. Cheng AL, et al. Challenges of combination therapy with immune checkpoint inhibitors for hepatocellular carcinoma. *J Hepatol*. (2020) 72:307–19. doi: 10.1016/j.jhep.2019.09.025

54. El Dika I, Khalil DN, Abou-Alfa GK. Immune checkpoint inhibitors for hepatocellular carcinoma. *Cancer*. (2019) 125:3312–9. doi: 10.1002/cncr.v125.19

55. Théry C, Amigorena S. The cell biology of antigen presentation in dendritic cells. *Curr Opin Immunol*. (2001) 13:45–51. doi: 10.1016/S0952-7915(00)00180-1

56. Unanue ER, Cerottini JC. Antigen presentation. *FASEB J*. (1989) 3:2496–502. doi: 10.1096/fasebj.3.13.2572499

57. Knight SC, Burke F, Bedford PA. Dendritic cells, antigen distribution and the initiation of primary immune responses to self and non-self antigens. *Semin Cancer Biol*. (2002) 12:301–8. doi: 10.1016/S1044-579X(02)00016-0

58. Argüello RJ, Reverendo M, Gatti E, Pierre P. Regulation of protein synthesis and autophagy in activated dendritic cells: implications for antigen processing and presentation. *Immunol Rev*. (2016) 272(1):28–38. doi: 10.1111/imr.12427

59. Edelson RL. Cutaneous T cell lymphoma: the helping hand of dendritic cells. *Ann N Y Acad Sci*. (2001) 941:1–11. doi: 10.1111/j.1749-6632.2001.tb03705.x

60. Mbongue JC, Nieves HA, Torrez TW, Langridge WH. The role of dendritic cell maturation in the induction of insulin-dependent diabetes mellitus. *Front Immunol*. (2017) 8:327. doi: 10.3389/fimmu.2017.00327

61. Scales HE, Meehan GR, Hayes AJ, Benson RA, Watson E, Walters A, et al. A novel cellular pathway of antigen presentation and CD4 T cell activation in vivo. *Front Immunol*. (2018) 9:2684. doi: 10.3389/fimmu.2018.02684

62. Knight SC. Dendritic cell-T-cell circuitry in health and changes in inflammatory bowel disease and its treatment. *Dig Dis*. (2016) 34:51–7. doi: 10.1159/000442926

63. Erokhina SA, Streltsova MA, Kanevskiy LM, Grechikhina MV, Sapozhnikov AM, Kovalenko EI. HLA-DR-expressing NK cells: Effective killers suspected for antigen presentation. *J Leukoc Biol*. (2021) 109(2):327–37. doi: 10.1002/JLB.3RU0420-668RR

64. Nakamura T, Sato T, Endo R, Sasaki S, Takahashi N, Sato Y, et al. STING agonist loaded lipid nanoparticles overcome anti-PD-1 resistance in melanoma lung metastasis via *NK cell activation*. *J Immunother Cancer*. (2021) 9(7). doi: 10.1136/jitc-2021-002852

65. Costa-García M, Ataya M, Moraru M, Vilches C, López-Botet M, Muntasell A. Human cytomegalovirus antigen presentation by HLA-DR+ NKG2C+ Adaptive NK cells specifically activates polyfunctional effector memory CD4+ T lymphocytes. *Front Immunol*. (2019) 10:687. doi: 10.3389/fimmu.2019.00687

66. Pishesha N, Harmand TJ, Ploegh HL. A guide to antigen processing and presentation. *Nat Rev Immunol*. (2022) 22:751–64. doi: 10.1038/s41577-022-00707-2

67. Moustaki A, Crawford JC, Alli S, Fan Y, Boi S, Zamora AE, et al. Antigen cross-presentation in young tumor-bearing hosts promotes CD8(+) T cell terminal differentiation. *Sci Immunol*. (2022) 7(68):eabf6136. doi: 10.1126/sciimmunol.abf6136

68. MacNabb BW, Tumuluru S, Chen X, Godfrey J, Kasal DN, Yu J, et al. Dendritic cells can prime anti-tumor CD8(+) T cell responses through major histocompatibility complex cross-dressing. *Immunity*. (2022) 55(6):982–97.e8. doi: 10.1016/j.immuni.2022.04.016

69. Kilian M, Sheinin R, Tan CL, Friedrich M, Krämer C, Kaminitz A, et al. MHC class II-restricted antigen presentation is required to prevent dysfunction of cytotoxic T cells by blood-borne myeloids in brain tumors. *Cancer Cell*. (2023) 41(2):235–51.e9. doi: 10.1016/j.ccell.2022.12.007

70. Zhu X, Mulcahy LA, Mohammed RA, Lee AH, Franks HA, Kilpatrick L, et al. IL-17 expression by breast-cancer-associated macrophages: IL-17 promotes invasiveness of breast cancer cell lines. *Breast Cancer Res*. (2008) 10(6):R95. doi: 10.1186/bcr2195

71. Franco OE, Jiang M, Strand DW, Peacock J, Fernandez S, Jackson RS 2nd, et al. Altered TGF-β signaling in a subpopulation of human stromal cells promotes prostatic carcinogenesis. *Cancer Res*. (2011) 71(4):1272–81. doi: 10.1158/0008-5472.CAN-10-3142

72. Kong P, Yang H, Tong Q, Dong X, Yi MA, Yan D. Expression of tumor-associated macrophages and PD-L1 in patients with hepatocellular carcinoma and construction of a prognostic model. *J Cancer Res Clin Oncol*. (2023) 149:10685–700. doi: 10.1007/s00432-023-04949-y

73. Morad G, Helmink BA, Sharma P, Wargo JA. Hallmarks of response, resistance, and toxicity to immune checkpoint blockade. *Cell*. (2021) 184(21):5309–37. doi: 10.1016/j.cell.2021.09.020

74. Yao H, Shen N, Ji G, Huang J, Sun J, Wang G, et al. Cisplatin nanoparticles promote intratumoral CD8(+) T cell priming via *antigen presentation and T cell receptor crosstalk*. *Nano Lett*. (2022) 22(8):3328–39. doi: 10.1021/acs.nanolett.2c00478

75. de Vries NL, van de Haar J, Veninga V, Chalabi M, Ijsselsteijn ME, van der Ploeg M, et al. γδ T cells are effectors of immunotherapy in cancers with HLA class I defects. *Nature*. (2023) 613(7945):743–50. doi: 10.1038/s41586-022-05593-1

76. Hack SP, Zhu AX, Wang Y. Augmenting anticancer immunity through combined targeting of angiogenic and PD-1/PD-L1 pathways: challenges and opportunities. *Front Immunol*. (2020) 11:598877. doi: 10.3389/fimmu.2020.598877

77. Minnar CM, Chariou PL, Horn LA, Hicks KC, Palena C, Schlom J, et al. Tumor-targeted interleukin-12 synergizes with entinostat to overcome PD-1/PD-L1 blockade-resistant tumors harboring MHC-I and APM deficiencies. *J Immunother Cancer*. (2022) 10(6). doi: 10.1136/jitc-2022-004561

78. Xu S, Zheng Y, Ye M, Shen T, Zhang D, Li Z, et al. Comprehensive pan-cancer analysis reveals EPHB2 is a novel predictive biomarker for prognosis and immunotherapy response. *BMC Cancer*. (2024) 24(1):1064. doi: 10.1186/s12885-024-12843-0

79. Mei K, Qin S, Chen Z, Liu Y, Wang L, Zou J. Camrelizumab in combination with apatinib in second-line or above therapy for advanced primary liver cancer: cohort A report in a multicenter phase Ib/II trial. *J Immunother Cancer*. (2021) 9(3). doi: 10.1136/jitc-2020-002191

80. Finn RS, Ryoo BY, Merle P, Kudo M, Bouattour M, Lim HY, et al. Pembrolizumab as second-line therapy in patients with advanced hepatocellular carcinoma in KEYNOTE-240: A randomized, double-blind, phase III trial. *J Clin Oncol*. (2020) 38(3):193–202. doi: 10.1200/JCO.19.01307

81. Guo M, Qi F, Rao Q, Sun J, Du X, Qi Z, et al. Serum LAG-3 predicts outcome and treatment response in hepatocellular carcinoma patients with transarterial chemoembolization. *Front Immunol*. (2021) 12:754961. doi: 10.3389/fimmu.2021.754961

82. Baysal H, Siozopoulou V, Zaryouh H, Hermans C, Lau HW, Lambrechts H, et al. The prognostic impact of the immune signature in head and neck squamous cell carcinoma. *Front Immunol*. (2022) 13:1001161. doi: 10.3389/fimmu.2022.1001161

83. Miao Y, Yuan Q, Wang C, Feng X, Ren J, Wang C. Comprehensive characterization of RNA-binding proteins in colon adenocarcinoma identifies a novel prognostic signature for predicting clinical outcomes and immunotherapy responses based on machine learning. *Comb Chem High Throughput Screen*. (2023) 26(1):163–82. doi: 10.2174/1386207325666220404125228

84. Yau T, Park JW, Finn RS, Cheng AL, Mathurin P, Edeline J, et al. Nivolumab versus sorafenib in advanced hepatocellular carcinoma (CheckMate 459): a randomised, multicentre, open-label, phase 3 trial. *Lancet Oncol*. (2022) 23(1):77–90. doi: 10.1016/S1470-2045(21)00604-5

85. Sperandio RC, Pestana RC, Miyamura BV, Kaseb AO. Hepatocellular carcinoma immunotherapy. *Annu Rev Med*. (2022) 73:267–78. doi: 10.1146/annurev-med-042220-021121

86. Sung PS, Park DJ, Roh PR, Mun KD, Cho SW, Lee GW, et al. Intrahepatic inflammatory IgA(+)PD-L1(high) monocytes in hepatocellular carcinoma development and immunotherapy. *J Immunother Cancer*. (2022) 10(5). doi: 10.1136/jitc-2021-003618

87. Zheng X, Jin W, Wang S, Ding H. Progression on the roles and mechanisms of tumor-infiltrating T lymphocytes in patients with hepatocellular carcinoma. *Front Immunol*. (2021) 12:729705. doi: 10.3389/fimmu.2021.729705

88. Lu C, Rong D, Zhang B, Zheng W, Wang X, Chen Z, et al. Current perspectives on the immunosuppressive tumor microenvironment in hepatocellular carcinoma: challenges and opportunities. *Mol Cancer*. (2019) 18(1):130. doi: 10.1186/s12943-019-1047-6

89. Kim HD, Song GW, Park S, Jung MK, Kim MH, Kang HJ, et al. Association between expression level of PD1 by tumor-infiltrating CD8(+) T cells and features of hepatocellular carcinoma. *Gastroenterology*. (2018) 155(6):1936–50.e17. doi: 10.1053/j.gastro.2018.08.030

90. Zhang Q, He Y, Luo N, Patel SJ, Han Y, Gao R, et al. Landscape and dynamics of single immune cells in hepatocellular carcinoma. *Cell*. (2019) 179(4):829–45.e20. doi: 10.1016/j.cell.2019.10.003

91. Krishna S, Lowery FJ, Copeland AR, Bahadiroglu E, Mukherjee R, Jia L, et al. Stem-like CD8 T cells mediate response of adoptive cell immunotherapy against human cancer. *Science*. (2020) 370(6522):1328–34. doi: 10.1126/science.abb9847

92. Castella M, Caballero-Baños M, Ortiz-Maldonado V, González-Navarro EA, Suñé G, Antoñana-Vidósola A, et al. Point-of-care CAR T-cell production (ARI-0001) using a closed semi-automatic bioreactor: experience from an academic phase I clinical trial. *Front Immunol*. (2020) 11:482. doi: 10.3389/fimmu.2020.00482

93. Nguyen A, Ho L, Hogg R, Chen L, Walsh SR, Wan Y. HDACi promotes inflammatory remodeling of the tumor microenvironment to enhance epitope spreading and antitumor immunity. *J Clin Invest*. (2022) 132(19). doi: 10.1172/JCI159283

94. Cai Z, Su X, Qiu L, Li Z, Li X, Dong X, et al. Personalized neoantigen vaccine prevents postoperative recurrence in hepatocellular carcinoma patients with vascular invasion. *Mol Cancer*. (2021) 20(1):164. doi: 10.1186/s12943-021-01467-8

95. Löffler MW, Gori S, Izzo F, Mayer-Mokler A, Ascierto PA, Königsrainer A, et al. Phase I/II multicenter trial of a novel therapeutic cancer vaccine, hepaVac-101, for hepatocellular carcinoma. *Clin Cancer Res*. (2022) 28(12):2555–66. doi: 10.1158/1078-0432.CCR-21-4424

96. Chen H, Li Z, Qiu L, Dong X, Chen G, Shi Y, et al. Personalized neoantigen vaccine combined with PD-1 blockade increases CD8(+) tissue-resident memory T-cell infiltration in preclinical hepatocellular carcinoma models. *J Immunother Cancer*. (2022) 10(9). doi: 10.1136/jitc-2021-004389

97. Guo ZS, Lu B, Guo Z, Giehl E, Feist M, Dai E, et al. Vaccinia virus-mediated cancer immunotherapy: cancer vaccines and oncolytics. *J Immunother Cancer*. (2019) 7(1):6. doi: 10.1186/s40425-018-0495-7

98. Shi D, Shi Y, Kaseb AO, Qi X, Zhang Y, Chi J, et al. Chimeric antigen receptor-glypican-3 T-cell therapy for advanced hepatocellular carcinoma: results of phase I trials. *Clin Cancer Res*. (2020) 26(15):3979–89. doi: 10.1158/1078-0432.CCR-19-3259

99. Makkouk A, Yang XC, Barca T, Lucas A, Turkoz M, Wong JTS, et al. Off-the-shelf Vδ1 gamma delta T cells engineered with glypican-3 (GPC-3)-specific chimeric antigen receptor (CAR) and soluble IL-15 display robust antitumor efficacy against hepatocellular carcinoma. *J Immunother Cancer*. (2021) 9(12). doi: 10.1136/jitc-2021-003441

100. Sun Y, Dong Y, Sun R, Liu Y, Wang Y, Luo H, et al. Chimeric anti-GPC3 sFv-CD3ε receptor-modified T cells with IL7 co-expression for the treatment of solid tumors. *Mol Ther Oncolytics*. (2022) 25:160–73. doi: 10.1016/j.omto.2022.04.003

101. Sun Y, Wu L, Zhong Y, Zhou K, Hou Y, Wang Z, et al. Single-cell landscape of the ecosystem in early-relapse hepatocellular carcinoma. *Cell*. (2021) 184(2):404–21.e16. doi: 10.1016/j.cell.2020.11.041

102. Siwowska K, Guzik P, Domnanich KA, Monné Rodríguez JM, Bernhardt P, Ponsard B, et al. Therapeutic potential of (47)Sc in comparison to (177)Lu and (90)Y: preclinical investigations. *Pharmaceutics*. (2019) 11(8). doi: 10.3390/pharmaceutics11080424

103. Piñero F, Dirchwolf M, Pessôa MG. Biomarkers in hepatocellular carcinoma: diagnosis, prognosis and treatment response assessment. *Cells*. (2020) 9. doi: 10.3390/cells9061370

104. Tan DJH, Ng CH, Lin SY, Pan XH, Tay P, Lim WH, et al. Clinical characteristics, surveillance, treatment allocation, and outcomes of non-alcoholic fatty liver disease-related hepatocellular carcinoma: a systematic review and meta-analysis. *Lancet Oncol*. (2022) 23(4):521–30. doi: 10.1016/S1470-2045(22)00078-X

105. Liu P, Zhou Q, Li J. Integrated multi-omics data analysis reveals associations between glycosylation and stemness in hepatocellular carcinoma. *Front Oncol*. (2022) 12:913432. doi: 10.3389/fonc.2022.913432

106. Cui D, Li W, Jiang D, Wu J, Xie J, Wu Y. Advances in multi-omics applications in HBV-associated hepatocellular carcinoma. *Front Med (Lausanne)*. (2021) 8:754709. doi: 10.3389/fmed.2021.754709

107. Verduin M, Zindler JD, Martinussen HM, Jansen RL, Croes S, Hendriks LE, et al. Use of systemic therapy concurrent with cranial radiotherapy for cerebral metastases of solid tumors. *Oncologist*. (2017) 22(2):222–35. doi: 10.1634/theoncologist.2016-0117

108. Zhao G, Wang Y, Fan Z, Xiong J, Ertas YN, Ashammakhi N, et al. Nanomaterials in crossroad of autophagy control in human cancers: Amplification of cell death mechanisms. *Cancer Lett*. (2024) 591:216860. doi: 10.1016/j.canlet.2024.216860

109. Lu Y, Wang Y, Su H, Li H. PD-L1 is associated with the prognosis of penile cancer: A systematic review and meta-analysis. *Front Oncol*. (2022) 12:1013806. doi: 10.3389/fonc.2022.1013806

frontiers | Frontiers in Immunology

TYPE Original Research
PUBLISHED 06 December 2024
DOI 10.3389/fimmu.2024.1517312

OPEN ACCESS

EDITED BY
Bing Yang,
Tianjin Medical University, China

REVIEWED BY
Xin Hu,
National Center for Child Health and Development (NCCHD), Japan
Liwei Zheng,
University of Colorado, United States

*CORRESPONDENCE
Jiazhou Ye
yejiazhou@gxmu.edu.cn
Rong Liang
liangrong@gxmu.edu.cn
Zhihu Huang
huangzhihu@gxmu.edu.cn

†These authors have contributed equally to this work and share first authorship

RECEIVED 25 October 2024
ACCEPTED 18 November 2024
PUBLISHED 06 December 2024

CITATION
Li S, Lin Y, Gao X, Zeng D, Cen W, Su Y, Su J, Zeng C, Huang Z, Zeng H, Huang S, Tang M, Li X, Luo M, Huang Z, Liang R and Ye J (2024) Integrative multi-omics analysis reveals a novel subtype of hepatocellular carcinoma with biological and clinical relevance. *Front. Immunol.* 15:1517312. doi: 10.3389/fimmu.2024.1517312

Integrative multi-omics analysis reveals a novel subtype of hepatocellular carcinoma with biological and clinical relevance

Shizhou Li[1†], Yan Lin[2†], Xing Gao[2], Dandan Zeng[2], Weijie Cen[1], Yuejiao Su[2], Jingting Su[2], Can Zeng[1], Zhenbo Huang[1], Haoyu Zeng[2], Shilin Huang[2], Minchao Tang[1], Xiaoqing Li[2], Min Luo[2], Zhihu Huang[3*], Rong Liang[2*] and Jiazhou Ye[1*]

[1]Department of Hepatobiliary Surgery, Guangxi Medical University Cancer Hospital, Nanning, Guangxi, China, [2]Department of Medical Oncology, Guangxi Medical University Cancer Hospital, Nanning, Guangxi, China, [3]Department of Clinical Laboratory, Minzu Hospital Guangxi Zhuang Autonomous Region, Affiliated Minzu Hospital of Guangxi Medical University, Nanning, Guangxi, China

Background: Hepatocellular carcinoma (HCC) is a highly heterogeneous tumor, and the development of accurate predictive models for prognosis and drug sensitivity remains challenging.

Methods: We integrated laboratory data and public cohorts to conduct a multi-omics analysis of HCC, which included bulk RNA sequencing, proteomic analysis, single-cell RNA sequencing (scRNA-seq), spatial transcriptomics sequencing (ST-seq), and genome sequencing. We constructed a tumor purity (TP) and tumor microenvironment (TME) prognostic risk model. Proteomic analysis validated the TP-TME-related signatures. Joint analysis of scRNA-seq and ST-seq revealed characteristic clusters associated with TP high-risk subtypes, and immunohistochemistry confirmed the expression of key genes. We conducted functional enrichment analysis, transcription factor activity inference, cell-cell interaction, drug efficacy analysis, and mutation information analysis to identify a novel subtype of HCC.

Results: Our analyses constructed a robust HCC prognostic risk prediction model. The patients with TP-TME high-risk subtypes predominantly exhibit hypoxia and activation of the Wnt/beta-catenin, Notch, and TGF-beta signaling pathways. Furthermore, we identified a novel subtype, XPO1+Epithelial. This subtype expresses signatures of the TP risk subtype and aligns with the biological behavior of high-risk patients. Additional analyses revealed that XPO1+Epithelial is influenced primarily by fibroblasts via ligand-receptor interactions, such as FN1-(ITGAV+ITGB1), and constitute a significant component of the TP-TME subtype. Moreover, XPO1+Epithelial interact with monocytes/macrophages, T/NK cells, and endothelial cells through ligand-receptor pairs, including MIF-(CD74+CXCR4), MIF-(CD74+CD44), and VEGFA-VEGFR1R2, respectively, thereby promoting the recruitment of immune-suppressive cells and angiogenesis. The ST-seq cohort treated with Tyrosine Kinase Inhibitors (TKIs) and Programmed Cell Death Protein 1 (PD-1) presented elevated levels of TP and TME risk subtype signature genes, as well as XPO1+Epithelial, T-cell, and

endothelial cell infiltration in the treatment response group. Drug sensitivity analyses indicated that TP-TME high-risk subtypes, including sorafenib and pembrolizumab, were associated with sensitivity to multiple drugs. Further exploratory analyses revealed that CTLA4, PDCD1, and the cancer antigens MSLN, MUC1, EPCAM, and PROM1 presented significantly increase expression levels in the high-risk subtype group.

Conclusions: This study constructed a robust prognostic model for HCC and identified novel subgroups at the single-cell level, potentially assisting in the assessment of prognostic risk for HCC patients and facilitating personalized drug therapy.

KEYWORDS

hepatocellular carcinoma, tumor purity, tumor microenvironment, single-cell RNA sequencing, spatial transcriptomics, immunotherapy, precision medicine

1 Introduction

Hepatocellular carcinoma (HCC) is the most prevalent primary liver cancer, ranking as the sixth most common tumor and the third leading cause of cancer-related mortality (1, 2). The progression of HCC is a complex, multifactorial, and multistep process that involves the accumulation of genomic alterations in somatic driver genes, in addition to epigenetic changes, resulting in significant molecular heterogeneity. Therefore, understanding the molecular mechanisms driving this heterogeneity is crucial for the development of targeted therapies (3–5).

Current staging and subtyping systems for HCC primarily rely on radiological, serological, and pathological assessments of the tumor load (6). However, HCC at the same stage can exhibit distinct molecular characteristics (7), highlighting the need for more precise subtyping systems that can better predict prognosis and treatment response. Tumor tissues consist not only tumor cells but also non-tumor cells, including immune cells, and stromal cells, all of which collectively influence tumor development (8). Tumor purity (TP) is defined as the proportion of tumor cells relative to the total cell population in a sample (9). Research has shown that TP is significantly correlated with various clinical characteristics, genomic expression, and the biological properties of patients with tumors (10, 11). Furthermore, heterogeneity of the tumor microenvironment (TME) is a key contributor to tumor diversity in HCC (12, 75). Persistent tumor stimulation affects the remodeling of the TME, which subsequently influences the response of tumors to various treatments (13, 76). Targeting the TME is considered a promising strategy to overcome barriers to anticancer immune responses and enhance the efficacy of immunotherapy. With rapid advancements in high-throughput sequencing and single-cell sequencing (scRNA-seq), numerous approaches have been developed to identify disease biomarkers, leading to significant progress in disease prognosis prediction (14–16). However, only a few molecular classifications of HCC have integrated both malignant cells and TME-associated molecules. In recent years, single-cell histological studies, particularly those employing scRNA-seq technology, have substantially enhanced our understanding of tumor cell heterogeneity, tumor-infiltrating immune cell clusters, and tumor-associated stromal cell characteristics at the single-cell level (17). Nevertheless, the ability of scRNA-seq to investigate tumor spatial structure is limited because of the loss of spatial and morphological information when tissues are dissociated into single-cell suspensions. The advent of spatial transcriptomics sequencing (ST-seq) has addressed the limitations of scRNA-seq, enabling the exploration of the spatial architecture of tumors (18).

In this study, we first established a novel prognostic model for HCC via bulk RNA sequencing, which was based on the expression patterns of TP-related and TME-related genes. The expression levels of these TP and TME-related genes were subsequently validated through proteomic analysis. We then conducted an in-depth exploration of the expression patterns and biological functions of the characteristic genes associated with TP risk subtypes via scRNA-seq and ST-seq. Notably, we identified XPO1+Epithelial within the tumor that may promote tumor progression and contribute to the regulation of the TME through cellular communication networks. Finally, we conducted a preliminary assessment of the relevance and potential mechanisms of the TP-TME risk subtypes in relation to HCC targeting and immunotherapy.

2 Materials and methods

2.1 Data processing

Six HCC samples were obtained from six patients who underwent hepatectomy as the initial treatment, along with one normal liver sample provided by a hepatic hemangioma patient

through surgical resection, at the Cancer Hospital of Guangxi Medical University. These samples were utilized for proteomic analysis, scRNA-seq, and ST-seq. The patients were enrolled at the Cancer Hospital of Guangxi Medical University from June to September 2021. Detailed information on the diagnostic criteria for HCC, along with patient inclusion and exclusion criteria, has been reported previously (19). In summary, all enrolled patients with HCC were newly diagnosed, pathologically confirmed, and free from other cancer types. Additionally, tumor and adjacent tissues were collected from 40 HCC patients who were diagnosed and treated with radical surgery between January 2021 and January 2024 at the Cancer Hospital of Guangxi Medical University for immunohistochemical (IHC) experiments. The detailed clinical information is present in Supplementary Table S1.

We screened the HCCDB database (http://lifeome.net/database/hccdb/home.html) (20) to identify the candidate datasets. The inclusion criteria were as follows: 1) the dataset included both gene expression profiles and the prognosis of patients with HCC, 2) the number of patients with a survival of more than 30 days should be more than 100, and 3) the gene expression profile of the dataset should contain more than 10,000 genes. In the HCCDB database, four datasets met the above criteria. We selected and downloaded the three largest datasets by sample size (GSE14520_GPL3921, TCGA-LIHC, and LIRI-JP) for analysis. The dataset GSE14520_GPL3921 (21) containing 225 HCC and 220 tumor-adjacent liver tissue samples was utilized to develop our subtyping systems. The TCGA-LIHC dataset, which contains RNA-seq data and clinical information for 356 HCC patients from The Cancer Genome Atlas (TCGA) (https://www.cancer.gov/tcga), and the LIRI-JP data set containing RNA-seq data and clinical information for 212 HCC patients from the JP Project from the International Cancer Genome Consortium (https://dcc.icgc.org/), were used to validate the subtyping systems.

Finally, we gathered proteomic analysis data of tumor and tumor adjacent tissues from 159 cases of HBV-associated HCC reported in Gao's study (22). This served as a validation of the proteomic analysis to confirm our findings. We also collected the ST-seq cohort GSE238264 (23), which was diagnosed with HCC and treated with a combination of tyrosine kinase inhibitors (TKIs) and programmed cell death protein 1 (PD-1) inhibitors, serving as a validation cohort sourced from the GEO database. The workflow of the present study is illustrated in Figure 1.

2.2 Calculation of the TP and TME scores and identification of differentially expressed genes

The gene expression profiles of GSE14520_GPL3921 were first utilized to calculate TP via the ESTIMATE package (24). GSE14520_GPL3921 was also used to calculate the TME score via the xCell tool (https://xcell.ucsf.edu/) (25) with the xCell gene signature. The DEGs in HCC compared to tumor-adjacent liver tissue were identified via the R package limma (v3.54.2) (26). Genes with fold changes > 1.5 and P (adjusted by false discovery rate) values < 0.05 were considered significant.

2.3 Normality test and correlation analysis

The TP and TME scores were separately analyzed via the Shapiro-Wilk test. Spearman or Pearson correlation analyses were performed to calculate the correlation between DEGs and the TP and the TME scores. A DEG that was positively correlated with TP and negatively correlated with the TME score was considered a TP-related gene, whereas a DEG that was negatively correlated with TP and positively correlated the TME score was considered a TME-related gene. In addition, the TME-related genes do not include marker genes of TME cells in the xCell signature.

2.4 Functional and pathway enrichment analysis

The online Metascape tool (https://metascape.org/) was used for functional enrichment analysis of DEGs in HCC and tumor-adjacent liver tissues. We performed GSEA (27, 28) on the GSE14520_GPL3921 dataset via the GSEA Java software (http://www.gsea-msigdb.org/gsea/index.jsp). Hallmark and canonical pathway gene sets derived from the Kyoto Encyclopedia of Genes and Genomes (KEGG) pathway database were downloaded from the Molecular Signatures Database (MSigDB) (28, 29) and used as reference gene sets. The threshold was set to a nominal P (NOM P) value < 0.05 and FDR q value < 0.25. Functional enrichment analyses of DEGs between single-cell clusters were performed via the R package clusterProfiler (v.4.6.2) (29), which is based on the Gene Ontology (GO) or MsigDB. The corrected enrichment terms with P<0.05 were considered statistically significant. Functional scoring was performed via AddModuleScore in the R package Seurat for gene sets in the MsigDB. Functional enrichment analyses of DEGs among single-cell clusters were conducted via the R package clusterProfiler (version 4.6.2) (30), which utilizes the GO framework or data from MsigDB. Enrichment terms with a corrected p-value of less than 0.05 were deemed statistically significant. Additionally, functional scoring was performed via the AddModuleScore function in the R package Seurat for gene sets derived from MsigDB.

2.5 Protein-protein interaction networks

The PPI networks of TP-related and TME-related genes were obtained from the STRING database (v11.5) (31) to preliminarily reveal the crosstalk between tumor cells and TME. The interactions with high confidence (>0.7) were included in the present study and visualized via Cytoscape software (v 3.8.0) (32).

2.6 Development of the TP- and TME-related gene-based polygenic risk scores

First, to develop the TP-related polygenic risk score (PRS), overall survival (OS)-associated TP-related genes were identified via univariate Cox regression analysis. Second, the expression

10.3389/fimmu.2024.1517312

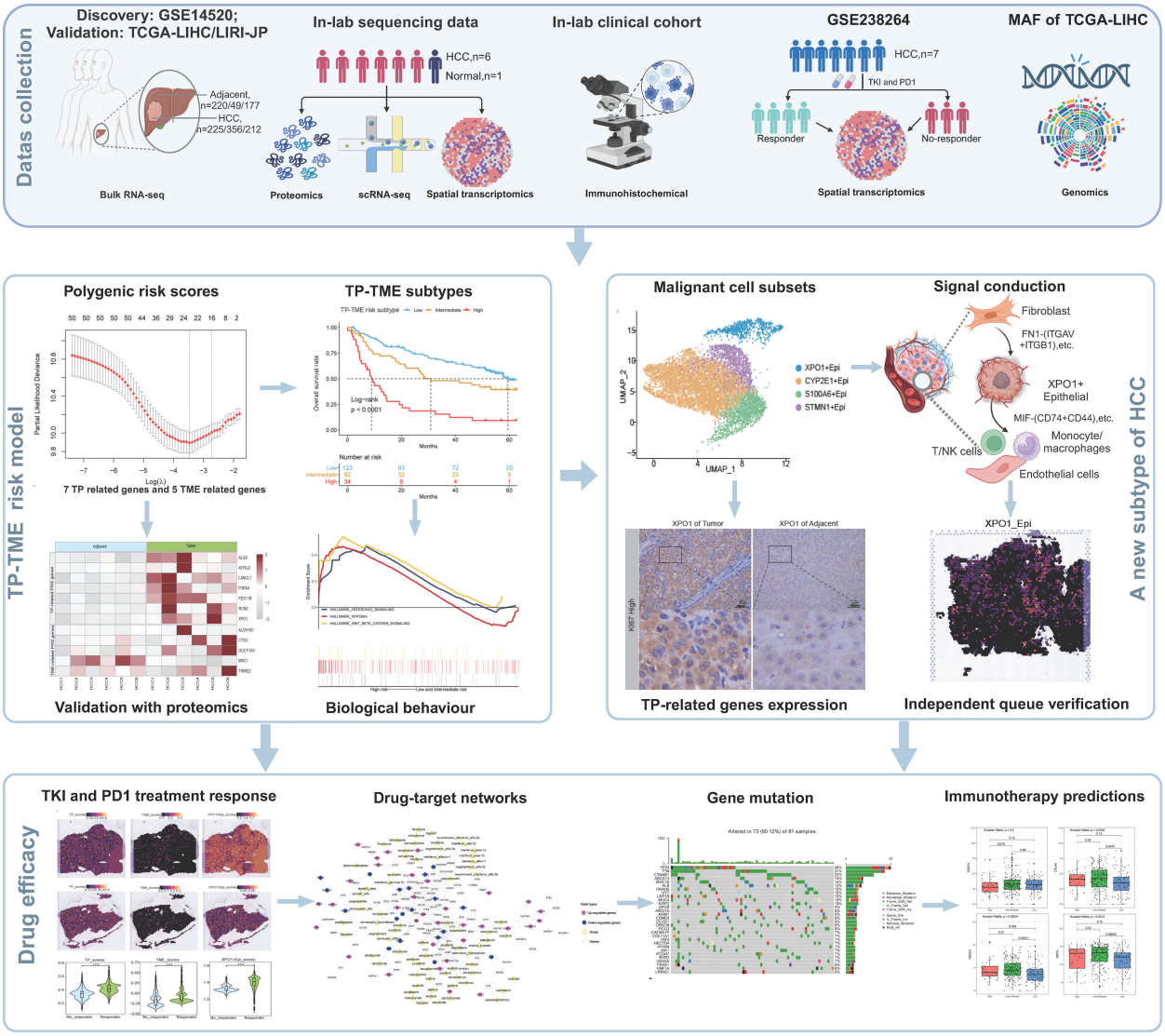

FIGURE 1
A flowchart showing the overall idea of this study. The figure was created with biorender.com.

profiles of the OS-associated TP-related genes were used to carry out least absolute shrinkage and selection operator (LASSO) Cox regression model analysis with leave-one-out cross validation via the glmnet package (33). The genes with nonzero coefficients were considered the optimal features and subjected to multivariate Cox regression and stepwise regression analysis. The TP-related PRS was subsequently developed via the following formula: TP-related PRS = Σ (Expression$_i$ $*$ Coeffient$_i$) where "Coeffient" and "Expression" represent the risk coefficient and expression of each gene in the multivariate Cox regression and stepwise regression analysis, respectively. The TME-related PRS was also developed according to the same method as above.

2.7 The TP-TME subtypes of HCC

The optimal cutoffs of the TP-related and TME-related PRS were identified vis the surv_cutpoint function from the Survminer package (https://CRAN.R-project.org/package=survminer) to separately divide patients into high and low TP- and TME-related PRS groups. Each individual received a TP- and a TME-related PRS levels, and we developed the TP-TME subtype according to the TP- and TME-related PRS levels. Patients with high TP- and TME-related PRS were considered the high-risk subtype, those possessing low TP- and TME-related PRS were considered the low-risk subtype, and the remaining patients with high TP-related and low

TME-related PRS or a low TP-related and high TME-related PRS were considered the intermediate-risk subtype.

2.8 Proteomic analysis

The protein samples were extracted, digested, and labeled with Tandem Mass Tag (TMT) according to the experimental specifications. A 10 μL aliquot of the supernatant was injected into a nanoflow HPLC system (Thermo Scientific) linked to an Orbitrap Fusion Lumos mass spectrometer (Thermo Scientific). The extracts were then applied to an Acclaim PepMap100 C18 column and separated on an EASY-Spray C18 column. In the Orbitrap mode, the mass spectrometer performed a comprehensive mass spectrometry (MS) scan across the 300-1500 m/z range in positive ion mode (with a source voltage fixed at 2.1 kV) and achieved a resolution of 120,000. After the complete MS scan, the 20 most abundant ions with different charge states were selected for high-energy collisional dissociation fragmentation analysis. For this experiment, the UniProt HUMAN database, which was downloaded on April 20, 2019, served as the database. MS/MS data were analyzed via Proteome Discoverer 1.4.

2.9 Preprocessing and quality control of single-cell transcriptome data

Raw FASTQ data were processed via Cell Ranger (version 8.0.0; 10× Genomics, USA), generating gene count matrices on the basis of the human genome reference set GRCh38 with all default parameter settings. The output filtered gene expression matrix for each sample was analyzed via the R package Seurat (v.4.3.0) (34). We calculated the doublet fraction for each cell via the R package DoubletFinder (v.2.0.4) (35) with aim of removing potential doublets with a target value of 7.6% per 1000 droplets. Additionally, for each sample, cells with fewer than 300 unique molecular identifiers (UMIs), or expressing more than 7000 or fewer than 300 genes were excluded. To eliminate dead or dying cells, we further removed cells with more than 10% UMIs originating from the mitochondrial genome. Next, the "FindVariableFeatures" function in Seurat and the vst method were employed to screen for the 2000 variable genes exhibiting the largest normalized variance, which were subsequently processed for principal component analysis (PCA). The "RunHarmony" function from the Harmony package (v.1.2.0) (36) was then utilized for sample batch correction. The "RunUMAP" function was applied to perform UMAP downscaling of the first 20 principal components according to the aforementioned steps. Finally, the "FindNeighbors" and "FindClusters" functions were employed to identify cell clusters.

2.10 Cell type identification

We collected typical marker genes for the identification of the major cell types. Epithelial cells were identified by the expression of ALB, APOA2, and EPCAM; fibroblasts were characterized by COL1A1, COL1A2, and DCN; endothelial cells were identified via PECAM1, VWF, and PLVAP; T/NK cells were marked via CD3D, CD3E, and CD2; B cells were identified via CD79A and MZB1; monocytes/macrophages were characterized via LYZ, CD86, and C1QC; mast cells were identified via TPSB2, CPA3, and KIT; neutrophils were marked via G0S2, CXCL8, and CSF3R; and dividing cells were identified via MKI67 and STMN1.

2.11 Immunohistochemistry experiments

Following tissue collection, samples from patients were fixed in 10% formaldehyde for 12 hours. The tissues were subsequently dehydrated, clarified, paraffin embedded, and sectioned at a thickness of 4 μm for both H&E and IHC staining. The staining procedures were performed according to the manufacturer's guidelines. Sections stained with H&E were examined under a light microscope (OLYMPUS BX43) via a ×10 eyepiece and a ×40 objective lens, with images captured using ImageView 4.15 (Pooher) software. For immunohistochemical analysis, the sections were scanned with a Pannoramic digital section scanner (3DHISTECH). Two pathologists, blinded to the clinical characteristics and findings of the patients, independently evaluated all the sections. Scoring was conducted on a 4-point scale on the basis of the intensity of cellular staining: no positive staining (negative) received a score of 0, yellowish (weakly positive) scored a score of 1, tan (positive) scored a score of 2, and tan (strongly positive) scored a score of 3. Additionally, a 4-point scale based on the percentage of positive cells was employed, with ≤25% scoring 1, 26%-50% scoring 2, 51%-75% scoring 3, and >75% scoring 4. The final score was derived by multiplying the two individual scores. The following primary antibodies were used to bind specific IHC proteins: XPO1 (Proteintech, 27917-1-AP) and RCN2 (Proteintech, 10193-2-AP), and the secondary antibody used was horse anti-mouse/rabbit IgG (Vector, ZF1028). Raw data for 40 HCC patients were uploaded (Supplementary File 1).

2.12 Chromosome copy number variation analysis

The R package InferCNV (v1.21.0) (https://github.com/broadinstitute/inferCNV) was used to infer CNV changes in the scRNA-seq data. The raw gene expression counts extracted from the Seurat object were imported into the Infercnv object via the "InfercnvObject()" function. T/NK cells and B cells were selected as control datasets for reference. The CNV value for each cell was estimated via the "run()" function in InferCNV with a cutoff value of 0.1.

2.13 Transcription factors activity analyses

Activity analyses of TFs were performed to pinpoint key regulatory TFs in the selected cell clusters, and SCENIC analysis

was conducted via the pySCENIC (37) package. The necessary databases for executing SCENIC, which include the TF database (cisTarget.hg38.mc9nr.feather) and the subject annotation database (hgnc.v9.1.0), were acquired from the pySCENIC website (https://github.com/aertslab/pySCENIC). The normalized expression matrix generated by Seurat served as the input matrix for the pySCENIC. TF activity was determined by the area under the recovery curve (AUC), and detailed findings from the transcription factor activity analyses are shown in Supplementary Table S2.

2.14 Cell-cell communication analyses

Cell-cell communication was inferred via the R software version of CellChat (v1.6.1) (38) and an existing database of ligand-receptor interactions. The apparent overexpression of ligands and receptors in specific cell clusters was initially identified via CellChat. The probability of communication occurring between two interacting clusters was quantified on the basis of the average expression level of the ligand in one cluster and the average expression level of the receptor in the other. The significance of communication was assessed via a permutation test. Interaction pairs with a P value < 0.05 were selected to assess intercellular communication. The detailed results of the cell-cell communication analysis are listed in Supplementary Table S3.

2.15 Spatial transcriptome data analyses

The expression matrices from the ST-seq data were processed via Seurat. "SCTransform()" normalised the values at each point, and "RunPCA()" retained the first 20 principal components (PCs) to reduce dimensionality. The top 30 DEGs for each cell cluster in the scRNA-seq cohort were used as input. Scores were assigned to individual points in the ST-seq dataset via the "gsva()" function of the R package GSVA (v1.46) (39) with default parameters. The spatial feature expression plots were generated via the "SpatialFeaturePlot()" function in Seurat.

2.16 Analyses of gene mutations and stemness scores

Gene mutation data from the TCGA-LIHC dataset were extracted from mutation annotation format (MAF) files via the *GDCquery_Maf* function in the "TCGAbiolinks" package (40). The gene mutation frequencies of each risk subtype were visualized as a waterfall plot via the *oncoplot* function in the "TCGAbiolinks" package. The tumor mutational burden (TMB) of each sample was obtained from a previous study (41). The stemness score (42) was calculated for each individual in the TCGA-LIHC dataset via the TCGA analyze_Stemness function in the "TCGAbiolinks" package.

2.17 Prediction of the efficacy of therapy

For the TP-TME risk subtypes, we compared the expression levels of two immune checkpoints (PDL1 and CTLA4) and five antigens (CD133, EPCAM, GCP3, MSLN, and MUC1) (43) to predict the potential response to these treatments. In addition, we performed drug repositioning analysis for the high-risk subtype via the PATHOME-Drug (http://statgen.snu.ac.kr/software/pathome/) web tool.

2.18 Statistical analysis

Unless otherwise stated, all analyses were performed in R (version 4.2.3). We identified DEGs via unpaired t-tests provided via the limma package. The Shapiro-Wilk test was used for the normality test. Time-dependent receiver operating characteristic (tROC) curve analysis was carried out using the tROC package (44). Kaplan–Meier survival curves for OS and progression free survival (PFS) were compared in different subtypes using the log-rank method in the "survival" package (https://CRAN.R-project.org/package=survival) and the "survminer" package (https://CRAN.R-project.org/package=survminer). Intergroup differences in continuous variables were assessed for significance via Wilcoxon, Kruskal–Wallis, or unpaired t tests. All tests were two-sided, and unless otherwise stated, we set P value < 0.05 to indicate statistical significance. Visualization was done vis the "ggplot2" R package.

3 Results

3.1 Biological functions and interactions of TP-related and TME-related genes

Using the GSE14520_GPL3921 dataset, we identified a total of 2,263 differentially expressed genes (DEGs) in HCC compared with tumor-adjacent liver tissue (Figure 2A). A total of 451 TP-related genes and 121 TME-related genes were identified through Spearman correlation analysis. Bidirectional hierarchical clustering revealed that the expression patterns of these genes could largely distinguish between HCC and tumor-adjacent liver tissue (Figure 2B). Unsurprisingly, the TP-related genes were enriched in mainly cancer-related Gene Ontology (GO) terms and pathways, such as the cell cycle and mismatch repair (Figure 2C). In contrast, TME-related genes were associated primarily with immune system processes (Figure 2D). The PPI networks of the TP-related and TME-related genes contain 342 nodes and 1177 edges (Supplementary Figure S1). In the PPI networks, red nodes indicate genes whose expression is upregulated, and blue nodes indicate genes whose expression is downregulated in tumors. Circular nodes represent TP-related genes, whereas rhombic nodes represent TME-related genes.

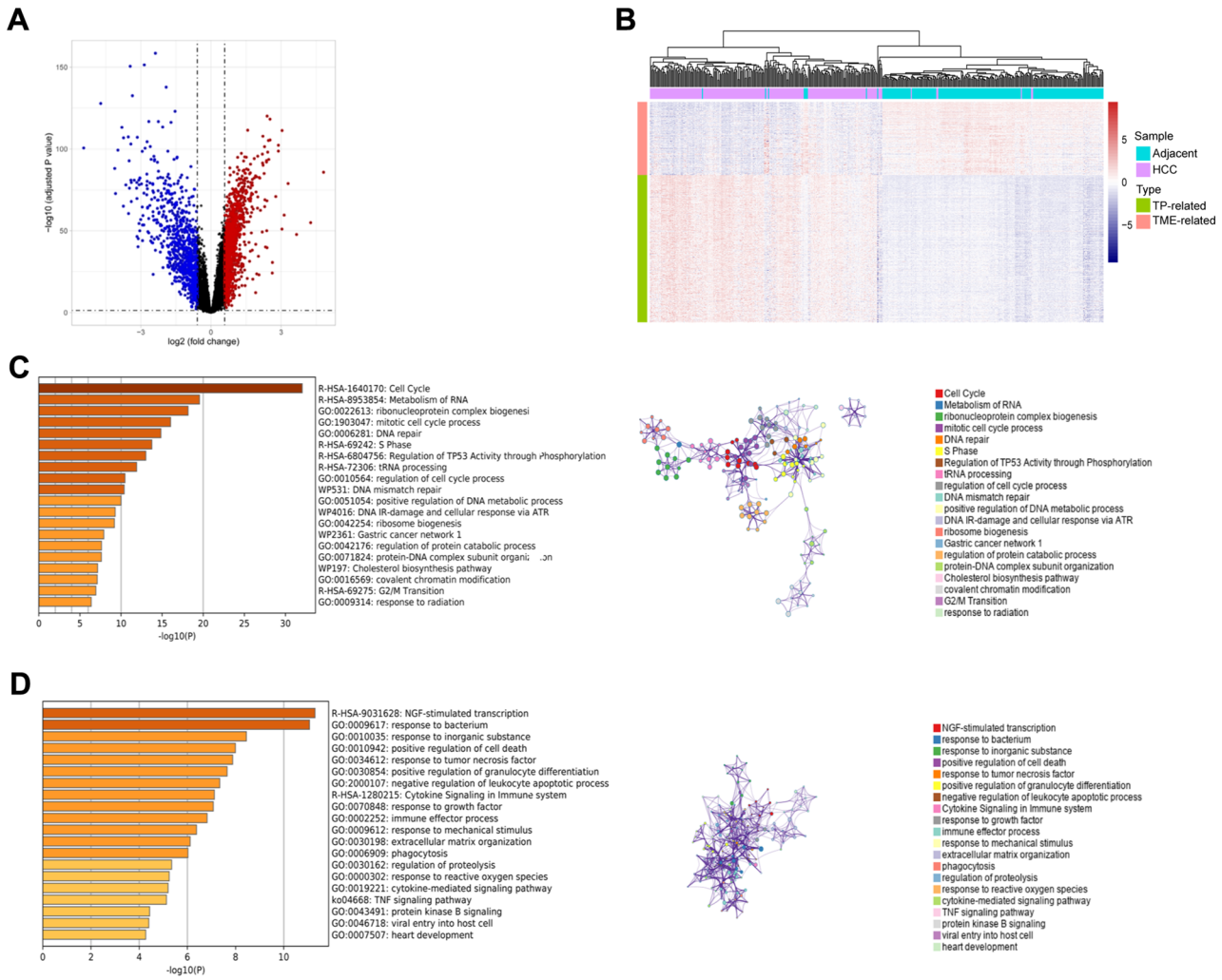

FIGURE 2
Identification, enrichment analysis, and protein-protein interaction networks of the tumor purity-related genes and tumor microenvironment-related genes in GSE14520_GPL3921. **(A)** Volcano plot of the differentially expressed genes. **(B)** Hierarchical clustering showing that the expression patterns of TP-related and TME-related genes basically distinguish HCC and tumor-adjacent liver tissues. **(C)** Functional enrichment analysis of the TP-related genes. *Left panel:* GO terms and pathways involving TP-related genes, and *right panel*: interactions among the GO terms and pathways. **(D)** Functional enrichment analysis of TME-related genes. *Left panel:* GO terms and pathways involving TME-related genes, and *right panel*: interactions among the GO terms and pathways.

3.2 The TP-TME risk subtype is a robust prognostic prediction system

Fifty TP-related genes were identified as OS-associated genes, twenty-two of which presented nonzero coefficients (Figure 3A), and 11 genes (ALG6, ATP5MF, CNIH4, ESM1, HEY1, LANCL1, P2RX4, PEX11B, POP7, RCN2, and XPO1) were used to generate the TP-related PRS (Supplementary Table S4). The TP-related PRS was significantly associated with OS [P < 0.0001, hazard ratio (HR) = 2.718 (95% CI for HR = 2.147-3.442)], and the area under the curve (AUC) of the tROC analysis was stable at approximately 0.8 (Figure 3B). The HCC patients with high TP-related PRS had shorter OS than did those with low TP-related PRS (P < 0.0001) (Figure 3C). Among the TME-related genes, twelve genes were identified as OS-associated genes, ten of which had nonzero coefficients (Figure 3D), and seven genes (ALDH1B1, CTSC, GUCY1A1, MRC1, SPRY2, TARP, and TRIM22) were used to generate the TME-related PRS (Supplementary Table S5). The TME-related PRS was also significantly associated with OS [P < 0.0001, HR = 2.718 (95%CI for HR = 1.978-3.735)], and the AUC of tROC analysis was 0.7-0.8 (Figure 3E). HCC patients with a high TME-related PRS had shorter OS than did those with low TP-related PRS (P < 0.0001) (Figure 3F). Our TP-TME risk subtype was generated on the basis of two PRSs, and 34, 52, and 123 patients with HCC were divided into high-, intermediate-, and low-risk subtypes, respectively. Patients in the high-risk subtype had the poorest survival, those in the low-risk subtype had the best survival, and those in the intermediate-risk cases had a better

10.3389/fimmu.2024.1517312

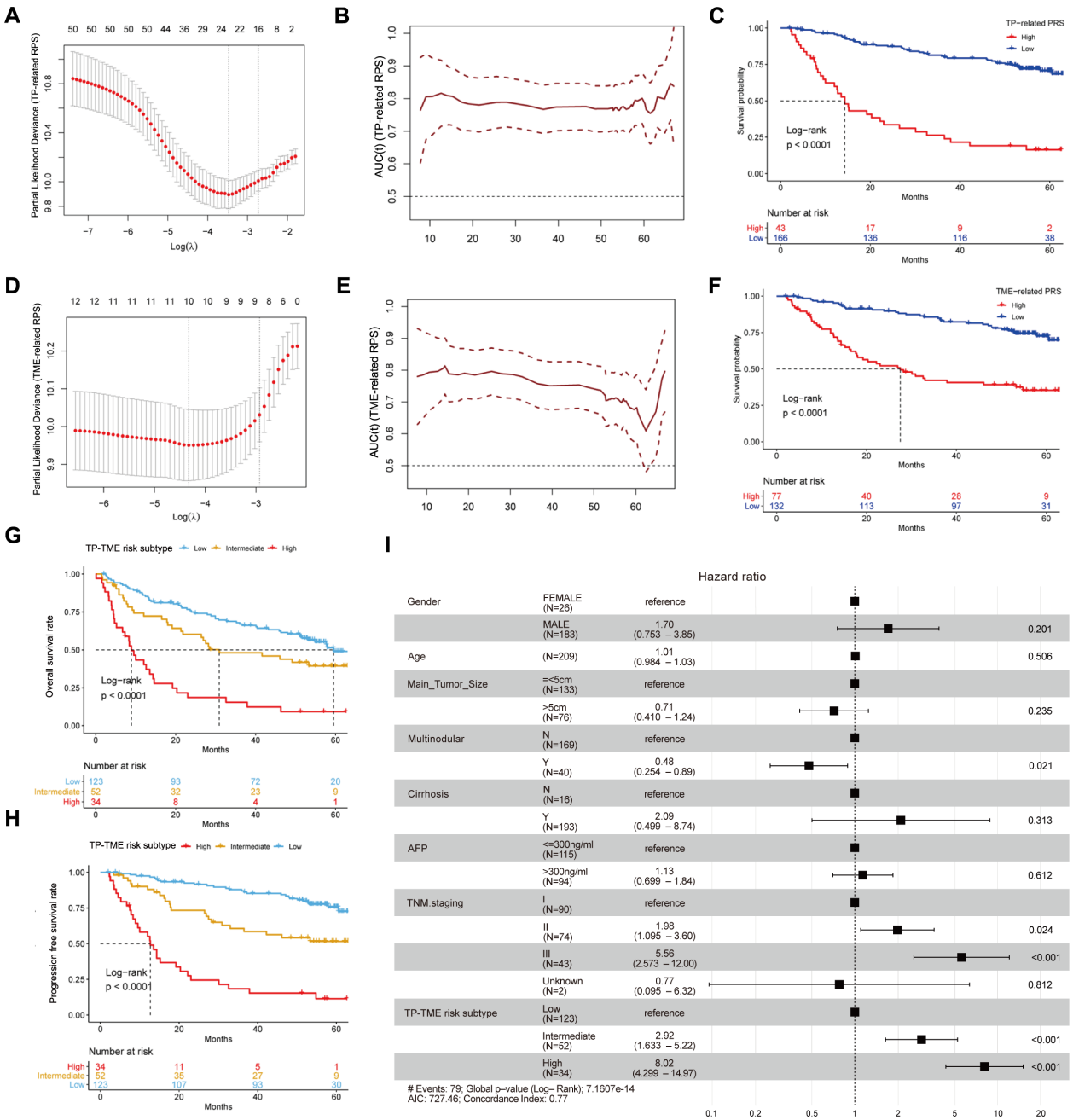

FIGURE 3
Development and validation of TP-TME risk subtypes in GSE14520_GPL3921. **(A)** Twenty-two TP-related genes had nonzero coefficients in the LASSO Cox regression model analysis; **(B)** Time-dependent ROC curve analysis for the TP-related PRS; **(C)** HCC with high TP-related PRS had shorter overall survival than those with low TP-related PRS. **(D)** Ten TME-related genes had nonzero coefficients in the LASSO Cox regression model analysis; **(E)** Time-dependent ROC curve analysis for the TME-related polygenic risk score; **(F)** HCC with high TME-related PRS had shorter overall survival than those with low TME-related PRS. **(G)** There were significant differences in overall survival among the three subtypes of the TP-TME risk subtypes. **(H)** There were significantly differences in progression-free survival among the three subtypes of the TP-TME risk subtypes. **(I)** The TP-TME risk subtype system was proven to be an independent prognostic factor, after adjusting for other clinicopathological characteristics.

prognosis than did those in the high-risk subtype and worse prognosis than did those in the low-risk subtype did (Figure 3G). A similar trend was also observed for PFS (Figure 3H). Furthermore, the TP-TME risk subtyping system demonstrated superior prognostic predictive power compared to routine clinicopathological features and remained independent of these features (Figure 3I). As in the GSE14520_GPL3921 dataset, the TP-related PRS and the TME-related PRS in the TCGA-LIHC and LIRI-JP datasets were calculated according to the abovementioned formulas. We found similar results in the TCGA-LIHC cohort (Supplementary Figures S2A–E) and the LIRI-JP cohort (Supplementary Figures S2F–I). Overall, TP-TME risk subtype is a robust prognostic prediction system.

10.3389/fimmu.2024.1517312

3.3 The biological functions of characteristic genes involved in TP-TME risk subtype

Compared with those in the TP-TME intermediate- and high-risk subtypes, the liver function-related HALLMARK (Figure 4A) and metabolism-related KEGG (Figure 4B) gene sets were significantly enriched in the TP-TME low-risk subtype. These findings suggest that the TP-TME low-risk subtype of HCC is well- differentiated. The TP-TME intermediate-risk subtype was characterized by enrichment of transcription factor E2F and MYC targets (Figure 4C) and cell cycle pathways (Figure 4D), whereas the TP-TME high-risk subtype was characterized by enrichment of hypoxia, Wnt/beta-catenin signaling (Figure 4E), the Notch signaling pathway and the TGF-beta signaling pathway (Figure 4F). These results indicate that there is significant biological heterogeneity among these three subtypes.

To validate the expression of genes characterizing the TP-TME risk subtype at the protein level, we collected tumor and adjacent-tumor tissues from 6 HCC patients for proteomic analysis. Analysis of the protein expression levels of genes associated with the HCC-TP-TME risk subtype showed, that XPO1, RCN2, PEX11B, P2RX4, LANCL1, ATP5MF, ALG6, TRIM22, GUCY1A3, CTSC, and ALDH1B1 were significantly elevated in tumor tissues compared with adjacent tumor tissues (Figure 4G). Furthermore, we validated these findings via published data from Gao et al. (22), which corroborated our results in an independent cohort (Figure 4H). Collectively, these results indicate that the characteristic genes of the TP-TME risk subtypes identified in our study have important clinical implications for the prognostic assessment of HCC and

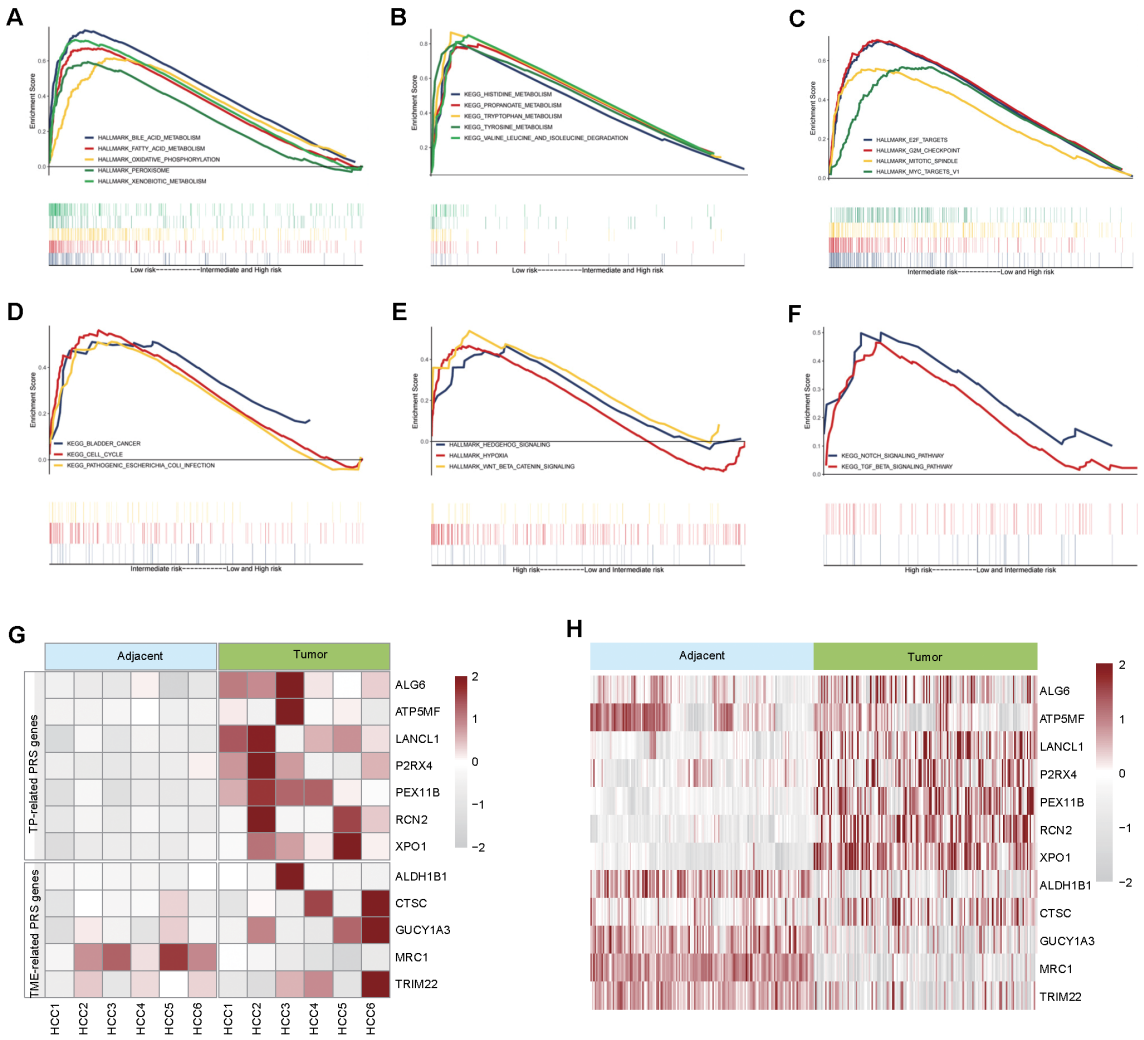

FIGURE 4
Biological behavior and characteristic gene protein expression levels of TP-TME risk subtypes. **(A)** The hallmark gene sets enriched in the TP-TME low-risk subtype. **(B)** The KEGG pathway gene sets enriched in the TP-TME low-risk subtype. **(C)** The hallmark gene sets enriched in the TP-TME intermediate-risk subtype. **(D)** The KEGG pathway gene sets enriched in the TP-TME intermediate-risk subtype. **(E)** The hallmark gene sets enriched in the TP-TME high-risk subtype. **(F)** The KEGG pathway gene sets enriched in the TP-TME high-risk subtype. **(G)** Heatmap showing the protein expression levels of genes associated with the TP-TME risk subtypes. **(H)** Heatmap showing protein expression levels of genes associated with the TP-TME risk subtypes reported by Gao et al.

warrant further investigation into the biological functions of these genes.

3.4 Exploring the expression patterns and biological functions of genes characterizing TP-TME risk subtypes in HCC via scRNA-seq

By analyzing the scRNA-seq data for HCC, we obtained 62,163 high-quality cells. Nine distinct cell types were identified on the basis of known markers: epithelial cells, fibroblasts, endothelial cells, T/NK cells, B cells, monocytes/macrophages, mast cells, neutrophils, and cycling cells (Figures 5A–C). Furthermore, we analyzed the proportions of various cell types across different patients and found that, although all cell types were present in each patient, the predominant infiltrating cell types varied, which may reflect heterogeneity among HCC patients (Figure 5D).

Next, we re-clustered the epithelial cells on the basis of their differentially expressed genes, identifying 4 clusters: XPO1+Epithelial, CYP2E1+Epithelial, S100A6+Epithelial, and STMN1+Epithelial (Figure 5E). The bubble diagram illustrates the highly expressed genes in each cluster (Figure 5F). Functional enrichment analysis revealed that XPO1+Epithelial was predominantly associated with the acute inflammatory response, cell growth, positive regulation of angiogenesis, and epithelial cell proliferation, indicating its potential role in tumor progression. In contrast, CYP2E1+Epithelial were primarily linked to material and energy metabolism, whereas S100A6+Epithelial were associated with the regulation of ubiquitin-protein ligase activity, among other functions. STMN1+Epithelial exhibited characteristics related to cytokinesis (Figure 5F). We subsequently analyzed the chromosome copy number variation in these epithelial cells via inferCNV. The results indicated that all four clusters presented significant chromosome amplifications and deletions (Supplementary Figure S3A). Additionally, we observed minimal capture of epithelial cells in normal liver tissue samples (Figure 5D), leading us to conclude that all four clusters consisted of malignant epithelial cells.

We found that 7 genes characterizing TME risk subtypes were expressed at varying levels across multiple cell types within the TME (Supplementary Figure S3B). However, 11 genes associated with the TP risk subtype signatures exhibited significantly increased expression in the XPO1+Epithelial. Specifically, the expression levels of XPO1, RCN2, P2RX4, PEX11B, LANCL1, HEY1, and ESM1 were significantly increase in this cluster than in the other clusters (Figures 5G, H). Consequently, we focused on this cluster characterized by high expression of genes in the XPO1+Epithelial group. Next, we collected tumor tissues and adjacent-tumor tissues from 40 HCC patients for immunohistochemical staining (Figure 5I) to validate our findings. We observed that the expression levels of XPO1 and RCN2 were elevated in tumor tissues compared with adjacent-tumor tissues (Figure 5J). Further analysis indicated that the expression of XPO1 and RCN2 was greater in tumor tissues with high Ki67 expression (Figures 5I, K, L). These results suggest that the elevated expression of XPO1 and RCN2 is closely associated with the proliferation of HCC.

Further analysis revealed that the XPO1+Epithelial cluster scored significantly increase than other clusters did in terms of functions associated with the TGF-beta signaling pathway, WNT/beta-catenin signaling, Notch signaling, Hedgehog signaling, and hypoxia signaling (Figure 6A). This finding was consistent with the upregulation of these functions observed in high-risk patients within the TP-TME risk model (Figures 4A–F). Additionally, compared with the other clusters, the XPO1+Epithelial cluster presented significantly increase scores for proliferation, migration, epithelial-mesenchymal transition (EMT), and angiogenesis (Figure 6A). Our analysis of the key TFs driving the distinct functions of these clusters revealed that the ten most active transcription factors in XPO1+Epithelial were predominantly associated with tumor proliferation, migration, and invasion (Figure 6B). For example, MEF2A may play a dual role in promoting tumor proliferation and metastasis by inducing the activation of EMT and WNT/beta -catenin signaling (45), whereas TCF7L2 serves as a core TF of the WNT signaling pathway, and is involved in regulating tumor cell proliferation and migration (46). Furthermore, we observed that patients exhibiting high expression of XPO1+Epithelial signatures had significantly shorter OS and PFS in the TCGA cohort (Figure 6C).

In summary, we found that XPO1+Epithelial constitute a cluster of cells characterized by TP high-risk subtypes, which exhibit elevated expression in cancer tissues. This cluster shows higher expression levels in patients with tumors that have high proliferation rates and is positively correlated with poor patient prognosis. The underlying mechanism may involve the contribution of this cluster to tumor progression through pathways such as EMT and WNT/beta-catenin signaling.

3.5 Crosstalk between XPO1+ Epithelial and TME

To further explore the crosstalk between XPO1+Epithelial and the TME in HCC, we performed intercellular communication analysis via 'CellChat'. The results indicated that among the four epithelial cell clusters, XPO1+Epithelial exhibited the highest degree of communication with TME components (Figure 7A). XPO1+Epithelial was regulated primarily by fibroblasts (Figure 7B). Additionally, signals sent by XPO1+Epithelial predominantly regulate monocyte/macrophages, endothelial cells, and T/NK cells (Figure 7C). Our further analysis of key ligand-receptor pairs that interact with XPO1+Epithelial (Figures 7D, E) revealed that fibroblasts regulate XPO1+Epithelial mainly through ligand-receptor pairs such as CD99-CD99 and FN1-(ITGAV+ITGB1) (Figure 7D). Conversely, XPO1+Epithelial promotes monocyte/macrophage recruitment by regulating monocytes through MIF-(CD74+CXCR4) and MIF-(CD74+CD44), as well as C3-(ITGAX+ITGB2). Furthermore, the iso-ligand receptors MIF-(CD74+CXCR4) and MIF-(CD74+CD44) regulate T/NK cells (Figure 7E), potentially facilitating tumor cell evasion of immune surveillance

10.3389/fimmu.2024.1517312

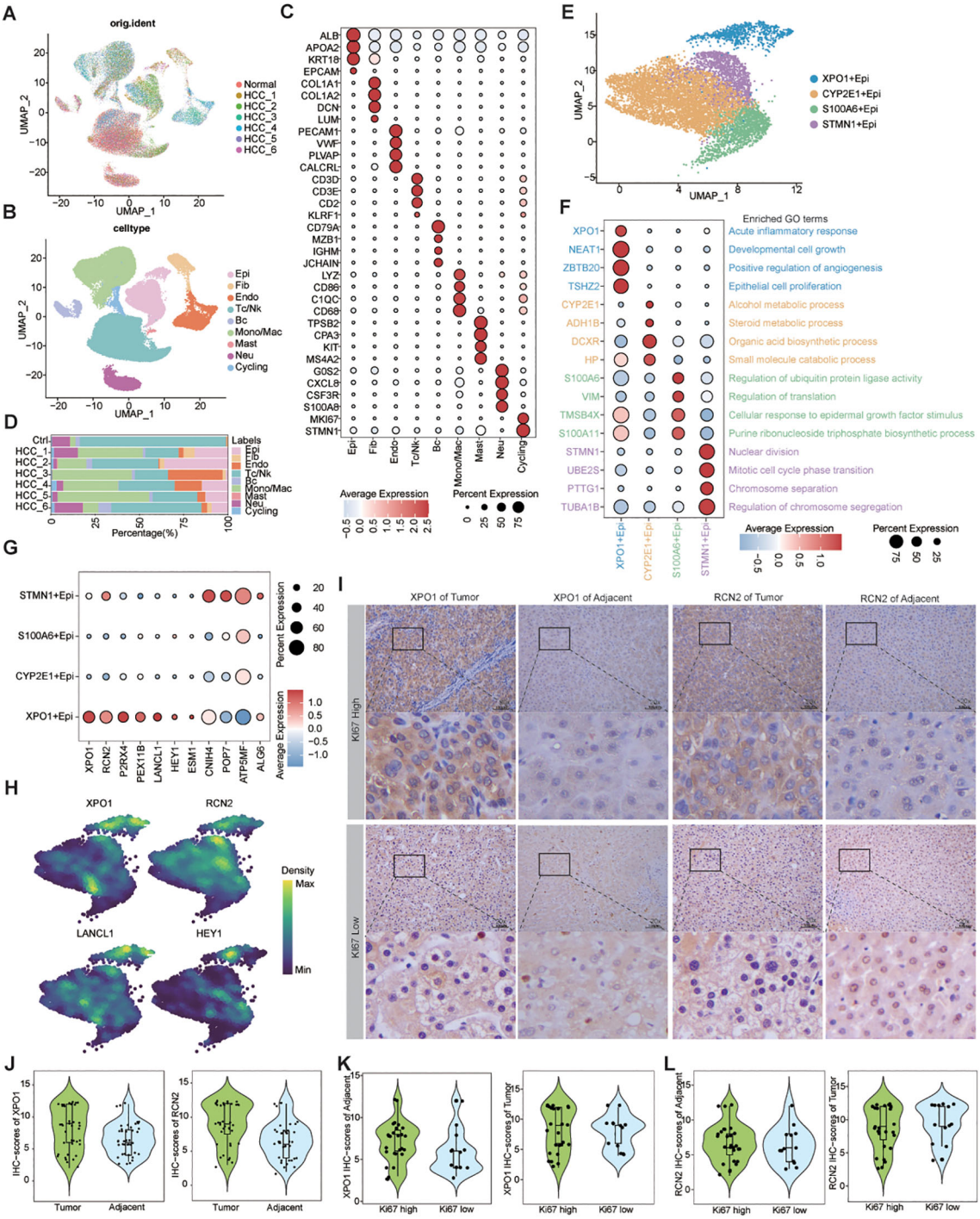

FIGURE 5
Single-cell resolution exploration of the expression profiles of genes characterizing TP-TME risk subtypes in HCC. **(A)** UMAP plot illustrating the distribution of cells across different samples, with distinct colors representing each sample; **(B)** UMAP plot depicting the transcriptomic landscape of 62,163 high-quality cells across nine cell types, with different colors indicating the various cell types: Epi (epithelial cell), Fib (fibroblast cell), Endo (endothelial cell), Tc/NK (T cell/natural killer cell), Bc (B cell), Mono/Mac (monocyte/macrophage cell), Mast (mast cell), Neu (neutrophil cell), and Cycling (cycling cell). **(C)** Bubble plots displaying the percentage expression of classical marker genes across the nine cell types, alongside average expression levels. **(D)** Bar graph illustrating the distribution of the nine cell types across different tissues, color-coded by cell type. **(E)** UMAP plot showing the cluster of epithelial cells divided into four distinct cell clusters. **(F)** Bubble plots highlighting the percentage and average expression levels of genes with high expression specific to different epithelial cell clusters, as well as GO-BP functional enrichment. **(G)** Bubble plots presenting the expression percentages and average expression levels of genes characterizing the TP risk subtype across different epithelial cell clusters. **(H)** Density map illustrating the distribution of TP-related genes within epithelial cell clusters. **(I)** IHC staining of XPO1 and RCN2 in clinical samples from HCC adjacent and tumor tissues. **(J)** Violin plot demonstrating the statistical analysis of IHC scores for XPO1 and RCN2 genes. **(K, L)** Violin plots displaying IHC scoring statistics for XPO1 **(K)** and RCN2 **(L)** under varying levels of Ki67 expression.

10.3389/fimmu.2024.1517312

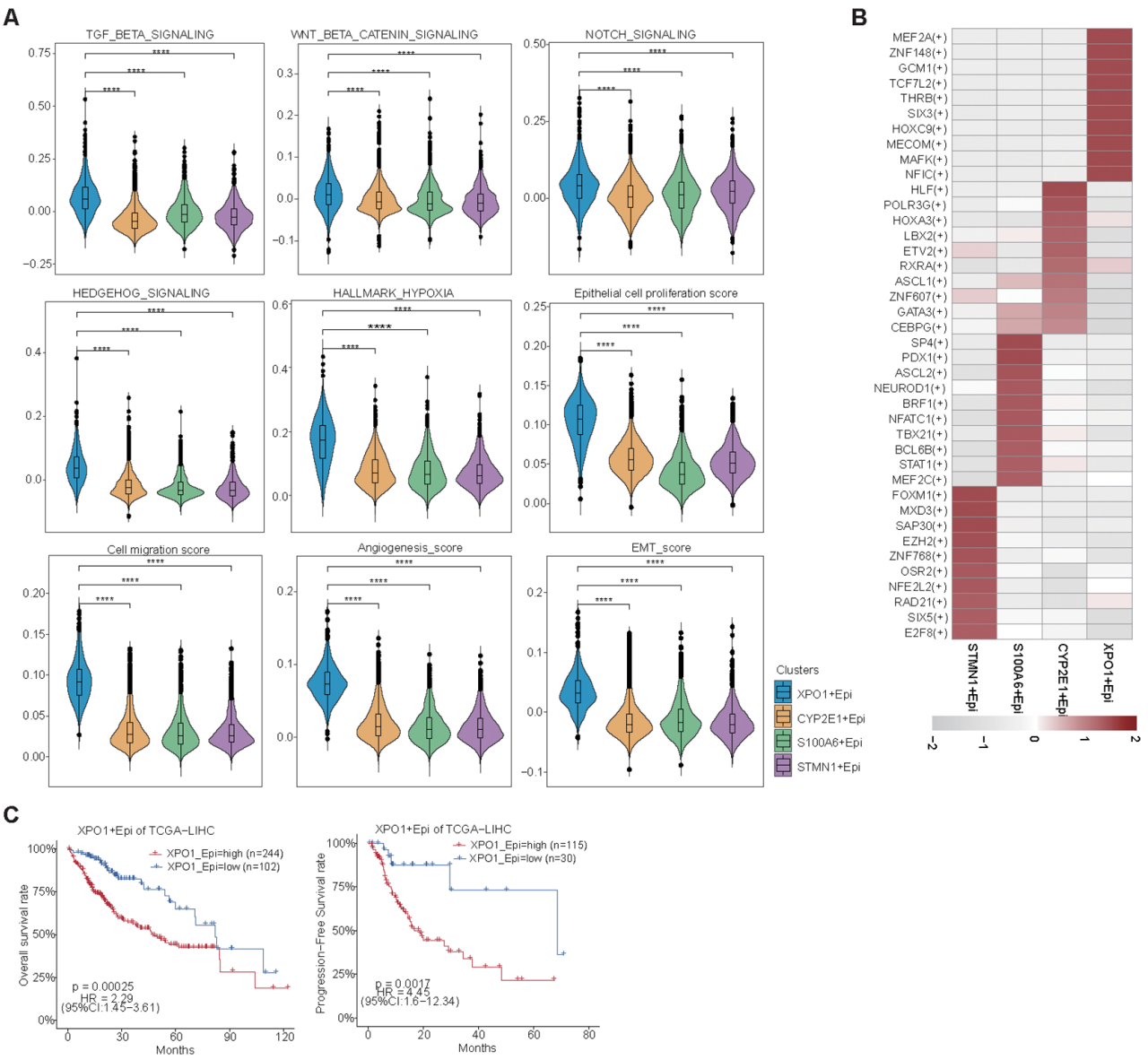

FIGURE 6
Biological function scoring and survival analysis of epithelial cells. **(A)** Violin plots illustrating various epithelial cell clusters in relation to TGF-beta signaling, Wnt beta/catenin signaling, Notch signaling, Hedgehog signaling, hypoxia, epithelial cell proliferation, cell migration, angiogenesis, and EMT scores. The Wilcoxon test was employed to evaluate the differences between groups. Statistical significance is indicated by '****', corresponding to $P < 0.0001$, respectively. **(B)** Heatmap displaying the top 10 transcription factors with the highest activity across different epithelial cell clusters. **(C)** A line graph depicting the overall survival and progression-free survival of XPO1+ epithelial cells.

(47, 48). Additionally, XPO1+Epithelial regulates endothelial cells via VEGFA-VEGFR1R2 and VEGFA-VEGFR1, which may be associated with promoting tumor vascular production (49, 50).

To confirm the results observed in the cell-cell communication analyses, we validated our findings via the TCGA-LIHC cohort at the bulk RNA-seq level. These data corroborated the positive correlation between the expression levels of specific receptors in the target cells (Figure 7F; Supplementary Figure S4A). Further evidence was provided by spatial transcriptome analysis (Figure 7G; Supplementary Figure S4B), which consistently demonstrated that fibroblasts co-localized with XPO1+Epithelial in specific physical locations. Additionally, the scores for both cell types were positively correlated, and fibroblasts regulated the co-localization of the primary ligand receptor for XPO1+Epithelial cells. Similarly, we observed physical positional co-localization between XPO1 +Epithelial and monocytes/macrophages, T/NK cells, endothelial cells, and their corresponding ligands and receptors, suggesting communication exchanges among these cell types. Thus, we validated the interaction network between XPO1+Epithelial cells and the TME via multi-omics.

In summary, our findings indicate that XPO1+Epithelial cells are key components in the remodeling of the TME, and are regulated primarily by ligand signaling from fibroblasts. This interaction may

10.3389/fimmu.2024.1517312

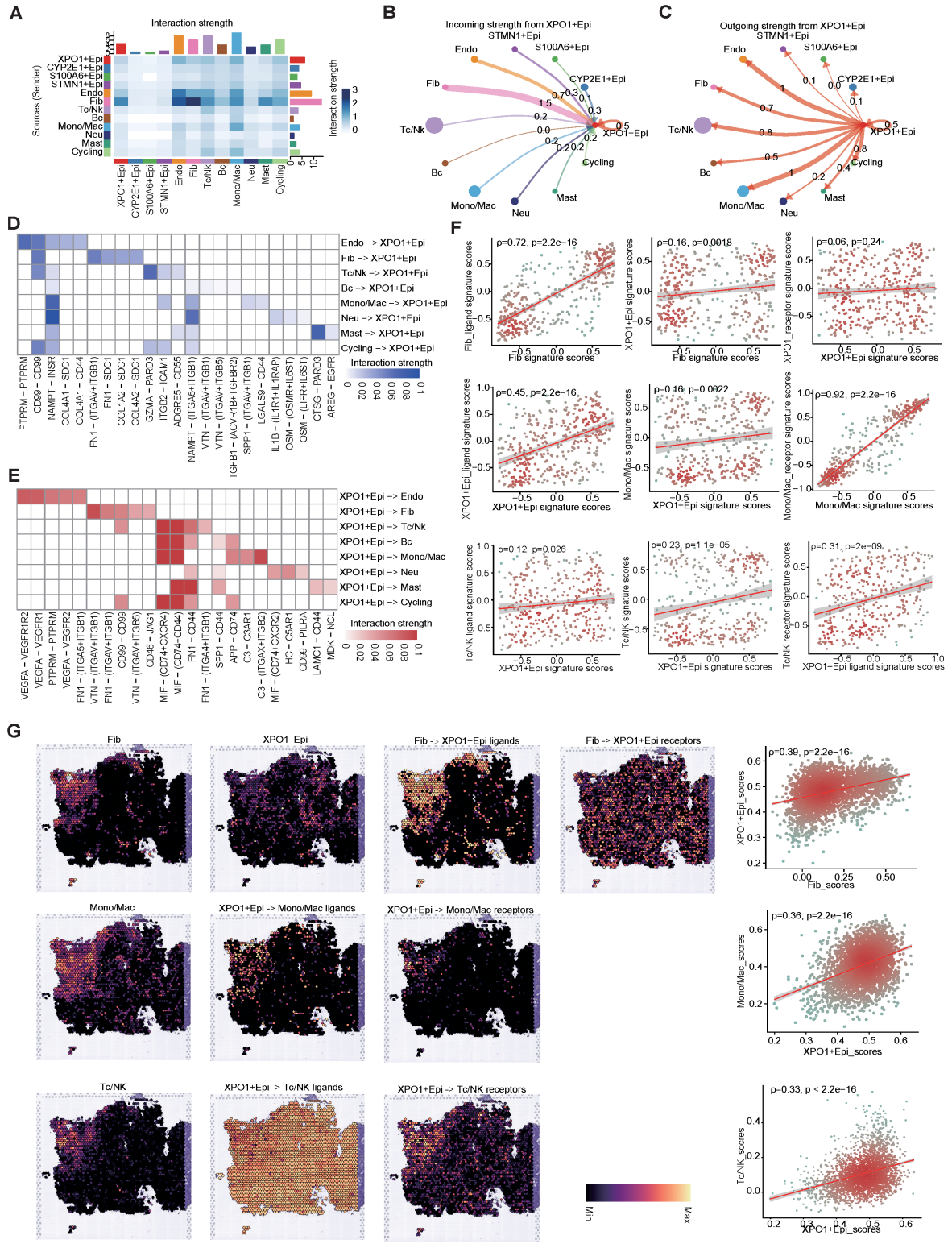

FIGURE 7
Cell-cell interaction network of HCC epithelial cells. **(A)** Heatmap illustrating the interaction intensities among various cell types in HCC. **(B, C)** Circular plot depicting the interaction intensities of incoming **(B)** and outgoing **(C)** interactions involving XPO1+Epithelial. **(D, E)** Heatmaps demonstrating the enhancement of ligand-receptor interaction intensities between XPO1+Epithelial and other cell types, with **(D)** focusing on incoming interactions and **(E)** on outgoing interactions. **(F)** A scatter plot revealing the correlation between XPO1+Epithelial and fibroblasts, monocytes/macrophages, and T/NK cells, along with their associated ligand receptors within the TCGA-LIHC cohort (n=374). **(G)** ST-seq was used to assess the spatial distribution and correlation between XPO1+Epithelial, fibroblasts, monocytes/macrophages, T/NK cells, and their interacting ligand receptors in HCC.

modulate endothelial cells, monocyte macrophages, and T-cells through seeded ligand receptors, potentially influencing immune cell recruitment, immunosuppression, and pro-angiogenesis.

3.6 Analysis and mechanistic exploration of the correlation between TP-TME risk subtypes and drug efficacy

In light of the analyses conducted at both the scRNA-seq and ST-seq levels, we determined that XPO1+Epithelial in HCC significant interacts with endothelial cells and T cells. This observation led us to speculate that XPO1+Epithelial may serve as a potential target for anti-angiogenic therapies and immunotherapy. To further investigate this hypothesis, we validated our findings via spatial transcriptome samples from the HCC treatment cohort. Compared with the nonresponsive group, the group that responded to the combination of TKIs and PD-1 treatment presented significantly increase signature gene scores (Figures 8A, B) for TP-TME risk subtypes, as well as elevated scores for XPO1 +Epithelial (Figure 8C). Additionally, T-cell and endothelial cell infiltration was notably more pronounced in the combination treatment response group (Figures 8D, E).

Through PATHOME-Drug analysis, we constructed drug-target networks to identify potentially effective drugs for the high-risk subtypes (Supplementary Figure S5A). The identified drugs included recommended agents, such as sorafenib, regorafenib, cabozantinib, and pembrolizumab (Supplementary Table S6). Collectively, these results suggest that TP-TME risk subtypes may be used to predict the efficacy of targeted and immunological therapies, warranting further investigation in follow-up cohort studies.

We conducted a preliminary exploration of the potential mechanisms associated with the genes that characterize the TP-TME risk subtypes and their implications for immunotherapy efficacy. Analysis of the top 30 mutated genes (Figures 8F–H) across the high-, intermediate-, and low-risk subtypes revealed that the genes with the highest mutation percentages in the different risk groups included TP53, TTN, and CTNNB1. Notably, the mutation percentages are greater in the intermediate- and high-risk groups, and these mutations are closely linked to the onset and progression of various tumors. There are currently few known drugs that target these mutated genes. Additionally, we observed that the tumor mutational burden (TMB) was low in HCC patients and did not differ significantly among the three subtypes (Supplementary Figure S5B), indicating that TMB may not serve as a valid biomarker for selecting HCC patients for treatment with immune checkpoint inhibitors (ICIs). Furthermore, our analyses revealed no significant differences in the stemness scores among the three risk subtypes (Supplementary Figure S5C). Although no significant differences were observed in the expression of CD274 (also known as PDL1) among the three risk subtypes, the expression levels of CTLA4 and PDCD1 were significantly increase in the intermediate- and high-risk subtypes than in compared to the low-risk subtype (Figure 8I). Consequently, the response rates of the intermediate- and high-risk subtypes to ICIs treatment may be greater than that those of the low-risk subtype. Furthermore, the three risk subtypes of the TP-TME presented distinct expression levels of the 5 cancer antigens targeted in chimeric antigen receptor-modified T cell (CAR-T) therapy (Figure 8I). Specifically, GPC3 expression was elevated in the intermediate-risk subtype relative to the low-risk subtype, whereas MSLN expression was higher in both the intermediate- and high-risk subtypes than in the low-risk subtype. The highest expression levels of MUC1, EPCAM, and PROM1 were observed in the high-risk subtype. Therefore, the three TP-TME risk subtypes may exhibit varying therapeutic responses to the corresponding CAR-T therapies.

4 Discussion

The heterogeneity of HCC is attributed to various etiologies, such as vial or parasitic infections, chemical carcinogens, cigarette smoking, excess alcohol intake, and dietary factors (51, 77). One of the essential efforts for improving the poor outcome of HCC is to provide a subtyping system that is capable of accurately defining tumor risk subtypes, each displaying unique molecular characteristics linked to potentially druggable driver genes, in order to provide personalized treatment choices on basis of the subtyping system. Although many efforts, which have focused mainly on malignant cells, have focused on intertumor heterogeneity and proposed various single- or multi-omics-based molecular typing systems (52, 53), their effectiveness for providing precision treatment remains limited. Given that the crucial role of the TME in cancers has been confirmed (54), TME-related molecules should contribute to the subtyping of HCC. Another challenge of previous molecular typing methods is cost effectiveness, because hundreds of genes or even multiple omics data types are needed.

In the present study, we first identified the genes of related to TP and the TME and subsequently generated a TP-related PRS and a TME-related PRS according to the expression patterns of these types of genes, and further proposed a novel risk subtyping method that could successfully divide patients with HCC into three risk subtypes. Similar to other molecular typing systems (55–58), our subtypes have distinct prognoses and were validated in two independent external datasets.

Unsurprisingly, some of these candidates eleven TP-related PRS genes and seven TME-related genes have been associated with HCC or other types of cancers in previous studies. ESM1 was identified as a biomarker of macrotrabecular-massive HCC (59). HEY1 plays a critical role in the hypoxia-related regulation of mitochondrial activity in HCC (60). The interactions between CTSC and the TNF-α/p38 MAPK signaling pathway are associated with proliferation and metastasis in HCC (61). LANCL1 was reported to protect prostate cancer cells from oxidative stress (62). XPO1 not only regulates tumor proliferation but also enhances sorafenib resistance by promoting EMT (63, 64). It has been identified as a therapeutic target for HCC (65). RCN2 promotes HCC progression by activating the MYC signaling pathway and regulating the EGFR-ERK pathway. In this context, our proteomic analysis revealed that

10.3389/fimmu.2024.1517312

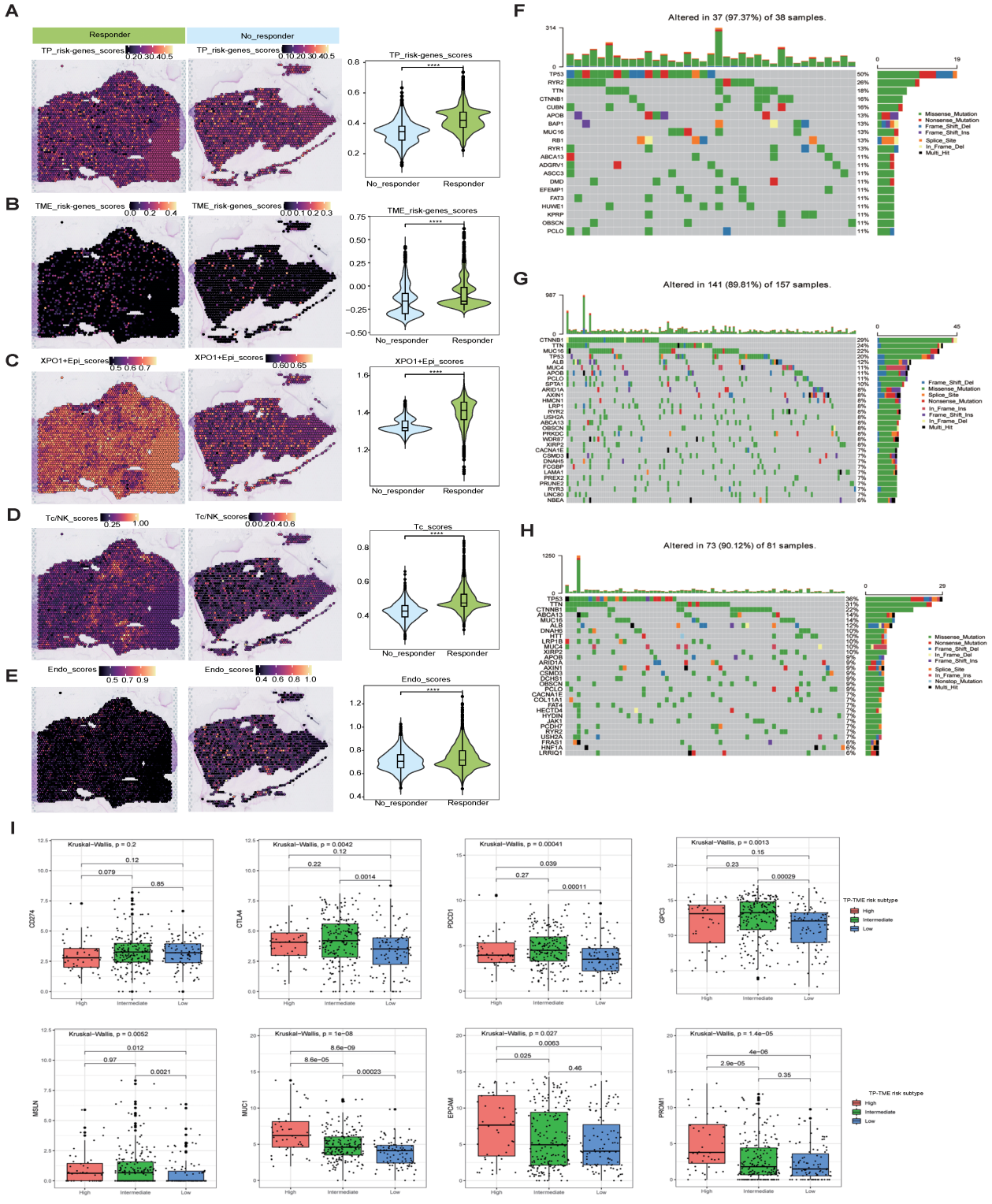

FIGURE 8
Mutation, stemness, and immunotherapeutic efficacy analysis. **(A–E)** Spatial transcriptomics data (GSE238264) reveal genes associated with TP risk profiles **(A)**, genes linked to TME risk profiles **(B)**, the spatial distribution of XPO1+Epi **(C)**, T/NK cells **(D)**, and endothelial cells **(E)**, and their statistical quantification in patients who either responded or did not respond to TKIs in combination with PD1 therapy. The Wilcoxon test was employed to evaluate differences between groups, with significance levels indicated as follows: '****', corresponding to P<0.0001, respectively. **(F–H)** Violin plots illustrating the top 30 mutated genes across three risk subtypes: **(F)** TP-TME high-risk subtype, **(G)** TP-TME intermediate-risk subtype, and **(H)** TP-TME low-risk subtype. **(I)** The expression levels of CD274, CTLA4, PDCD1, GPC3, MSLN, MUC1, EPCAM, and PROM1 are presented across the three TP-TME risk subtypes.

the protein levels of several tumor progression-related PRS genes were elevated in cancer tissues from patients with HCC.

Our research revealed indicates that the genes characterizing the TP risk subtypes, such as XPO1 and RCN2, in HCC have not yet been examined at the single-cell level. In this context, we investigated the critical functions of genes defining TP risk subtypes in HCC at single-cell resolution. We identified a previously unreported malignant cell cluster, XPO1+Epithelial, exhibiting features associated with the TP-TME risk subtype. This cluster involves the upregulation of the TFs MEF2A, TCF7L2, and ZNF148, which significant activate the TGF-beta signaling pathway, and the WNT/beta -catenin signaling pathway, and promote EMT, all of which play a crucial pro-oncogenic roles (45, 46, 66–68). Furthermore, these factors are associated with elevated tumorigenic characteristics such as proliferation and migration. Collectively, these findings suggest that the XPO1 +Epithelial, with TP-TME risk subtype-related features, can serve as a predictor of tumor malignancy.

There is a consensus regarding the significant impact of the TME on various tumor phenotypes. Accordingly, we further analyzed the cell-cell communication between XPO1+ Epithelial and various components of the TME. Our findings indicate that fibroblasts are the predominant cell type regulating XPO1+ Epithelial, primarily through enhanced ligand-receptor interactions, such as those involving FN1-(ITGAV+ITGB1) and CD99-CD99. These interactions, which are consistent with previous reports, correlated with increased up-regulation of tumor EMT through ligand-receptor signaling. Furthermore, XPO1+ Epithelial can modulate monocyte macrophages, T cells, and endothelial cells through multiple ligand-receptor pairs. For example, XPO1+ Epithelial can interact with immune cells via several ligand-receptor pairs, such as MIF-(CD74+CXCR4) and MIF-(CD74 +CD44), which, as previously reported, function as recruiters of immunosuppressive cells and thus promote immunosuppression, enabling tumor cells to evade immune surveillance (47, 48, 69). Additionally, XPO1+ Epithelial can promote angiogenesis via VEGFA-VEGFR1/R2, thereby facilitating tumor growth, which aligns with our previous study (19). We fully validated these findings through multi-omics, utilizing both the TCGA-LIHC cohort and the paired ST-seq cohort.

By analyzing ST-seq data from HCC patients treated with TKIs in combination with PD-1 inhibitors, we observed that the scores of TP, TME-RPS-related genes, and XPO1+Epithelial genes were significantly increase in the responsive group. Furthermore, endothelial cell and T-cell infiltration were significantly increase in the responsive group than in the nonresponsive group. This strongly suggests that the TP-TME high-risk subtype may exhibit greater sensitivity to TKIs combined with PD-1 therapy; however, this finding requires validation through further studies. Additionally, while further research is necessary, we propose potential immunotherapies and drugs for high-risk subtypes, which may aid in clinical decision-making.

Mutations in several key genes play crucial roles in tumorigenesis (70). Consistent with previous studies, both TP53 and CTNNB1 presented high mutation probabilities across different risk groups (71). Research has demonstrated that HCC with CTNNB1 mutations tends to be well differentiated and associated with a better prognosis. In contrast, HCC with TP53 mutations, particularly in the absence of CTNNB1 mutations, is more aggressive and strongly linked to poor outcomes (72). Our findings indicate that a higher mutation probability of TP53, coupled with a lower mutation probability of CTNNB1, is prevalent in high-risk groups, strongly suggesting that HCC classified within the TP-TME high-risk subtype is more aggressive.

Furthermore, we investigated the sensitivity of various TP-TME risk subtypes to immunotherapy. Our comparative analysis of immune checkpoint expression across different TP-TME risk subtypes revealed elevated levels of immune checkpoints such as PDCD1 and CTLA4, in intermediate- and high-risk subtypes. These findings suggest that these risk subtypes may respond more effectively to immune checkpoint inhibitors (73). Additionally, the expression levels of antigens used in CAR-T therapy vary among the different risk subtypes, indicating that the three TP-TME risk subtypes may exhibit distinct responses to CAR-T therapy.

Owing to the low sensitivity of conventional diagnostic techniques and the lack of pronounced early symptoms, HCC is often diagnosed at an advanced stage (2, 78). Despite recent advancements in HCC treatment, many patients still experience treatment resistance and disease progression (74, 79). Our proposed classification method aims to improve prognosis evaluation in HCC and identify patients likely to benefit from TKIs and PD-1 inhibitors. By leveraging a risk score and the proportion of XPO1 +Epithelial expression, clinicians can predict patient responses to TKIs and PD-1 therapy, facilitating the development of personalized immunotherapy regimens designed to improve patient outcomes.

Although our current study introduces a novel molecular classification system and elaborates on the biological and clinical significance of the XPO1+Epithelial, several noteworthy limitations exist. First, the TP-TME risk model was derived from retrospective analyses and needs to be validated and optimized in future prospective trials to ensure its applicability and accuracy in different populations and settings. Second, our sample of included scRNA-seq data was limited; despite the use of ST-seq and bulk RNA-seq for validation, the findings must still be validated in a larger cohort. For future research directions, in addition to validating the risk subtype model, further investigations of subtype-specific responses to immunotherapy are crucial. Future studies could initiate exploratory clinical trials tailored to the characteristics of TP-TME high-risk subtypes, allowing for the assessment of their responses to existing or novel immunotherapies, thereby supporting individualized treatment strategies. Specifically, targeting particular molecular markers that may be present in XPO1+ Epithelial cells could facilitate the further development and optimization of targeted drugs, ultimately enhancing therapeutic efficacy while minimizing toxic side effects.

5 Conclusion

We proposed and validated a novel risk subtype system for HCC that is based on tumor progression in the TP-TME.

Additionally, we identified and validated the biological behavior and clinical significance of XPO1+Epithelial, a novel category among the TP risk subtypes characterized, across multiple cohorts. These findings enhance prognostic risk prediction for HCC patients and provide valuable insights for predicting personalized targeted therapy and immunotherapy.

Data availability statement

The original contributions presented in the study are included in the article/Supplementary Material. Further inquiries can be directed to the corresponding authors.

Ethics statement

The studies involving humans were approved by Guangxi Medical University Cancer Hospital (Ethics Code: KY2020025). The studies were conducted in accordance with the local legislation and institutional requirements. The participants provided their written informed consent to participate in this study.

Author contributions

SL: Data curation, Formal analysis, Investigation, Methodology, Project administration, Software, Writing – original draft, Writing – review & editing. YL: Conceptualization, Funding acquisition, Project administration, Resources, Supervision, Writing – original draft. XG: Data curation, Methodology, Supervision, Writing – original draft. DZ: Methodology, Validation, Writing – original draft. WC: Investigation, Methodology, Project administration, Validation, Writing – original draft. YS: Investigation, Methodology, Writing – original draft. JS: Formal analysis, Methodology, Writing – original draft. CZ: Data curation, Writing – original draft. ZBH: Data curation, Methodology, Writing – original draft. HZ: Investigation, Writing – original draft. SH: Methodology, Project administration, Writing – original draft. MT: Methodology, Writing – original draft. XL: Methodology, Writing – original draft. ML: Funding acquisition, Investigation, Writing – original draft. ZHH: Conceptualization, Funding acquisition, Investigation, Resources, Supervision, Writing – review & editing. RL: Conceptualization, Funding acquisition, Resources, Supervision, Writing – original draft, Writing – review & editing. JY: Conceptualization, Funding acquisition, Resources, Writing – review & editing.

Funding

The author(s) declare financial support was received for the research, authorship, and/or publication of this article. This research was supported by the Guangxi Natural Science Foundation (NO. 2024GXNSFDA010046, 2024GXNSFAA010401, 2024GXNSFBA010071), National Natural Science Foundation of China (NO. 82060427, 82103297), Advanced Innovation Teams and Xinghu Scholars Program of Guangxi Medical University, Guangxi Medical University Outstanding Young Talents Training Program, Guangxi Scholarship Fund of Guangxi Education Department, Nanning Qingxiu District Science and Technology Project (No. 2020037, 2020038, 2021007), Guangxi Medical and health key discipline construction project, Guangxi Medical and health key cultivation discipline construction project, Guangxi Key Laboratory of Basic and Translational Research for Colorectal Cancer.

Conflict of interest

The authors declare that the research was conducted in the absence of any commercial or financial relationships that could be construed as a potential conflict of interest.

Generative AI statement

The author(s) declare that no Generative AI was used in the creation of this manuscript.

Publisher's note

Supplementary material

The Supplementary Material for this article can be found online at: https://www.frontiersin.org/articles/10.3389/fimmu.2024.1517312/full#supplementary-material

SUPPLEMENTARY FIGURE 1
Protein-protein interaction networks of the TP-related genes and TME-related genes. Red represents upregulated, and blue represents downregulated genes in hepatocellular carcinoma. The circular nodes represent TP-related genes, and the diamond nodes represent TME-related genes.

SUPPLEMENTARY FIGURE 2
Validation of TP-TME risk subtypes in multiple cohorts. **(A–E)** Validation of TP-TME risk subtypes in the TCGA-LIHC. **(A)** HCC with high TP-related PRS had shorter overall survival than those with low TP-related PRS. **(B)** HCC with high TME-related PRS had shorter overall survival than those with low TME-related PRS. **(C)** There were significant differences in overall survival among the three subtypes of the TP-TME risk subtypes. **(D)** There were significant differences in progression-free survival among the three subtypes of the TP-TME risk subtypes. **(E)** The TP-TME risk subtype system was proven to be an independent prognostic factor, after adjusting for other clinicopathological characteristics. **(F–I)** Validation of TP-TME risk subtypes in LIRI-JP. **(F)** HCC with high TP-related PRS had shorter overall survival than those with low TP-related PRS. **(G)** HCC with high TME-related PRS had shorter overall survival

than those with low TME-related PRS. **(H)** There were significant differences in overall survival among the three subtypes in the TP-TME risk subtypes. **(I)** The TP-TME risk subtype system was proved to be an independent prognostic factor, after adjusting for other clinicopathological characteristics.

SUPPLEMENTARY FIGURE 3

Illustrates the functional scoring of epithelial cells. **(A)** Hierarchical heatmap displaying large-scale copy number variations (CNVs) in epithelial cells. **(B)** Bubble plots depict the average expression and percentage of expression of the TME risk subtype signature genes across various cell types.

SUPPLEMENTARY FIGURE 4

XPO1+Epi and endothelial cell interactions in the TCGA-LIHC cohort and spatial transcriptome cohort correlations. **(A)** A scatterplot illustrating the correlation between XPO1+Epithelial and endothelial cells, along with their ligand receptors, in the TCGA-LIHC cohort (n=374). **(B)** ST-seq analysis revealing the spatial distribution and correlation between endothelial cells and ligand receptors of XPO1+Epithelial interacting with endothelial cells in HCC.

SUPPLEMENTARY FIGURE 5

Drug-target networks for potentially effective drugs for the TP-TME high-risk subtypes. **(A)** Drug-target networks for potentially effective drugs for the TP-TME high-risk subtypes. Red represents upregulated, and blue represents downregulated in the TP-TME high-risk subtypes. The Wilcox test was used to assess the differences between groups. **(B)** Tumor mutation burden scores of the three TP-TME risk subtypes. **(C)** Stemness scores of the three TP-TME risk subtypes.

References

1. Siegel RL, Giaquinto AN, Jemal A. Cancer statistics, 2024. *CA Cancer J Clin*. (2024) 74:12–49. doi: 10.3322/caac.21820

2. Forner A, Reig M, Bruix J. Hepatocellular carcinoma. *Lancet*. (2018) 391:1301–14. doi: 10.1016/S0140-6736(18)30010-2

3. Caruso S, Calatayud AL, Pilet J, La Bella T, Rekik S, Imbeaud S, et al. Analysis of liver cancer cell lines identifies agents with likely efficacy against hepatocellular carcinoma and markers of response. *Gastroenterology*. (2019) 157:760–76. doi: 10.1053/j.gastro.2019.05.001

4. de Bono JS, Ashworth A. Translating cancer research into targeted therapeutics. *Nature*. (2010) 467:543–9. doi: 10.1038/nature09339

5. Losic B, Craig AJ, Villacorta-Martin C, Martins-Filho SN, Akers N, Chen X, et al. Intratumoral heterogeneity and clonal evolution in liver cancer. *Nat Commun*. (2020) 11:291. doi: 10.1038/s41467-019-14050-z

6. Minagawa M, Ikai I, Matsuyama Y, Yamaoka Y, Makuuchi M. Staging of hepatocellular carcinoma: assessment of the Japanese TNM and AJCC/UICC TNM systems in a cohort of 13,772 patients in Japan. *Ann Surg*. (2007) 245:909–22. doi: 10.1097/01.sla.0000254368.65878.da

7. Nault JC, Martin Y, Caruso S, Hirsch TZ, Bayard Q, Calderaro J, et al. Clinical impact of genomic diversity from early to advanced hepatocellular carcinoma. *Hepatology*. (2020) 71:164–82. doi: 10.1002/hep.30811

8. Joyce JA, Pollard JW. Microenvironmental regulation of metastasis. *Nat Rev Cancer*. (2009) 9:239–52. doi: 10.1038/nrc2618

9. Zhang C, Cheng W, Ren X, Wang Z, Liu X, Li G, et al. Tumor purity as an underlying key factor in glioma. *Clin Cancer Res*. (2017) 23:6279–91. doi: 10.1158/1078-0432.CCR-16-2598

10. Aran D, Sirota M, Butte AJ. Systematic pan-cancer analysis of tumour purity. *Nat Commun*. (2015) 6:8971. doi: 10.1038/ncomms9971

11. Rhee JK, Jung YC, Kim KR, Yoo J, Kim J, Lee YJ, et al. Impact of tumor purity on immune gene expression and clustering analyses across multiple cancer types. *Cancer Immunol Res*. (2018) 6:87–97. doi: 10.1158/2326-6066.CIR-17-0201

12. Hanahan D, Coussens LM. Accessories to the crime: functions of cells recruited to the tumor microenvironment. *Cancer Cell*. (2012) 21:309–22. doi: 10.1016/j.ccr.2012.02.022

13. Pitt JM, Marabelle A, Eggermont A, Soria JC, Kroemer G, Zitvogel L. Targeting the tumor microenvironment: removing obstruction to anticancer immune responses and immunotherapy. *Ann Oncol*. (2016) 27:1482–92. doi: 10.1093/annonc/mdw168

14. Mayakonda A, Lin DC, Assenov Y, Plass C, Koeffler HP. Maftools: efficient and comprehensive analysis of somatic variants in cancer. *Genome Res*. (2018) 28:1747–56. doi: 10.1101/gr.239244.118

15. Miao YR, Zhang Q, Lei Q, Luo M, Xie GY, Wang H, et al. ImmuCellAI: A unique method for comprehensive T-cell subsets abundance prediction and its application in cancer immunotherapy. *Adv Sci (Weinh)*. (2020) 7:1902880. doi: 10.1002/advs.201902880

16. Lu J, Chen Y, Zhang X, Guo J, Xu K, Li L. A novel prognostic model based on single-cell RNA sequencing data for hepatocellular carcinoma. *Cancer Cell Int*. (2022) 22:38. doi: 10.1186/s12935-022-02469-2

17. Gulati GS, D'Silva JP, Liu Y, Wang L, Newman AM. Profiling cell identity and tissue architecture with single-cell and spatial transcriptomics. *Nat Rev Mol Cell Biol*. (2024). doi: 10.1038/s41580-024-00768-2

18. Bressan D, Battistoni G, Hannon GJ. The dawn of spatial omics. *Science*. (2023) 381:eabq4964. doi: 10.1126/science.abq4964

19. Ye J, Gao X, Huang X, Huang S, Zeng D, Luo W, et al. Integrating single-cell and spatial transcriptomics to uncover and elucidate GP73-mediated pro-angiogenic regulatory networks in hepatocellular carcinoma. *Res (Wash D C)*. (2024) 7:0387. doi: 10.34133/research.0387

20. Lian Q, Wang S, Zhang G, Wang D, Luo G, Tang J, et al. HCCDB: A database of hepatocellular carcinoma expression atlas. *Genomics Proteomics Bioinf*. (2018) 16:269–75. doi: 10.1016/j.gpb.2018.07.003

21. Roessler S, Jia HL, Budhu A, Forgues M, Ye QH, Lee JS, et al. A unique metastasis gene signature enables prediction of tumor relapse in early-stage hepatocellular carcinoma patients. *Cancer Res*. (2010) 70:10202–12. doi: 10.1158/0008-5472.CAN-10-2607

22. Gao Q, Zhu H, Dong L, Shi W, Chen R, Song Z, et al. Integrated proteogenomic characterization of HBV-related hepatocellular carcinoma. *Cell*. (2019) 179:561–77.e22. doi: 10.1016/j.cell.2019.10.038

23. Zhang S, Yuan L, Danilova L, Mo G, Zhu Q, Deshpande A, et al. Spatial transcriptomics analysis of neoadjuvant cabozantinib and nivolumab in advanced hepatocellular carcinoma identifies independent mechanisms of resistance and recurrence. *Genome Med*. (2023) 15:72. doi: 10.1186/s13073-023-01218-y

24. Yoshihara K, Shahmoradgoli M, Martínez E, Vegesna R, Kim H, Torres-Garcia W, et al. Inferring tumour purity and stromal and immune cell admixture from expression data. *Nat Commun*. (2013) 4:2612. doi: 10.1038/ncomms3612

25. Aran D, Hu Z, Butte AJ. xCell: digitally portraying the tissue cellular heterogeneity landscape. *Genome Biol*. (2017) 18:220. doi: 10.1186/s13059-017-1349-1

26. Ritchie ME, Phipson B, Wu D, Hu Y, Law CW, Shi W, et al. limma powers differential expression analyses for RNA-sequencing and microarray studies. *Nucleic Acids Res*. (2015) 43:e47. doi: 10.1093/nar/gkv007

27. Mootha VK, Lindgren CM, Eriksson KF, Subramanian A, Sihag S, Lehar J, et al. PGC-1alpha-responsive genes involved in oxidative phosphorylation are coordinately downregulated in human diabetes. *Nat Genet*. (2003) 34:267–73. doi: 10.1038/ng1180

28. Subramanian A, Tamayo P, Mootha VK, Mukherjee S, Ebert BL, Gillette MA, et al. Gene set enrichment analysis: a knowledge-based approach for interpreting genome-wide expression profiles. *Proc Natl Acad Sci U S A*. (2005) 102:15545–50. doi: 10.1073/pnas.0506580102

29. Liberzon A, Subramanian A, Pinchback R, Thorvaldsdóttir H, Tamayo P, Mesirov JP. Molecular signatures database (MSigDB) 3.0. *Bioinformatics*. (2011) 27:1739–40. doi: 10.1093/bioinformatics/btr260

30. Wu T, Hu E, Xu S, Chen M, Guo P, Dai Z, et al. clusterProfiler 4.0: A universal enrichment tool for interpreting omics data. *Innovation (Camb)*. (2021) 2:100141. doi: 10.1016/j.xinn.2021.100141

31. Szklarczyk D, Gable AL, Lyon D, Junge A, Wyder S, Huerta-Cepas J, et al. STRING v11: protein-protein association networks with increased coverage, supporting functional discovery in genome-wide experimental datasets. *Nucleic Acids Res*. (2019) 47:D607–d13. doi: 10.1093/nar/gky1131

32. Shannon P, Markiel A, Ozier O, Baliga NS, Wang JT, Ramage D, et al. Cytoscape: a software environment for integrated models of biomolecular interaction networks. *Genome Res*. (2003) 13:2498–504. doi: 10.1101/gr.1239303

33. Friedman J, Hastie T, Tibshirani R. Regularization paths for generalized linear models via coordinate descent. *J Stat Softw*. (2010) 33:1–22. doi: 10.18637/jss.v033.i01

34. Hao Y, Hao S, Andersen-Nissen E, Mauck WM 3rd, Zheng S, Butler A, et al. Integrated analysis of multimodal single-cell data. *Cell*. (2021) 184:3573–87.e29. doi: 10.1016/j.cell.2021.04.048

35. McGinnis CS, Murrow LM, Gartner ZJ. DoubletFinder: doublet detection in single-cell RNA sequencing data using artificial nearest neighbors. *Cell Syst*. (2019) 8:329–37.e4. doi: 10.1016/j.cels.2019.03.003

36. Korsunsky I, Millard N, Fan J, Slowikowski K, Zhang F, Wei K, et al. Fast, sensitive and accurate integration of single-cell data with Harmony. *Nat Methods*. (2019) 16:1289–96. doi: 10.1038/s41592-019-0619-0

37. Van de Sande B, Flerin C, Davie K, De Waegeneer M, Hulselmans G, Aibar S, et al. A scalable SCENIC workflow for single-cell gene regulatory network analysis. *Nat Protoc*. (2020) 15:2247–76. doi: 10.1038/s41596-020-0336-2

38. Jin S, Guerrero-Juarez CF, Zhang L, Chang I, Ramos R, Kuan CH, et al. Inference and analysis of cell-cell communication using CellChat. *Nat Commun*. (2021) 12:1088. doi: 10.1038/s41467-021-21246-9

39. Hänzelmann S, Castelo R, Guinney J. GSVA: gene set variation analysis for microarray and RNA-seq data. *BMC Bioinf*. (2013) 14:7. doi: 10.1186/1471-2105-14-7

40. Colaprico A, Silva TC, Olsen C, Garofano L, Cava C, Garolini D, et al. TCGAbiolinks: an R/Bioconductor package for integrative analysis of TCGA data. *Nucleic Acids Res*. (2016) 44:e71. doi: 10.1093/nar/gkv1507

41. Thorsson V, Gibbs DL, Brown SD, Wolf D, Bortone DS, Ou Yang TH, et al. The immune landscape of cancer. *Immunity*. (2018) 48:812–30.e14. doi: 10.1016/j.immuni.2018.03.023

42. Malta TM, Sokolov A, Gentles AJ, Burzykowski T, Poisson L, Weinstein JN, et al. Machine learning identifies stemness features associated with oncogenic dedifferentiation. *Cell*. (2018) 173:338–54.e15. doi: 10.1016/j.cell.2018.03.034

43. Ma S, Li X, Wang X, Cheng L, Li Z, Zhang C, et al. Current progress in CAR-T cell therapy for solid tumors. *Int J Biol Sci*. (2019) 15:2548–60. doi: 10.7150/ijbs.34213

44. Blanche P, Dartigues JF, Jacqmin-Gadda H. Estimating and comparing time-dependent areas under receiver operating characteristic curves for censored event times with competing risks. *Stat Med*. (2013) 32:5381–97. doi: 10.1002/sim.v32.30

45. Xiao Q, Gan Y, Li Y, Fan L, Liu J, Lu P, et al. MEF2A transcriptionally upregulates the expression of ZEB2 and CTNNB1 in colorectal cancer to promote tumor progression. *Oncogene*. (2021) 40:3364–77. doi: 10.1038/s41388-021-01774-w

46. Ravindranath AJ, Cadigan KM. The role of the C-clamp in wnt-related colorectal cancers. *Cancers (Basel)*. (2016) 8(8):74. doi: 10.3390/cancers8080074

47. Schwartz V, Lue H, Kraemer S, Korbiel J, Krohn R, Ohl K, et al. A functional heteromeric MIF receptor formed by CD74 and CXCR4. *FEBS Lett*. (2009) 583:2749–57. doi: 10.1016/j.febslet.2009.07.058

48. Borghese F, Clanchy FI. CD74: an emerging opportunity as a therapeutic target in cancer and autoimmune disease. *Expert Opin Ther Targets*. (2011) 15:237–51. doi: 10.1517/14728222.2011.550879

49. Shibuya M. Vascular endothelial growth factor receptor-1 (VEGFR-1/Flt-1): a dual regulator for angiogenesis. *Angiogenesis*. (2006) 9:225–30; discussion 31. doi: 10.1007/s10456-006-9055-8

50. Mabeta P, Steenkamp V. The VEGF/VEGFR axis revisited: implications for cancer therapy. *Int J Mol Sci*. (2022) 23(24):15585. doi: 10.3390/ijms232415585

51. Schulze K, Nault JC, Villanueva A. Genetic profiling of hepatocellular carcinoma using next-generation sequencing. *J Hepatol*. (2016) 65:1031–42. doi: 10.1016/j.jhep.2016.05.035

52. Wu Y, Liu Z, Xu X. Molecular subtyping of hepatocellular carcinoma: A step toward precision medicine. *Cancer Commun (Lond)*. (2020) 40:681–93. doi: 10.1002/cac2.v40.12

53. Lu LC, Hsu CH, Hsu C, Cheng AL. Tumor heterogeneity in hepatocellular carcinoma: facing the challenges. *Liver Cancer*. (2016) 5:128–38. doi: 10.1159/000367754

54. Hinshaw DC, Shevde LA. The tumor microenvironment innately modulates cancer progression. *Cancer Res*. (2019) 79:4557–66. doi: 10.1158/0008-5472.CAN-18-3962

55. Cancer Genome Atlas Research Network, Ley TJ, Miller C, Ding L, Raphael BJ, Mungall AJ, et al. Comprehensive and integrative genomic characterization of hepatocellular carcinoma. *Cell*. (2017) 169:1327–41.e23. doi: 10.1016/j.cell.2017.05.046

56. Fujimoto A, Furuta M, Totoki Y, Tsunoda T, Kato M, Shiraishi Y, et al. Whole-genome mutational landscape and characterization of noncoding and structural mutations in liver cancer. *Nat Genet*. (2016) 48:500–9. doi: 10.1038/ng.3547

57. Lee JS, Chu IS, Heo J, Calvisi DF, Sun Z, Roskams T, et al. Classification and prediction of survival in hepatocellular carcinoma by gene expression profiling. *Hepatology*. (2004) 40:667–76. doi: 10.1002/hep.20375

58. Jiang Y, Sun A, Zhao Y, Ying W, Sun H, Yang X, et al. Proteomics identifies new therapeutic targets of early-stage hepatocellular carcinoma. *Nature*. (2019) 567:257–61. doi: 10.1038/s41586-019-0987-8

59. Calderaro J, Meunier L, Nguyen CT, Boubaya M, Caruso S, Luciani A, et al. ESM1 as a marker of macrotrabecular-massive hepatocellular carcinoma. *Clin Cancer Res*. (2019) 25:5859–65. doi: 10.1158/1078-0432.CCR-19-0859

60. Kung-Chun Chiu D, Pui-Wah Tse A, Law CT, Ming-Jing Xu I, Lee D, Chen M, et al. Hypoxia regulates the mitochondrial activity of hepatocellular carcinoma cells through HIF/HEY1/PINK1 pathway. *Cell Death Dis*. (2019) 10:934. doi: 10.1038/s41419-019-2155-3

61. Zhang GP, Yue X, Li SQ. Cathepsin C interacts with TNF-α/p38 MAPK signaling pathway to promote proliferation and metastasis in hepatocellular carcinoma. *Cancer Res Treat*. (2020) 52:10–23. doi: 10.4143/crt.2019.145

62. Wang J, Xiao Q, Chen X, Tong S, Sun J, Lv R, et al. LanCL1 protects prostate cancer cells from oxidative stress via suppression of JNK pathway. *Cell Death Dis*. (2018) 9:197. doi: 10.1038/s41419-017-0207-0

63. Zheng Y, Gery S, Sun H, Shacham S, Kauffman M, Koeffler HP. KPT-330 inhibitor of XPO1-mediated nuclear export has anti-proliferative activity in hepatocellular carcinoma. *Cancer Chemother Pharmacol*. (2014) 74:487–95. doi: 10.1007/s00280-014-2495-8

64. Wang Z, Pan B, Yao Y, Qiu J, Zhang X, Wu X, et al. XPO1 intensifies sorafenib resistance by stabilizing acetylation of NPM1 and enhancing epithelial-mesenchymal transition in hepatocellular carcinoma. *BioMed Pharmacother*. (2023) 160:114402. doi: 10.1016/j.biopha.2023.114402

65. Azizian NG, Li Y. XPO1-dependent nuclear export as a target for cancer therapy. *J Hematol Oncol*. (2020) 13:61. doi: 10.1186/s13045-020-00903-4

66. Zhang CZ, Chen GG, Lai PB. Transcription factor ZBP-89 in cancer growth and apoptosis. *Biochim Biophys Acta*. (2010) 1806:36–41. doi: 10.1016/j.bbcan.2010.03.002

67. Wang N, Li MY, Liu Y, Yu J, Ren J, Zheng Z, et al. ZBP-89 negatively regulates self-renewal of liver cancer stem cells via suppression of Notch1 signaling pathway. *Cancer Lett*. (2020) 472:70–80. doi: 10.1016/j.canlet.2019.12.026

68. He S, Tang S. WNT/β-catenin signaling in the development of liver cancers. *BioMed Pharmacother*. (2020) 132:110851. doi: 10.1016/j.biopha.2020.110851

69. Gore Y, Starlets D, Maharshak N, Becker-Herman S, Kaneyuki U, Leng L, et al. Macrophage migration inhibitory factor induces B cell survival by activation of a CD74-CD44 receptor complex. *J Biol Chem*. (2008) 283:2784–92. doi: 10.1074/jbc.M703265200

70. Hu HF, Ye Z, Qin Y, Xu XW, Yu XJ, Zhuo QF, et al. Mutations in key driver genes of pancreatic cancer: molecularly targeted therapies and other clinical implications. *Acta Pharmacol Sin*. (2021) 42:1725–41. doi: 10.1038/s41401-020-00584-2

71. Zucman-Rossi J, Villanueva A, Nault JC, Llovet JM. Genetic landscape and biomarkers of hepatocellular carcinoma. *Gastroenterology*. (2015) 149:1226–39.e4. doi: 10.1053/j.gastro.2015.05.061

72. Nishida N, Nishimura T, Kaido T, Minaga K, Yamao K, Kamata K, et al. Molecular scoring of hepatocellular carcinoma for predicting metastatic recurrence and requirements of systemic chemotherapy. *Cancers (Basel)*. (2018) 10(10):367. doi: 10.3390/cancers10100367

73. Shi J, Liu J, Tu X, Li B, Tong Z, Wang T, et al. Single-cell immune signature for detecting early-stage HCC and early assessing anti-PD-1 immunotherapy efficacy. *J Immunother Cancer*. (2022) 10(1):e003133. doi: 10.1136/jitc-2021-003133

74. Yang X, Yang C, Zhang S, Geng H, Zhu AX, Bernards R, et al. Precision treatment in advanced hepatocellular carcinoma. *Cancer Cell*. (2024) 42:180–97. doi: 10.1016/j.ccell.2024.01.007

75. Ye J, Lin Y, Liao Z, Gao X, Lu C, Lu L, et al. Single cell-spatial transcriptomics and bulk multi-omics analysis of heterogeneity and ecosystems in hepatocellular carcinoma. *NPJ Precis Oncol*. (2024) 8(1):262. doi: 10.1038/s41698-024-00752-1

76. Ruff SM, Pawlik TM. The role of immune checkpoint inhibitors and/or Yttrium-90 radioembolization in the management of hepatocellular carcinoma: challenges of treatment sequence. *Hepatoma Res*. (2024) 10:33. doi: 10.20517/2394-5079.2024.59

77. Singh A, Anjum B, Naz Q, Raza S, Sinha RA, Ahmad MK, et al. Night shift-induced circadian disruption: links to initiation of non-alcoholic fatty liver disease/non-alcoholic steatohepatitis and risk of hepatic cancer. *Hepatoma Res*. (2024), 2394-5079.2024.88. doi: 10.20517/2394-5079.2024.88

78. Ainiwaer A, Chen Y, Lu Y. Precise staging of advanced HCC promotes higher quality of personalized treatment management: Chinese experts consensus on precision diagnosis and management of advanced hepatocellular carcinoma (2023). *Hepatoma Res*. (2024) 10:4. doi: 10.20517/2394-5079.2023.155

79. Liang R, Zhang J, Liu Z, Liu Z, Li Q, Luo X, et al. Mechanism and Molecular network of RBM8A-mediated regulation of oxaliplatin resistance in hepatocellular carcinoma. *Front Oncol*. (2021) 10:585452. doi: 10.3389/fonc.2020.585452

Glossary

HCC	Hepatocellular carcinoma
scRNA-seq	Single-cell RNA sequencing
ST-seq	Spatial transcriptomics sequencing
TP	Tumor purity
TME	Tumor microenvironment
EMT	Epithelial-mesenchymal transition
TKIs	Tyrosine Kinase Inhibitors
PD-1	Programmed Cell Death Protein 1
IHC	Immunohistochemical
TCGA	The Cancer Genome Atlas Program
DEGs	Differentially expressed genes
HR	Hazard Ratio
AUC	Area under curve
KEGG	The Kyoto Encyclopedia of Genes and Genomes
MSigDB	The Molecular Signatures Database
GO	The Gene Ontology
PPI	Protein-protein interaction
PRS	Polygenic risk score
OS	Overall survival
PFS	Progression free survival
LASSO	The least absolute shrinkage and selection operator
CNV	Chromosome copy number variation
TFs	Transcription factors
MAF	Mutation annotation format
TMB	Tumor mutational burden
tROC	Time-dependent receiver operating characteristic curve
L-R	Ligand-receptor
Epi	Epithelial cell
Fib	Fibrobalst cell
Endo	Endothlial cell
Tc/Nk	T cell/Natural killer cell
Bc	B cell
Mono/Mac	Monocytes/Macrophages cell
Mast	Mast cell
Neu	Neutrophil cell
Cycling	Cycling cell

frontiers | Frontiers in Immunology

TYPE Review
PUBLISHED 20 December 2024
DOI 10.3389/fimmu.2024.1520398

OPEN ACCESS

EDITED BY
Bing Yang,
Tianjin Medical University, China

REVIEWED BY
Chong Yin,
Affiliated Hospital of North Sichuan Medical College, China
Liwei Zheng,
University of Colorado Anschutz Medical Campus, United States

*CORRESPONDENCE
Xiufeng Chu
chuxiufeng831031@gmail.com

†These authors have contributed equally to this work

RECEIVED 31 October 2024
ACCEPTED 02 December 2024
PUBLISHED 20 December 2024

CITATION
Bukhari I, Li M, Li G, Xu J, Zheng P and Chu X (2024) Pinpointing the integration of artificial intelligence in liver cancer immune microenvironment.
Front. Immunol. 15:1520398.
doi: 10.3389/fimmu.2024.1520398

Pinpointing the integration of artificial intelligence in liver cancer immune microenvironment

Ihtisham Bukhari[1,2†], Mengxue Li[2†], Guangyuan Li[1†], Jixuan Xu[3], Pengyuan Zheng[2] and Xiufeng Chu[1,2*]

[1]Department of Oncology, The Fifth Affiliated Hospital of Zhengzhou University, Zhengzhou, China, [2]Marshall B. J. Medical Research Center, Zhengzhou University, Zhengzhou, Henan, China, [3]Department of Gastrointestinal & Thyroid Surgery, The Fifth Affiliated Hospital of Zhengzhou University, Zhengzhou, China

Liver cancer remains one of the most formidable challenges in modern medicine, characterized by its high incidence and mortality rate. Emerging evidence underscores the critical roles of the immune microenvironment in tumor initiation, development, prognosis, and therapeutic responsiveness. However, the composition of the immune microenvironment of liver cancer (LC-IME) and its association with clinicopathological significance remain unelucidated. In this review, we present the recent developments related to the use of artificial intelligence (AI) for studying the immune microenvironment of liver cancer, focusing on the deciphering of complex high-throughput data. Additionally, we discussed the current challenges of data harmonization and algorithm interpretability for studying LC-IME.

KEYWORDS

liver cancer, immune microenvironment, artificial intelligence, machine learning, ScRNA-seq

1 Introduction

Liver cancer poses huge health challenges due to escalating global incidence, notably in transitional regions like East and Southeast Asia. It currently ranks 6th in cancer incidence and 3rd in mortality, surpassed only by lung and colorectal cancers (1). Surgery provides relatively satisfactory outcomes when detected at an early stage, liver transplantation at early-stage liver cancer patients achieved a 5-year survival of about 70-80.0%. Surgical resection or tumor ablation can reach a 5-year survival rate of 50% to 70% (2–5). For patients with locally advanced liver cancer, Trans-arterial Chemoembolization (TACE), either in combination with other treatments or as a standalone therapy, yields a 5-year survival rate of 20% to 40% (4, 6).

Systemic therapy has witnessed significant breakthroughs in targeted therapy and immune therapy in the past two decades, which have not only improved survival in advanced patients but also made some of them suitable for surgical removal. Even so, liver cancer remains one of the worst-prognosed diseases due to late diagnosis, drug resistance, and frequent recurrence and metastasis (7). The chances of survival of the patients with liver cancer at late stage are low due to the lack of effective drugs, meaning that patients typically live for only 6 to 20 months after diagnosis (8). This underscores the urgent need for effective treatments (9).

Liver cancer has several subtypes, including hepatocellular carcinoma (HCC), bile-duct cancer, hepatoblastoma, and various liver sarcomas and carcinomas. Among them, HCC is the most common worldwide, whereas, in some Asian countries, bile-duct cancer is more common than HCC. This regional variation may result from different risk factors, such as hepatitis B virus, hepatitis C virus, fungi, aflatoxin, alcohol, poor diet, and parasitic flatworm (10, 11). It is still unclear that why some people can live with liver disease for many years, whereas others develop fatal cancer. Increasing evidence suggests the alterations of the liver immune microenvironment play a key role during cancer transformation and drug resistance. However, the heterogeneity and intricate molecular dynamics impede a deep understanding of the immune microenvironment of liver cancer.

In this review, we first provide a brief overview of AI and describe its common applications in cancer research. We also illustrated the immunological characteristics of the liver and its pathological alterations during cancer development. Subsequently, we explored the latest applications of AI and current challenges within the context of LC-IME.

2 Applications of AI in cancer research

2.1 AI and machine learning

AI technology involves the development of systems capable of executing tasks typically requiring human intelligence, such as reasoning, learning, and problem-solving. It is designed to replicate cognitive processes like perception, language processing, and decision-making, these systems draw from a diverse range of disciplines, including computer science, mathematics, psychology, and linguistics. AI technology has penetrated all aspects of human activities (12–15). In the cancer research field, AI is characterized by the use of machine learning and deep learning algorithms (16), which are important in processing and analyzing large-scale datasets (17–19).

Machine learning (ML), an integral part of artificial intelligence, encapsulates the autonomous identification of patterns and formulations within vast datasets (20). By discerning and extracting significant features from the data, ML can make accurate predictions and decisions .It fundamentally extracts patterns and rules from the data and apply them to new data. The workflow of ML comprises the acquisition, pre-processing, feature extraction of the data, model training, and evaluation optimization application of the obtained model. During model training, parameters are adjusted to minimize the discrepancy between predicted and actual outcomes, known as 'error' or 'loss,' which is quantified to direct the optimization process towards enhanced accuracy. Based on the model training approaches, there are four different types of ML: supervised (21), unsupervised (22, 23), semi-supervised (24), and reinforcement learning (25) (Figure 1).

Deep learning (DL), a subfield of machine learning, employs artificial neural networks (26) to represent important information from massive amounts of data. DL comprises an input layer, multiple hidden layers, and an output layer, each of which receives the output of the previous layer as input and performs nonlinear transformations that progressively distill raw data into meaningful feature abstractions. There are several popular DL architectures: multilayer perceptron (MLP), convolutional neural networks (CNNs), recurrent neural networks (RNNs), auto-encoders (AEs), generative adversarial networks (GANs) and transformer (Figure 2). These architectures can be used according to the specificity of the data.

2.2 Application of AI in cancer research

Early cancer detection: By facilitating cancer detection at the precancer stage, AI allows for early interventions that significantly prolong the overall survival time of the patients. For example, Klein et al. used a blood-based multi-cancer early detection (MCED) test and applied cell-free DNA sequencing, combined with machine learning, which predicted the origin of cancer signals with high specificity and accuracy in a variety of cancers (27). Similarly, Stark et al. constructed machine learning models using Gail model inputs and personal health data. These models exhibit strong performance in predicting breast cancer risk and can be used as non-invasive tools to increase early detection and prevention of breast cancer (28). Additionally, to develop a machine learning model to predict the risk of lymph node metastasis in renal carcinoma, Feng et al. filtered clinical features through LASSO and univariate and multivariate logistic regression analyses and then used statistically significant risk factors to build the XGB model. It could distinguish about 89% of LNM patients when the threshold probability was set to 54.6%, suggesting a promising application prospect in the clinic (29).

Machine learning and deep learning emerge as potent tools to identify biomarkers from intricate datasets (30). For example, Halner et al. established a random forest-based machine learning

Abbreviations: CSF1/CSF1R, Colony Stimulating Factor 1/Colony Stimulating Factor 1 Receptor; PD-L1, programmed death-ligand 1; TIM-3, T cell immunoglobulin and mucin domain-3; IGF-1, insulin-like growth factor-1; CCL20, C-C motif ligand 20; IFN-γ, interferon-γ; NAD+, nicotinamide adenine dinucleotide; NMN, nicotinamide mononucleotide; ICOS, T-cell co-stimulator; GM-CSF, colony-stimulating factor; PGE2, prostaglandin E2; TOX, thymocyte selection associated high mobility group box; CTLA-4, cytotoxic T-lymphocyte antigen 4; LAG3, lymphocyte activation gene 3.

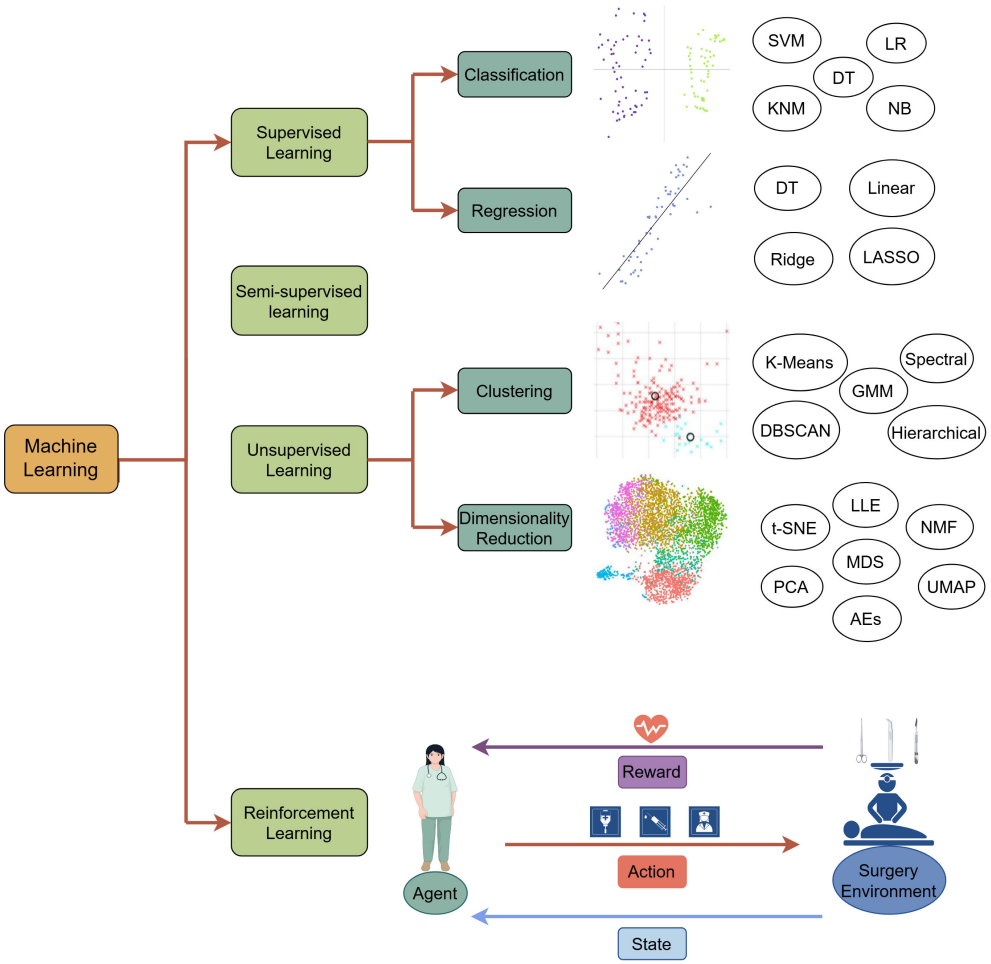

FIGURE 1
The overview of machine learning paradigms. Supervised learning: Trains models on a labeled dataset, where the training dataset consists of input data and corresponding output labels, allowing the model to be able to make accurate predictions on classification and regression tasks. Semi-supervised learning: Trains the model with a small amount of labeled data and applies the model trained to annotate unlabeled data. Unsupervised learning: Discovers hidden patterns, structures, or subgroups in the unlabeled data through clustering and dimensionality reduction. It uses datasets without clear notice of the dependent (response) variable. Unsupervised means that the machine or computer should learn patterns from the data without referring to any specific response. Unsupervised learning aims to explore the data structure and generate a hypothesis rather than to test any hypothesis by statistical methods or to construct prediction or classification models on the basis of a set of conditions and a specified response. Algorithms for unsupervised learning can be subdivided into two categories: (1) clustering algorithms and (2) dimensionality reduction. Reinforcement learning: Identifies a sequence of actions to increase the probability of achieving a predetermined goal. A RL problem is solved through a trial-and-error learning process. A RL agent interacts with an environment to maximize the cumulative reward resulting from its actions. Generally, RL problems are modeled and solved using a Markov Decision Process (MDP), guided by Bellman's equation. There are four components: (1) a state that represents the environment at each time step; (2) an action the agent takes at each time step that influences the next state; (3) a transition probability that provides an estimate for reaching different subsequent states, which reflects the environment in which an agent interacts; and (4) a reward function, which is the observed feedback given a state-action pair. LR, Logistic Regression; DT, Decision Tree; NB, Naïve Bayes; SVM, Support Vector Machine; NN, K-nearest Neighbor; Ridge, Ridge Regression; Linear, Linear Regression; LASSO, Least Absolute Shrinkage and Selection Operator; GMM, Gaussian Mixture Model; DBSCAN, Density-Based Spatial Clustering of Applications with Noise; PCA, Principal Component Analysis; MDS, Multidimensional Scaling; NMF, Non-negative Matrix Factorization; LLE, Locally Linear embedding; t-SNE, t-Distributed Stochastic Neighbor Embedding Algorithm; UMAP, Uniform Manifold Approximation and Projection; AEs, Autoencoders.

pipeline, "Decancer," to analyze liquid biopsies. Decanter enhanced the sensitivity for detecting stage I cancer from 48% to 90% regardless of cancer type. Promisingly, DEcancer's performance using a 14-43 protein panel is comparable to 1,000 original proteins (31). To identify metabolomic biomarkers for the diagnosis and prognosis of gastric cancer, Chen et al. used the LASSO regression algorithm to build a 10-metabolite GC diagnostic model, which is validated in an external test set with a sensitivity of 0.905. This model exhibited superior performance to traditional models that utilized clinical parameters and identified two distinct biomarker panels, enabling early diagnosis and prognosis of cancer (32). Tayob et al. developed the parametric empirical Bayes algorithm and the Bayesian screening algorithm to improve the early detection of cancer, which improved sensitivity to cancer biomarkers (33). Furthermore, Konstantinos et al. tested the miRNA expression profiles of Gastrointestinal stromal tumors (GISTs) and applied machine learning to identify the miRNAs associated with the risk of GIST development. They found that several miRNAs, with hsa-

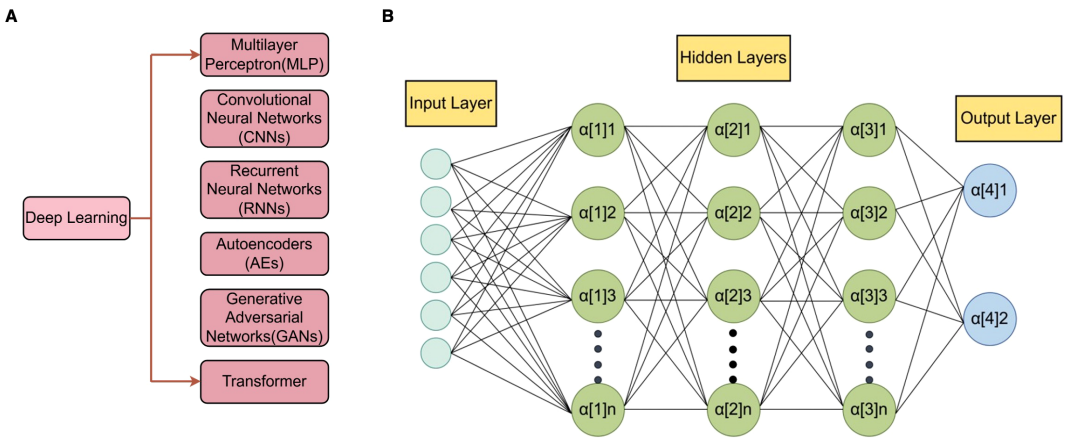

FIGURE 2
The overview of deep learning paradigms. **(A)**, Deep learning is a subfield of machine learning. It employs artificial neural networks for representation learning from massive amounts of data. A deep neural network consists of an input layer, multiple hidden layers, and an output layer, each of which receives the output of the previous layer of neurons as input and performs nonlinear transformation processing, thereby gradually transforming the raw data into meaningful feature representations. **(B)**, The composition of multilayer perceptron (MLP) is shown as an example of deep learning. The input layer receives data, where each neuron corresponds to a feature of the input data. The hidden layers perform computations and transformations on the input data through weighted sums and non-linear activation functions. These processed signals are then conveyed to the output layer, which generates the final output of the network.

miR218-5p as the best, may strongly affect the prognosis of GISTs and can serve as predictors for their development (34). In short, the application of AI and machine learning in oncology clinics has improved diagnostic time and clinical outcomes in various cancers.

Medical imaging: Imaging is at the forefront of clinical care. The integration of AI into image interpretation helps radiologists streamline workflow and improve patient care (35). Within imaging, convolutional neural networks (CNNs) and Deep Learning (DL) are exceptionally useful in computer vision and enable machines to see and interpret visual data (36, 37). Al-Masni et al. developed the ROI-based Convolutional Neural Network "You Only Look Once (YOLO)" to accurately detect and classify the masses in mammograms. It achieves an overall accuracy of 96.33% in detecting the mass location and 85.52% in distinguishing between benign and malignant lesions (38). Zhao et al. built the deep-learning-based, fully automated lymph node detection and segmentation (auto-LNDS) model based on multiparametric magnetic resonance imaging (mpMRI). The auto-LNDS achieved a sensitivity, PPV, and FP/vol of 80.0%, 73.5%, and 8.6 in internal testing and 62.6%, 64.5%, and 8.2 in external testing, respectively, significantly better than the performance of junior radiologists, therefore holding great potential for facilitating N-staging in clinical practice (39). Jin et al. developed a CNN-based algorithm to Improve the accuracy in Optical Diagnosis of Colorectal Polyps. It increased the accuracy of novice endoscopists to 85.6% and significantly reduced the skill-level dependence of endoscopists and costs (40).

Pathological identification: As the gold standard for confirming cancer, pathological identification holds paramount significance in diagnosis, prognosis, and therapeutic strategies. However, the heterogeneity of tumors poses a big challenge to precise diagnosis (41, 42). AI has transformed the landscape of cancer pathology by empowering it with enhanced diagnostic accuracy and streamlined decision-making frameworks, leveraging sophisticated histology image analysis (43). For example, to achieve an AI-based pathological prediction of the origins of unknown cancers. Lu et al. build the Tumor Origin Assessment via Deep Learning (TOAD), a deep-learning-based algorithm that provides a differential diagnosis for the origin of the primary tumor based on routinely acquired histology slides (44). In addition, Lee et al. presented a graph deep neural-network model to analyze the whole-slide images (45). This model considers histopathological features from the tumor microenvironment. in gigapixel-sized WSIs in a semi-supervised manner and was trained to provide interpretable prognostic biomarkers in patients with kidney, breast, lung, and uterine cancers.

Treatment: The outcomes of cancer treatment are affected by several key factors, such as the patient`s health status, cancer subtype, and stage. Additionally, molecular cancer research has recently revealed the contribution of genetic mutations to patients` responses to a specific treatment. The complex interplay of the above factors in the real world poses a significant challenge for oncologists in selecting the appropriate treatment regimen for a specific patient.

In this scenario, AI is inherently a powerful approach to the integration and aggregation of intricate and multi-dimensional datasets and providing comprehensive data support for decision-making (46, 47). For example, Luo et al. proposed a collaborative filtering method with machine learning. It can identify the most suitable compounds for patients without genetic data, making it feasible to predict drug sensitivity and achieve personalized drug selection in a cost-effective way (48). Abajian et al. used Supervised Machine Learning with both Logistic Regression (LR) and Random Forest (RF) algorithms to explore the treatment response to transarterial chemoembolization for hepatocellular carcinoma. Both LR and RF models achieved an overall accuracy of 78% and

identified cirrhosis status and relative tumor signal intensity (>27.0) as the two strongest predictors of treatment response (49). Kong et al. introduced a NetBio-based machine learning, which accurately predicted the treatment responses to Immune checkpoint inhibitors (ICIs) in three different cancer types-melanoma, gastric cancer, and bladder cancer. This model demonstrated superior performance in comparison with conventional ICI treatment biomarkers, such as the expression profiles of ICI targets (50).

Prognosis and management: Understanding the progression and survival time of patients is essential for cancer management. Oncologists used to predict patients' prognoses based on their experience of understanding patients' clinical profiles (age, health status) and tumor characteristics (subtype, stage, and grade). Nevertheless, this strategy is inherently limited and has a low predictive capability due to individual variation. AI has exhibited great promise to deal with these constraints and achieves accurate prognosis prediction for individual patients (51). Qiu et al. developed an XGBoost model to help physicians make clinical decisions. It employed clinicopathological information and predicted the risk of distant metastasis in patients with rectal cancer (52). Based on LASSO regression and Pearson correlation coefficients, Cai et al. identified metastasis-associated genes from different cancer tissues and then used them to build a CNN-based model, "Multi-Dimensional Convolutional Neural Network (MDCNN)." It achieved satisfactory prediction accuracy in bone metastasis, lung metastasis, and liver metastasis (53). The combination of AI and the Internet of Things (IoT) technology enables telemedicine and intelligent monitoring functions, allowing patients to receive scenario-based remote management (54).

Drug Discovery: Drug discovery and development of anti-cancer drugs is the goal of translational medicine. However, this work is quite a costly and time-consuming operation. Additionally, although the advances in muti-omics and clinical trials provide quite meaningful information, their complexity also imposes a huge obstacle. AI and computer-aided drug design, along with modern experimental technical knowledge, has energized data mining for faster drug design and development in the pharmaceutical industry (55). For example, AlphaFold2, a deep neural network algorithm, demonstrates high accuracy in predicting the three-dimensional structures of proteins, particularly when sequences of multiple homologs are available. It helps us understand protein function changes underlying carcinogenesis and improve our approaches to counter them (56). Meanwhile, low-cost cancer drug repurposing can be achieved by deep learning approaches, which aid the modeling of existing drugs for discovering novel drug targets. For example, Zhou et al. designed a prediction approach called an ensemble of multiple drug repositioning approaches (EMUDRA). Using EMUDRA, they predicted and experimentally validated the antibiotic rifabutin as an anti-cancer drug for triple-negative breast cancer (57).

3 Liver immune microenvironment and its alterations in cancer

The liver is not only an important metabolic organ but also possesses significant immune functions, and it contains a vast array of immune cells (Table 1). Several factors contribute to the unique immune functions of the liver. Firstly, the liver is a hematopoietic organ during embryonic development. Secondly, the flow of portal venous blood carries components from the gastrointestinal tract and spleen (58). Thirdly, the liver participates in mucosal immunity through the biliary system. Due to the liver's direct exposure to many antigens from the gastrointestinal tract, it has developed a unique immune tolerance, which is manifested as intrinsic tolerance mechanisms in both innate and adaptive immune responses. Therefore, the liver can protect itself from autoimmune damage caused by the extensive presentation of gastrointestinal antigens (59, 60). However, in the context of liver injury and disease, various liver cells participate in complex pro-inflammatory responses, which may lead to hepatocyte death and further disease progression (61).

TABLE 1 Properties of immune cells in the liver.

Cell type	Markers	Functions in liver
Macrophages	F4/80, CD68 (Kupffer) CD86 (M1) CD68, CD163 (M2)	Engulf pathogens and dead cells, participate in antigen presentation, and produce various cytokines to regulate immune responses.
NK Cells	CD56, CD16	Identify and kill cells infected with viruses and tumor cells.
Dendritic Cells	CD1a, CD11c	Maintain immune tolerance and regulate liver-specific immune responses
cDCs	XCR1, CLEC9A (cDC1) CD11b, CD172a (cDC2)	Process antigens and present them to T cells, triggering an immune response against pathogens or tumor cells (cDC1). Induce regulatory T cell responses, promote coordination between humoral and cellular immunity. Regulate immune responses to pathogens in the liver and stimulate B cells to produce antibodies (cDC2).
pDCs	B220, PDCA-1 (mouse) BDCA-2, BDCA-4 (human)	When viruses invade, pDCs rapidly activate and secrete cytokines such as interferon, activating other immune cells and initiating an antiviral immune response.
Neutrophils	CD66b, Ly6G	The first line of defense in acute inflammation, phagocytosis and killing of invading microorganisms.
T Cells	CD3, CD4, CD8	Directly kill target cells or secrete cytokines to clear viral infections, monitor tumor development, and participate in liver transplant rejection responses.
$CD4^+$ T	IFN-γ (Th1) IL-4, IL-5, IL-13 (Th2) IL-17 (Th17) CD4	Assist in immune response (activate other immune cells, promote antibody production), immune regulation (maintain immune balance, inhibit inflammatory response), and participate in liver repair (promote liver cell regeneration, regulate fibrosis).

(Continued)

TABLE 1 Continued

Cell type	Markers	Functions in liver
$CD8^+$ T	CD8	Have cytotoxic function, participates in adaptive immune responses, and can recognize and eliminate cells that are infected with viruses or have mutations.
NKT	CD161, NK1.1	Secrete cytokines to regulate immune responses, with anti-tumor and immune surveillance functions.
Tregs	CD4, CD25, FoxP3	Maintain liver immune tolerance.
B Cells	CD19, CD20	Produce specific antibodies, participate in antigen presentation, and regulate the activity of other immune cells.

Innate immune system: In the liver, the innate immune system forms the first line of defense against pathogens, present at birth and lasts throughout life. Immunity against various pathogens or malignant cells is provided by different types of immune cells (62). These cells include neutrophils, natural killer cells, Kupffer cells, monocytes, dendritic cells, and natural killer T cells (NKT) (63). Neutrophils, the most abundant group of circulating white blood cells, constitute the first line of defense in acute inflammation by phagocytosing and killing invading microorganisms (64). Natural killer cells Identify and kill cells infected with viruses and tumor cells (65). They don't require secondary activation for their cytolytic activity. Instead, they induce apoptosis in tumor cells by activating FasL or TRAIL (66, 67). In case of their inactivation or restricted infiltration to the liver, tumor cells grow rapidly (68, 69). Kupffer cells are resident macrophages in the liver and constantly in contact with antigens from the gastrointestinal tract (70–72). Bleriot et al. identified two distinct populations of Kupffer cells, which share core molecular characteristics but express different genes and proteins (73). Additionally, the liver also recruits a large number of monocytes from peripheral blood and converts them into macrophages in the liver microenvironment (monocyte-derived macrophages). Different subtypes of macrophages can be distinguished with the specific expression of cell markers, such as CD11b, CCR2, and F4/80 (74–76). M1 macrophages mainly express CD16 and CD32, etc., and also produce TNFα, nitric oxide (NO), and reactive oxygen intermediates (ROI) to play antitumor roles, while M2 macrophages express several surface molecules such as CD163, Dectin-1, etc., and release interleukins (IL-4 and IL-13) and glucocorticoids, mainly perform the immunosuppressive pro-tumor activity (77, 78). Dendritic cells, also known as antigen-presenting cells, identify affected cells or pathogens and present them to other immune cells, thus maintaining immune tolerance and regulating liver-specific immune responses (79). NKT cells are unconventional T cells that are activated by glycolipid antigens (80, 81). They have both NK cell surface markers and antigen receptor characteristics of T cells and serve as a bridge between innate and adaptive immunity (82). The NKT cells that are located in hepatic sinusoids provide intravascular immune surveillance (83) where they may mediate proinflammatory effects through type I NKT cell subsets or exhibit immunosuppressive functions via type II NKT cells (84). In short, these immune cells coordinate with each other to accomplish the innate immune response in three steps: early inflammation, amplification of the inflammatory signal, and resolution.

Adaptive immune system: Several subtypes of T cells abundantly exist in healthy liver, including $CD4^+$ helper T (Th) cells, $CD8^+$ cytotoxic T cells, and regulatory T cells (Tregs) (85). $CD4^+$ T cells are crucial for preventing tumorigenesis by facilitating the elimination of malignant cells (86–88). They typically act as initiators of antitumor responses and correlate with favorable responses to immunotherapy. $CD8^+$ cytotoxic T cells serve as the primary effector cells of the cellular immune system, which recognize presented antigens and kill infected or malignant cells (89). Additionally, a population of CD8+ tissue-resident memory (TRM) cells exist in the liver, functioning as local immune sentinels (90, 91). Tregs are a subset of $CD4^+$ T cells with immunosuppressive properties. These cells are crucial for maintaining homeostasis and immune tolerance (92, 93). Accumulation of Tregs has been implicated in facilitating immune evasion and hepatocarcinogenesis (92, 93).

B cells are a group of specialized cells that produce specific antibodies, participate in antigen presentation, and regulate the activities of other immune cells (94).

The development of liver cancer is highly related to infection and inflammation, which foster the unique Immunosuppressive microenvironment of liver cancer. It is characterized by blunted anti-tumor immunity, an enrichment of tumor-promoting immunosuppressive cell types, and impaired innate and adaptive immunity (95–99). Recently, immune checkpoint inhibitors (ICIs) have demonstrated promising clinical benefits in HCC, thus emphasizing the importance of immunotherapy (100). Apart from ICIs, immunotherapy also encompasses adoptive cell therapy, oncolytic virotherapy, and cancer vaccine therapy. These approaches can improve T-cell function and enhance cellular immunity, thereby leading to the elimination of LC-IME and the inhibition of tumor growth. To guide the application of immunotherapy, more efforts are needed to gain a deeper understanding of LC-IME.

4 The integration of AI and the immune microenvironment of liver cancer

In liver cancer, the intricate heterogeneity, consisting of diverse immune and stromal cells, significantly contributes to metastasis, relapse, and drug resistance (101–103). The exploration of the tumor immune microenvironment and complex cellular interactions can provide crucial insights for developing more effective, tailored immune-oncology therapies. However, the sheer volume and complexity of data from single-cell RNA sequencing (scRNA-seq) and multi-omics pose challenges for direct clinical application. In addressing these challenges, artificial intelligence (AI) is increasingly recognized as a potent tool that enhances our understanding of these large-scale datasets.

4.1 The integration of AI and omics data

scRNA-seq analysis: scRNA-seq allows researchers to conduct in-depth analysis of molecular characteristics, such as gene expression and epigenetic modifications within individual cells, generating vast amounts of genetic information data (104). The analysis of these data is crucial for revealing cellular heterogeneity and functional characteristics (105). With the intervention of AI, rapid processing and interpretation of massive scRNA-seq data can be achieved with enhanced data accuracy. AI algorithms can automatically identify and filter out noise, retaining the true biological differences between cells and thereby improving data reliability (106). Additionally, batch effects, a common issue in scRNA-seq analysis, can be caused by various factors such as experimental samples, platforms, and library construction methods. AI technologies can effectively eliminate these batch effects while preserving biological differences by projecting high-dimensional data into a low-dimensional cellular embedding space through an asymmetric autoencoder structure (107). In fact, these methods not only improve the accuracy of data integration but also enable online data integration and comparative analysis of new data with existing data.

By use of different machine learning approaches, cell type identification models are developed to recognize cell types and subtypes (108). These models can extract key biological insights to predict the changes in gene expression levels or even dynamic changes in gene interaction networks. For example, scRobust, a self-supervised learning strategy built on the transformer architecture, has demonstrated effectiveness in cell-type annotation and drug tolerance detection (109). A deep learning model "Enformer Celltyping" predicts epigenetic signals across cell types. It overcomes the limitations of existing machine learning approaches, which are confined to the cell types they were trained on (110). Here, we summarized cell-type identification models in Table 2.

Multi-omics analysis: Complex and dynamic networks of molecules in LC-IME make a single layer of "omics" unable to provide deep insights into the underlying mechanisms. Recent technological advancement in high-throughput measurement of genome (111, 112), epigenome (113, 114), metabolome (115), transcriptome (116), and proteome (117) allows comprehensive multi-omic studies. Multi-omics approaches are pivotal in identifying new therapeutic targets (118) and predicting patients' responses to treatments (119). The data from different omics can be cross-fused and mutually verified, providing a more reliable, comprehensive, and systematic perspective (120, 121). Through the integrated analysis of omics data, in-depth biological data that cannot be obtained by a single omics technology can be uncovered (122, 123). However, the advantage of multi-omics data integration comes with the extra complexity deriving from inherently diverse types of omics datasets, which may pose a challenge to integrateing the omics data in a biologically meaningful manner (124). The experimental data generated across diverse laboratories often cannot be seamlessly amalgamated due to inherent constraints. Additionally, the inherent heterogeneity of multi-omic datasets, stemming from technical, biological, chemical, and physical sources, poses significant challenges for interpretation (125).

With the continuous development of AI technologies, the integration of AI and multi-omics has emerged as one powerful solution to these challenges (126–128). AI has remarkable capabilities in deciphering complex patterns and extracting meaningful insights from large and intricate datasets (129–131). This enables researchers to more systematically analyze the complexity of biological systems (132), reveal the interactions and regulatory mechanisms between different molecular layers, and more accurately identify disease-related molecular markers and potential drug targets (133, 134). This subsequently contributes to the development of personalized medicine and precise treatment plans, improving therapeutic effects and reducing side effects (16, 135, 136).

TABLE 2 Cell-type identification models for scRNA-seq analysis.

Models	Paradigm	Algorithm
Scmap	Unsupervised-Graph based	Nearest neighbor
Seurat	Unsupervised-Graph based	Nearest neighbor
scType	Unsupervised-Graph based	Nearest neighbor
ScScope	Unsupervised-Deep learning based	Recurrent network
DESC	Unsupervised-Deep learning based	Autoencoder
ScAIDE	Unsupervised-Deep learning based	Autoencoder
scETM	Unsupervised-Deep learning based	Autoencoder
scVI	Unsupervised-Deep learning based	Hierarchical Bayesian
DISC	Semi-supervised-Deep learning based	Autoencoder
ScDCC	Semi-supervised-Deep learning based	Autoencoder
ScLearn	Supervised-Similarity-based	
CaSTLe	Supervised-General classifier-based	XGBoost
SCCAF	Supervised-General classifier-based	Logistic regression
ScID	Supervised-General classifier-based	Fisher's linear discriminant analysis
ScDeepSort	Supervised-Deep learning based	Weighted GNN
NeuCA	Supervised-Deep learning based	Hierarchical FFNN
ItClust	Supervised-Transfer learning based	
SCTL	Supervised-Transfer learning based	

Data-based Integration. This methodology has proven effective in several studies. Zhang Team merged information from single-nucleotide polymorphisms (SNPs) and transcriptomic profiles into a single matrix, which uses a Bayesian integrative model to facilitate the investigation of their interplay and enable the prediction of quantitative phenotypes (137). To predict remission rates and survival outcomes in ovarian cancer, Mankoo and colleagues integrated the data of copy number alteration, DNA methylation, microRNA, and gene expression and performed a multivariate Cox-LASSO analysis (138). Shen et al. proposed the iCluster framework for glioblastoma subtyping. This framework harmoniously and integrated, with a common set of latent variables, three distinct omics data of copy number alteration, gene expression, and DNA methylation (139).

Model-based Integration. In a model-centric integration framework, distinct models tailored to individual data perspectives are initially formulated, subsequently converging through a fusion process of their respective outputs. For example, the ATHENA tool (140–142), which is designed for investigating heritable and environmental network associations, integrates different omics data of copy number alterations, DNA methylation, miRNA, and gene expression to uncover correlations with clinical endpoints. This integration involves constructing foundational models and neural networks per omics type, ultimately leading to the construction of an integrated model (137). Wang's team used Similarity Network Fusion (SNF) for cancer subtyping. It begins by creating patient similarity matrices based on DNA methylation and the expression of mRNA expression or miRNA and moves to an iterative nonlinear integration, where the three foundational similarity matrices converge into a unified matrix (143). To predict drug resistance in HIV protease mutants, Dr. Ghici and Potter devised an ensemble-based strategy. It sets up the basic predictive models with structural characteristics of the HIV protease-drug inhibitor complex and DNA sequence variations, respectively, and then orchestrates a majority voting system to enhance the accuracy of drug resistance prediction (144).

4.2 Current achievements of AI-guided scRNA-seq for cellular identification in LC-IME

4.2.1 Neutrophil

Neutrophils play a key role during the initiation of innate immunity and the shaping of adaptive immunity. Several subtypes of Tumor-associated neutrophils (TANs) exist with different functions and markers: the antitumor N1, the protumor N2, and polymorphonuclear myeloid-derived suppressor cells (PMN-MDSCs) (145, 146). Tumor cells or other stromal cells in LC-IME educate TANs polarization towards pro-tumor phenotype through the secretion of cytokines or chemokines, such as GM-CSF, IL-6, TGF-β, and E2 PGE2 (147). Furthermore, the elevated neutrophil-lymphocyte ratio is associated with advanced cancer stage, aggressive tumor characteristics, as well as recurrence after resection but varies with etiology (148). Neutrophil extracellular traps (NETs), a unique structure produced during neutrophil death, have been shown to promote HCC metastasis by provoking inflammatory responses (149–152). However, due to the existence of high heterogeneity, some subsets of neutrophils have pro-tumor effects, while others appear to have anti-tumor effects, the overall influence of neutrophils on cancer therapy remains obscure (153–155). Zhang's team performed scRNA-seq analysis and stratified patients into five subtypes, including immune activation, immune suppression mediated by myeloid or stromal cells, immune exclusion, and immune residence phenotypes, which were spatially organized and associated with chemokine networks and genomic features. Notably, the abundance of tumor-associated neutrophils (TANs), particularly prominent within the myeloid-cell-dominated subtype, emerged as a harbinger of an adverse clinical prognosis. Depletion of TANs in mouse models significantly attenuated tumor progression, thereby shedding a promising light on therapeutic targets for innovative immunotherapeutic strategies (156). Neutrophils also showed resistance to anti-PDL-1 therapy in HCC via T-cell exhaustion (156). Interestingly, due to shorter lifespan and less abundance of RNAs, Neutrophils are difficult to identify by single-cell sequencing. However, application of optimized workflows (such as no enrichment strategy) (156) or capture methods (such as the BD Rhapsody platform) (157) made it possible to identify them. Still, some neutrophils with unique transcriptomic and functional features are identified in HCC by scRNA sequencing. Neutrophils expressing MMP8, CD74, SPP1, etc in HCC are considered tumor-associated neutrophils. Importantly, Particularly, CD10+ ALPL+ neutrophils hinder anti-PD-1 therapy by permanently destroying the T-cell (153). Suggesting that identifying and targeting neutrophils in HCC is essential for successful clinical outcomes.

4.2.2 Macrophages

Tumor-associated macrophages (TAMs) are one of the most abundant innate immune cells and are observed at all stages of tumor progression in the LC-IME (95). According to the difference of functions in tumor progression, there are the classical M1 subtype and the alternative M2 subtype. The M1 phenotype is induced by pro-inflammatory cytokines such as IL-1β, IL-6, IL-12, and tumor necrosis factor-α (TNF-α), whereas the M2 phenotype is polarized by immunomodulatory molecules such as IL-4, IL-10, macrophage colony-stimulating factor (M-CSF), and transforming growth factor-β (TGF-β) (158). TAMs promote liver cancer progression through various approaches, including angiogenesis, cancer cell proliferation, immunosuppression, extracellular matrix remodeling, and drug resistance to therapeutic agents (159). TAMs express inhibitory immune checkpoint proteins, such as PD-1, PD-L1, and TIM-3, secret the immunosuppressive cytokine IL-6, and recruit Tregs (160–162). Furthermore, TAMs are important bridges between tumor cells and other immune effector cells. M2 TAMs secrete IGF-1 and CCL20 to recruit Tregs and impair CD8+ T cell function (163). $FasL^{+}CD11b^{+}F4/80^{+}$ monocyte-derived macrophages interact with the activated antigen-specific $Fas^{+}CD8^{+}$ T cells and make them undergo apoptosis. The

elimination of these hepatic macrophages significantly increased the survival of hepatic T cells (164). Moreover, Osteopontin (OPN), a pro-metastatic gene, promotes macrophage infiltration and PD-L1 expression in HCC by activating CSF1/CSF1R pathway (165). Conversely, upon appropriate stimulation, macrophages exhibit remarkable anti-tumor capabilities, such as phagocytosis of cancer cells and cytotoxic tumor eradication (159). Therefore, Macrophage-targeting strategies have the potential to synergize with current therapeutic tools to improve the outcomes of patients with liver cancer. Single-cell sequencing has identified several new subtypes of macrophages in HCC. For instance, there are two major types of macrophages: C1QA+ and THBS1+ macrophages (166). Among them, THBS1+ macrophages are myeloid-derived suppressor cells (MDSC)-like cells. However, C1QA+ are considered TAM-like macrophages, which have properties of both M1 and M2 macrophages and highly express APOE, GPNMB, and SLC40A1 (98) and are associated with poor prognosis of liver cancer. The accumulation of LAIR1+ and TIM3+ TAM macrophages reduced the infiltration of CD8+T cells and was associated with poor prognosis of HCC patients (167). Similarly, the abundance of the APOC1+ macrophages was comparatively higher in HCC tissues, inhibiting APOC1 improves the effects of anti-PD-1 therapy by reshaping M2 macrophages into the M1 macrophages (168). Considering the key role of macrophages (TAM) in cancer development, chemical inhibitors are being trialed, such as the combination of CCR2/CCR5 antagonists (targeting macrophages) with Nivolumab is currently in phase II clinical trials (NCT04123379). The complex functions of TAMs have sparked great interest in developing new therapeutic strategies targeting macrophages.

4.2.3 Dendritic cells

Dendritic cells (DCs), functioning as antigen-presenting cells (APCs), interact with diverse immune cells and form a vital mediator between innate and adaptive immunity. There are two types of DCs, including Conventional DCs (cDCs) and plasmacytoid DCs (pDCs). The primary responsibility of cDCs (either cDC1 or cDC2) is antigen presentation, whereas pDCs are specialized for antiviral and antitumor immunity via the secretion of type I interferons (169),

In immunosuppressive tumor microenvironment, DC cells can be functionally reshaped and lose their antitumor functions. Tregs suppress the expression of HLA-DR and impair the antigen-presenting function of cDC2 cells (170, 171). DC cells often play an immunosuppressive role, and the enrichment of tumor-infiltrating pDCs was correlated with Tregs infiltration as well as poor prognosis in patients with HCC (172, 173). As the immune response to immunotherapy largely depends on DC cells, many strategies have been evaluated for stimulating DC cells in HCC patients, such as DC vaccines (174), nanodrugs (175, 176), and DC-derived exosomes (177), some of which have been demonstrated to activate tumor-specific immunity. Advanced scRNA-seq has identified the heterogeneous nature of dendritic cells (DC) in HCC, thus revealing diversity in their functions. These heterogeneous mature DCs, including CCR7+ LAMP3+ DCs, can migrate from tumors to lymph nodes, interfering with T cell function, including exhausted T cells (TEX) and Tregs cells (98). They are also found in lung cancer because they also express immune regulatory markers (Cd274, Pdcd1lg2, and Cd200) and maturation markers (Cd40, Ccr7, and Il12b); thus, they are named as mature dendritic cells enriched in immune regulatory molecules (mregDCs) (178). In the context of ICI treatment, a cellular triad composed of mregDCs, CXCL13+ helper T (Th) cells, and PD-1^{hi} progenitor CD8+ T cells is significantly enriched in the HCC microenvironment. Communication between mregDCs and CXCL13+ Th cells within these cellular triads helps in the differentiation of progenitor CD8+ T cells into effector antitumor CD8+ T cells (179). Similarly, CXCR3+ CD8+ effector memory T (TEM) cells and HLA-DR+ cDC1 recruited to determine the responsiveness of HCC to ICI (180).

4.2.4 T cells

CD8+T cells exhibit an exhausted phenotype and are incapable of halting tumor progression in HCC, and the enrichment of exhausted CD8+T is negatively correlated with the response to immunotherapy and prognosis in patients in patients with HCC (181). It has been demonstrated that dysfunction of $CD8^+$ T cells occurs within a few hours after they encounter tumor antigens, even before undergoing cell division T (182). This rapid divergence of T cell fate prior to cell division provides us a clue for timely application of immunotherapy. Additionally, tissue-resident memory CD8+ T (TRM) cells are also enriched in tumors, especially in HBV-related HCC (183). A high TRM proportion is associated with better outcomes following ICI therapy (181, 184).

Under the co-stimulation of activated APCs and different cytokines, Naïve CD4+ T cells proliferate and differentiate into different subsets, including Th cells (specifically, Th1, Th2, and Th17), follicular helper T (Tfh) cells, and Treg cells (185). Among them, Th1 cells secret IFN-γ and IL-2 and promote the anti-tumor effect of CD8+ T cells (186). Furthermore, Th1 cells facilitate dendritic cell (DC) maturation through the CD40-CD40L signaling axis (187). On the other hand, Th17 cells are abundant in HCC and are associated with unfavorable clinical outcomes (188). Moreover, Th17 cells contribute to resistance against PD-L1 therapy by upregulating PD-L1 expression in HCC cells through the secretion of IL-17A (189). Treg cells are significantly increased in HCC and are correlated with dysfunction of CD8 T-cells, reduced clinical benefits of anti-PD-L1 plus anti-VEGFR, and poor survival (190–192). Given the crucial role of Tregs in maintaining immune homeostasis and preventing auto-immune diseases, there is a pressing need for innovative approaches that precisely target tumor-infiltrating Tregs and spare the physiological function of Tregs. Currently, little is known about the roles of Th2 and Tfh cells in HCC, which require further investigation. Both exhausted CD8+T and Treg cells are characterized by upregulated expression of a series of inhibitory receptors, such as PD-1 and CTLA-4 (193, 194). In pre-tumoral HCC tissues, monocytes express higher levels of CD93, which inhibit the infiltration of CD8 T cells (195). Thus, targeting CD93-expressing monocytes can help increase the activation and infiltration of the CD8 T cells. Multi-

omics is commonly used to identify the T-cells in tumors, but standard AI-based systems for efficiently detecting T-cells in liver TME are not available. Questions regarding advanced AI intervention in the detection of T cells in solid tumors, especially liver cancer, remain unclear.

4.2.5 B cells

Tumor-infiltrating B cells play pivotal roles in tumor immunity, including antigen presentation, antibody production, and other functions (196). Their presence is notably a favorable marker for HCC prognosis (94, 197). Additionally, the presence of intratumoral tertiary lymphoid structures (TLS) is correlated with a reduced risk of early recurrence in HCC patients after surgical resection (198). Within TLS, abundant B cells transform into plasma cells and produce IgG antibodies that effectively combat tumors (199). However, there are some subtypes of B cells that play pro-tumor roles in HCC. IgA-producing B cells enhanced the expression of PD-L1 and exert an inhibitory influence on T-cell activation (200). Furthermore, regulatory B cells (Bregs), which are characterized by IL-10 secretion, not only dampen T-cell responsiveness but also contribute to HCC progression via the CD40/CD154 signaling axis (201). Given the intricate and diverse functions exhibited by various B-cell subsets in HCC, further research endeavors are required to unlock their full potential in therapeutic strategies. As aforementioned, single-cell sequencing is commonly used to identify the cellular composition of tumors. The level of B cells in liver tumors was detected using conventional sc-seq (202), but AI-guided sc-seq is not generally applied.

4.2.6 NK cells and other innate lymphoid cells

Innate lymphoid cells (ILCs) are a highly heterogeneous family, which comprise NK cells, ILCs also include ILC1s, ILC2s, and ILC3s. In the human liver, NK cells constitute a prominent subtype of lymphocyte, accounting for about 50% of the total intrahepatic lymphocytes (203). These NK cells can be categorically split into two distinct subsets: cytotoxic NK cells marked by $CD56^{dim}CD16^{high}$ expression and immunoregulatory NK cells characterized by $CD56^{bright}CD16^{low}$ expression (204). Cytokines, such as IL-10 and TGF-β, induce the exhaustion phenotype of CD11b-/CD27-NK cells through the upregulation of NKG2A and CD96, respectively. The blockade of IL-10 or TGF-β pathway can reverse the dysfunction of NK cells (205, 206). Furthermore, a significant reduction of NAD+ in NK cells causes their dysfunction. Supplementation with NMN, a NAD+ precursor, restores the anti-tumor effects of NK cells (207). Due to its potent cytotoxicity against tumors without dependence on secondary activation, various innovative NK cell-based therapeutic strategies have been explored in HCC (208). For example, bispecific antibodies are designed to bridge the gap between NK cells and tumor cells (209–211). These antibodies possess dual specificity, enabling them to simultaneously bind to a tumor-associated antigen on HCC cells and an activating receptor on NK cells. This interaction triggers potent antibody-dependent cellular cytotoxicity (ADCC), NK cells are activated and directed toward the tumor, leading to their direct killing via the release of cytotoxic granules containing perforin and granzymes. Furthermore, adoptive cell transfer (ACT) therapies have emerged as a promising avenue for NK cell-based treatments. NK cells are either expanded ex vivo or subsequently modified to enhance their tumor-targeting and killing capabilities. These modifications can be achieved through the engineering of chimeric antigen receptors (CARs) into NK cells (212) or the activating killing-ability of NK cells with cytokines (213).

Not like the cytolytic NK cells, ILC1s, ILC2s, and ILC3s function through cytokine secretion. Interestingly, the secretion behaviors of ILC1s, ILC2s, and ILC3s mirror the functions and characteristics of CD4+ helper T cell subsets. The three ILC subtypes secrete IFN-γ/TNF-α, IL-4/IL-5/IL-13, and IL-17/IL-22, which are signatures of characteristics of Th1, Th2, and Th17 cells, respectively (204, 214). Currently, their roles in liver cancer are still controversial. For example, ICOS+ILC2a cells were enriched in HCC and associated with poor prognosis (215). However, in another study, a high ILC2/ILC1 ratio is associated with enhanced anti-tumor immune responses and better prognosis (216). Further studies are needed to define the contribution of these cytokine-secretion ILCs in HCC.

5 Challenges and Future Prospects

In the past several years, a drastic rise in data digitization has been seen in many sectors, including the medical sector. However, it comes with challenges, especially in acquiring and scrutinizing suitable data to solve various complex problems. LC-IME is highly heterogeneous and complex, and so far, no AI system has been constructed to identify various cell types and signaling pathways (217, 218). The cellular composition of the LC-IME is usually determined by conventional single-cell sequencing; AI intervention can improve the overall outcome. With enhanced automation, AI has the power to handle large-scale data because AI-guided tools can learn from input data and independently draw conclusions according to the given objectives. On the other hand, conventional methods require stepwise monitoring and human input for manual analysis and drawing conclusions. However, several limitations still exist for freely applying AI in LC-IME. First, there is a long way to go in building highly accurate AI algorithms and models that are both explainable and trustworthy. Further integration of constraints into the models, based on biological domain knowledge in a principled manner, is necessary to improve both the accuracy and interpretability of models being applied to LC-IME. Second, the reliability of most studies is limited by small sample sizes. Future rigorous, large-scale longitudinal studies on LC-IME are needed for feature decomposition and to reduce the large number of variables. Third, research growth in this area is hindered by the lack of international guidelines or models that specify where AI is more likely to be useful in monitoring the integration of large data. There is a need for transparent, accessible, and curated data sharing. Moreover, interdisciplinary approaches, supplemented by rigorous co-production and co-design processes alongside individuals with liver cancer, are key to progress in this area. These research directions are expected to drive the in-depth

application of AI technology in LC-IME field, thereby providing new solutions for precision medicine of liver cancer and significantly improving treatment outcomes and quality of life for patients.

6 Conclusion

With the rapid development of high-throughput sequencing technology and computer science, the amount of large omics data has increased exponentially, the advantages of multi-omics analysis have gradually emerged, and the application of artificial intelligence has become more and more extensive. Overall, this review has highlighted the potential, current applications, and implementation framework for integrating AI in the discovery and validation of biomarkers in HCC. Finally, we briefly explained the current challenges of multi-omics analysis and artificial intelligence in order to provide new research ideas for the medical industry and to promote the development and application of precision medicine.

Author contributions

XC: Writing – original draft, Writing – review & editing, Conceptualization. IB: Writing – review & editing. ML: Writing – review & editing. GL: Methodology, Visualization, Writing – review & editing. JX: Writing – review & editing. PZ: Supervision, Writing – review & editing.

Funding

The author(s) declare financial support was received for the research, authorship, and/or publication of this article. This project was supported by Research Fund for the Doctoral program of the Fifth Affiliated Hospital of Zhengzhou University (pb2024kyqdj03), Supporting Program for Young Talent Innovation Teams of Zhengzhou University (32320688), Henan Medical Key Technologies R & D Program (LHGJ20220570).

Acknowledgments

We are deeply grateful to Xinfeng Liang for her crucial management and coordination in the planning and execution of the research activity. Her efforts have ensured the smooth progress and successful outcome of our endeavors.

Conflict of interest

The authors declare that the research was conducted in the absence of any commercial or financial relationships that could be construed as a potential conflict of interest.

Generative AI statement

The author(s) declare that no Generative AI was used in the creation of this manuscript.

Publisher's note

References

1. Bray F, Laversanne M, Sung H, Ferlay J, Siegel RL, Soerjomataram I, et al. Global cancer statistics 2022: GLOBOCAN estimates of incidence and mortality worldwide for 36 cancers in 185 countries. *CA Cancer J Clin*. (2024) 74:229–63. doi: 10.3322/caac.21834

2. Jianyong L, Lunan Y, Dajiang L, Wentao W, Liver Surgery G. Comparison of open liver resection and RFA for the treatment of solitary 3-5-cmhepatocellular carcinoma: a retrospective study. *BMC Surg*. (2019) 19:195. doi: 10.1186/s12893-019-0663-9

3. Sugawara Y, Hibi T. Surgical treatment of hepatocellular carcinoma. *Biosci Trends*. (2021) 15:138–41. doi: 10.5582/bst.2021.01094

4. Cassinotto C, Nogue E, Durand Q, Panaro F, Assenat E, Dohan A, et al. Life expectancy of patients with hepatocellular carcinoma according to the upfront treatment: A nationwide analysis. *Diagn Interv Imaging*. (2023) 104:192–9. doi: 10.1016/j.diii.2023.01.002

5. Lee MW, Kang D, Lim HK, Cho J, Sinn DH, Kang TW, et al. Updated 10-year outcomes of percutaneous radiofrequency ablation as first-line therapy for single hepatocellular carcinoma < 3 cm: emphasis on association of local tumor progression and overall survival. *Eur Radiol*. (2020) 30:2391–400. doi: 10.1007/s00330-019-06575-0

6. National Clinical Research Center for Infectious D, Society of Hepatology BMA and Translational Medicine Branch CAoG, Geriatrics. Expert consensus on precise diagnosis and management of primary hepatocellular carcinoma in advanced stage (2023 version). *Zhonghua Gan Zang Bing Za Zhi*. (2023) 31:910–20. doi: 10.3760/cma.j.cn501113-20230717-00006

7. Brown ZJ, Greten TF, Heinrich B. Adjuvant treatment of hepatocellular carcinoma: prospect of immunotherapy. *Hepatology*. (2019) 70:1437–42. doi: 10.1002/hep.30633

8. Scudellari M. Drug development: try and try again. *Nature*. (2014) 516:S4–6. doi: 10.1038/516S4a

9. Gravitz L. Liver cancer. *Nature*. (2014) 516:S1. doi: 10.1038/516S1a

10. Laursen L. A preventable cancer. *Nature*. (2014) 516:S2–3. doi: 10.1038/516S2a

11. Llovet JM, Kelley RK, Villanueva A, Singal AG, Pikarsky E, Roayaie S, et al. Hepatocellular carcinoma. *Nat Rev Dis Primers*. (2021) 7:6. doi: 10.1038/s41572-020-00240-3

12. Pashkov VM, Harkusha AO, Soloviov OS. The impact of the introduction of artificial intelligence technologies on the current human rights and freedoms concept. *Pol Merkur Lekarski*. (2023) 51:646–53. doi: 10.36740/Merkur

13. Hou Y, Dong Q, Wang D, Liu J. Introduction to 'Artificial intelligence in failure analysis of transportation infrastructure and materials'. *Philos Trans A Math Phys Eng Sci*. (2023) 381:20220177. doi: 10.1098/rsta.2022.0177

14. Bundy A, Chater N, Muggleton S. Introduction to 'Cognitive artificial intelligence'. *Philos Trans A Math Phys Eng Sci*. (2023) 381:20220051. doi: 10.1098/rsta.2022.0051

15. Xiao F, Ke J. Pricing, management and decision-making of financial markets with artificial intelligence: introduction to the issue. *Financ Innov*. (2021) 7:85. doi: 10.1186/s40854-021-00302-9

16. Li L, Sun M, Wang J, Wan S. Multi-omics based artificial intelligence for cancer research. *Adv Cancer Res*. (2024) 163:303–56. doi: 10.1016/bs.acr.2024.06.005

17. Wang F, Preininger A. AI in health: state of the art, challenges, and future directions. *Yearb Med Inform*. (2019) 28:16–26. doi: 10.1055/s-0039-1677908

18. Mintz Y, Brodie R. Introduction to artificial intelligence in medicine. *Minim Invasive Ther Allied Technol*. (2019) 28:73–81. doi: 10.1080/13645706.2019.1575882

19. Sung JJY. Introduction to artificial intelligence in medicine. *Singapore Med J*. (2024) 65:132. doi: 10.4103/singaporemedj.SMJ-2024-060

20. Sarker IH. Machine learning: algorithms, real-world applications and research directions. *SN Comput Sci*. (2021) 2:160. doi: 10.1007/s42979-021-00592-x

21. Jiang T, Gradus JL, Rosellini AJ. Supervised machine learning: A brief primer. *Behav Ther*. (2020) 51:675–87. doi: 10.1016/j.beth.2020.05.002

22. Eckhardt CM, Madjarova SJ, Williams RJ, Ollivier M, Karlsson J, Pareek A, et al. Unsupervised machine learning methods and emerging applications in healthcare. *Knee Surg Sports Traumatol Arthrosc*. (2023) 31:376–81. doi: 10.1007/s00167-022-07233-7

23. Valkenborg D, Rousseau AJ, Geubbelmans M, Burzykowski T. Unsupervised learning. *Am J Orthod Dentofacial Orthop*. (2023) 163:877–82. doi: 10.1016/j.ajodo.2023.04.001

24. Reddy YCAP, Viswanath P, Eswara Reddy B. Semi-supervised learning: A brief review. *Int J Eng Technol*. (2018) 7:81. doi: 10.14419/ijet.v7i1.8.9977

25. Datta S, Li Y, Ruppert MM, Ren Y, Shickel B, Ozrazgat-Baslanti T, et al. Reinforcement learning in surgery. *Surgery*. (2021) 170:329–32. doi: 10.1016/j.surg.2020.11.040

26. Hassoun MH. *Fundamentals of artificial neural networks*. MIT Press (1995).

27. Klein EA, Richards D, Cohn A, Tummala M, Lapham R, Cosgrove D, et al. Clinical validation of a targeted methylation-based multi-cancer early detection test using an independent validation set. *Ann Oncol*. (2021) 32:1167–77. doi: 10.1016/j.annonc.2021.05.806

28. Stark GF, Hart GR, Nartowt BJ, Deng J. Predicting breast cancer risk using personal health data and machine learning models. *PloS One*. (2019) 14:e0226765. doi: 10.1371/journal.pone.0226765

29. Feng X, Hong T, Liu W, Xu C, Li W, Yang B, et al. Development and validation of a machine learning model to predict the risk of lymph node metastasis in renal carcinoma. *Front Endocrinol (Lausanne)*. (2022) 13:1054358. doi: 10.3389/fendo.2022.1054358

30. Rodland KD, Webb-Robertson BJ, Srivastava S. Introduction to the special issue on Applications of Artificial Intelligence in Biomarker Research. *Cancer biomark*. (2022) 33:171–2. doi: 10.3233/CBM-229001

31. Halner A, Hankey L, Liang Z, Pozzetti F, Szulc D, Mi E, et al. DEcancer: Machine learning framework tailored to liquid biopsy based cancer detection and biomarker signature selection. *iScience*. (2023) 26:106610. doi: 10.1016/j.isci.2023.106610

32. Chen Y, Wang B, Zhao Y, Shao X, Wang M, Ma F, et al. Metabolomic machine learning predictor for diagnosis and prognosis of gastric cancer. *Nat Commun*. (2024) 15:1657. doi: 10.1038/s41467-024-46043-y

33. Tayob N, Feng Z. Personalized statistical learning algorithms to improve the early detection of cancer using longitudinal biomarkers. *Cancer biomark*. (2022) 33:199–210. doi: 10.3233/CBM-210307

34. Stefanou IK, Dovrolis N, Gazouli M, Theodorou D, Zografos GK, Toutouzas KG. miRNAs expression pattern and machine learning models elucidate risk for gastric GIST. *Cancer biomark*. (2022) 33:237–47. doi: 10.3233/CBM-210173

35. Starikov A, Al'Aref SJ, Singh G, Min JK. Artificial intelligence in clinical imaging: An introduction. *Clin Imaging*. (2018) 49:vii–ix. doi: 10.1016/j.clinimag.2018.04.001

36. Lee JG, Jun S, Cho YW, Lee H, Kim GB, Seo JB, et al. Deep learning in medical imaging: general overview. *Korean J Radiol*. (2017) 18:570–84. doi: 10.3348/kjr.2017.18.4.570

37. Kourounis G, Elmahmudi AA, Thomson B, Hunter J, Ugail H, Wilson C. Computer image analysis with artificial intelligence: a practical introduction to convolutional neural networks for medical professionals. *Postgrad Med J*. (2023) 99:1287–94. doi: 10.1093/postmj/qgad095

38. Al-Masni MA, Al-Antari MA, Park JM, Gi G, Kim TY, Rivera P, et al. Detection and classification of the breast abnormalities in digital mammograms via regional Convolutional Neural Network. *Annu Int Conf IEEE Eng Med Biol Soc*. (2017) 2017:1230–3. doi: 10.1109/EMBC.2017.8037053

39. Zhao X, Xie P, Wang M, Li W, Pickhardt PJ, Xia W, et al. Deep learning-based fully automated detection and segmentation of lymph nodes on multiparametric-mri for rectal cancer: A multicentre study. *EBioMedicine*. (2020) 56:102780. doi: 10.1016/j.ebiom.2020.102780

40. Jin EH, Lee D, Bae JH, Kang HY, Kwak MS, Seo JY, et al. Improved accuracy in optical diagnosis of colorectal polyps using convolutional neural networks with visual explanations. *Gastroenterology*. (2020) 158:2169–79 e8. doi: 10.1053/j.gastro.2020.02.036

41. Ramon YCS, Sese M, Capdevila C, Aasen T, De Mattos-Arruda L, Diaz-Cano SJ, et al. Clinical implications of intratumor heterogeneity: challenges and opportunities. *J Mol Med (Berl)*. (2020) 98:161–77. doi: 10.1007/s00109-020-01874-2

42. Marusyk A, Janiszewska M, Polyak K. Intratumor heterogeneity: the rosetta stone of therapy resistance. *Cancer Cell*. (2020) 37:471–84. doi: 10.1016/j.ccell.2020.03.007

43. Shmatko A, Ghaffari Laleh N, Gerstung M, Kather JN. Artificial intelligence in histopathology: enhancing cancer research and clinical oncology. *Nat Cancer*. (2022) 3:1026–38. doi: 10.1038/s43018-022-00436-4

44. Lu MY, Chen TY, Williamson DFK, Zhao M, Shady M, Lipkova J, et al. AI-based pathology predicts origins for cancers of unknown primary. *Nature*. (2021) 594:106–10. doi: 10.1038/s41586-021-03512-4

45. Lee Y, Park JH, Oh S, Shin K, Sun J, Jung M, et al. Derivation of prognostic contextual histopathological features from whole-slide images of tumours via graph deep learning. *Nat BioMed Eng*. (2022). doi: 10.1038/s41551-022-00923-0

46. Pei Q, Luo Y, Chen Y, Li J, Xie D, Ye T. Artificial intelligence in clinical applications for lung cancer: diagnosis, treatment and prognosis. *Clin Chem Lab Med*. (2022) 60:1974–83. doi: 10.1515/cclm-2022-0291

47. Mitsala A, Tsalikidis C, Pitiakoudis M, Simopoulos C, Tsaroucha AK. Artificial intelligence in colorectal cancer screening, diagnosis and treatment. *A New Era Curr Oncol*. (2021) 28:1581–607. doi: 10.3390/curroncol28030149

48. Luo S, Xu J, Jiang Z, Liu L, Wu Q, Leung EL, et al. Artificial intelligence-based collaborative filtering method with ensemble learning for personalized lung cancer medicine without genetic sequencing. *Pharmacol Res*. (2020) 160:105037. doi: 10.1016/j.phrs.2020.105037

49. Abajian A, Murali N, Savic LJ, Laage-Gaupp FM, Nezami N, Duncan JS, et al. Predicting treatment response to intra-arterial therapies for hepatocellular carcinoma with the use of supervised machine learning-an artificial intelligence concept. *J Vasc Interv Radiol*. (2018) 29:850–7 e1. doi: 10.1016/j.jvir.2018.01.769

50. Kong J, Ha D, Lee J, Kim I, Park M, Im SH, et al. Network-based machine learning approach to predict immunotherapy response in cancer patients. *Nat Commun*. (2022) 13:3703. doi: 10.1038/s41467-022-31535-6

51. Levy EI, Taussky P, Cohen JE, Kan P. Introduction. Neurosurgical management of stroke, organization of stroke management, and artificial intelligence applications. *Neurosurg Focus*. (2021) 51:E1. doi: 10.3171/2021.4.FOCUS21264

52. Qiu B, Shen Z, Wu S, Qin X, Yang D, Wang Q. A machine learning-based model for predicting distant metastasis in patients with rectal cancer. *Front Oncol*. (2023) 13:1235121. doi: 10.3389/fonc.2023.1235121

53. Cai WL, Cheng M, Wang Y, Xu PH, Yang X, Sun ZW, et al. Prediction and related genes of cancer distant metastasis based on deep learning. *Comput Biol Med*. (2024) 168:107664. doi: 10.1016/j.compbiomed.2023.107664

54. Lu ZX, Qian P, Bi D, Ye ZW, He X, Zhao YH, et al. Application of AI and ioT in clinical medicine: summary and challenges. *Curr Med Sci*. (2021) 41:1134–50. doi: 10.1007/s11596-021-2486-z

55. Sarkar C, Das B, Rawat VS, Wahlang JB, Nongpiur A, Tiewsoh I, et al. Artificial intelligence and machine learning technology driven modern drug discovery and development. *Int J Mol Sci*. (2023) 24:2026. doi: 10.3390/ijms24032026

56. Qiu X, Li H, Ver Steeg G, Godzik A. Advances in AI for protein structure prediction: implications for cancer drug discovery and development. *Biomolecules*. (2024) 14:339. doi: 10.3390/biom14030339

57. Zhou X, Wang M, Katsyv I, Irie H, Zhang B. EMUDRA: Ensemble of Multiple Drug Repositioning Approaches to improve prediction accuracy. *Bioinformatics*. (2018) 34:3151–9. doi: 10.1093/bioinformatics/bty325

58. Jenne CN, Kubes P. Immune surveillance by the liver. *Nat Immunol*. (2013) 14:996–1006. doi: 10.1038/ni.2691

59. Zheng M, Tian Z. Liver-mediated adaptive immune tolerance. *Front Immunol*. (2019) 10:2525. doi: 10.3389/fimmu.2019.02525

60. Schramm C, Oo YH, Lohse AW. Tolerance and autoimmunity in the liver. *Semin Immunopathol*. (2022) 44:393–5. doi: 10.1007/s00281-022-00952-6

61. Koo SY, Park EJ, Lee CW. Immunological distinctions between nonalcoholic steatohepatitis and hepatocellular carcinoma. *Exp Mol Med*. (2020) 52:1209–19. doi: 10.1038/s12276-020-0480-3

62. Yang Zhou J. Innate immunity and early liver inflammation. *Front Immunol*. (2023) 14:1175147. doi: 10.3389/fimmu.2023.1175147

63. Meyer M, Schwarzler J, Jukic A, Tilg H. Innate immunity and MASLD. *Biomolecules*. (2024) 14:476. doi: 10.3390/biom14040476

64. Tang J, Yan Z, Feng Q, Yu L, Wang H. The roles of neutrophils in the pathogenesis of liver diseases. *Front Immunol*. (2021) 12:625472. doi: 10.3389/fimmu.2021.625472

65. Kahraman A, Schlattjan M, Kocabayoglu P, Yildiz-Meziletoglu S, Schlensak M, Fingas CD, et al. Major histocompatibility complex class I-related chains A and B (MIC A/B): a novel role in nonalcoholic steatohepatitis. *Hepatology*. (2010) 51:92–102. doi: 10.1002/hep.23253

66. Backes CS, Friedmann KS, Mang S, Knorck A, Hoth M, Kummerow C. Natural killer cells induce distinct modes of cancer cell death: Discrimination, quantification, and modulation of apoptosis, necrosis, and mixed forms. *J Biol Chem*. (2018) 293:16348–63. doi: 10.1074/jbc.RA118.004549

67. Zhang Y, Wu Y, Shen W, Wang B, Yuan X. Crosstalk between NK cells and hepatic stellate cells in liver fibrosis (Review). *Mol Med Rep*. (2022) 25:208. doi: 10.1186/s10020-021-00415-y

68. Kumar S. Natural killer cell cytotoxicity and its regulation by inhibitory receptors. *Immunology*. (2018) 154:383–93. doi: 10.1111/imm.2018.154.issue-3

69. Doherty DG. Immunity, tolerance and autoimmunity in the liver: A comprehensive review. *J Autoimmun*. (2016) 66:60–75. doi: 10.1016/j.jaut.2015.08.020

70. Racanelli V, Rehermann B. The liver as an immunological organ. *Hepatology*. (2006) 43:S54–62. doi: 10.1002/hep.21060

71. Nakamoto N, Kanai T. Role of toll-like receptors in immune activation and tolerance in the liver. *Front Immunol*. (2014) 5:221. doi: 10.3389/fimmu.2014.00221

72. Tacke F. Targeting hepatic macrophages to treat liver diseases. *J Hepatol*. (2017) 66:1300–12. doi: 10.1016/j.jhep.2017.02.026

73. Bleriot C, Barreby E, Dunsmore G, Ballaire R, Chakarov S, Ficht X, et al. A subset of Kupffer cells regulates metabolism through the expression of CD36. *Immunity*. (2021) 54:2101–16 e6. doi: 10.1016/j.immuni.2021.08.006

74. Holt MP, Cheng L, Ju C. Identification and characterization of infiltrating macrophages in acetaminophen-induced liver injury. *J Leukoc Biol*. (2008) 84:1410–21. doi: 10.1189/jlb.0308173

75. Obstfeld AE, Sugaru E, Thearle M, Francisco AM, Gayet C, Ginsberg HN, et al. C-C chemokine receptor 2 (CCR2) regulates the hepatic recruitment of myeloid cells that promote obesity-induced hepatic steatosis. *Diabetes*. (2010) 59:916–25. doi: 10.2337/db09-1403

76. Stienstra R, Saudale F, Duval C, Keshtkar S, Groener JE, van Rooijen N, et al. Kupffer cells promote hepatic steatosis via interleukin-1beta-dependent suppression of peroxisome proliferator-activated receptor alpha activity. *Hepatology*. (2010) 51:511–22. doi: 10.1002/hep.23337

77. Strizova Z, Benesova I, Bartolini R, Novysedlak R, Cecrdlova E, Foley LK, et al. M1/M2 macrophages and their overlaps - myth or reality? *Clin Sci (Lond)*. (2023) 137:1067–93. doi: 10.1042/CS20220531

78. Liu J, Geng X, Hou J, Wu G. New insights into M1/M2 macrophages: key modulators in cancer progression. *Cancer Cell Int*. (2021) 21:389. doi: 10.1186/s12935-021-02089-2

79. Crispe IN. Liver antigen-presenting cells. *J Hepatol*. (2011) 54:357–65. doi: 10.1016/j.jhep.2010.10.005

80. Poddighe D, Maulenkul T, Zhubanova G, Akhmaldtinova L, Dossybayeva K. Natural killer T (NKT) cells in autoimmune hepatitis: current evidence from basic and clinical research. *Cells*. (2023) 12:2854. doi: 10.3390/cells12242854

81. Gan J, Mao XR, Zheng SJ, Li JF. Invariant natural killer T cells: Not to be ignored in liver disease. *J Dig Dis*. (2021) 22:136–42. doi: 10.1111/1751-2980.12968

82. Arrese M, Cabrera D, Kalergis AM, Feldstein AE. Innate immunity and inflammation in NAFLD/NASH. *Dig Dis Sci*. (2016) 61:1294–303. doi: 10.1007/s10620-016-4049-x

83. Geissmann F, Cameron TO, Sidobre S, Manlongat N, Kronenberg M, Briskin MJ, et al. Intravascular immune surveillance by CXCR6+ NKT cells patrolling liver sinusoids. *PloS Biol*. (2005) 3:e113. doi: 10.1371/journal.pbio.0030113

84. Kumar V. NKT-cell subsets: promoters and protectors in inflammatory liver disease. *J Hepatol*. (2013) 59:618–20. doi: 10.1016/j.jhep.2013.02.032

85. Ramadori P, Kam S, Heikenwalder M. T cells: Friends and foes in NASH pathogenesis and hepatocarcinogenesis. *Hepatology*. (2022) 75:1038–49. doi: 10.1002/hep.32336

86. Rakhra K, Bachireddy P, Zabuawala T, Zeiser R, Xu L, Kopelman A, et al. CD4 (+) T cells contribute to the remodeling of the microenvironment required for sustained tumor regression upon oncogene inactivation. *Cancer Cell*. (2010) 18:485–98. doi: 10.1016/j.ccr.2010.10.002

87. Kang TW, Yevsa T, Woller N, Hoenicke L, Wuestefeld T, Dauch D, et al. Senescence surveillance of pre-malignant hepatocytes limits liver cancer development. *Nature*. (2011) 479:547–51. doi: 10.1038/nature10599

88. Heinrich B, Brown ZJ, Diggs LP, Vormehr M, Ma C, Subramanyam V, et al. Steatohepatitis impairs T-cell-directed immunotherapies against liver tumors in mice. *Gastroenterology*. (2021) 160:331–45 e6. doi: 10.1053/j.gastro.2020.09.031

89. Van Herck MA, Weyler J, Kwanten WJ, Dirinck EL, De Winter BY, Francque SM, et al. The differential roles of T cells in non-alcoholic fatty liver disease and obesity. *Front Immunol*. (2019) 10:82. doi: 10.3389/fimmu.2019.00082

90. Hirsova P, Bamidele AO, Wang H, Povero D, Revelo XS. Emerging roles of T cells in the pathogenesis of nonalcoholic steatohepatitis and hepatocellular carcinoma. *Front Endocrinol (Lausanne)*. (2021) 12:760860. doi: 10.3389/fendo.2021.760860

91. MacParland SA, Liu JC, Ma XZ, Innes BT, Bartczak AM, Gage BK, et al. Single cell RNA sequencing of human liver reveals distinct intrahepatic macrophage populations. *Nat Commun*. (2018) 9:4383. doi: 10.1038/s41467-018-06318-7

92. Togashi Y, Shitara K, Nishikawa H. Regulatory T cells in cancer immunosuppression - implications for anticancer therapy. *Nat Rev Clin Oncol*. (2019) 16:356–71. doi: 10.1038/s41571-019-0175-7

93. Wang H, Zhang H, Wang Y, Brown ZJ, Xia Y, Huang Z, et al. Regulatory T-cell and neutrophil extracellular trap interaction contributes to carcinogenesis in non-alcoholic steatohepatitis. *J Hepatol*. (2021) 75:1271–83. doi: 10.1016/j.jhep.2021.07.032

94. Garnelo M, Tan A, Her Z, Yeong J, Lim CJ, Chen J, et al. Interaction between tumour-infiltrating B cells and T cells controls the progression of hepatocellular carcinoma. *Gut*. (2017) 66:342–51. doi: 10.1136/gutjnl-2015-310814

95. Cheng K, Cai N, Zhu J, Yang X, Liang H, Zhang W. Tumor-associated macrophages in liver cancer: From mechanisms to therapy. *Cancer Commun (Lond)*. (2022) 42:1112–40. doi: 10.1002/cac2.v42.11

96. Sangro B, Sarobe P, Hervas-Stubbs S, Melero I. Advances in immunotherapy for hepatocellular carcinoma. *Nat Rev Gastroenterol Hepatol*. (2021) 18:525–43. doi: 10.1038/s41575-021-00438-0

97. Zheng C, Zheng L, Yoo JK, Guo H, Zhang Y, Guo X, et al. Landscape of infiltrating T cells in liver cancer revealed by single-cell sequencing. *Cell*. (2017) 169:1342–56 e16. doi: 10.1016/j.cell.2017.05.035

98. Zhang Q, He Y, Luo N, Patel SJ, Han Y, Gao R, et al. Landscape and dynamics of single immune cells in hepatocellular carcinoma. *Cell*. (2019) 179:829–45 e20. doi: 10.1016/j.cell.2019.10.003

99. Llovet JM, Castet F, Heikenwalder M, Maini MK, Mazzaferro V, Pinato DJ, et al. Immunotherapies for hepatocellular carcinoma. *Nat Rev Clin Oncol*. (2022) 19:151–72. doi: 10.1038/s41571-021-00573-2

100. Harkus U, Wankell M, Palamuthusingam P, McFarlane C, Hebbard L. Immune checkpoint inhibitors in HCC: Cellular, molecular and systemic data. *Semin Cancer Biol*. (2022) 86:799–815. doi: 10.1016/j.semcancer.2022.01.005

101. Binnewies M, Roberts EW, Kersten K, Chan V, Fearon DF, Merad M, et al. Understanding the tumor immune microenvironment (TIME) for effective therapy. *Nat Med*. (2018) 24:541–50. doi: 10.1038/s41591-018-0014-x

102. Thorsson V, Gibbs DL, Brown SD, Wolf D, Bortone DS, Ou Yang TH, et al. The immune landscape of cancer. *Immunity*. (2018) 48:812–30 e14. doi: 10.1016/j.immuni.2018.03.023

103. Li X, Ramadori P, Pfister D, Seehawer M, Zender L, Heikenwalder M. The immunological and metabolic landscape in primary and metastatic liver cancer. *Nat Rev Cancer*. (2021) 21:541–57. doi: 10.1038/s41568-021-00383-9

104. Cheng C, Chen W, Jin H, Chen X. A review of single-cell RNA-seq annotation, integration, and cell-cell communication. *Cells*. (2023) 12:1970. doi: 10.3390/cells12151970

105. Lu J, Sheng Y, Qian W, Pan M, Zhao X, Ge Q. scRNA-seq data analysis method to improve analysis performance. *IET Nanobiotechnol*. (2023) 17:246–56. doi: 10.1049/nbt2.12115

106. Brendel M, Su C, Bai Z, Zhang H, Elemento O, Wang F. Application of deep learning on single-cell RNA sequencing data analysis: A review. *Genomics Proteomics Bioinf*. (2022) 20:814–35. doi: 10.1016/j.gpb.2022.11.011

107. Ryu Y, Han GH, Jung E, Hwang D. Integration of single-cell RNA-seq datasets: A review of computational methods. *Mol Cells*. (2023) 46:106–19. doi: 10.14348/molcells.2023.0009

108. Madadi Y, Monavarfeshani A, Chen H, Stamer WD, Williams RW, Yousefi S. Artificial intelligence models for cell type and subtype identification based on single-cell RNA sequencing data in vision science. *IEEE/ACM Trans Comput Biol Bioinform*. (2023) 20:2837–52. doi: 10.1109/TCBB.2023.3284795

109. Park S, Lee H. Robust self-supervised learning strategy to tackle the inherent sparsity in single-cell RNA-seq data. *Brief Bioinform*. (2024) 25:bbae586. doi: 10.1093/bib/bbae586

110. Murphy AE, Beardall W, Rei M, Phuycharoen M, Skene NG. Predicting cell type-specific epigenomic profiles accounting for distal genetic effects. *Nat Commun*. (2024) 15:9951. doi: 10.1038/s41467-024-54441-5

111. Consortium GT. Human genomics. The Genotype-Tissue Expression (GTEx) pilot analysis: multitissue gene regulation in humans. *Science*. (2015) 348:648–60. doi: 10.1126/science.1262110

112. Wellcome Trust Case Control C. Genome-wide association study of 14,000 cases of seven common diseases and 3,000 shared controls. *Nature*. (2007) 447:661–78. doi: 10.1038/nature05911

113. Roadmap Epigenomics C, Kundaje A, Meuleman W, Ernst J, Bilenky M, Yen A, et al. Integrative analysis of 111 reference human epigenomes. *Nature*. (2015) 518:317–30. doi: 10.1038/nature14248

114. Ziller MJ, Gu H, Muller F, Donaghey J, Tsai LT, Kohlbacher O, et al. Charting a dynamic DNA methylation landscape of the human genome. *Nature*. (2013) 500:477–81. doi: 10.1038/nature12433

115. Shin SY, Fauman EB, Petersen AK, Krumsiek J, Santos R, Huang J, et al. An atlas of genetic influences on human blood metabolites. *Nat Genet*. (2014) 46:543–50. doi: 10.1038/ng.2982

116. Trapnell C, Roberts A, Goff L, Pertea G, Kim D, Kelley DR, et al. Differential gene and transcript expression analysis of RNA-seq experiments with TopHat and Cufflinks. *Nat Protoc*. (2012) 7:562–78. doi: 10.1038/nprot.2012.016

117. Kim MS, Pinto SM, Getnet D, Nirujogi RS, Manda SS, Chaerkady R, et al. A draft map of the human proteome. *Nature*. (2014) 509:575–81. doi: 10.1038/nature13302

118. Ivanisevic T, Sewduth RN. Multi-omics integration for the design of novel therapies and the identification of novel biomarkers. *Proteomes*. (2023) 11:34. doi: 10.3390/proteomes11040034

119. Lapuente-Santana O, van Genderen M, Hilbers PAJ, Finotello F, Eduati F. Interpretable systems biomarkers predict response to immune-checkpoint inhibitors. *Patterns (N Y)*. (2021) 2:100293. doi: 10.1016/j.patter.2021.100293

120. Hasin Y, Seldin M, Lusis A. Multi-omics approaches to disease. *Genome Biol*. (2017) 18:83. doi: 10.1186/s13059-017-1215-1

121. Scarpa JR, Elemento O. Multi-omic molecular profiling and network biology for precision anaesthesiology: a narrative review. *Br J Anaesth*. (2023) 131:26–36. doi: 10.1016/j.bja.2023.03.006

122. Sun YV, Hu YJ. Integrative analysis of multi-omics data for discovery and functional studies of complex human diseases. *Adv Genet*. (2016) 93:147–90. doi: 10.1016/bs.adgen.2015.11.004

123. Subramanian I, Verma S, Kumar S, Jere A, Anamika K. Multi-omics data integration, interpretation, and its application. *Bioinform Biol Insights*. (2020) 14:1177932219899051. doi: 10.1177/1177932219899051

124. Rautenstrauch P, Vlot AHC, Saran S, Ohler U. Intricacies of single-cell multi-omics data integration. *Trends Genet*. (2022) 38:128–39. doi: 10.1016/j.tig.2021.08.012

125. Das T, Andrieux G, Ahmed M, Chakraborty S. Integration of online omics-data resources for cancer research. *Front Genet*. (2020) 11:578345. doi: 10.3389/fgene.2020.578345

126. Acosta JN, Falcone GJ, Rajpurkar P, Topol EJ. Multimodal biomedical AI. *Nat Med*. (2022) 28:1773–84. doi: 10.1038/s41591-022-01981-2

127. Cai Z, Poulos RC, Liu J, Zhong Q. Machine learning for multi-omics data integration in cancer. *iScience*. (2022) 25:103798. doi: 10.1016/j.isci.2022.103798

128. Wu X, Li W, Tu H. Big data and artificial intelligence in cancer research. *Trends Cancer*. (2024) 10:147–60. doi: 10.1016/j.trecan.2023.10.006

129. Haas R, Zelezniak A, Iacovacci J, Kamrad S, Townsend S, Ralser M. Designing and interpreting 'multi-omic' experiments that may change our understanding of biology. *Curr Opin Syst Biol*. (2017) 6:37–45. doi: 10.1016/j.coisb.2017.08.009

130. Wang XY, Qu HZ, Fang XD. Omics big data and medical artificial intelligence. *Yi Chuan*. (2021) 43:930–7. doi: 10.16288/j.yczz.21-215

131. Xu Y, Liu X, Cao X, Huang C, Liu E, Qian S, et al. Artificial intelligence: A powerful paradigm for scientific research. *Innovation (Camb)*. (2021) 2:100179. doi: 10.1016/j.xinn.2021.100179

132. Glass DR, Tsai AG, Oliveria JP, Hartmann FJ, Kimmey SC, Calderon AA, et al. An integrated multi-omic single-cell atlas of human B cell identity. *Immunity*. (2020) 53:217–32 e5. doi: 10.1016/j.immuni.2020.06.013

133. Mann M, Kumar C, Zeng WF, Strauss MT. Artificial intelligence for proteomics and biomarker discovery. *Cell Syst*. (2021) 12:759–70. doi: 10.1016/j.cels.2021.06.006

134. Adeoye J, Su YX. Artificial intelligence in salivary biomarker discovery and validation for oral diseases. *Oral Dis*. (2024) 30:23–37. doi: 10.1111/odi.14641

135. He X, Liu X, Zuo F, Shi H, Jing J. Artificial intelligence-based multi-omics analysis fuels cancer precision medicine. *Semin Cancer Biol*. (2023) 88:187–200. doi: 10.1016/j.semcancer.2022.12.009

136. Swanson K, Wu E, Zhang A, Alizadeh AA, Zou J. From patterns to patients: Advances in clinical machine learning for cancer diagnosis, prognosis, and treatment. *Cell*. (2023) 186:1772–91. doi: 10.1016/j.cell.2023.01.035

137. Fridley BL, Lund S, Jenkins GD, Wang L. A Bayesian integrative genomic model for pathway analysis of complex traits. *Genet Epidemiol*. (2012) 36:352–9. doi: 10.1002/gepi.2012.36.issue-4

138. Mankoo PK, Shen R, Schultz N, Levine DA, Sander C. Time to recurrence and survival in serous ovarian tumors predicted from integrated genomic profiles. *PloS One*. (2011) 6:e24709. doi: 10.1371/journal.pone.0024709

139. Shen R, Mo Q, Schultz N, Seshan VE, Olshen AB, Huse J, et al. Integrative subtype discovery in glioblastoma using iCluster. *PloS One*. (2012) 7:e35236. doi: 10.1371/journal.pone.0035236

140. Holzinger ER, Dudek SM, Frase AT, Pendergrass SA, Ritchie MD. ATHENA: the analysis tool for heritable and environmental network associations. *Bioinformatics*. (2014) 30:698–705. doi: 10.1093/bioinformatics/btt572

141. Kim S, Yeganova L, Comeau DC, Wilbur WJ, Lu Z. PubMed Phrases, an open set of coherent phrases for searching biomedical literature. *Sci Data*. (2018) 5:180104. doi: 10.1038/sdata.2018.104

142. Turner SD, Dudek SM, Ritchie MD. ATHENA: A knowledge-based hybrid backpropagation-grammatical evolution neural network algorithm for discovering epistasis among quantitative trait Loci. *BioData Min*. (2010) 3:5. doi: 10.1186/1756-0381-3-5

143. Wang B, Mezlini AM, Demir F, Fiume M, Tu Z, Brudno M, et al. Similarity network fusion for aggregating data types on a genomic scale. *Nat Methods*. (2014) 11:333–7. doi: 10.1038/nmeth.2810

144. Draghici S, Potter RB. Predicting HIV drug resistance with neural networks. *Bioinformatics*. (2003) 19:98–107. doi: 10.1093/bioinformatics/19.1.98

145. Zhou SL, Yin D, Hu ZQ, Luo CB, Zhou ZJ, Xin HY, et al. A positive feedback loop between cancer stem-like cells and tumor-associated neutrophils controls hepatocellular carcinoma progression. *Hepatology*. (2019) 70:1214–30. doi: 10.1002/hep.30630

146. Yu SJ, Ma C, Heinrich B, Brown ZJ, Sandhu M, Zhang Q, et al. Targeting the crosstalk between cytokine-induced killer cells and myeloid-derived suppressor cells in hepatocellular carcinoma. *J Hepatol*. (2019) 70:449–57. doi: 10.1016/j.jhep.2018.10.040

147. Geh D, Leslie J, Rumney R, Reeves HL, Bird TG, Mann DA. Neutrophils as potential therapeutic targets in hepatocellular carcinoma. *Nat Rev Gastroenterol Hepatol*. (2022) 19:257–73. doi: 10.1038/s41575-021-00568-5

148. Wong L, Bozhilov K, Hernandez B, Kwee S, Chan O, Ellis L, et al. Underlying liver disease and advanced stage liver cancer are associated with elevated neutrophil-lymphocyte ratio. *Clin Mol Hepatol*. (2019) 25:305–16. doi: 10.3350/cmh.2019.0004

149. Yang L, Liu Q, Zhang X, Liu X, Zhou B, Chen J, et al. DNA of neutrophil extracellular traps promotes cancer metastasis via CCDC25. *Nature*. (2020) 583:133–8. doi: 10.1038/s41586-020-2394-6

150. Xiao Y, Cong M, Li J, He D, Wu Q, Tian P, et al. Cathepsin C promotes breast cancer lung metastasis by modulating neutrophil infiltration and neutrophil extracellular trap formation. *Cancer Cell*. (2021) 39:423–37 e7. doi: 10.1016/j.ccell.2020.12.012

151. van der Windt DJ, Sud V, Zhang H, Varley PR, Goswami J, Yazdani HO, et al. Neutrophil extracellular traps promote inflammation and development of hepatocellular carcinoma in nonalcoholic steatohepatitis. *Hepatology*. (2018) 68:1347–60. doi: 10.1002/hep.29914

152. Yang LY, Luo Q, Lu L, Zhu WW, Sun HT, Wei R, et al. Increased neutrophil extracellular traps promote metastasis potential of hepatocellular carcinoma via provoking tumorous inflammatory response. *J Hematol Oncol*. (2020) 13:3. doi: 10.1186/s13045-019-0836-0

153. Meng Y, Ye F, Nie P, Zhao Q, An L, Wang W, et al. Immunosuppressive CD10(+)ALPL(+) neutrophils promote resistance to anti-PD-1 therapy in HCC by mediating irreversible exhaustion of T cells. *J Hepatol*. (2023) 79:1435–49. doi: 10.1016/j.jhep.2023.08.024

154. Gungabeesoon J, Gort-Freitas NA, Kiss M, Bolli E, Messemaker M, Siwicki M, et al. A neutrophil response linked to tumor control in immunotherapy. *Cell*. (2023) 186:1448–64 e20. doi: 10.1016/j.cell.2023.02.032

155. Hirschhorn D, Budhu S, Kraehenbuehl L, Gigoux M, Schroder D, Chow A, et al. T cell immunotherapies engage neutrophils to eliminate tumor antigen escape variants. *Cell*. (2023) 186:1432–47 e17. doi: 10.1016/j.cell.2023.03.007

156. Xue R, Zhang Q, Cao Q, Kong R, Xiang X, Liu H, et al. Liver tumour immune microenvironment subtypes and neutrophil heterogeneity. *Nature*. (2022) 612:141–7. doi: 10.1038/s41586-022-05400-x

157. Wang L, Liu Y, Dai Y, Tang X, Yin T, Wang C, et al. Single-cell RNA-seq analysis reveals BHLHE40-driven pro-tumour neutrophils with hyperactivated glycolysis in pancreatic tumour microenvironment. *Gut*. (2023) 72:958–71. doi: 10.1136/gutjnl-2021-326070

158. Chen S, Saeed A, Liu Q, Jiang Q, Xu H, Xiao GG, et al. Macrophages in immunoregulation and therapeutics. *Signal Transduct Target Ther*. (2023) 8:207. doi: 10.1038/s41392-023-01452-1

159. Mantovani A, Allavena P, Marchesi F, Garlanda C. Macrophages as tools and targets in cancer therapy. *Nat Rev Drug Discovery*. (2022) 21:799–820. doi: 10.1038/s41573-022-00520-5

160. Li X, Yao W, Yuan Y, Chen P, Li B, Li J, et al. Targeting of tumour-infiltrating macrophages via CCL2/CCR2 signalling as a therapeutic strategy against hepatocellular carcinoma. *Gut*. (2017) 66:157–67. doi: 10.1136/gutjnl-2015-310514

161. Gordon SR, Maute RL, Dulken BW, Hutter G, George BM, McCracken MN, et al. PD-1 expression by tumour-associated macrophages inhibits phagocytosis and tumour immunity. *Nature*. (2017) 545:495–9. doi: 10.1038/nature22396

162. Lu LG, Zhou ZL, Wang XY, Liu BY, Lu JY, Liu S, et al. PD-L1 blockade liberates intrinsic antitumourigenic properties of glycolytic macrophages in hepatocellular carcinoma. *Gut*. (2022) 71:2551–60. doi: 10.1136/gutjnl-2021-326350

163. Sprinzl MF, Puschnik A, Schlitter AM, SChad A, Ackermann K, Esposito I, et al. Sorafenib inhibits macrophage-induced growth of hepatoma cells by interference with insulin-like growth factor-1 secretion. *J Hepatol*. (2015) 62:863–70. doi: 10.1016/j.jhep.2014.11.011

164. Yu J, Green MD, Li S, Sun Y, Journey SN, Choi JE, et al. Liver metastasis restrains immunotherapy efficacy via macrophage-mediated T cell elimination. *Nat Med*. (2021) 27:152–64. doi: 10.1038/s41591-020-1131-x

165. Zhu Y, Yang J, Xu D, Gao XM, Zhang Z, Hsu JL, et al. Disruption of tumour-associated macrophage trafficking by the osteopontin-induced colony-stimulating factor-1 signalling sensitises hepatocellular carcinoma to anti-PD-L1 blockade. *Gut*. (2019) 68:1653–66. doi: 10.1136/gutjnl-2019-318419

166. Giraud J, Chalopin D, Ramel E, Boyer T, Zouine A, Derieppe MA, et al. THBS1(+) myeloid cells expand in SLD hepatocellular carcinoma and contribute to immunosuppression and unfavorable prognosis through TREM1. *Cell Rep*. (2024) 43:113773. doi: 10.1016/j.celrep.2024.113773

167. Ho DW, Tsui YM, Chan LK, Sze KM, Zhang X, Cheu JW, et al. Single-cell RNA sequencing shows the immunosuppressive landscape and tumor heterogeneity of HBV-associated hepatocellular carcinoma. *Nat Commun*. (2021) 12:3684. doi: 10.1038/s41467-021-24010-1

168. Hao X, Zheng Z, Liu H, Zhang Y, Kang J, Kong X, et al. Inhibition of APOC1 promotes the transformation of M2 into M1 macrophages via the ferroptosis pathway and enhances anti-PD1 immunotherapy in hepatocellular carcinoma based on single-cell RNA sequencing. *Redox Biol*. (2022) 56:102463. doi: 10.1016/j.redox.2022.102463

169. Del Prete A, Salvi V, Soriani A, Laffranchi M, Sozio F, Bosisio D, et al. Dendritic cell subsets in cancer immunity and tumor antigen sensing. *Cell Mol Immunol*. (2023) 20:432–47. doi: 10.1038/s41423-023-00990-6

170. Suthen S, Lim CJ, Nguyen PHD, Dutertre CA, Lai HLH, Wasser M, et al. Hypoxia-driven immunosuppression by Treg and type-2 conventional dendritic cells in HCC. *Hepatology*. (2022) 76:1329–44. doi: 10.1002/hep.32419

171. Akkaya B, Oya Y, Akkaya M, Al Souz J, Holstein AH, Kamenyeva O, et al. Regulatory T cells mediate specific suppression by depleting peptide-MHC class II from dendritic cells. *Nat Immunol*. (2019) 20:218–31. doi: 10.1038/s41590-018-0280-2

172. Pang L, Ng KT, Liu J, Yeung WO, Zhu J, Chiu TS, et al. Plasmacytoid dendritic cells recruited by HIF-1alpha/eADO/ADORA1 signaling induce immunosuppression in hepatocellular carcinoma. *Cancer Lett*. (2021) 522:80–92. doi: 10.1016/j.canlet.2021.09.022

173. Pedroza-Gonzalez A, Zhou G, Vargas-Mendez E, Boor PP, Mancham S, Verhoef C, et al. Tumor-infiltrating plasmacytoid dendritic cells promote immunosuppression by Tr1 cells in human liver tumors. *Oncoimmunology*. (2015) 4:e1008355. doi: 10.1080/2162402X.2015.1008355

174. Chen C, Ma YH, Zhang YT, Zhang F, Zhou N, Wang X, et al. Effect of dendritic cell-based immunotherapy on hepatocellular carcinoma: A systematic review and meta-analysis. *Cytotherapy*. (2018) 20:975–89. doi: 10.1016/j.jcyt.2018.06.002

175. Xiao Z, Li T, Zheng X, Lin L, Wang X, Li B, et al. Nanodrug enhances post-ablation immunotherapy of hepatocellular carcinoma via promoting dendritic cell maturation and antigen presentation. *Bioact Mater*. (2023) 21:57–68. doi: 10.1016/j.bioactmat.2022.07.027

176. Zhang D, Lin Z, Wu M, Cai Z, Zheng Y, He L, et al. Cytosolic delivery of thiolated neoantigen nano-vaccine combined with immune checkpoint blockade to boost anti-cancer T cell immunity. *Adv Sci (Weinh)*. (2021) 8:2003504. doi: 10.1002/advs.202003504

177. Lu Z, Zuo B, Jing R, Gao X, Rao Q, Liu Z, et al. Dendritic cell-derived exosomes elicit tumor regression in autochthonous hepatocellular carcinoma mouse models. *J Hepatol*. (2017) 67:739–48. doi: 10.1016/j.jhep.2017.05.019

178. Maier B, Leader AM, Chen ST, Tung N, Chang C, LeBerichel J, et al. A conserved dendritic-cell regulatory program limits antitumour immunity. *Nature*. (2020) 580:257–62. doi: 10.1038/s41586-020-2134-y

179. Magen A, Hamon P, Fiaschi N, Soong BY, Park MD, Mattiuz R, et al. Intratumoral dendritic cell-CD4(+) T helper cell niches enable CD8(+) T cell differentiation following PD-1 blockade in hepatocellular carcinoma. *Nat Med*. (2023) 29:1389–99. doi: 10.1038/s41591-023-02345-0

180. Chuah S, Lee J, Song Y, Kim HD, Wasser M, Kaya NA, et al. Uncoupling immune trajectories of response and adverse events from anti-PD-1 immunotherapy in hepatocellular carcinoma. *J Hepatol*. (2022) 77:683–94. doi: 10.1016/j.jhep.2022.03.039

181. Barsch M, Salie H, Schlaak AE, Zhang Z, Hess M, Mayer LS, et al. T-cell exhaustion and residency dynamics inform clinical outcomes in hepatocellular carcinoma. *J Hepatol*. (2022) 77:397–409. doi: 10.1016/j.jhep.2022.02.032

182. Rudloff MW, Zumbo P, Favret NR, Roetman JJ, Detres Roman CR, Erwin MM, et al. Hallmarks of CD8(+) T cell dysfunction are established within hours of tumor antigen encounter before cell division. *Nat Immunol*. (2023) 24:1527–39. doi: 10.1038/s41590-023-01578-y

183. Lim CJ, Lee YH, Pan L, Lai L, Chua C, Wasser M, et al. Multidimensional analyses reveal distinct immune microenvironment in hepatitis B virus-related hepatocellular carcinoma. *Gut*. (2019) 68:916–27. doi: 10.1136/gutjnl-2018-316510

184. Cheng Y, Gunasegaran B, Singh HD, Dutertre CA, Loh CY, Lim JQ, et al. Non-terminally exhausted tumor-resident memory HBV-specific T cell responses correlate with relapse-free survival in hepatocellular carcinoma. *Immunity*. (2021) 54:1825–40 e7. doi: 10.1016/j.immuni.2021.06.013

185. Sun L, Su Y, Jiao A, Wang X, Zhang B. T cells in health and disease. *Signal Transduct Target Ther*. (2023) 8:235. doi: 10.1038/s41392-023-01471-y

186. Borst J, Ahrends T, Babala N, Melief CJM, Kastenmuller W. CD4(+) T cell help in cancer immunology and immunotherapy. *Nat Rev Immunol*. (2018) 18:635–47. doi: 10.1038/s41577-018-0044-0

187. Ruterbusch M, Pruner KB, Shehata L, Pepper M. *In vivo* CD4(+) T cell differentiation and function: revisiting the th1/th2 paradigm. *Annu Rev Immunol*. (2020) 38:705–25. doi: 10.1146/annurev-immunol-103019-085803

188. Zhang JP, Yan J, Xu J, Pang XH, Chen MS, Li L, et al. Increased intratumoral IL-17-producing cells correlate with poor survival in hepatocellular carcinoma patients. *J Hepatol*. (2009) 50:980–9. doi: 10.1016/j.jhep.2008.12.033

189. Song M, Wang L, Jiang S, Liang J, Li W, Rao W, et al. Pathogenic Th17 cell-mediated liver fibrosis contributes to resistance to PD-L1 antibody immunotherapy in hepatocellular carcinoma. *Int Immunopharmacol*. (2024) 129:111601. doi: 10.1016/j.intimp.2024.111601

190. Fu J, Xu D, Liu Z, Shi M, Zhao P, Fu B, et al. Increased regulatory T cells correlate with CD8 T-cell impairment and poor survival in hepatocellular carcinoma patients. *Gastroenterology*. (2007) 132:2328–39. doi: 10.1053/j.gastro.2007.03.102

191. Gao Q, Qiu SJ, Fan J, Zhou J, Wang XY, Xiao YS, et al. Intratumoral balance of regulatory and cytotoxic T cells is associated with prognosis of hepatocellular carcinoma after resection. *J Clin Oncol*. (2007) 25:2586–93. doi: 10.1200/JCO.2006.09.4565

192. Zhu AX, Abbas AR, de Galarreta MR, Guan Y, Lu S, Koeppen H, et al. Molecular correlates of clinical response and resistance to atezolizumab in combination with bevacizumab in advanced hepatocellular carcinoma. *Nat Med*. (2022) 28:1599–611. doi: 10.1038/s41591-022-01868-2

193. Khan O, Giles JR, McDonald S, Manne S, Ngiow SF, Patel KP, et al. TOX transcriptionally and epigenetically programs CD8(+) T cell exhaustion. *Nature*. (2019) 571:211–8. doi: 10.1038/s41586-019-1325-x

194. McLane LM, Abdel-Hakeem MS, Wherry EJ. CD8 T cell exhaustion during chronic viral infection and cancer. *Annu Rev Immunol*. (2019) 37:457–95. doi: 10.1146/annurev-immunol-041015-055318

195. Jiang D, Huang A, Zhu BX, Gong J, Ruan YH, Liu XC, et al. Targeting CD93 on monocytes revitalizes antitumor immunity by enhancing the function and infiltration of CD8(+) T cells. *J Immunother Cancer*. (2024) 12:e010148. doi: 10.1136/jitc-2024-010148

196. Laumont CM, Banville AC, Gilardi M, Hollern DP, Nelson BH. Tumour-infiltrating B cells: immunological mechanisms, clinical impact and therapeutic opportunities. *Nat Rev Cancer*. (2022) 22:414–30. doi: 10.1038/s41568-022-00466-1

197. Kurebayashi Y, Ojima H, Tsujikawa H, Kubota N, Maehara J, Abe Y, et al. Landscape of immune microenvironment in hepatocellular carcinoma and its additional impact on histological and molecular classification. *Hepatology*. (2018) 68:1025–41. doi: 10.1002/hep.29904

198. Calderaro J, Petitprez F, Becht E, Laurent A, Hirsch TZ, Rousseau B, et al. Intra-tumoral tertiary lymphoid structures are associated with a low risk of early recurrence of hepatocellular carcinoma. *J Hepatol*. (2019) 70:58–65. doi: 10.1016/j.jhep.2018.09.003

199. Fridman WH, Meylan M, Pupier G, Calvez A, Hernandez I, Sautes-Fridman C. Tertiary lymphoid structures and B cells: An intratumoral immunity cycle. *Immunity*. (2023) 56:2254–69. doi: 10.1016/j.immuni.2023.08.009

200. Barrow F, Khan S, Wang H, Revelo XS. The emerging role of B cells in the pathogenesis of NAFLD. *Hepatology*. (2021) 74:2277–86. doi: 10.1002/hep.31889

201. Shao Y, Lo CM, Ling CC, Liu XB, Ng KT, Chu AC, et al. Regulatory B cells accelerate hepatocellular carcinoma progression via CD40/CD154 signaling pathway. *Cancer Lett*. (2014) 355:264–72. doi: 10.1016/j.canlet.2014.09.026

202. Li Y, Huang H, Wang Q, Zheng X, Zhou Y, Kong X, et al. Identification of prognostic risk model based on plasma cell markers in hepatocellular carcinoma through single-cell sequencing analysis. *Front Genet*. (2024) 15:1363197. doi: 10.3389/fgene.2024.1363197

203. Sharma A, Seow JJW, Dutertre CA, Pai R, Bleriot C, Mishra A, et al. Onco-fetal reprogramming of endothelial cells drives immunosuppressive macrophages in hepatocellular carcinoma. *Cell*. (2020) 183:377–94 e21. doi: 10.1016/j.cell.2020.08.040

204. Ruf B, Heinrich B, Greten TF. Immunobiology and immunotherapy of HCC: spotlight on innate and innate-like immune cells. *Cell Mol Immunol*. (2021) 18:112–27. doi: 10.1038/s41423-020-00572-w

205. Sun C, Xu J, Huang Q, Huang M, Wen H, Zhang C, et al. High NKG2A expression contributes to NK cell exhaustion and predicts a poor prognosis of patients with liver cancer. *Oncoimmunology*. (2017) 6:e1264562. doi: 10.1080/2162402X.2016.1264562

206. Sun H, Huang Q, Huang M, Wen H, Lin R, Zheng M, et al. Human CD96 correlates to natural killer cell exhaustion and predicts the prognosis of human hepatocellular carcinoma. *Hepatology*. (2019) 70:168–83. doi: 10.1002/hep.30347

207. Guo X, Tan S, Wang T, Sun R, Li S, Tian P, et al. NAD + salvage governs mitochondrial metabolism, invigorating natural killer cell antitumor immunity. *Hepatology*. (2023) 78:468–85. doi: 10.1002/hep.32658

208. Mantovani S, Oliviero B, Varchetta S, Mele D, Mondelli MU. Natural killer cell responses in hepatocellular carcinoma: implications for novel immunotherapeutic approaches. *Cancers (Basel)*. (2020) 12:926. doi: 10.3390/cancers12040926

209. Vallera DA, Felices M, McElmurry R, McCullar V, Zhou X, Schmohl JU, et al. IL15 trispecific killer engagers (TriKE) make natural killer cells specific to CD33+ Targets while also inducing persistence, *in vivo* expansion, and enhanced function. *Clin Cancer Res*. (2016) 22:3440–50. doi: 10.1158/1078-0432.CCR-15-2710

210. Davis ZB, Vallera DA, Miller JS, Felices M. Natural killer cells unleashed: Checkpoint receptor blockade and BiKE/TriKE utilization in NK-mediated anti-tumor immunotherapy. *Semin Immunol*. (2017) 31:64–75. doi: 10.1016/j.smim.2017.07.011

211. Chan WK, Kang S, Youssef Y, Glankler EN, Barrett ER, Carter AM, et al. A CS1-NKG2D bispecific antibody collectively activates cytolytic immune cells against multiple myeloma. *Cancer Immunol Res*. (2018) 6:776–87. doi: 10.1158/2326-6066.CIR-17-0649

212. Xiao L, Cen D, Gan H, Sun Y, Huang N, Xiong H, et al. Adoptive transfer of NKG2D CAR mRNA-engineered natural killer cells in colorectal cancer patients. *Mol Ther*. (2019) 27:1114–25. doi: 10.1016/j.ymthe.2019.03.011

213. Lee JH, Lee JH, Lim YS, Yeon JE, Song TJ, Yu SJ, et al. Adjuvant immunotherapy with autologous cytokine-induced killer cells for hepatocellular carcinoma. *Gastroenterology*. (2015) 148:1383–91 e6. doi: 10.1053/j.gastro.2015.02.055

214. Curio S, Belz GT. The unique role of innate lymphoid cells in cancer and the hepatic microenvironment. *Cell Mol Immunol*. (2022) 19:1012–29. doi: 10.1038/s41423-022-00901-1

215. He Y, Luo J, Zhang G, Jin Y, Wang N, Lu J, et al. Single-cell profiling of human CD127(+) innate lymphoid cells reveals diverse immune phenotypes in hepatocellular carcinoma. *Hepatology*. (2022) 76:1013–29. doi: 10.1002/hep.32444

216. Heinrich B, Gertz EM, Schaffer AA, Craig A, Ruf B, Subramanyam V, et al. The tumour microenvironment shapes innate lymphoid cells in patients with hepatocellular carcinoma. *Gut*. (2022) 71:1161–75. doi: 10.1136/gutjnl-2021-325288

217. Chen C, Wang Z, Ding Y, Qin Y. Tumor microenvironment-mediated immune evasion in hepatocellular carcinoma. *Front Immunol*. (2023) 14:1133308. doi: 10.3389/fimmu.2023.1133308

218. Santhakumar C, Gane EJ, Liu K, McCaughan GW. Current perspectives on the tumor microenvironment in hepatocellular carcinoma. *Hepatol Int*. (2020) 14:947–57. doi: 10.1007/s12072-020-10104-3

frontiers | Frontiers in Oncology

TYPE Original Research
PUBLISHED 10 January 2025
DOI 10.3389/fonc.2024.1511958

OPEN ACCESS

EDITED BY
Bing Yang,
Tianjin Medical University, China

REVIEWED BY
Jun Hu,
Tianjin Medical University Cancer Institute and Hospital, China
Liwei Zheng,
University of Colorado Anschutz Medical Campus, United States

*CORRESPONDENCE
Shibing Cao
doc99cao@sina.com
Taiyang Zhu
343155405@qq.com
Xindong Yin
yinxindong1226@sina.com

†These authors have contributed equally to this work and share first authorship

RECEIVED 15 October 2024
ACCEPTED 19 December 2024
PUBLISHED 10 January 2025

CITATION
Xing W, Zhou Y, Long Q, Yi N, Wang G, Shi R, Huang J, Yin X, Zhu T and Cao S (2025) Multiomic analysis of lactylation and mitochondria-related genes in hepatocellular carcinoma identified MRPL3 as a new prognostic biomarker.
Front. Oncol. 14:1511958.
doi: 10.3389/fonc.2024.1511958

Multiomic analysis of lactylation and mitochondria-related genes in hepatocellular carcinoma identified MRPL3 as a new prognostic biomarker

Wenya Xing[1†], Yuanzi Zhou[1†], Qiuzi Long[2†], Nan Yi[1], Gaoyuan Wang[1], Rongwei Shi[3], Jinlong Huang[2], Xindong Yin[1*], Taiyang Zhu[1*] and Shibing Cao[1*]

[1]Department of General Surgery, Affiliated Hospital of Nanjing University of Chinese Medicine, Jiangsu Province Hospital of Chinese Medicine, Nanjing, China, [2]Nanjing University of Chinese Medicine, Nanjing, China, [3]Department of General Internal Medicine, Affiliated Hospital of Nanjing University of Chinese Medicine, Jiangsu Province Hospital of Chinese Medicine, Nanjing, China

Background: Recent research has highlighted lactate's crucial role in epigenetic regulation, particularly by influencing histone modifications that drive the initiation and progression of hepatocellular carcinoma (HCC). While mitochondria are known to regulate tumor behavior, the interaction between lactate metabolism and mitochondrial function in cancer tissues remains underexplored. Understanding this relationship may provide deeper insights into tumor metabolic reprogramming and reveal novel therapeutic targets for HCC and other malignancies.

Methods: We conducted a comprehensive screening of lactylation- and mitochondria-associated genes (LMRGs) in HCC patients, followed by clustering based on these genes. Prognostic outcomes and pathway enrichment were analyzed across the identified clusters. Additionally, we developed a prognostic model based on LMRGs, examining its implications for survival, immune response, and drug sensitivity. *In vitro* experiments were performed to validate the expression patterns and functional role of MRPL3 in HCC.

Results: We developed a prognostic model, named the LMRG model, incorporating three key genes: ACACA, MRPL3, and MRPS23. This model revealed significant differences in survival outcomes, immune responses, and drug sensitivity between patients with high and low LMRG scores. MRPL3 was found to be overexpressed in HCC, playing a critical role in tumor growth and metastasis. These results were further validated through *in vitro* experiments, confirming MRPL3's role in HCC cell proliferation and invasion.

Conclusion: We created a predictive model, LMRG, and identified MRPL3 as a key biomarker. Our findings suggest that MRPL3 has significant potential as a reliable predictive biomarker for clinical applications in HCC diagnosis and treatment.

KEYWORDS

hepatocellular carcinoma, lactylation, epigenetic regulation, MRPL3, prognostic biomarkers

1 Introduction

As of 2022, primary liver cancer ranks as the sixth most prevalent cancer and the third leading cause of cancer-related deaths globally (1). The predominant subtype of primary liver cancer is hepatocellular carcinoma (HCC), followed by cholangiocarcinoma (CC) (2, 3). The primary risk factors for HCC include chronic infections with hepatitis B virus (HBV) and hepatitis C virus (HCV), as well as alcoholic and non-alcoholic fatty liver diseases (4). Although surgery remains the main treatment for HCC, recurrence and metastasis are common challenges (5). Ablation therapies, such as microwave ablation (MWA), are effective for early-stage HCC (6). Other treatment modalities, including intra-arterial therapy, radiotherapy, and systemic therapies (standard cytotoxic chemotherapy, targeted therapy), offer additional options but are often hindered by drug resistance, hepatic impairment, and tumor resilience mechanisms (7, 8).

The limitations of current therapeutic approaches underscore a critical need to delve deeper into the gene regulatory mechanisms underlying HCC. For instance, resistance to chemotherapy and radiotherapy is frequently linked to dysregulated signaling pathways and epigenetic modifications that enable tumor progression and survival under treatment pressures (9). Moreover, understanding how HCC evolves in the context of its complex etiology and microenvironment could provide novel insights into therapeutic vulnerabilities. Thus, exploring gene regulatory networks is not only vital for uncovering the molecular underpinnings of HCC but also for identifying biomarkers for early diagnosis and developing targeted therapies that circumvent resistance.

In recent years, lactate and mitochondrial function have emerged as critical factors influencing cancer biology, including HCC. While lactate accumulation is a hallmark of altered tumor metabolism under the Warburg effect (10), mitochondria, despite reduced reliance on oxidative phosphorylation in many tumors, remain pivotal in producing reactive oxygen species (ROS) and supporting biosynthetic pathways essential for rapid tumor growth (11). These two elements are intricately linked through metabolic signaling networks, highlighting their potential role in HCC progression and therapeutic resistance.

Lactate, traditionally seen as a glycolysis byproduct, plays a critical role in cancer metabolism. The Warburg effect highlights tumor cells' reliance on glycolysis, leading to elevated lactate production (10, 12). Beyond metabolism, lactate acts as a regulatory molecule influencing immune modulation (12) and histone lysine lactylation, which translates metabolic signals into transcriptional changes (13, 14). In HCC, Gao et al. showed that K28 lactylation promotes proliferation and metastasis by inhibiting adenylate kinase 2 (AK2) (15), while Xu et al. found that Demethylzeylasteral (DML) suppresses H3K9la and H3K56la lactylation, inhibiting HCC progression (16). Bioinformatics studies by Chen et al. revealed that lactylation-related genes predict HCC prognosis, immunity, mutations, and drug sensitivity (17). These findings position lactylation as a promising epigenetic target in cancer research.

Mitochondria are vital for ATP production via oxidative phosphorylation and play key roles in respiration, metabolism, and apoptosis (18). Their genome encodes components of the electron transport chain (ETC), a major source of reactive oxygen species (ROS), which trigger signaling pathways, promote proliferation, and drive tumor progression (19, 20). The interplay between glycolysis and mitochondrial metabolism regulates tumor microenvironment adaptation, with glycolysis-derived lactate altering mitochondrial functions and mitochondria-generated ROS influencing histone lactylation. Oncogenic factors like c-Myc, HIF-1α, PI3K/Akt, and p53 modulate these interactions, linking mitochondria to HCC progression and therapy resistance (21–24). Prognostic models using mitochondria-related genes, such as those by Zhang B et al. (eight genes) and another study (six genes), highlight mitochondria's critical role in HCC diagnostics and therapeutics (25, 26).

Pyruvate from glycolysis is converted to lactate under hypoxia, creating an immunosuppressive environment and promoting cancer growth. Lactate also modifies histone lysines, regulating gene expression (27). Leah I. Susser et al. showed that mitochondrial fragmentation increases lactate, driving histone lactylation and M2-like macrophage responses (28), demonstrating a bidirectional link between lactate and mitochondrial dynamics. This highlights a bidirectional relationship where glycolytic intermediates such as lactate influence mitochondrial dynamics, and mitochondrial processes

modulate epigenetic reprogramming through lactylation. Thompson's group revealed lactate activates the electron transport chain in mitochondria, boosting ATP production (29). Jingwei Ma et al. found lithium carbonate enhances T-cell anti-tumor activity by driving lactic acid into mitochondria. However, research on lactylation and mitochondria in HCC remains scarce.

First, we screened for genes associated with lactylation and mitochondria, termed LMRGs and analyzed their differential expression across databases such as The Cancer Genome Atlas (TCGA), Gene Expression Omnibus (GEO), and the International Cancer Genome Consortium (ICGC). Using least absolute shrinkage and selection operator (LASSO) regression, we established an LMRG model to identify prognosis-related genes. We then performed mutational, immunological, and drug sensitivity analyses. Additionally, we selected a key gene, MRPL3, from the model for clinical and immune correlation analyses. By linking lactylation and mitochondrial functions, we aimed to unveil novel regulatory mechanisms and identify actionable biomarkers for HCC, addressing critical gaps in existing research.

2 Materials and methods

2.1 The source of the LMRGs

Zhao Y et al. first identified histone lactylation and its regulatory role in cellular functions (13). Based on their findings, lactylation-related genes were identified by extracting genes directly reported to be involved in lactylation processes or significantly impacted by lactylation in their study. These genes were included based on their functional relevance to lactylation, as demonstrated through experimental evidence or validated mechanisms. For mitochondria-related genes, we utilized the Human MitoCarta3.0 database, a comprehensive resource cataloging mitochondrial proteins and pathways (30), available at https://www.broadinstitute.org/mitocarta/mitocarta30-inventory-mammalian-mitochondrial-proteins-and-pathways. Genes annotated as mitochondrial components or pathways in MitoCarta3.0 were selected for further analysis. To define the lactylation-mitochondria-related genes (LMRGs), we intersected the identified lactylation-related gene set with the mitochondria-related gene set. This intersection highlighted genes simultaneously associated with lactylation and mitochondrial functions.

2.2 Collection of analytical data

We retrieved expression and clinical data about HCC from multiple sources, including TCGA (https://portal.gdc.cancer.gov/), GEO (https://www.ncbi.nlm.nih.gov/geo/), and ICGC (https://dcc.icgc.org/). TCGA's dataset was notably supplemented with mutation data and copy number variation (CNV) information. The expression and clinical data were subsequently integrated into a matrix file using Strawberry Perl software (version 5.30.0.1). Data for pan-cancer were sourced from the University of California Santa Cruz Xena browser (UCSC Xena) database (http://xena.ucsc.edu/), RNAseq data in TCGA and Genotype-Tissue Expression (GTEx) in TPM format and their corresponding normal tissue data were processed uniformly by the Toil program (31). We have organized the data used and presented it in a tabular form (Table 1).

2.3 Recognition of differentially expressed LMRGs

The differentially expressed genes between normal and tumor tissues from TCGA and GEO were identified by the "limma" R package, we set the cutoff criteria for significant fold changes and false discovery rates (FDR) to ensure robust identification of key genes. Specifically, genes with a fold change ($|\log FC|$) > 2 or< 0.5 and an FDR< 0.05 were considered significant. These thresholds were chosen based on widely accepted standards in transcriptomic analysis and were further validated for consistency with the biological relevance of identified genes. Take the intersection of DEGs and LMRGs to get the final differentially expressed LMRGs (DE-LMRGs). For the identified DE-LMRGs, we conducted tumor mutation burden (TMB) analysis by TCGA dataset. The frequency of CNV in DE-LMRGs was calculated based on gene copy number gain and deletion. A functional enrichment analysis of DE-LMRGs was conducted, encompassing Gene Ontology (GO) and Kyoto Encyclopedia of Genes and Genomes (KEGG) analysis, utilizing the "clusterProfiler" R package.

2.4 Clustering analysis on the basis of DE-LMRGs

The TCGA and GEO expression and survival data were merged and batch effects were removed using the "ComBat function" of the "SVA" R package. Based on the DE-LMRGs, we conducted a clustering analysis of the merged data by the "ConsensusClusterPlus" R package, the HCC patients were thus classified into different LMRG clusters. To verify the accuracy of the clustering, Principal Component Analysis (PCA) was performed to show the overall differences between different clusters. We analyzed the survival differences between patients in different clusters and plotted the survival curves using the "survival" R package. By the "pheatmap" R package, a heatmap of gene expression linked to clinical information was created. Gene Set Variation Analysis (GSVA) based on the "c2.cp.kegg.symbols.gmt" gene set was performed to explore the functional pathways of HCC between different clusters. To determine the immune cell content between different clusters, Single Sample Gene Set Enrichment Analysis (ssGSEA) was subsequently conducted. Both processes are realized by the "GSVA" and "GSEABase" R packages.

2.5 Construction and validation of the LMRG prognostic model

In order to further explore the role of LMRGs on prognosis, we developed the LMRG score. Regarding the clinical features of HCC, univariate Cox (uniCox) analysis was performed on the merged

TABLE 1 The clinical features of HCC patients from TCGA, GEO, and ICGC datasets.

Clinical features	Total patients(851)		TCGA(424)		GSE76427(167)		ICGC(260)	
	Number	Percentage (%)	Number	Percentage (%)	Number	Percentage (%)	Number	Percentage (%)
Type								
Tumor	749	88.01%	374	88.21%	115	68.86%	260	100%
Normal	102	11.99%	50	11.79%	52	31.14%	0	0%
Fustat								
Alive	201	26.73%	132	35.01%	23	20.00%	46	17.69%
Dead	551	73.27%	245	64.99%	92	80.00%	214	82.31%
Age								
≤65	398	52.93%	235	62.33%	65	56.52%	98	37.69%
>65	353	46.94%	141	37.40%	50	43.48%	162	62.31%
Unknown	1	0.13%	1	0.27%	0	0%	0	0%
Gender								
Female	212	28.19%	122	32.36%	22	19.13%	68	26.15%
Male	540	71.81%	255	67.64%	93	80.87%	192	73.85%
Stage								
I-II	509	67.69%	262	69.50%	90	78.26%	157	60.38%
III-IV	219	29.12%	91	24.14%	25	21.74%	103	39.62%
Unknown	24	3.19%	24	6.37%	0	0%	0	0%

data. Then, we added the ICGC data as an external test set and the merged data as an internal training set to build the LMRG model using LASSO regression, subsequently the LMRG score is calculated according to the following formula:

$$LMRG\ \ Score = \sum coef\ (LMRGs)\ \times\ exp\ (LMRGs)$$

The median LMRG score was used to stratify HCC patients into high- and low-LMRG-score groups. Subsequently, risk plots and expression heatmaps were constructed, leveraging the prognosis-related LMRGs, to facilitate a more intuitive understanding of the disparities in gene expression profiles between the distinct LMRG groups. We did Kaplan-Meier (KM) analysis using the "survminer" and "survival" R packages.

The Receiver Operating Characteristic (ROC) curve was employed to demonstrate the predictive capacity of the model, and Principal Component Analysis (PCA) and t-distribution Stochastic Neighbor Embedding (t-SNE) were designed to better distinguish different LMRG groups, which were implemented by the "timeROC" and "Rtsne" R packages, respectively.

2.6 Prognosis analysis of the clinical

To ascertain the correlation between the LMRG score and clinical status, we performed both uniCox and multivariate Cox (muiCox) analyses. Subsequently, the LMRG score of HCC patients and their clinical features were finely mapped to 1-, 3-, and 5-year overall survival with the "rms" R package. To validate the precision and reliability of the nomogram for clinical utilization, in-depth calibration curves were generated and analyzed. Furthermore, the discrepancies in LMRG score were examined in relation to various clinical characteristics, which were represented in box-and-line plots.

2.7 Correlation between the LMRG model and LMRG clusters

We investigated the differences in LMRG score between the two clusters to define whether the LMRG model could be applied to clustering. Then, correlations between the LMRG clusters, LMRG score, and survival outcome were assessed and depicted by using the "galluvial" R package.

2.8 PPI network and enrichment analysis

A Protein-Protein Interaction (PPI) network of prognosis-related LMRGs and DE-LMRGs was constructed through the STRING website (https://cn.string-db.org/cgi/input.pl). Furthermore, we performed GO and KEGG enrichment analysis on the prognosis-related LMRGs to elucidate the underlying pathways that are pertinent to our model.

2.9 Immunological and tumor stem cell analysis

Immune cell infiltration levels across all samples were quantitatively assessed utilizing the CIBERSORT algorithm, permitting us to subsequently evaluate the relationship between the LMRG score and derived immune score. The correlations between prognosis-related LMRGs, LMRG score, and immune cells were also analyzed. These steps were visualized through the "ggpubr," "ggplot," and "reshape2" R packages. We scored the tumor microenvironment (TME) by the ESTIMATE algorithm on three dimensions: StromalScore, ImmuneScore, and ESTIMATEScore. And differences in the distributions of high- and low-LMRG-score groups were visually represented and compared using violin plots. In addition, we conducted tumor stem cell correlation analysis of the LMRG model based on RNA stemness scores (RNAss).

2.10 Chemotherapy drug sensitivity analysis

Data on drugs were taken from the Genomics of Drug Sensitivity in Cancer (GDSC) website (https://www.cancerrxgene.org). The half-maximal inhibitory concentration (IC50) was employed to evaluate drug sensitivity between the high- and low-LMRG-score groups using the "oncoPredict" R package.

2.11 Expression and prognostic analysis of MRPL3

We extracted the ENSG00000114686.8 (MRPL3) molecule from the UCSC database, performed $\log2^{(TPM+1)}$ transformation of the expression values, and analyzed the data differences using the "stats" R package. Moreover, we extracted this molecule in the TCGA-ALL database according to the same method and performed a paired-sample difference analysis using the same R package. We obtained the TCGA prognostic dataset (32), excluding samples with a follow-up duration of less than 30 days, and employed the "survival" package to construct a Cox proportional hazards regression model, which aimed to elucidate the correlation between gene expression profiles and prognosis within each tumor type. The outcomes of this analysis were then graphically represented using the "ggplot2" R package.

2.12 Single-cell sequencing analysis of MRPL3

This step was achieved on the Tumor Immunity Single Cell Center 2 (TISCH2) flat (http://tisch.compgenomics.org/home/). The GEO scRNA-seq dataset (GSE140228), which contains 62,530 cells from 5 HCC tissues, was selected for this study, and the scRNA-seq was performed using a 10x Genomics platform. The "NormalizeData" function in "Seurat" was used to normalize the data. The raw count (UMI) in each cell was 10,000.

2.13 Cell culture and tissue collection of HCC

The human hepatic normal cell line (THLE2) and five HCC cell lines (Huh7, Hep3B, HepG2, HCC-LM3, Li-7) for this experiment were cultured using DMEM medium (Gibco, USA) containing 10% fetal bovine serum (BiologicalIndustries, Israel). In addition, 30 pairs of primary HCC tumors and adjacent tissues were collected at Jiangsu Province Hospital of Chinese Medicine (Nanjing, China). The research project was granted ethical approval by the Ethics Committee of Jiangsu Province Hospital of Chinese Medicine (No. 2023NL-132-01), and written informed consent was obtained from all participants.

2.14 Real-time reverse transcriptase PCR

RNA was extracted from tissues and cells using TRIzol reagent (Gibco, USA) and Complementary DNA (cDNA) synthesis was performed using PrimeScript®RT Kit (TaKaRa, Japan). Subsequently, a fluorescent quantitative PCR instrument and primers were used for RT-qPCR analysis of this cDNA, which was repeated thrice per sample.

2.15 Knockdown of MRPL3 via transfection

A specific shRNA, designed to downregulate MRPL3 expression, was synthesized by GenePharma Co., Ltd. (Shanghai, China), with pLKO.1 serving as a control. Lentiviral packaging and transfection were then performed in 293T cells. The concentrated lentivirus, along with hexadimethrine bromide (Beyotime, China), was introduced into HCC cell lines (Hep3B, HCC-LM3). The transfected stable cell lines were selected using puromycin (Solarbio, China). Cell Counting Kit-8 assay (CCK-8).

The cells were categorized into sh-NC, sh-MRPL3 of the Hep3B, and HCC-LM3 after transfection and were uniformly planted in 96-well plates, respectively. After 24h of incubation, 100μl of fresh DMEM medium and 10μl of CCK8 solution were subsequently added to every well. The plates were incubated again for 4h, and then the absorbance at 450nm was measured on an enzyme-linked immunoassay detector (Tecan, Switzerland).

2.16 Flow cytometric apoptosis assay

Hep3B, HCC-LM3 cells were incubated with RNase A and propidium iodide (Sigma, USA) for 15 min at 20°C away from light. Then, the cells were treated with Annexin V-FITC/PI Apoptosis Detection Kit (Roche, Switzerland) in accordance with the instructions provided by the manufacturer. The distribution of

cell cycle phases was ultimately analyzed using flow cytometry (BD, USA), and the apoptosis level was analyzed.

2.17 Western blot assay

Total protein extraction from Hep3B cells and 5 pairs of patients' tissues was conducted using a protein extraction kit (Beyotime, China), and determination of protein concentration was performed by a BCA kit (Beyotime). The extracted proteins were separated on a 10% SDS-PAGE gel and transferred to PVDF membranes (Millipore, USA). The membranes with cell proteins were blocked and incubated with primary antibodies (Cleaved-Caspase3, Cleaved-Caspase9, Bcl-2, E-cadherin, vimentin, GAPDH) overnight, while the membranes with tissue proteins were blocked and incubated with MRPL3 antibody overnight. After incubation with secondary antibodies (Goat anti-rabbit IgG (h+l), HRP), bands were detected by chemiluminescence using an imaging system. All antibodies used were purchased from Affinity Biosciences (USA).

2.18 Wound-healing assay

After spreading Hep3B, HCC-LM3 cells to complete fusion, a line of cells was removed by scratching at the bottom of the culture dish using a sterile gun tip. The influence of cell proliferation was excluded by changing the serum-free medium, and the healing of the scratch was photographed and recorded at predetermined time points (0h, 48h). The capacity of the cells to migrate was evaluated by quantifying the alteration in the width of the scratch.

2.19 Cell migration and invasion assays

Matrigel (BD, USA) was applied to the upper layer of Transwell chambers (Costar, USA) to test the invasive ability of cells; the step is not necessary when detecting cell migration ability. The experimental cell lines were inoculated into the upper layer of Transwell chambers containing serum-free medium, and the lower layer was placed in a 10% FBS medium for chemotaxis. Following a 24-hour incubation period, non-migrating or non-invasive cells were meticulously removed with cotton swabs. Subsequently, methanol was employed to immobilize the remaining cells, which were then stained with crystal violet. Three views of each chamber were selected and counted under a microscope (Olympus, Japan) to quantify the capacity for cell migration and invasion.

2.20 Statistical analysis

The statistical analyses in this study were conducted using R software (version 4.2.1). The specific statistical tests employed include Student's t-test for comparing two groups, one-way ANOVA followed by Tukey's *post hoc* test for multiple group comparisons, and Kaplan-Meier survival analysis with the log-rank test for survival comparisons. The rationale for selecting these tests was to ensure that the methods align with the data distribution and study objectives. For instance, the t-test and ANOVA were chosen based on the assumption of normal distribution, which was verified using the Shapiro-Wilk test prior to analysis. For non-normally distributed data, non-parametric tests such as the Mann-Whitney U test or Kruskal-Wallis test were applied as appropriate.

Additionally, Pearson's or Spearman's correlation analyses were conducted depending on the data distribution to explore relationships between variables. To mitigate the risk of type I errors in multiple comparisons, we applied the Benjamini-Hochberg procedure to adjust p-values when necessary. The statistical significance threshold was set at $p<0.05$ for all tests. Data are presented as mean ± standard deviation (SD) unless otherwise specified. Visualizations, including scatter plots, boxplots, and Kaplan-Meier survival curves, were generated using GraphPad Prism version 9 (GraphPad Software, San Diego, CA, USA) to enhance the clarity and reproducibility of the results.

3 Results

3.1 Identification and functional analysis of lactylation-mitochondria-related genes in HCC

We searched for 1223 lactylation-related genes from the Supplementary file of Zhao's article (33) and 1136 mitochondria-related genes from the MitoCarta website, taking the intersection of the two, and ended up with 82 LMRGs (Figure 1A). The 82 genes identified in this study are presented in detail in Supplementary Table S1. In addition, gene expressions between normal and tumor samples in TCGA and GEO datasets were analyzed separately, resulting in 24,951 differential genes in TCGA and 5,692 differential genes in GSE76427 (Figures 1B, C). Taking the overlap of these differentially expressed genes with LMRG, we finally gained 23 DE-LMRGs (Figure 1D).

To initially explore LMRGs, we first analyzed the TMB and CNV incidence of DE-LMRGs in samples of HCC (Figures 1E, F). As shown in the figure, the mutation frequency of these genes was low and there was no obvious consistency in copy number variation, as we visualized the variation of DE-LMRGs on specific chromosomes (Figure 1G). Next, we analyzed the enrichment, and DE-LMRGs were predominantly enriched within amino acid metabolic process under biological processes (BP); mitochondrial matrix under cellular components (CC), and flavin adenine dinucleotide binging under molecule function (MF) (Figures 1H, I). The predominant enrichment of KEGG pathways was observed in propanoate metabolism and lipoic acid metabolism (Figures 1J, K).

3.2 Clustering analysis and immune profiling of LMRG clusters in HCC

The HCC samples from TCGA and GSE76427 datasets were merged and batch-corrected. After that, we clustered the merged

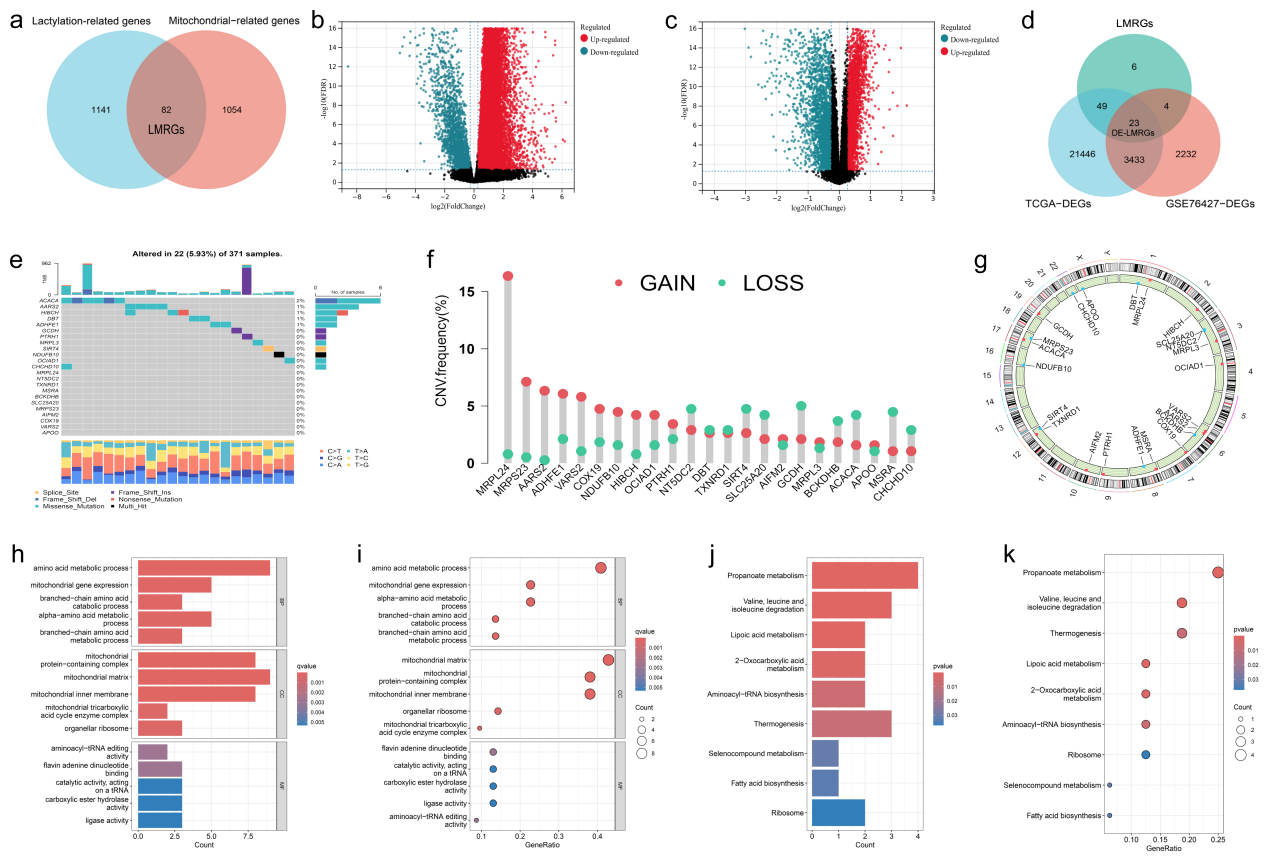

FIGURE 1
Identification and Functional Enrichment Analysis of Lactylation-Mitochondria-Related Genes (LMRGs) in HCC. **(A)** Venn plot of LMRGs. **(B)** Volcano plot of gene expression variation between hepatic normal and HCC tissues in TCGA dataset and **(C)** in GEO dataset. **(D)** Identification of DE-LMRGs. **(E)** Waterfall plot of mutation frequencies and types of DE-LMRGs in HCC. **(F)** Frequency of copy number variation in DE-LMRGs. **(G)** Circos plots of chromosome distributions among DE-LMRGs. **(H, I)** GO enrichment analysis of DE-LMRGs. **(J, K)** KEGG pathway enrichment analysis of DE-LMRGs.

data, and the difference between LMRG clusters was clearest when the number of groups was 2 (Figures 2A, B), and PCA results showed that the samples between the two clusters could be discerned with clarity (Figure 2C). In terms of OS, there were significant differences between LMRG clusters ($p<0.01$) (Figure 2D). Finally, we plotted the heatmap of gene expression and clinical features (Figure 2E).

GSVA analysis was performed between two clusters and demonstrated that most of the differential pathways between the clusters were related to acid metabolism (Figure 2F). In addition, we quantified the relative amounts of 23 different immune cell types in two LMRG clusters by ssGSEA analysis. Results showed that most of the differences between the clusters were in T cell types (Figure 2G).

To avoid LMRG model overfitting, LASSO regression was applied for further screening. The 10 genes mentioned above associated with prognosis were assigned coefficients, and 3 prognosis-related LMRGs (ACACA, MRPL3, MRPS23) were screened by lambda.min (Figures 3A, B). Subsequently, the LMRG score for each sample is calculated utilizing the following methodology: LMRG Score = [exp (ACACA)*0.0798] +[exp (MRPL3)*0.2829]+[exp(MRPS23)*0.1586]. The sample was categorized into the high- and low-LMRG-score groups, whereby the median score was used as the cut-off point. Expression of these 3 prognosis-related LMRGs in different LMRG groups is demonstrated by the heatmap (Figure 3E).

3.3 Prognostic analysis and risk scoring model based on LMRGs in HCC

To identify LMRGs associated with prognosis, we performed uniCox analysis on the merged data. As results revealed, of 23 DE-LMRGs, 10 genes were associated with HCC prognosis, and 8 of them (NT5DC2, TXNRD1, MRPS23, AIFM2, ACACA, MRPL3, APOO, SIRT4) were associated with poor prognosis, and 2 of them (GCDH, ADHFE1) were associated with good prognosis (Figure 2H).

3.4 Validation of the LMRG model validation and clinical application of the LMRG-based prognostic model in HCC

The above-merged data was taken as the internal training set, and another HCC data from the ICGC dataset was used as the external test set; the samples in the test set were also classified into high- and low-LMRG-score groups in accordance with the above methodology. The KM curves demonstrated that the high-LMRG-score group

exhibited a poorer prognosis than the low-LMRG-score group in both the training and test sets (Figures 3C, D). Furthermore, the risk curves and survival status plots illustrated the risk and survival status of the samples in the training and test sets (Figures 3H-K). Next, we validated the model using ROC curves, PCA analysis, and t-SNE analysis, respectively. We visualized the Area Under Curve (AUC) values for survival times of 1-, 2-, and 3-year, which were 0.728, 0.647, and 0.664 for the training set and 0.697, 0.650, and 0.664 for the test set (Figures 3F, G). PCA and t-SNE plots showed little overlap between high- and low-LMRG-score groups and a significant tendency toward clustering within the two groups (Figures 3L-O).

Moreover, when the clinical features of HCC were analyzed by uniCox and multiCox in the training set, we discovered that "stage" and "LMRG Score" were independently associated with a poor prognosis for patients with HCC (Figures 4A, B), and this result was verified in the test set (Figures 4C, D).

When comparing the differences in LMRG score across various clinical features, we found that age and gender factors did not have a statistically significant impact on LMRG score. However, tumor stage significantly influenced the LMRG score, demonstrating notable statistical differences (Supplementary Figure S1).

Finally, the nomogram based on the LMRG model could predict the 1-, 3-, and 5-year survival rates of HCC patients (Figure 4E). Moreover, the calibration curves demonstrated the accuracy and reliability of the aforementioned predictions (Figure 4F).

Additionally, we investigated the correlation between the LMRG clusters and the LMRG model, observing a statistically significant difference in LMRG score between the two clusters

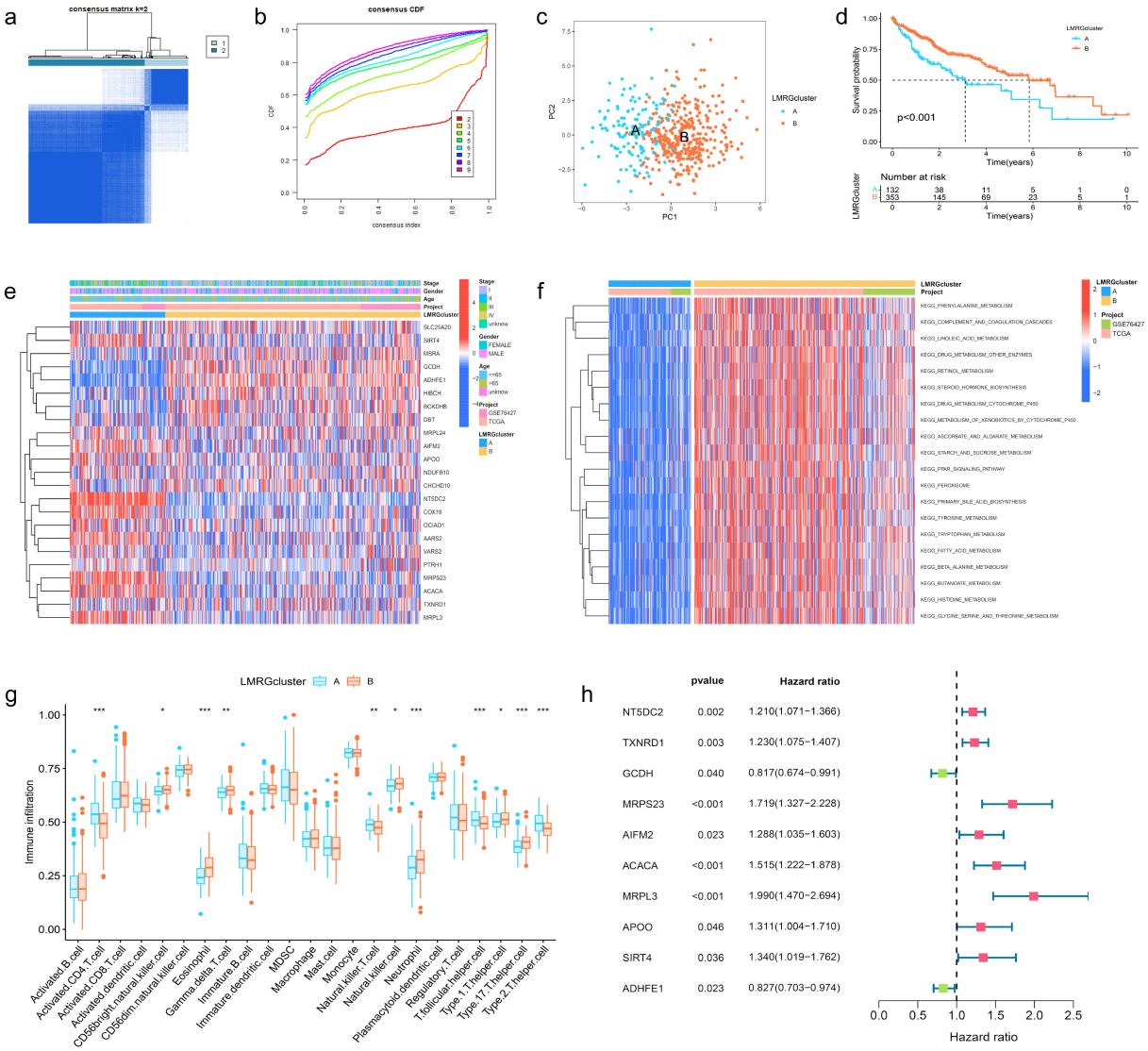

FIGURE 2
Clustering, Immune Profiling, and Prognostic Analysis of LMRG Clusters in HCC. **(A)** The patients were divided into 2 clusters. **(B)** CDF curves when k=2-9. **(C)** PCA plot showing independence between two clusters. **(D)** Survival analysis between LMRG clusters. **(E)** Heatmap of DE-LMRGs expression, clusters, and clinical features. **(F)** GSVA analysis of the KEGG pathways in LMRG clusters. **(G)** Immune infiltration level of LMRG clusters (*p<0.05; **p<0.01; ***p<0.001). **(H)** Forest plot of univariate Cox regression analysis for DE-LMRGs.

(p<2.22e-16) (Figure 4G). LMRG clusters, LMRG score, and survival status of HCC patients can be visualized by the Sankey plot (Figure 4H).

3.5 Immune profiling, tumor microenvironment, and functional enrichment of the LMRG model in HCC

In order to investigate the relationship between the LMRG model and tumor immune cells, we performed sample immune cell score assignments using the CIBERSOFT algorithm and found that the LMRG score showed a positive correlation with Macrophages M2 cell but a negative correlation with T cells CD4 memory resting (Figures 5A, B). However, no significant correlation was found in the remaining cells. The overall correlation plot is shown in the Supplementary Material (Supplementary Figure S2). Next, the TME analysis revealed that the low-LMRG-score group exhibited elevated StromalScore, ImmuneScore, and ESTIMATEScore values (Figure 5D). Stem cell analysis reveals a positive correlation between RNAss and LMRG score (Figure 5C). The gene mutation data of HCC from TCGA were visualized between different LMRG

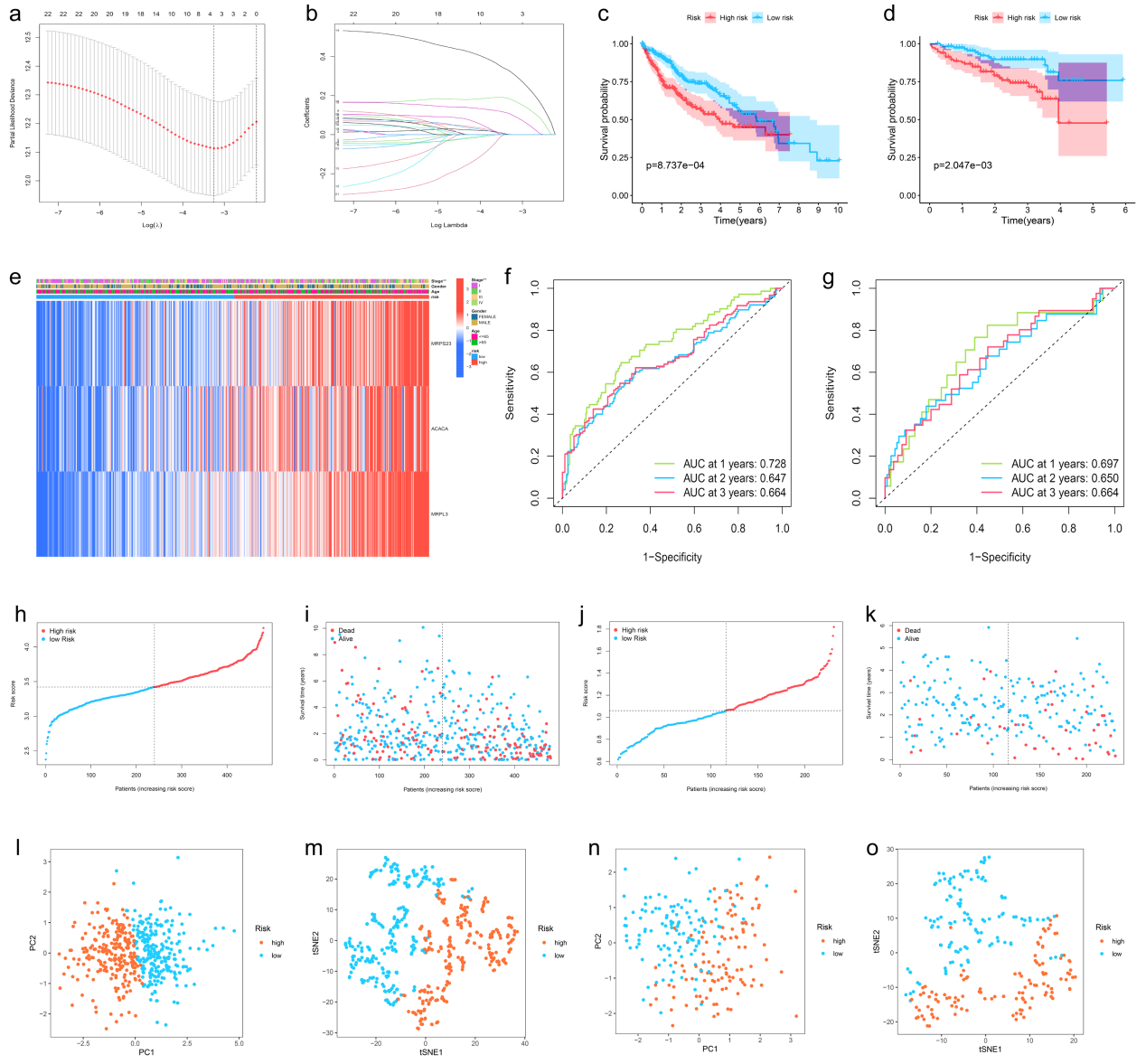

FIGURE 3
Development, Validation, and Visualization of the LMRG-Based Prognostic Risk Model in HCC. **(A)** Selection of the optimal penalty parameter for LASSO regression. **(B)** LASSO coefficient configuration. **(C)** Kaplan-Meier survival curves between high- and low-LMRG-score groups in the internal training set and **(D)** in the ICGC external test set. **(E)** Heatmap of prognosis-related LMRGs expression in the training set. **(F)** ROC curves for OS in the training set and **(G)** in the ICGC test set. **(H, I)** Patients' LMRG score distribution, survival status, and time distribution in the training set and **(J, K)** in the ICGC test set. **(L, M)** PCA and t-NSE plot in the training set and **(N, O)** in the ICGC test set.

groups by waterfall plots, with TP53, CTNNB1, TNN, MUC16, and PCLO being the most commonly mutated genes (Figures 5E, F). Although 157 of the 178 (88.2%) samples in the high-LMRG-score group had tumor mutations, compared to 148 (83.15%) in the low-LMRG-score samples, the results revealed no statistically significant differences between the two groups (Supplementary Figure S3). The 3 prognosis-related LMRGs in the model were analyzed for enrichment and were mainly enriched for the fatty-acyl-CoA biosynthetic process in BP, for the mitochondrial inner membrane in CC, and for the structural constituent of the ribosome in MF (Figures 5G, H). In terms of pathway enrichment, they were mainly present in AMPK signaling, Pyruvate metabolism, and Propanoate metabolism pathways (Figures 5I, J).

3.6 Identification of drug sensitivities associated with the LMRG model in HCC

To find effective drugs for the treatment of HCC, we calculated IC50 values of 198 chemotherapeutic drugs in HCC samples and identified 86 drugs with significant differences. We listed 8 drugs, 5 (ML323, BPD-00008900, Sepantronium bromide, MK-1775, Daporinad) of which had elevated IC50 values in the low-LMRG-score group, thus more sensitive to the treatment of high-LMRG-score patients (Figures 6A-J). And 3 (AZD2014, Doramapimod, SB505124) of which were more favorable for the treatment of patients in the low-LMRG-score group (Figures 6K-P). Other drugs sensitive to HCC are detailed in the Supplementary Material (Supplementary Table S2).

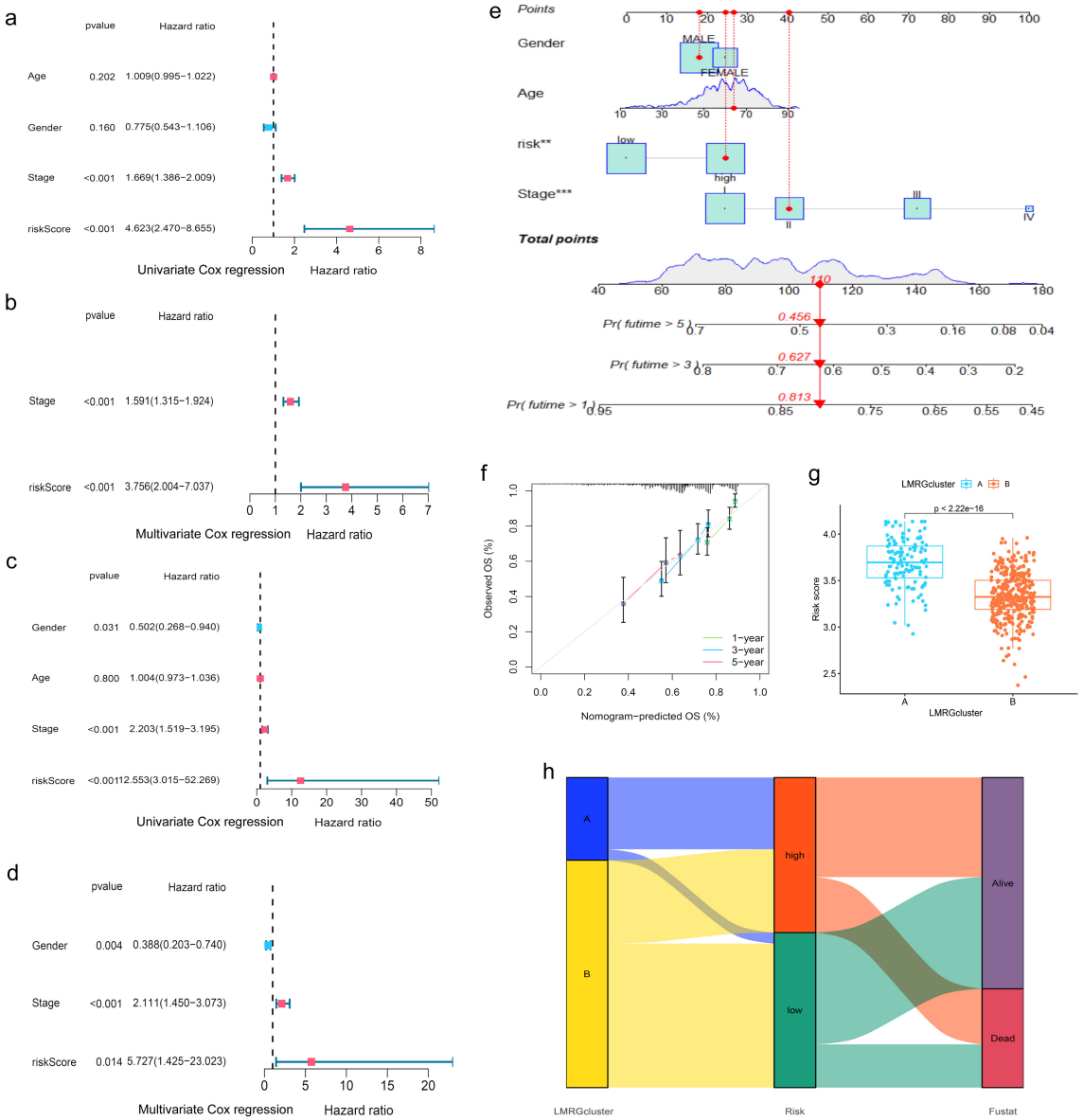

FIGURE 4
Evaluation of the prognostic efficiency of the LMRG model. **(A, B)** Cox analysis in the training group. **(C, D)** Cox analysis in the test group. **(E)** Nomogram Predicts Patient Survival at 1, 3, and 5 years. **(F)** Calibration of Nomogram. **(G)** Distribution profile of LMRG score in two LMRG clusters. **(H)** Sankey plot of LMRG clusters, LMRG score, and survival outcome. **p<0.01; ***p<0.001.

3.7 Visualization of immune cell distribution and MRPL3 expression in HCC samples

We selected GSE140228 for visualization, a chip containing 5 samples, and first showed the percentage of each cell in each as well as in the total sample, found that CD8T and CD4T cells have high occupancy content (Figures 7A, B). By descending to two dimensions, the distribution of immune cells can be observed (Figures 7D, E). The distribution of MRPL3 was then demonstrated as well, and it was found to be predominantly aggregated in DC, ILC, Plasma, and Tprolif cells (Figures 7C, F).

3.8 MRPL3 as a prognostic biomarker and therapeutic target in HCC: expression patterns, survival analysis, and experimental validation

MRPL3 had the highest coefficient value in the LMRG model, and no articles targeting this gene for the treatment of HCC were

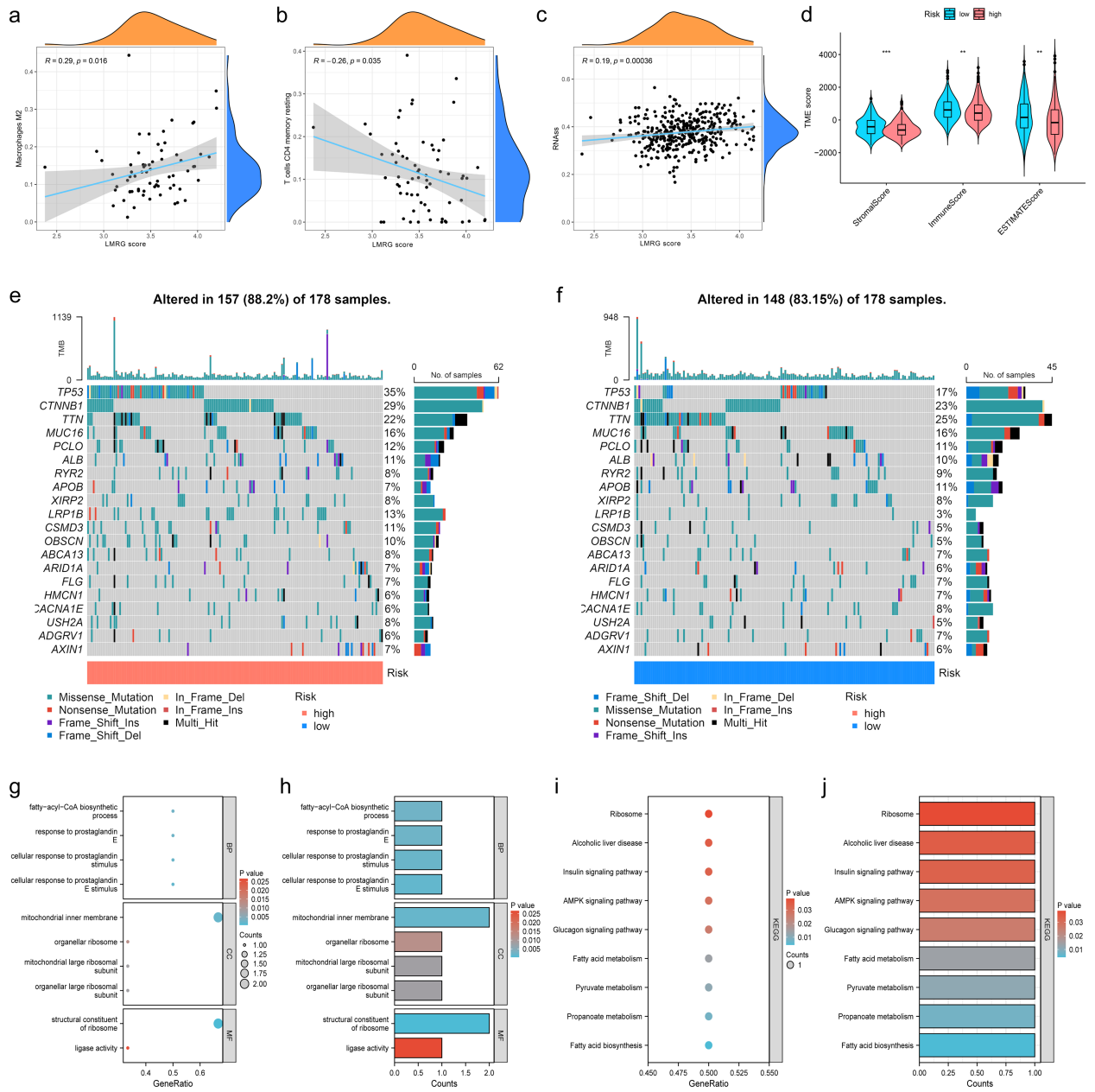

FIGURE 5
Immunization, mutation and enrichment analysis of the LMRG model. **(A)** M2 immune cell correlation. **(B)** CD4 T-cell immune cell correlation. **(C)** Correlation between the LMRG score and RNAss. **(D)** TME scores between the high- and low-LMRG-score groups. **(E, F)** Waterfall plot of mutation frequencies for the LMRG model. **(G, H)** GO enrichment analysis of prognosis-related LMRGs. **(I, J)** KEGG pathway enrichment analysis of prognosis-related LMRGs. **p<0.01; ***p<0.001.

found. Thus, we performed a single gene analysis for MRPL3. Moreover, we showed the PPI profiles of all DE-LMRGs (Figure 8A) and found that HIBCH as a hub protein linked to other proteins that can tightly link the prognosis-related LMRGs (ACACA, MRPL3) to other DE-LMRGs.

Among 33 tumors, we found that MRPL3 showed high expression in most tumors, compared to paracancerous tissue (Figure 8F). As paired samples were present in TCGA, we also performed differential expression analysis of MRPL3 in paired samples, and the results were as above (Figure 8G). This was also true in TCGA-HCC, with high expression in HCC tissue and low expression in paracancerous tissue (Figure 8B). Next, we analyzed the survival profile of MRPL3 in 33 tumors using Hazard Ratio (HR) values to indicate their prognosis and found that MRPL3 was correlated with a poor prognosis in the majority of tumor types (Figure 8J), as was the case for TCGA-HCC (Figure 8H). MRPL3 demonstrated remarkable predictive efficacy in forecasting the prognosis of HCC patients, with the AUC value was 0.786 (Figure 8I). To validate the expression of MRPL3 in HCC, we performed RT-qPCR and Western blot experiments. The results demonstrated a notable elevation in the expression level of MRPL3 in HCC tissues in comparison to normal hepatic tissues (Figures 8C, E). Consistent with this finding, cellular experiments revealed that all five HCC cell lines exhibited higher expression of MRPL3 than the hepatic normal cell line (Figure 8D). Abbreviations for all tumors are detailed in the supplemental document (Supplementary Table S3).

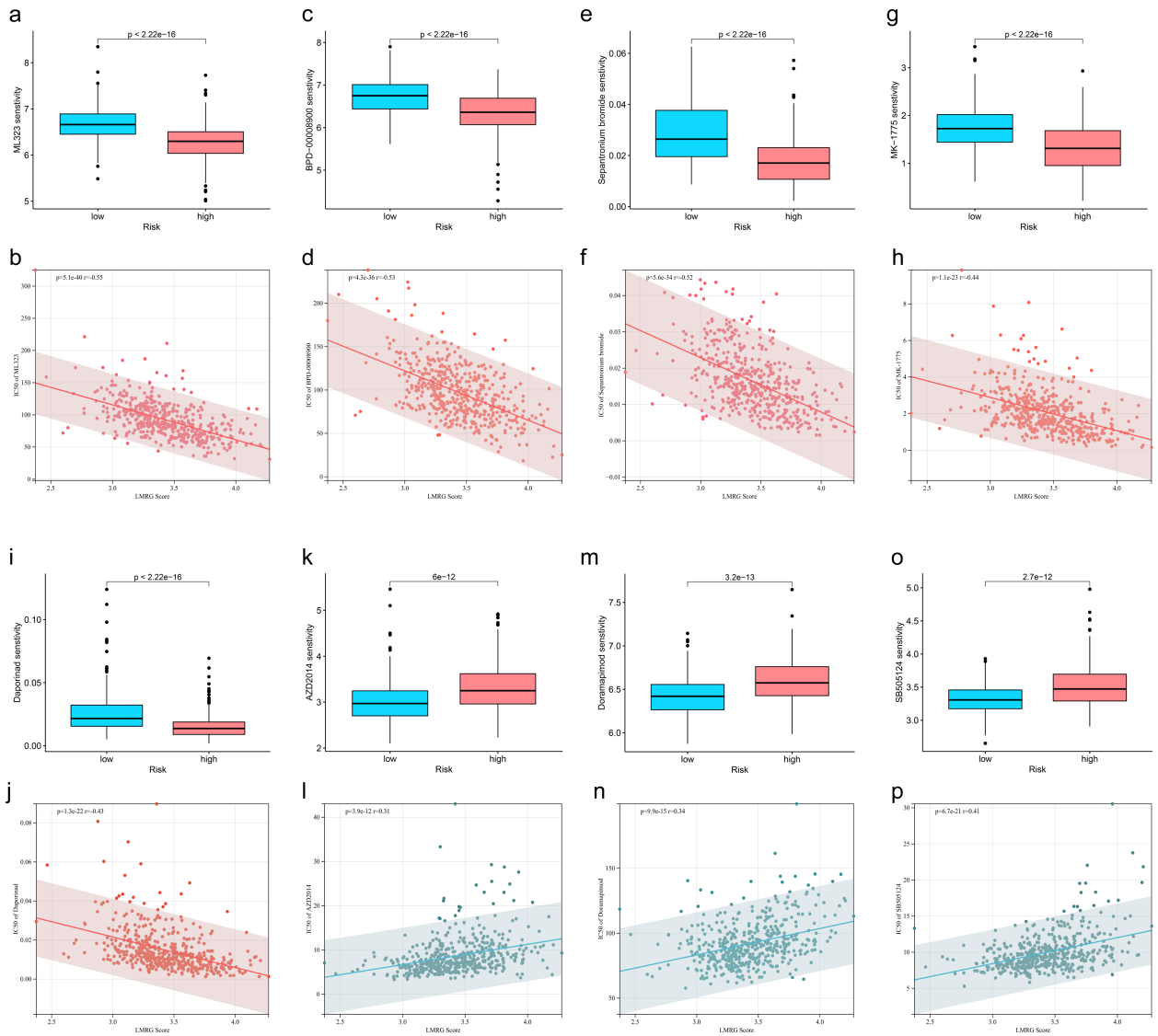

FIGURE 6
Association between LMRG score and susceptibility to chemotherapy. **(A, B)** ML323, **(C, D)** BPD-00008900, **(E, F)** Sepantronium bromide, **(G, H)** MK-1775, **(I, J)** Selumetinib, **(K, L)** AZD2014, **(M, N)** Doramapimod, **(O, P)** SB505124.

10.3389/fonc.2024.1511958

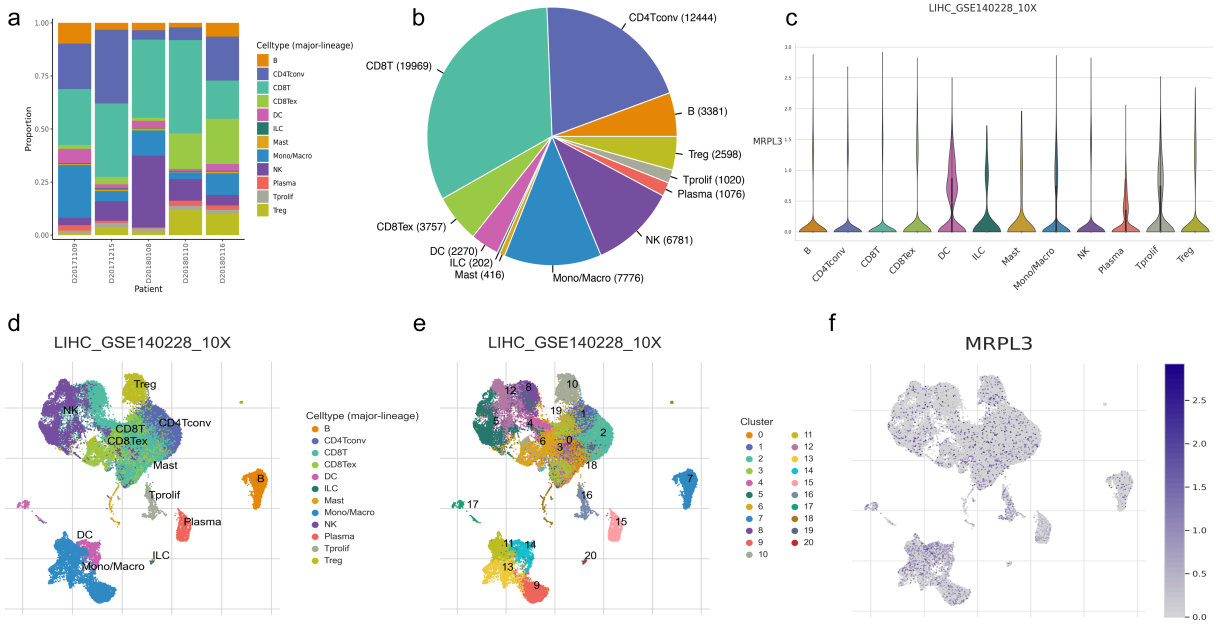

FIGURE 7
Immune cell composition and mrpl3 expression analysis in HCC by single-cell sequencing analysis. **(A, B)** Content of various cell types. **(C)** Expression of MRPL3 in various immune cells. **(D, E)** Two-dimensional distribution of cells in tissues. **(F)** Two-dimensional distribution of MRPL3 in tissues.

3.9 Functional characterization of MRPL3: impact on proliferation, apoptosis, migration, and invasion in HCC cells

To further identify the biological function of MRPL3, sh-RNA was utilized to knockdown MRPL3 in Hep3B and HCC-LM3 cell lines for subsequent experiments (Figure 9A). CCK-8 revealed a significant reduction in cell viability following the knockdown of MRPL3 in Hep3B cells, with effective inhibition of cell proliferation observed at 72 hours ($p<0.01$) (Figure 9B). The same result was obtained in HCC-LM3 cells (Figure 9C). Flow cytometry also revealed that knockdown of MRPL3 promoted apoptosis in Hep3B and HCC-LM3 cells (Figure 9D, F), with a majority of apoptotic cells observed in the late stage (Figures 9E, G). Western blotting results (Figure 9H) indicated that in Hep3B cells, compared to sh-NC, sh-MRPL3 exhibited significantly increased expression levels of apoptotic proteins (c-caspase3 and c-caspase9). Additionally, there was increased expression of E-cadherin and decreased expression of vimentin, which are associated with tumor suppression and progression, respectively. These findings suggest that knockdown of MRPL3 may not only promote apoptosis in HCC cells but also potentially enhance their invasion and migration.

Furthermore, wound-healing assays revealed that the downregulation of MRPL3 significantly hindered the migratory capacity of Hep3B and HCC-LM3 cells (Figure 10A). Transwell assays observed that the knockdown of MRPL3 not only suppressed the migration of the HCC cells but also inhibited the invasion abilities (Figure 10B). These experimental results uncover the central biological functions of MRPL3 in HCC.

4 Discussion

Lactate, a byproduct of tumor metabolism, plays a dual role in tumorigenesis, progression, and immunosuppression (34). Recent studies have also revealed its epigenetic impact, including histone modification, which regulates gene expression (13). Mitochondria, essential for energy production, are similarly vital for tumor cells. Mutations in mitochondrial genes can drive tumor development, while inhibiting mitochondrial function disrupts tumor metabolism, potentially inducing cell death (35, 36). Under aerobic conditions, pyruvate enters the TCA cycle as acetyl-CoA, but in anaerobic conditions, lactate is produced as an alternative (37). This underscores a strong connection between lactylation and mitochondria. To explore this relationship, we conducted molecular-genetic bioinformatics analyses using public datasets. We identified 82 lactylation-mitochondria-related genes (LMRGs) by intersecting lactylation-related genes from original studies with mitochondria-related genes from MitoCarta3.0.

Lactylation, a recently identified post-translational modification, has been implicated in the metabolic reprogramming of cancer cells. In hepatocellular carcinoma (HCC), lactylation of specific proteins can modulate mitochondrial function, thereby influencing tumor progression. For example, the lactylation of lysine at position K28 of the AK2 protein has been shown to promote HCC deterioration. Additionally, SIRT3-mediated de-lactylation of CCNE2 inhibits liver cancer cell proliferation, underscoring the regulatory role of lactylation in cell cycle control (15). Recent studies have also revealed that histone lactylation is associated with enhanced transcription of mitochondrial biogenesis regulators, linking metabolic reprogramming with epigenetic

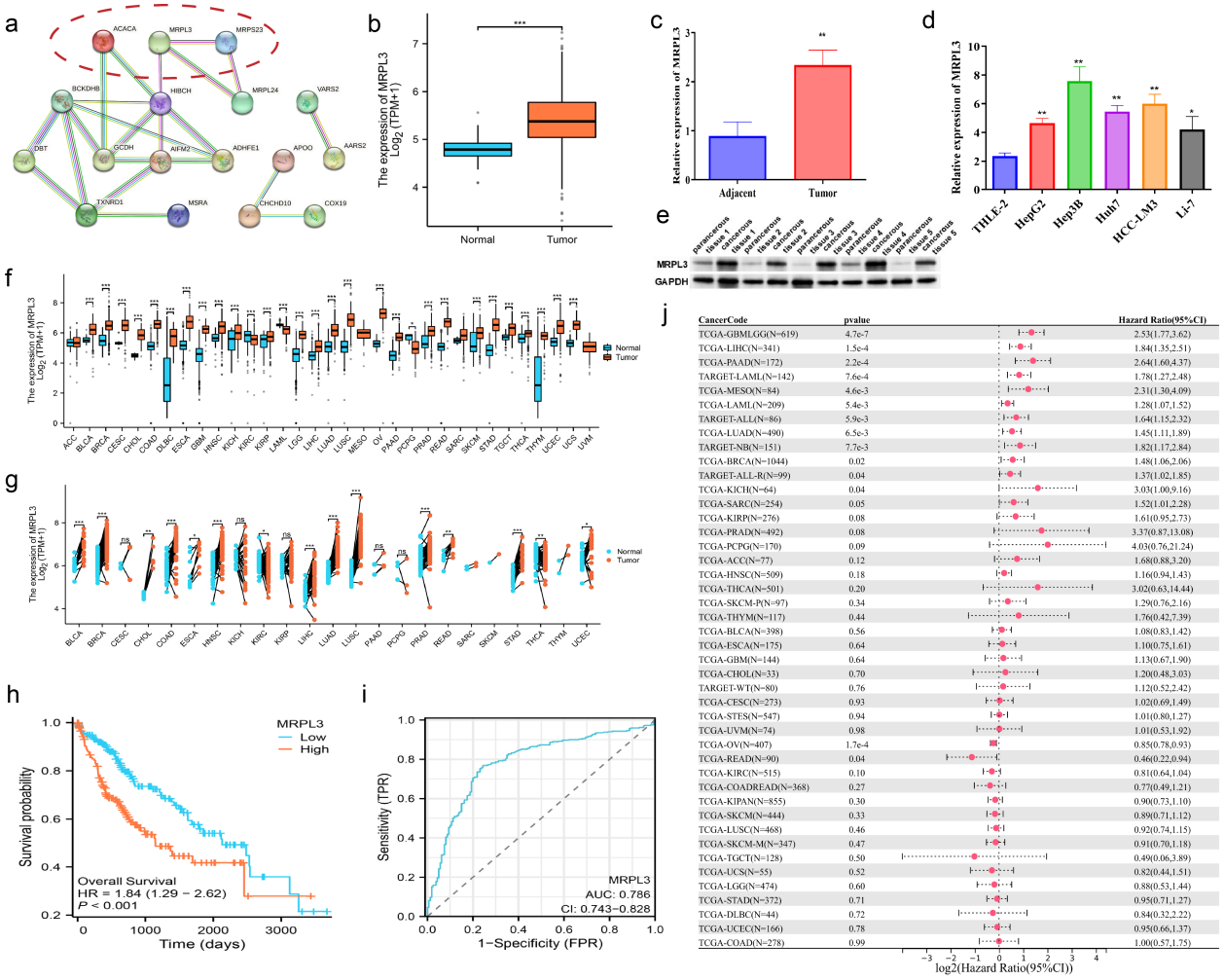

FIGURE 8
Comprehensive Analysis of MRPL3 Expression, Prognostic Significance, and Diagnostic Value in HCC. **(A)** PPI network of all DE-LMRGs. **(B)** Differential expression of MRPL3 in hepatic normal and HCC tissues according to TCGA dataset. **(C)** RT-qPCR results of MRPL3 in hepatic normal and HCC tissues. **(D)** RT-qPCR results of MRPL3 in hepatic normal cell line and five HCC cell lines. **(E)** Western blot results of MRPL3 in hepatic normal and HCC tissues. **(F)** Expression of MRPL3 in 33 tumors. **(G)** Differential expression of MRPL3 in paired samples. **(H)** Differential expression of MRPL3 in multiple normal and tumor tissues. **(I)** The plausibility of MRPL3 for HCC survival prediction. **(J)** MRPL3 prognostic HR values in multiple tumor types. *p<0.05; **p<0.01; ***p<0.001.

control (16). These findings suggest that targeting lactylation could offer new therapeutic avenues for HCC treatment (17).

Based on LMRGs, we successfully clustered HCC patients into distinct groups with high intra-cluster consistency. We then developed a prognostic model for HCC using LMRGs, which demonstrated strong predictive accuracy for patient survival. Among the identified prognosis-related LMRGs, ACACA, MRPS23, and MRPL3 emerged as key candidates for HCC diagnosis and treatment. ACACA promotes HCC malignancy by aberrantly activating the Wnt/β-catenin signaling pathway. Its downregulation significantly suppresses HCC cell migration, invasion, proliferation, and EMT, while inducing cell cycle arrest (38). MRPS23 is an independent prognostic marker associated with tumor size, TNM stage, and overall survival (OS). Silencing MRPS23 reduces HCC proliferation both *in vitro* and *in vivo* (39). MRPL3, primarily studied in early embryonic development, impacts ribosome assembly and mitochondrial translation. It has been linked to lymph node metastasis, higher SBR grading, and Ki-67 expression in breast cancer, suggesting a role in tumor proliferation (40–42). However, the connection between MRPL3 and HCC remains largely unexplored, requiring further investigation.

Hence, we conducted a series of analyses for MRPL3, which has the highest coefficient in the LMRG model, to explore its association with HCC. MRPL3, which is fully known as mitochondrial ribosomal protein L3. Whereas mitochondrial ribosomes are found within eukaryotic cells, which are responsible for accomplishing the translation process within an organelle like the mitochondrion (43), its instability and tumor development can lead to a vicious cycle (44). Therefore, MRP family genes can be used as markers for cancer diagnosis and prognostic status (45). We analyzed the expression level of MRPL3 across 33 types of cancer and discovered that it was significantly elevated in tumor tissues for most cancers, including HCC. Furthermore, high levels of MRPL3 expression were associated with poor prognoses in many cancers,

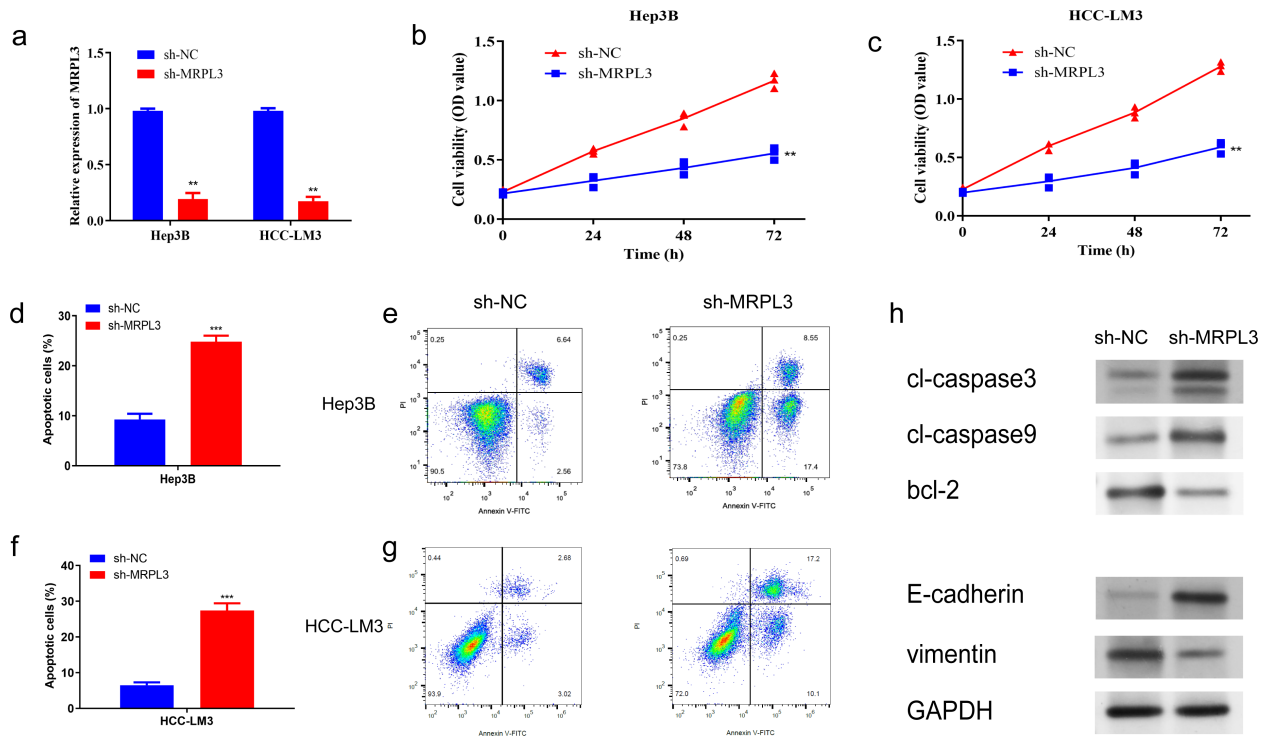

FIGURE 9
Impact of MRPL3 Knockdown on Proliferation and Apoptosis in Hep3B and HCC-LM3. **(A)** Expression of MRPL3 after silencing. **(B, C)** Silencing of MRPL3 in Hep3B and HCC-LM3 cells, respectively, and CCK-8 assay of cell proliferative activity. **(D, E)** Apoptosis after silencing of MRPL3 in Hep3B cells. **(F, G)** Apoptosis after silencing of MRPL3 in HCC-LM3 cells. **(H)** Western blot detection of MRPL3 apoptosis, migration and invasion related proteins after silencing in Hep3B cells. **p<0.01; ***p<0.001.

such as prostate and colorectal cancer, which was consistent with the bioinformatics analysis of the MRP family by the article of Yu L et al. (46). We probed the correlation between MRPL3 and HCC with *in vitro* experiments. MRPL3 expression was markedly elevated in HCC compared to hepatic normal cells and tissues in RT-qPCR experiments. More promisingly, MRPL3 proved to be a reliable predictor of prognosis in HCC patients. Experimental results demonstrated that MRPL3 knockdown influenced key proteins related to apoptosis, cell proliferation, and migration. A significant downregulation of MRPL3 markedly impeded the growth and migration of HCC cells while simultaneously enhancing their apoptotic response. These researches demonstrated that MRPL3 may serve as a target to inhibit HCC tumor progression, thus providing strong support for clinical decision-making.

To further elucidate the mechanistic relevance of MRPL3 in HCC, we explored its roles in lactylation and mitochondrial functions, which revealed its potential as a crucial mediator in tumor metabolic reprogramming and epigenetic regulation. MRPL3, identified as a key component of the LMRG model, is intricately associated with both lactylation and mitochondrial functions. As a mitochondrial ribosomal protein, MRPL3 is essential for mitochondrial translation and maintaining mitochondrial integrity, a critical factor for oxidative phosphorylation and energy metabolism. Dysregulation of MRPL3 can destabilize mitochondrial ribosome assembly, impairing the electron transport chain and leading to metabolic reprogramming that supports tumorigenesis. Furthermore, MRPL3's overexpression in HCC tissues and cell lines correlates with metabolic shifts toward glycolysis and lactate accumulation, hallmarks of cancer metabolism. Lactate, in turn, promotes histone lactylation, a process influencing gene expression relevant to tumor proliferation and immune evasion. Our study revealed a significant correlation between MRPL3 expression and poor prognosis in HCC, highlighting its role in metabolic adaptation and tumor progression. PPI analysis further linked MRPL3 with HIBCH, an enzyme vital for mitochondrial amino acid metabolism, suggesting a cooperative role in regulating mitochondrial and lactylation-mediated metabolic pathways. Experimental validation confirmed that silencing MRPL3 disrupted mitochondrial function and inhibited HCC cell proliferation, migration, and invasion. These findings suggest that MRPL3 not only contributes to mitochondrial metabolism but also integrates lactylation-related epigenetic regulation, underpinning its critical role in HCC pathophysiology.

Besides, the PPI network revealed that MRPL3 is not only tightly linked to MRP family genes (MRPS23, MRPL24), but also closely associated with HIBCH (47). Upregulation of HIBCH is shown to be connected with poor prognosis in other tumors (48), which is the same as the upregulation of MRPL3. HIBCH acts as a hub gene associating prognosis-related LMRGs with other DE-LMRGs, and its importance in biological processes cannot be overstated. Research has demonstrated that HIBCH is crucial for

amino acid metabolism, with its proper function being closely linked to overall cellular metabolic processes. Mutations in HIBCH may trigger abnormalities in mitochondrial respiratory chain enzymes and pyruvate dehydrogenase, which in turn disrupts respiration and metabolism (49). However, the underlying link between HIBCH and MRP family members is currently under-explored. We venture to speculate in this paper that there may be some as-yet-unknown mechanism of interaction between MRPL3 and HIBCH capable of modulating the progression of tumor and thus interfering with respiration and the TCA cycle.

The LMRG score and MRPL3 both positively correlate with M2 macrophage infiltration, with Chen DY et al. highlighting MRPL3's role in M2 macrophage polarization (40). M2 tumor-associated macrophages suppress inflammation, promote tumor proliferation, and aid immune evasion (50). Targeting MRPL3 through immunotherapy may help rebalance the M1/M2 ratio by reprogramming M2-like macrophage metabolism, potentially enhancing tumor treatment. The LMRG score also negatively correlates with CD4+ T memory cells, though MRPL3 shows no significant association. This discrepancy may stem from ACACA in the LMRG model, as ACACA deficiency is known to enhance CD4+ T memory cell generation by affecting fatty acid biosynthesis (51). Immune-enhancing drugs might downregulate prognosis-related LMRG expression, reducing HCC incidence. Drug sensitivity analysis identified ML323 as a promising candidate for HCC therapy. As a USP1 inhibitor, ML323 reduces macrophage infiltration, regulates CD4+ T cell differentiation, and inhibits Th17 cell development, maintaining immune balance and exerting anti-tumor effects (52–54). While these findings inform HCC treatment, they require validation through extensive clinical trials. Additionally, our LMRG model, based on public datasets, needs further testing with clinical samples.

Compared to traditional HCC biomarkers such as AFP, DCP, and GPC3, MRPL3 demonstrated superior predictive power and a stronger correlation with advanced clinicopathological features. While AFP is widely used in clinical practice, its sensitivity and specificity are often limited, particularly in early-stage HCC (55, 56). Similarly, DCP and GPC3, although valuable, lack the integrative insights provided by MRPL3 into mitochondrial dysfunction and metabolic reprogramming (57, 58). Our analysis showed that combining MRPL3 with AFP in a composite prognostic model further improved predictive accuracy, emphasizing MRPL3's additive clinical utility. These results underscore MRPL3's potential

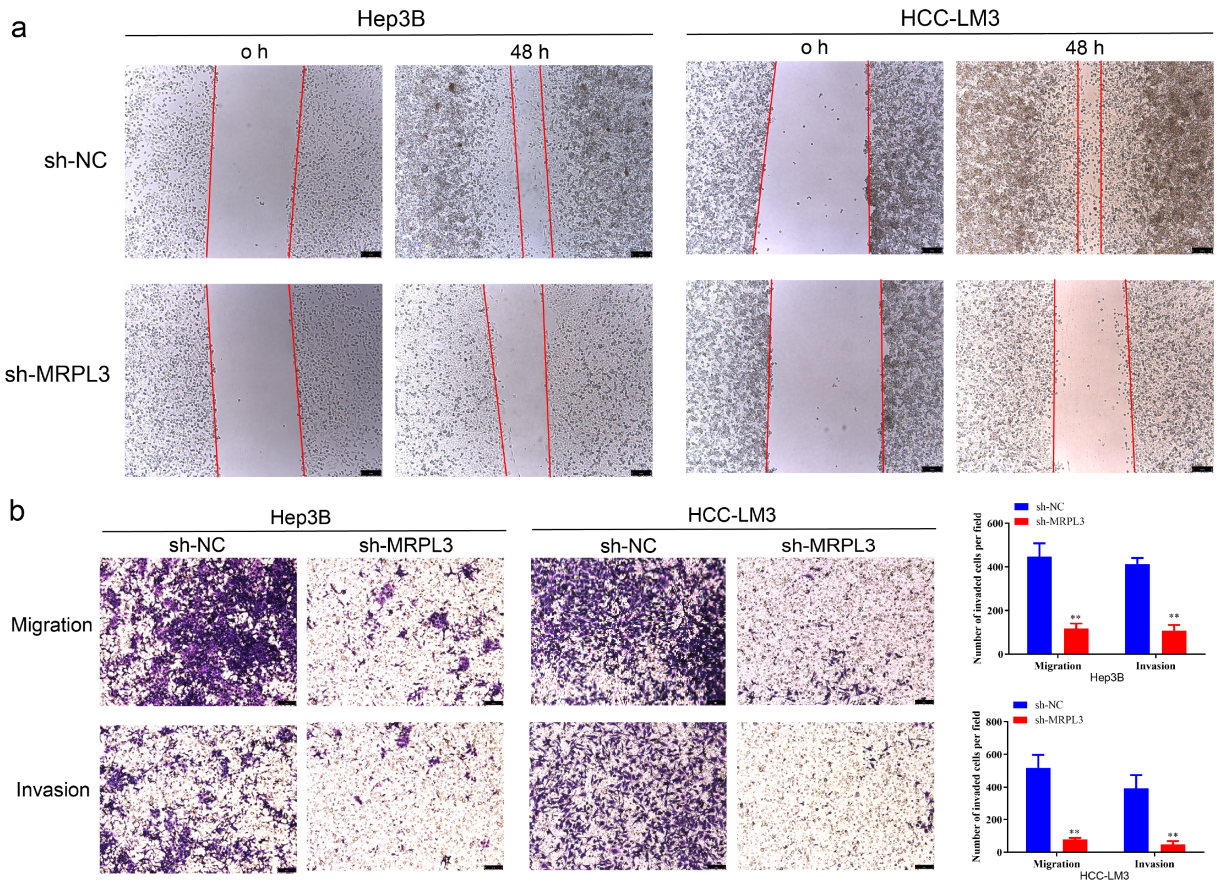

FIGURE 10
Migration and invasion ability of MRPL3 in HCC cell lines. **(A)** Wound-healing assay of silencing MRPL3 in Hep3B and HCC-LM3 cells. **(B)** Cell migration and invasion ability of silencing MRPL3 in Hep3B and HCC-LM3 cells. **p<0.01.

not only as a standalone biomarker but also as a complementary factor in enhancing the prognostic capacity of existing models.

The features of the article are the LMRG-based prognosis-related genes as novel options for the diagnosis and treatment of HCC, with MRPL3 among them available as a new immunotherapeutic target. Patients with HCC can undergo genetic testing based on their LMRG score, allowing for classification in a high- or low-LMRG-score groups so that patients can be given appropriate treatment. This will bring new inspiration for the clinical treatment of HCC.

Data availability statement

The original contributions presented in the study are included in the article/Supplementary Material. Further inquiries can be directed to the corresponding authors.

Ethics statement

The studies involving humans were approved by the Ethics Committee of Jiangsu Province Hospital of Chinese Medicine (No. 2023NL-132-01). The studies were conducted in accordance with the local legislation and institutional requirements. Written informed consent for participation in this study was provided by the participants' legal guardians/next of kin.

Author contributions

WX: Conceptualization, Investigation, Methodology, Writing – original draft, Writing – review & editing. YZ: Formal analysis, Methodology, Writing – review & editing. QL: Formal analysis, Software, Visualization, Writing – review & editing. NY: Formal analysis, Software, Visualization, Writing – review & editing. GW: Funding acquisition, Project administration, Supervision, Writing – review & editing. RS: Conceptualization, Data curation, Funding acquisition, Investigation, Project administration, Resources, Supervision, Writing – review & editing. JH: Funding acquisition, Project administration, Writing – review & editing. XY: Validation, Visualization, Writing – review & editing. TZ: Funding acquisition, Project administration, Writing – review & editing. SC: Conceptualization, Data curation, Investigation, Resources, Validation, Writing – review & editing.

Funding

The author(s) declare financial support was received for the research, authorship, and/or publication of this article. This work was supported by the National Natural Science Foundation of China (NSFC). Grant number is 8207150765.

Conflict of interest

The authors declare that the research was conducted in the absence of any commercial or financial relationships that could be construed as a potential conflict of interest.

Generative AI statement

The author(s) declare that no Generative AI was used in the creation of this manuscript.

Publisher's note

Supplementary material

The Supplementary Material for this article can be found online at: https://www.frontiersin.org/articles/10.3389/fonc.2024.1511958/full#supplementary-material

References

1. Bray F, Laversanne M, Sung H, Ferlay J, Siegel RL, Soerjomataram I, et al. Global cancer statistics 2022: GLOBOCAN estimates of incidence and mortality worldwide for 36 cancers in 185 countries. *CA: A Cancer J Clin*. (2024) 74:229–63. doi: 10.3322/caac.21834

2. Moris D, Palta M, Kim C, Allen PJ, Morse MA, Lidsky ME. Advances in the treatment of intrahepatic cholangiocarcinoma: An overview of the current and future therapeutic landscape for clinicians. *CA: A Cancer J Clin*. (2023) 73:198–222. doi: 10.3322/caac.21759

3. Sun L, Ke X, Guan A, Jin B, Qu J, Wang Y, et al. Intratumoural microbiome can predict the prognosis of hepatocellular carcinoma after surgery. *Clin Trans Med*. (2023) 13:e1331. doi: 10.1002/ctm2.1331

4. Kulik L, El-Serag HB. Epidemiology and management of hepatocellular carcinoma. *Gastroenterology*. (2019) 156:477–491.e1. doi: 10.1053/j.gastro.2018.08.065

5. Brown ZJ, Tsilimigras DI, Ruff SM, Mohseni A, Kamel IR, Cloyd JM, et al. Management of hepatocellular carcinoma: A review. *JAMA Surg*. (2023) 158:410–20. doi: 10.1001/jamasurg.2022.7989

6. Couillard AB, Knott EA, Zlevor AM, Mezrich JD, Cristescu MM, Agarwal P, et al. Microwave ablation as bridging to liver transplant for patients with hepatocellular carcinoma: A single-center retrospective analysis. *J Vasc interv radiol: JVIR*. (2022) 33:1045–53. doi: 10.1016/j.jvir.2022.05.019

7. Vogel A, Meyer T, Sapisochin G, Salem R, Saborowski A. Hepatocellular carcinoma. *Lancet (London England)*. (2022) 400:1345–62. doi: 10.1016/S0140-6736(22)01200-4

8. Yang Y, Xiong L, Li M, Jiang P, Wang J, Li C. Advances in radiotherapy and immunity in hepatocellular carcinoma. *J Trans Med*. (2023) 21:526. doi: 10.1186/s12967-023-04386-y

9. Ha S, Wong VW, Zhang X, Yu J. Interplay between gut microbiome, host genetic and epigenetic modifications in MASLD and MASLD-related hepatocellular carcinoma. *Gut*. (2024) 74:141–52. doi: 10.1136/gutjnl-2024-332398

10. Heim CE, Bosch ME, Yamada KJ, Aldrich AL, Chaudhari SS, Klinkebiel D, et al. Lactate production by Staphylococcus aureus biofilm inhibits HDAC11 to reprogramme the host immune response during persistent infection. *Nat Microbiol*. (2020) 5:1271–84. doi: 10.1038/s41564-020-0756-3

11. Lee J, Gong YX, Xie DP, Jeong H, Seo H, Kim J, et al. Anticancer effect of ERM210 on liver cancer cells through ROS/mitochondria-dependent apoptosis signaling pathways. *In Vivo*. (2021) 35:2599–608. doi: 10.21873/invivo.12542

12. Liberti MV, Locasale JW. The warburg effect: how does it benefit cancer cells? *Trends Biochem Sci*. (2016) 41:211–8. doi: 10.1016/j.tibs.2015.12.001

13. Zhang D, Tang Z, Huang H, Zhou G, Cui C, Weng Y, et al. Metabolic regulation of gene expression by histone lactylation. *Nature*. (2019) 574:575–80. doi: 10.1038/s41586-019-1678-1

14. Wang X, Ying T, Yuan J, Wang Y, Su X, Chen S, et al. BRAFV600E restructures cellular lactylation to promote anaplastic thyroid cancer proliferation. *Endocr Relat Cancer*. (2023) 30:e220344. doi: 10.1530/ERC-22-0344

15. Yang Z, Yan C, Ma J, Peng P, Ren X, Cai S, et al. Lactylome analysis suggests lactylation-dependent mechanisms of metabolic adaptation in hepatocellular carcinoma. *Nat Metab*. (2023) 5:61–79. doi: 10.1038/s42255-022-00710-w

16. Pan L, Feng F, Wu J, Fan S, Han J, Wang S, et al. Demethylzeylasteral targets lactate by inhibiting histone lactylation to suppress the tumorigenicity of liver cancer stem cells. *Pharmacol Res*. (2022) 181:106270. doi: 10.1016/j.phrs.2022.106270

17. Cheng Z, Huang H, Li M, Liang X, Tan Y, Chen Y. Lactylation-related gene signature effectively predicts prognosis and treatment responsiveness in hepatocellular carcinoma. *Pharm (Basel Switzerland)*. (2023) 16:644. doi: 10.3390/ph16050644

18. Harrington JS, Ryter SW, Plataki M, Price DR, Choi AMK. Mitochondria in health, disease, and aging. *Physiol Rev*. (2023) 103:2349–422. doi: 10.1152/physrev.00058.2021

19. Wallace DC. Mitochondria and cancer. *Nat Rev Cancer*. (2012) 12:685–98. doi: 10.1038/nrc3365

20. Shadel GS, Horvath TL. Mitochondrial ROS signaling in organismal homeostasis. *Cell*. (2015) 163:560–9. doi: 10.1016/j.cell.2015.10.001

21. Jeong SM, Lee A, Lee J, Haigis MC. SIRT4 protein suppresses tumor formation in genetic models of Myc-induced B cell lymphoma. *J Biol Chem*. (2014) 289:4135–44. doi: 10.1074/jbc.M113.525949

22. Mucaj V, Shay JES, Simon MC. Effects of hypoxia and HIFs on cancer metabolism. *Int J Hematol*. (2012) 95:464–70. doi: 10.1007/s12185-012-1070-5

23. Ghosh JC, Siegelin MD, Vaira V, Faversani A, Tavecchio M, Chae YC, et al. Adaptive mitochondrial reprogramming and resistance to PI3K therapy. *J Natl Cancer Institute*. (2015) 107:dju502. doi: 10.1093/jnci/dju502

24. Jiang D, LaGory EL, Brož DK, Bieging KT, Brady CA, Link N, et al. Analysis of p53 transactivation domain mutants reveals Acad11 as a metabolic target important for p53 pro-survival function. *Cell Rep*. (2015) 10:1096–109. doi: 10.1016/j.celrep.2015.01.043

25. Wang Y, Wang D-Y, Bu K-N, Gao J-D, Zhang B-L. Prognosis prediction and risk stratification of breast cancer patients based on a mitochondria-related gene signature. *Sci Rep*. (2024) 14:2859. doi: 10.1038/s41598-024-52981-w

26. Shi Y, Huang G, Jiang F, Zhu J, Xu Q, Fang H, et al. Deciphering a mitochondria-related signature to supervise prognosis and immunotherapy in hepatocellular carcinoma. *Front Immunol*. (2022) 13:1070593. doi: 10.3389/fimmu.2022.1070593

27. Hammond MJ, Nenarokova A, Butenko A, Zoltner M, Dobáková EL, Field MC, et al. A uniquely complex mitochondrial proteome from euglena gracilis. *Mol Biol Evol*. (2020) 37:2173–91. doi: 10.1093/molbev/msaa061

28. Susser LI, Nguyen MA, Geoffrion M, Emerton C, Ouimet M, Khacho M, et al. Mitochondrial fragmentation promotes inflammation resolution responses in macrophages via histone lactylation. *Mol Cell Biol*. (2023) 43:531–46. doi: 10.1080/10985549.2023.2253131

29. Cai X, Ng CP, Jones O, Fung TS, Ryu KW, Li D, et al. Lactate activates the mitochondrial electron transport chain independently of its metabolism. *Mol Cell*. (2023) 83:3904–3920.e7. doi: 10.1016/j.molcel.2023.09.034

30. Rath S, Sharma R, Gupta R, Ast T, Chan C, Durham TJ, et al. MitoCarta3.0: an updated mitochondrial proteome now with sub-organelle localization and pathway annotations. *Nucleic Acids Res*. (2021) 49:D1541–7. doi: 10.1093/nar/gkaa1011

31. Vivian J, Rao AA, Nothaft FA, Ketchum C, Armstrong J, Novak A, et al. Toil enables reproducible, open source, big biomedical data analyses. *Nat Biotechnol*. (2017) 35:314–6. doi: 10.1038/nbt.3772

32. Liu J, Lichtenberg T, Hoadley KA, Poisson LM, Lazar AJ, Cherniack AD, et al. An integrated TCGA pan-cancer clinical data resource to drive high-quality survival outcome analytics. *Cell*. (2018) 173:400–416.e11. doi: 10.1016/j.cell.2018.02.052

33. Ippolito L, Morandi A, Giannoni E, Chiarugi P. Lactate: A metabolic driver in the tumour landscape. *Trends Biochem Sci*. (2019) 44:153–66. doi: 10.1016/j.tibs.2018.10.011

34. Rabinowitz JD, Enerbäck S. Lactate: the ugly duckling of energy metabolism. *Nat Metab*. (2020) 2:566–71. doi: 10.1038/s42255-020-0243-4

35. Averbeck D, Rodriguez-Lafrasse C. Role of mitochondria in radiation responses: epigenetic, metabolic, and signaling impacts. *Int J Mol Sci*. (2021) 22:11047. doi: 10.3390/ijms222011047

36. Borcherding N, Brestoff JR. The power and potential of mitochondria transfer. *Nature*. (2023) 623:283–91. doi: 10.1038/s41586-023-06537-z

37. Cunnane SC, Trushina E, Morland C, Prigione A, Casadesus G, Andrews ZB, et al. Brain energy rescue: an emerging therapeutic concept for neurodegenerative disorders of ageing. *Nat Rev Drug Discovery*. (2020) 19:609–33. doi: 10.1038/s41573-020-0072-x

38. Shen Y, Wang X, Ni Z, Xu S, Qiu S, Zheng W, et al. Identification of acetyl-CoA carboxylase alpha as a prognostic and targeted candidate for hepatocellular carcinoma. *Clin Trans Oncol: Off Publ Fed Spanish Oncol Soc Natl Cancer Institute Mexico*. (2023) 25:2499–513. doi: 10.1007/s12094-023-03137-1

39. Pu M, Wang J, Huang Q, Zhao G, Xia C, Shang R, et al. High MRPS23 expression contributes to hepatocellular carcinoma proliferation and indicates poor survival outcomes. *Tumour Biol: J Int Soc Oncodev Biol Med*. (2017) 39:1010428317709127. doi: 10.1177/1010428317709127

40. Galmiche L, Serre V, Beinat M, Assouline Z, Lebre A-S, Chretien D, et al. Exome sequencing identifies MRPL3 mutation in mitochondrial cardiomyopathy. *Hum Mutat*. (2011) 32:1225–31. doi: 10.1002/humu.21562

41. Cahill LS, Cameron JM, Winterburn J, Macos P, Hoggarth J, Dzamba M, et al. Structural variant in mitochondrial-associated gene (MRPL3) induces adult-onset neurodegeneration with memory impairment in the mouse. *J Neurosci: Off J Soc Neurosci*. (2020) 40:4576–85. doi: 10.1523/JNEUROSCI.0013-20.2020

42. Yin J, Lin C, Jiang M, Tang X, Xie D, Chen J, et al. CENPL, ISG20L2, LSM4, MRPL3 are four novel hub genes and may serve as diagnostic and prognostic markers in breast cancer. *Sci Rep*. (2021) 11:15610. doi: 10.1038/s41598-021-95068-6

43. Cheong A, Lingutla R, Mager J. Expression analysis of mammalian mitochondrial ribosomal protein genes. *Gene Expression patterns: GEP*. (2020) 38:119147. doi: 10.1016/j.gep.2020.119147

44. Yang Y, Karakhanova S, Hartwig W, D'Haese JG, Philippov PP, Werner J, et al. Mitochondria and mitochondrial ROS in cancer: novel targets for anticancer therapy. *J Cell Physiol*. (2016) 231:2570–81. doi: 10.1002/jcp.25349

45. Chandrashekar DS, Karthikeyan SK, Korla PK, Patel H, Shovon AR, Athar M, et al. UALCAN: An update to the integrated cancer data analysis platform. *Neoplasia (New York N.Y.)*. (2022) 25:18–27. doi: 10.1016/j.neo.2022.01.001

46. Zhao J-W, Zhao W-Y, Cui X-H, Xing L, Shi J-C, Yu L. The role of the mitochondrial ribosomal protein family in detecting hepatocellular carcinoma and predicting prognosis, immune features, and drug sensitivity. *Clin Trans Oncol: Off Publ Fed Spanish Oncol Soc Natl Cancer Institute Mexico*. (2024) 26:496–514. doi: 10.1007/s12094-023-03269-4

47. Gillette MA, Satpathy S, Cao S, Dhanasekaran SM, Vasaikar SV, Krug K, et al. Proteogenomic characterization reveals therapeutic vulnerabilities in lung adenocarcinoma. *Cell*. (2020) 182:200–225.e35. doi: 10.1016/j.cell.2020.06.013

48. Shan Y, Gao Y, Jin W, Fan M, Wang Y, Gu Y, et al. Targeting HIBCH to reprogram valine metabolism for the treatment of colorectal cancer. *Cell Death Dis*. (2019) 10:618. doi: 10.1038/s41419-019-1832-6

49. Ferdinandusse S, Waterham HR, Heales SJR, Brown GK, Hargreaves IP, Taanman J-W, et al. HIBCH mutations can cause Leigh-like disease with combined deficiency of multiple mitochondrial respiratory chain enzymes and pyruvate dehydrogenase. *Orphanet J Rare Dis*. (2013) 8:188. doi: 10.1186/1750-1172-8-188

50. Bosco MC. Macrophage polarization: Reaching across the aisle? *J Allergy Clin Immunol*. (2019) 143:1348–50. doi: 10.1016/j.jaci.2018.12.995

51. Endo Y, Onodera A, Obata-Ninomiya K, Koyama-Nasu R, Asou HK, Ito T, et al. ACC1 determines memory potential of individual CD4+ T cells by regulating *de novo* fatty acid biosynthesis. *Nat Metab*. (2019) 1:261–75. doi: 10.1038/s42255-018-0025-4

52. Kim MS, Baek J-H, Lee J, Sivaraman A, Lee K, Chun K-H. Deubiquitinase USP1 enhances CCAAT/enhancer-binding protein beta (C/EBPβ) stability and accelerates adipogenesis and lipid accumulation. *Cell Death Dis*. (2023) 14:776. doi: 10.1038/s41419-023-06317-7

53. Zhu X, Wang P, Zhan X, Zhang Y, Sheng J, He S, et al. USP1-regulated reciprocal differentiation of Th17 cells and Treg cells by deubiquitinating and stabilizing TAZ. *Cell Mol Immunol*. (2023) 20:252–63. doi: 10.1038/s41423-022-00969-9

54. Zhao Y, Xue C, Xie Z, Ouyang X, Li L. Comprehensive analysis of ubiquitin-specific protease 1 reveals its importance in hepatocellular carcinoma. *Cell Prolif*. (2020) 53:e12908. doi: 10.1111/cpr.12908

55. Zhou J, Sun HC, Wang Z, Cong WM, Wang JH, Zeng MS, et al. Guidelines for diagnosis and treatment of primary liver cancer in China (2017 edition). *Liver Cancer*. (2018) 7:235–60. doi: 10.1159/000488035

56. Luo P, Yin P, Hua R, Tan Y, Li Z, Qiu G, et al. multicenter serum metabolite biomarker identification study for the early detection of hepatocellular carcinoma. *Hepatology*. (2018) 67:662–75. doi: 10.1002/hep.29561

57. Tsuchiya N, Sawada Y, Endo I, Saito K, Uemura Y, Nakatsura T. Biomarkers for the early diagnosis of hepatocellular carcinoma. *World J Gastroenterol*. (2015) 21:10573–83. doi: 10.3748/wjg.v21.i37.10573

58. Marrero JA, Kulik LM, Sirlin CB, Zhu AX, Finn RS, Abecassis MM, et al. Diagnosis, staging, and management of hepatocellular carcinoma: 2018 practice guidance by the american association for the study of liver diseases. *Hepatology*. (2018) 68:723–50. doi: 10.1002/hep.29913

frontiers | Frontiers in Immunology

TYPE Original Research
PUBLISHED 30 January 2025
DOI 10.3389/fimmu.2025.1516848

OPEN ACCESS

EDITED BY
Bing Yang,
Tianjin Medical University, China

REVIEWED BY
Xin Hu,
National Center for Child Health and Development (NCCHD), Japan
Xinya Zhao,
Shandong Provincial Chest Hospital, China
Jun Hu,
Tianjin Medical University Cancer Institute and Hospital, China

*CORRESPONDENCE
Bin Song
Songlab_radiology@163.com
Yi Wei
drweiyi057@163.com

†These authors have contributed equally to this work and share first authorship

RECEIVED 25 October 2024
ACCEPTED 02 January 2025
PUBLISHED 30 January 2025

CITATION
Li Q, Zhang T, Yao S, Gao F, Nie L, Tang H, Song B and Wei Y (2025) Preoperative assessment of liver regeneration using T1 mapping and the functional liver imaging score derived from Gd-EOB-DTPA-enhanced magnetic resonance for patient with hepatocellular carcinoma after hepatectomy. *Front. Immunol.* 16:1516848. doi: 10.3389/fimmu.2025.1516848

Preoperative assessment of liver regeneration using T1 mapping and the functional liver imaging score derived from Gd-EOB-DTPA-enhanced magnetic resonance for patient with hepatocellular carcinoma after hepatectomy

Qian Li[1†], Tong Zhang[1†], Shan Yao[1], Feifei Gao[1], Lisha Nie[2], Hehan Tang[1], Bin Song[1,3*] and Yi Wei[1*]

[1]Department of Radiology, West China Hospital, Sichuan University, Chengdu, China, [2]MRI Research, GE Healthcare (China), Beijing, China, [3]Department of Radiology, Sanya People's Hospital, Sanya, China

Objectives: To explore whether T1 mapping parameters and the functional liver imaging score (FLIS) based on Gd-EOB-DTPA MRI could evaluate liver regeneration after hepatectomy for HCC patient.

Methods: This retrospective study finally included 60 HCC patients (48 men and 12 women, with a median age of 53 years). T1 relaxation time of liver before gadoxetic acid injection ($T1_{pre}$) and during the hepatobiliary phase ($T1_{HBP}$), reduction rate (Δ%) and FLIS were calculated, their correlations with liver fibrosis stage, hepatic steatosis, and liver regeneration, quantified as regeneration index (RI), were assessed by Kendall's tau-b correlation test or Spearman's correlation test. Multivariate linear regression analyses were used to explore the indicator of RI.

Results: $T1_{pre}$, $T1_{HBP}$, Δ%, and FLIS manifested significant correlation with fibrosis stage ($r = 0.434$, $P = 0.001$; $r = 0.546$, $P < 0.001$; $r = -0.356$, $P = 0.005$; $r = -0.653$, $P < 0.001$, respectively). $T1_{pre}$ showed significant correction with steatosis grade ($r = 0.415$, $P = 0.001$). Fibrosis stage and steatosis grade were associated with RI ($r = -0.436$, $P<0.001$; $r = -0.338$, $P = 0.008$). Accordingly, $T1_{pre}$, $T1_{HBP}$ and FLIS were the significant predictors ($P<0.05$) of RI in multivariate analysis. Similarly, in the patients undergoing minor hepatectomy (n=35), $T1_{HBP}$, Δ% and FLIS were related to RI ($P<0.05$) in multivariate analysis. Nevertheless, in the patients undergoing major hepatectomy (n=25), no T1 mapping parameter and FLIS was the independent predictor of RI.

Conclusions: T1 mapping parameters and FLIS were the potential noninvasive indicators of liver regeneration, except for HCC patients undergoing major hepatectomy.

Clinical relevance statement: The value of T1 mapping and FLIS with Gd-EOB-DTPA MRI for accurate preoperative evaluation of liver regeneration is critical to prevent liver failure and improve prognosis of HCC patients.

KEYWORDS

liver regeneration, t1 mapping, gadolinium ethoxybenzyl DTPA, carcinoma, hepatocellular, hepatectomy

Highlights

- Accurate preoperative evaluation of liver regeneration is critical to prevent liver failure.
- T1 mapping parameters and FLIS were associated with fibrosis stage and liver regeneration.
- T1 mapping parameters and FLIS were the potential noninvasive indicators of liver regeneration for HCC patients.

Introduction

Hepatocellular carcinoma (HCC) is the sixth most common malignant tumor and the third leading cause of cancer-related death worldwide (1). Although liver regeneration could occur after the first-line curative treatment for HCC, i.e., surgical resection, liver impairment or injury may exceed its hyperplastic ability, leading to post-operative liver failure (2, 3). Hence, accurate preoperative evaluation of liver regeneration (LR) is critical to the prognosis assessment and clinical management.

Advanced liver fibrosis and fatty liver are closely associated with the poor capacity of LR (4, 5). Currently, liver biopsy, magnetic resonance elastography (MRE), shear wave elastography (SWE), Intravoxel incoherent motion (IVIM) diffusion-weighted imaging and texture analysis have been used for preoperative evaluation of liver fibrosis and hepatic steatosis. However, invasiveness, sampling error, interobserver variability, low stability, the need of specific equipment and field strength dependency limit their clinical application (6–10). Evidence has proved that the change in the cell function and histological characteristics, concentration of extracellular matrix proteins, and activation of hepatic stellate cells, accompanied with the progression of liver fibrosis, would result in the changes in T1 relaxation time in fibrotic tissues (11, 12). Besides, hepatic steatosis induces a mixture of water and fat, and the fat is generally out-of-phase with water. In out-of-phase mixture of water and fat, the signal is subtracted by the fat component, resulting in slow T1 recovery and longer T1 relaxation time (13, 14). Liver fibrosis could also alter the expression levels of organic anion transporting polypeptides (Oatps) and multidrug resistance associated protein (Mrp), leading to an increased T1 relaxation time of the liver parenchyma in hepatobiliary phase with Gd-EOB-DTPA-enhanced MR (15). The T1 mapping sequence based on Gd-EOB-DTPA-enhanced MR do not depend on the device itself and directly reflect the true T1 value of tissues, thus providing more reliable and less subjective quantitative evaluation of liver function (15). Previous studies (16, 17) have proven that these metrics derived from T1mapping of pre-contrast ($T1_{pre}$) and 20-min hepatobiliary phase ($T1_{HBP}$ and T1 reduction rate) were suitable for detecting liver fibrosis(≥ F2)($T1_{pre}$: AUC, 0.70-0.89; $T1_{HBP}$: AUC,0.86; T1 reduction rate;AUC,0.89), and these metrics were also significantly correlated with hepatic steatosis($T1_{pre}$: r=-0.695, P<0.001; $T1_{HBP}$: r=0.263, P<0.046 and T1 reduction rate: r=-0.310, P=0.018). Meanwhile, a functional liver imaging score (FLIS) that takes into account three features of gadoxetic acid–enhanced MRI of the liver: enhancement quality, rate of biliary contrast excretion, and persistence of signal intensity in the portal vein, was also associated with the severity of diffuse liver disease, FLIS ≤ 3 and FLIS≥ 5 were the optimal cutoff for distinguish ALBI grade 3 (AUC, 0.974-0.994) and Child-Pugh A or diffuse liver disease (AUC, 0.93), respectively (18, 19). Hence, T1 mapping of pre-contrast, 20-min

Abbreviations: ALB, albumin; HCC, Hepatocellular carcinoma; HBP, hepatobiliary phase; IVIM, Intravoxel incoherent motion; ICC, intra-class correlation coefficient; SWE, shear wave elastography; LR, liver regeneration; LVpre, volume of preoperative future remnant liver; LVpost, volume of postoperative remnant liver; MRE, magnetic resonance elastography; Mrp, multidrug resistance associated protein; MOLLI, Modifed lock-locker inversion recovery; Oatps, organic anion transporting polypeptides; FLIS, a functional liver imaging score; PHRR, parenchymal hepatic resection rate; RI, regeneration index; SMART1Map, adaptive recovery times for T1 mapping sequence; T1pre, T1 relaxation time of the liver before gadoxetic acid injection; $T1_{HBP}$, T1 relaxation time of the liver 20 min after gadoxetic acid injection; VIF, Variance Inflation Factor; Δ%, the reduction rate of T1 relaxation time.

hepatobiliary phase and FLIS are essential for preoperative assessment of LR capacity.

According to the previous studies (7, 20, 21), the resected volume is of vital importance for LR, and the large resected volume with major hepatectomy may cause high regeneration indices, such as regeneration index (RI), and hide the importance of liver itself on liver regeneration. Thus, it is warrant to separate out the analysis for patients who had minor vs. major hepatectomies.

The aim of our study is to evaluate the capacity of LR by Gd-EOB-DTPA-enhanced T1 mapping and FLIS score in HCC patients, and go on subgroup analysis with the type of hepatectomy.

Materials and methods

Participants and data collection

This retrospective study was conducted in accordance with the ethical guidelines of the Declaration of Helsinki and was approved by the Institutional Review Board of Sichuan university, West China Hospital. Due to the retrospective nature, written informed consent was waived. A total of 224 pathological confirmed HCC patients, undergoing curative-intent hepatectomy and preoperative T1-mapping imaging examination derived from Gd-EOB-DTPA-enhanced magnetic resonance between September 2018 and May 2022, were consecutively recruited. The inclusion criteria were as follows: (1) patients were aged ≥18 years; (2) the time interval between preoperative T1-mapping imaging examination and hepatectomy was less than 4 weeks; (3) primary HCC without treatment; (4) have follow-up contrast-enhanced CT. Additionally, patients were excluded according to the following exclusion criteria (Figure 1): 1) received any anti-HCC treatments, such as hepatectomy, TACE, chemotherapy or radiofrequency ablation prior to hepatectomy, due to that anti-HCC treatment would cause uncertain impact on image quality, such as like signal interference and artifact, finally affecting the accuracy of imaging evaluation in liver parenchymal function. (n=10); 2) had diffuse recurrence or intrahepatic metastasis on follow-up computed tomography (CT) which would cause technical segmentation failure(n=18). The main reason was that the recurrent lesions and metastases spread throughout the liver parenchyma in patients with diffuse recurrence or intrahepatic metastasis, and it was difficult to

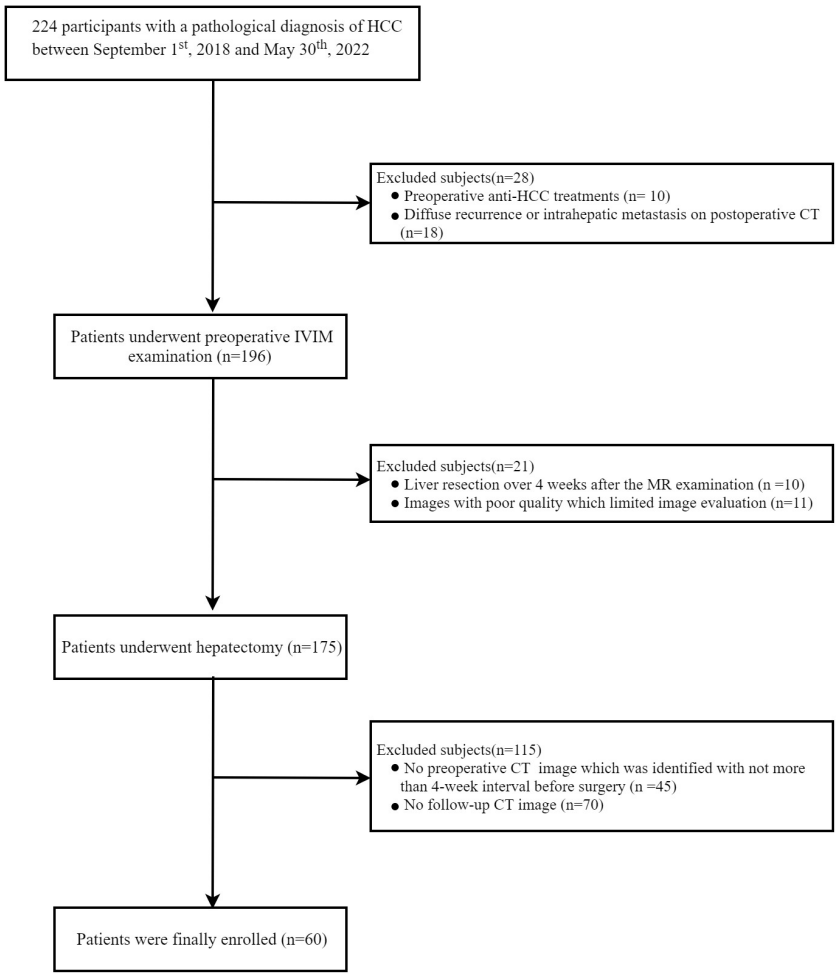

FIGURE 1
Flow diagram of the study population. RI, regeneration index.

segment hepatic parenchyma technically; 3) the time interval between hepatectomy and MR imaging was more than 4 weeks (n =11); 4) images with poor quality (e.g., severe artifact) that limited image evaluation (n=10); 5) no preoperative CT image from less than 4-weeks before hepatectomy (n=45); and 6) lacked follow-up contrast-enhanced CT in one year after hepatectomy (n=70). Finally, 60 patients with HCC were included in the final study cohort. Clinicopathologic variables, fibrosis stage confirmed by histological examination of a resected specimen (according to the METAVIR scoring system (22), F0-1 as no to mild fibrosis, F2 as significant fibrosis, F3 as advanced fibrosis, and F4 as cirrhosis), inflammation grade confirmed by histological examination of a resected specimen [according to the Scheuer scoring system (23)], steatosis grade confirmed by histological examination of a resected specimen [according to the amount of surface area of the parenchyma that was visually determined to be affected by steatosis (24), hepatic steatosis was divided into none (S0, < 5%), mild (S1, 5–33%), and moderate–severe (S2–3, > 33%)].

MR imaging

A 3.0-T MR system (Discovery MR 750w, GE Healthcare) with a 16-channel phased-array torso coil (GE Medical System) was used for MRI examinations. Every patient fast for 6-8 hours before MR imaging. Saturation method using adaptive recovery times for T1 mapping sequence (SMART1Map) was used for T1 mapping scan. The parameters were as follows: TE/TR/flip-angle: 1.64msec/3.3msec/50°, slice thickness 8.0 mm, slice gap 2 mm, FOV 40 × 36 cm^2, matrix 192 × 128, NEX 1. T1 mapping was performed before and 20 min after injection of Gd-EOB-DTPA (0.025mmol/kg; Primovist; Bayer Pharma AG, Berlin, Germany), which was administered intravenously using a bolus injection at the injection rate of 1 mL/s and followed by a 20-mL saline flush. T1 mapping images were then transferred to a T1 mapping and quantitative dynamic contrast enhanced MRI software package (Omni-Kinetics, GE Healthcare). And Omni-Kinetics using the VFA method automatically generated T1 maps.

CT techniques

All patients underwent two multi-slice CT scan (preoperative CT and postoperative CT) by Revolution CT (GE Healthcare) or SOMATOM definition (Siemens). The scanning parameters were as follows: tube voltage: 100 kVp or 120 kVp, tube current: 200–450 mA, slice thickness: 1.5-5 mm, pitch: 0.992: 1, rotation speed: 0.5 s/rot, ASIR-V: 20%. All patients received an intravenous, nonionic contrast medium (iodine concentration, 300-370 mg/mL; volume, 1.5–2.0 ml/kg; contrast type, Iopromide Injection, Bayer Pharma AG) at a rate of 2-3 ml/s, and then a 20 mL saline was injected for the flush. The arterial phase and portal venous phases started at about 30-35 s and 60-75 s, respectively, after the contrast injection.

Imaging analysis

Two independent radiologists (LQ and YW), with 10 and 6 years of experience in abdominal imaging, blinded to the clinical data, laboratory tests, and histopathological results, reviewed all the T1 mapping images. T1 mapping was generated automatically inline based on a pixel-by-pixel fitting. The ROIs were kept in the same position before and after enhancement. According to the resection margin based on postoperative contrast-enhanced CT image, the section of largest future remnant liver parenchyma was selected to measure related relaxation values by referring to the HBP imaging, avoiding visible vessels and artifacts and maintaining a 0.5 cm distance to the surface of the liver. The mean T1 relaxation time for three ROIs was considered as the representative T1 relaxation time for the liver. Δ% refers to the reduction rate of T1 relaxation time, which was calculated as $[(T1_{pre}) - (T1_{HBP})]/(T1_{HBP}) \times 100\%$, where $T1_{pre}$ and $T1_{HBP}$ are the T1 relaxation time of the liver before and 20 min after gadoxetic acid injection. The mean value measured by the two radiologists was used for further statistical analysis. Additionally, the respective measures obtained by the two radiologists were used to determine inter-observer agreement expressed in terms of the intra-class correlation coefficient (ICC).

Two independent radiologists (SY and TZ), with 6 and 12 years of experience in abdominal imaging, blinded to the clinical data, laboratory tests, and histopathological results, reviewed all HBP–enhanced images. The radiologists assigned an FLIS to each patient independently. When the FLIS ranged from 0 to 6 points and was calculated by summing scores for liver parenchymal enhancement, biliary contrast excretion, and portal vein sign (18, 25):

1. Enhancement quality score of 0, 1, or 2 compared the liver to right kidney uptake. A score of 0, 1, or 2 meant the liver was hypo-, iso-, or hyperintense, respectively, to the right kidney.
2. Excretion quality score of 0, 1, or 2 was determined on the basis of the degree of contrast agent excretion into the biliary tract. A score of 0, 1, or 2 meant there was no biliary tract contrast excretion, excretion into peripheral intrahepatic bile ducts or the right and/or left hepatic duct(s), or excretion into the common hepatic duct, the common bile duct, or the duodenum, respectively.
3. The portal vein sign quality score of 0, 1, or 2 was on the basis of the portal vein relative to liver parenchymal signal intensity. A score of 0, 1, or 2 meant the portal vein was hyper-, iso-, or hypointense to the liver parenchyma, respectively.

Preoperative CT liver volume

The liver evaluation software embedded on a post-processing workstation (uWs-CT, R005, United-Imaging Healthcare, Shanghai, China) was used for liver volume assessment based on preoperative contrast-enhanced CT. The entire liver parenchyma

and vessels (mainly including the hepatic artery, portal vein, hepatic vein, and their main branches) were automatically extracted by this software. Manual corrections of liver contours were performed by an experienced radiologist (TZ) with 10 years of abdominal CT experience when necessary. Secondly, a straight line along the maximum diameter of the tumor was manually drawn by the above experienced radiologist, and the tumor was then semiautomatically segmented. The volume of the total functional liver (removing tumor volume and vessel volume) was automatically calculated and displayed. Besides, the above experienced radiologist drew a virtual curve along the surgical margin according to the postoperative CT image. Finally, the volume of the preoperative remnant liver (LV_{pre} removing volume of vessels) was calculated automatically. The parenchymal hepatic resection rate (PHRR) (20) was calculated using the following equation:

$$PHRR = \frac{(Volume\ of\ the\ total\ functionalliver) - LVpre}{Volume\ of\ total\ functional\ liver} \times 100\%$$

Postoperative CT liver volume

Since the retrospective nature and there was no routine protocol for postoperative follow-up CT, the timing of follow-up CT was varied. The remnant liver volume often regenerates dramatically in the 6th month after hepatectomy. Accordingly, the follow-up portal phase CT images acquired closest to the 6th month after surgery were utilized to calculate the volume of the postoperative remnant liver (LV_{post}). As described previously, LV_{post} and major intrahepatic vessels were automatically extracted and manually corrected, and then the LV_{post} (after subtracting the volume of vessels) was automatically calculated. The regeneration index (RI) was calculated using the following equation:

$$RI = \frac{LVpost - LVpre}{LVpre} \times\ 100\ \%$$

Statistical analysis

Categorical variables were summarized as frequencies and proportions, while continuous variables were expressed as means with standard deviations or medians with interquartile ranges, depending on the distribution assessed by the Kolmogorov–Smirnov test. Independent sample t test or Mann–Whitney U test was used to assess the differences of baseline characteristics between patients undergoing minor or major hepatectomy for continuous variables, the chi-square test or Fisher's exact test or Wilcoxon rank sum test was used for categorical variables. Correlations between baseline characteristics and RI were evaluated by Spearman's correlation test. The relation between T1 mapping parameters and fibrosis stage, fibrosis stage and RI were assessed using Kendall's tau-b correlation test. Multivariate linear regression analyses were used to find the factors related to RI, and only those parameters which had statistical significance ($P<0.05$) in Spearman's correlation test were subsequently included in further multivariate regression analysis. VIF (Variance Inflation Factor) was used to evaluate multicollinearity between variables in multivariate analysis, and VIF >10 considered indicative of multicollinearity.

Intra-class correlation coefficient (ICC) with the two-way random method was used to check the interobserver agreement toward the diffusion parameters (values < 0.50 poor agreement, 0.51–0.75 moderate agreement, 0.76–0.90 good agreement, > 0.91 excellent agreement). PASS software was used to ensure robust sample size determination and power analysis in multiple linear regression. All statistical tests were performed using SPSS software (Version 26, IBM) and R software (Version 4.0.2). All *P* value less than 0.05 were considered significant.

Results

The baseline characteristics of the included patients

Finally, a total of 60 HCC patients (48 men and 12 women, with a median age of 53 years) were included in this study, and the sample size was in the adequate range for the study. The follow-up period from surgery to postoperative CT scans ranged from 1.5–11.5 months. LV_{pre}, LV_{post}, PHRR and RI of all the patients were 729.18 ± 32.25, mL; 1022.29 ± 28.83, mL; 38.61 ± 2.40, %;50.84 ± 6.08, %, respectively. There were 25 patients receiving major hepatectomy, and the remaining patients (n=35) underwent minor hepatectomy. Compared with the patients undergoing major hepatectomy, these undergoing minor hepatectomy had higher LV_{pre} (867.50 ± 201.31, mL VS. 535.54 ± 170.40.52, mL, $P<0.001$) and LV_{post} (1081.58 ± 197.61, mL VS. 939.28 ± 234.42, mL, $P=0.014$), lower PHRR (26.57 ± 12.35, % VS. 55.47 ± 11.22, %, $P<0.001$) and RI (27.91 ± 24.82, % VS. 82.94 ± 52.39, %, $P<0.001$). However, the other clinical characteristics were not significant different (all $P>0.05$)between the two subgroups. Detailed information about the baseline characteristics were summarized in Table 1.

When considering T1 mapping parameters and FLIS, detailed values of $T1_{pre}$ (ms), $T1_{HBP}$ (ms), Δ% and FLIS of all the 60 patients included in the study was listed in Supplementary Table S1. The ICC value of the two radiologists for $T1_{pre}$, $T1_{HBP}$, Δ% and FLIS were 0.881 (95% CI, 0.808-0.927), 0.920 (95% CI, 0.895-0.936), 0.903 (95% CI, 0.889-0.918) and 0.933 (95% CI, 0.921-0.946) respectively. No significant difference of T1 mapping parameters and FLIS (all $P>0.05$) manifested between patients receiving minor and major hepatectomy (Table 2). Due to the excellent agreement in ICCs of FLIS, for simplicity, only the FLIS assessed by the more experienced radiologist 2 were used in the analyses.

The relations between T1 mapping parameters, FLIS and liver fibrosis

In all the patients, $T1_{pre}$ and $T1_{HBP}$ manifested a significant tendency of positive correlation with fibrosis stage (r = 0.434,

10.3389/fimmu.2025.1516848

TABLE 1 Baseline characteristics of the included patients.

Baseline characteristics	Total patients (n=60)	Minor hepatectomy (n=35)	Major hepatectomy (n=25)	*P* value
Clinical characteristics				
Age (years)	53.00 (44.00,58.00)	55.50 (43.75,60.25)	51.00 (42.50,56.00)	0.103
Gender				0.513
Male	48 (80.00)	27 (77.14)	21 (84.00)	
Female	12 (20.00)	8 (22.86)	4 (16.00)	
BMI	23.78±0.45	23.73±4.04	23.67±2.51	0.946
ALT (IU/L)	37.00 (23.00,63.50)	33.00 (21.75,48.50)	44.00 (28.50,68.00)	0.081
AST (IU/L)	35.50 (25.50,51.00)	28.50 (22.50,38.00)	36.00 (28.60,42.00)	0.082
ALP (IU/L)	91.00 (80.00,136.25)	88.00 (76.75,118.25)	83.50 (73.00,96.00)	0.254
GGT (IU/L)	71.00 (38.50,146.25)	48.00 (30.75,85.75)	60.00 (41.20,92.00)	0.006
ALB (g/L)	42.45±0.70	41.94±5.46	43.16±5.39	0.397
TBIL (umol/L)	13.60 (10.55,16.63)	12.55 (9.55,16.40)	14.80 (11.60,19.05)	0.146
DBIL (umol/l)	4.85 (2.40,6.00)	4.10 (3.28,5.43)	5.20 (4.00,7.20)	0.057
HGB (g/L)	141.76±2.68	140.38±20.91	143.04±19.91	0.624
PLT (10^9/L)	157.90±10.34	151.88±76.40	168.48±81.76	0.427
PT (s)	11.35 (10.90,11.93)	11.10 (10.70,11.70)	11.60 (11.25,12.35)	0.684
INR	1.01 (0.96,1.05)	1.00 (0.96,1.05)	1.02 (0.98,1.08)	0.113
HbsAg (Positive, %)	51 (85)	29 (82.86)	22 (88)	0.722
HBeAg (Positive, %)	5 (8.33)	5 (14.29)	0 (0)	0.069
Anti-HCV (Positive, %)	0 (0)	0 (0)	0 (0)	1.000
ALBI grade				0.337
I	48 (80.00)	27 (77.14)	21 (84.00)	
II	10 (16.67)	6 (17.14)	4 (16.00)	
III	2 (3.33)	2 (5.71)	0 (0.00)	
LVpre (mL)	729.18±32.25	867.50±201.31	535.54±170.40	<0.001*
LVpost (mL)	1022.29±28.83	1081.57±197.61	939.28±234.42	0.014*
PHRR (%)	38.61±2.40	26.57±12.35	55.47±11.22	<0.001*
RI (%)	50.84±6.08	27.91±24.82	82.94±52.39	<0.001*
FLIS	3 (2,5.95)	3 (2,6)	3 (2,5.7)	0.497
Pathological characteristics				
Inflammation grade				0.767
A0	0 (0.00)	0 (0.00)	0 (0.00)	
A1	6 (10.00)	3 (8.57)	3 (12.00)	
A2	22 (36.67)	12 (34.29)	10 (40.00)	
A3	32 (53.33)	20 (57.14)	12 (48.00)	
Fibrosis stage				0.134
F0-1	16 (26.67)	9 (25.71)	7 (28.00)	
F2	9 (15.00)	3 (8.57)	6 (24.00)	

(Continued)

TABLE 1 Continued

Baseline characteristics	Total patients (n=60)	Minor hepatectomy (n=35)	Major hepatectomy (n=25)	*P* value
F3	15 (25.00)	12 (34.29)	3 (12.00)	
F4	20 (33.33)	11 (31.43)	9 (36.00)	
Steatosis grade				0.844
S0	25 (41.67)	14 (40.00)	11 (44.00)	
S1	33 (55.00)	20 (57.14)	13 (52.00)	
S2-3	2 (3.33)	1 (2.86)	1 (4.00)	
T1 mapping parameters				
T1-pre (ms)	992.65±10.05	1003.72±60.96	977.15±58.88	0.195
T1-HBP (ms)	485.67±8.52	496.01±588.27	471.20±74.35	0.153
Δ%	51.06±0.73	50.54±5.56	51.79±5.86	0.405

Data are represented in mean ± SD or medians with interquartile ranges, or frequency (%); And Data were evaluated by independent t test or Mann-Whitney U test for continuous variables and the Chi-square test or Fisher's exact test or Wilcoxon rank sum test for categorical variables; * referred to P<0.05; RI, regeneration index; PHRR, parenchymal hepatic resection rate; BMI, body mass index; ALT, Alanine aminotransferase; AST, Aspartate aminotransferase; ALP, alkaline phosphatase; GGT, γ-Glutamyl Transferase; ALB, albumin; TBIL, total bilirubin; DBIL, direct bilirubin; HGB, hemoglobin; PLT, Platelet count; PT, Prothrombin time; INR, international normalized ratio; ALBI, albumin-bilirubin grade; LVpre: volume of preoperative future remnant liver; LVpost: volume of postoperative remnant liver, RI, regeneration index; PHRR, parenchymal hepatic resection rate; T1-pre, T1 relaxation time of the liver before gadoxetic acid injection; T1-HBP, T1 relaxation time of the liver 20 min after gadoxetic acid injection; Δ%, the reduction rate of T1 relaxation time.

TABLE 2 Results of the univariate analysis of correlations between the regeneration index and preoperative variables.

Variables	Total patients (n=60)		Minor hepatectomy (n=35)		Major hepatectomy (n=25)	
	Correlation coefficient	*P* value	Correlation coefficient	*P* value	Correlation coefficient	*P* value
Age (years)	-0.176	0.178	-0.116	0.333	-0.128	0.542
Gender	0.022	0.870	0.148	0.395	0.061	0.774
PHRR (%)	0.770	<0.001*	0.444	0.007*	0.609	0.001*
BMI	0.089	0.504	0.196	0.267	-0.120	0.566
ALB (g/L)	0.316	0.014*	0.199	0.251	0.480	0.015*
ALT (IU/L)	0.097	0.464	-0.289	0.097	0.276	0.181
AST (IU/L)	0.183	0.163	-0.320	0.061	0.182	0.384
ALP (IU/L)	0.067	0.611	-0.041	0.816	-0.065	0.759
GGT (IU/L)	0.095	0.472	-0.290	0.091	-0.324	0.115
TBIL (umol/L)	-0.005	0.970	-0.248	0.151	-0.131	0.532
DBIL (umol/L)	-0.031	0.816	-0.189	0.278	-0.158	0.452
HGB (g/L)	-0.137	0.302	-0.148	0.404	-0.218	0.296
PLT (10^9/L)	0.242	0.065	0.307	0.077	0.104	0.622
PT (s)	0.125	0.346	-0.090	0.614	-0.290	0.159
INR	0.048	0.716	-0.067	0.705	-0.148	0.479
HbsAg	-0.026	0.846	0.060	0.732	-0.273	0.186
HBeAg	-0.203	0.120	-0.194	0.264	–	–
ALBI grade	-0.014	0.914	-0.162	0.353	–	–

(Continued)

TABLE 2 Continued

Variables	Total patients (n=60)		Minor hepatectomy (n=35)		Major hepatectomy (n=25)	
	Correlation coefficient	*P* value	Correlation coefficient	*P* value	Correlation coefficient	*P* value
Type of partial hepatectomy	0.671	<0.001*	–	–		
FLIS	0.300	0.020*	0.484	0.003*	0.275	0.076
LVpre (mL)	-0.817	<0.001*	-0.578	<0.001*	-0.603	0.001*
T1-pre (ms)	-0.467	<0.001*	-0.378	0.025*	-0.575	0.003*
T1-HBP(ms)	-0.592	<0.001*	-0.725	<0.001*	-0.430	0.032*
Δ%	0.395	0.002*	0.587	<0.001*	0.081	0.701

* referred to *P*<0.05; RI, regeneration index; PHRR, parenchymal hepatic resection rate; BMI, body mass index; ALT, Alanine aminotransferase; AST, Aspartate aminotransferase; ALP, alkaline phosphatase; GGT, γ-Glutamyl Transferase; ALB, albumin; TBIL, total bilirubin; DBIL, direct bilirubin; HGB, hemoglobin; PLT, Platelet count; PT, Prothrombin time; INR, international normalized ratio; ALBI, albumin-bilirubin grade; LVpre: volume of preoperative future remnant liver; LVpost: volume of postoperative remnant liver; T1-pre, T1 relaxation time of the liver before gadoxetic acid injection; T1-HBP, T1 relaxation time of the liver 20 min after gadoxetic acid injection; Δ%, the reduction rate of T1 relaxation time.

P =0.001 and r = 0.546, *P* < 0.001, respectively, Figure 2A), and a significant tendency of negative correlation also showed between Δ% and fibrosis stage (r = -0.356, *P* =0.005, Figure 2A). FLIS also showed significant correlation with fibrosis stage (r = -0.653, *P* <0.001, Figure 2B). Meanwhile, $T1_{pre}$, $T1_{HBP,}$ Δ% and FLIS also showed significant correlations with fibrosis stage ($T1_{pre}$: r =0.442, *P*=0.008; $T1_{HBP}$: r =0.600, *P*<0.001; Δ%: r =-0.433, *P*=0.009; FLIS, r =-0.579, *P*=0.001, Figures 3A, B) in the patients undergoing minor hepatectomy. While in the patients undergoing major hepatectomy, moderate correlation showed between $T1_{pre}$ and fibrosis stage (r = 0.408, *P*=0.043, Figure 4A), $T1_{HBP}$ and fibrosis stage (r = 0.440, *P*=0.028, Figure 4A), FLIS and fibrosis stage (r =-0.435, *P*=0.001, Figure 4B).

The relations between liver fibrosis and RI

In the total patients, fibrosis stage and RI manifested a statistically significant negative correlation (r = -0.436, *P*<0.001, Figure 2C). Besides, a significant correlation occurred between fibrosis stage and RI (r = -0.590, *P*<0.001, Figure 3C) in the patients undergoing minor hepatectomy. However, fibrosis stage did not show a significant negative correlation with RI (r =-0.368, *P*= 0.071, Figure 4C) in the patients undergoing major hepatectomy.

The relations between T1 mapping parameters, FLIS and hepatic steatosis

Whether in the total patients or subgroups undergoing minor or major hepatectomy, $T1_{pre}$ manifested significant correlation with steatosis grade (total patients: r = 0.415, *P* =0.001, Supplementary Figure S1A; patients undergoing minor hepatectomy: r = 0.470, *P* =0.004, Supplementary Figure S2A; patients undergoing major hepatectomy: r = 0.413, *P* =0.040, Supplementary Figure S3A), however, $T1_{HBP,}$ Δ% and FLIS did not show significant correlation with steatosis grade (all *P*>0.05, Supplementary Figures S1–S3A, S1–S3B).

The relations between hepatic steatosis and RI

Whether in the total patients or subgroups undergoing minor hepatectomy, significant correlation was observed between steatosis

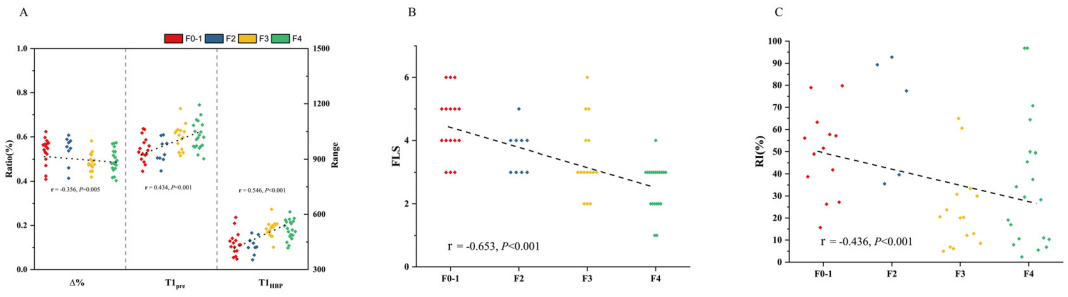

FIGURE 2
The relation between T1 mapping parameters and fibrosis stage **(A)**, FLIS and fibrosis stage **(B)**, fibrosis stage and RI **(C)** in total patients. RI, regeneration index; T1pre, T1 relaxation time of the liver before gadoxetic acid injection; T1HBP, T1 relaxation time of the liver 20 min after gadoxetic acid injection; Δ%, the reduction rate of T1 relaxation time; FLIS a functional liver imaging score.

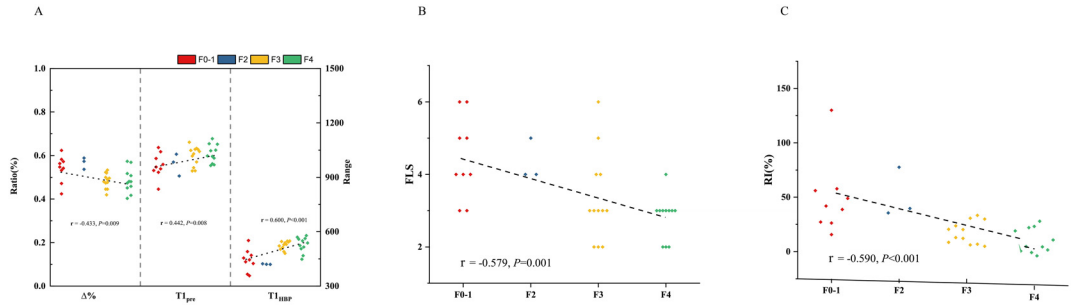

FIGURE 3
The relation between T1 mapping parameters and fibrosis stage **(A)**, FLIS and fibrosis stage **(B)**, fibrosis stage and RI **(C)** in patients undergoing minor hepatectomy. RI, regeneration index; T1pre, T1 relaxation time of the liver before gadoxetic acid injection; T1HBP, T1 relaxation time of the liver 20 min after gadoxetic acid injection; Δ%, the reduction rate of T1 relaxation time; FLIS, a functional liver imaging score.

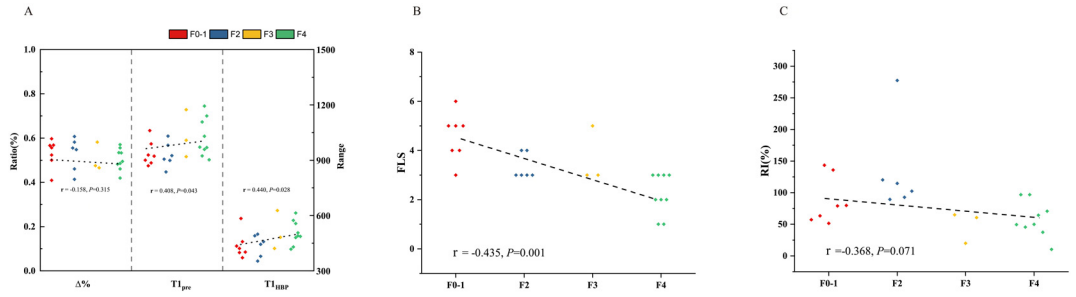

FIGURE 4
The relation between T1 mapping parameters and fibrosis stage **(A)**, FLIS and fibrosis stage **(B)**, fibrosis stage and RI **(C)** in patients undergoing major hepatectomy. RI, regeneration index; T1pre, T1 relaxation time of the liver before gadoxetic acid injection; T1HBP, T1 relaxation time of the liver 20 min after gadoxetic acid injection; Δ%, the reduction rate of T1 relaxation time; FLIS, a functional liver imaging score.

grade and RI (total patients: r = -0.338, P =0.008, Supplementary Figure S1C; patients undergoing minor hepatectomy: r = -0.403, P =0.004, Supplementary Figure S2C). However, no statistically significant correlation was observed between steatosis grade and RI in the patients undergoing major hepatectomy (r = -0.188, P =0.369, Supplementary Figure S3C).

The relations between T1 mapping parameters and RI

Total patients

In the total patients, in addition to PHRR (r = 0.770, P<0.001), ALB (r = 0.316, P=0.014), type of partial hepatectomy (r = 0.671, P<0.001) and LVpre(r = -0.817, P<0.001), T1pre(r = -0.467, P<0.001), $T1_{HBP}$(r = -0.592, P <0.026) and Δ% (r = 0.395, P = 0.002), FLIS (r = 0.300, P=0.020) were also identified as significant predictors of RI in spearman relation analysis (Table 2, Figure 5).

Multicollinearity occurs If two variables with the strong intercorrelation were simultaneously included in multivariate analysis; hence, only one variable was included to avoid the occurrence of multicollinearity. Considering the strong intercorrelation between PHRR and LV_{pre} (r= -0.785, P<0.001, Supplementary Figure S4A), PHRR and type of partial hepatectomy (r= 0.794, P<0.001, Supplementary Figure S4B), LV_{pre} and type of partial hepatectomy (r= -0.785, P<0.001, Supplementary Figure S4C), $T1_{pre}$ and $T1_{HBP}$(r= 0.485, P<0.001, Supplementary Figure S5A), $T1_{HBP}$ and Δ% (r= -0.834, P<0.001, Supplementary Figure S5C), FLIS and $T1_{pre}$(r= -0.213, P=0.029, Supplementary Figure S5D), FLIS and $T1_{HBP}$(r= -0.398, P<0.001, Supplementary Figure S5E), FLIS and Δ% (r=0.286, P=0.003, Supplementary Figure S5F). Accordingly, 9 independent models in multivariate analysis were tested (Model 1 included ALB, PHRR, T1pre and Δ%; Model 2 included ALB, PHRR and $T1_{HBP}$; Model 3 included ALB, Type of partial hepatectomy, T1pre and Δ%; Model 4 included ALB, Type of partial hepatectomy and $T1_{HBP}$; Model 5 included ALB, LVpre, T1pre and Δ%; Model 6 included ALB, LVpre and $T1_{HBP,}$ Model 7 included ALB, LVpre and FLIS; Model 8 included ALB, Type of partial hepatectomy and FLIS; Model 9 included ALB, PHRR and FLIS), Model 1 achieved the highest adjusted R^2 of 0.594. T1pre, $T1_{HBP}$ and FLIS showed significantly negative or positive linear associations with RI in all the models ($T1_{pre}$:Model 1, Standardized β = -0.346, P< 0.001; Model 3, Standardized β = -0.386, P<0.001; Model 5: Standardized β = -0.305, P=0.003; $T1_{HBP}$: Model 2, Standardized β = -0.272, P=0.006; Model 4, Standardized β = -0.362, P<0.001; Model 6:

10.3389/fimmu.2025.1516848

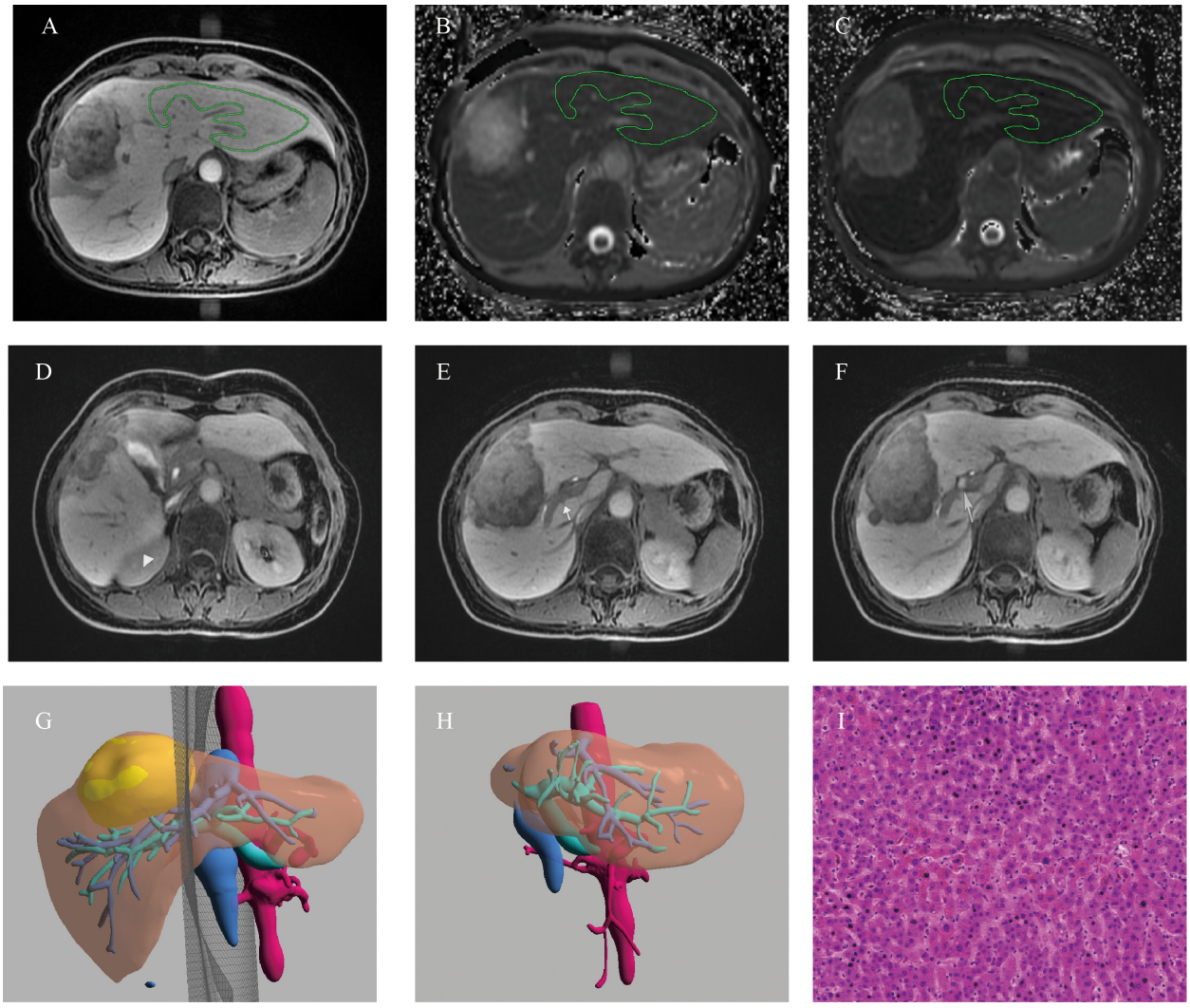

FIGURE 5
Example of a 52-years old female patients with HCC. **(A)** The ROI placement of live parenchyma based on HBP, **(B)** the T1pre was 921.79 ms, **(C)** the $T1_{HBP}$ was 371.71 ms, and Δ% was 59.73%; **(D)**The signal intensity of liver parenchyma was isointense to the right kidney (triangle, score 1); **(E)** biliary contrast excreted into the common bile duct (dovetail arrow, score 2); **(F)** the portal vein (arrow) demonstrated hypointensity relative to thehepatic parenchyma (score 2), hence, the functional liver imaging score (FLIS) was 5; **(G)**The axial cross section image of the preoperative simulated surgical tangent; **(H)**The axial image of the actual remnant liver on the sixth month after surgery, and RI was 78.94%; **(I)** The fibrosis stage of lesion-free area was histopathologically proven to be F1 (original magnification, ×20); RI, regeneration index; T1pre, T1 relaxation time of the liver before gadoxetic acid injection; $T1_{HBP}$, T1 relaxation time of the liver 20 min after gadoxetic acid injection; Δ%, The reduction rate of T1 relaxation time, FLIS, a functional liver imaging score.

Standardized β = -0.183, *P*= 0.005; FLIS: Model 7, Standardized β = 0.233, *P*=0.037; Model 8, Standardized β = 0.256, *P*=0.040; Model 9, Standardized β = 0.231, *P*=0.033, Table 3). The whole VIFs were under 10, and it meant that no multicollinearity occurred between variables in all the multivariate model.

Patients undergoing minor or major hepatectomy

Similarly, considering the strong intercorrelation between PHRR and LV_{pre} (r= -0.495, *P*=0.003, Supplementary Figure S6A), $T1_{HBP}$ and Δ% (r= 0.879, *P*<0.001, Supplementary Figure S6D), $T1_{HBP}$ and FLIS (r= -0.478, *P*=0.001, Supplementary Figure S6F), Δ% and FLIS (r=0.386, *P*=0.003, Supplementary Figure S6G) in patients undergoing minor hepatectomy, accordingly, 6 independent models in multivariate analysis were tested (Model 1 included PHRR, $T1_{pre}$ and $T1_{HBP}$; Model 2 included PHRR, $T1_{pre}$ and Δ%; Model 3 included LV_{pre}, $T1_{pre}$ and $T1_{HBP}$, $T1_{pre}$ and Δ%; Model 4 included LV_{pre}, $T1_{pre}$ and Δ%; Model 5 included LV_{pre}, $T1_{pre}$ and FLIS; Model included PHRR, $T1_{pre}$ and FLIS), $T1_{HBP}$, Δ% and FLIS still showed significantly negative or positive linear associations with RI in all the models ($T1_{HBP}$: Model 1, Standardized β = -0.549, *P*< 0.001; Model 3, Standardized β = -0.510, *P*<0.001; Δ%:Model 2: Standardized β = 0.532,*P*<0.003; Model 4, Standardized β = 0.497, *P*=0.001; FLIS: Model 5, Standardized β = 0.029, *P*=0.017; Model 6, Standardized β = 0.349, *P*=0.017, Table 3). And all the VIFs were under 10.

Meanwhile, in consideration of the strong intercorrelation between PHRR and LV_{pre} (r= -0.579, *P*=0.002, Supplementary Figure S7A), $T1_{pre}$ and $T1_{HBP}$ (r= 0.532, *P*=0.006, Supplementary

TABLE 3 Results of the multivariate linear regressions with RI as the dependent variable in total patients, in patients undergoing minor hepatectomy, and in patients undergoing major hepatectomy.

	Covariates	Standardized β	*P* value	Adjusted R^2 of the Model	VIF
Total Patients (n=60)	Model 1			0.594	
	ALB	0.096	0.278		1.034
	PHRR	0.570	<0.001*		1.151
	$T1_{pre}$	-0.346	<0.001*		1.054
	Δ%	0.104	0.246		1.071
	Model 2			0.517	
	ALB	0.103	0.269		1.032
	PHRR	0.580	<0.001*		1.147
	$T1_{HBP}$	-0.272	0.006*		1.113
	Model 3			0.495	
	Type of partial hepatectomy	0.479	<0.001*		1.057
	ALB	0.140	0.139		1.014
	$T1_{pre}$	-0.386	<0.001*		1.033
	Δ%	0.188	0.048*		1.016
	Model 4			0.456	
	Type of partial hepatectomy	0.497	<0.001*		1.049
	ALB	0.146	0.138		1.013
	$T1_{HBP}$	-0.362	<0.001*		1.036
	Model 5			0.501	
	LV_{pre}	-0.565	<0.001*		1.435
	ALB	0.042	0.662		1.102
	$T1_{pre}$	-0.305	0.003*		1.120
	Δ%	0.020	0.842		1.227
	Model 6			0.448	
	LV_{pre}	-0569	<0.001*		1.422
	ALB	0.051	0.617		1.097
	$T1_{HBP}$	-0.183	0.005*		1.321
	Model 7			0.462	
	LV_{pre}	-0.561	<0.001		1.331
	ALB	0.001	0.992		1.086
	FLIS	0.233	0.037		1.312
	Model 8			0.372	
	Type of partial hepatectomy	0.443	<0.001		1.326
	ALB	0.093	0.383		1.062
	FLIS	0.256	0.040		1.390
	Model 9			0.490	

(Continued)

TABLE 3 Continued

	Covariates	Standardized β	*P* value	Adjusted R^2 of the Model	VIF
	PHRR	0.572	<0.001		1.250
	ALB	0.051	0.596		1.067
	FLIS	0.231	0.033		1.293
Patients undergoing minor hepatectomy (n=35)	Model 1			0.594	
	PHRR	0.324	0.010*		1.157
	$T1_{pre}$	-0.180	0.140		1.189
	$T1_{HBP}$	-0.549	<0.001*		1.340
	Model 2			0.609	
	PHRR	0.316	0.010*		1.161
	$T1_{pre}$	-0.455	<0.001*		1.020
	Δ%	0.532	<0.001*		1.182
	Model 3			0.573	
	LV_{pre}	-0.310	0.024*		1.350
	$T1_{pre}$	-0.163	0.191		1.176
	$T1_{HBP}$	-0.510	<0.001*		1.552
	Model 4			0.586	
	LV_{pre}	-0.297	0.028		1.363
	$T1_{pre}$	-0.420	0.001*		1.052
	Δ%	0.497	0.001*		1.378
	Model 5			0.492	
	LV_{pre}	-0.474	0.001		1.069
	$T1_{pre}$	-0.217	0.107		1.144
	FLIS	0.029	0.017		1.214
	Model 6			0.457	
	PHRR	0.434	0.002		1.060
	$T1_{pre}$	-0.261	0.064		1.156
	FLIS	0.349	0.017		1.212
Patients undergoing major hepatectomy (n=25)	Model 1			0.223	
	PHRR	0.436	0.027*		1.047
	ALB (g/L)	-0.208	0.267		1.028
	$T1_{HBP}$	-0.243	0.206		1.076
	Model 2			0.159	
	LV_{pre}	-0.407	0.042*		1.311
	ALB (g/L)	0.189	0.333		1.035
	$T1_{HBP}$	-0.136	0.537		1.347
	Model 3			0.194	
	LV_{pre}	-0.342	0.140		1.469
	ALB	0.043	0.835		1.239
	$T1_{pre}$	-0.338	0.114		1.237

(Continued)

TABLE 3 Continued

	Covariates	Standardized β	*P* value	Adjusted R^2 of the Model	VIF
	Δ%	0.127	0.550		1.303
	FLIS	0.080	0.700		1.240
	Model 4			0.261	
	PHRR	0.380	0.048		1.087
	ALB	0.050	0.800		1.240
	$T1_{pre}$	-0.348	0.080		1.150
	Δ%	0.050	0.797		1.202
	FLIS	0.170	0.376		

* referred to $P<0.05$; PHRR, parenchymal hepatic resection rate; LVpre: volume of preoperative future remnant liver; T1-pre, T1 relaxation time of the liver before gadoxetic acid injection; T1-HBP, T1 relaxation time of the liver 20 min after gadoxetic acid injection; Δ%, the reduction rate of T1 relaxation time.

Figure S7B) and $T1_{HBP}$ and Δ% (r= -0.821, $P<0.001$, Supplementary Figure S7D), $T1_{HBP}$ and FLIS(r= -0.340, $P=0.028$, Supplementary Figure S7F) in patients undergoing major hepatectomy, accordingly, 4 independent models in multivariate analysis were tested(Model 1 included ALB, PHRR and $T1_{HBP}$; Model 2 included ALB, LV_{pre} and $T1_{HBP}$; Model 3 included ALB, LV_{pre}, $T1_{pre}$, Δ% and FLIS; Model 4 included ALB, PHRR, $T1_{pre}$, Δ% and FLIS), however, no T1 mapping parameters and FLIS (all $P>0.05$)showed a significantly linear association with RI.

Discussion

This present study explored the utility of T1-mapping parameters of pre-contrast, 20-min hepatobiliary phase (HBP), FLIS for liver regeneration assessment in HCC patients undergoing hepatectomy. The results demonstrated that $T1_{pre}$, $T1_{HBP}$, Δ% and FLIS score were the significant preoperative biomarkers of liver regeneration whether in univariate or multivariable analysis. They may help optimize patient selection for hepatectomy, promote individualized therapy, and reduce the occurrence of potential complications. Meanwhile, T1 mapping parameters and FLIS were closely associated with the severity of liver fibrosis, which are of vital importance for LR assessment. Besides, $T1_{pre}$ was also related to the severity of steatosis. However, for patients undergoing major hepatectomy, although T1 mapping parameters and FLIS were still related to liver fibrosis, they were not effective indicators of liver regeneration.

In line with our study, the increase of T1 relaxation times ($T1_{pre}$) before contrast injection correspond with the stage of hepatic fibrosis, due to the fact that the progression of hepatic fibrosis is believed to be accompanied with to an increase in extracellular water and protein concentration, finally leading to the increase the T1 relaxation time of liver parenchyma (11, 26, 27). Moreover, along with the increasing degree of fibrosis, disrupted architecture, aberrant hepatocyte regeneration, increased extracellular constituents, and vascular changes of liver parenchyma would cause a decreased number of normally functioning hepatocytes, a decreasing trend in Oatps level and an increasing trend in Mrps level with disturbed transporting system (28–30). The uptake of Gd-EOB-DTPA in hepatocytes occurs via Oatps expressed at the sinusoidal membrane, and its biliary excretion occurs via Mrps at the canalicular membrane (31). Accordingly, with the progression of liver fibrosis, the uptake of Gd-EOB-DTPA in hepatocytes would be in decrease and the secretion would be in increase due to the decreasing Oatps expression and the increasing Mrps expression, finally resulting in the significant increase of T1 relaxation times ($T1_{HBP}$) and the significant decrease of signal enhancement of parenchyma after Gd-EOB-DTPA injection. Hence, FLIS score, based on the signal enhancement of liver parenchyma after Gd-EOB-DTPA injection, was reasonable to be in decrease due to the decreasing Oatps expression, further negatively associated with the stage of liver fibrosis. Δ%, which was calculated as $[(T1_{pre}) - (T1_{HBP})]/(T1_{HBP}) \times 100\%$, showed significantly negative relation with the stage of liver fibrosis in this study. This may be explained that $T1_{pre}$ increased by a lower degree than $T1_{HBP}$ in the progression of liver fibrosis, which have been found in Sheng's study [32]. In line with our study, previous studies (32, 33) has also found that $T1_{HBP}$ was in an increasing trend while Δ% gradually decreased with the progression of liver fibrosis. Meanwhile, consistent with our study, steatosis grade had strong correlation with $T1_{pre}$ (17). The potential reason was that hepatic steatosis would induce a mixture of water and fat, the fat would be generally out-of-phase with water, and the MR signal would be subtracted by the fat component, resulting in longer T1 relaxation time ($T1_{pre}$) (13, 14). However, compared with that Oatps expression was in decrease and Mrps expression was in increase due to liver fibrosis, hepatic steatosis was often along with the descending expression of Oatps and unchanged or even decreasing expression of Mrps (34, 35). Accordingly, the uptake of Gd-EOB-DTPA in hepatocytes would be in decrease and the secretion decelerated. Thus, the clearance rate of Gd-EOB-DTPA in hepatocytes due to hepatic steatosis was slower than that due to liver fibrosis, finally leading to that the increase of T1 relaxation times ($T1_{HBP}$) and the decrease of signal enhancement of parenchyma after Gd-EOB-DTPA injection due to hepatic steatosis was by a lower degree than that due to liver fibrosis. This was the potential reason why $T1_{HBP}$, Δ% and FLIS showed significant correlation with fibrosis stage but no statistical correlation with steatosis grade. Similar to our study, Yang et al. found only $T1_{pre}$ was

significantly associated with liver steatosis at multiple regression analysis while $T1_{HBP}$ and Δ% was not. Moreover, consistent with our study, the severity of liver fibrosis was associated with the capacity of liver regeneration (36, 37). Fibrosis overrides liver regeneration through differential recruitment of pro-regenerative CXCR7-Id1 versus pro-fibrotic FGFR1-CXCR4 angiocrine pathways in vascular niche (38). When overstimulated, selective CXCR4 activation in liver sinusoidal endothelial cells could abrogate regeneration. Meanwhile, evidence (39) has also proven that liver fibrosis would cause the shortening of hepatocyte telomeres, leading to a decrease in the number of cell divisions of primary human cells, finally restraining liver regeneration. Besides, hepatic steatosis would cause lipid overloading, which is associated with endoplasmic reticulum stress and oxidative stress, leading to delayed hepatocyte DNA replication, finally resulting in the impair of liver regeneration (40). Hence, it is reasonable that T1 mapping parameters and FLIS are closely associated with liver regeneration. Although T1 mapping and FLIS on Gd-EOB-DTPA-enhanced MRI require the injection of contrast agent, reduced or absent hepatocyte function is the major pathophysiologic impairment in severely fibrotic and cirrhotic patients with low capacity of liver regeneration. T1 mapping on Gd-EOB-DTPA-enhanced MRI could directly reflect hepatocyte function through effectively assessing the ability of hepatocytes to uptake Gd-EOB-DTPA, while IVIM-DWI and MRE can only indirectly assess hepatocyte function by reflecting liver stiffness, the diffusion of water molecules and the liver blood perfusion (41). Hence, it is of pivotal importance for the use of T1 mapping parameters and FLIS based on Gd-EOB-DTPA-enhanced MRI in liver regeneration assessment for that it could directly reflect hepatocyte function. However, there is lack of direct comparisons whether T1 mapping on Gd-EOB-DTPA-enhanced MRI is superior over IVIM-DWI and MRE in the liver regeneration estimation, and it is warranted to go on comparison in the further study.

However, in the patients undergoing major hepatectomy, not only hepatic steatosis, liver fibrosis was also not associated with liver regeneration, which was in line with finding from Jang's study (7). We hypothesize that the factors affecting hepatic function are of secondary importance for liver regeneration after a large liver resection (where the liver remnant is relatively small). Compared with minor hepatectomy, major hepatectomy often means the increase in the ratio of blood flow to the remnant liver and relatively more remnant liver cells, which is in need to preserve appropriate liver function and support the metabolic needs. These changes may lead to a greater concentration of cytokines and the more effective hepatic proliferation, finally promoting liver regeneration (2, 42). Accordingly, it is conceivable that although $T1_{pre}$, $T1_{HBP}$ and FLIS showed moderate correlation with liver fibrosis stage, significant correlation was observed between $T1_{pre}$ and hepatic steatosis, no T1 mapping parameters and FLIS were related to liver regeneration in patients undergoing major hepatectomy.

All of T1 mapping parameters in present study were not associated with grading inflammation (The details are shown in Supplementary Table S2), which was not in line with previous study (27). It may be explained by that all the patients in present study were confirmed as HCC, their inflammation grade was more serious and the majority (90%) was in inflammation grade 2-3.

Larger PHRR are often accompanied with larger resection volume and smaller LV_{pre} (20). Thus, there is reasonable intercorrelation between PHRR, LV_{pre} and type of hepatectomy. PHRR, LV_{pre} and the type of hepatectomy were associated with LR in previous studies (43, 44). Compared with PHRR, the type of hepatectomy and LV_{pre} overlooked the considerable interpatient variability in the size of the various liver segments. And it may be the possible cause that the model including PHRR achieved the better adjusted R^2 whether in the total patient or patient undergoing major or minor hepatectomy. In the present study, ALB was a relevant factor affecting liver regeneration, which was consistent with previous studies (21, 45). It is likely that liver fibrosis, accompanied by the damage of liver regeneration, could cause a reduction in normal hepatocytes, finally resulting in lower ALB levels (46).

This present study is based on saturation method using adaptive recovery times for T1 mapping sequence (SMART1Map), rather than modifed lock-locker inversion recovery (MOLLI). Compared with MOLLI, SMART1Map is less sensitive to imaging parameters, such as T2 times and magnetization transfer, does not require correction (47, 48). Therefore, T1 mapping parameters based on SAMRT1Map for liver regeneration assessment are more stable and reliable. Gadoxetic acid disodium is a liver specific contrast agent which has reported to achieve comparable diagnostic performance with extra cellular contrast agent but provided additional hepatobiliary phase (HBP). For liver regeneration assessment, $T1_{HBP}$ could reflect both water molecules in liver parenchyma, which could also be evaluated by T1pre, and Oatp1a1 level with disturbed transporting system, and Δ% were calculated as $(T1_{pre}\text{-}T1_{HBP})/T1_{pre} \times 100\%$. FLIS takes into account three features of gadoxetic acid–enhanced MRI of the liver: enhancement quality, rate of biliary contrast excretion, and persistence of signal intensity in the portal vein. Thus, it is reasonable for the existence of intercorrelation between $T1_{pre}$ and $T1_{HBP}$, $T1_{HBP}$ and Δ%, $T1_{pre}$ and FLIS, $T1_{HBP}$ and FLIS, Δ% and FLIS.

When considering the potential clinical complication of T1 mapping parameters and FLIS score, they may serve as useful tips tools to inform a potential paradigm shift in treating HCC patients. Specifically, for HCC patients exhibiting higher $T1_{pre}$ and $T1_{HBP}$ values, coupled with lower Δ% and FLIS values, there is a greater tendency for them to have a higher degree of liver fibrosis and hepatic steatosis, a reduced capacity for liver regeneration, thereby increasing the likelihood of developing postoperative liver failure. These patients may be considered as more suitable candidates for alternative treatment approaches rather than upfront surgery. For instance, along with the higher $T1_{pre}$ and $T1_{HBP}$ values, coupled with lower Δ% and FLIS values, the progression of liver fibrosis and the decline of liver regeneration capacity could alter hepatic immune microenvironment, leading to the presence of tumor-infiltrating lymphocytes such as $CD8^+$and $CD4^+$T cells, and the upregulation of exhaustion markers such as PD-L1, and CTLA-4 (49, 50). Immune checkpoint inhibition, such as anti-CTLA-4 therapy and anti-PD-L1 therapy, may be new treatment option.

Due to the relatively small sample size and the nature of exploratory research without uniform threshold to distinguish low regeneration capacity from high regeneration capacity, no threshold of T1 mapping parameters and FLIS score were explored to distinguish regeneration capacity and guide clinical interventions, and it is warranted in the further study.

Limitation

Our study has several limitations. Firstly, the relatively small size of the retrospective study population based on a single research institution limit the quality of evidence that no T1 mapping parameters and FLIS score were associated with liver regeneration for patients undergoing major hepatectomy. In the subsequent research, prospective studies with a larger sample based on multi-institution are warranted to further verify this tendency and provide higher quality evidence. In order to address the variability and ensure the reliability of the research, the standardize scanning protocols and standardized training for participating researchers would be used to reduce systemic errors and variability between different institution, and the influence of different institution would be taken into account as a covariate in statistical analysis. Secondly, due to the retrospective study, the non-uniform interval between postoperative CT image and surgery in the range of 1.5–11.5 months. In fact, due to that it is still unclear when regeneration is complete, the postoperative course of liver regeneration assessment was an inconsistent time such as 1–6 months (51). Besides, it has proven that the first week after surgery is the period with high speed in liver regeneration, and then the speed of regeneration slows down (52, 53). In our study, for patients undergoing multiple postoperative CT scan, the difference of RIs based on the multiple CT images ranged of 0.49%-19.55% (mean: 8.78%). Thus, the non-uniform interval between postoperative CT image and surgery in this present study was within limits of acceptability. A prospective study with uniform time interval for postoperative follow-up CT is warranted in the future. Thirdly, it is better to measure the preoperative volume using the immediate postsurgical CT. However, due to the respective nature, the patient usually underwent an abdominal plain CT scan after immediate hepatectomy. It is difficult to remove the hepatic portal vein, hepatic vein, and their main branches. Similar to previous studies (7, 20, 54), the present study used the previous CT image to calculate the preoperative volume, In the subsequent research, it is better to go on an immediate postsurgical measurement based on prospective nature. Besides, it is better to assess the fibrosis stage based on the preoperative remnant liver. However, it is unreasonable to go on liver biopsy of preoperative remnant liver, according to the previous study (7), surgical specimen was used for fibrosis stage assessment. In the subsequent prospective research, additional evaluation using US shear-wave elastography or acoustic radiation force impulse imaging can be done for liver fibrosis assessment. Finally, due to the retrospective nature, no comparison went on between T1 mapping with the alternative noninvasive methods included indocyanine green (ICG) clearance (55), MRE (7) and IVIM (56) for liver regeneration evaluation. In the subsequent research, alternative noninvasive methods for comparison are in need.

Conclusion

In conclusion, T1pre, $T1_{HBP}$, Δ% values and FLIS score of Gd-EOB-DTPA-enhanced MRI could be noninvasive imaging indicators for liver regeneration assessment, expect for patients undergoing major hepatectomy.

Data availability statement

The raw data supporting the conclusions of this article will be made available by the authors, without undue reservation.

Ethics statement

The studies involving humans were approved by the Institutional Review Board of Sichuan university, West China Hospital. The studies were conducted in accordance with the local legislation and institutional requirements. The ethics committee/institutional review board waived the requirement of written informed consent for participation from the participants or the participants' legal guardians/next of kin because This is a Retrospective study, hence, the written informed consent was waived. Written informed consent was obtained from the individual(s) for the publication of any potentially identifiable images or data included in this article.

Author contributions

QL: Conceptualization, Data curation, Formal analysis, Funding acquisition, Methodology, Software, Supervision, Validation, Visualization, Writing – original draft. TZ: Conceptualization, Formal analysis, Methodology, Project administration, Software, Validation, Writing – original draft. SY: Investigation, Methodology, Project administration, Software, Supervision, Writing – review & editing. FG: Methodology, Project administration, Supervision, Validation, Writing – review & editing. LN: Software, Supervision, Visualization, Writing – review & editing. HT: Investigation, Project administration, Software, Validation, Writing – review & editing. BS: Conceptualization, Funding acquisition, Investigation, Supervision, Validation, Visualization, Writing – review & editing. YW: Funding acquisition, Investigation, Software, Supervision, Validation, Writing – review & editing.

Funding

The author(s) declare financial support was received for the research, authorship, and/or publication of this article. This project was supported by research and development funds from the National Natural Science Foundation of China (grant number 82202117 and 82402243), Science and Technology Support Program of Sichuan Province (grant number

23NSFSC3065, 24ZDYF0416, and 2024YFFK0256) and China Postdoctoral Science Foundation (2024M762238).

Conflict of interest

Author LN was employed by the company GE Healthcare.

The remaining authors declare that the research was conducted in the absence of any commercial or financial relationships that could be construed as a potential conflict of interest.

Generative AI statement

The author(s) declare that no Generative AI was used in the creation of this manuscript.

Publisher's note

Supplementary material

The Supplementary Material for this article can be found online at: https://www.frontiersin.org/articles/10.3389/fimmu.2025.1516848/full#supplementary-material

References

1. Sung H, Ferlay J, Siegel RL, Laversanne M, Soerjomataram I, Jemal A, et al. Global cancer statistics 2020: GLOBOCAN estimates of incidence and mortality worldwide for 36 cancers in 185 countries. *CA Cancer J Clin*. (2021) 71:209–49. doi: 10.3322/caac.21660

2. Inoue Y, Fujii K, Ishii M, Kagota S, Tomioka A, Hamamoto H, et al. Volumetric and functional regeneration of remnant liver after hepatectomy. *J Gastrointest Surg*. (2019) 23:914–21. doi: 10.1007/s11605-018-3985-5

3. Cieslak KP, Runge JH, Heger M, Stoker J, Bennink RJ, van Gulik TM. New perspectives in the assessment of future remnant liver. *Dig Surg*. (2014) 31:255–68. doi: 10.1159/000364836

4. Marrone G, Shah VH, Gracia-Sancho J. Sinusoidal communication in liver fibrosis and regeneration. *J Hepatol*. (2016) 65:608–17. doi: 10.1016/j.jhep.2016.04.018

5. Allaire M, Gilgenkrantz H. The impact of steatosis on liver regeneration. *Horm Mol Biol Clin Investig*. (2018) 41. doi: 10.1515/hmbci-2018-0050

6. Li YT, Cercueil JP, Yuan J, Chen W, Loffroy R, Wáng YX. Liver intravoxel incoherent motion (IVIM) magnetic resonance imaging: a comprehensive review of published data on normal values and applications for fibrosis and tumor evaluation. *Quant Imaging Med Surg*. (2017) 7:59–78. doi: 10.21037/qims.2017.02.03

7. Jang S, Lee JM, Lee DH, Joo I, Yoon JH, Chang W, et al. Value of MR elastography for the preoperative estimation of liver regeneration capacity in patients with hepatocellular carcinoma. *J Magn Reson Imaging*. (2017) 45:1627–36. doi: 10.1002/jmri.25517

8. Gao Y, Zheng J, Liang P, Tong M, Wang J, Wu C, et al. Liver fibrosis with two-dimensional US shear-wave elastography in participants with chronic hepatitis B: A prospective multicenter study. *Radiology*. (2018) 289:407–15. doi: 10.1148/radiol.2018172479

9. Ramos Rubio E, Llado Garriga L. Usefulness of pre-surgical biopsy in selecting patients with hepatocellular carcinoma for liver transplant. *Cir Esp*. (2010) 87:133–8. doi: 10.1016/j.ciresp.2009.11.026

10. Shin HJ, Yoon H, Kim MJ, Han SJ, Koh H, Kim S, et al. Liver intravoxel incoherent motion diffusion-weighted imaging for the assessment of hepatic steatosis and fibrosis in children. *World J Gastroenterol*. (2018) 24:3013–20. doi: 10.3748/wjg.v24.i27.3013

11. Li Z, Sun J, Hu X, Huang N, Han G, Chen L, et al. Assessment of liver fibrosis by variable flip angle T1 mapping at 3.0T. *J Magn Reson Imaging*. (2016) 43:698–703. doi: 10.1002/jmri.25030

12. Xu XY, Wang WS, Zhang QM, Li JL, Sun JB, Qin TT, et al. Performance of common imaging techniques vs serum biomarkers in assessing fibrosis in patients with chronic hepatitis B: A systematic review and meta-analysis. *World J Clin cases*. (2019) 7:2022–37. doi: 10.12998/wjcc.v7.i15.2022

13. Ahn JH, Yu JS, Park KS, Kang SH, Huh JH, Chang JS, et al. Effect of hepatic steatosis on native T1 mapping of 3T magnetic resonance imaging in the assessment of T1 values for patients with non-alcoholic fatty liver disease. *Magn Reson Imaging*. (2021) 80:1–8. doi: 10.1016/j.mri.2021.03.015

14. Mozes FE, Tunnicliffe EM, Pavlides M, Robson MD. Influence of fat on liver T1 measurements using modified Look-Locker inversion recovery (MOLLI) methods at 3T. *J Magn Reson Imaging*. (2016) 44:105–11. doi: 10.1002/jmri.25146

15. Kim JE, Kim HO, Bae K, Choi DS, Nickel D. T1 mapping for liver function evaluation in gadoxetic acid-enhanced MR imaging: comparison of look-locker inversion recovery and B(1) inhomogeneity-corrected variable flip angle method. *Eur Radiol*. (2019) 29:3584–94. doi: 10.1007/s00330-018-5947-4

16. Li J, Liu H, Zhang C, Yang S, Wang Y, Chen W, et al. Native T1 mapping compared to ultrasound elastography for staging and monitoring liver fibrosis: an animal study of repeatability, reproducibility, and accuracy. *Eur Radiol*. (2020) 30:337–45. doi: 10.1007/s00330-019-06335-0

17. Yang R, Chen Z, Pan J, Yang S, Hu F. Non-contrast T1ρ dispersion versus Gd-EOB-DTPA-enhanced T1mapping for the risk stratification of non-alcoholic fatty liver disease in rabbit models. *Magn Reson Imaging*. (2024) 107:130–7. doi: 10.1016/j.mri.2024.01.013

18. Lee HJ, Hong SB, Lee NK, Kim S, Seo HI, Kim DU, et al. Validation of functional liver imaging scores (FLIS) derived from gadoxetic acid-enhanced MRI in patients with chronic liver disease and liver cirrhosis: the relationship between Child-Pugh score and FLIS. *Eur Radiol*. (2021) 31:8606–14. doi: 10.1007/s00330-021-07955-1

19. Aslan S, Eryuruk U, Tasdemir MN, Cakir IM. Determining the efficacy of functional liver imaging score (FLIS) obtained from gadoxetic acid-enhanced MRI in patients with chronic liver disease and liver cirrhosis: the relationship between Albumin-Bilirubin (ALBI) grade and FLIS. *Abdom Radiol (NY)*. (2022) 47:2325–34. doi: 10.1007/s00261-022-03557-7

20. Kele PG, de Boer M, van der Jagt EJ, Lisman T, Porte RJ. Early hepatic regeneration index and completeness of regeneration at 6 months after partial hepatectomy. *Br J Surg*. (2012) 99:1113–9. doi: 10.1002/bjs.8807

21. Zhang T, Li Q, Wei Y, Yao S, Yuan Y, Deng L, et al. Preoperative evaluation of liver regeneration following hepatectomy in hepatocellular carcinoma using magnetic resonance elastography. *Quant Imaging Med Surg*. (2022) 12:5433–51. doi: 10.21037/qims-22-306

22. Bedossa P, Poynard T. An algorithm for the grading of activity in chronic hepatitis C. The METAVIR Cooperative Study Group. *Hepatology*. (1996) 24:289–93. doi: 10.1002/hep.510240201

23. Scheuer PJ. Classification of chronic viral hepatitis: a need for reassessment. *J Hepatol*. (1991) 13:372–4. doi: 10.1016/0168-8278(91)90084-O

24. Huang Z, Zhou J, Lu X, Zhang T, Xu S, Jin J, et al. How does liver steatosis affect diagnostic performance of 2D-SWE.SSI: assessment from aspects of steatosis degree and pathological types. *Eur Radiol*. (2021) 31:3207–15. doi: 10.1007/s00330-020-07288-5

25. Bastati N, Beer L, Mandorfer M, Poetter-Lang S, Tamandl D, Bican Y, et al. Does the functional liver imaging score derived from gadoxetic acid-enhanced MRI predict outcomes in chronic liver disease? *Radiology*. (2020) 294:98–107. doi: 10.1148/radiol.2019190734

26. Hoad CL, Palaniyappan N, Kaye P, Chernova Y, James MW, Costigan C, et al. A study of T_1 relaxation time as a measure of liver fibrosis and the influence of confounding histological factors. *NMR BioMed*. (2015) 28:706–14. doi: 10.1002/nbm.3299

27. von Ulmenstein S, Bogdanovic S, Honcharova-Biletska H, Blümel S, Deibel AR, Segna D, et al. Assessment of hepatic fibrosis and inflammation with look-locker T1 mapping and magnetic resonance elastography with histopathology as reference standard. *Abdom Radiol (NY)*. (2022) 47:3746–57. doi: 10.1007/s00261-022-03647-6

28. Besa C, Bane O, Jajamovich G, Marchione J, Taouli B. 3D T1 relaxometry pre and post gadoxetic acid injection for the assessment of liver cirrhosis and liver function. *Magn Reson Imaging*. (2015) 33:1075–82. doi: 10.1016/j.mri.2015.06.013

29. Ogasawara K, Terada T, Katsura T, Hatano E, Ikai I, Yamaoka Y, et al. Hepatitis C virus-related cirrhosis is a major determinant of the expression levels of hepatic drug transporters. *Drug Metab Pharmacokinet*. (2010) 25:190–9. doi: 10.2133/dmpk.25.190

30. Lagadec M, Doblas S, Giraudeau C, Ronot M, Lambert SA, Fasseu M, et al. Advanced fibrosis: Correlation between pharmacokinetic parameters at dynamic gadoxetate-enhanced MR imaging and hepatocyte organic anion transporter expression in rat liver. *Radiology*. (2015) 274:379–86. doi: 10.1148/radiol.14140313

31. Kimura Y, Sato S, Hitomi E, Ohyama M, Adachi K, Inagaki Y, et al. Coexpression of organic anion-transporting polypeptides 1B3 and multidrug-resistant proteins 2 increases the enhancement effect of gadolinium-ethoxybenzyl-diethylenetriamine pentaacetic acid on hepatocellular carcinoma in magnetic resonance imaging. *Hepatol Res*. (2014) 44:327–37. doi: 10.1111/hepr.2014.44.issue-3

32. Sheng RF, Wang HQ, Yang L, Jin KP, Xie YH, Fu CX, et al. Assessment of liver fibrosis using T1 mapping on Gd-EOB-DTPA-enhanced magnetic resonance. *Dig Liver Dis*. (2017) 49:789–95. doi: 10.1016/j.dld.2017.02.006

33. Pan S, Wang XQ, Guo QY. Quantitative assessment of hepatic fibrosis in chronic hepatitis B and C: T1 mapping on Gd-EOB-DTPA-enhanced liver magnetic resonance imaging. *World J Gastroenterol*. (2018) 24:2024–35. doi: 10.3748/wjg.v24.i18.2024

34. Fisher CD, Lickteig AJ, Augustine LM, Oude Elferink RP, Besselsen DG, Erickson RP, et al. Experimental non-alcoholic fatty liver disease results in decreased hepatic uptake transporter expression and function in rats. *Eur J Pharmacol*. (2009) 613:119–27. doi: 10.1016/j.ejphar.2009.04.002

35. Lickteig AJ, Fisher CD, Augustine LM, Aleksunes LM, Besselsen DG, Slitt AL, et al. Efflux transporter expression and acetaminophen metabolite excretion are altered in rodent models of nonalcoholic fatty liver disease. *Drug Metab Dispos*. (2007) 35:1970–8. doi: 10.1124/dmd.107.015107

36. Aierken Y, Kong LX, Li B, Liu XJ, Lu S, Yang JY. Liver fibrosis is a major risk factor for liver regeneration: A comparison between healthy and fibrotic liver. *Med (Baltimore)*. (2020) 99:e20003. doi: 10.1097/MD.0000000000020003

37. Cordero-Espinoza L, Huch M. The balancing act of the liver: tissue regeneration versus fibrosis. *J Clin Invest*. (2018) 128:85–96. doi: 10.1172/JCI93562

38. Huebert RC, Shah VH. Sinusoidal endothelial cells direct traffic at the intersection of regeneration and fibrosis. *Hepatology*. (2014) 60:754–6. doi: 10.1002/hep.27116

39. Wiemann SU, Satyanarayana A, Tsahuridu M, Tillmann HL, Zender L, Klempnauer J, et al. Hepatocyte telomere shortening and senescence are general markers of human liver cirrhosis. *FASEB J*. (2002) 16:935–42. doi: 10.1096/fj.01-0977com

40. Hamano M, Ezaki H, Kiso S, Furuta K, Egawa M, Kizu T, et al. Lipid overloading during liver regeneration causes delayed hepatocyte DNA replication by increasing ER stress in mice with simple hepatic steatosis. *J Gastroenterol*. (2014) 49:305–16. doi: 10.1007/s00535-013-0780-7

41. Yoon JH, Lee JM, Kim E, Okuaki T, Han JK. Quantitative liver function analysis: volumetric T1 mapping with fast multisection B(1) inhomogeneity correction in hepatocyte-specific contrast-enhanced liver MR imaging. *Radiology*. (2017) 282:408–17. doi: 10.1148/radiol.2016152800

42. Gruttadauria S, Parikh V, Pagano D, Tuzzolino F, Cintorino D, Miraglia R, et al. Early regeneration of the remnant liver volume after right hepatectomy for living donation: a multiple regression analysis. *Liver Transpl*. (2012) 18:907–13. doi: 10.1002/lt.23450

43. Kim JE, Kim JH, Park SJ, Choi SY, Yi NJ, Han JK. Prediction of liver remnant regeneration after living donor liver transplantation using preoperative CT texture analysis. *Abdom Radiol (NY)*. (2019) 44:1785–94. doi: 10.1007/s00261-018-01892-2

44. Meier M, Andersen KJ, Knudsen AR, Nyengaard JR, Hamilton-Dutoit S, Mortensen FV. Liver regeneration is dependent on the extent of hepatectomy. *J Surg Res*. (2016) 205:76–84. doi: 10.1016/j.jss.2016.06.020

45. Zhang T, Wei Y, He X, Yuan Y, Yuan F, Ye Z, et al. Prediction of remnant liver regeneration after right hepatectomy in patients with hepatocellular carcinoma using preoperative CT texture analysis and clinical features. *Contrast Media Mol Imaging*. (2021) 2021:5572470. doi: 10.1155/2021/5572470

46. Ma HY, Dong L, Quan SZ, Li RY, Wang XR. Comparison of four markers of hepatic fibrosis and hepatic function indices in patients with liver cirrhosis and hepatoma. *Ann Palliat Med*. (2021) 10:4108–21. doi: 10.21037/apm-20-1623

47. Matsumoto S, Okuda S, Yamada Y, Suzuki T, Tanimoto A, Nozaki A, et al. Myocardial T1 values in healthy volunteers measured with saturation method using adaptive recovery times for T1 mapping (SMART1Map) at 1.5 T and 3 T. *Heart Vessels*. (2019) 34:1889–94. doi: 10.1007/s00380-019-01401-5

48. Slavin GS, Stainsby JA. True T1 mapping with SMART1Map (saturation method using adaptive recovery times for cardiac T1 mapping): a comparison with MOLLI. *J Cardiovasc Magnet Resonance*. (2013) 15:P3. doi: 10.1186/1532-429X-15-S1-P3

49. Keenan BP, Fong L, Kelley RK. Immunotherapy in hepatocellular carcinoma: the complex interface between inflammation, fibrosis, and the immune response. *J Immunother Cancer*. (2019) 7:267. doi: 10.1186/s40425-019-0749-z

50. Zhu AX, Finn RS, Edeline J, Cattan S, Ogasawara S, Palmer D, et al. Pembrolizumab in patients with advanced hepatocellular carcinoma previously treated with sorafenib (KEYNOTE-224): a non-randomised, open-label phase 2 trial. *Lancet Oncol*. (2018) 19:940–52. doi: 10.1016/S1470-2045(18)30351-6

51. Yokoi H, Isaji S, Yamagiwa K, Tabata M, Sakurai H, Usui M, et al. Donor outcome and liver regeneration after right-lobe graft donation. *Transpl Int*. (2005) 18:915–22. doi: 10.1111/j.1432-2277.2005.00158.x

52. Gong WF, Zhong JH, Lu Z, Zhang QM, Zhang ZY, Chen CZ, et al. Evaluation of liver regeneration and post-hepatectomy liver failure after hemihepatectomy in patients with hepatocellular carcinoma. *Biosci Rep*. (2019) 39. doi: 10.1042/BSR20190088

53. Haga J, Shimazu M, Wakabayashi G, Tanabe M, Kawachi S, Fuchimoto Y, et al. Liver regeneration in donors and adult recipients after living donor liver transplantation. *Liver Transpl*. (2008) 14:1718–24. doi: 10.1002/lt.21622

54. Zappa M, Dondero F, Sibert A, Vullierme MP, Belghiti J, Vilgrain V. Liver regeneration at day 7 after right hepatectomy: global and segmental volumetric analysis by using CT. *Radiology*. (2009) 252:426–32. doi: 10.1148/radiol.2522080922

55. de Graaf W, Bennink RJ, Heger M, Maas A, de Bruin K, van Gulik TM. Quantitative assessment of hepatic function during liver regeneration in a standardized rat model. *J Nucl Med*. (2011) 52:294–302. doi: 10.2967/jnumed.110.078360

56. Li Q, Zhang T, Che F, Yao S, Gao F, Nie L, et al. Intravoxel incoherent motion diffusion weighted imaging for preoperative evaluation of liver regeneration after hepatectomy in hepatocellular carcinoma. *Eur Radiol*. (2023) 33:5222–35. doi: 10.1007/s00330-023-09496-1

frontiers | Frontiers in Immunology

TYPE Original Research
PUBLISHED 16 June 2025
DOI 10.3389/fimmu.2025.1614683

OPEN ACCESS

EDITED BY
Bing Yang,
Tianjin Medical University, China

REVIEWED BY
Shitang Ma,
West Anhui University, China
Yidan Sun,
Washington University in St. Louis, United States

*CORRESPONDENCE
Zheng Lu
luzhengdr@bbmc.edu.cn

†These authors have contributed equally to this work and share first authorship

RECEIVED 19 April 2025
ACCEPTED 30 May 2025
PUBLISHED 16 June 2025

CITATION
Zhang D, Li X, Wang Z, Fan J, Yang Y, Han S, Sun W, Wang D, Zhou S, Liu Z, Chen S, Yang Y, Zhu Y and Lu Z (2025) Machine learning-driven prediction of immune checkpoint inhibitor responses against cholangiocarcinoma: a bile biopsy perspective. *Front. Immunol.* 16:1614683. doi: 10.3389/fimmu.2025.1614683

Machine learning-driven prediction of immune checkpoint inhibitor responses against cholangiocarcinoma: a bile biopsy perspective

Dengyong Zhang[1†], Xinrui Li[2†], Zhonglin Wang[3†], Jingyuan Fan[4], Yuhang Yang[1], Sophia Han[5], Wanliang Sun[1], Dongdong Wang[1], Shuo Zhou[1], Zhong Liu[1], Shihao Chen[6], Yan Yang[7], Yan Zhu[6] and Zheng Lu[1*]

[1]Department of General Surgery, The First Affiliated Hospital of Bengbu Medical University, Bengbu, Anhui, China, [2]Biology Department, Bates College, Lewiston, ME, United States, [3]School of Public Policy & Management, Tsinghua University, Beijing, China, [4]The Biology Department, Carnegie Vanguard High School, Houston, TX, United States, [5]The Biology Department, Awty International School, Houston, TX, United States, [6]Institute of Epigenetics and Epigenomics and University of Animal Science and Technology, Yangzhou University, Yangzhou, China, [7]Department of Oncology, The First Affiliated Hospital of Bengbu Medical University, Bengbu, Anhui, China

Background: The treatment of cholangiocarcinoma (CCA) continues to face numerous clinical challenges, including the prediction of sensitivity to immunotherapy and the development of preoperative diagnostic models.

Methods: In this study, we aimed to address these challenges by collecting bile samples from CCA patients for metabolomic and microbiomic analyses. We also performed immunofluorescence (IF) staining on tissue formalin-fixed, paraffin-embedded (FFPE) blocks to assess the expression of relevant biomarkers. Additionally, we followed up with patients to analyze prognostic indicators based on their survival times. Using advanced machine learning techniques, specifically LASSO regression, we constructed a predictive model to determine the effectiveness of programmed cell death protein 1 (PD-1) inhibitors in treating CCA. The model integrates bile metabolomic data with an Immune Hot-Cold Index (IHC Index) derived from IF results, providing a comprehensive metric of the patient's immune environment.

Results: Our findings revealed significant differences in metabolomic profiles between CCA patients and those with non-malignant liver diseases, as well as between patients with different genetic mutations. The IHC Index successfully differentiated between immune "hot" and "cold" states, correlating strongly with patient responses to immunotherapy. Furthermore, in one CCA patient, the model's predictions were validated, demonstrating high accuracy and clinical relevance.

Conclusion: Our predictive model offers a robust tool for assessing the sensitivity of CCA patients to PD-1 inhibitors, potentially guiding personalized treatment strategies. Additionally, the integration of bile metabolomics with IF data provides a promising approach for developing preoperative diagnostic models, enhancing early detection and treatment planning for CCA.

KEYWORDS

cholangiocarcinoma, immune checkpoint inhibitors, bile metabolomics, machine learning, programmed cell death protein 1 (PD-1) therapy, immune hot-cold index, metabolites, biomarker prediction

1 Introduction

Cholangiocarcinoma (CCA) is a heterogeneous malignant tumor originating from bile duct, with an incidence rate second only to that of hepatocellular carcinoma (HCC) among primary liver tumors. CCA accounts for approximately 1% of all cancers in the population and about 10-15% of all primary liver cancers (1–3). Most patients are asymptomatic in the early stage and lack of effective diagnostic biomarkers, making early clinical diagnosis challenging. Consequently, only about one-third of patients are candidates for surgical resection at the time of diagnosis (4). Current treatment options for inoperable patients are limited, with gemcitabine combined with platinum chemotherapy being the most commonly used regimen. However, the clinical efficacy of this treatment is extremely poor (5, 6).

As a novel class of immunotherapeutic agents, immune check point inhibitors targeting programmed cell death protein 1 (PD-1) have shown clinical efficacy in treating various tumors (7, 8), but their role in CCA remains in the exploratory stages, with ongoing clinical trials. In the Phase I of clinical treatment of advanced CCA, the median overall survival time was reported to be 15 ± 4 months, with 11 of 30 patients achieving objective remission (9). The ongoing TOPAZ-1 project used durvalumab combined with platinum and gemcitabine to treat advanced CCA in Phase III clinical trial, demonstrating partial clinical efficacy (10, 11). However, not all patients benefit from this treatment regimen. At present, there is no reliable index to predict whether patients are effective in PD-1 treatment, which is crucial for guiding patients in clinical treatment. Therefore, developing predictive tools to for this purpose is essential. Clinically, patients with CCA are often accompanied by obstructive jaundice. To mitigate liver function damage, percutaneous transhepatic cholangial drainage (PTCD) puncture and drainage of bile are needed to improve liver function, which also serves as a reserve for subsequent drug treatments. This procedure facilitates the collection of bile samples in a clinical setting.

Existing research predominantly focused on the relationship between specific metabolites in bile and CCA. Hashim AbdAlla et al. (12) focused on phosphatidylcholine (PtC) and bile acids, comparing their levels in bile from CCA patients and those with benign biliary diseases. Similarly, Sharif et al. (13) analyzed glycine-conjugated bile acids, primary bile acids, and PtC in bile from CCA patients. Albiin et al. (14) studied the levels of PtC, bile acids, lipid, and cholesterol in bile, highlighting significant differences between CCA patients and those with benign biliary conditions. Volinsky et al. (15) explored oxidized phosphatidylcholines in cellular signaling and their role in various diseases, including CCA. Won-Suk Song et al. (16) identified glycocholic acid (GCA) and taurochenodeoxycholic acid (TCDCA) as specific metabolic biomarkers for CCA. Gomez et al. (17) developed and validated an LC-MS/MS method for quantifying various bile acids, highlighting the significance of free and conjugated bile acids in disease mechanisms.

Although these studies have provided significant insights, they are limited by their focus on specific metabolites. Concentrating solely on individual metabolites can overlook broader metabolic interactions and comprehensive biochemical alterations associated with CCA. This narrow scope may miss potential biomarkers and therapeutic targets that could be identified through a more holistic analysis. Metabolomics, the comprehensive study of metabolites in a biological system, reveals that cancer's metabolic reprogramming affects numerous pathways and involves a wide array of metabolites. Therefore, analyzing bile as a whole can offer a more complete picture of the disease and its interactions, potentially leading to more effective predictive models and therapeutic strategies (18).

To address these limitations, our research aims to take a comprehensive approach by analyzing bile as a whole and exploring its association with CCA. By examining the entire spectrum of bile metabolites, we hope to develop a more robust predictive model for PD-1 inhibitor response in CCA patients. In this study, we used bile samples from patients with CCA for metabolomics and microbiology detection, sequenced exons of corresponding cancer tissue samples of patients, and detected the expression of immune-related indicators in tissues by immunofluorescence (IF). We then built a prediction model for the therapeutic effect of PD-1 on CCA through machine learning and verified the model in some patients treated with PD-1.

2 Methods and materials

2.1 Human subjects

Bile was collected from patients between January 2019 and July 2023 at The First Affiliated Hospital of Bengbu Medical University. A total of 66 CCA patients who had not received neoadjuvant therapy were selected for this study. Among them, 62 patients underwent surgical procedures for tumor collection. Additionally, bile from 38 patients with non-malignant liver diseases, such as gallbladder stones or liver hemangioma, was collected and used as a negative control. The collection and preservation of bile samples followed the same protocols described in our previous publication (19). Written informed consent was obtained from each patient, and the study was approved by the Ethics Committee of Bengbu Medical University (No. 2021230 and No. 2019035).

2.2 Metabolomics

Completed by Huada Gene Company (Shenzhen, China) in the same way as the previous published articles (19).

2.3 Microbiology (16S)

Completed by Huada Gene Company (Shenzhen, China). The microbial community DNA was extracted using MagPure Stool DNA KF kit B(Magen, China) following the manufacturer's instructions. DNA was quantified with a Qubit Fluorometer by using Qubit dsDNA BR Assay kit (Invitrogen, USA) and the quality was checked by running aliquot on 1% agarose gel. Variable regions V4 of bacterial 16S rRNA gene was amplified with degenerate PCR primers, 515F (5-GTGCCAGCMGCCGCGGTAA-3') and 806R (5'-GGACTACHVGGGTWTCTAAT-3'). Both forward and reverse primers were tagged with Illumina adapter, pad and linker sequences. Then do PCR reaction. The Libraries were qualified by the Agilent Technologies 2100 bioanalyzer. The validated libraries were used for sequencing on MGISEQ-2000 platform (BGI, Shenzhen, China) following the standard pipelines of Illumina, and generating 2 × 250 bp paired-end reads.

2.4 Whole-exome sequencing

Completed by LC Bio Tech (Hangzhou, China). We sequenced exons of 61 formalin fixed paraffin embedded (FFPE) blocks in these patients with CCA. The total DNA was extracted using QIAGEN DNeasy Blood & Tissue Kit (69506, QIAGEN) or QIAamp DNA FFPE Tissue (56404, QIAGEN). Then the DNA which was fragmented by using Covaris M220 Focused-ultrasonicator were subjected to sequencing library construction. Exome capture was performed using the Human Exome 2.0 Plus (Twist Bioscience) following the vendor's recommended protocol. The final libraries were sequenced for paired-end 150 bp using the Illumina NovaSeq 6000 Sequencing System (Illumina) at LC-Bio Technology Co., Ltd (Hangzhou, China).

2.5 Immunofluorescence

The routine steps for IF are detailed in the literature. Briefly, the process involves dewaxing FFPE blocks to water, antigen repair, blocking endogenous peroxidase with 3% hydrogen peroxide, serum blocking, and sequentially adding primary and secondary antibodies. In this study, we detected 12 protein indexes in 62 cases

TABLE 1 Primary and secondary antibodies used for multiplex immunofluorescence staining of FFPE blocks.

Primary antibody	Cat no.	Company	Species	Ratio	Secondary antibody
OX40	AB264466	Abcam	Rab	1:4000	CY3(red)
ICOS	A00291-3	BOSTER Biological Technology	Rab	1:400	488(green)
CD20	60271-1-AP	Proteintech Group	Mou	1:400	CY5(pink)
CD86	AB239075	Abcam	Rab	1:200	594 (yellow)
LAG3	AB209236	Abcam	Rab	1:1000	CY3(red)
TIM3	AB241332	Abcam	Rab	1:1000	488(green)
PD-1	GB12338	Servicebio	Mou	1:1000	CY5(pink)
VISTA	24849-1-AP	Proteintech Group	Rab	1:200	594(yellow)
CD3	GB13014	Servicebio	Rab	1:200	CY3(red)
CD206	AB64693	Abcam	Rab	1:500	488(green)
CD8	GB12068	Servicebio	Mou	1:500	CY5(pink)
CD4	AB133616	Abcam	Rab	1:500	594(yellow)

This table lists the 12 immune-related protein markers analyzed in 62 cholangiocarcinoma (CCA) tissue samples. For each marker, the primary antibody name, catalog number, source company, host species, dilution ratio, and the corresponding fluorophore-conjugated secondary antibody are provided.

of CCA using a four-label fluorescence staining method. The first antibody was stained and photographed, followed by antigen repair and blocking steps, repeated until the fourth antibody was obtained. We tested the following 12 indexes on the same FFPE block. The details of the primary and secondary antibodies used for multiplex immunofluorescence are summarized in (Table 1).

2.6 Calculation and assessment of the Immune Hot-Cold Index

We utilized IHC results to indicate the overall level of a patient's immune environment, characterized by a specific metric. This involves treating OX40, ICOS, CD20, CD86, LAG3, TIM3, PD-1, VISTA, CD3, CD206, CD8, and CD4 as twelve dimensions of vectors, thereby creating a patient-specific IHC vector space. Within this space, we calculated the Euclidean distance between the 12-dimensional vectors and a zero vector, which serves as a measure of immune response strength—denoted as the IHC index. The Euclidean distance formula used is:

$$IHC\ \ index = d(p,q)^2 = \sqrt{(\sum_{i=1}^{N}(p_i - q_i)^2)}$$

where p and q represent the two vectors (data points).

We adopted the same computational approach as in previous studies, compared the clustering results, and assessed the scoring method based on recall, F1 score, precision, and accuracy. Additionally, t-SNE was employed for visualization.

2.7 Model construction

After testing various machine learning algorithms, we selected the Least Absolute Shrinkage and Selection Operator (LASSO) regression for our dataset. Our focus was on predicting a continuous variable, the immune hot-cold index, using biliary metabolomic sequencing data. LASSO regression's advantage lies in its ability to assume coefficient sparsity, which reduces overfitting by setting the coefficients of less significant variables to zero. This method enhances the model's interpretability, allowing us to identify promising targets among numerous metabolic products.

To prevent overfitting, we initially used Spearman correlation to reduce the number of metabolic products used as inputs to the model. Following this, we employed a five-fold cross-validation to establish the predictive model using LASSO regression. This approach ensured robust model performance by testing it on multiple subsets of the data. Finally, we tested statistical hypotheses to determine the optimal parameters for the model, ensuring its accuracy and reliability.

2.8 Statistical analysis

Statistical test was finished by t test in excel (version 16.58) and p value < 0.05 was determined as significance.

3 Results

3.1 Patient characteristics

A total of 66 CCA patients (intrahepatic CCA n= 17; extrahepatic CCA n= 49) that did not receive neoadjuvant therapy were selected for this study. 62 CCA samples (intrahepatic CCA n= 15; extrahepatic CCA n= 47) underwent surgery to collect tumors. Among 66 CCA patients, 39% were female and with a median age of 66 years (range, 40–83; Supplementary Table 1). Forty percent of patients were alive at the latest follow-up. Ninety seven percent of patients were diagnosed at advanced stages (T2 or higher). Bile from 38 patient with non-malignant liver diseases, such as gallbladder stone or liver hemangioma, were collected as negative control: 45% were female and with a median age of 59 years (range, 25–90; Supplementary Table 1).

3.2 The significant difference in metabolites instead of microbes between CCA and control

We identified 8783 substances in the metabolism-related database (1132 were down-regulated and 1459 were up-regulated by the criteria: p-value<0.05). We also identified 1316 substances in the microbe-related database (12 microbes shows significant changes by the criteria: p-value<0.05). The heatmap of top 100 up/down-regulated metabolisms and microbes shows in Figures 1A–C. Due to the limited changes in microbes, we will focus on metabolites in following research.

3.3 The significant difference in metabolites between patients harboring mutated and wild-type genes

We examined metabolite profiles in patients harboring specific mutations. Among 62 CCA patients, 21 of them harbor TP53 mutations (Supplementary Table 1). Compared with wild-type patients, 236 metabolites show significant changes by the criteria: p-value<0.05 (98 up-regulated and 138 down-regulated, Figure 2A). Besides, in seven patients harboring K-Ras mutations, 446 metabolites up-regulated while only 18 metabolites down-regulated (Figure 2B). These results suggest that mutations in oncogenes and tumor suppressor genes show different impact on the profile of metabolites in bile.

3.4 The expression of immune cell and immune checkpoint markers

All 62 samples underwent singleplex IHC for 12 immune cell and immune checkpoint markers. Representative examples of staining are shown in Figure 3A and the positive rates of each marker are shown in Figure 3B. To further explore the relationships between these markers, we examined their correlations (Figure 3C). As expected,

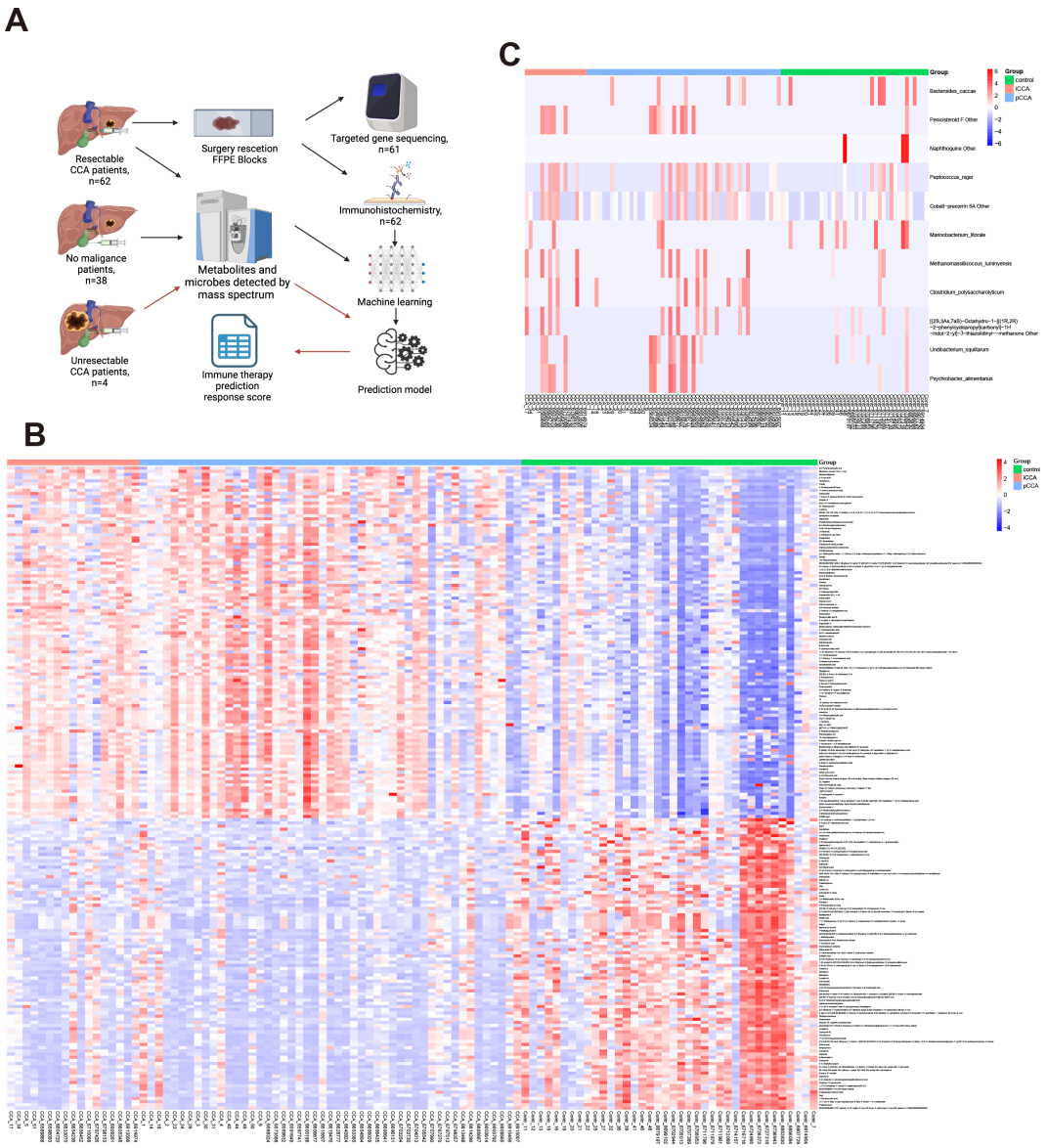

FIGURE 1
Overview of study design and comparison of metabolomic and microbial profiles between CCA and control groups. **(A)** Schematic of patient selection, sample collection, and processing workflow. **(B)** Heatmap showing the top 100 up- and down-regulated metabolites in bile samples between CCA and control groups. **(C)** Heatmap showing microbial taxa significantly altered between CCA and control groups based on 16S rRNA sequencing.

high correlations in CD4:CD8 ($\rho = 0.42$) and CD20:CD8 ($\rho = 0.52$) are observed. Notably, the correlation between CD3 and CD8 is rather low ($\rho = 0.14$). While few other strong correlations were observed, including CD206:CD3 ($\rho = 0.46$), CD206:CD4 ($\rho = 0.46$), CD20:CD4 ($\rho = 0.45$), and CD3:CD4 ($\rho = 0.57$).

3.5 Validation and universality of the IHC Index

In the following step, we calculated the IHC Index in each sample based on the expression of immune cell and immune checkpoint markers.

First, we illustrated the three-dimensional projection of all patients' immune vectors in the IHC vector space after dimensionality reduction using t-SNE (Figure 4A), which provides a continuous scalar value representing an individual's overall level of immune hotness or coldness. To validate the reliability of this method, we subsequently applied this methodology to retrospectively assess a previous study of 96 patients with intrahepatic cholangiocarcinoma (iCCA) (https://pubmed.ncbi.nlm.nih.gov/34510503/), achieving convincing results (Figure 4B). This retrospective validation suggests that our approach may be applicable to multi-target IHC data; however, additional datasets and prospective studies are needed to confirm its broader applicability. The study identified two groups—immune

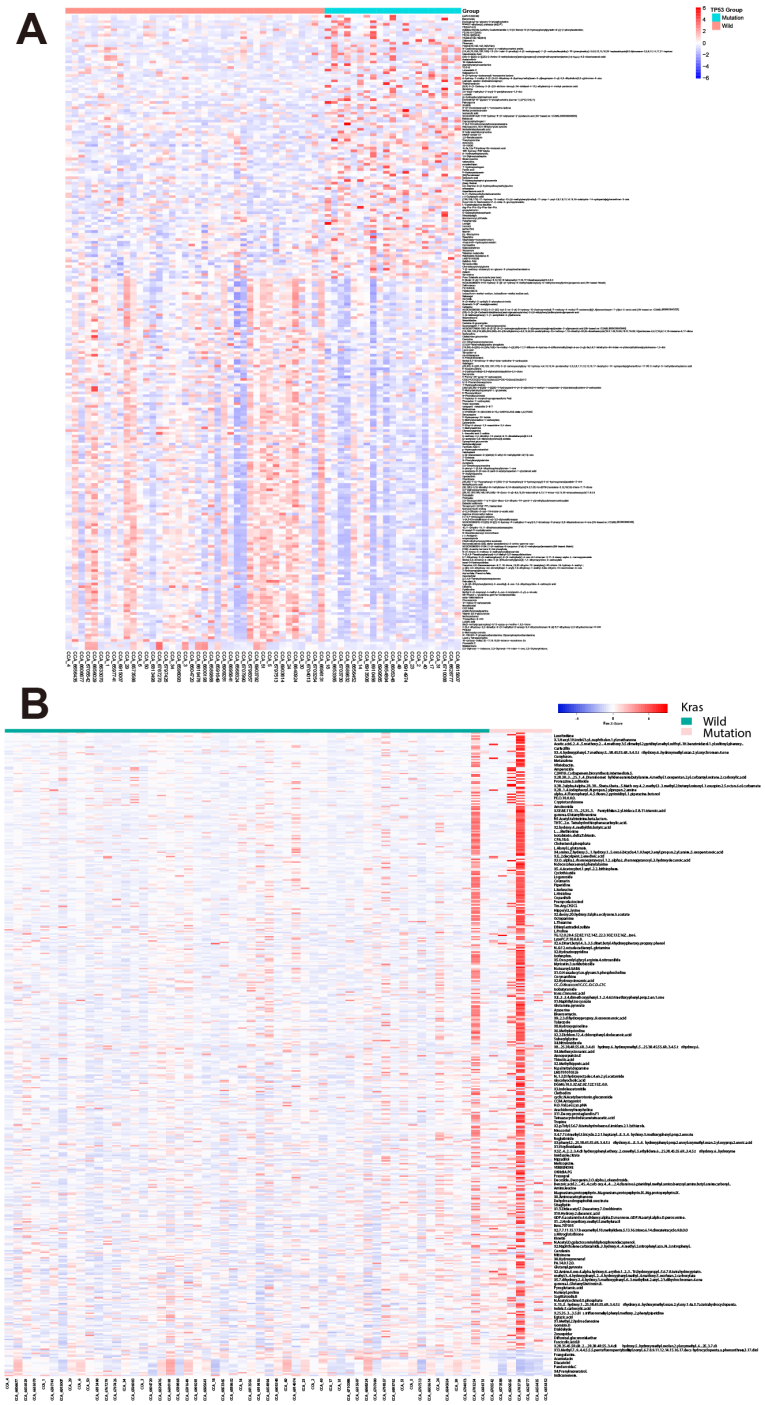

FIGURE 2
Differential bile metabolite profiles in CCA patients with TP53 and K-Ras mutations. **(A)** Volcano plot showing significantly altered metabolites in patients harboring TP53 mutations versus wild-type. **(B)** Volcano plot showing significantly altered metabolites in patients harboring K-Ras mutations versus wild-type.

"hot" and immune "cold"—and provided IHC data targeting similar markers as our current work. Additionally, it presented a code set of 773 immune genes associated with immune exhaustion, affirming the reliability of IHC-based groupings. Figure 4B shows the calculation of the IHC index using our method on this dataset, where using a single threshold accurately distinguished between the original hot and cold groups with an accuracy of 1, proving our defined IHC index's ability to continuously describe and universally address similar issues, solving previous challenges associated with the lack of a continuous scale.

10.3389/fimmu.2025.1614683

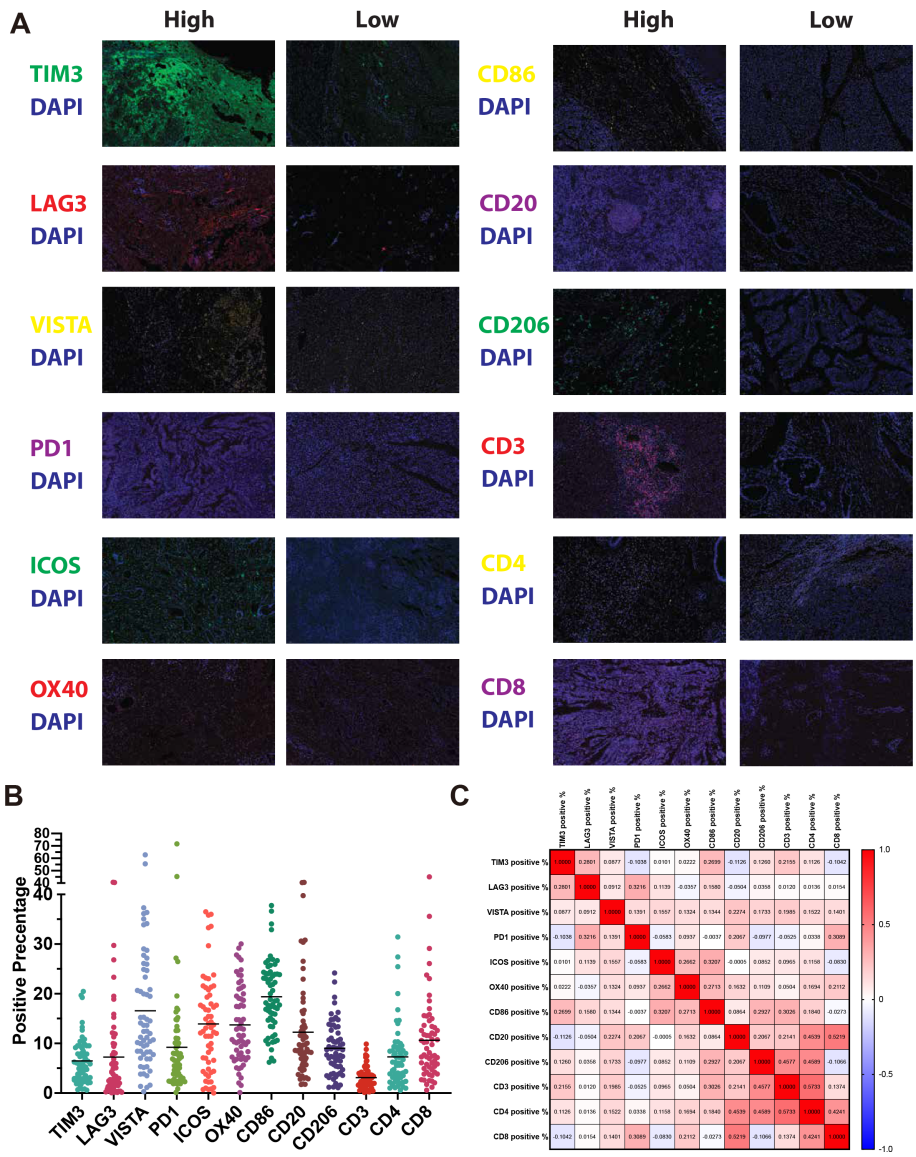

FIGURE 3
Immune profiling of CCA tissues using immunofluorescence. **(A)** Representative photomicrographs of CCA tissue samples showing high and low expression of immune markers. **(B)** Dot plot summarizing the percentage of positive staining for each of the 12 immune markers across all patients. **(C)** Correlation matrix showing Spearman correlations between expression levels of immune cell and immune checkpoint markers.

3.6 Establishment of the IHC index predictive model

Initially, based on Spearman correlation (setting significance at $p<0.05$), we identified 163 metabolic products strongly correlated with the IHC index to minimize overfitting in model predictions. Figures 4C, D display the correlation between these selected metabolites and their predictive values.

Using the LASSO regression method, we developed a predictive model; Figure 4E illustrates its performance on the test and training sets, showcasing R^2 values of 0.83 and 0.58, respectively. The grey dashed line represents a perfect prediction, and while the model's performance slightly diminishes at higher score ranges, it does not deviate significantly from the ideal fit line, demonstrating that our model captures the data characteristics well and exhibits good predictive performance.

Figures 4F–H respectively display the model's residuals values, residuals distribution, and Q-Q plot. The residuals values are scattered equally on both sides of a horizontal red line, follow a normal distribution, and ordered residuals align closely with the red line, thus fulfilling the model assumptions of normality, linearity, equality of variance, and independence.

Figures 5A, B show the LASSO model's selection of alphas and the optimal alpha used in this model. Figure 5C presents predictions of the IHC index for newly recruited patients. Figure 5D displays these predictions as a boxplot, which falls into four quartiles,

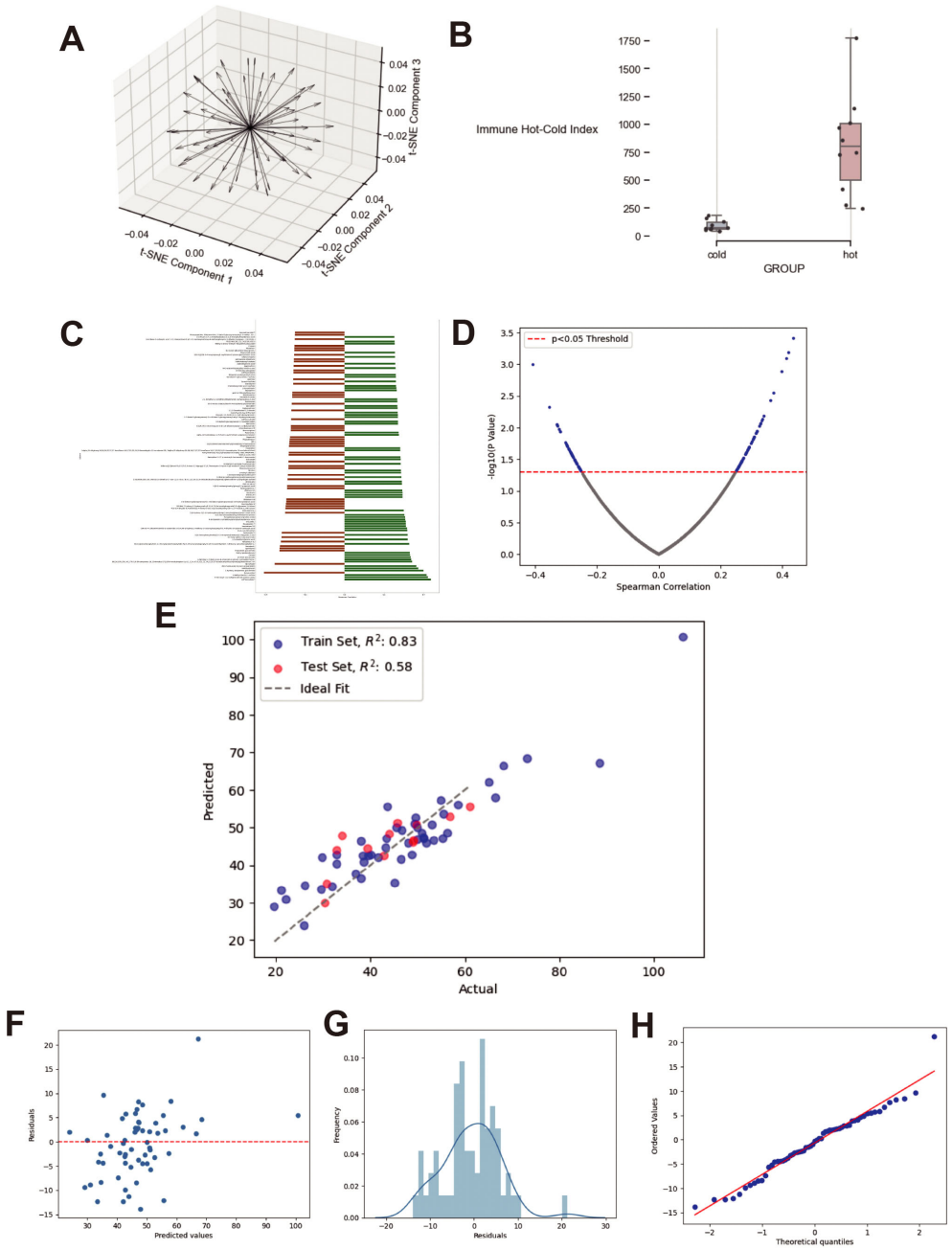

FIGURE 4
Construction and validation of the Immune Hot-Cold (IHC) index and predictive model. **(A)** Three-dimensional projection of IHC vectors from patient samples using t-SNE dimensionality reduction. **(B)** Validation of the IHC index using an external iCCA cohort (PMID: 34510503), demonstrating separation of immune "hot" and "cold" groups. **(C)** Spearman correlation between bile metabolites and the IHC index. **(D)** Scatter plot of selected metabolites significantly associated with IHC index ($p < 0.05$). **(E)** Predicted vs actual values of the IHC index using LASSO regression in training and test sets. **(F)** Residual plot showing homoscedasticity. **(G)** Histogram of residuals indicating normality assumption. **(H)** Q-Q plot confirming the normal distribution of residuals.

highlighting the predictive model's effectiveness and consistency. Based on these four quartiles, we calculated the survival curve of CCA patients. As shown in Figure 5D, Q1 group with the lowest scores shows significant lower survival rate compared with other three groups. Figure 5E presents CT images from a representative patient before and after PD-1 inhibitor treatment, demonstrating a notable reduction in tumor size that enabled successful surgical resection.

3.7 The clinical validation of this model

Among four unresectable patients, the predicted IHC index values were 81.6, 23.1, 28.5, and 75.8, respectively. The patient with the highest IHC index (81.6) underwent PD-1 inhibitor treatment and subsequently demonstrated a favorable clinical response.

At initial presentation (March 22, 2022), the patient had a CA19–9 level exceeding 1200 IU/mL and was diagnosed with

10.3389/fimmu.2025.1614683

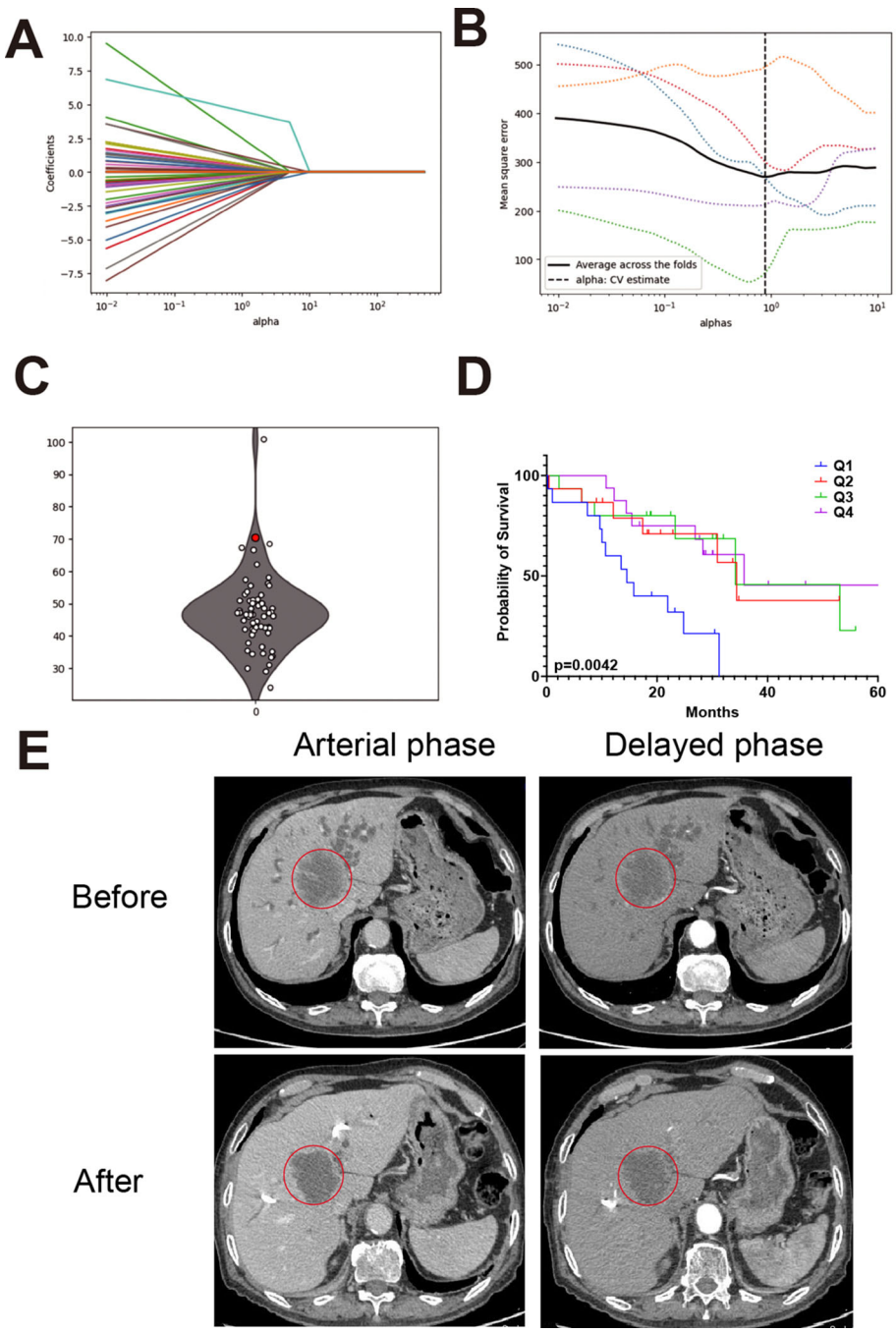

FIGURE 5
Model performance and case validation in clinical settings. **(A)** Cross-validation curve for LASSO regression showing the relationship between lambda values and model error. **(B)** Optimal alpha value selected for the final model based on lowest cross-validation error. **(C)** Predicted IHC index values for newly recruited patients using the trained model. **(D)** Boxplot categorizing patients into IHC index quartiles with a red dot highlighting an unresectable patient enrolled in immunotherapy. **(E)** CT images from a representative patient before and after PD-1 inhibitor treatment, showing a reduction in tumor size and successful surgical resection.

unresectable intrahepatic cholangiocarcinoma. After four cycles of PD-1 inhibitor therapy, the CA19–9 level dropped to 118.07 IU/mL (June 18, 2022). A preoperative measurement on July 25, 2022, showed a sustained decline at 299.68 IU/mL. CT imaging revealed a 35% reduction in tumor size, leading to surgical eligibility. Surgery was performed on July 29, 2022, with frozen section confirming negative margins. Final pathology (August 3, 2022) reported a resected 5.5×4.0×3.0 cm hilar cholangiocarcinoma with necrosis and no lymph node involvement (0/5).

This case illustrates the potential clinical utility of the IHC index in identifying immunologically active tumors that are more likely to respond to PD-1 inhibitors and become surgically resectable.

4 Discussion

Intrahepatic cholangiocarcinoma is the second most common liver tumor, characterized by high malignancy, resistance to chemotherapy, and poor prognosis. Anti-PD-1 immunotherapy (Nivolumab, durvalumab, etc.) has shown certain effects in treating intrahepatic cholangiocarcinoma (20). The Phase II of the KEYNOTE-158 trial evaluated the efficacy of PD-1 inhibitory monoclonal antibody pembrolizumab in a cohort of 104 patients with advanced biliary cancer who received standard chemotherapy. The results showed an objective remission rate of 5.8% (21). Consequently, PD-1 inhibitors have been increasingly used in clinical practice for treating cholangiocarcinoma. However, there is a current challenge in evaluating the sensitivity of patients to PD-1 inhibitors and selecting the appropriate PD-1 drugs. There are few related studies at present.

We present, for the first time, a numerical standard for assessing the overall immune environment's heat level based on multi-target IF. Traditional metrics for measuring immune heat have significant limitations, often focusing on PD-L1 or just 1–3 IF targets. They typically rely on the percentage of stained cells for stratification, using a 0–2 criterion to describe the overall level of immune heat, such as 1,2. These immune scores do not provide a continuous quantitative evaluation. Our newly created index offers a promising framework to this issue, based on a multi-dimensional vector length constructed from the percentage of cells stained for multiple IF targets, straightforwardly reflecting the definition of immune heat intensity. It is crucial to note that while some target expression levels are considered to have positive or negative associations with immune responses, there is evidence that they are also involved in regulatory processes and immune responses in other, deeper ways. Our focus is on the overall immune response strength, hence, considering the positive or negative impact of individual targets on immune response strength is limited. Our metric preserves the intensity information of individual targets to the greatest extent.

Our study also examined the genetic aspects of CCA, identifying significant differences in metabolomic profiles between patients with specific mutations, such as TP53 and K-Ras. Research indicates that these mutations are commonly found in iCCA and significantly influence the disease's development and progression. For instance, mutations in TP53 and K-Ras can lead to distinct metabolic alterations, which are known to impact the bile metabolomic profiles, adding complexity to the understanding of CCA. The presence of these mutations is associated with changes in metabolic pathways that are critical for tumor growth and response to therapy (22). This highlights the necessity for personalized therapeutic approaches, considering the unique genetic and metabolic landscape of each patient.

To translate the IHC index into clinically actionable insights, we aimed to identify a low-cost, clinically oriented bridge through biliary metabolites that could provide convenient, rapid, and accurate predictions for cholangiocarcinoma patients' responses to immune checkpoint inhibitors.

During model development, we initially tested fully connected neural networks, ResNet, and XGBoost regressors. However, these models exhibited notable overfitting and poor generalization in our relatively small-sample, high-dimensional dataset, even after applying pruning and other regularization strategies. LASSO regression was therefore selected for its superior stability and interpretability in this context. Before using LASSO regression, we also compared its performance with these alternative methods, but LASSO consistently yielded more reliable results, particularly in terms of avoiding overfitting and maintaining model clarity. Therefore, LASSO was ultimately chosen to ensure the majority of parameters are zero-valued.

Furthermore, our research illustrates the broader implications of integrating multi-omic data in clinical diagnostics. The combination of metabolomics with IF data may improve the predictive performance of our model and provide additional insights into the tumor microenvironment, though further validation is required. This integrative approach has the potential to be extended to other cancer types and may inform the development of future diagnostic and prognostic tools.

We also attempted to construct a preoperative diagnostic model of cholangiocarcinoma based on bile metabolomics, supplemented by microbiome analysis. However, the microbiome results revealed only 12 taxa with statistically significant differences between CCA and control groups, and no strong overall microbial signal was observed. Given the known antimicrobial properties of bile and its typically low microbial biomass, the diversity and functional relevance of bile microbiota may be inherently limited compared to other compartments like the gut. These biological constraints, combined with the limited statistical differences detected, led us to deprioritize the microbiomic data and focus our model development on metabolomics. Although preliminary attempts at diagnostic modeling using bile metabolomics alone were not yet satisfactory, we plan to expand our sample size and consider additional molecular layers, such as virology or proteomics, in future work to enhance diagnostic potential.

Despite the promising results, our study has limitations that need to be addressed in future research. The relatively small sample size and the single-center nature of the study may limit the generalizability of our findings. To mitigate the sample size limitation, we used LASSO regression, which performs well in small-sample, high-dimensional contexts by penalizing less informative features. Spearman correlation-based preselection and five-fold cross-validation further helped control for overfitting. In addition, we retrospectively validated the IHC Index using a previously published iCCA dataset (PMID: 34510503), achieving accurate classification of immune 'hot' and 'cold' profiles. Although complete external validation of the bile metabolomics model is limited by data availability, these findings support the model's robustness and potential generalizability. Future studies should aim to include larger, multi-center cohorts to validate and refine our predictive model further. Additionally, while our model focuses on bile metabolomics and immune biomarkers, incorporating other omics data, such as proteomics and transcriptomics, could provide a more comprehensive understanding of CCA and its response to immunotherapy.

Moreover, the dynamic nature of the immune response and its interaction with metabolic pathways suggest that longitudinal

studies are necessary to capture these changes over time. Such studies could provide insights into the temporal aspects of treatment response and resistance, further enhancing the clinical utility of our predictive model (23).

Our findings offer an early observation that may contribute to understanding the relationship between metabolomic and immune profiles. However, the mechanistic links between individual bile metabolites and specific immune signaling pathways remain to be fully elucidated. While prior studies have identified compounds such as glycocholic acid (GCA) and taurochenodeoxycholic acid (TCDCA) as biomarkers for CCA, their direct roles in modulating T-cell responses or immune checkpoints are not well established. Future studies involving pathway-based metabolomic analysis and experimental validation will be needed to explore how specific bile metabolites contribute to immune regulation in the CCA microenvironment. Figure 4B demonstrates that our defined IHC index reliably captures the variables measured in comparable studies. This accuracy is further validated by the immune exhaustion gene code set provided in the referenced study. We anticipate that future research will continue to utilize and refine this standard, thereby enhancing its application and validity in diverse contexts.

5 Conclusions

In summary, our study presents a novel, integrative approach to predicting PD-1 inhibitor responses in CCA patients. By combining bile metabolomics with immune biomarkers, we have developed a preliminary predictive model that shows potential for informing personalized treatment strategies. Our findings underscore the importance of a holistic approach in cancer research, paving the way for more effective and tailored therapeutic interventions. Future research should continue to build on these findings, expanding the scope of biomarker discovery and refining predictive models to enhance the clinical management of CCA.

Data availability statement

The original contributions presented in the study are included in the article/Supplementary Material. Further inquiries can be directed to the corresponding author.

Ethics statement

The studies involving humans were approved by the Ethics Committee of Bengbu Medical University. The studies were conducted in accordance with the local legislation and institutional requirements. The participants provided their written informed consent to participate in this study. Written informed consent was obtained from the individual(s) for the publication of any potentially identifiable images or data included in this article.

Author contributions

ZLi: Writing – original draft, Investigation. DZ: Conceptualization, Writing – original draft, Funding acquisition. YZ: Software, Writing – original draft, Validation, Formal Analysis. ZW: Data curation, Writing – original draft, Software, Visualization, Formal Analysis. XL: Investigation, Writing – original draft. JF: Formal Analysis, Writing – original draft, Investigation. YY: Writing – original draft, Investigation. SH: Formal Analysis, Investigation, Writing – original draft. WS: Investigation, Writing – original draft, Resources. DW: Investigation, Writing – original draft. SZ: Investigation, Writing – original draft. ZLu: Writing – review & editing, Conceptualization. SC: Investigation, Writing – original draft. YY: Writing – original draft, Formal Analysis.

Funding

The author(s) declare that financial support was received for the research and/or publication of this article. This study was supported by Anhui Provincial Natural Science Foundation (202308085MH271), Anhui province health scientific research project (AHWJ2023A20076), and the sixth batch of "special support plan" leading talent projects in Anhui Province.

Conflict of interest

The authors declare that the research was conducted in the absence of any commercial or financial relationships that could be construed as a potential conflict of interest.

Generative AI statement

The author(s) declare that no Generative AI was used in the creation of this manuscript.

Publisher's note

Supplementary material

The Supplementary Material for this article can be found online at: https://www.frontiersin.org/articles/10.3389/fimmu.2025.1614683/full#supplementary-material

References

1. Valle JW, Kelley RK, Nervi B, Oh DY, Zhu AX. Biliary tract cancer. *Lancet*. (2021) 397:428–44. doi: 10.1016/S0140-6736(21)00153-7

2. Ilyas SI, Khan SA, Hallemeier CL, Kelley RK, Gores GJ. Cholangiocarcinoma - evolving concepts and therapeutic strategies. *Nat Rev Clin Oncol*. (2018) 15:95–111. doi: 10.1038/nrclinonc.2017.157

3. Banales JM, Marin JJG, Lamarca A, Rodrigues PM, Khan SA, Roberts LR, et al. Cholangiocarcinoma 2020: the next horizon in mechanisms and management. *Nat Rev Gastroenterol hepatol*. (2020) 17:557–88. doi: 10.1038/s41575-020-0310-z

4. Izquierdo-Sanchez L, Lamarca A, La Casta A, Buettner S, Utpatel K, Klumpen HJ, et al. Cholangiocarcinoma landscape in Europe: Diagnostic, prognostic and therapeutic insights from the ENSCCA Registry. *J hepatol*. (2022) 76:1109–21. doi: 10.1016/j.jhep.2021.12.010

5. Ilyas SI, Affo S, Goyal L, Lamarca A, Sapisochin G, Yang JD, et al. Cholangiocarcinoma - novel biological insights and therapeutic strategies. *Nat Rev Clin Oncol*. (2023) 20:470–86. doi: 10.1038/s41571-023-00770-1

6. Elvevi A, Laffusa A, Scaravaglio M, Rossi RE, Longarini R, Stagno AM, et al. Clinical treatment of cholangiocarcinoma: an updated comprehensive review. *Ann hepatol*. (2022) 27:100737. doi: 10.1016/j.aohep.2022.100737

7. Galluzzi L, Humeau J, Buque A, Zitvogel L, Kroemer G. Immunostimulation with chemotherapy in the era of immune checkpoint inhibitors. *Nat Rev Clin Oncol*. (2020) 17:725–41. doi: 10.1038/s41571-020-0413-z

8. Xu F, Jin T, Zhu Y, Dai C. Immune checkpoint therapy in liver cancer. *J Exp Clin Cancer research: CR*. (2018) 37:110. doi: 10.1186/s13046-018-0777-4

9. Ueno M, Ikeda M, Morizane C, Kobayashi S, Ohno I, Kondo S, et al. Nivolumab alone or in combination with cisplatin plus gemcitabine in Japanese patients with unresectable or recurrent biliary tract cancer: a non-randomised, multicentre, open-label, phase 1 study. *Lancet Gastroenterol hepatol*. (2019) 4:611–21. doi: 10.1016/S2468-1253(19)30086-X

10. Ebia MI, Sankar K, Osipov A, Hendifar AE, Gong J. TOPAZ-1: a new standard of care for advanced biliary tract cancers? *Immunotherapy*. (2023) 15:473–6. doi: 10.2217/imt-2022-0269

11. Burris HA 3rd, Okusaka T, Vogel A, Lee MA, Takahashi H, Breder V, et al. Durvalumab plus gemcitabine and cisplatin in advanced biliary tract cancer (TOPAZ-1): patient-reported outcomes from a randomised, double-blind, placebo-controlled, phase 3 trial. *Lancet Oncol*. (2024) 25:626–35. doi: 10.1016/S1470-2045(24)00082-2

12. Hashim Abdalla MS, Taylor-Robinson SD, Sharif AW, Williams HR, Crossey MM, Badra GA, et al. Differences in phosphatidylcholine and bile acids in bile from Egyptian and UK patients with and without cholangiocarcinoma. *HPB*. (2011) 13:385–90. doi: 10.1111/j.1477-2574.2011.00296.x

13. Sharif AW, Williams HR, Lampejo T, Khan SA, Bansi DS, Westaby D, et al. Metabolic profiling of bile in cholangiocarcinoma using *in vitro* magnetic resonance spectroscopy. *HPB*. (2010) 12:396–402. doi: 10.1111/j.1477-2574.2010.00185.x

14. Albiin N, Smith IC, Arnelo U, Lindberg B, Bergquist A, Dolenko B, et al. Detection of cholangiocarcinoma with magnetic resonance spectroscopy of bile in patients with and without primary sclerosing cholangitis. *Acta Radiol*. (2008) 49:855–62. doi: 10.1080/02841850802220092

15. Volinsky R, Kinnunen PK. Oxidized phosphatidylcholines in membrane-level cellular signaling: from biophysics to physiology and molecular pathology. *FEBS J*. (2013) 280:2806–16. doi: 10.1111/febs.2013.280.issue-12

16. Song WS, Park HM, Ha JM, Shin SG, Park HG, Kim J, et al. Discovery of glycocholic acid and taurochenodeoxycholic acid as phenotypic biomarkers in cholangiocarcinoma. *Sci Rep*. (2018) 8:11088. doi: 10.1038/s41598-018-29445-z

17. Gomez C, Stucheli S, Kratschmar DV, Bouitbir J, Odermatt A. Development and validation of a highly sensitive LC-MS/MS method for the analysis of bile acids in serum, plasma, and liver tissue samples. *Metabolites*. (2020) 10(7):282. doi: 10.3390/metabo10070282

18. Wang W, Rong Z, Wang G, Hou Y, Yang F, Qiu M. Cancer metabolites: promising biomarkers for cancer liquid biopsy. *biomark Res*. (2023) 11:66. doi: 10.1186/s40364-023-00507-3

19. Zhang D, Zhao G, Sun W, Wang D, Zhou S, Liu Z, et al. Bile metabolites as diagnostic biomarkers for perihilar cholangiocarcinoma. *Sci Rep*. (2023) 13:3177. doi: 10.1038/s41598-023-27603-6

20. Oh DY, Lee KH, Lee DW, Yoon J, Kim TY, Bang JH, et al. Gemcitabine and cisplatin plus durvalumab with or without tremelimumab in chemotherapy-naive patients with advanced biliary tract cancer: an open-label, single-centre, phase 2 study. *Lancet Gastroenterol hepatol*. (2022) 7:522–32. doi: 10.1016/S2468-1253(22)00043-7

21. Piha-Paul SA, Oh DY, Ueno M, Malka D, Chung HC, Nagrial A, et al. Efficacy and safety of pembrolizumab for the treatment of advanced biliary cancer: Results from the KEYNOTE-158 and KEYNOTE-028 studies. *Int J cancer*. (2020) 147:2190–8. doi: 10.1002/ijc.33013

22. Hill MA, Alexander WB, Guo B, Kato Y, Patra K, O'Dell MR, et al. Kras and Tp53 mutations cause cholangiocyte- and hepatocyte-derived cholangiocarcinoma. *Cancer Res*. (2018) 78:4445–51. doi: 10.1158/0008-5472.CAN-17-1123

23. Gutierrez-Larranaga M, Gonzalez-Lopez E, Roa-Bautista A, Rodrigues PM, Diaz-Gonzalez A, Banales JM, et al. Immune checkpoint inhibitors: the emerging cornerstone in cholangiocarcinoma therapy? *Liver Cancer*. (2021) 10:545–60. doi: 10.1159/000518104

frontiers | Frontiers in Immunology

TYPE Original Research
PUBLISHED 23 July 2025
DOI 10.3389/fimmu.2025.1592259

OPEN ACCESS

EDITED BY
Bing Yang,
Tianjin Medical University, China

REVIEWED BY
Xin Hu,
National Center for Child Health and Development (NCCHD), Japan
Santosh Chokkakula,
Chungbuk National University, Republic of Korea

*CORRESPONDENCE
Xuesong Zhang
zhangxuesongdy2y@163.com

†These authors have contributed equally to this work and share first authorship

RECEIVED 12 March 2025
ACCEPTED 03 July 2025
PUBLISHED 23 July 2025

CITATION
Wang Z, Zhou G, Cao R, Zhang G, Zhang Y, Xiao M, Liu L and Zhang X (2025) Harnessing multi-omics and artificial intelligence: revolutionizing prognosis and treatment in hepatocellular carcinoma.
Front. Immunol. 16:1592259.
doi: 10.3389/fimmu.2025.1592259

Harnessing multi-omics and artificial intelligence: revolutionizing prognosis and treatment in hepatocellular carcinoma

Zhen Wang[1,2,3†], Gangchen Zhou[1,2†], Rongchuan Cao[2,4†], Guolin Zhang[2,5†], Yongxu Zhang[2,4], Mingyue Xiao[2], Longbi Liu[1,2] and Xuesong Zhang[1*]

[1]Department of Interventional Therapy, Zuanshiwan Campus, The Second Hospital of Dalian Medical University, Dalian, Liaoning, China, [2]Department of Graduate, Dalian Medical University, Dalian, Liaoning, China, [3]Department of General Surgery, The First Affiliated Hospital of Dalian Medical University, Dalian, Liaoning, China, [4]Department of Orthopedics, The Second Hospital of Dalian Medical University, Dalian, Liaoning, China, [5]Department of Cardiology II, The Second Hospital of Dalian Medical University, Dalian, Liaoning, China

Background: Hepatocellular carcinoma (HCC) is the most prevalent form of liver cancer, characterized by elevated mortality rates and heterogeneity. Despite advancements in treatment, the development of personalized therapeutic strategies for HCC remains a substantial challenge due to the intricate molecular characteristics of the disease. A multi-omics approach has the potential to offer more profound insights into HCC subtypes and enhance patient stratification for personalized treatments.

Methods: A comprehensive data set comprising clinical, transcriptomic, genomic and epigenomic information from HCC patients was retrieved from the TCGA, ICGC, GEO and CPTAC databases. To identify distinct molecular subtypes, a multi-omics data integration approach was employed, utilizing 10 distinct clustering algorithms. Survival analysis, immune infiltration profiling and drug sensitivity predictions were then used to evaluate the prognostic significance and therapeutic responses of these subtypes. Furthermore, machine learning models were employed to develop the artificial intelligence-derived risk score (AIDRS) with the aim of predicting patient outcomes and guiding personalized therapy. *In vitro* and vivo experiments were conducted to assess the role of CEP55 in tumor progression.

Results: The present study identified two distinct HCC subtypes (CS1 and CS2, respectively), each exhibiting different clinical outcomes and molecular characteristics. CS1 was associated with better overall survival, while CS2 exhibited higher mutation burden and immune suppression. The AIDRS, constructed using a multi-step machine learning approach, effectively predicted patient prognosis across multiple cohorts. High AIDRS score correlated with poor prognosis and a limited response to immunotherapy. Furthermore, the study identified CEP55 as a potential therapeutic target, as it was found to be overexpressed in CS2 and associated with poorer outcomes. *In vitro* experiments confirmed that CEP55 knockdown reduced HCC cell

proliferation, migration, and invasion. Moreover, in xenograft models, CEP55 knockdown significantly reduced tumor growth and proliferation.

Conclusions: The integration of multi-omics data has been demonstrated to provide a comprehensive understanding of HCC subtypes, thus enhancing the prediction of prognosis and guiding personalized treatment strategies. The development of the AIDRS offers a robust tool for risk stratification, while CEP55 has emerged as a promising target for therapeutic intervention in HCC.

KEYWORDS

hepatocellular carcinoma (HCC), multi-omics, artificial intelligence-derived risk score (AIDRS), molecular subtypes, sorafenib, transcatheter arterial chemoembolization (TACE), immunotherapy, CEP55

1 Introduction

Primary liver cancer is the sixth most prevalent form of cancer worldwide and the third leading cause of cancer-related fatalities. Hepatocellular carcinoma (HCC) accounts for approximately 75% to 85% of liver cancer cases (1). According to global cancer statistics in 2022 (2), the incidence of HCC is highest in East Asia and sub-Saharan Africa, particularly in countries like China, Japan and Mongolia. The major risk factors for HCC include chronic hepatitis B and C infections, excessive alcohol consumption and non-alcoholic fatty liver disease (NAFLD). Surgical resection is regarded as the optimal treatment option for HCC, given its status as a radical therapy. However, the majority of patients present with late-stage disease, by which point the opportunity for surgical intervention has often been missed, and the recurrence rate after surgery remains high. It is evident that local treatments such as transcatheter arterial chemoembolization (TACE) and systemic treatments, including radiotherapy, chemotherapy and immunotherapy, have become significant treatment options for HCC (1, 3, 4). Among these, sorafenib, a multi-target tyrosine kinase inhibitor, is the first targeted chemotherapeutic drug to be approved for the treatment of HCC. Although it has been shown to prolong patient survival, its efficacy is limited and drug resistance is also a prominent problem (5–7).

Recent years have seen a shift towards immunotherapy and combination targeted therapies as the prevailing trend in the treatment of HCC (1, 8, 9). A notable development is the combination of the anti- VEGFA monoclonal antibody bevacizumab and the PD-L1 inhibitor atezolizumab, which has emerged as the first treatment regimen to demonstrate a significant improvement in overall survival (OS) when compared to sorafenib (10). Furthermore, targeted drugs like lenvatinib and PD-1/PD-L1 inhibitors such as pembrolizumab have exhibited promising results (11, 12). However, systemic therapy is usually accompanied by adverse effects on normal hepatocytes, and the survival time and quality of life of patients is often seriously affected by side effects, mainly vomiting and immunosuppression (11–14). Therefore, the selection and implementation of personalized treatment regimens for HCC patients is a key challenge that needs to be addressed.

HCC is characterized by significant heterogeneity, which poses a substantial challenge to its treatment. However, this heterogeneity also presents opportunities for the development of personalized treatment strategies (1, 13). The molecular heterogeneity of HCC patients can be categorized into distinct subtypes, each with unique biological characteristics, prognosis and response to treatment (15). Elucidation of these subtypes facilitates the development of more precise and personalized treatment strategies, thereby enhancing treatment efficacy and reducing unnecessary side effects. The advent of high-throughput sequencing technology has been instrumental in facilitating the analysis of molecular subtypes of HCC, with it offering significant contributions to the prognosis, prediction and precision treatment of HCC patients (16–18). However, the majority of current research is confined to the utilization of single omics methods such as transcriptomics (19), proteomics (20) and metabolomics (21), or analysis is restricted to specific biological pathways, such as fatty acid metabolism (21). There is a paucity of systematic subtype analysis incorporating multi-omics perspectives, including genomics, transcriptomics and epigenomics, and multiple biological levels. This has impeded our ability to fully elucidate the complex biological characteristics and clinical behavior of HCC and hindered the development of more accurate predictive tools, new classification standards and biomarkers to guide individualized treatment of HCC.

In this study, we integrated multi-omics data, incorporating genomics, transcriptomics and epigenomics, to distinguish stable HCC subtypes and conduct an in-depth molecular characterization. Utilizing multiple machine learning techniques, we developed more accurate prognostic prediction models and artificial intelligence-derived risk score (AIDRS), which provide targeted guidance for specific treatment strategies for patients. This approach will contribute to the establishment of a more comprehensive and accurate personalized therapeutic strategy for HCC, ultimately improving treatment outcomes and quality of life for HCC patients.

2 Materials and methods

2.1 Multi-omics data collection and pre-processing

Clinical details, transcriptome expression (FPKM format), DNA methylation (methylation 450k format), somatic mutations (masked format) and copy number variants (gistic2 format) from TCGA-LIHC in The Cancer Genome Atlas (TCGA) database (https://portal.gdc.cancer.gov/) were downloaded using the R package "TCGAbiolinks" (v.2.28.3) (22). lncRNA and mRNA data were annotated using official website files followed by log2 (FPKM+1) calculations to make them more comparable. The somatic mutation analysis was all performed by R package "maftools" (v.2.16.0) (23). For DNA methylation data, β-values were log-transformed. The external validation cohorts ICGC-LIRI was obtained from the International Cancer Genome Consortium (ICGC) database (https://dcc.icgc.org/) and GSE14520 (24), GSE144269 (25), GSE141200 (26) and GSE141198 (26) were obtained from the NCBI Gene Expression Omnibus (GEO) database (https://www.ncbi.nlm.nih.gov/geo/). For genes with duplicates, the average value was taken. The samples were identified and only the data from the tumor tissue was kept.

Expression matrix and treatment response information for 67 HCC patients treated with sorafenib were extracted from the GSE109211 (27) dataset to assess whether subtypes were sensitive to sorafenib. GSE104580 containing 147 HCC patients treated with TACE was recruited to assess subtype sensitivity to TACE. In addition, GSE215011 (28) and GSE202069 (29), including 10 and 24 HCC patients respectively, were included to evaluate the association between molecular subtypes and immunotherapy response.

To further explore the proteomic characteristics of subtypes, protein expression matrix and corresponding clinical information of 151 HCC patients were obtained from the Clinical Proteomic Tumor Analysis Consortium (CPTAC) cohort (20). This dataset was utilized to validate subtype-specific molecular features at the proteomic level and to assess their clinical relevance.

The single-cell RNA sequencing (scRNA-seq) data were downloaded from the NCBI Gene GSE151530 (28), GSE156625 (29), GSE189903 (30) and GSE202642 (31). Among each sample, cells with fewer than 1000 UMI counts and genes expressed in less than 300 cells were excluded. In addition, a total of 273 genes associated with mitochondria, heat shock proteins and ribosomes were excluded to avoid expression artifacts from undetected noise and dissociation. After the quality filtering, 249012 cells were selected for the following analysis.

2.2 Data integration and molecular subtype identification

A new classification of HCC was established based on multi-omics data of mRNA expression, LncRNA expression, DNA methylation and somatic mutation data. The factors most associated with OS were extracted based on Cox regression survival analysis, ensuring that these factors were all $P \leq 0.001$. Finally, 1000 mRNA, 100 lncRNA and 100 DNA methylation sites were recruited. Meanwhile, 11 genes with mutation frequencies greater than 3% were enrolled for multi-omics analysis.

To minimize noise while retaining important features, CPI and Gaps-statistics were used to obtain the optimal number of clusters. Subsequently, 10 algorithms (iClusterBayes, moCluster, CIMLR, IntNMF, ConsensusClustering, COCA, NEMO, PINSPlus, SNF and LRA) built into the R package "MOVICS" (32) are used to cluster the samples and the clustering results of different algorithms are integrated to improve the robustness of the clustering. In addition, the nearest template prediction (NTP) was run in external validation cohorts to verify the stability of the subtypes.

2.3 Survival analysis and comparison of clinical features

Survival analysis was conducted for different cohorts using the subtypes and Kaplan-Meier curves were plotted and Log-Rank tests were performed. At the same time, the differences in clinical characteristics were compared. In addition, in order to clarify the potential impact of subtypes on the prognosis of HCC patients, univariate and multivariate Cox survival analysis were conducted sequentially for different cohorts. The results were presented in forest plots and $P < 0.05$ considered significant.

2.4 Genomic characterization and tumor microenvironment analysis

The R package "maftools" (23) (v.2.16.0) was used to somatic mutation analysis. The 'mafCompare' function was used to identify differentially mutated genes between CS1 and CS2 and the top 20 were visualized by the 'coOncoplot' function. The 'trinucleotideMatrix' and 'extractSignatures' functions were used to identify retained characteristic mutation patterns in the cancer progression processes, thus enabling the interpretation of mutations as potential mutagenic processes. Mutant-allele tumor heterogeneity (MATH) and tumor mutation burden (TMB) was calculated for the TCGA-LIHC and ICGC-IRLI cohorts, and the mutation frequencies of TP53 and CNTTB1 were also compared between subtypes.

Download the snp6.na35.remap.hg38.subset.txt.gz file from GitHub (https://github.com/NCI-GDC/dnacopy-tool/) as a marker file. Split the masked copy number segment according to the subtype and use them as the segment file for CS1 and CS2 respectively. The maker file and segment file were uploaded to the GenePattern (https://www.genepattern.org/) website, while Human_hg38.UCSC.add_mir.160920.mat was selected as the reference file. Finally, the GISTIC 2.0 (33) module was run to investigate the CNVs of CS1 and CS2. After the run results are obtained, the R package "BSgenome.Hsapiens.UCSC.hg38" (v.1.4.5) was used to identify the chromosomal location of any amplification or deletion events.

In order to provide further clarification regarding the potential impact of CNV events on gene expression, genes corresponding to

specific copy number variation events in CS1 and CS2 were extracted and integrated into an expression matrix, respectively. The RNA-seq (count format) data were analyzed using DEseq2 (34) (v.1.40.2), whereby genes with $P < 0.05$ and $|\log2FC| \geq 1$ was defined as differentially expressed genes (DEGs). Furthermore, the copy number values corresponding to the aforementioned differentially expressed genes were extracted from the file entitled "broad_data_by_genes.txt" and normalized to "Nor_CNV". The student t-test was then used to identify "Nor_CNV" that differed significantly among subtypes and their corresponding genes were integrated with the DEGs in order to obtain the genes most likely to have altered expression due to copy number variation. Finally, the expression of genes was compared between subtypes and correlation curves were plotted between gene expression and "Nor_CNV".

The tumor microenvironment (TME) of three independent study cohorts was decoded using xCell (35), quantiseq (36), TIMER (37) and MCPcounter (38) algorithms. The differences in cell type-specific immune infiltration scores between subtypes were analyzed using the limma (39) (v.3.56.2) algorithm. The results were then normalized and presented as heatmap.

2.5 Dimension reduction, integration and unsupervised clustering of single-cell RNA sequencing data

Single-cell RNA sequencing data from this study were analyzed uniformly using the R package "SCP" (v.0.5.6) (https://github.com/zhanghao-njmu/SCP). NormalizeData and ScaleData were used to normalize and scale the preprocessed data, respectively, while FindVariableGenes was used to identify highly variable genes. The "RunPCA" function was used to estimate the principal components (PCs). Then, the dimension range was set to 1:40, and the "RunUMAP" functions were used to perform the uniform manifold approximation and projection downscaling (UMAP). In order to eliminate the batch effect caused by the difference of sample sources, we used the "Harmony" function of the R package "harmony" (0.1.1) (40) for data integration. Set integration_method = "Harmony", linear_reduction_dims_use = 1:50, and use the function FindNeighbors to allocate cells. In addition, set different resolutions and run FindClusters for unsupervised clustering. In conclusion, we displayed the clustering of cells at various resolutions in a tree format. We then selected the stable outcomes (cluster_resolution = 0.6) for further analysis. Based on published classical cell markers, six cell types were identified: B cells (*CD79A, CD79B*), Endothelial (*VWF, PECAM1*), Fibroblasts (*COL1A1, COL1A2*), Hepatocytes (*ALB, APOA2*), Myeloid (*LYZ, C1QB, S100A9*) and T/NK Cells (*CD1C, CD3D, CD3E*).

2.6 Identifying subtype-related subpopulations by integrating bulk and single-cell RNA sequencing data

We identified subtype-related subpopulations by the Scissor (41) algorithm. Briefly, we used CS1 and CS2 as the phenotype while collating a single-cell RNA sequencing data (scRNA-seq) expression matrix and bulk profiling data. The above three files were used as input data for Scissor, where CS2 was defined as a positive outcome and CS1 as a negative outcome. A regression model was built against the dichotomous variables to calculate the regression coefficients for each cell against the phenotype. Cells with negative regression coefficients are highly correlated with CS1, described as "Scissor_CS1", cells with positive regression coefficients are highly correlated with CS2, described as " Scissor_CS2", and cells with zero regression coefficients are background cells, described as "NULL".

2.7 Prediction of precise therapy strategies

Drug sensitivity analysis was performed using the oncoPredict (42) algorithm for subtypes, extracting results that were consistent across three independent cohorts for normalization, and ggplot2 for visualization. To assess the sensitivity of immunotherapy, the R package "easier" was used to calculate the Estimate Systems Immunotherapy response (EaSIeR) score (43). Based on the outcomes, the patients were classified into two groups, namely non-response (NR) and response (R). Bar graphs were used to compare the proportion of patients responding to treatment in different subtypes. At the same time, the Tumor Immune Dysfunction and Exclusion (TIDE) score were calculated using the TIDE algorithm under a Linux system (44). Additionally, four independent cohorts (GSE109211, GSE104580, GSE215011 and GSE202069) containing treatment information, were further used to compare differences in sensitivity between sorafenib, TACE and immunotherapy treatment between subtypes. For all comparisons, $P < 0.05$ was considered significant.

2.8 Construction and evaluation of the artificial intelligence-derived risk score

The AIDRS was developed following a well-established analytical framework from the R package "Mime" (v.0.0.0.9) (38), which integrates ten classical machine learning algorithms: random forest (RSF), elastic network (Enet), stepwise Cox (StepCox), CoxBoost, partial least squares regression for Cox (plsRcox), supervised principal components (superpc), generalized boosted regression models (GBM), survival support vector machine (survivalsvm), Ridge, and least absolute shrinkage and selection operator (Lasso). Among these, RSF, Lasso, CoxBoost, and different variants of StepCox (both directions and backward selection) were employed in the initial feature selection stately generating 117 distinct algorithmic combinations for model construction. AIDRS was developed using a structured multi-step process (1): Differential gene expression analysis was performed on both the training and validation cohorts, and input matrices were constructed by extracting genes that were differentially expressed in the three cohorts at the same time (2). Univariate Cox regression analysis was conducted using the coxph function from the R package

"survival" (v.3.8-3) on both the training and validation cohorts. Candidate prognostic genes (CPGs) were identified based on $P \leq 0.01$ and consistent hazard ratios (HR > 1 or HR < 1) across both datasets (3). Feature selection and model fitting were performed using the 117 algorithmic combinations, where selected CPGs were incorporated into prognostic models trained on the Z-score normalized gene expression values (4). Model evaluation was conducted by computing risk scores for patients in the training, validation and independent test sets, utilizing the predict function from the respective model packages (5). Performance assessment was based on Harrell's concordance index (C-index), which was calculated via univariate Cox regression analysis on the risk scores across all datasets (6). The final optimal model was automatically selected based on the highest average C-index across all three cohorts. The corresponding risk score derived from this model was defined as the AIDRS.

After construction, several strategies were used to further assess the predictive efficacy of the AIDRS in both the training and validation cohorts (1): Calculate the median risk score, categorize the HCC patients into high-risk and low-risk groups, plot the Kaplan-Meier curves and run the Log-Rank test to compare the differences in survival (2). Time-dependent ROC curve analysis was performed and the area under the curve (AUC) was calculated (3). Meta-analysis was performed for univariate Cox regression.

2.9 Multidimensional validation of AIDRS

The predictive efficacy of AIDRS was extensively and comprehensively validated using multi-omics data. Specifically, the AIDRS between subtypes in the training and validation cohorts were first compared to clarify differences between groups. Second, patients were grouped according to the median AIDRS and the Kaplan-Meier curves were plotted to compare survival differences. Subsequently, patients were differentiated on the basis of clinical characteristics and differences in AIDRS between groups were compared. In addition, patients in the TCGA-LIHC and ICGC-LIRC cohort were grouped according to whether TP53 and CTNNB1 were mutated or not, to verify the association between AIDRS and gene mutations. Further, the correlation between different treatment scores and AIDRS was calculated and correlation curves were plotted. Finally, AIDRS was calculated for scRNA-seq data using three methods ("Seurat", "AUCell" and "UCell"), while comparing the intensity in different cell types.

2.10 Identification of key genes in AIDRS

The following steps were taken in order to identify overlapping genes included in the AIDRS model in the training and validation cohorts, along with multiple strategies to further identify key genes for AIDRS (1): AIDRS-associated genes were extracted from different study cohorts and overlapping genes were identified using veen plots (2). The multiplicity of differences in gene expression between subtypes will be compared (3). The prognostic hazard ratios of genes will be calculated based on univariate Cox regression (4). The Pearson correlation coefficient between gene expression and AIDRS will be calculated (5). Calculate the area under the curve (AUC) values of genes and compare the efficacy of genes in classifying subtypes (6). Group patients based on median gene expression, plot Kaplan-Meier curves and compare survival differences between groups using the Log-Rank test (7). Further validate the key genes based on scRNA-seq data.

2.11 Cell culture

The human HCC cell lines Bel-7402 and Hep-3B were obtained from the Cell Bank of Type Culture Collection of the Chinese Academy of Sciences (Shanghai, China). Both cell lines were maintained in Dulbecco's Modified Eagle's Medium (DMEM) (BasalMedia, Shanghai, China) supplemented with 10% fetal bovine serum (FBS, ExCell, Suzhou, China). Cells were incubated under standard culture conditions at 37°C with 5% CO_2 in a humidified incubator.

2.12 Cell transfection and CEP55 knockdown

To achieve effective CEP55 knockdown, small interfering RNA (siRNA) specifically targeting CEP55 was designed and synthesized by RiboBio (Guangzhou, China). A non-targeting siRNA was used as the negative control (NC). Transfection efficiency was confirmed through quantitative real-time polymerase chain reaction (qRT-PCR).

2.13 Cell Counting Kit-8 assay

Transfected Bel-7402 and Hep-3B cells were seeded into 96-well plates and incubated under optimal conditions for 24, 48 and 72 h. The Cell Counting Kit-8 (CCK-8) (US Everbright, Suzhou, China) assay was performed according to the manufacturer's protocol. Absorbance was measured at 450 nm using a microplate reader (Infinite F50, Tecan, Switzerland) to assess cell viability.

2.14 Colony formation assay

Transfected Bel-7402 and Hep-3B cells were trypsinized, counted and plated in 6-well plates at a density of 200 cells per well. The cells were cultured for 14 days to allow colony formation. Colonies were then fixed with 4% paraformaldehyde for 30 minutes, washed with phosphate-buffered saline (PBS), and stained with 0.1% crystal violet solution (Solarbio, Beijing, China) for 30 minutes. The number of colonies was counted and analyzed statistically.

2.15 Transwell migration assays

Cell migration ability was evaluated using transwell chambers with 24-μm pores. Briefly, 2.5×10^4 transfected cells resuspended in serum-free DMEM were seeded into the upper chamber, while the lower chamber contained DMEM supplemented with 10% FBS. After 48 h of incubation at 37°C, non-migrated cells were carefully removed, and migrated cells were fixed, stained and counted under a light microscope.

2.16 Wound-healing assays

To further assess the migration capability of CEP55-silenced cells, a scratch wound healing assay was performed. Transfected cells were seeded into 6-well plates and grown to near confluence. A 200-μL pipette tip was used to create a straight scratch in the cell monolayer. Images were captured at 0 and 48 h to evaluate the wound closure rate, which was used to quantify the migratory potential of the cells.

2.17 Xenograft tumor model in nude mice

BALB/c nude mice (4–6 weeks old, male) were purchased from the Comparative Medicine Center of Yangzhou University (SYXK (Su) 2023-0019) and housed in a specific pathogen-free (SPF) facility with controlled temperature, humidity, and a 12 h light/dark cycle. All animal procedures were approved by the Dalian Medical University Animal Care and Ethics Committee (XL250423013) and were performed in accordance with the guidelines for the Care and Use of Laboratory Animals.

CEP55 knockdown and control groups were established against Bel-7402 and Hep-3B cell lines. Each group was injected subcutaneously into the dorsal axilla of nude mice (5×10^6 cells in 100 μL PBS per mouse). Tumor growth and the health condition of the mice were monitored weekly. After 5 weeks, mice were euthanized by cervical dislocation, and tumors were excised, weighed, and measured. Tumor volume was calculated using the formula: V (cm^3) = 1/2 × length × $width^2$. The harvested tumor tissues were separated into two sections (1): preserved at -80°C for cryopreservation (2). fixed in a 4% paraformaldehyde solution.

2.18 Western blotting

Total protein was extracted from xenograft tumor tissues using a lysis buffer containing protease inhibitors. Protein concentration was determined using a BCA Protein Assay Kit (P0010, Beyotime Biotechnology, Shanghai, China). Equal amounts of protein were separated by 10% SDS-PAGE (S8010, Solarbio, Beijing, China) and transferred to PVDF membranes (ISEQ00010, Millipore, USA). The membranes were blocked with 5% non-fat milk and then incubated overnight at 4 °C with primary antibodies against CEP55 (1:1000, PA5-96976, Thermo, MA, USA) and GAPDH (1:500, ab8245, Abcam, Shanghai, China). After washing, the membranes were incubated with HRP-conjugated secondary antibodies at room temperature for 2 h. Protein bands were visualized using enhanced chemiluminescence (ECL) reagents (180-5001, Tanon, Shanghai, China). Band intensities were quantified using ImageJ software, and the relative expression levels of target proteins were normalized to GAPDH.

2.19 Immunohistochemistry

Tumor tissues were fixed in 4% paraformaldehyde, embedded in paraffin, and sectioned at 4 μm thickness. Sections were deparaffinized with xylene and rehydrated through graded ethanol. Antigen retrieval was performed using heated citrate buffer (C1010, Solarbio, Beijing, China) for 15 minutes. Endogenous peroxidase activity was blocked with 3% hydrogen peroxide for 20 minutes at room temperature. After blocking with normal serum, sections were incubated overnight at 4 °C with a primary antibody against CEP55 (1:50, 23891-1-AP, Proteintech, Wuhan, China) and Ki-67 (1:500, ab15580, Abcam, Shanghai, China), followed by incubation with an appropriate HRP-conjugated secondary antibody for 1 h at room temperature. DAB (Diaminobenzidine) was used for chromogenic detection, and hematoxylin was used for nuclear counterstaining. After dehydration and mounting, the stained sections were imaged using a brightfield microscope (NIB900, Leica Microsystems, Germany). The histochemistry score were evaluated semi-quantitatively.

2.20 Statistics and visualization

All statistical analyses for the figures were conducted using rstatix (v.0.7.2) and visualizations were generated with ggplot2 (v.3.4.3), except for methods where default tools were applied. Group comparisons were performed using parametric tests, such as Student's t-test or Welch's ANOVA test, provided the data followed normality and homogeneity of variance assumptions. In cases where data deviated from normality, non-parametric tests, including the Wilcoxon test or Kruskal-Wallis test, were employed, followed by Tukey's *post-hoc* analysis. The Chi-square test was used to determine whether the sample distribution of a categorical variable is consistent. When identical statistical methods or color schemes are used in multiple parts of the manuscript, only the initial reference will include detailed annotations. All subsequent references will follow the same format and statistical approach as stated initially.

3 Results

3.1 Identify two molecular subtypes of HCC patients based on consensus clustering

After applying stringent data filtering, a total of 355 HCC patients with complete datasets across mRNA, lncRNA expression, DNA methylation, gene mutations and OS outcomes

from the TCGA-LIHC cohort were selected for consensus clustering to identify molecular subtypes. Based on the optimal number of multi-omics clusters determined by the clustering prediction index (CPI) and Gap statistics, we identified two molecular subtypes for further analysis (Supplementary Figure 1A). Ten classical clustering algorithms available in the R package "MOVICs" (34) were employed to assign patients to these predefined molecular subtypes, followed by an ensemble consensus to ensure the robustness of the classification. The silhouette analysis further validated the clustering, demonstrating a moderate similarity among the samples in each subtype, with silhouette scores of 0.56 and 0.80 for CS1 and CS2, respectively (Supplementary Figure 1B). The distribution of the multi-omics data across these subtypes, along with associated clinicopathological features was shown in Figure 1A. For instance, CS1 displayed a higher DNA methylation profile, with patients carrying mutations in CTNNB1 primarily grouped in this subtype. CS2 was characterized by higher prevalence of mutations in TP53. In addition, most of the incorporated mRNA and lncRNA were highly expressed in CS2, including SPP1, S100A10, SNHG3, SNHG4 and so on.

The clinical prognostic outcome of HCC patients is a crucial factor in determining subsequent treatment options. We indicated that CS1 exhibited significantly superior overall survival (OS), progression-free interval (PFI), disease-specific survival (DSS) and disease-free interval (DFI) when compared to CS2, indicating a higher prognosis ($P \leq 0.01$) (Figures 1B–E). In addition, the TCGA-LIHC cohort demonstrated that the nearest template prediction algorithm predictions were consistent with the original typing, thereby indicating stable and reliable CS subtypes and confirming the rationality of subtype extrapolation using nearest template prediction algorithm (Figure 1F).

3.2 Molecular subtypes further confirmed in independent cohort

In order to validate the external stability of the CS subtypes, the nearest template prediction algorithm was employed for the identification of subtypes against the ICGC-LIRI and GSE14520 cohorts. The ICGC-LIRI cohort comprised 223 HCC patients, of whom 149 were classified as CS1 and 74 as CS2, while the GSE14520 cohort contained 237 HCC patients, with 123 designated as CS1 and 114 as CS2 (Figures 1G, I). Furthermore, in both the ICGC-LIRI and GSE14520 cohorts, CS1, in comparison with CS2, exhibited superior overall survival (OS) and disease-free survival (PFI) ($P \leq 0.01$) (Figures 1H, J, K).

3.3 Patients with different molecular subtypes face different clinicopathologic and functional features

In comparisons targeting clinicopathological features between subtypes, we found that CS2 patients in three independent cohorts (TCGA-LIHC, ICGC-LIRI and GSE14520) were mostly in advanced tumor stage, along with higher alpha-fetoprotein (AFP), longer prothrombin time (PT), and larger tumor size compared to CS1 ($P < 0.05$) (Figures 2A–C). Second, in the univariate Cox regression of prognostic factors for HCC patients, CS subtypes were shown to be a prognostic risk factor in both the training and validation cohorts, with hazard ratios of 2.8, 2.3 and 2.2 in that order ($P < 0.05$) (Figure 2D). The hazard ratios of CS subtypes were similar to the tumor stage, which is often used to evaluate the patient's prognosis in the clinic and were significantly superior to those of AFP, albumin (ALB) and PT ($P < 0.05$) (Figure 2D). In addition, after further incorporating the statistically significant prognostic factors into the multivariate Cox regression, we found that the statistical efficacy of a variety of metrics, including AFP, ALB and PT, was significantly reduced ($P < 0.05$) (Figures 2E–G). In contrast, CS subtypes and tumor stage were statistically different in the three independent cohorts, with hazard ratios for CS subtypes being: 2.2, 2.1 and 1.73, respectively ($P < 0.05$) (Figures 2E–G).

The differential expression analysis among subtypes yielded 4562, 2638 and 556 differentially expressed genes in the three study cohorts, respectively. Of these, 73 were concurrently expressed upregulated genes and 99 were expressed downregulated genes (Supplementary Figure 1C). GO enrichment analysis subsequently revealed that 172 DEGs were closely associated with metabolism-related biological processes, including xenobiotic metabolic process, small molecule metabolic process and oxoacid metabolic process ($P < 0.05$). Additionally, these genes were found to be actively involved in immune responses, such as positive regulation of immune system process ($P < 0.05$) (Supplementary Figure 1D). The KEGG analysis indicated that the DEGs were significantly enriched in pathways such as the Toll-like receptor signaling pathway, metabolic pathways and the IL-17 signaling pathway ($P < 0.05$) (Supplementary Figure 1E). Furthermore, an analysis of the differences in feature scores across three distinct study cohorts revealed that scores associated with immune activation-related pathways were significantly elevated in CS1, including "TMEscoreA_CIR", "TIP_Recognition_of_cancer_cells_by_T_cells_1", "TIP_Infiltration_of_immune_cells_into_tumors_2" and so on ($P < 0.05$) (Supplementary Figure 1F). Conversely, scores for biological metabolic pathways such as "Tyrosine_Metabolism", "Tryptophan_Metabolism", "Steroid_Hormone_Metabolism" were significantly lower in CS1 compared to CS2 ($P < 0.05$) (Supplementary Figure 1G). Overall, CS1 exhibited significant immune activity, while CS2 was closely associated with biological metabolic pathways.

3.4 Genomic alterations with different molecular subtypes

Following the sorting of the top twenty genes according to mutation frequency, it was established that the top three mutated genes in the TCGA-LIHC cohort were TP53 (28%), CTNNB1 (26%) and TTN (24%) (Figure 3A). Twenty genes were identified as mutated in both CS1 and CS2, and no specific genes were found

10.3389/fimmu.2025.1592259

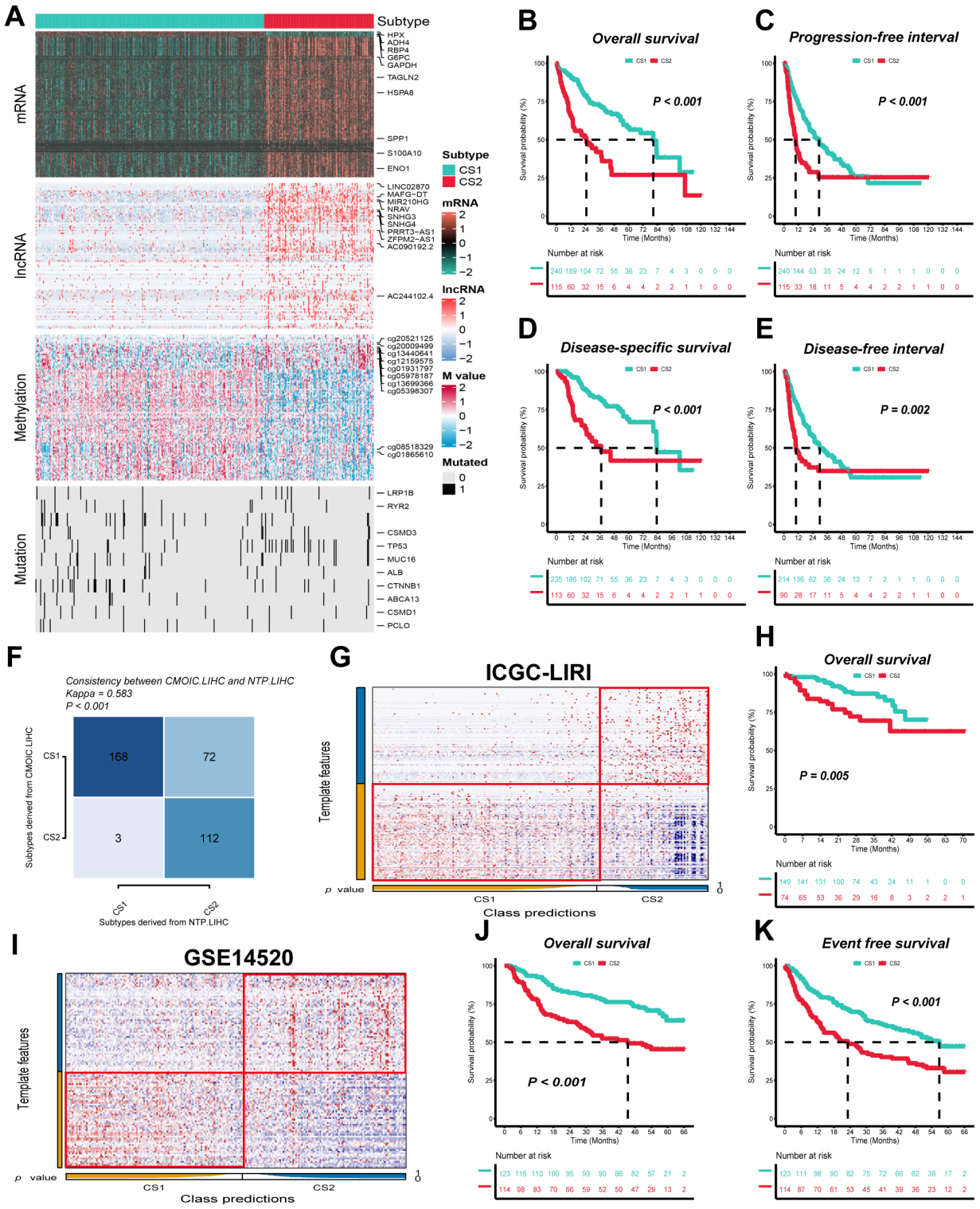

FIGURE 1
Two distinct molecular subtypes were identified through consensus clustering of multi-omics data, and clinical outcomes and stability were assessed. **(A)** Multi-omics features corresponding to CS1 and CS2 in the TCGA-LIHC cohort. M value, methylation value; CS, clustering subtype. **(B–E)** Kaplan–Meier curves corresponding to subtypes in the TCGA-LIHC cohort for overall survival, progression-free interval, disease-specific survival, and disease-free interval. **(F)** Consistency of subtype with nearest template prediction in the TCGA-LIHC cohort. **(G)** Evaluation of CS1 and CS2 subtypes in the ICGC-LIRI cohort. **(H)** Kaplan–Meier curves corresponding to subtypes in the GSE14520 cohort for overall survival. **(I)** Evaluation of CS1 and CS2 subtypes in the GSE14520 cohort. **(J, K)** Kaplan–Meier curves corresponding to subtypes in the GSE14520 cohort for overall survival and disease-free survival. Log-rank test was used in **(B, C, D, E, H, J, K)**.

to be mutated only in one subtype. However, a significant variation in the frequency of gene mutation was observed among the different subtypes. For instance, the mutation frequency of the CTNNB1 gene was approximately 75% in CS1, which is considerably higher than the 25% observed in CS2. Conversely, mutations in the TP53 gene were present in about 67.5% of all CS2 individuals, compared to only about 47.5% of individuals with mutations in CS1 ($P \leq 0.001$) (Figure 3B). Furthermore, CS2 exhibited higher TMB and lower MATH compared to CS1 ($P < 0.05$) (Figure 3E). Significant differences in TP53 and CTNNB1 mutation frequency, TMB and MATH between subtypes were likewise confirmed in the validation cohort ICGC-LIRI ($P < 0.05$) (Figures 3F, G). In the analysis of mutations against genes, we found that mutations in CS1 were enriched for defective DNA mismatch repair features (COSMIC_6), exposure to aristolochic acid (COSMIC_22) and exposure to tobacco (smoking) mutagens (COSMIC_4), whereas mutations in CS2 were mainly enriched for exposure to aristolochic acid (COSMIC_22) (Figures 3C, D).

For CNVs, the frequency of mutation events on different chromosomes and the corresponding p-values were calculated separately after grouping them according to subtypes. The results showed a higher frequency of gene copy number deletions on chromosomes 4 and 13–16 and a lower frequency of gene copy number duplications on chromosomes 5 and 8 in CS2 compared to CS1 (Figures 4A, B). Concurrently, the statistical efficacy of copy number variation events in CS1 and CS2 was inadequate, particularly in the context of gene copy number deletion events (Figure 4C). In the subsequent integrated analysis, it was found that CNV events involved a total of 415 genes, of which 62 genes were differentially expressed between subtypes, containing 42 upregulated and 20 downregulated genes (Figure 4D). Among them, only CPB2 and DLEU7 genes showed simultaneous differences in expression and copy number values between subtypes ($P < 0.05$) (Figures 4E–G). Furthermore, the correlation analysis for gene expression and copy number values revealed a consistent positive correlation for the CPB2 gene in both CS1 and CS2 ($P < 0.05$), while the correlation for the DLEU7 gene did not satisfy the statistical difference ($P \geq 0.05$) (Figure 4G).

3.5 CS1 has abundant immune infiltration and CS2 has dense tumor cells

The present study evaluated the cell types in the tumor microenvironment of HCC patients in three independent study cohorts, utilizing four distinct inverse convolution algorithms. The analysis revealed that CS1 exhibited a higher abundance of $CD8^+$ T, $CD4^+$ T, NK Cells and M1-type macrophages, indicative of a more pronounced immune cell infiltration compared to CS2 ($P < 0.05$). Conversely, CS2 demonstrated a higher prevalence of non-immune cells, including hepatocytes, endothelial cells, fibroblasts and pericytes, exhibiting significant disparities among the various subtypes ($P < 0.05$) (Figure 5A).

Following the initial quality control and dimensionality reduction clustering, a single-cell atlas of HCC patients containing 249012 cells with 39 cell subpopulations was established. Initially, the cell subpopulations were separated from each other according to the sample source, which exhibited a significant batch effect (Supplementary Figure 2A). Following data integration by the "harmony" algorithm (40), the distributions of cells from different samples overlapped with each other in the two-dimensional space, thereby effectively avoiding the generation of aberrant cell clusters from the sample source (Supplementary Figure 2B). Subsequently, the cells were distinguished into six categories based on classical marker genes (Supplementary Figure 2C; Figure 5B). Following the mapping of CS subtypes to single-cell atlases based on the "Scissor" algorithm (41), it was found that the results in the three study cohorts varied greatly (Figures 5C–E). For example, CS1 was found to be concentrated in the fibroblast subpopulation in the ICGC-LIRI cohort, but not in the TCGA-LIHC and GSE14520 cohorts. A similar observation was made in the GSE14520 cohort, where CS2 was found to be concentrated in B cells, endothelial cells, fibroblasts and hepatocyte subpopulations. However, its distribution was not found to be simultaneous in the other two cohorts. It is noteworthy that all three study cohorts exhibited a centralized distribution of CS2 in the hepatocyte subpopulation, with percentages of 70%, 56%, and 64%, respectively (Figures 5C–E). This was significantly higher than the percentage of CS1. This finding indicates that CS2 exhibits a strong association with hepatocyte subpopulations, the inverse convolution results that is further validated by this conclusion.

3.6 CS1 is sensitive to immunotherapy, CS2 is more suitable for sorafenib and TACE

In order to ascertain the most appropriate treatment for the various subtypes of HCC, the oncoPredict algorithm (42) was utilized to evaluate patients' therapeutic sensitivity. The findings revealed that CS1 exhibited high sensitivity to treatment with drugs such as nutlin-3 and ruxolitinib ($P < 0.05$), while microtubule inhibitors such as paclitaxel and vinblastine appeared to be more suitable for the treatment of CS2 (Figure 6A). Furthermore, in the analysis for the sorafenib treatment cohort GSE109211, patients categorized as CS2 demonstrated a treatment response rate of approximately 70%, whereas CS1 was even less than 5% (Figure 6F). Similarly, in the TACE treatment cohort GSE104580, about 75% of CS2 belonged to the treatment-responsive population, and far fewer, just about 27% for CS1 ($P \leq 0.0001$) (Figure 6G).

In terms of predicting immunotherapy response in HCC patients, CS2 had higher EaSleR score than CS1, with a significant difference between the two ($P < 0.05$) (Figure 6B). Accordingly, CS1 had a similar response rate of approximately 60% across the three study cohorts, while CS2 had a peak response rate of only 30% ($P \leq 0.0001$) (Figure 6B). In addition, the TIDE algorithm (44) was used to further evaluate a number of predictors in HCC patients that have been shown to potentially influence immunotherapy response. The results showed that CS1 had higher MSI score and IFNG compared to CS2, which was consistent across

10.3389/fimmu.2025.1592259

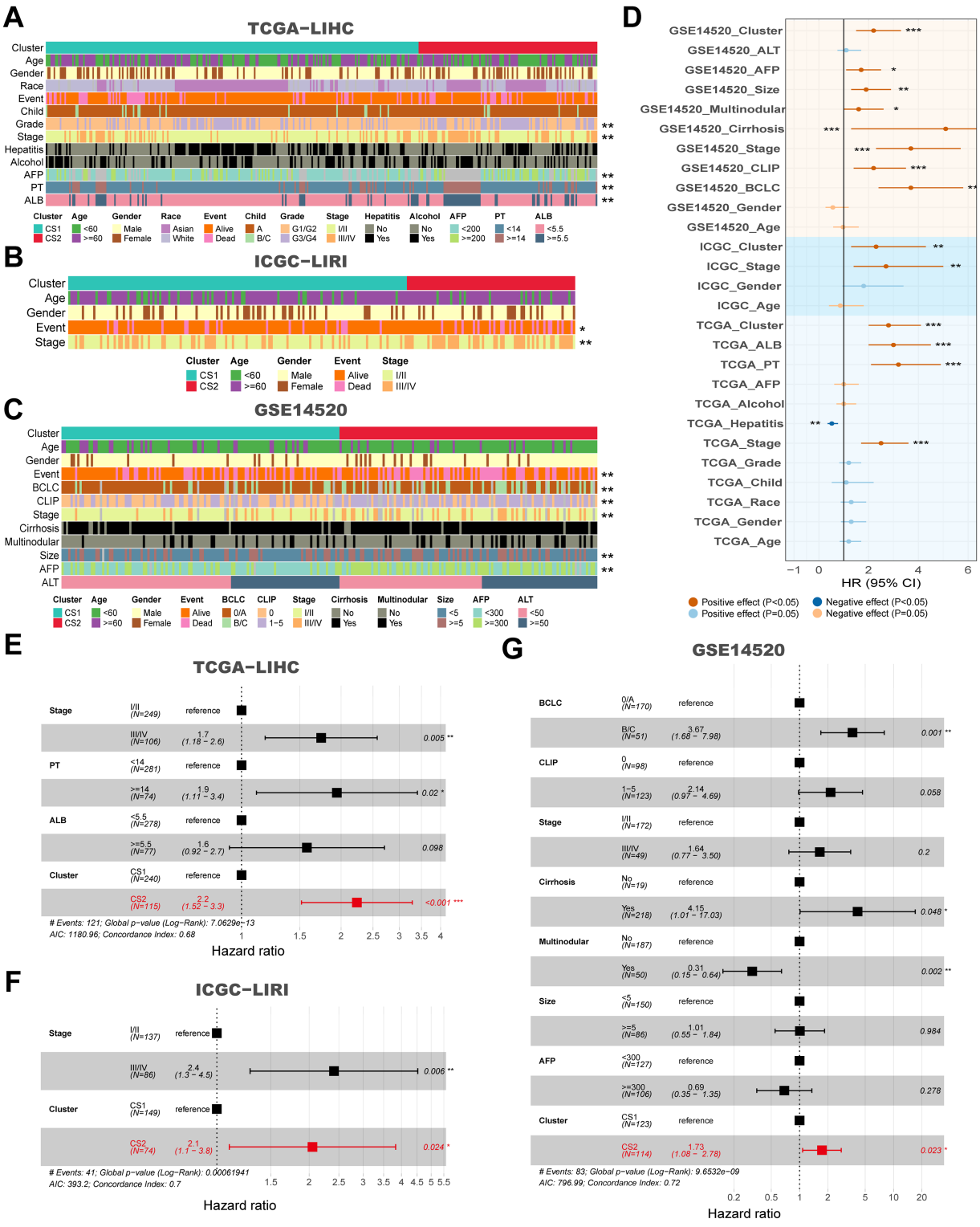

FIGURE 2
Clinical and molecular characteristics associated with subtypes across multiple cohorts, and their impact on survival. **(A)** Clinical features corresponding to CS1 and CS2 in the TCGA-LIHC cohort. **(B)** Clinical features corresponding to CS1 and CS2 in the ICGC-LIRI cohort. **(C)** Clinical features corresponding to CS1 and CS2 in the GSE14520 cohort. **(D)** Forest plot for univariate Cox of clinical variables and subtypes in the TCGA-LIHC, ICGC-LIRI and GSE14520 cohorts. **(E)** Hazard ratios for clinical features and CS subtypes in relation to overall survival based on multivariate Cox analysis in the TCGA-LIHC cohort. **(F)** Hazard ratios for clinical features and subtypes in relation to overall survival based on multivariate Cox analysis in the ICGC-LIRI cohort. **(G)** Hazard ratios for clinical features and subtypes in relation to overall survival based on multivariate Cox analysis in the GSE14520 cohort. *$P < 0.05$, **$P \leq 0.01$, ***$P \leq 0.001$.

10.3389/fimmu.2025.1592259

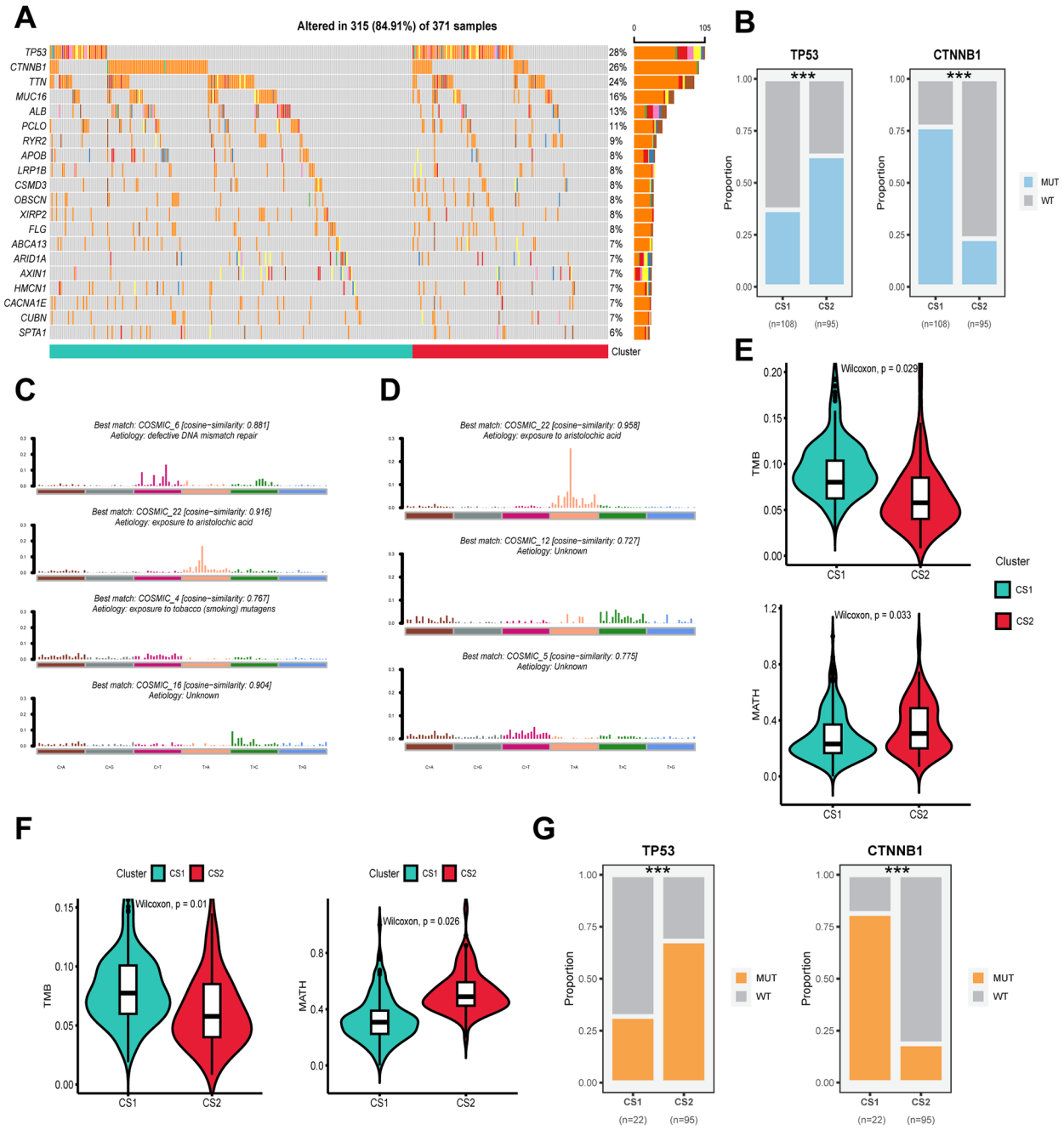

FIGURE 3
Genomic alterations, mutation signatures and mutational burden in subtypes across cohorts. **(A)** Oncoplot showing the distribution of somatic mutations across the most frequently altered genes for CS1 and CS2 in the TCGA-LIHC cohort. **(B)** Proportions of mutations in TP53 and CTNNB1 for CS1 and CS2 in the TCGA-LIHC cohort. **(C)** The best matching COSMIC mutational signatures (with similarity scores) for CS1. **(D)** The best matching COSMIC mutational signatures (with similarity scores) for CS2. **(E)** Violin plots showing the distribution of tumor mutational burden (TMB) in CS1 and CS2 subtypes in the TCGA-LIHC cohort. **(F)** Violin plots showing the distribution of TMB in CS1 and CS2 subtypes in the ICGC-LIRC cohort. **(G)** Mutation status of TP53 and CTNNB1 in CS1 and CS2 subtypes, showing the proportion of wild-type (WT) and mutant (MUT) alleles for each gene in the different clusters. Wilcoxon test was used in **(E, F)** Chi-square test was used in **(B, G)** $***P \leq 0.001$.

the three study cohorts ($P < 0.05$) (Figure 6C). CS2 had higher levels of MDSC, CAF and M2-type TAM, which are associated with the immunosuppressive microenvironment ($P < 0.05$) (Figure 6D). Meanwhile, CS1 had a lower cytotoxic T-cell dysfunction and exclusion score, suggesting its potential immune-activating activity ($P < 0.05$) (Figure 6E). Notably, the results of the explorations for the two real-world immunotherapy cohorts were consistent with our computational predictions, confirming that CS1 patients responded significantly better to immunotherapy than CS2 patients. Specifically, the majority of CS1 patients in GSE215011

10.3389/fimmu.2025.1592259

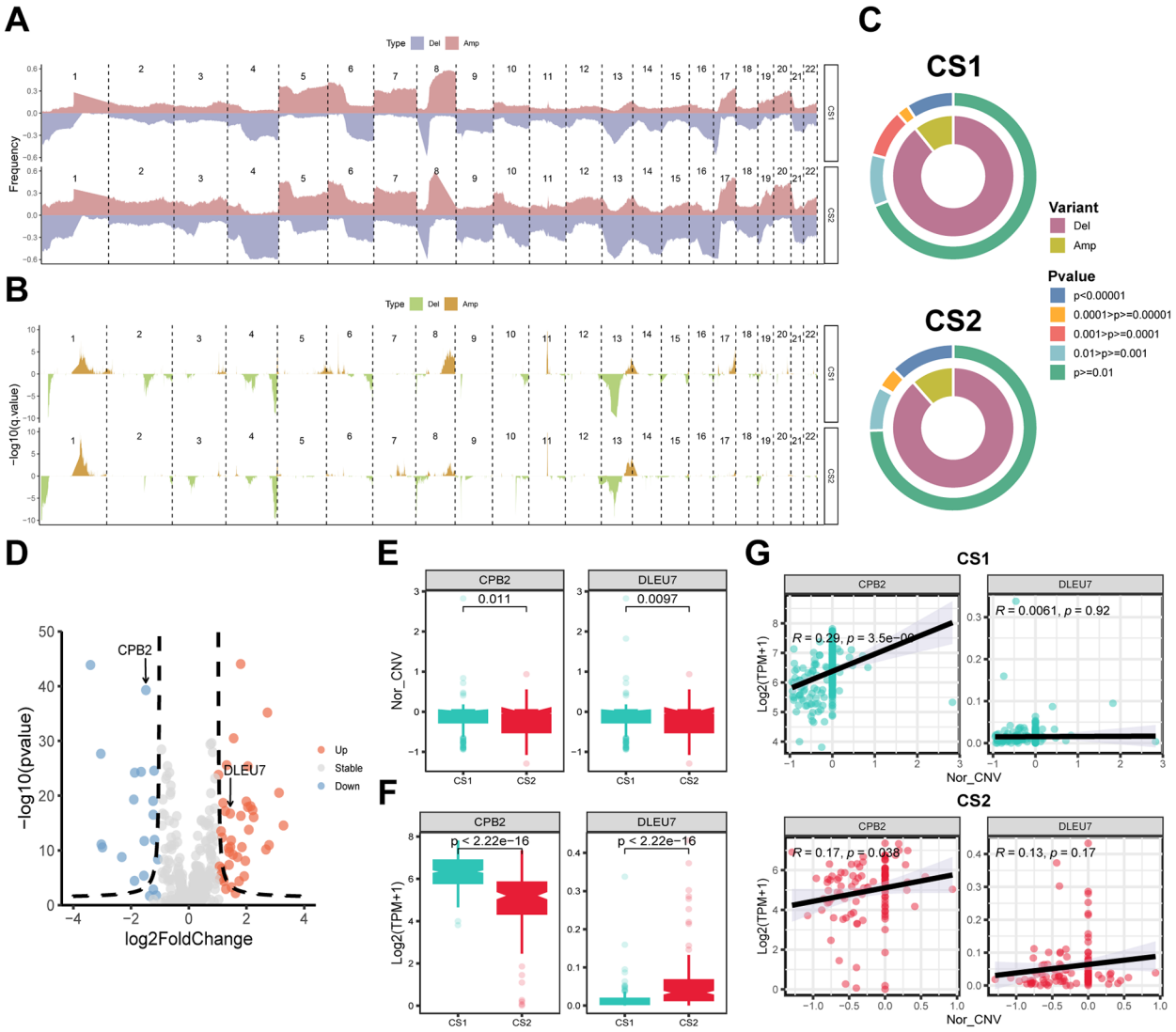

FIGURE 4
Copy number alterations (CNA), gene expression and their correlation with subtypes. **(A)** Frequency plot showing the distribution of CNA across chromosomes for CS1 and CS2, with deletions (Del) and amplifications (Amp) indicated. **(B)** Statistical significance of CNA events with -log10 p-values shown for each region. **(C)** Circular plots depicting the distribution of CNA variants (Del and Amp) and their statistical significance across CS1 and CS2. Colors represent different levels of significance. **(D)** Volcano plot showing differentially expressed genes (DEGs). Red indicates upregulated genes and blue indicates downregulated ones. **(E)** Box plots showing the copy number variation (CNV) score of CPB2 and DLEU7 in CS1 and CS2. **(F)** Box plots presenting the gene expression of CPB2 and DLEU7 in CS1 and CS2. **(G)** Correlation analysis between CPB2 and DLEU7 gene expression and CNV score in CS1 and CS2. Pearson correlation coefficients and p-values are indicated. Wilcoxon test was used in **(E, F)**.

and GSE202069 demonstrated a positive response to treatment, with response rates as high as 75% and 80% for CS1 patients compared to less than 25% for CS2 patients, respectively ($P \leq 0.0001$) (Supplementary Figures S2D, E).

3.7 Integrated machine learning algorithms to develop artificial intelligence-driven risk score

A comprehensive analysis of these 172 overlapping DEGs was conducted using 10 machine learning algorithms, which resulted in the creation of 117 prognostic prediction models. The consistency indices of these models were then calculated for each cohort and their mean values were determined within the overall study cohort. Of all the models, the StepCox[forward]+Ent[a=0.1] model demonstrated the most consistent prognostic prediction efficacy, exhibiting the highest average consistency indices of 0.703 and 0.075 (Figure 7A).

In the univariate Cox regression analysis for the training and validation cohorts, the StepCox[forward]+Ent[a=0.1] model corresponded to hazard ratio (HR) of 2.31, 5.34, and 2.83, respectively ($P \leq 0.001$) (Figure 7B). Meanwhile, in the Meta-analysis of HR for the StepCox[forward]+Ent[a=0.1] model across

10.3389/fimmu.2025.1592259

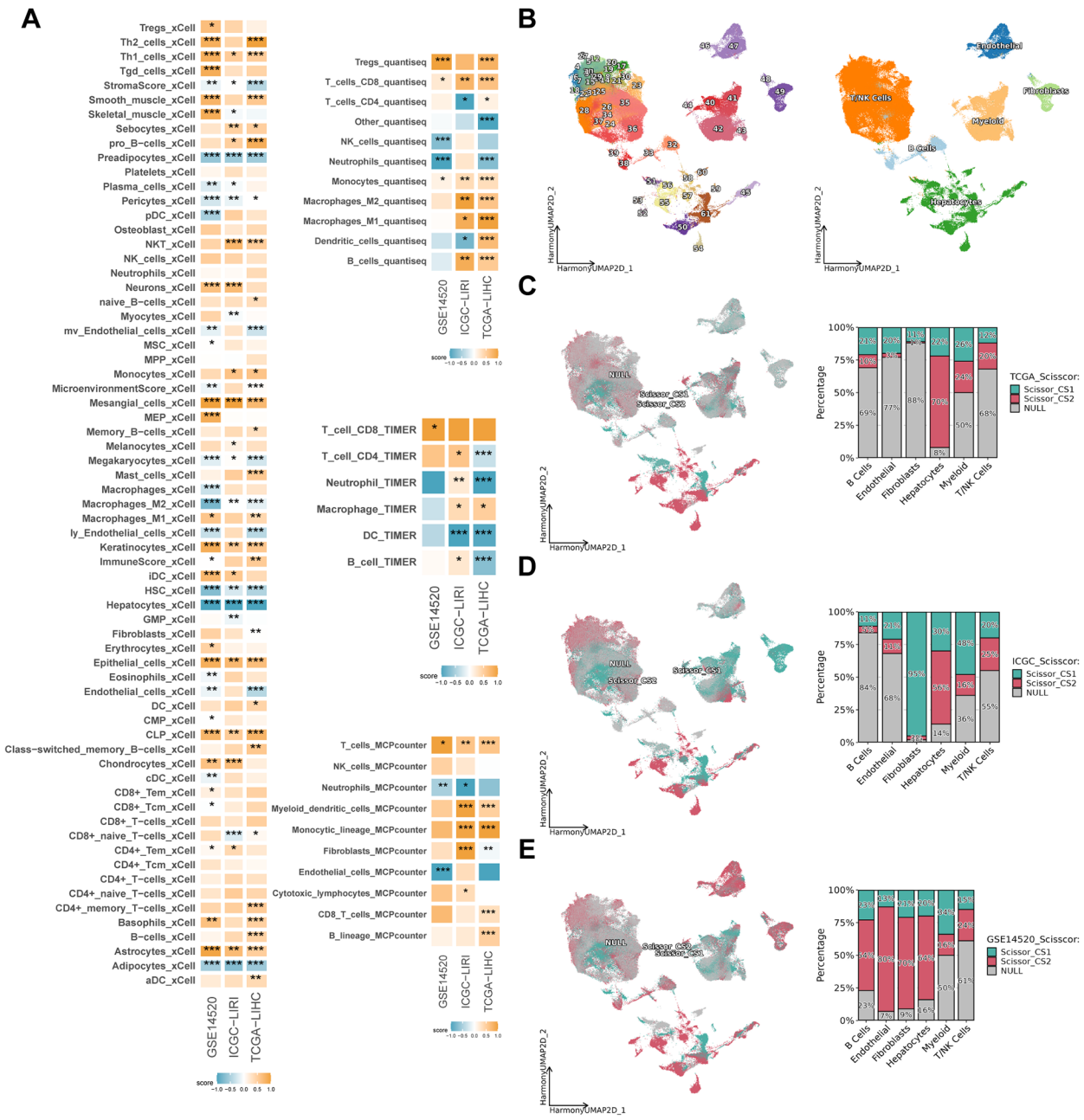

FIGURE 5
Immune infiltration and subtypes distribution across different datasets. **(A)** Heatmap showing the enrichment scores of various immune and stromal cell types in CS1 and CS2 across TCGA-LIHC, ICGC-LIRI and GSE14520 cohorts. The color intensity represents the degree of enrichment. **(B)** Uniform manifold approximation and projection (UMAP) of scRNA-seq data, depicting different cell populations across the dataset, with major cell types labeled. **(C–E)** Scissor-based subtypes distribution of CS1 and CS2 in TCGA-LIHC, ICGC-LIRI and GSE14520 cohorts. The left panels display UMAP projections with cells color-coded by subtype (CS1: red, CS2: cyan, NULL: gray). The right bar plots illustrate the proportion of different cell types within each subtype. *$P < 0.05$, **$P \leq 0.01$, ***$P \leq 0.001$.

the three study cohorts, the random-effects model and the mixed-effects model corresponded to HR of 2.88 and 2.75, respectively, and met the statistical differences ($P \leq 0.001$) (Figure 7B). In addition, the prognostic predictive efficacy of the StepCox[forward]+Ent [a=0.1] model was found to be superior and accurate at 1, 3, and 5 years, respectively, and relatively stable across cohorts. The corresponding AUC values ranged from 0.824 to 0.659 (Figure 7C). It is noteworthy that the average AUC of the model gradually decreased with the prolongation of follow-up time, which is consistent with the actual situation.

Following the determination of the optimal prognostic model, the prognostic risk score, herein referred to as AIDRS, was calculated for each patient with HCC. Subsequent analyses revealed that patients with HCC exhibiting a high AIDRS demonstrated a worse prognosis in both the training and validation cohorts, corresponding to prognostic HR of 2.29, 5.24,

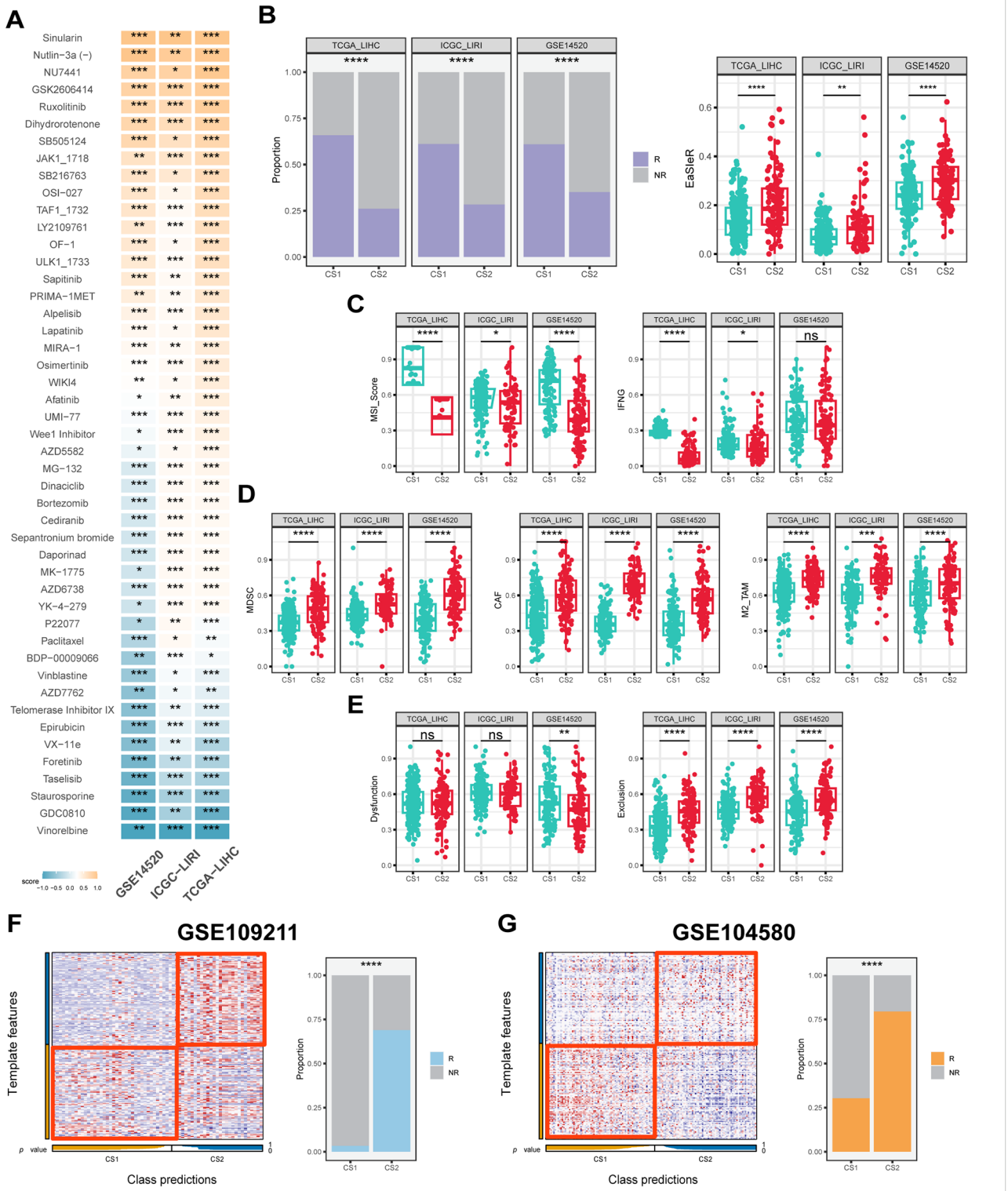

FIGURE 6
Drug response, immune score and predictive classification across different datasets. **(A)** Heatmap of drug response in CS1 and CS2 across the TCGA-LIHC, ICGC-LIRI and GSE14520 cohorts. The color represents drug response in each subtype, with yellow signifies CS1 sensitivity and blue signifies CS2 sensitivity. **(B)** Proportion of immunotherapy response and boxplots of EasleR score in CS1 and CS2 across the TCGA-LIHC, ICGC-LIRI and GSE14520 cohorts. **(C)** Boxplots showing MSI score and INFG in CS1 and CS2 across the TCGA-LIHC, ICGC-LIRI and GSE14520 cohorts. **(D)** Boxplots showing MDSC, CAF and M2-TAMs in CS1 and CS2 across the TCGA-LIHC, ICGC-LIRI and GSE14520 cohorts. **(E)** Boxplots showing T cell dysfunction and exclusion score in CS1 and CS2 across the TCGA-LIHC, ICGC-LIRI and GSE14520 cohorts. **(F)** Evaluation of CS1 and CS2 in the GSE109211 cohort. **(G)** Evaluation of CS1 and CS2 in the GSE104580 cohort. R indicates response, NR indicates no response. Wilcoxon test was used in **(A–E)** Chi-square test was used in **(B, F, G)** ns $P \geq 0.05$, *$P < 0.05$, **$P \leq 0.01$, ***$P \leq 0.001$, ****$P \leq 0.0001$.

and 2.8, respectively ($P \leq 0.001$) (Figure 7D). This finding suggests that AIDRS is a key risk factor for the prognosis of patients with HCC.

3.8 Association between AIDRS and patient prognosis, clinicopathological features, genomic alterations, and personalized therapy

In each of the six mutually independent study cohorts, CS2 exhibited significantly higher AIDRS than CS1 ($P \leq 0.0001$) (Figure 8A). Meanwhile, AIDRS was calculated separately for scRNA-seq data using three different algorithms: "Seurat", "AUcell" and "Ucell". The results demonstrated that hepatocytes exhibited higher AIDRS ($P \leq 0.0001$) (Figure 8B). This finding was consistent across the TCGA-LIHC, ICGCI-LIRI and GSE14520 cohorts. Subsequently, survival analysis revealed that patients in the high AIDRS group corresponded to more fatal events and had a worse prognosis, and this finding was consistent across the TCGA-LIHC, ICGCI-LIRI and GSE14520 cohorts ($P \leq 0.0001$) (Figures 8C–E).

Further analyses addressed AIDRS and clinicopathological features, revealing that patients with advanced tumors exhibited higher AIDRS ($P \leq 0.01$) (Figures 8F–H). Similarly, prognostic risk factors such as AFP, PT and tumor volume were approximately significant, with higher AIDRS correlating with increased risk ($P \leq 0.01$) (Figures 8F–H). Furthermore, patients with TP53 mutant HCC patients exhibited a higher AIDRS in comparison to those with the wild type ($P \leq 0.0001$) (Figure 8I). Conversely, patients with CTNNB1 mutant patients demonstrated a lower AIDRS ($P \leq 0.01$) (Figure 8I). The correlation analysis between AIDRS and immunotherapy response-related scores revealed that higher AIDRS was associated with higher EaSleR score and T-cell exclusion score, and lower MSI score and T-cell dysfunction score ($P \leq 0.01$) (Figures 7J–M). These findings suggest that higher AIDRS is associated with a limited benefit from immunotherapy.

3.9 CEP55 has good predictive efficacy and positively influences patient prognosis

The genes corresponding to the StepCox[forward]+Ent[a=0.1] model in the three study cohorts were extracted, 79, 56, and 118, respectively, with 26 overlapping genes among the three (Figure 9A). Differential expression analysis of the subtypes showed that 18 genes in CS2, including CEP55, showed consistent upregulation of expression in the three study cohorts, while the remaining 8 genes were down-regulated ($P < 0.05$) (Figure 9B). Subsequent univariate Cox regression and correlation analysis revealed that all genes with upregulated expression in CS2 belonged to the prognostic risk factors for HCC patients and were significantly positively associated with AIDRS ($P < 0.05$) (Figures 9C, D). Conversely, genes downregulated in CS2 showed protective factors for HCC prognosis and were significantly negatively correlated with AIDRS ($P < 0.05$) (Figures 9C, D). Furthermore, the proteomics cohort CPTAC revealed that patients exhibiting low CEP55 expression exhibited significantly prolonged overall survival when compared to those exhibiting high CEP55 expression ($P \leq 0.01$) (Supplementary Figure 2F). Concurrently, patients in the CEP55 high-expression exhibited elevated AIDRS ($P < 0.05$) (Supplementary Figure 2G), and CEP55 protein expression levels demonstrated a significant positive correlation with AIDRS ($R = 0.27$, $P < 0.05$) (Supplementary Figure 2H).

In analyses targeting the predictive efficacy of subtypes, CEP55 exhibited higher AUC compared to other genes in both the training and validation cohorts, with 0.942, 0.785, and 0.822, respectively (Figures 9E, F). For subsequent survival analyses, we found that HCC patients with high expression of CEP55 were more likely to experience a fatal event during the follow-up period, which was consistent among the three cohorts of independent studies of each other ($P < 0.05$) (Figures 9G–J). Furthermore, scRNA-seq data indicated that CEP55 was expressed at the highest level in hepatocytes ($P \leq 0.0001$) (Figure 9K).

3.10 Knockdown of CEP55 inhibited cell proliferation, migration and invasion of HCC cells

In order to validate the critical role of CEP55 in HCC, two different types of CEP55 knockdown phenotypes were constructed for two HCC cell lines, Bel-7402 and Hep-3B. The presence of CEP55 in both HCC cell lines was indicative of the CEP55 knockdown phenotypes. Following the targeting of siRNAs, the gene expression of CEP55 was significantly reduced in cell lines Bel-7402 and Hep-3B ($P < 0.05$) (Figure 10A), thus confirming the success of the construction of the CEP55 knockdown phenotypes. Subsequent functional assays revealed that CEP55 knockdown phenotypes Si-1 and Si-2 exhibited diminished cell viability and reduced cell clone number, indicating that CEP55 knockdown inhibited HCC cell proliferation ($P < 0.05$) (Figures 10B, C). Furthermore, CEP55 knockdown significantly impeded the migration and invasion of cell lines A and B in the transwell assay and scratch wound healing assay ($P < 0.05$) (Figures 10D, E).

3.11 Knockdown of CEP55 inhibits tumor growth and proliferation in xenograft models

In order to investigate the effect of CEP55 on tumor growth *in vivo*, xenograft models were established in BALB/c nude mice using Bel-7402 and Hep-3B HCC cell lines with CEP55 knockdown. During the observation period, the activity levels, grooming behavior, and overall health status of the mice remained within normal parameters, exhibiting a downward trend in weight ($P \leq 0.01$) (Figures 11A, B). The body weight of the mice decreased gradually over time, with a more significant decrease observed in the shCEP55

10.3389/fimmu.2025.1592259

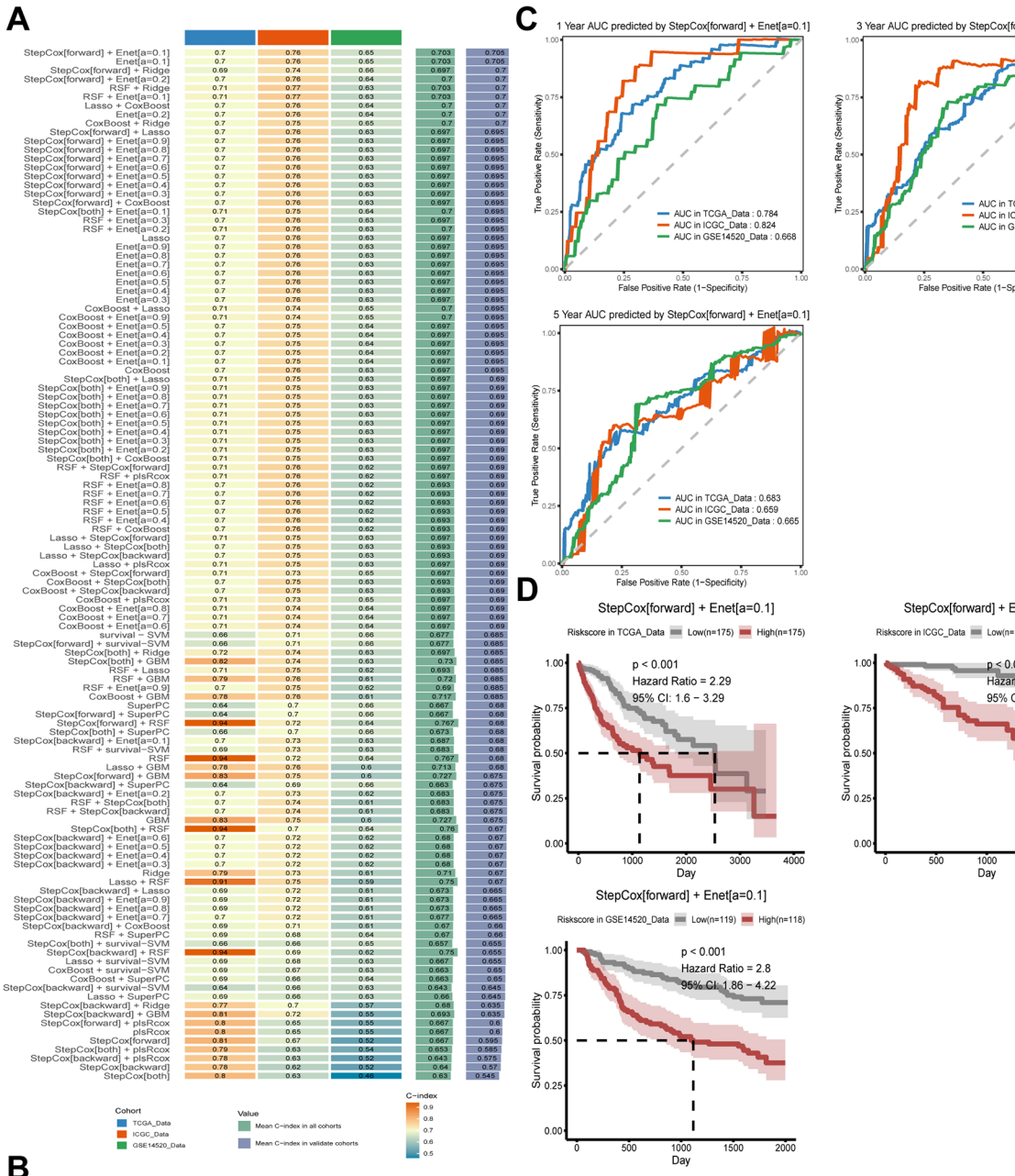

FIGURE 7
Construction and evaluation of prognostic models across different datasets. **(A)** C-index of each model among different datasets sorted by the average of C-index in validation cohorts. **(B)** Meta-analysis of univariate Cox result of the best model StepCox[forward]+Ent[a=0.1] across the TCGA-LIHC, ICGC-LIRC and GSE14520 cohorts. **(C)** Receiver operating characteristic (ROC) curves showing the prediction performance of the StepCox [forward]+Ent[a=0.1] model for 1-year (top left), 3-year (top right), and 5-year (bottom left) survival data across the TCGA-LIHC, ICGC-LIRC and GSE14520 cohorts. **(D)** Kaplan-Meier curves showing the survival probability for high-risk and low-risk groups predicted by the risk score calculated by StepCox[forward]+Ent[a=0.1] model across TCGA-LIHC (left), ICGC-LIRC (right), and GSE14520 (bottom) cohorts. Log-rank test was used in **(D)**.

10.3389/fimmu.2025.1592259

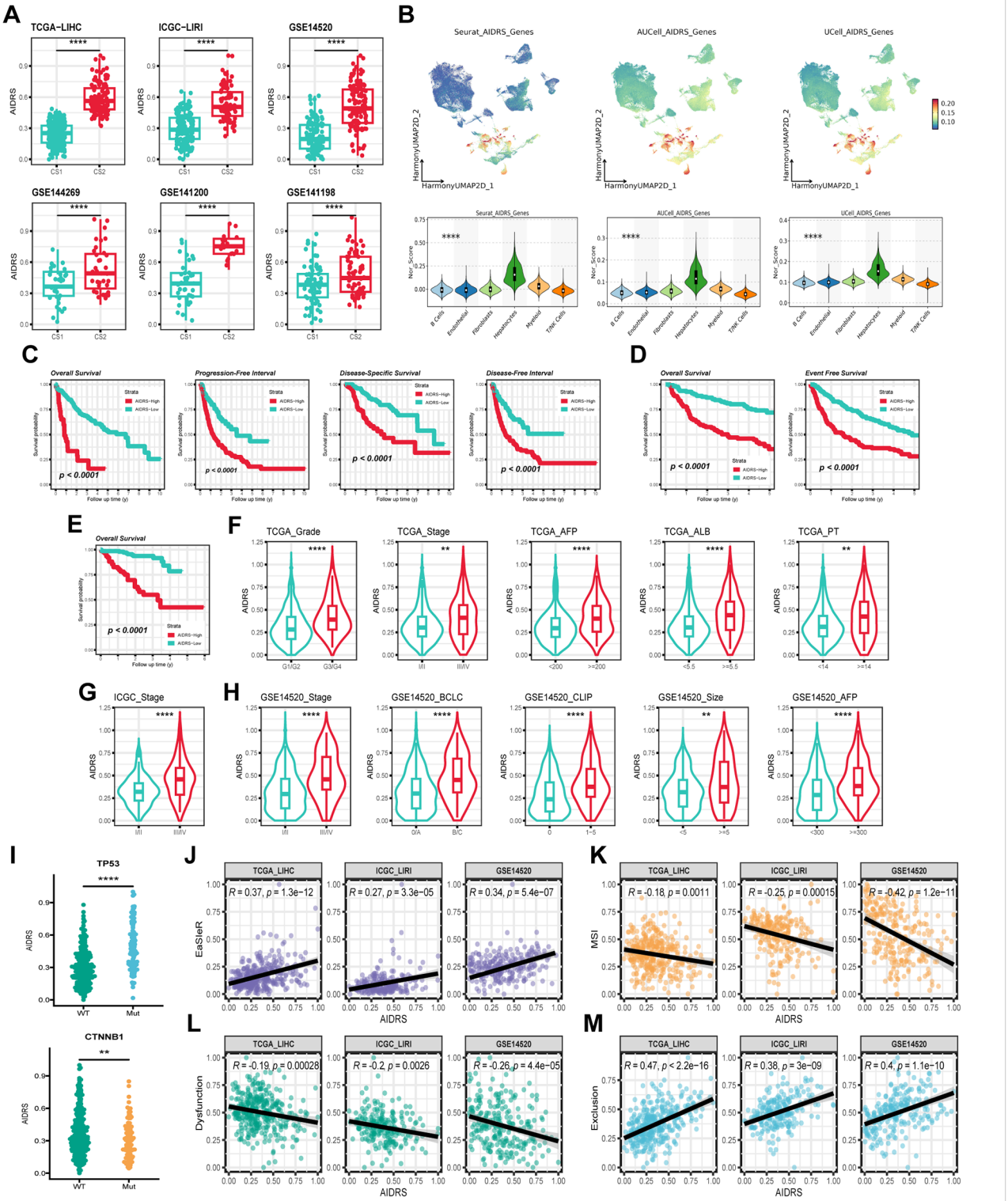

FIGURE 8 (Continued)

FIGURE 8 (Continued)
Correlation of AIDRS with clinicopathological features, immune score, and survival outcomes across different datasets. **(A)** Boxplots displaying the AIDRS across the CS1 and CS2 for the TCGA-LIHC, ICGC-LIRI and GSE14520 cohorts. **(B)** UMAP plots (top) and violin plots (bottom) showing the expression distribution of AIDRS-related genes across the TCGA-LIHC, ICGC-LIRI and GSE14520 cohorts. **(C)** Kaplan-Meier curves showing the overall survival, progression-free interval, disease-specific survival and disease-free interval for high- and low-risk groups in the TCGA-LIHC cohort. **(D)** Kaplan-Meier curves showing the overall survival and progression-free interval in the ICGC-LIRI cohort. **(E)** Kaplan-Meier curve showing the overall survival in the GSE14520 cohort. **(F)** Violin plots illustrating the distribution of AIDRS based on clinicopathological features such as Grade, Stage, AFP, ALB and PT across the TCGA-LIHC cohort. **(G)** Violin plots comparing AIDRS across Stage in the ICGC-LIRI cohort. **(H)** Violin plots showing AIDRS based on clinicopathological features such as Stage, CLIP, AFP and tumor size across the GSE14520 cohort. **(J)** Scatter plots showing the correlation between AIDRS and EasleR score in the TCGA-LIHC, ICGC-LIRI and GSE14520 cohorts. **(K)** Scatter plots showing the correlation between AIDRS and MSI score in the in the TCGA-LIHC, ICGC-LIRI and GSE14520 cohorts. **(L)** Scatter plots showing the correlation between AIDRS and T cell dysfunction score in the in the TCGA-LIHC, ICGC-LIRI and GSE14520 cohorts. **(M)** Scatter plots showing the correlation between AIDRS and T cell exclusion score in the in the TCGA-LIHC, ICGC-LIRI and GSE14520 cohorts. Log-rank test was used in **(C, D, E)** Wilcoxon test was used in **(A, F, G, H, I)** Welch's ANOVA test was used in **(B)** $^{**}P \leq 0.01$, $^{****}P \leq 0.0001$.

group ($P \leq 0.01$) (Figures 11A, B). Western blotting analysis demonstrated that, in comparison with the control group, the expression levels of CEP55 in the xenograft tumors of the shCEP55 group were significantly reduced, thus indicating that CEP55 knockdown was effective at this particular time ($P \leq 0.01$) (Figures 11C, D). Moreover, CEP55 knockdown effectively inhibited the growth of xenograft tumors derived from Bel-7402 and Hep-3B cells, with tumor volumes in the shCEP55 group being significantly smaller than those in the control group (Figures 11A, B). Furthermore, it was found that in xenograft tumors derived from the two different sources, Bel-7402 and Hep-3B, the histochemistry score of CEP55 and Ki-67 in the shCEP55 group were significantly lower than those in the control group, further confirming the inhibitory effect of CEP55 knockdown on tumor cell proliferation ($P \leq 0.01$) (Figures 11E, F).

4 Discussion

HCC is a highly heterogeneous malignancy, which poses significant challenges to both treatment and prognosis. Despite advancements in systemic therapies, including targeted and immunotherapies, the clinical outcomes for many patients remain suboptimal, particularly in advanced-stage disease. In recent years, multiple molecular subtypes have been proposed for HCC to better understand this heterogeneity and guide personalized treatment. For instance, Hoshida et al. (19) identified three robust HCC subtypes based on transcriptomics: S1, S2, and S3. Among them, S2 has the largest tumor volume and the highest AFP, and has the worst prognosis. In terms of molecular characteristics, S1 exhibits abnormal activation of the WNT signaling pathway, S2 is characterized by cell proliferation, and S3 corresponds to the process of hepatocyte differentiation. In a proteomic study by Guo et al. (20), hepatitis B virus-related HCC patients were divided into metabolic subgroups, microenvironment dysfunction subgroups and proliferation subgroups. S-Mb is characterized by high levels of proteins involved in cancer metabolism and is associated with the best prognosis. In contrast, S-Me is characterized by high levels of proteins involved in immunity and inflammation and is associated with a poorer prognosis when compared with S-Mb. In a systematic study of metabolic gene expression profiles, Chen et al. (45) also identified three subtypes of HCC (C1, C2 and C3). Subtype C1 exhibits high metabolic activity, subtype C2 shows high sensitivity to immunotherapy, and subtype C3 has the highest AFP and the worst prognosis. These efforts have proposed distinct molecular subtypes of HCC and confirmed that these subtypes are associated with treatment response. Nevertheless, studies that focus on a single omics approach or specific biological pathways frequently fail to capture the full complexity of the disease. To address this limitation, our study integrates multi-omics data from genomics, transcriptomics and epigenomics, identifying two molecular subtypes of HCC, CS1 and CS2, with distinct clinical and biological characteristics (Figure 12).

In light of the intricacy involved in data integration and the necessity for ensuring the reproducibility of subtypes, the study employed the consensus clustering framework MOVICs (34), a methodology that has been demonstrated to be efficacious in other cancer studies, for the identification of molecular subtypes of HCC. For instance, Ji et al. (46) utilized MOVICs to distinguish between IDH-mutant glioblastoma subtypes, class 1 and class 2, elucidating the disparities in molecular characteristics while identifying drugs, temozolomide and navitoclax, that are sensitive to each of these subtypes. In a similar vein, studies on lung adenocarcinoma (47), colorectal cancer (48), and breast cancer (49) have also employed MOVICs to perform multi-omics typing, thereby enhancing the understanding of tumor heterogeneity and optimizing treatment options for patients. In a manner analogous to these studies, the present study identifies and characterizes HCC subtypes from multiple dimensions, including clinicopathologic features, genetic mutations, DNA methylation patterns, immune microenvironment composition and so on. In this study, we found that CS1 had a more favorable prognosis, while CS2 was associated with poorer clinical outcomes. CS2 was found to have higher serum levels of AFP, longer PT, and larger tumor volume when compared with CS1. As corroborated by both univariate and multivariate Cox regression analysis, underscore the significance of the CS subtype as a critical prognostic factor for patients diagnosed with HCC. The hazard ratio associated with CS1 is notably more effective in predicting outcomes when compared with conventional biomarkers such as AFP, ALB and PT. At the genomic level, CS1 was found to exhibit elevated levels of CTNNB1 mutations and high TMB, while CS2 was predominantly characterized by TP53 mutations and high MATH. It has been demonstrated that gene mutations can induce tumor cells to produce neoantigens by means of regulating gene expression. This,

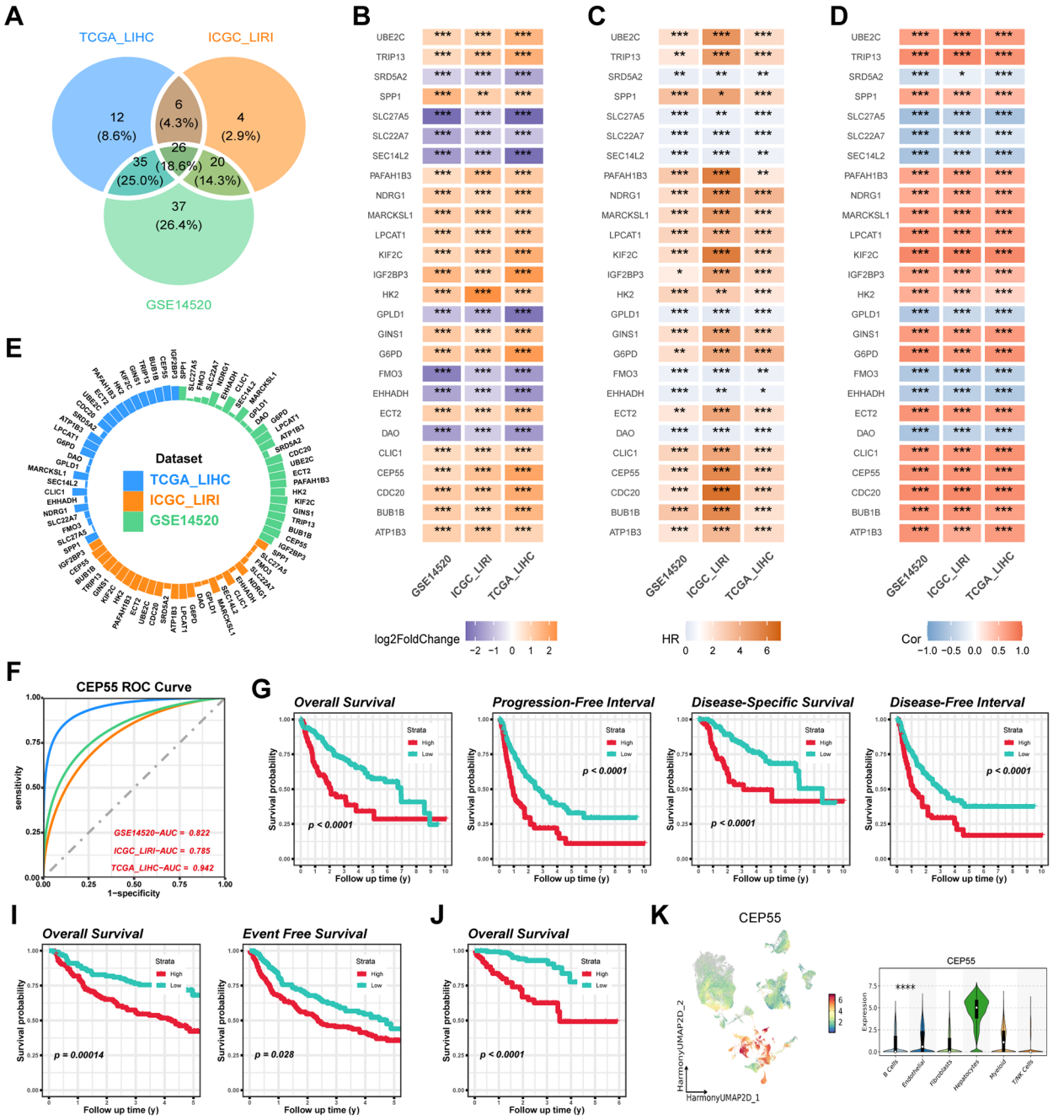

FIGURE 9
Identification and validation of CEP55 as a prognostic biomarker across multiple datasets. **(A)** Overlapping differentially expressed genes (DEGs) among the TCGA-LIHC, ICGC-LIRI and GSE14520 cohorts. **(B)** Log2 fold change (log2FC) values of overlapping DEGs across the TCGA-LIHC, ICGC-LIRI and GSE14520 datasets. **(C)** Univariate Cox regression for overlapping DEGs associated with survival outcomes in TCGA-LIHC, ICGC-LIRI and GSE14520 cohorts. **(D)** Correlation heatmap showing the association of AIDRS and overlapping DEGs across the datasets. The color intensity represents the strength of the correlation. **(E)** Circular plot displaying the AUC value of overlapping DEGs, with each dataset (TCGA-LIHC, ICGC-LIRI and GSE14520) represented in different colors. **(F)** ROC curves illustrating the predictive accuracy of CEP55 in TCGA-LIHC, ICGC-LIRI and GSE14520 datasets. **(G)** Kaplan-Meier curves for overall survival, progression-free interval, disease-specific survival and disease-free interval of high and low CEP55 expression groups in the TCGA-LIHC cohort. **(H)** Kaplan-Meier curves for overall survival and event-free survival of high and low CEP55 expression groups in the ICGC-LIRI dataset. **(I)** Kaplan-Meier curve for overall survival in the GSE14520 dataset, showing significant survival differences between high and low CEP55 expression groups. **(J)** UMAP plot displaying the expression of CEP55 across different cell populations. The violin plot on the right shows the distribution of CEP55 expression across major cell types. Log-rank test was used in **(G, I, J)** Welch's ANOVA test was used in **(K)** *$P < 0.05$, **$P \leq 0.01$, ***$P \leq 0.001$, ****$P \leq 0.0001$.

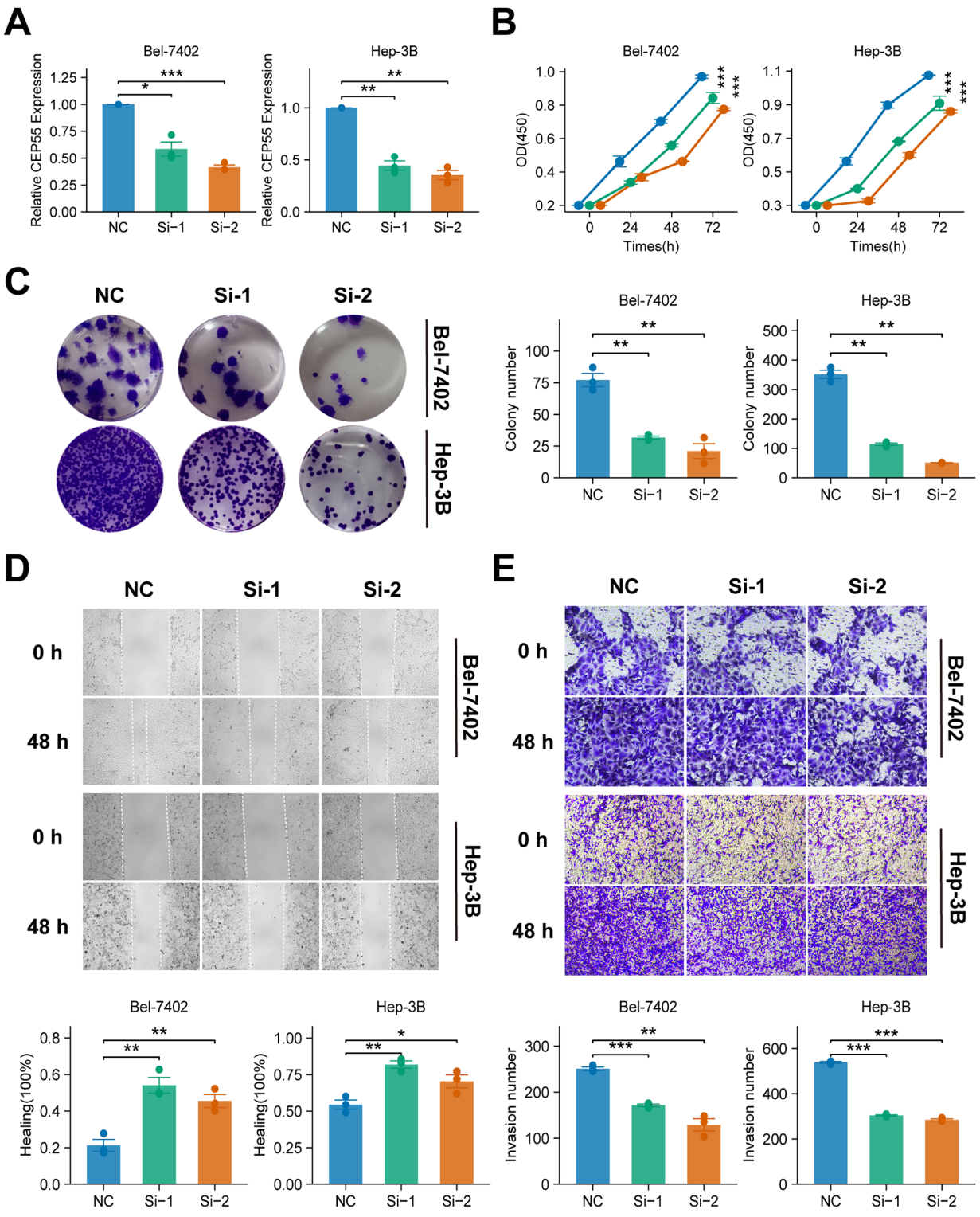

FIGURE 10
Effects of CEP55 knockdown on cell proliferation, migration and invasion in Bel-7402 and Hep-3B cell lines. **(A)** Quantitative PCR analysis showing the relative expression of CEP55 in Bel-7402 and Hep-3B cells after transfection with siRNA (Si-1 and Si-2) compared to the negative control (NC). **(B)** Cell viability measured at 24, 48, and 72 h in Bel-7402 and Hep-3B cells. Proliferation was significantly reduced in siRNA-treated cells compared to NC. **(C)** Representative images (upper) and quantification (lower) of colony formation in Bel-7402 and Hep-3B cells after CEP55 knockdown. **(D)** Representative images of wound healing at 0 and 48 h (upper) and quantification of healing percentage (lower) in Bel-7402 and Hep-3B cells. **(E)** Representative images (upper) and quantification of invaded cells (lower) in Bel-7402 and Hep-3B cells at 0 and 48 h after CEP55 knockdown. Wilcoxon test was used in A, C, D, **(E)** Chi-square test was used in **(B)** $^{*}P < 0.05$, $^{**}P \leq 0.01$, $^{***}P \leq 0.001$.

10.3389/fimmu.2025.1592259

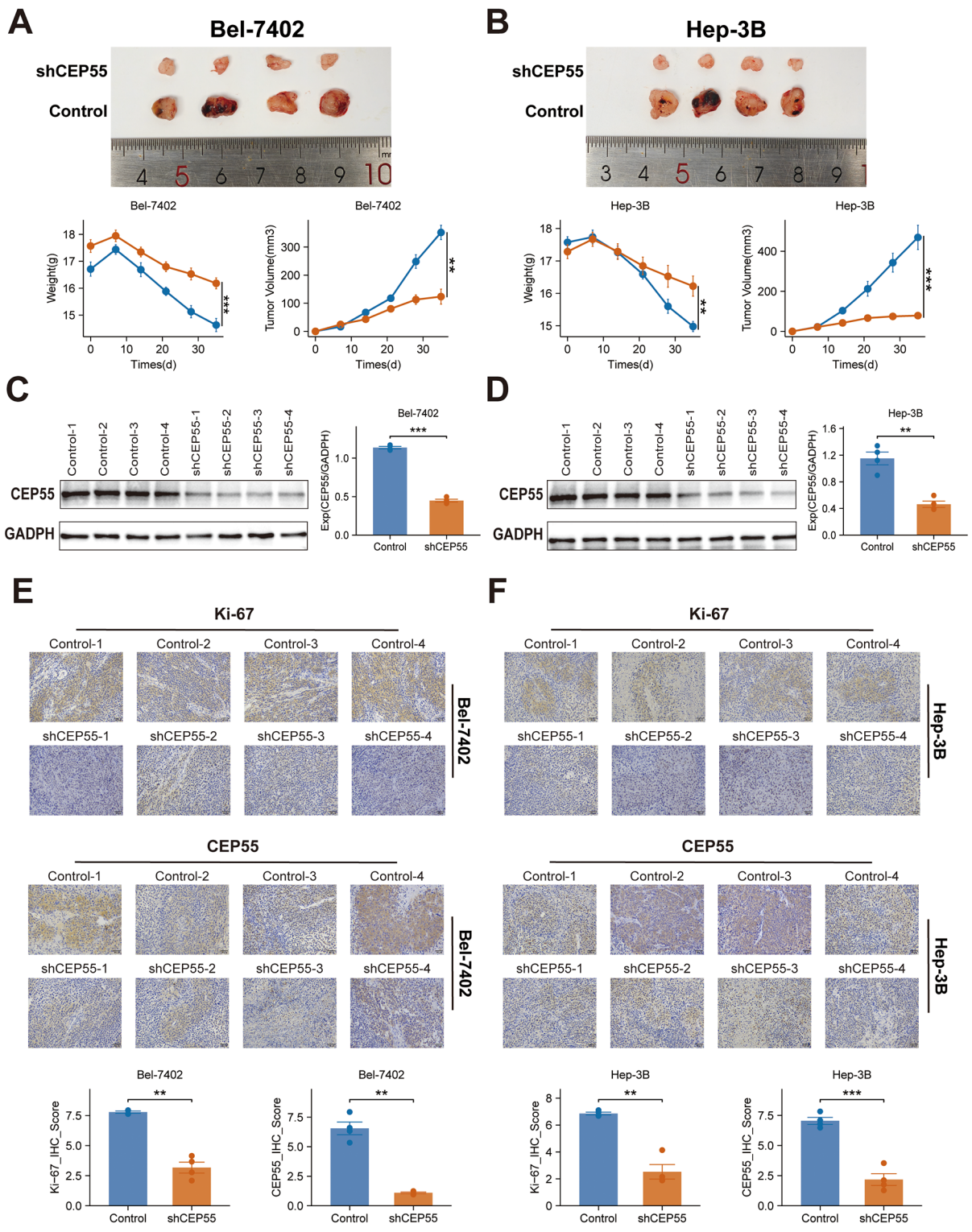

FIGURE 11
Effects of CEP55 knockdown on tumor growth and proliferation in Bel-7402 and Hep-3B xenograft models. **(A)** Representative images (upper) and quantification (lower) of tumor weight and volume in Bel-7402 xenografts after CEP55 knockdown (shCEP55) and control treatments. **(B)** Representative images (upper) and quantification (lower) of tumor weight and volume in Hep-3B xenografts. **(C)** Western blotting analysis of CEP55 expression in Bel-7402 xenograft tumors. **(D)** Western blotting analysis of CEP55 expression in Hep-3B xenograft tumors. **(E)** Immunohistochemistry staining of Ki-67 and CEP55 in Bel-7402 xenograft tumors (upper) and corresponding quantification of Ki-67 and CEP55 staining (lower). **(F)** Immunohistochemistry staining of Ki-67 and CEP55 in Hep-3B xenograft tumors (upper) and corresponding quantification (lower). *$P < 0.05$, **$P \leq 0.01$, ***$P \leq 0.001$..

10.3389/fimmu.2025.1592259

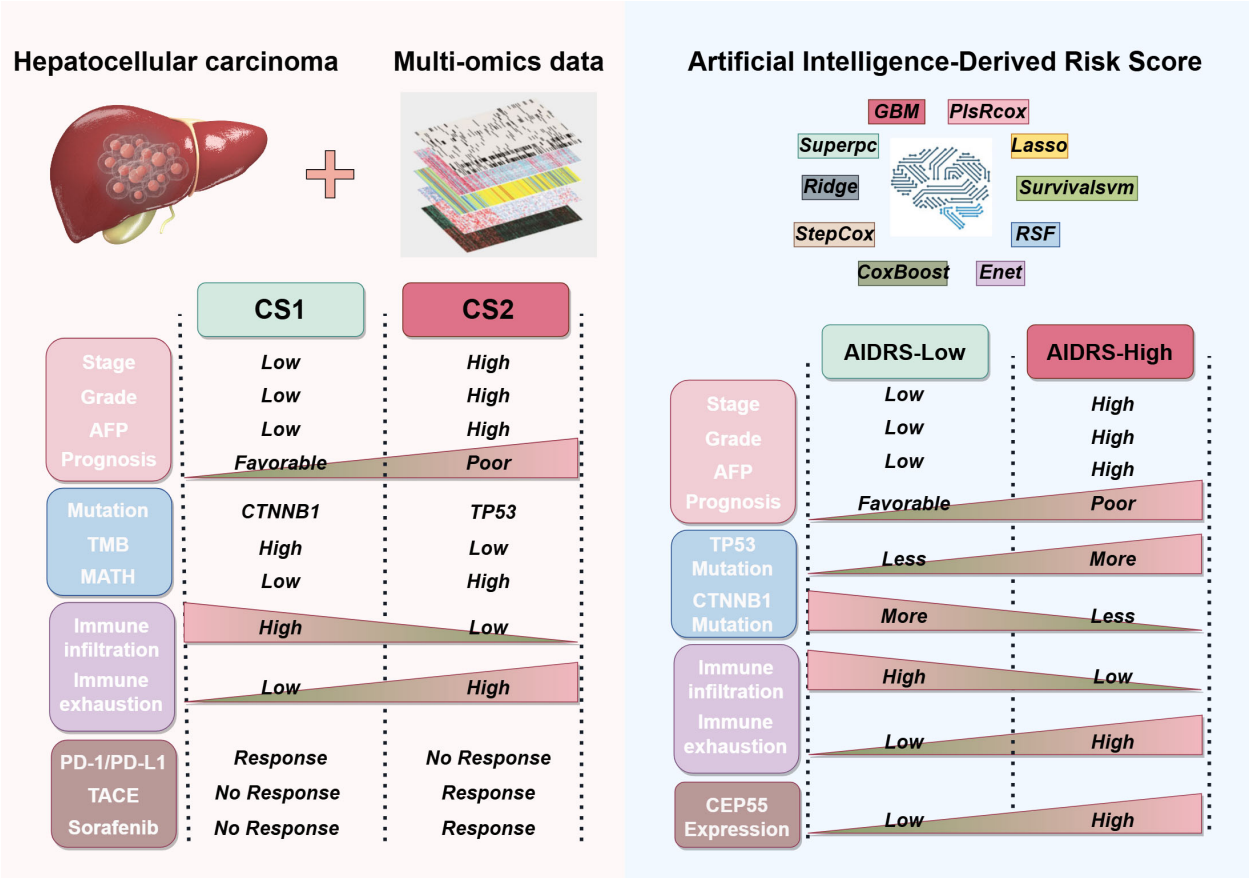

FIGURE 12
Sketch diagram illustrating the clinicopathological features, genetic alterations, immune status, and treatment responses among CS1 and CS2 based on multi-omics data, as well as the artificial intelligence-derived risk score (AIDRS) classification.

in turn, activates immune cells to recognize and eliminate the tumor cells, thus enhancing the efficacy of immunotherapy (50, 51). In this study, functional enrichment analysis indicated that CS1 with high TMB exhibited significant activation of immune-related pathways, and the infiltration levels of various immune cells, including $CD8^+$ T cells, NK cells, and M1 macrophages were significantly higher than those in CS2. Moreover, both computational predictions and real-world data indicated that CS1 exhibited a higher response to immunotherapy. Conversely, Li et al. (52) discovered that TP53 mutations can upregulate MTFHD2 expression to enhance one-carbon metabolism activity in tumor cells, thereby promoting cell proliferation and survival, rendering it an important factor influencing tumor malignant behavior. In a similar vein, it was ascertained that CS2, characterized by a high prevalence of TP53 mutations, exhibited a strong correlation with multiple metabolic pathways. At the same time, Nian et al. (53) demonstrated that TP53 mutations can induce metabolic reprogramming in TAMs in HCC, thereby suppressing the anti-tumor immunity of $CD8^+$ T cells. Similarly, it was determined that the CS2 tumor microenvironment is characterized by the predominance of cells, including MDSCs and CAFs, that contribute to immune suppression and immune escape, thereby leading to reduced tumor immunogenicity and immunotherapy response rates. In summary, it is hypothesized that high TMB and high TP53 mutations may be significant driving factors leading to substantial differences in molecular characteristics and clinical outcomes between CS1 and CS2.

As a small molecule inhibitor, nutlin-3 activates the p53 pathway, inducing cell cycle arrest and apoptosis in tumor cells without exerting toxic effects on normal cells (48). It has been demonstrated to possess excellent anti-cancer activity and safety in preclinical studies of retinoblastoma (54), lymphoma (55) and other malignant tumors (56, 57). In this study, we found that CS1 is sensitive to nutlin-3, suggesting that it may benefit significantly from nutlin-3. Conversely, CS1 demonstrated heightened sensitivity to the JAK2 inhibitor ruxolitinib in comparison to CS2. This observation is particularly noteworthy in light of the documented enhanced effect of targeting the JAK2/STAT3 pathway on tumor immunogenicity (58). We hypothesize that this heightened sensitivity is associated with its regulatory influence on the immune microenvironment. Consequently, the combination of ruxolitinib with immune checkpoint inhibitors (ICIs) may yield a more pronounced therapeutic effect for CS1. Conversely, CS2 appears to demonstrate heightened sensitivity to chemotherapeutic agents such as paclitaxel and vinblastine, which are conventional anti-microtubule drugs that have received the Food and Drug Administration (FDA) approval for the treatment of various malignant tumors (59–61), including ovarian

cancer, non-small cell lung cancer and breast cancer. However, studies conducted on HCC have thus far been confined to phase II clinical trials (NCT02423239 and NCT04175912). Maybe, the differences between them in drugs sensitivity to CS subtypes may provide a valuable information for subsequent research.

Sorafenib is a first-line treatment for patients with advanced HCC (1). A phase 3 clinical study (5) conducted by the SHARP investigators study group demonstrated that sorafenib can prolong the median survival and time to radiographic progression by nearly 3 months in patients with advanced HCC. However, it is important to note that only a small proportion (20%–40%) of patients with advanced HCC are reported to be sensitive to sorafenib treatment and these patients usually progress after sorafenib treatment (secondary or acquired resistance) (6, 7). For this reason, some special technical methods, such as TACE, are recommended as an important supplementary means of first-line treatment for HCC (62, 63). The current research indicates that the survival outcomes of TACE treatment are variable, with only some patients demonstrating survival benefits (64–66). This study found that patients sensitive to sorafenib and TACE treatment are more concentrated in the CS2 subtype. The tumor microenvironment of CS2 is rich in non-immune cells, such as hepatocytes and fibroblasts, which is undoubtedly optimal for sorafenib and TACE, which exert anti-cancer activity through tumor toxicity. In recent years, there has been vigorous development in research into ICIs for malignant tumors, and related drugs have been widely used in clinical practice (8). The results are not so promising, and some patients have not significantly improved their survival endpoints due to the low response rate (1, 67). However, there is a subset of patients for whom the response to therapy is more favorable, and in whom the immune system can mount a more effective response due to the high immunogenicity of the tumors. This is exemplified by melanoma. By contrast, “cold tumors”, such as those observed in pancreatic cancer and prostate cancer, are characterized by a dense tumor tissue, which hinders the infiltration of immune cells. The immunosuppressive microenvironment of these hinders the effectiveness of immunotherapy. Similarly, CS1 was demonstrated higher immunogenicity due to its abundance of immune cell infiltrations, rendering it more susceptible to immunotherapy.

The application of machine learning (ML) in various fields has led to a growing body of research that substantiates the efficacy of ML technology in predicting disease outcomes, treatment responses, and patient prognoses (68–71). Nevertheless, the selection of the most appropriate model remains challenging due to the heterogeneity of file types, system parameters and dataset formats employed by disparate machine learning algorithms. To address this challenge, this study utilized the Mime framework (72), which integrates 117 distinct machine learning models to construct a prognostic model for HCC patients associated with CS subtypes (72). The “StepCox[forward]+Ent [a=0.1]” model, which demonstrated the highest prediction accuracy, was identified through a comparative analysis of model performance across multiple independent study cohorts. To enhance interpretability and streamline application, artificial intelligence-derived risk score (AIDRS) was further developed based on the model. The findings of this study revealed that elevated AIDRS score were associated with a more unfavorable prognosis for HCC patients with larger tumor volumes, elevated AFP, and longer PT. Six independent study cohorts all confirmed that the AIDRS score for CS2 was significantly higher than that for CS1. Furthermore, the study demonstrated that elevated AIDRS scores are associated with improved immunotherapy efficacy, as evidenced by increased EaSleR and T cell rejection scores, as well as reduced microsatellite instability (MSI) and T cell dysfunction scores. It is evident that AIDRS scores serve a dual purpose; they function as an excellent prognostic risk prediction tool and aid in identifying HCC patient CS subtypes through transcriptomics. This enhances the convenience and universality of subtype classification, thereby guiding personalized treatment for HCC patients. Specifically, patients with higher AIDRS scores tend to belong to CS2. In combination with the elevated response rates documented in CS2 patients to sorafenib or TACE treatment, this substantiates the prioritization of sorafenib or TACE as primary treatment modalities. Conversely, patients exhibiting lower AIDRS scores are more aptly categorized as CS1, signifying a predilection for immunotherapy. Moreover, our findings indicate that CEP55 is a pivotal contributor to AIDRS and associated with unfavorable prognose. In addition, it exhibited an excellent predictive capacity for CS subtypes, with AUC values of 0.942 and 0.822 in the training and validation sets, respectively. Consequently, these findings suggest that CEP55 can serve as a reliable biomarker for distinguishing CS subtypes in HCC patients, which is fully consistent with the AIDRS score. So, the consideration of CEP55 expression may prove advantageous in the development of personalized treatment strategies for HCC patients.

CEP55, a centromere protein, has been shown to be overexpressed in various human cancers, including liver cancer (73), breast cancer (74), and renal cell carcinoma (75). The study (76) found that CEP55 can activate PI3K/AKT and FOXM1-related pathways to intervene in the process of cytokinesis, thereby promoting tumorigenesis, proliferation, and metastasis. In addition, Yang et al. (77) found that patients with HCC overexpressing CEP55 generally had higher histological grades, more lymph node metastases and a poorer prognosis, which is consistent with the findings of the current study. The functional studies of CEP55 in HCC cell lines (Bel-7402 and Hep-3B) demonstrated that CEP55 knockdown inhibited cell proliferation, migration and invasion. Moreover, in xenograft models, CEP55 knockdown significantly reduced tumor growth and proliferation, as evidenced by decreased tumor volume, lower CEP55 and Ki-67 expression. A pan-cancer study by Xie et al. (78) revealed that CEP55 is closely associated with immune-related pathways, such as the IL-6/JAK-STAT3 signaling pathway and the IFN-α/γ response pathway. Additionally, in most malignant tumors, including HCC, CEP55 expression is significantly positively correlated with the infiltration levels of MDSCs and Th2 cells in the tumor microenvironment, leading to immune suppression. In the study, CS2 with high CEP55 expression was found to correspond to higher T cell rejection scores and lower T cell dysfunction scores, overall exhibiting low immunogenicity. On the basis of these findings, it can be speculated that targeting CEP55 may not only directly inhibit tumor cell proliferation and migration but also modulate tumor immunogenicity by influencing immune-related pathways, including the IL-6/JAK-STAT3 and IFN-α/γ pathways, thereby enhancing sensitivity to relevant therapies, particularly immunotherapy.

While the present study provides valuable insights into the molecular subtypes of HCC, there are several limitations that should be acknowledged. Firstly, the retrospective nature of the cohort means that the results may be subject to bias and prospective validation in larger, more diverse patient populations is essential. Secondly, the multi-omics data utilized were limited to genomics, transcriptomics, epigenomics and proteomics. Incorporating additional omics layers, such as metabolomics, could further enhance the predictive power of the models. In addition, while it was demonstrated that the AIDRS had the capacity to predict patient prognosis and guide treatment decisions, its clinical applicability must be confirmed through prospective, multi-central studies. Moreover, further research is required to explore how other therapies, such as combination immune checkpoint inhibitors or novel targeted agents could benefit patients.

5 Conclusion

In conclusion, this study successfully identifies and characterizes two distinct HCC subtypes, CS1 and CS2, through the integration of multi-omics data, highlighting their significant differences in clinical outcomes, molecular characteristics and immune features. The development of the AIDRS provides an effective prognostic tool, enabling precise risk stratification and guiding personalized treatment decisions for HCC patients. Of particular note is the identification of CEP55 as a pivotal gene associated with poor prognosis and progression, suggesting that its targeting may offer a promising therapeutic strategy. These findings contribute to a more profound understanding of HCC heterogeneity and lay the foundation for more tailored approaches to treatment, thereby enhancing the precision of clinical interventions in the management of HCC.

Data availability statement

The original contributions presented in the study are included in the article/Supplementary Material. Further inquiries can be directed to the corresponding author.

Ethics statement

The animal study was approved by Dalian Medical University Animal Care and Ethics Committee. The study was conducted in accordance with the local legislation and institutional requirements.

Author contributions

ZW: Investigation, Methodology, Software, Validation, Visualization, Writing – original draft, Writing – review & editing. GaZ: Data curation, Methodology, Validation, Writing - review & editing. RC: Data curation, Methodology, Validation, Writing - review & editing. GuZ: Data curation, Methodology, Validation, Writing – original draft. YZ: Data curation, Investigation, Writing – original draft. MX: Data curation, Investigation, Writing – original draft. LL: Data curation, Investigation, Writing – original draft. XZ: Conceptualization, Project administration, Supervision, Writing – review & editing.

Funding

The author(s) declare that no financial support was received for the research and/or publication of this article.

Acknowledgments

The Figure 12 (license code: TTWPR15d55) in the manuscript were drawn by Figdraw (https://www.figdraw.com/). We acknowledge the TCGA (https://portal.gdc.cancer.gov/), ICGC (https://dcc.icgc.org/), CPTAC (https://proteomics.cancer.gov/programs/cptac/) and GEO (https://www.ncbi.nlm.nih.gov/geo/) database for providing their platforms and contributors for uploading their meaningful datasets. We thank Dr.Jianming Zeng (University of Macau), and all the members of his bioinformatics team, biotrainee, for generously sharing their experience and codes. We also thank Biotrainee and Shanghai HS Biotech Co.,Ltd for providing the biorstudio high performance computing cluster (https://biorstudio.cloud) for conducting the research reported in this paper.

Conflict of interest

The authors declare that the research was conducted in the absence of any commercial or financial relationships that could be construed as a potential conflict of interest.

Generative AI statement

The author(s) declare that no Generative AI was used in the creation of this manuscript.

Publisher's note

Supplementary material

The Supplementary Material for this article can be found online at: https://www.frontiersin.org/articles/10.3389/fimmu.2025.1592259/full#supplementary-material

References

1. Llovet JM, Kelley RK, Villanueva A, Singal AG, Pikarsky E, Roayaie S, et al. Hepatocellular carcinoma. *Nat Rev Dis Primer*. (2021) 7:1–28. doi: 10.1038/s41572-020-00240-3

2. Bray F, Laversanne M, Sung H, Ferlay J, Siegel RL, Soerjomataram I, et al. Global cancer statistics 2022: GLOBOCAN estimates of incidence and mortality worldwide for 36 cancers in 185 countries. *CA Cancer J Clin*. (2024) 74:229–63. doi: 10.3322/caac.21834

3. Reig M, Forner A, Rimola J, Ferrer-Fàbrega J, Burrel M, Garcia-Criado Á, et al. BCLC strategy for prognosis prediction and treatment recommendation: The 2022 update. *J Hepatol*. (2022) 76:681–93. doi: 10.1016/j.jhep.2021.11.018

4. Finn RS, Qin S, Ikeda M, Galle PR, Ducreux M, Kim T-Y, et al. Atezolizumab plus bevacizumab in unresectable hepatocellular carcinoma. *N Engl J Med*. (2020) 382:1894–905. doi: 10.1056/NEJMoa1915745

5. Llovet JM, Ricci S, Mazzaferro V, Hilgard P, Gane E, Blanc J-F, et al. Sorafenib in advanced hepatocellular carcinoma. *N Engl J Med*. (2008) 359:378–90. doi: 10.1056/NEJMoa0708857

6. He Y, Luo Y, Huang L, Zhang D, Wang X, Ji J, et al. New frontiers against sorafenib resistance in renal cell carcinoma: From molecular mechanisms to predictive biomarkers. *Pharmacol Res*. (2021) 170:105732. doi: 10.1016/j.phrs.2021.105732

7. Zhu Y, Zheng B, Wang H, Chen L. New knowledge of the mechanisms of sorafenib resistance in liver cancer. *Acta Pharmacol Sin*. (2017) 38:614–22. doi: 10.1038/aps.2017.5

8. Sharma P, Siddiqui BA, Anandhan S, Yadav SS, Subudhi SK, Gao J, et al. The next decade of immune checkpoint therapy. *Cancer Discov*. (2021) 11:838–57. doi: 10.1158/2159-8290.CD-20-1680

9. Wang Y-Y, Yang X, Wang Y-C, Long J-Y, Sun H-S, Li Y-R, et al. Clinical outcomes of lenvatinib plus transarterial chemoembolization with or without programmed death receptor-1 inhibitors in unresectable hepatocellular carcinoma. *World J Gastroenterol*. (2023) 29:1614–26. doi: 10.3748/wjg.v29.i10.1614

10. Llovet JM, Castet F, Heikenwalder M, Maini MK, Mazzaferro V, Pinato DJ, et al. Immunotherapies for hepatocellular carcinoma. *Nat Rev Clin Oncol*. (2022) 19:151–72. doi: 10.1038/s41571-021-00573-2

11. Llovet JM, Pinyol R, Yarchoan M, Singal AG, Marron TU, Schwartz M, et al. Adjuvant and neoadjuvant immunotherapies in hepatocellular carcinoma. *Nat Rev Clin Oncol*. (2024) 21:294–311. doi: 10.1038/s41571-024-00868-0

12. Llovet JM, Pinyol R, Kelley RK, El-Khoueiry A, Reeves HL, Wang XW, et al. Molecular pathogenesis and systemic therapies for hepatocellular carcinoma. *Nat Cancer*. (2022) 3:386–401. doi: 10.1038/s43018-022-00357-2

13. Yang X, Yang C, Zhang S, Geng H, Zhu AX, Bernards R, et al. Precision treatment in advanced hepatocellular carcinoma. *Cancer Cell*. (2024) 42:180–97. doi: 10.1016/j.ccell.2024.01.007

14. Tabrizian P, Abdelrahim M, Schwartz M. Immunotherapy and transplantation for hepatocellular carcinoma. *J Hepatol*. (2024) 80:822–5. doi: 10.1016/j.jhep.2024.01.011

15. Rebouissou S, Nault J-C. Advances in molecular classification and precision oncology in hepatocellular carcinoma. *J Hepatol*. (2020) 72:215–29. doi: 10.1016/j.jhep.2019.08.017

16. Reuter JA, Spacek D, Snyder MP. High-throughput sequencing technologies. *Mol Cell*. (2015) 58:586–97. doi: 10.1016/j.molcel.2015.05.004

17. Adam G, Rampášek L, Safikhani Z, Smirnov P, Haibe-Kains B, Goldenberg A. Machine learning approaches to drug response prediction: challenges and recent progress. *NPJ Precis Oncol*. (2020) 4:19. doi: 10.1038/s41698-020-0122-1

18. Ding L, Bailey MH, Porta-Pardo E, Thorsson V, Colaprico A, Bertrand D, et al. Perspective on oncogenic processes at the end of the beginning of cancer genomics. *Cell*. (2018) 173:305–320.e10. doi: 10.1016/j.cell.2018.03.033

19. Hoshida Y, Nijman SMB, Kobayashi M, Chan JA, Brunet J-P, Chiang DY, et al. Integrative transcriptome analysis reveals common molecular subclasses of human hepatocellular carcinoma. *Cancer Res*. (2009) 69:7385–92. doi: 10.1158/0008-5472.CAN-09-1089

20. Gao Q, Zhu H, Dong L, Shi W, Chen R, Song Z, et al. Integrated proteogenomic characterization of HBV-related hepatocellular carcinoma. *Cell*. (2019) 179:1240. doi: 10.1016/j.cell.2019.10.038

21. Li B, Li Y, Zhou H, Xu Y, Cao Y, Cheng C, et al. Multiomics identifies metabolic subtypes based on fatty acid degradation allocating personalized treatment in hepatocellular carcinoma. *Hepatol Baltim Md*. (2024) 79:289–306. doi: 10.1097/HEP.0000000000000553

22. Colaprico A, Silva TC, Olsen C, Garofano L, Cava C, Garolini D, et al. TCGAbiolinks: an R/Bioconductor package for integrative analysis of TCGA data. *Nucleic Acids Res*. (2016) 44:e71. doi: 10.1093/nar/gkv1507

23. Mayakonda A, Lin D-C, Assenov Y, Plass C, Koeffler HP. Maftools: efficient and comprehensive analysis of somatic variants in cancer. *Genome Res*. (2018) 28:1747–56. doi: 10.1101/gr.239244.118

24. Roessler S, Jia H-L, Budhu A, Forgues M, Ye Q-H, Lee J-S, et al. A unique metastasis gene signature enables prediction of tumor relapse in early-stage hepatocellular carcinoma patients. *Cancer Res*. (2010) 70:10202–12. doi: 10.1158/0008-5472.CAN-10-2607

25. Candia J, Bayarsaikhan E, Tandon M, Budhu A, Forgues M, Tovuu L-O, et al. The genomic landscape of Mongolian hepatocellular carcinoma. *Nat Commun*. (2020) 11:4383. doi: 10.1038/s41467-020-18186-1

26. Hsu C-L, Ou D-L, Bai L-Y, Chen C-W, Lin L, Huang S-F, et al. Exploring markers of exhausted CD8 T cells to predict response to immune checkpoint inhibitor therapy for hepatocellular carcinoma. *Liver Cancer*. (2021) 10:346–59. doi: 10.1159/000515305

27. Pinyol R, Montal R, Bassaganyas L, Sia D, Takayama T, Chau G-Y, et al. Molecular predictors of prevention of recurrence in HCC with sorafenib as adjuvant treatment and prognostic factors in the phase 3 STORM trial. *Gut*. (2019) 68:1065–75. doi: 10.1136/gutjnl-2018-316408

28. Liu C, Zhou C, Xia W, Zhou Y, Qiu Y, Weng J, et al. Targeting ALK averts ribonuclease 1-induced immunosuppression and enhances antitumor immunity in hepatocellular carcinoma. *Nat Commun*. (2024) 15:1009. doi: 10.1038/s41467-024-45215-0

29. Wang Y-P, Yu G-R, Lee M-J, Lee S-Y, Chu I-S, Leem S-H, et al. Lipocalin-2 negatively modulates the epithelial-to-mesenchymal transition in hepatocellular carcinoma through the epidermal growth factor (TGF-beta1)/Lcn2/Twist1 pathway. *Hepatol Baltim Md*. (2013) 58:1349–61. doi: 10.1002/hep.26467

30. Ma L, Hernandez MO, Zhao Y, Mehta M, Tran B, Kelly M, et al. Tumor cell biodiversity drives microenvironmental reprogramming in liver cancer. *Cancer Cell*. (2019) 36:418–430.e6. doi: 10.1016/j.ccell.2019.08.007

31. Sharma A, Seow JJW, Dutertre C-A, Pai R, Blériot C, Mishra A, et al. Onco-fetal reprogramming of endothelial cells drives immunosuppressive macrophages in hepatocellular carcinoma. *Cell*. (2020) 183:377–394.e21. doi: 10.1016/j.cell.2020.08.040

32. Ma L, Heinrich S, Wang L, Keggenhoff FL, Khatib S, Forgues M, et al. Multiregional single-cell dissection of tumor and immune cells reveals stable lock-and-key features in liver cancer. *Nat Commun*. (2022) 13:7533. doi: 10.1038/s41467-022-35291-5

33. Zhu G-Q, Tang Z, Huang R, Qu W-F, Fang Y, Yang R, et al. CD36+ cancer-associated fibroblasts provide immunosuppressive microenvironment for hepatocellular carcinoma via secretion of macrophage migration inhibitory factor. *Cell Discov*. (2023) 9:25. doi: 10.1038/s41421-023-00529-z

34. Lu X, Meng J, Zhou Y, Jiang L, Yan F. MOVICS: an R package for multi-omics integration and visualization in cancer subtyping. *Bioinforma Oxf Engl*. (2021) 36:22–3. doi: 10.1093/bioinformatics/btaa1018

35. Aran D, Hu Z, Butte AJ. xCell: digitally portraying the tissue cellular heterogeneity landscape. *Genome Biol*. (2017) 18:220. doi: 10.1186/s13059-017-1349-1

36. Finotello F, Mayer C, Plattner C, Laschober G, Rieder D, Hackl H, et al. Molecular and pharmacological modulators of the tumor immune contexture revealed by deconvolution of RNA-seq data. *Genome Med*. (2019) 11:34. doi: 10.1186/s13073-019-0638-6

37. Li T, Fu J, Zeng Z, Cohen D, Li J, Chen Q, et al. TIMER2.0 for analysis of tumor-infiltrating immune cells. *Nucleic Acids Res*. (2020) 48:W509–14. doi: 10.1093/nar/gkaa407

38. Becht E, Giraldo NA, Lacroix L, Buttard B, Elarouci N, Petitprez F, et al. Estimating the population abundance of tissue-infiltrating immune and stromal cell populations using gene expression. *Genome Biol*. (2016) 17:218. doi: 10.1186/s13059-016-1070-5

39. Ritchie ME, Phipson B, Wu D, Hu Y, Law CW, Shi W, et al. limma powers differential expression analyses for RNA-sequencing and microarray studies. *Nucleic Acids Res*. (2015) 43:e47–7. doi: 10.1093/nar/gkv007

40. Korsunsky I, Millard N, Fan J, Slowikowski K, Zhang F, Wei K, et al. Fast, sensitive and accurate integration of single-cell data with Harmony. *Nat Methods*. (2019) 16:1289–96. doi: 10.1038/s41592-019-0619-0

41. Sun D, Guan X, Moran AE, Wu L-Y, Qian DZ, Schedin P, et al. Identifying phenotype-associated subpopulations by integrating bulk and single-cell sequencing data. *Nat Biotechnol*. (2022) 40:527–38. doi: 10.1038/s41587-021-01091-3

42. Maeser D, Gruener RF, Huang RS. oncoPredict: an R package for predicting *in vivo* or cancer patient drug response and biomarkers from cell line screening data. *Brief Bioinform*. (2021) 22:bbab260. doi: 10.1093/bib/bbab260

43. Lapuente-Santana Ó, van Genderen M, Hilbers PAJ, Finotello F, Eduati F. Interpretable systems biomarkers predict response to immune-checkpoint inhibitors. *Patterns N Y N*. (2021) 2:100293. doi: 10.1016/j.patter.2021.100293

44. Jiang P, Gu S, Pan D, Fu J, Sahu A, Hu X, et al. Signatures of T cell dysfunction and exclusion predict cancer immunotherapy response. *Nat Med*. (2018) 24:1550–8. doi: 10.1038/s41591-018-0136-1

45. Yang C, Huang X, Liu Z, Qin W, Wang C. Metabolism-associated molecular classification of hepatocellular carcinoma. *Mol Oncol*. (2020) 14:896–913. doi: 10.1002/1878-0261.12639

46. Ji Q, Zheng Y, Zhou L, Chen F, Li W. Unveiling divergent treatment prognoses in IDHwt-GBM subtypes through multiomics clustering: a swift dual MRI-mRNA model for precise subtype prediction. *J Transl Med*. (2024) 22:578. doi: 10.1186/s12967-024-05401-6

47. Han T, Bai Y, Liu Y, Dong Y, Liang C, Gao L, et al. Integrated multi-omics analysis and machine learning to refine molecular subtypes, prognosis, and immunotherapy in lung adenocarcinoma. *Funct Integr Genomics*. (2024) 24:118. doi: 10.1007/s10142-024-01388-x

48. Zheng X, Ma Y, Bai Y, Huang T, Lv X, Deng J, et al. Identification and validation of immunotherapy for four novel clusters of colorectal cancer based on the tumor microenvironment. *Front Immunol*. (2022) 13:984480. doi: 10.3389/fimmu.2022.984480

49. He Y, Duan S, Wang W, Yang H, Pan S, Cheng W, et al. Integrative radiomics clustering analysis to decipher breast cancer heterogeneity and prognostic indicators through multiparametric MRI. *NPJ Breast Cancer*. (2024) 10:72. doi: 10.1038/s41523-024-00678-8

50. Klebanov N, Artomov M, Goggins WB, Daly E, Daly MJ, Tsao H. Burden of unique and low prevalence somatic mutations correlates with cancer survival. *Sci Rep*. (2019) 9:4848. doi: 10.1038/s41598-019-41015-5

51. Rizvi NA, Hellmann MD, Snyder A, Kvistborg P, Makarov V, Havel JJ, et al. Mutational landscape determines sensitivity to PD-1 blockade in non–small cell lung cancer. *Science*. (2015). doi: 10.1126/science.aaa1348

52. Li G, Wu J, Li L, Jiang P. p53 deficiency induces MTHFD2 transcription to promote cell proliferation and restrain DNA damage. *Proc Natl Acad Sci U.S.A*. (2021) 118:e2019822118. doi: 10.1073/pnas.2019822118

53. Nian Z, Dou Y, Shen Y, Liu J, Du X, Jiang Y, et al. Interleukin-34-orchestrated tumor-associated macrophage reprogramming is required for tumor immune escape driven by p53 inactivation. *Immunity*. (2024) 57:2344–2361.e7. doi: 10.1016/j.immuni.2024.08.015

54. Romani A, Zauli E, Zauli G, AlMesfer S, Al-Swailem S, Voltan R. MDM2 inhibitors-mediated disruption of mitochondrial metabolism: A novel therapeutic strategy for retinoblastoma. *Front Oncol*. (2022) 12:1000677. doi: 10.3389/fonc.2022.1000677

55. Voltan R, di Iasio MG, Bosco R, Valeri N, Pekarski Y, Tiribelli M, et al. Nutlin-3 downregulates the expression of the oncogene TCL1 in primary B chronic lymphocytic leukemic cells. *Clin Cancer Res Off J Am Assoc Cancer Res*. (2011) 17:5649–55. doi: 10.1158/1078-0432.CCR-11-1064

56. Romani A, Lodi G, Casciano F, Gonelli A, Secchiero P, Zauli G, et al. Enhanced Anti-Melanoma Activity of Nutlin-3a Delivered via Ethosomes: Targeting p53-Mediated Apoptosis in HT144 Cells. *Cells*. (2024) 13(20):1678. doi: 10.3390/cells13201678

57. Vassilev LT. p53 Activation by small molecules: application in oncology. *J Med Chem*. (2005) 48:4491–9. doi: 10.1021/jm058174k

58. Wang Z, Chen Y, Fang H, Xiao K, Wu Z, Xie X, et al. Reprogramming cellular senescence in the tumor microenvironment augments cancer immunotherapy through multifunctional nanocrystals. *Sci Adv*. (2024) 10:eadp7022. doi: 10.1126/sciadv.adp7022

59. Wong PY, Chan CYK, Xue HDG, Goh CC, Cheu JWS, Tse APW, et al. Cell cycle inhibitors activate the hypoxia-induced DDX41/STING pathway to mediate antitumor immune response in liver cancer. *JCI Insight*. (2024) 9:e170532. doi: 10.1172/jci.insight.170532

60. Petroni G, Formenti SC, Chen-Kiang S, Galluzzi L. Immunomodulation by anticancer cell cycle inhibitors. *Nat Rev Immunol*. (2020) 20:669–79. doi: 10.1038/s41577-020-0300-y

61. Suski JM, Braun M, Strmiska V, Sicinski P. Targeting cell-cycle machinery in cancer. *Cancer Cell*. (2021) 39:759–78. doi: 10.1016/j.ccell.2021.03.010

62. Forner A, Gilabert M, Bruix J, Raoul J-L. Treatment of intermediate-stage hepatocellular carcinoma. *Nat Rev Clin Oncol*. (2014) 11:525–35. doi: 10.1038/nrclinonc.2014.122

63. Habib A, Desai K, Hickey R, Thornburg B, Lewandowski R, Salem R. Transarterial approaches to primary and secondary hepatic Malignancies. *Nat Rev Clin Oncol*. (2015) 12:481–9. doi: 10.1038/nrclinonc.2015.78

64. Zhou Y, Zhang X, Wu L, Ye F, Su X, Shi L, et al. Meta-analysis: preoperative transcatheter arterial chemoembolization does not improve prognosis of patients with resectable hepatocellular carcinoma. *BMC Gastroenterol*. (2013) 13:51. doi: 10.1186/1471-230X-13-51

65. Bruix J, Sala M, Llovet JM. Chemoembolization for hepatocellular carcinoma. *Gastroenterology*. (2004) 127:S179–188. doi: 10.1053/j.gastro.2004.09.032

66. Li K-W, Li X, Wen T-F, Lu W-S. The effect of postoperative TACE on prognosis of HCC: an update. *Hepatogastroenterology*. (2013) 60:248–51. doi: 10.5754/hge12665

67. Cheng A-L, Hsu C, Chan SL, Choo S-P, Kudo M. Challenges of combination therapy with immune checkpoint inhibitors for hepatocellular carcinoma. *J Hepatol*. (2020) 72:307–19. doi: 10.1016/j.jhep.2019.09.025

68. Hashizume T, Ying B-W. Challenges in developing cell culture media using machine learning. *Biotechnol Adv*. (2024) 70:108293. doi: 10.1016/j.bioteChadv.2023.108293

69. Roisman LC, Kian W, Anoze A, Fuchs V, Spector M, Steiner R, et al. Radiological artificial intelligence - predicting personalized immunotherapy outcomes in lung cancer. *NPJ Precis Oncol*. (2023) 7:125. doi: 10.1038/s41698-023-00473-x

70. Kim H-J, Gong E-J, Bang C-S. Application of machine learning based on structured medical data in gastroenterology. *Biomimetics*. (2023) 8:512. doi: 10.3390/biomimetics8070512

71. Liu Z, Liu L, Weng S, Guo C, Dang Q, Xu H, et al. Machine learning-based integration develops an immune-derived lncRNA signature for improving outcomes in colorectal cancer. *Nat Commun*. (2022) 13:816. doi: 10.1038/s41467-022-28421-6

72. Liu H, Zhang W, Zhang Y, Adegboro AA, Fasoranti DO, Dai L, et al. Mime: A flexible machine-learning framework to construct and visualize models for clinical characteristics prediction and feature selection. *Comput Struct Biotechnol J*. (2024) 23:2798–810. doi: 10.1016/j.csbj.2024.06.035

73. Yang Y-F, Zhang M-F, Tian Q-H, Fu J, Yang X, Zhang CZ, et al. SPAG5 interacts with CEP55 and exerts oncogenic activities via PI3K/AKT pathway in hepatocellular carcinoma. *Mol Cancer*. (2018) 17:117. doi: 10.1186/s12943-018-0872-3

74. Kalimutho M, Sinha D, Jeffery J, Nones K, Srihari S, Fernando WC, et al. CEP55 is a determinant of cell fate during perturbed mitosis in breast cancer. *EMBO Mol Med*. (2018) 10:e8566. doi: 10.15252/emmm.201708566

75. Zhou L, Zhu Y, Guo F, Long H, Yin M. Pan-cancer analysis of oncogenic role of CEP55 and experiment validation in clear cell renal cell carcinoma. *Sci Rep*. (2024) 14:28279. doi: 10.1038/s41598-024-80057-2

76. Tandon D, Banerjee M. Centrosomal protein 55: A new paradigm in tumorigenesis. *Eur J Cell Biol*. (2020) 99:151086. doi: 10.1016/j.ejcb.2020.151086

77. Yang L, He Y, Zhang Z, Wang W. Upregulation of CEP55 predicts dismal prognosis in patients with liver cancer. *BioMed Res Int*. (2020) 2020:4139320. doi: 10.1155/2020/4139320

78. Xie X, Liang H, Jiangting W, Wang Y, Ma X, Tan Z, et al. Cancer-testis antigen CEP55 serves as a prognostic biomarker and is correlated with immune infiltration and immunotherapy efficacy in pan-cancer. *Front Mol Biosci*. (2023) 10:1198557. doi: 10.3389/fmolb.2023.1198557

Glossary

AIDRS	Artificial Intelligence-Derived Risk Score
AFP	Alpha-Fetoprotein
ALB	Albumin
AUC	Area Under the Curve
CCK-8	Cell Counting Kit-8
CIMLR	Cancer Integration via Multikernel Learning
CNV	Copy Number Variation
COCA	Cluster of Clusters Analysis
CPGs	Candidate Prognostic Genes
CPI	Clustering Prediction Index
CS1/CS2	Clustering Subtypes 1 and 2
CTNNB1	Catenin Beta 1
DEGs	Differentially Expressed Genes
DLEU7	Deleted in Lymphocytic Leukemia 7
DMEM	Dulbecco's Modified Eagle's Medium
DNA	Deoxyribonucleic Acid
DSS	Disease Specific Survival
EaSIeR	Estimate Systems Immunotherapy Response
EGFR	Epidermal Growth Factor Receptor
Enet	Elastic Network
FBS	Fetal Bovine Serum
FDA	Food and Drug Administration
FPKM	Fragments Per Kilobase of transcript per Million mapped reads
GBM	Generalized Boosted Regression Models
GEO	Gene Expression Omnibus
GISTIC	Genomic Identification of Significant Targets in Cancer
HCC	Hepatocellular Carcinoma
HR	Hazard Ratio
ICGC	International Cancer Genome Consortium
IDH	Isocitrate Dehydrogenase
IFNG	Interferon-Gamma
IntNMF	Integrative Nonnegative Matrix Factorization
JAK2	Janus Kinase 2
Lasso	Least Absolute Shrinkage and Selection Operator
lncRNA	Long Non-Coding RNA
MATH	Mutant-Allele Tumor Heterogeneity
MCPcounter	Microenvironment Cell Populations-counter
MDSC	Myeloid-Derived Suppressor Cells
MET	Mesenchymal-Epithelial Transition
ML	Machine Learning
MOVICS	Multi-Omics integration and Visualization in Cancer Subtyping
MSI	Microsatellite Instability
NC	Negative Control
NCBI	National Center for Biotechnology Information
NF-κB	Nuclear Factor Kappa-Light-Chain-Enhancer of Activated B Cells
NGS	Next-Generation Sequencing
NTP	Nearest Template Prediction
OS	Overall Survival
PBS	Phosphate Buffered Saline
PCs	Principal Components
PECAM1	Platelet and Endothelial Cell Adhesion Molecule 1
PFI	Progression Free Interval
plsRcox	Partial Least Squares Regression for Cox model
PT	Prothrombin Time
qRT-PCR	Quantitative Real-Time Polymerase Chain Reaction
ROC	Receiver Operating Characteristic
RNA-seq	RNA Sequencing
RSF	Random Survival Forest
scRNA-seq	Single-Cell RNA Sequencing
siRNA	Small Interfering RNA
SNP	Single Nucleotide Polymorphism
SNF	Similarity Network Fusion
SPP1	Secreted Phosphoprotein 1
StepCox	Stepwise Cox Regression Model
Superpc	Supervised Principal Components
TACE	Transcatheter Arterial Chemoembolization
TCGA	The Cancer Genome Atlas
TIDE	Tumor Immune Dysfunction and Exclusion
TIMER	Tumor Immune Estimation Resource
TMB	Tumor Mutation Burden
TME	Tumor Microenvironment
TP53	Tumor Protein P53
TTN	Titin
UMAP	Uniform Manifold Approximation and Projection
UMI	Unique Molecular Identifier
VEGF	Vascular Endothelial Growth Factor
VEGFA	Vascular Endothelial Growth Factor A
VWF	Von Willebrand Factor
WNT	Wingless/Integrated Signaling Pathway

Frontiers in Immunology

Explores novel approaches and diagnoses to treat immune disorders.

The official journal of the International Union of Immunological Societies (IUIS) and the most cited in its field, leading the way for research across basic, translational and clinical immunology.

Discover the latest Research Topics

See more →

Frontiers

Avenue du Tribunal-Fédéral 34
1005 Lausanne, Switzerland
frontiersin.org

Contact us

+41 (0)21 510 17 00
frontiersin.org/about/contact